SERDP

FINAL REPORT

Development and Laboratory Validation of Mathematical Modeling Tools for Prediction of PFAS Transformation, Transport, and Retention in AFFF Source Areas

Linda Abriola
Masoud Arshadi
Tufts University

Simin Akbariyeh
Uriel Garza
Kurt Pennell
Brown University

Thomas Phelan
U.S. Air Force Academy

John Christ
S&B Christ Consulting

September 2023

SERDP Project ER18-1149

DISTRIBUTION STATEMENT A
This document has been cleared for public release.

This report was prepared under contract to the Department of Defense Strategic Environmental Research and Development Program (SERDP). The publication of this report does not indicate endorsement by the Department of Defense, nor should the contents be construed as reflecting the official policy or position of the Department of Defense. Reference herein to any specific commercial product, process, or service by trade name, trademark, manufacturer, or otherwise, does not necessarily constitute or imply its endorsement, recommendation, or favoring by the Department of Defense.

REPORT DOCUMENTATION PAGE

Form Approved
OMB No. 0704-0188

Public reporting burden for this collection of information is estimated to average 1 hour per response, including the time for reviewing instructions, searching existing data sources, gathering and maintaining the data needed, and completing and reviewing this collection of information. Send comments regarding this burden estimate or any other aspect of this collection of information, including suggestions for reducing this burden to Department of Defense, Washington Headquarters Services, Directorate for Information Operations and Reports (0704-0188), 1215 Jefferson Davis Highway, Suite 1204, Arlington, VA 22202-4302. Respondents should be aware that notwithstanding any other provision of law, no person shall be subject to any penalty for failing to comply with a collection of information if it does not display a currently valid OMB control number. **PLEASE DO NOT RETURN YOUR FORM TO THE ABOVE ADDRESS.**

1. REPORT DATE *(DD-MM-YYYY)*	**2. REPORT TYPE**	**3. DATES COVERED** *(From - To)*
06-09-2023	SERDP Final Report	6/5/2018 - 6/5/2023

4. TITLE AND SUBTITLE

Development and Laboratory Validation of Mathematical Modeling Tools for Prediction of PFAS Transformation, Transport, and Retention in AFFF Source Areas

5a. CONTRACT NUMBER
W912HQ-18-C-0014

5b. GRANT NUMBER
ER18-1149

5c. PROGRAM ELEMENT NUMBER

6. AUTHOR(S)

Abriola, Linda M.
Cápiro Natalie L.
Phelan, Thomas J.
Pennell, Kurt D.
Christ, John A.

5d. PROJECT NUMBER

5e. TASK NUMBER
Subtask 5.6

5f. WORK UNIT NUMBER

7. PERFORMING ORGANIZATION NAME(S) AND ADDRESS(ES)

Tufts University
TRUSTEES OF TUFTS COLLEGE INC
169 HOLLAND ST FL 3
SOMERVILLE MA 02144-2401

8. PERFORMING ORGANIZATION REPORT NUMBER

ER18-1149

9. SPONSORING / MONITORING AGENCY NAME(S) AND ADDRESS(ES)

Office of the Deputy Assistant Secretary of Defense (Energy Resilience & Optimization)
3500 Defense Pentagon, RM 5C646
Washington, DC 20301-3500

10. SPONSOR/MONITOR'S ACRONYM(S)
SERDP

11. SPONSOR/MONITOR'S REPORT NUMBER(S)
ER18-1149

12. DISTRIBUTION / AVAILABILITY STATEMENT

DISTRIBUTION STATEMENT A. Approved for public release: distribution unlimited.

13. SUPPLEMENTARY NOTES

14. ABSTRACT

This integrated experimental and modeling research was designed to address data gaps associated with PFAS transport and transformation in natural subsurface environments and to develop models and decision tools that could aid site managers in the assessment of PFAS mobility and persistence in complex AFFF source areas. A matrix of experiments of increasing scale and complexity was undertaken with individual PFAS and mixtures, employing reference media and natural aquifer materials collected from PFAS-impacted sites. Experiments encompassed air-water and nonaqueous phase liquid (NAPL)-water interfacial tension and soil sorption measurements, biotransformation microcosm experiments for selected PFAS precursors, and single and multiphase column transport experiments. Mathematical models based upon research findings were used to explore potential PFAS transport and fate under representative field conditions. Research findings revealed that PFAS migration and retention are greatly influenced by interfacial processes. Under conditions consistent with AFFF releases, competitive sorption effects were found to be pronounced, and spill conditions were shown to have a strong influence on PFAS mobility and mass fluxes at the water table. Experimental observations improved our understanding of the potential for biotransformation of fluorotelomerization (FT)- and electrochemical fluorination (ECF)-based precursors in AFFF-impacted soils under various environmental conditions. Results provide insight into the structure-relevant stability of PFAS and a starting point for screening microbes and functional genes engaged in PFAS biotransformation. Field-scale model applications led to development of a meta-analysis table for use by practitioners that depicts the extent of correlation of important transport metrics with AFFF release parameters and site conditions.

15. SUBJECT TERMS

AFFF-Impacted Soils; Aqueous Film Forming Foam (AFFF); Field-Scale Model Applications; Interfacial Accumulation Mathematical Models for Flow and Transport; Natural Subsurface Environments; Interfacial Accumulation; PFAS Biotransformation

16. SECURITY CLASSIFICATION OF:			**17. LIMITATION OF ABSTRACT**	**18. NUMBER OF PAGES**	**19a. NAME OF RESPONSIBLE PERSON**
a. REPORT	**b. ABSTRACT**	**c. THIS PAGE**			Linda Abriola
UNCLASS	UNCLASS	UNCLASS	UNCLASS	398	**19b. TELEPHONE NUMBER** *(include area code)* 617-627-8685

Standard Form 298 (Rev. 8-98)
Prescribed by ANSI Std. Z39.18

Table of Contents

Table of Contents i
List of Tables ix
List of Figures xiv
List of Acronyms xxviii
Keywords xxx
Acknowledgements xxxi
Abstract 1
Graphical Abstract 2
Executive Summary 3
Introduction 3
Objectives 3
Technical Approach 3
Results and Discussion 4
Partitioning Studies 4
Microcosm Experiments with AFFF-Impacted Soils 6
Column Studies 8
Field-Scale Model Applications and Decision Tool Development 10
Implications for Future Research and Benefits 11
1. Objectives 13
2. Background 14
2.1 PFAS contamination at AFFF source areas 14
2.2 Interfacial processes and interphase mass transfer 15
2.3 Biotransformation 18
2.4 Transport modeling 19
3. Materials and Methods 21
3.1 Batch Studies 21
3.1.1 PFAS Accumulation at the Air-Water Interface 21
3.1.1.1 Materials 21
3.1.1.2 Preparation of PFAS Solutions 21
3.1.1.3 Surface Tension Measurements 22
3.1.1.4 Analytical Methods 22
3.1.2 PFAS mixture accumulation at NAPL-water interfaces 24

3.1.2.1 PFOA, PFOS, FOSA, and AFFF Solutions 24
3.1.2.2 Interfacial Tension Measurements 25
3.1.2.3 Surface Excess Calculations 25
3.2 Batch biotransformation studies 26
3.2.1 Chemicals and Materials 26
3.2.2 Microcosm set-up and preparations 27
3.2.2.1 Microcosms for aerobic biotransformation of FOSA, 8:2 FTOH, 6:2 FTS and AFFF mixture 27
3.3 Microcosms for anaerobic biotransformation of 8:2 FTOH 28
3.3.1 Microcosm sampling and preparation 29
3.3.2 Targeted PFAS Analysis 30
3.3.3 Non-targeted PFAS Analysis 31
3.3.4 Microbial Community Analysis 32
3.3.5 Microbial co-occurrence network analysis 33
3.3.6 Functional analysis 34
3.4 Abiotic transport studies 34
3.4.1 Influence of Aqueous Film Forming Foams on the Solubility and Mobilization of Non-Aqueous Phase Liquid Contaminants 34
3.4.1.1 Materials 34
3.4.1.2 Density, viscosity, interfacial tension, and NAPL solubility measurements. 36
3.4.1.3 Column mobilization studies 37
3.4.2 Influence of Residual Nonaqueous-Phase Liquids (NAPLs) on the Transport and Retention of Perfluoroalkyl Substances 38
3.4.2.1 Materials 38
3.4.2.2 Batch soil adsorption and phase partitioning experiments 38
3.4.2.3 Column experiments 39
3.5 Abiotic-biotic transport studies 41
3.5.1 Biotransformation of 6:2 FTS in 1-D flow-through columns 41
3.5.1.1 Column design and preparation 41
3.5.1.2 Synthetic groundwater preparation 42
3.5.1.3 Column operation and sampling 42
3.5.1.4 Targeted and Non-Targeted PFAS Analysis 43
3.5.1.5 DNA Extraction and llumina MiSeq Sequencing 44
3.6 Mathematical Modeling of PFAS Transport and Retention 44
3.6.1 NAPL Column studies 44

3.6.1.1 Mathematical Model 44
3.6.2 Field-scale transport scenarios 45
3.6.2.1 Mathematical Model 45
3.6.2.2 Simulation scenario development 47
4. Results and Discussion 51
4.1 Batch partitioning studies 51
4.1.1 PFAS accumulation at the air-water interface 51
4.1.1.1 Surface Tension Measurements 51
4.1.1.2 Surface Excess Calculations 53
4.1.1.3 Concluding remarks 60
4.1.2 PFAS mixture accumulation at NAPL-water interfaces 61
4.1.2.1 Interfacial Tension Measurements 61
4.1.2.2 Surface Excess Concentration 66
4.1.2.3 Impact of Calculated vs. Measured Concentrations on Surface Excess 70
4.1.2.4 Mass Distribution in Unsaturated Soil 71
4.1.2.5 Concluding remarks 73
4.2 Batch biotransformation studies 73
4.2.1 Aerobic biotransformation of FOSA in Loring and Hudson soil 73
4.2.1.1 Biotransformation rates 73
4.2.1.2 Quantification of biotransformation products and mass balance 74
4.2.1.3 Biotransformation Comparison of the biotransformation of FOSA and FOSA precursors. 76
4.2.1.4 Microbial communities in Loring and Hudson soil microcosms. 77
4.2.1.4.1 Diversity and Richness. 77
4.2.1.4.2 Shifts in microbial community compositions 78
4.2.1.5 Concluding remarks 80
4.2.2 Aerobic biotransformation of 8:2 FTOH in Robins and Loring soil 81
4.2.2.1 Biotransformation of 8:2 FTOH in Robins soil 81
4.2.2.1.1 Parent compound biotransformation and kinetics 81
4.2.2.1.2 Parent compound biotransformation and kinetics. 82
4.2.2.1.3 Mass balance. 84
4.2.2.2 Biotransformation of 8:2 FTOH in Loring soil 84
4.2.2.3 Novel 8:2 FTOH biotransformation products and proposed pathways 85
4.2.2.3.1 Potential novel transformation products identified by non-targeted analysis. 85

4.2.2.3.2 Aerobic biotransformation pathways of 8:2 FTOH. 86
4.2.2.4 Microbial community dynamics during aerobic biotransformation of 8:2 FTOH 88
4.2.2.4.1 Microbial community richness and diversity. 88
4.2.2.4.2 Microbial community composition shifts in the Robins biotransformation experiment..... 89
4.2.2.4.3 Microbial community composition shifts in the Loring biotransformation experiment..... 90
4.2.2.5 Concluding remarks 92
4.2.3 Biotransformation of 8:2 FTOH under nitrate-, sulfate-, and iron-reducing conditions 93
4.2.3.1 Biotransformation of 8:2 FTOH under nitrate-reducing conditions 93
4.2.3.1.1 Biotransformation rates. 93
4.2.3.1.2 Biotransformation products quantified by LC-MS/MS targeted analysis... 94
4.2.3.1.3 Biotransformation products identified by LC-HRMS..... 96
4.2.3.2 Biotransformation of 8:2 FTOH under sulfate-reducing and iron-reducing conditions 98
4.2.3.2.1 Biotransformation rates and products quantified by LC-MS/MS targeted analysis. 98
4.2.3.2.2 Biotransformation product identified by LC-HRMS analysis. 99
4.2.3.3 Distinct 8:2 FTOH biotransformation pathways under different redox conditions 100
4.2.3.3.1 Comparison of biotransformation under sulfate- and iron-reducing conditions with that under nitrate-reducing conditions. 100
4.2.3.3.2 Comparison of microbial communities under different redox conditions. 101
4.2.3.4 Comprehensive biotransformation pathways of 8:2 FTOH 102
4.2.3.5 Concluding remarks 105
4.2.4 Aerobic biotransformation of 6:2 FTS in Robins and Loring soil 106
4.2.4.1 Experimental system 106
4.2.4.2 Biotransformation of 6:2 FTS in Loring and Robins soil microcosms..... 106
4.2.4.2.1 Biotransformation rates. 106
4.2.4.2.2 Biotransformation products quantified by LC-MS/MS targeted analysis. 107
4.2.4.2.3 Comparison of 6:2 FTS biotransformation. 109
4.2.4.2.4 Factors impacting 6:2 FTS biotransformation. 110
4.2.4.3 Identification of novel biotransformation products by LC-HRMS analysis 112
4.2.4.4 Biotransformation pathways of 6:2 FTS in AFFF-impacted soil..... 113

4.2.4.5 Concluding remarks 116
4.2.5 Aerobic biotransformation of PFAS mixtures in AFFF formulation 116
4.2.5.1 PFAS identified by LC-HRMS in AFFF-amended microcosms..... 116
4.2.5.1.1 PFAS identified as AFFF components and associated transformation potential 118
4.2.5.1.2 PFAS identified as transformation products and associated potential of further transformation 121
4.2.5.2 Structurally relevant factors impacting the stability of identified AFFF-derived PFAS 123
4.2.5.3 Transformation pathways of identified AFFF-derived PFAS 126
4.2.5.4 Concluding remarks 129
4.2.6 Potential Microbial Taxa in Soil Microbial Communities and Functional Genes Related to Fluorotelomer Biotransformation 130
4.2.6.1 Microbial co-occurrence network 130
4.2.6.1.1 Microbial community compositions, topological properties, and modules 130
4.2.6.1.2 Generalist taxa and co-occurrent microbes 133
4.2.6.1.3 Keystone taxa 135
4.2.6.2 Microbial functional profiles 137
4.2.6.2.1 Functional genes that may be involved in fluorotelomer biotransformation 137
4.2.6.2.2 Other interesting functional genes..... 139
4.2.6.3 Association between functional genes/enzymes and microorganisms 139
4.2.6.4 Concluding remarks 140
4.3 Abiotic Transport Studies..... 143
4.3.1 Influence of Aqueous Film Forming Foams on the Solubility and Mobilization of Non-Aqueous Phase Liquid Contaminants 143
4.3.1.1 NAPL Solubility 143
4.3.1.2 NAPL-water interfacial tension 143
4.3.1.3 NAPL mobilization 145
4.3.1.4 NAPL desaturation curves 150
4.3.1.5 Concluding remarks 152
4.3.2 Influence of Residual Nonaqueous-Phase Liquids (NAPLs) on the Transport and Retention of Perfluoroalkyl Substances..... 153
4.3.2.1 PFAS accumulation at the PCE-NAPL water interface. 153
4.3.2.2 PFAS Partitioning into PCE-NAPL 155

4.3.2.3 PFAS Adsorption on Ottawa sand 157
4.3.2.4 Effect of residual PCE-NAPL on PFOS and PFNA transport 161
4.3.2.5 Effect of residual PCE-NAPL on the transport of PFAS mixtures 162
4.3.2.6 Concluding remarks 167
4.4 Abiotic-biotic transport studies 168
4.4.1 Biotransformation of 6:2 FTS in 1-D flow-through columns 168
4.4.1.1 Biotransformation of 6:2 FTS under dynamic flow conditions 168
4.4.1.1.1 Profiles of 6:2 FTS and LC-MS/MS quantified biotransformation products in biotic column effluents 169
4.4.1.1.2 Biotransformation of 6:2 FTS along flowing path 172
4.4.1.1.3 Biotransformation products of 6:2 FTS identified by LC-HRMS in effluent and side-port samples. 175
4.4.1.1.4 Comparison of 6:2 FTS biotransformation between microcosm and column experiments. 175
4.4.1.2 Dynamics of microbial communities throughout the column experiments 176
4.4.1.2.1 Diversity of microbial communities 176
4.4.1.2.2 Dynamics of FL microbial communities 177
4.4.1.2.3 Spatial distribution of PMA microbial communities 179
4.4.1.3 Concluding remarks 180
4.5 Field-Scale Mathematical Modeling 181
4.5.1 Field-scale transport simulations 181
4.5.1.1 Influence of climatic conditions 185
4.5.1.2 Effect of spill conditions on transport of AFFF constituents 186
4.5.1.3 Qualitative comparison of simulations with field data 187
4.5.1.4 Influence of interfacial accumulation processes on transport predictions .. 189
4.5.2 Decision matrix 190
4.5.2.1 Peak Concentration at the Water Table 191
4.5.2.2 Rate of Contaminant Migration 192
4.5.2.3 Mass Distribution in the Contaminant Source Zone 195
4.5.2.4 Concluding remarks 200
5. Conclusions and Implications for Future Research/Implementation 201
5.1 Conclusions 201
5.1.1 Interfacial Processes 201
5.1.2 Biotransformation 201
5.1.3 Field Scale Modeling 203

5.2 Implications for Future Research 204
5.2.1 Interfacial Processes 204
5.2.2 PFAS Biotransformation 205
6. Literature Cited 206
Appendix A: Supporting Data 230
A.1 Appropriateness of using the Freundlich Equation to Fit Surface Tension 230
A.2 Organic and inorganic content analysis 231
A.3 Criteria for identification of potential important taxa in network analysis 231
A.4 Calculation of NAPL-Water Interfacial Area 231
A.5 Modifications to the HYDRUS 1-D Code 232
A.6 Estimation of Sorption Isotherms for Field-Scale Simulations 232
A.7 Development of Spill Scenarios for Field-Scale Modeling 233
A.7.1 AFCEC Database 233
A.7.2 Site selection 233
A.7.3 Spill selection 234
A.7.4 Soil profile and parameters 234
A.8 Selected Sites for Field-Scale Simulations 235
A.8.1 Wright-Patterson AFB 235
A.8.2 Tyndall AFB 235
A.8.3 Ellsworth 236
A.9 Observations of PFOA and PFOS Separate Phase Formation 236
A.10 Calculation of PFOA and PFOS Mass Distribution in an Unsaturated Soil 237
A.11 PFAS Phase Distribution Calculations 237
A.12 Fluoride detection 239
A.13 Establishment of nitrate-, sulfate-, and iron-reducing microcosms 239
A.14 Background levels of legacy PFAS in Loring AFB soil 240
A.15 Background levels of 6:2 FTS and its potential transformation products in Loring and Robins soils. 240
A.16 Diversity and richness of microbial community. 241
A.17 The impacts of 6:2 FTS and its biotransformation products on the microbial community compositions 242
A.18 Supplementary files 242
A.19 Supplementary tables 243
A.20 Supplementary figures 285
Appendix B: List of Scientific/Technical Publications 344

B.1 Peer-Reviewed Papers 344
B.2 Presentations/Posters: 344
Appendix C: Other Supporting Materials 347
C.1 Per- and Polyfluoroalkyl Substances (PFAS) Analyte List 347
C.2 Standard Operating Procedures for PFAS Sample Collection Preparation, and Analysis 349
C.3 Analytical Confirmation Whitepaper 355
C.3.1 Analytical Methodology Overview 355
C.3.2 Analytical Confirmatory Analysis of Soil Samples 357
C.3.3 Analytical Confirmatory Analysis of Water Samples 362

List of Tables

Table 3.1 Microcosm set-up examining aerobic biotransformation of FOSA, 8:2 FTOH, 6:2 FTS and AFFF mixture. 28

Table 3.2 Experimental set-up of 8:2 FTOH biotransformation microcosms under nitrate-, sulfate-, and iron-reducing conditions 29

Table 3.3 Concentrations of per- and polyfluoroalkyl substances (PFAS) measured in 3M FC-783F 3% wt. concentrate. 36

Table 3.4 Summary of experimental parameters and results of PCE column studies. 41

Table 3.5 High-level summary of site-specific conditions for field-scale simulations. 47

Table 3.6 Spill scenario Parameters for field-scale simulations. 48

Table 3.7 Langmuir-Szyszkowski parameters for field-scale simulations. 49

Table 3.8 Concentration of PFOA, PFOS, and MASS in mixtures for field-scale simulations... 50

Table 4.1 Szyszkowski fitted parameters for PFOA concentration range from 0 to 25 mg/L. 57

Table 4.2 Szyszkowski fitted parameters for PFOS concentration range from 0 to 90 mg/L..... 57

Table 4.3 Fitted Langmuir/Szyszkowski equations for the maximum surface excess (Γ_{max}) of PFOA and PFOS at the air-water interface in solutions as a function of total dissolved solids (TDS) 58

Table 4.4 Comparison of air-water partitioning coefficients (K_i) and surface excess (Γ) for PFOA using the Linear, Natural Log and Szyszkowski methods. 59

Table 4.5 Comparison of air-water partitioning coefficients (K_i) and surface excess (Γ) for PFOS using the Linear, Natural Log and Szyszkowski methods. 59

Table 4.6 Calculated maximum surface excess concentrations (Γm, mg/m^2) 66

Table 4.7 Calculated surface activity values (b, mg/L) 66

Table 4.8 An overview of the prior and current studies investigating biotransformation of FOSA and FOSA precursors. 77

Table 4.9 Fitting parameters of the first-order double exponential decay model..... 82

Table 4.10 Taxonomy of generalists ASVs and their significant (P-value < 0.01) co-occurrent ASVs 134

Table 4.11 Szyszkowski equation fitted parameters for NAPL-water interfacial tension data in the presence of AFFF. 145

Table 4.12 Properties of the displacing fluids and porous media used in the NAPL mobilization column studies 146

Table 4.13 Residual saturations of JP-4, TCE and PCE in 20-30 mesh and 60-80 mesh Ottawa sand following sequential injection of background electrolyte (500 mg/L $CaCl_2$), 3% wt. AFFF, and 4% wt. 1:1 Aerosol AY/OT solutions. 150

Table 4.14 Fitted NAPL-water partitioning coefficients (K_{nw}) for PFNA, PFOS and 6 PFAS compounds in the mixture. 157

Table 4.15 Fitted Kd values obtained from batch reactor and control column experiments. 159

Table 4.16 Fitted parameters (equilibrium interfacial adsorption constant Keq and maximum surface excess Γmax) for mixtures of 6 PFAS and 2 PFAS at PCE-water interface. 167

Table 4.17 Modeling predictions and measurements of PFAS in soil and pore water at Ellsworth AFB. 188

Table 4.18 Meta-analysis of model results to show correlation between inputs and outputs for PFOA and PFOS transport. 199

Table A.1 Surface excess values obtained for a concentration of 1 mg/L. 243

Table A.2 Fitted parameters obtained using Eq. A-1. 243

Table A.3 Properties of representative porous medium 243

Table A.4 Chemical names, acronyms, molecular structures, and suppliers of target poly- and perfluoroalkyl substances (PFAS) for LC-MS/MS quantitative analysis. 244

Table A.5 Physical and chemical properties of Robins, Loring, and Hudson soils. 245

Table A.6 Targeted mass inclusion list used in LC-MS analysis. 245

Table A.7 Limits of detection (LODs) and limits of quantification (LOQs) of targeted PFAS. 245

Table A.8 Instrument conditions and LC gradient used for the detection and quantification of 8:2 FTOH, 6:2 FTS and their polyfluorinated transformation products by UPLC-MS/MS. 246

Table A.9 Multiple reaction monitoring (MRM) parameters used for the detection and quantification of 8:2 FTOH, 6:2 FTS and their polyfluorinated transformation products by UPLC-MS/MS. 247

Table A.10 Instrument conditions and LC gradient used for the detection and quantification of PFAAs by UPLC-MS/MS. 248

Table A.11 Multiple reaction monitoring (MRM) parameters used for the detection and quantification of PFAAs by UPLC-MS/MS. 249

Table A.12 Limits of detection (LODs) and limits of quantification (LOQs) of target PFAS. 250

Table A.13 The number and the time points of the effluent and side-port samples collected from biotic columns for targeted and non-targeted PFAS analysis, ORP measurement, and DNA extraction throughout the experiments. 251

Table A.14 Changes in the mass (nmole) of FOSA and PFOS in Loring soil microcosms. 252

Table A.15 Partitioning of FOSA and PFOS in aqueous and solid phases of Loring and Hudson live treatments (percentage (%) of mass in each phase relative to the total mass). 252

Table A.16 Microbial richness and diversity in Loring and Hudson soils. 252

Table A.17 Fitting parameters of the first-order exponential decay model[a] 252

Table A.18 Molar percentage of 8:2 FTOH and 7:2 sFTOH being removed by headspace sampling over the initially spiked 8:2 FTOH in Robins biotransformation experiment during 90-day incubation. 253

Table A.19 Molar percentage (mol%) of 8:2 FTOH and its biotransformation products over the initially spiked 8:2 FTOH at the end of 90-day Loring biotransformation experiment. 253

Table A.20 Identification confidence level of potential 8:2 FTOH transformation products. 254

Table A.21 Microbial richness and diversity in Loring and Robins AFB soils. 255

Table A.22 Concentrations (nanomole per gram soil/dry weight) of individual PFAS in Loring AFB soil. 255

Table A.23 Potential biotransformation products of 8:2 FTOH identified by LC-HRMS analysis 256

Table A.24 Background levels (nmole/g dw) of 6:2 FTS and its potential per- and polyfluorinated transformation products in Loring and Robins soils. 256

Table A.25 Changes in the mass (nmole) of 6:2 FTS and its potential transformation products in Loring soil microcosms. 257

Table A.26 Changes in the mass (nmole) of 6:2 FTS and its potential transformation products in Robins soil microcosms. 258

Table A.27 Comparison of 6:2 FTS biotransformation in environmental matrices and pure cultures under aerobic conditions. 259

Table A.28 Microbial richness and diversity in Loring and Robins soils. 260

Table A.29 Potential biotransformation products of 6:2 FTS identified by HRMS analysis 260

Table A.30 The full names and corresponding acronyms of classified PFAS identified in non-targeted LC-HRMS analysis. 261

Table A.31 Identification of 16 classes of PFAS in non-targeted LC-HRMS analysis. 263

Table A.32 The average log2-fold changes (LFCs) of classified PFAS in the associated peak areas between certain sampling points and the initial sampling point (day 0) 265

Table A.33 Topological properties of the microbial co-occurrence networks in soils under different redox conditions (the control and constructed networks) and random networks with the same size as the constructed network. 267

Table A.34 Correlation coefficients (Cramer's *V* value) and significances (Chi-square *P*-value) between module and environmental factors. 267

Table A.35 Count of genes with significant changes in abundance between treatment (microcosms exposed to fluorotelomer) and control (microcosms without fluorotelomer addition) in each set of microcosm experiment according to PICRUSt2 results. 267

Table A.36 Potential functional genes encoding dehydrogenases and reductases identified in this study. 268

Table A.37 Potential functional genes encoding oxygenases identified in this study. 269

Table A.38 Potential functional genes encoding other enzymes except oxidoreductases identified in this study. 270

Table A.39 Functional genes encoding enzymes involved in microbial defluorination and fluorotelomer transformation in prior studies. 270

Table A.40 Packed dry porous media mass, total porosity, and pore volume (PV) for experimental columns. 271

Table A.41 Oxidation-reduction potential (ORP) of biotic column samples collected at different time points. 271

Table A.42 The average molar yields of 6:2 FTS and its biotransformation products (unit: mol%) in different phases. 271

Table A.43 Potential biotransformation products of 6:2 FTS identified by LC-HRMS analysis in the present column experiments and prior microcosms (Yan et al., 2022). 272

Table A.44 The average molar yields of 6:2 FTS and its biotransformation products (unit: mol%) at different time points in prior microcosm study (Yan et al., 2022). 273

Table A.45 Richness and diversity of the free-living (FL) and porous media-attached (PMA) microbial communities in the biotic columns. 273

Table A.46 Regression parameters to obtain Freundlich coefficients (Kf and n) from soil properties according to equations (A-6) and (A-7). 274

Table A.47 Description of spills for field-scale simulations. 275

Table A.48 Soil properties for Wright-Patterson Scenario 1 (AFFF Area 8). 278

Table A.49 Soil properties for Wright-Patterson Scenario 2 (AFFF Area 22). 279

Table A.50 Soil properties for Tyndall Scenario (Map Unit 13) 280

Table A.51 Soil properties for Ellsworth Scenario (Nunn clay loam, NcA). 281

Table A.52 Soil properties for Ellsworth Scenario (LY210109 within area OU1). 282

Table A.53 Estimated sorption parameters for Wright-Patterson Scenario 1. 283

Table A.54 Estimated sorption parameters for Wright-Patterson Scenario 2. 283

Table A.55 Estimated sorption parameters for Tyndall. 283

Table A.56 Estimated sorption parameters for Ellsworth (Nunn clay loam, NcA). 283

Table A.57 Estimated sorption parameters for Ellsworth (LY210109 within area OU1). 284

Table C.1 Target PFAS Analyte List 356

Table C.2 Confirmatory Analysis of Soil Samples (Borehole 2, 0-6” depth) 357

Table C.3 Confirmatory Analysis of Soil Samples (Borehole 2, 12-18” depth) 358

Table C.4 Confirmatory Analysis of Soil Samples (Borehole 3, 0-6” depth) 359

Table C.5 Confirmatory Analysis of Soil Samples (Borehole 3, 12-18” depth) 360

Table C.6 Confirmatory Analysis of Soil Samples (Borehole 4, 0-6” depth) 361

Table C.7 Confirmatory Analysis of Water Scrubber Samples (LP1)..... 363
Table C.8 Confirmatory Analysis of Water Scrubber Samples (Field Blank)..... 364
Table C.9 Confirmatory Analysis of Water Scrubber Samples (LP2)..... 365
Table C.10 Confirmatory Analysis of Water Scrubber Samples (LP1)..... 366

List of Figures

Figure 3.1 Photograph of a typical column at residual PCE saturation. Note the PCE-NAPL was distributed uniformly along the column as small globules or ganglia. 40

Figure 3.2 Schematic diagrams of (a) column experimental set-up and (b) segments S1-S5 delineated for the dissection of solid phase at the termination of column experiments. Segment S1 was closest to the column inlet, and segment S5 was closest to the column outlet. Ports 1, 2, and 3 were located at the center of segments S2, S3, and S4, respectively. 44

Figure 4.1 Comparison of surface tension data for NaPFOA and PFOA in ultrapure water measured in this work (open boxes) to values obtained from the literature. 52

Figure 4.2 Comparison of surface tension data obtained for KPFOS measured in ultrapure water in this work (open boxes) to values for TEAPFOS, KPFOS, and NaPFOS obtained from the literature. 52

Figure 4.3 Air-Water surface tension of PFOA(a) and FPOS (b) reported as PFOS in solutions with major cations and anions found in groundwater. Lines are the Szyszkowski equation fit. .. 53

Figure 4.4 Linear fit of surface tension versus PFOA concentration using Eq. (4-4). 55

Figure 4.5 Linear fit of surface tension versus PFOS concentrations using Eq. (4-4). 55

Figure 4.6 Least squares regression fits of surface tension versus the natural log of PFOA concentration using Eq. (4-5). 56

Figure 4.7 Least squares regression fits of surface tension versus the natural log of PFOS concentrations using Eq. (4-5). 56

Figure 4.8 Comparison of surface excess values as a function of aqueous phase concentration calculated using the Linear, Natural Log and Langmuir-Szyszkwoski methods. 60

Figure 4.9 Distribution of PFOA or PFOS mass at the air-water interface and the mass dissolved in the aqueous phase and adsorbed onto the solids assuming a 1 mg/L aqueous concentration. It was assumed a water saturation at which surface area is 80 m^2 in 1 m^3 volume of soil. 61

Figure 4.10 Interfacial tension for PFOA (a), PFOS (b), or FOSA (c) in an aqueous solution with approximately 380 mg/L TDS. Air-water interfacial tension results for PFOA and PFOS were previously reported in Costanza et al. (2019). The lines shown in a-c are the fits of the Szyszkowski equation (Eq. (3-1) and (4-1) to (4-5)) to the measured interfacial tension values. 63

Figure 4.11 Interfacial tension for 3M AFFF in aqueous solution with 371 mg/L TDS, Ansul AFFF in aqueous solution with 379 mg/L TDS, or PFOS (from **Figure 4.2**) at the air-water (a), dodecane-water (b), PCE-water (c), or JP-4—Water (d) interface. AFFF concentration is for total mass added. The lines shown in a-d are the fits of the Szyszkowski equation (Eq (3-1)) to the measured interfacial tension values. Lower x-axis indicates PFOS concentration in 3M and Ansul formulations. 65

Figure 4.12 Surface excess concentration for PFOA (a), PFOS (b), or FOSA (c) at the air-water, dodecane-water, or JP-4—water interfaces. The lines shown Langmuir/Szyszkowski equation (Eq (3-3) using values from **Table 4.6** and **Table 4.7**. The line for PCE was omitted because it coincided with dodecane. 67

Figure 4.13 Surface excess concentrations for 3M AFFF, Ansul AFFF, or PFOS at the air-water (a), dodecane-water (b), or JP-4—water (c) interfaces. The lines are the Langmuir/Szyszkowski equation (3-3) using values from **Table 4.6** and **Table 4.7**. Lines for PCE not shown because they were similar to those for dodecane. 69

Figure 4.14 Calculated fraction of PFOA (a), PFOS (b), or FOSA (c) mass at the air-water or dodecane-water interface, dissolved in water, and adsorbed to a sandy soil as a function of bulk-water concentration. Soil with water saturation of 0.78, fraction of organic carbon of 0.2%, bulk density of 1.5 kg/L, air-water interfacial area of 8 m^2 at water content of 0.26, NAPL-water interfacial area of 2 m^2 at dodecane residual saturation of 2%. Linear isotherm with PFOA Kd of 0.216 L/kg, PFOS Kd of 1.14 L/kg, and PFOS Kd of 0.25 L/kg..... 72

Figure 4.15 Changes in molar ratios of residual FOSA during aerobic biotransformation in Loring (Panel A) and Hudson (Panel B) soil microcosms. Error bars represent the standard deviation of triplicate live treatment microcosms, and of duplicate control microcosms. 74

Figure 4.16 The formation of PFOS during FOSA aerobic biotransformation in Loring (Panel A) and Hudson (Panel B) soil microcosms. Error bars represent the standard deviation of triplicate live treatment microcosms, and of duplicate control microcosms..... 75

Figure 4.17 The relative abundance of microbial community composition at the phylum level in Loring (left) and Hudson (right) soil microcosms. 79

Figure 4.18 Profiles of 8:2 FTOH and its biotransformation products from the Robins biotransformation experiment during 90-day incubation: (a) residual molar percentage of 8:2 FTOH in the live treatment, abiotic control, and live control; error bars represent one standard deviation of triplicate live treatments and duplicate abiotic/live controls; (b) molar yields of quantified biotransformation products in the live treatment; error bars represent one standard deviation of triplicate live treatments. 82

Figure 4.19 Proposed aerobic biotransformation pathways of 8:2 FTOH based on this study and previous studies [49, 52, 175, 187, 189, 194]. Red and blue arrows represent the pathways harbored by microbial communities in Loring and Robins AFB soils, respectively. Compounds in the orange box were directly quantified by LC-MS/MS in this study, except for those with brackets. Compounds in brackets were not detected by LC-MS/MS in this study but have been documented as 8:2 FTOH biotransformation products. Compounds in dashed boxes are tentative biotransformation products identified in non-targeted analysis by LC-HRMS in this study. Compounds/pathway with dashed arrows in blue boxes are proposed based on prior literature. Compounds/pathway in green boxes with dashed arrows are newly identified in this study..... 88

Figure 4.20 Relative abundance of microbial community at the (a) phylum level and (b) genus level in the Robins biotransformation experiment..... 90

Figure 4.21 Relative abundance of microbial community at the (a) phylum level and (b) genus level in the Loring biotransformation experiment. 91

Figure 4.22 Changes in molar ratios of residual 8:2 FTOH during biotransformation under nitrate-reducing conditions in the electron-donor (ED) treatment, natural attenuation (NA) treatment, abiotic controls, and positive controls microcosms (Panel A). Molar yields of 8:2 FTOH biotransformation products (squares: 8:2 FTCA, circles: 8:2 FTUA, up triangles: 7:2 sFTOH, down triangles: PFOA) in the ED (solid black lines and solid symbols) and NA treatments (dash

red lines and open symbols) (Panel B). Panel C is a zoom view of B, showing the time course trends of PFOA molar yields..... 94

Figure 4.23 Changes in concentrations of targeted PFAS during 8:2 FTOH biotransformation under sulfate-reducing (Panels A and B), and iron-reducing conditions (Panels C and D). Panels A and C show 8:2 FTOH in the electron-donor (ED) treatment, natural attenuation (NA) treatment, abiotic control, and positive control. Panels B and D show the biotransformation products of 8:2 FTOH in ED and NA treatments. Note that the y-axis scale in Panel B is larger than the scale in Panel D..... 99

Figure 4.24 The relative abundance of microbial community composition at the phylum level (Panel A) and genus level (Panel B) in the initial Loring soil (Day 0), and in the nitrate-, sulfate-, and iron-reducing microcosms at the end of ca. 400 days incubation. Microcosms are classified as electron-donor (ED) treatment, natural attenuation (NA) treatment and positive control..... 101

Figure 4.25 Proposed comprehensive biotransformation pathways of 8:2 FTOH under various redox conditions. O2, NO3-, SO42-, Fe3+, and CO2 represent oxic, nitrate-reducing, sulfate-reducing, iron-reducing, and methanogenic conditions, respectively. The pathways under oxic and methanogenic conditions were proposed in previous studies [49, 52, 175, 189, 219], and they were observed in various environmental matrices (e.g., aerobic soil, activated sludge, digester sludge), which likely possessed different microbial communities from those in Loring soil (i.e., a historically AFFF-contaminated soil). The compounds in the solid rectangular boxes were quantitatively analyzed by LC-MS/MS, and the compounds in the dashed rectangular boxes were identified using non-targeted HRMS in the present study. The compounds in the brackets are the aerobic biotransformation products proposed and/or detected in previous studies whereas not detected in this study. The solid arrows indicate the biotransformation steps that would be expected to occur based on the current and/or previous studies. The dashed arrows indicate the potential reactions that may or may not occur. The double arrows indicate multiple enzymatic steps..... 103

Figure 4.26 Changes in molar ratios of residual 6:2 FTS during aerobic biotransformation in Loring (Panel A) and Robins (Panel B) soil microcosms. Error bars represent the standard deviation of triplicate live treatments and duplicate abiotic controls. 107

Figure 4.27 Changes in concentrations of per- (Panels A and C) and polyfluorinated (Panels B and D) biotransformation products during 6:2 FTS aerobic biotransformation in Loring (Panels A and B) and Robins (Panels C and D) soil microcosms. Error bars represent the standard deviation of triplicate live treatments. Note that different y-axis scales were used in Panels A-D. 109

Figure 4.28 Proposed aerobic biotransformation pathways of 6:2 FTS in AFFF-impacted soils. The compounds in the rectangular boxes were detected by LC-MS/MS analysis, and the compounds in the oval boxes were identified using non-targeted LC-HRMS analysis. The compounds in the brackets are proposed transformation products and were not detected in this study. The solid arrows represent the biotransformation steps expected to occur based on the present and previous studies [44, 53, 178]. The dashed arrows represent the proposed reactions that may occur. The double arrows represent multiple enzymatic steps involved. The two large, curved arrows in green illustrate the novel “fluorotelomer ketone to PFCA” pathway proposed in this study which elucidate the formation process of PFCAs. 114

Figure 4.29 Sixteen classes of PFAS identified by LC-HRMS in AFFF-amended microcosms, including 10 classes categorized as AFFF components (shaded in yellow), 8classes categorized as

transformation products (shaded in blue), and 2 classes as both AFFF components and transformation products (shaded in green). The chemical structures of the PFAS classes, and general trends of peak area in live treatment and abiotic control over the 308-day incubation of each homologue within each class were also illustrated..... 118

Figure 4.30 Log_2-fold changes (LFCs) in peak areas of different PFAS between day 308 and day 0. (a) and (b) show LFCs for the AFFF components detected live treatment and abiotic control, respectively. Error bars represent one standard deviation among replicate microcosms..... 126

Figure 4.31 Proposed transformation pathways of (a) sulfonamide-based and (b) carboxamide-based PFAS identified by LC-HRMS in AFFF-amended soil microcosms. Compounds in yellow and blue boxes were identified in this study as AFFF components and transformation products, respectively. Compounds in green box were identified in this study as both AFFF components and transformation products. Compounds in parentheses were not detected in this study, but detected or predicted as intermediates in previous studies [162, 236, 241]. Red and green arrows represent possible biotransformation and abiotic transformation steps, respectively. Dashed arrows indicate hypothetical multiple steps. 127

Figure 4.32 Microbial co-occurrence networks in fluorotelomer contaminated soils under different redox conditions (constructed networks). An edge (connection) between nodes (ASVs) indicates a strong and significant correlation between two nodes. The size of each node is proportional to the number of connections (degree). The nodes are colored according to (a) phylum taxa and (b) module assigned..... 132

Figure 4.33 UpSet plot for genes shared among different sets of microcosm experiments. The table (top, left panel) shows the contaminant, soil type, and redox condition in each set of microcosms. The horizontal bar plot (bottom, left panel) exhibits the total number of genes with significantly higher abundance in each set of microcosms. The vertical bar plot (top, right panel) depicts the number of genes shared by two or more of sets of microcosms. The matrix (bottom, right panel) indicates which sets of genes are represented by each bar..... 137

Figure 4.34 Sankey diagrams indicating the contribution of predicted functional genes by bacterial taxa across all microcosm experiments. Noted that the vertical nodes are not proportional to the size of relative abundance. The left column represents functional genes (a) that may be related to defluorination and (b) that were also identified as important functional genes in this study. The middle and right columns are taxonomic groups at phylum level and taxonomic groups at genus level, respectively. The colors are assigned based on the taxonomy at genus level. 142

Figure 4.35 Equilibrium solubilities of PCE and TCE in aqueous solutions of AFFF over a concentration range of 0 to 50 g/L (5 % wt.). For comparison purposes, previously reported solubilities of PCE and TCE in aqueous solutions of a nonionic surfactant, Tween® 80, over a similar concentration range are also presented. Errors bars represent standard error of duplicate measurements..... 144

Figure 4.36 NAPL-water interfacial tensions for (a) JP4, TCE and PCE as a function of AFFF concentration; data fit to Szyszkowski equation (solid lines), (b) enlarged graph of interfacial tension data below 4 mN/m, and (c) corresponding surface excess concentrations at the NAPL-water interface obtained using Langmuir/Szyszkowski equation..... 145

Figure 4.37 Vertical (downward) mobilization of TCE in 20-30 mesh Ottawa sand with 3% wt. AFFF as the displacing fluid: (a) prior to AFFF flush; (b) after injection of 0.8 PVs of 3 wt. %

AFFF solution (TCE moved downward and formed a bank); (c) after injection of 1.5 PVs of 3 wt. % AFFF solution, (TCE continued to migrate downward); (d) after injection of 3 PVs of 3% wt. AFFF solution. 147

Figure 4.38 Effluent samples showing TCE-DNAPL displaced by 3% wt. AFFT from column shown in Figure S1. Collection time (pore volumes) for each tube (left to right): 0.74, 0.89, 1.05, 1.17, 1.32, 1.47, 1.62, 1.77 PV. 147

Figure 4.39 Representative non-reactive tracer test showing effluent breakthrough curves obtained for bromide before and after flushing with a displacing fluid: (a) after 500mg/L CaCl2 flush, prior to AFFF flush, (b) after AFFF flush and (c) after AY/OT flush. Note the delayed tracer breakthrough after the AFFF flush(b) and AY/OT flush(c) since NAPL was displaced from the column and water pore volume was increased. 148

Figure 4.40 Vertical (downward) mobilization of TCE-DNAPL in 20-30 mesh Ottawa sand with 4% wt. Aerosol AY/OT solution as the displacing fluid: (a) prior to Aerosol AY/OT flush; (b) after injection of 0.5 PVs of 4% wt. Aerosol AY/OT solution (TCE moved downward and formed a bank); (c) after injection of 0.9 PVs of 4% wt. Aerosol AY/OT, (TCE continued to migrate downward); (d) after injection of 1.5 PVs of 4% wt. Aerosol AY/OT solution. 149

Figure 4.41 Effluent samples showing TCE-DNAPL displaced by 4% wt. Aerosol AY/OT solution from column shown in Figure S3. Collection time (pore volumes) for each tube (left to right): 0.33, 0.48, 0.63, 0.79, 0.94, 1.09, 1.24, 1.39 PV. 150

Figure 4.42 NAPL desaturation curves for (a) JP-4, (b) TCE and (c) PCE in 20-30 mesh and 60-80 mesh Ottawa sand expressed in terms of the total trapping number (N_T). The solid data points represent measured NAPL saturations obtained for the three displacing solutions: 500 mg/L $CaCl_2$, 3% wt. AFFF and 4% wt. Aerosol® AY/OT solutions. The open data points shown in (c) are results from previous study using 4% Tween® 80 and Aerosol® surfactants [36]. Errors bars represent standard error of duplicate or triplicate column experiments. 152

Figure 4.43 Interfacial tension (a) and corresponding surface excess (b) and interfacial partition coefficient (K_i) (c) of PCE-NAPL and solutions containing individual PFAS, a 1:1 mixture of PFNA and PFOS (PFAS mix-2), and a mixture of six PFAS (PFAS mix-6). Error bars in (a) indicate standard deviations in triplicate measurements. 154

Figure 4.44 (a) Surface excess (Γ) and (b) interfacial partition coefficient (K_i) of PFAS as single solute and in the PFAS mixtures over a concentration range of 0-100 mg/L. 155

Figure 4.45 PFAS partitioning isotherms into PCE-NAPL. The dashed lines indicate PFAS partitioning isotherm in mix-6, the solid lines are PFNA only and PFOS only partitioning isotherms. Error bar indicates standard deviations in triplicate measurements. 156

Figure 4.46 Single component (a) PFNA and (b) PFOS adsorption data for 60-80 mesh OS. Data were fit with the linear, Freundlich and Langmuir isotherm models. 158

Figure 4.47 Solid phase adsorption data for (a) PFBS, (b) PFHpA, (c) PFHxS, (d)PFOA, (e) PFNA and (f) PFOS in solutions containing mixtures of 6 PFAS. Data were fit with the linear, Freundlich and Langmuir isotherm models. 158

Figure 4.48 Breakthrough curves obtained for (a) PFNA only and (b) PFOS only in control columns (no PCE-NAPL). Data were fit with either the linear/equilibrium or linear/non-equilibrium solid phase adsorption models. 159

Figure 4.49 Breakthrough curves obtained for (a) PFNA and (b) PFOS in a control column (no PCE-NAPL) for a 1:1 PFNA:PFOS mixture. Data were fit with either the linear/equilibrium or linear/non-equilibrium solid phase adsorption models. 160

Figure 4.50 Breakthrough curves obtained for (a) PFBS, (b) PFHpA, (c) PFHxS, (d) PFOA, (e) PFNA and (f) PFOS in a control column (no PCE-NAPL) for a mixture of 6 PFAS. Data were fit using either a linear/equilibrium or linear/non-equilibrium solid phase adsorption model. 160

Figure 4.51 Measured and simulated effluent breakthrough curves obtained for (a) PFNA only and PFOS only columns and (b) 1:1 PFNA and PFOS binary mixture column at residual PCE-NAPL (~16%). Error bar indicates standard deviations in duplicate columns. 162

Figure 4.52 Comparison of Langmuir and Freundlich isotherms fits for NAPL-water Interfacial tension (a) and corresponding estimation of surface excess (b) for PFOS solutions. The Freundlich fitted parameters for PFOS surface excess are: $kfIA = 0.228\ (\mathrm{mg/m2})(\mathrm{L/mg})nIA\ , nIA = 0.493.$ 163

Figure 4.53 Comparison of Langmuir and Freundlich isotherms fits for NAPL-water Interfacial tension (a) and corresponding surface excess (b) for PFNA solutions. The Freundlich fitted parameters for PFOS surface excess are: $kfIA = 0.149\ (\mathrm{mg/m2})(\mathrm{L/mg})nIA\ , nIA = 0.561$.164

Figure 4.54 Breakthrough curves for PFOS in a control column (no PCE-NAPL) using a mixture of 6 PFAS mixture that were fit with (a) linear/equilibrium model, (b) nonlinear/equilibrium model, and (c) linear/non-equilibrium model. 164

Figure 4.55 Measured and simulated effluent breakthrough curves for injected solutions containing a mixture of six PFAS (~70-100 µg/L each) in columns containing residual PCE-NAPL (~16%). Error bar indicates standard deviations in duplicate columns. 166

Figure 4.56 Time-course of 6:2 FTS concentration in the effluents from abiotic and biotic columns. Error bars represent the standard deviation of duplicate abiotic and biotic columns. 169

Figure 4.57 Time-courses of 6:2 FTS biotransformation products quantified by LC-MS/MS analysis in biotic columns effluents. Error bars represent the standard deviation of duplicate biotic columns. Note that different y-axis scales were used in top and bottom plots. 170

Figure 4.58 The average molar yields of 6:2 FTS and LC-MS/MS quantified biotransformation products along flowing path (i.e., Port 1, Port 2, Port 3, and Effluent, See Fig. 1) in different subphases. Phases I-A and I-B were not included because an incorrect sampling technique was used initially for side-port sampling, which resulted in the collected samples were mostly from the side-port itself (i.e., a "dead zone") instead of the flowing stream. 173

Figure 4.59 Principal coordinate analysis (PCoA) plot based on microbial communities in aqueous side-port and solid samples from segments S1-S5. Each data point represents an individual sample. PCoA was calculated using weighted UniFrac distances. Samples collected at three side-ports and five segments along the column in Phase I, Phase II, and at the termination of the experiments are differentiated by color and shape. The ellipses represent 95% confidence interval around the cluster centroid. 177

Figure 4.60 Phylum-level microbial composition of free-living (FL) microbial communities in aqueous side-port samples collected during Phase I (a) and Phase II (b), and porous media-attached (PMA) microbial communities in solid samples from segments S1-S5 of two biotic columns (c) (d). 178

Figure 4.61 Genus-level microbial composition of free-living (FL) microbial communities in aqueous side-port samples collected during Phase I (a) and Phase II (b), and porous media-attached (PMA) microbial communities in solid samples from segments S1-S5 of two biotic columns (c) (d). 179

Figure 4.62 Simulation results for the first soil profile at Wright-Patterson AFB (WP-1) with four spills per year equivalent to 100 gal of AFFF concentrate (conditions Sp1). (a) Water content profiles (horizontal lines indicate the soil layers and water table); (b) AWIA profiles; (c) and (d) PFOA and PFOS total soil concentration profiles; (e) average mass fraction in each phase (PW = pore water, IA = AWIA, S = solids) in the vadose zone; and (f) breakthrough curves at the water table. 181

Figure 4.63 Close inspection of precipitation, average AWIA, and ratio of mass accumulated at the AWIA and sorbed mass in solid phase over the period from 15 to 20 years at WP-1. Interfacial to sorbed mass ratio varies with the change in available interfacial area, increasing in drier months and decreasing in wetter seasons 183

Figure 4.64 Comparison between the two soil profiles at Wright-Patterson AFB (WP-1 and WP-2) with spill conditions Sp1. (a) Position of the center of total mass in the vadose zone during the first 20 years, and (b) breakthrough of PFOA and PFOS at the water table. 184

Figure 4.65 Total soil concentration of PFOA (left) and PFOS (right) at the four soil scenarios on the top 100 cm after 1 year (top) and 5 years (bottom) from a single spill of 400 gal of AFFF concentrate (Sp6). 185

Figure 4.66 Breakthrough curves of PFOA (left) and PFOS (right) at the water table at Wright-Patterson, scenario 1 (top) and Tyndall (bottom) as a function of spill conditions. For each condtion, the legend indicates the spill frequency in a 10-year period and the cumulative volume of concentrate AFFF released per unit area. 186

Figure 4.67 Predicted breakthrough of PFOA and PFOS at the water table after periodic spills equivalent to (a) 100 gal and (b) 25 gal of 3% AFFF solution at Wright-Patterson considering (i) the base model of this manuscript, (ii) no competition at the air-water interface, and (iii) no moisture release from interfacial tension (IFT) reduction. 189

Figure 4.68 Maximum concentration at the water table as a function of the Equivalent Total Volume of AFFF Concentrate released per area for both (a) PFOA and (b) PFOS. Symbols enclosed by diamonds represent one-time spills. 191

Figure 4.69 Maximum concentration at the water table as a function of the water table depth for (a) PFOA and (b) PFOS. 192

Figure 4.70 Maximum concentration at the water table as a function of average net recharge for both (a) PFOA and (b) PFOS. 192

Figure 4.71 Depth to Water Table/Time to Reach Water Table plotted as a function of Average Permeability (log K) for both (a) PFOA and (b) PFOS. 193

Figure 4.72 Rate of Migration of Center of Mass for the first 10 years of simulation plotted as a function of Log(K) for both (a) PFOA and (b) PFOS. 194

Figure 4.73 Time to reach max concentration at the water table as a function of the net recharge averaged over one (1) year for both PFOA (blue symbols) and PFOS (orange symbols). 195

Figure 4.74 Ratio of mobile to immobile mass as a function of Equivalent Total Volume of AFFF Concentrate per area for both (a) PFOA and (b) PFOS. The colors of the symbols represent the different locations and the symbols enclosed by diamonds represent single-spill scenarios..... 196

Figure 4.75 Ratio of mobile to immobile mass as a function of log(K) for (a) PFOA and (b) PFOS. Note the colors represent the different contaminant sites. All data are plotted after a 40-year simulation except Tyndall, which are plotted at the end of 10 years. 196

Figure 4.76 Ratio of mobile to immobile mass as a function of the average Freundlich parameter for (a) PFOA and (b) PFOS. Note Tyndall is excluded. 197

Figure 4.77 (a) PFOA rate of migration of the center of mass and (b) time to reach the water table as a function of the Freundlich parameter. 198

Figure A.1 Separate phase formation in a solution of 5,000 mg/L PFOA in ultrapure water. ... 285

Figure A.2 Separate phase formation in a solution of 500 mg/L KPFOS in 1,741 mg/L Total Dissolved Solids..... 285

Figure A.3 Comparison between Freundlich and Szyszkowski fits of air-water surface tension curves for PFOS in 42 mM TDS solution. 286

Figure A.4 Surface excess for PFOS in 42 mM solution determined from the Freundlich and Langmuir-Szyszkowski equations. 286

Figure A.5 Compound Discoverer Workflow. 287

Figure A.6 Principal coordinate analysis (PCoA) plot of phylogenetic microbial community changes among the treatments from Loring and Hudson soil microcosms, as described by weighted UniFrac distance matrices. The PC1 and PC2 axes explain 40% and 22.1% of the variation, respectively. 287

Figure A.7 The relative abundance of microbial community composition at the genus level in Loring (left) and Hudson (right) soil microcosms. 288

Figure A.8 Total organic carbon (TOC) in (a) Robins biotransformation experiment during 90-day incubation. DGBE amendment were made to live treatment (black arrow) and live control (blue arrow) and (b) Loring biotransformation experiment during 90-day incubation. Identical amount of DGBE was amended into all three groups at the same time points (black arrow). Error bars represent one standard deviation of triplicate live treatments and duplicate abiotic/live controls. 288

Figure A.9 Molar percentage of residual 8:2 FTOH in live treatment in Robins biotransformation experiment during 90-day incubation along with fitting curve of first-order double exponential decay model. 289

Figure A.10 Mass of PFCAs (C5-C10) in Robins biotransformation experiment during 90-day incubation. Error bars represent one standard deviation of triplicate of live treatments and duplicate abiotic and live controls. Asterisks indicate statistically significant differences between the live treatment and abiotic/live control (two sample *t*-test). The single asterisk indicates $p < 0.05$ and double asterisks indicate $p < 0.01$. Note that the y-axis scales for each PFCA are different..... 290

Figure A.11 The total molar recovery in Robins biotransformation experiment during 90-day incubation. Error bars represent one standard deviation of triplicate live treatments and duplicate abiotic controls. 291

Figure A.12 Mass of PFCAs (C4-C10) in Loring biotransformation experiment. Asterisk indicates $p < 0.05$ compared with live control at day 90. Error bars represent one standard deviation of triplicate high-dose and low-dose treatments and duplicate live controls. 291

Figure A.13 Change of peak area count (mean value and standard error of three technical replicate) along with time at day 0 and day 90 for compounds selected by non-targeted analysis in Loring biotransformation experiment. 292

Figure A.14 Change of peak area count (mean value and standard error of three technical replicate) along with time at day 0 and day 90 for compounds selected by non-targeted analysis in Loring biotransformation experiment (Low-dose treatment only). 293

Figure A.15 Change of peak aera count (mean value and standard error of three technical replicate) along with time at day 0, day 28 and day 90 for compounds selected by non-targeted analysis in Robins biotransformation experiment. 294

Figure A.16 Illustration of the elucidated high-resolution MS2 spectrum obtained for 1H-perfluoroheptane, identified at the confirmed structure confidence level (level 1): (a) microcosm sample; (b) 1H-perfluoroheptane reference standard (1 μg/L). 295

Figure A.17 Principal coordinate analysis (PCoA) plot of phylogenetic microbial community changes across different 8:2 FTOH dose treatments with Loring AFB soil or Robins AFB soil as described by weighted UniFrac distance matrices. PC1 explains 67.9% of the variation while PC2 explains 14.4%. 296

Figure A.18 Concentrations of nitrate and organic acids in ED treatment/positive control (Panel A); concentrations of nitrate and total organic carbon (TOC) in NA treatment (Panel B); concentrations of nitrate and lactate in abiotic control (Panel C). The black, red, and gray arrows represent the individual amendments of 40 mM nitrate, 20 mM lactate, and 5 mM DGBE to the microcosms, respectively. Note that a total of 11 nitrate and 8 lactate amendments were made to ED treatment/positive control due to the rapid depletion of both electron donor and acceptor. Error bars represent the standard deviation of triplicate ED/NA microcosms, and of duplicate control microcosms. 297

Figure A.19 Concentrations of sulfate and organic acids in ED treatment/positive control (Panel A); concentrations of sulfate and total organic carbon (TOC) in NA treatment (Panel B); concentrations of sulfate and lactate in abiotic control (Panel C). The black, red, and gray arrows represent the individual amendments of 20 mM sulfate, 20 mM lactate, and 5 mM DGBE to the microcosms, respectively. Error bars represent the standard deviation of triplicate ED/NA microcosms, and of duplicate control microcosms. 298

Figure A.20 Concentrations of Fe(II) and organic acids in ED treatment/positive control (Panel A); concentrations of Fe(II) and total organic carbon (TOC) in NA treatment (Panel B); concentrations of Fe(II) and lactate in abiotic control (Panel C). The red, and gray arrows represent the individual amendments of 20 mM lactate, and 5 mM DGBE to the microcosms, respectively. Note that the time variation of pH in each treatment was also plotted in respective Panel. Error bars represent the standard deviation of triplicate ED/NA microcosms, and of duplicate control microcosms. 299

Figure A.21 Changes in molar ratio of residual 8:2 FTOH, and the fitting curves of single first-order kinetic models in ED and NA treatment under nitrate-reducing condition. 300

Figure A.22 Changes in the concentrations (nanomole per gram soil/dry weight) of 7:3 acid, and C4-C9 PFCAs in ED, NA treatment, abiotic controls, and positive controls under nitrate-reducing condition throughout the experiments. Note that the y-axis scales in PFOA plot is larger than the scales in other plots. 301

Figure A.23 The total molar recoveries (8:2 FTOH and quantifiable biotransformation products) during 8:2 FTOH biotransformation in ED, NA treatment, and abiotic controls under nitrate-reducing conditions (Panel A), sulfate-reducing conditions (Panel B), iron-reducing conditions (Panel C). 302

Figure A.24 The MS2 spectra of potential biotransformation products identified in the ED and/or NA treatments under nitrate, sulfate-, or iron-reducing conditions**.** Panel A, 7:3 U acid (F(CF2)7CH=CHCOOH, *m/z* 438.9822); Panel B, 3-OH-7:3 acid ($F(CF_2)_7CHOHCH_2COOH$, *m/z* 456.9930); Panel C, 3-F-7:3 acid ($F(CF_2)_7CFHCH_2COOH$, *m/z* 458.9885). 303

Figure A.25 The time trend of 7:3 U acid during 8:2 FTOH biotransformation in each treatment under (A) nitrate-reducing; (B) sulfate-reducing; and (C) iron-reducing conditions based on peak areas of extracted ion chromatograms. 304

Figure A.26 The time trend of 3-OH-7:3 acid during 8:2 FTOH biotransformation in each treatment under (A) nitrate-reducing; (B) sulfate-reducing; and (C) iron-reducing conditions based on peak areas of extracted ion chromatograms. 305

Figure A.27 The time trend of 7:3 U amide during 8:2 FTOH biotransformation in each treatment under (A) nitrate-reducing; (B) sulfate-reducing; and (C) iron-reducing conditions based on peak areas of extracted ion chromatograms. Note Panel A' is the zoom view of Panel A, excluding the NA treatment with a smaller y-axis scale, to illustrate the different time trends between the ED treatment and two controls. 306

Figure A.28 The MS2 spectra of a novel biotransformation product identified as 1H-perfluoroheptane (m/z 368.9764). Panel A is the spectrum of samples collected from 8:2 FTOH nitrate-reducing microcosms. Panel B is the spectrum of 1 ppb 1H-perfluoroheptane standard. 307

Figure A.29 The molar yields of 1H-perfluoroheptane during 8:2 FTOH biotransformation in each treatment under nitrate-reducing conditions, based on the GC-HRMS quantification results. .. 307

Figure A.30 Changes in the concentrations (nanomole per gram soil/dry weight) of 7:3 acid, and C4-C9 PFCAs in ED, NA treatment, abiotic controls, and positive controls under sulfate-reducing condition throughout the experiments. 308

Figure A.31 Changes in the concentrations (nanomole per gram soil/dry weight) of 7:3 acid, and C4-C9 PFCAs in ED, NA treatment, abiotic controls, and positive controls under iron-reducing condition throughout the experiments. 309

Figure A.32 The time trend of 3-F-7:3 acid during 8:2 FTOH biotransformation in each treatment under (A) nitrate-reducing; (B) sulfate-reducing; and (C) iron-reducing conditions based on peak areas of extracted ion chromatograms. 310

Figure A.33 Principal coordinate analysis (PCoA) plot of phylogenetic microbial community changes among the microcosms under different redox conditions, as described by weighted UniFrac distance matrices. 311

Figure A.34 Concentrations of dissolved organic carbon (DOC) in Loring (Panel A) and Robins (Panel B) soil microcosms. Solid arrows represent the amendment of 10 mM DGBE to live treatments and positive controls. Error bars represent the standard deviation of triplicate live treatment microcosms, and of duplicate control microcosms. 311

Figure A.35 Changes in sulfate concentrations during 6:2 FTS aerobic biotransformation in Loring (Panel A) and Robins (Panel B) soil microcosms. Error bars represent the standard deviation of triplicate live treatment microcosms, and of duplicate control microcosms. 312

Figure A.36 Principal coordinate analysis (PCoA) plot of phylogenetic microbial community changes among the treatments from Loring or Robins soil microcosms, as described by weighted UniFrac distance matrices. The PC1 and PC2 axes explain 44.2% and 27.2% of the variation, respectively. 312

Figure A.37 The relative abundance of microbial community composition at the phylum level in Loring (left) and Robins (right) soil microcosms. 313

Figure A.38 The relative abundance of microbial community composition at the genus level in Loring (left) and Robins (right) soil microcosms. 313

Figure A.39 The total molar recoveries (6:2 FTS and quantifiable biotransformation products) in live treatments and abiotic controls from Loring and Robins soil microcosms. 314

Figure A.40 The time trends of 1H-perfluoropentane (C_5HF_{11}, *m/z* 268.98271) and 1H-perfluorobutane (C_4HF_9, *m/z* 218.98587) during 6:2 FTS biotransformation in each treatment of Loring and Robins soil microcosms based on peak areas of extracted ion chromatograms..... 314

Figure A.41 The time trends of 1,2,2,3,3,4,4,4-Octafluorobutan-1-ol ($C_4H_2F_8O$, *m/z* 216.98912) and Perfluoropentanal (C_5HF_9O, *m/z* 246.9808) during 6:2 FTS biotransformation in each treatment of Loring and Robins soil microcosms based on peak areas of extracted ion chromatograms. 315

Figure A.42 The time trends of $C_7H_2F_8$ (m/z 236.99543), $C_7H_3F_9$ (m/z 257.00159), and m/z 292.98316 during 6:2 FTS biotransformation in each treatment of Loring and Robins soil microcosms based on peak areas of extracted ion chromatograms. 316

Figure A.43 MS^2 spectra of 1H-perfluoropentane (C_5HF_{11}, *m/z* 268.98271) obtained from the analysis of microcosm sample (Panel A), and the analysis of 1 ppb reference standard (Panel B). 317

Figure A.44 MS^2 spectra of 1H-perfluorobutane (C_4HF_9, *m/z* 218.98587) obtained from the analysis of microcosm sample (Panel A), and the analysis of 1 ppb reference standard (Panel B). 318

Figure A.45 MS^2 spectra of potential 6:2 FTS biotransformation products. Panel A, 1,2,2,3,3,4,4,4-octafluorobutan-1-ol ($C_4H_2F_8O$, m/z 216.98912); Panel B, $C_7H_2F_8$ (m/z 236.99543). 318

Figure A.46 Change of peak areas (mean value and standard error of three technical replicate) along with time (308 days) for **TAmPr-FASA** homologues with different perfluoroalkyl chain length (a) n = 4, (b) n = 5, (c) n =6. All these compounds were identified only in ESI+ mode. 319

Figure A.47 Change of peak areas (mean value and standard error of three technical replicate) along with time (308 days) for **AmPr-FASA** homologues with different perfluoroalkyl chain length (a-1) n = 4, ESI-, (a-2) n = 4, ESI+; (b-1) n = 5, ESI-, (b-2) n = 5, ESI+; (c-1) n =6, ESI-, (c-2) n = 6, ESI+; (d) n = 7, ESI+; (e) n = 8, ESI+. 320

Figure A.48 Change of peak areas (mean value and standard error of three technical replicate) along with time (308 days) for **CEt-AmPr-FASA-PrA** homologue with perfluoroalkyl chain length n = 4, identified in ESI+ mode. 321

Figure A.49 Change of peak areas (mean value and standard error of three technical replicate) along with time (308 days) for **AmPr-FASA-PrA/TAmPr-FASA-AA** homologues with different perfluoroalkyl chain length (a-1) n = 4, ESI-, (a-2) n = 4, ESI+; (b-1) n = 5, ESI-, (b-2) n = 5, ESI+; (c-1) n = 6, ESI-, (c-2) n = 6, ESI+; (d) n = 7, ESI+; (e) n = 8, ESI+ 322

Figure A.50 Change of peak areas (mean value and standard error of three technical replicate) along with time (308 days) for **6:2 FTAB** identified in ESI+ mode. 323

Figure A.51 Change of peak areas (mean value and standard error of three technical replicate) along with time (308 days) for **AmPr-FAAd** different with perfluoroalkyl chain length (a) n = 6 and (b) n = 7. 324

Figure A.52 Change of peak areas (mean value and standard error of three technical replicate) along with time (308 days) for **CEt-AmPr-FAAd** with perfluoroalkyl chain length n = 7 identified in ESI+ mode. 325

Figure A.53 Change of peak areas (mean value and standard error of three technical replicate) along with time (308 days) for **PFSA** homologues with different perfluoroalkyl chain length (a) n = 2, (b) n = 3, (c) n = 4, (d) n = 5, (e) n = 6, (f) n = 7, (g) n = 8, (h) n = 9, and (i) n = 10. All the homologues were identified in ESI- mode. 326

Figure A.54 Change of peak areas (mean value and standard error of three technical replicate) along with time (308 days) for **PFCA** homologues with different perfluoroalkyl chain length (a) n = 4, (b) n = 5, (c) n = 6, (d) n = 7, and (e) n = 9. All the homologues were identified in ESI- mode. 327

Figure A.55 Change of peak areas (mean value and standard error of three technical replicate) along with time (308 days) for **FASA** homologues with different perfluoroalkyl chain length (a) n = 3, (b-1) n = 4, (c) n = 5, (d) n = 6, and (e) n = 8. All the homologues were identified in ESI- mode. 328

Figure A.56 Change of peak areas (mean value and standard error of three technical replicate) along with time (308 days) for **M-AmPr-FASA** with perfluoroalkyl chain length n = 6 identified in (a-1) ESI- mode and (a-2) ESI+ mode. 329

Figure A.57 Change of peak areas (mean value and standard error of three technical replicate) along with time (308 days) for **OAmPr-FASA** homologues with different perfluoroalkyl chain length (a) n = 4, (b-1) and (b-2) n = 6, (c) n = 7, and (d) n = 8. Except for (b-1) identified in ESI- mode, others were all identified in ESI+ mode. 330

Figure A.58 Change of peak areas (mean value and standard error of three technical replicate) along with time (308 days) for **N-MeFASAA** with perfluoroalkyl chain length n = 6 identified in ESI- mode. 331

Figure A.59 Change of peak areas (mean value and standard error of three technical replicate) along with time (308 days) for **N-EtFASAA** with perfluoroalkyl chain length n = 6 identified in ESI- mode. 331

Figure A.60 Change of peak areas (mean value and standard error of three technical replicate) along with time (308 days) for **OAmPr-FAAd** homologues with different perfluoroalkyl chain length (a) n = 5, (b) n = 6, and (c) n = 7. All the homologues were identified in ESI+ mode.... 332

Figure A.61 Change of total mass (nanomole) over time (308 days) for C_6 homologue of AmPr-FASA based on LC-MS analysis. The red, green, and blue symbols/lines represent the live treatment, abiotic control, and live control, respectively. Error bar represents one standard deviation of replicates. 333

Figure A.62 Change of total mass (nanomole) over time (308 days) for homologues in PFCAs, PFSAs, and FASAs with available analytical standards based on LC-MS analysis: (a) PFBA, (b) PFPeA, (c) PFHxA, (d) PFHpA, (e) PFOA, (f) PFBS, (g) PFPeS, (h) PFHxS, (i) PFHpS, (j) PFOS, (k) FHxSA, and (l) FOSA. Error bar represents one standard deviation of replicates. 334

Figure A.63 Microbial co-occurrence networks in fluorotelomer contaminated soils under different redox conditions (constructed networks). An edge (connection) between nodes (ASVs) indicates a strong and significant correlation between two nodes. The size of each node is proportional to the number of connections (degree). The nodes are colored according to (a) contaminant added externally, (b) soil, and (c) redox condition maintained during the experiments. 335

Figure A.64 The node distribution in the Degree-Closeness centrality-Betweenness centrality space..... 336

Figure A.65 The node positions and regions of roles in the z–P parameter space. The nodes in the bottom region are peripheral nodes, or non-hubs, ($z < 0.9$); the nodes in the top left region are modular hubs ($z \geq 0.9$, $P \leq 0.30$); the nodes in the top middle region are connector hubs ($z \geq 0.9$, $0.30 < P \leq 0.75$); and the nodes in the top right region are network hubs ($z \geq 0.9$, $P > 0.75$). ... 336

Figure A.66 Heatmap of selected functional gene abundances predicted by PICRUSt2 in different treatments of microcosm experiments. The left panel are from 4 sets of aerobic microcosms and there are 2 columns for each set (left column: live treatment with fluorotelomer added; right column: control without fluorotelomer). A and E, 8:2 FTOH, Loring soil and Robins soil, respectively; F and G, 6:2 FTS, Loring soil and Robins soil, respectively. The right panel are from 3 sets of anerobic microcosms with 3 columns for each set (left: live treatment with fluorotelomer and lactate added as extra electron donor and carbon source to mimic biostimulation; middle column: live treatment with fluorotelomer and only diethylene glycol monobutyl ether as external electron donor and caron source to mimic natural attenuation; right column: control without fluorotelomer). B, C, and D, 8:2 FTOH, Loring soil, under nitrate-, sulfate-, and iron-reducing conditions, respectively. The values of gene abundance were normalized (Z-score) and colored from red to blue to indicate high-to-low relative abundances. 337

Figure A.67 Concentrations of dissolved organic carbon (DOC) in the effluent samples collected from abiotic and biotic columns. 338

Figure A.68 Aerobic biotransformation pathways of 6:2 FTS in AFFF-impacted soils proposed in the previous study [332]. The compounds in the rectangular boxes were detected by LC-MS/MS analysis, and the compounds in the oval boxes were identified using non-targeted LC-HRMS analysis. The compounds in the brackets are proposed transformation products. The solid arrows represent the biotransformation steps expected to occur based on the present and previous studies. The dashed arrows represent the proposed reactions that may occur. The double arrows represent multiple enzymatic steps involved. The two large, curved arrows in green illustrate the proposed "fluorotelomer ketone to PFCA" pathway which elucidate the formation process of PFCAs... 339

Figure A.69 The peak areas of extracted ion chromatograms of C_7HF_{11} (*m/z* 292.98325) in (a) abiotic and biotic column effluent, and (b) side-port and effluent samples from biotic columns during the column experiments..... 340

Figure A.70 Wright-Patterson Scenario 1. 341

Figure A.71 Wright-Patterson Scenario 2. 341

Figure A.72 Tyndall Scenario..... 342

Figure A.73 Ellsworth Scenario. 343

List of Acronyms

AFB	Air Force Base
AFFF	Aqueous film forming foam
AWIA	Air-water interfacial area
BTC	Breakthrough curve
CMC	Critical micelle concentration
DoD	Department of Defense
DGBE	Diethylene glycol butyl ether
DOC	Dissolved organic carbon
EL	Elsworth Airforce Base
ERSON	Environmental Restoration Statements of Need
FOSA	Perfluoro-1-octanesulfonamide
FTS	Fluorotelomer sulfonic acid
GC-MS	Gas chromatography mass spectrometer
HDPE	High-density polyethylene
HFPO-DA	Hexafluoropropylene oxide dimer acid
HOCs	Hydrophobic organic compounds
IFT	Interfacial tension
LC-MS/MS	Liquid chromatography tandem mass spectrometer
LOD	Limit of detection
LOQ	Limit of quantitation
MASS	Model alkyl sulfate salt
MS^2	Tandem mass spectrometry
NAPL	Nonaqueous phase liquids
NPDWR	National Primary Drinking Water Regulation
NT	Total trapping number
OC	Organic carbon
PCE	Perchloroethylene
PFAA	Perfluroalkyl acids
PFAS	Poly- and Perfluoroalkyl Substances
PFBA	Perfluorobutanoic acid
PFBS	Perfluorobutanesulfonic acid
PFDA	Perfluorodecanoic acid
PFDoA	Perfluorododecanoic acid
PFDoS	Perfluorododecane sulfonic acid
PFDS	Perfluorodecane sulfonic acid
PFHpA	Perfluoroheptanoic acid
PFHxA	Perfluorohexanoic acid
PFHxS	Perfluorohexanesulfonic acid
PFNA	Perfluorononanoic acid
PFNS	Perfluorononane sulfonic acid
PFOA	Perfluorooctanoic acid
PFOS	Perfluorooctane sulfonic acid
PFPeA	Perfluoropentanoic acid
PFPeS	Perfluoropentane sulfonic acid

PFTeDA	Perfluorotetradecanoic acid
PFTrDA	Perfluorotridecanoic acid
PFUnA	Perfluoroundecanoic acid
PV	Pore Volume
SDS	Sodium Dodecyl Sulfate
SERDP	Strategic Environmental Research and Development Program
Sp	Spill
TCE	Trichloroethylene
TDS	Total dissolved solids
TQ	Triple quadrupole
TY	Tyndall Airforce Base
UPLC	Ultra-performance liquid chromatography
USEPA	U.S. Environmental Protection Agency
WP	Wright-Patterson Airforce Base
WSRs	Weight solubilization ratios

Keywords

AFFF-Source Zones
Aqueous Film Forming Foam (AFFF)
Biotransformation
Interfacial Processes
Mathematical Modeling
Poly- and Perfluoroalkyl Substances (PFAS)
Subsurface Transport

Acknowledgements

In addition to co-PI's Dr. Linda M. Abriola, Dr. Kurt D. Pennell, Dr. Natalie L. Cápiro, Dr. John A. Christ, and Dr. Thomas J. Phelan, the following individuals contributed to the research presented in this report:

Tufts University: Ana Guedes (MS Student); Dr. Masoud Arshadi (Research Assistant Professor)

Brown University: Chen Liu (PhD Student), Dorothea Pinchbeck (Undergraduate Researcher), Dr. Jed Costanza (Research Engineer), Dr. Katherine E. Manz (Research Assistant Professor), Litzy Guevara (PhD student), Matthew J. Woodock (Research Engineer), Shuchi Liao (PhD Student), Dr. Uriel Garza-Rubalcava (Post Doctoral Fellow), and Zachary S. Saleeba (PhD Student).

Auburn University: Peng-Fei Yan (PhD student) and Sheng Dong (PhD student).

Baylor College of Medicine: Dr. Melissa P. Mezzari (Project Manager).

Woodard & Curran: J. Daniel Bryant (Director of Practices).

Funding for part of this research was also provided by SERDP contract W912HQ-18-C0002: "Development of Coupled Physiochemical and Biological Systems for In-Situ Remediation of Mixed Perfluorinated Chemical and Chlorinated Solvent Groundwater Plumes". The authors thank the Air Force Civil Engineer Center and Geosyntec Consultants for assistance in the collection of site materials at Robins AFB. We acknowledge Naji Akladiss at Maine Department of Environmental Protection (MDEP) for providing access to collect Loring soil. Sheng Dong and Peng-Fei Yan also acknowledge the financial support from the China Scholarship Council, and Auburn University Graduate School and Office of International Programs. Dr. Garza-Rubalcava's post-doctoral support from the Brown University Hope St Fellowship is also gratefully acknowledged. The high-resolution mass spectrometer used to identify reaction byproducts was partially funded by National Science Foundation (NSF) Major Research Instrumentation (MRI) award CBET-1919870.

Abstract

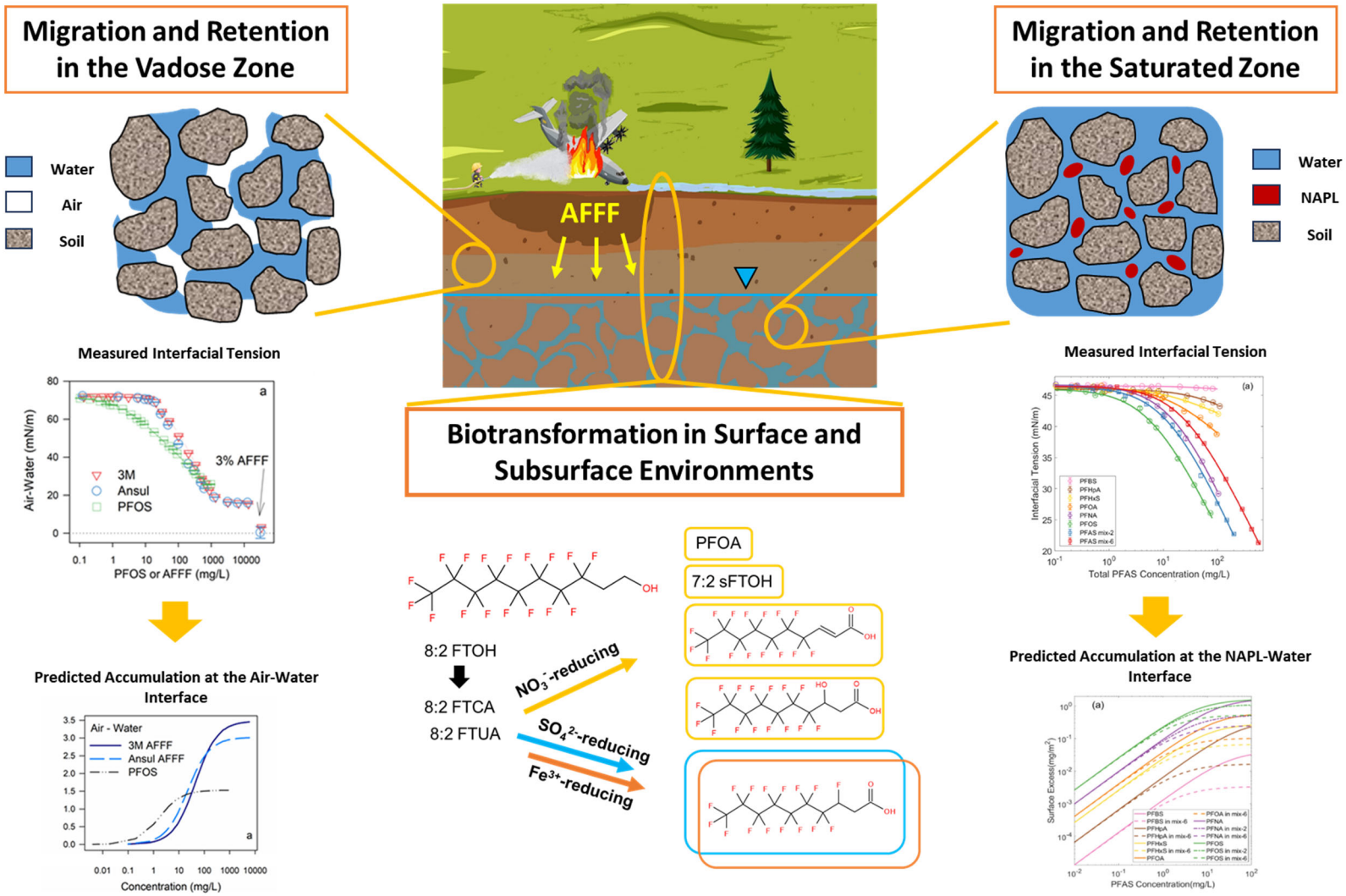
Introduction and Objectives. The repeated historic use of aqueous film forming foam (AFFF) in fire-fighting has resulted in groundwater contamination at hundreds of DoD sites, where per- and polyfluoroalkyl substance (PFAS) contamination is often commingled with hydrocarbons and solvents. This integrated experimental and modeling research was designed to address the data gaps associated with the processes that control the transport (e.g., sorption, interphase partitioning, interfacial accumulation) and (aerobic/anaerobic) transformation of PFAS in natural subsurface environments and to develop models and decision tools that could aid site managers in the assessment of PFAS mobility and persistence in complex AFFF source areas.

Technical Approach. A matrix of experiments of increasing scale and complexity was undertaken with individual PFAS and mixtures, employing reference media and natural aquifer materials collected from PFAS-impacted sites. Experiments encompassed air-water and nonaqueous phase liquid (NAPL)-water interfacial tension and soil sorption measurements, biotransformation microcosm experiments for selected PFAS precursors, and single and multiphase column transport experiments. These experiments supported the development and calibration/validation of mathematical modeling tools which were then used to explore potential PFAS transport and fate under representative field conditions and to formulate a decision matrix for use by site managers.

Results. Research findings revealed that PFAS migration is greatly influenced by interfacial processes. Air-water interfacial accumulation was shown to: (1) be a strong function of ionic strength; (2) lead to substantial mass retention in unsaturated soils; and (3) be a nonlinear function of concentration, with a limiting capacity at higher concentrations. Under conditions consistent with AFFF releases, competitive sorption effects were found to be pronounced, with more surface-active PFAS enhancing the transport of other PFAS. At AFFF field application levels, spill conditions were shown to have a strong influence on PFAS mobility and mass fluxes at the water table and to have the potential to reduce soil moisture and mobilize entrapped NAPLs. The biotransformation of three PFAS precursors, perfluoro-1-octanesulfonamide (FOSA), 8:2 fluorotelomer alcohol (8:2 FTOH), and 6:2 fluorotelomer sulfonic acid (FTS), as well as constituents of a legacy AFFF, was explored. The extent and rate of biotransformation of FOSA and 6:2 FTS were found to be strongly influenced by environmental factors, such as soil sorption capacity, availability of sulfur sources, and native microbial community composition. 8:2 FTOH was transformed rapidly by indigenous microbial communities from AFFF-impacted surface soils under aerobic conditions, and its biotransformation rates and pathways were found to be highly dependent upon redox conditions. Sixteen classes of PFAS in a historically used 3M AFFF formulation were identified, and multiple classes of ECF-based precursors and a wide range of homologues were demonstrated to be transformed under biotic and/or abiotic conditions.

Benefits. This research has improved our understanding of interfacial retention mechanisms of PFAS and supported the development/validation of mathematical models for prediction of PFAS transport at AFFF impacted sites. Representative model applications led to development of a meta-analysis table for use by practitioners that depicts the extent of correlation of important transport metrics with AFFF release parameters and site conditions. This project also improved our understanding of the potential for biotransformation of fluorotelomerization (FT)- and electrochemical fluorination (ECF)-based precursors in AFFF-impacted soils under various environmental conditions. Results provide insight into the structure-relevant stability of PFAS and a starting point for screening microbes and functional genes engaged in PFAS biotransformation.

Graphical Abstract



Executive Summary

Introduction

The repeated historic use of aqueous film forming foam (AFFF) in fire-fighting has resulted in groundwater contamination at hundreds of DoD sites, where per- and polyfluoroalkyl substance (PFAS) contamination is often commingled with hydrocarbons and solvents. In March 2023, the US EPA announced a proposed National Primary Drinking Water Regulation (NPDWR) for six PFAS, including perfluorooctanoic acid (PFOA) and perfluorooctanesulfonic acid (PFOS) at 4 ng/L. Given these stringent proposed regulatory levels, it is critical that the transport and fate of these and related compounds in the subsurface environment be understood. Several PFAS that are potential degradation precursors to PFOA and PFOS, such as perfluoro-1-octanesulfonamide (FOSA) and 8:2 fluorotelomer alcohol (8:2 FTOH), are also present in AFFF. Although considerable progress was made prior to 2019 (when this project was initiated) in advancing our understanding of perfluoroalkyl acid (PFAA) occurrence and sorption behavior, very little research focused on the retention and transformation of complex PFAS contaminant mixtures in natural porous media, particularly those that incorporated PFAA precursors. In addition, there was a paucity of laboratory experiments in flowing systemswhich could help guide the development and validation of mathematical modeling tools. This research was designed to address the data gaps associated with the processes that control the transport and transformation (natural attenuation) of complex PFAS mixtures in natural subsurface media and to develop models and decision tools that could aid site managers in the assessment of PFAS mobility and persistence. These goals directly responded to four specific objectives as outlined in the SERDP Statement of Need (ERSON-18-C1).

Objectives

The primary objectives of this integrated experimental and modeling research were: (1) to improve our understanding of sequestration mechanisms (e.g., sorption, interphase partitioning, interfacial accumulation) and abiotic/biotic (aerobic/anaerobic) transformations that control the transport and persistence of selected PFAS (including representative PFAA, as well as their precursors and transformation products) in natural aquifer materials; and (2) to develop and validate mathematical models and decision tools that describe the key processes governing transformation, transport, and retention of these selected PFAS in complex AFFF source areas.

Technical Approach

The research plan was organized around three tasks, encompassing (1) transport and partitioning experiments; (2) coupled abiotic and biotic transformation experiments; and (3) mathematical modeling and decision tool development. A matrix of batch and column experiments of increasing scale and complexity was undertaken with the selected PFASs individually and within mixtures,

employing reference media and natural aquifer materials collected from PFAS-impacted sites. Experiments encompassed air-water and nonaqueous phase liquid (NAPL)-water interfacial tension and soil sorption measurements, biotransformation microcosm experiments for selected PFAS precursors under different redox conditions, and single and multiphase transport experiments in packed sand and soil columns to explore interphase mass exchange and biotransformation processes under dynamic conditions. These experiments were designed to support the development and calibration/validation of mathematical modeling tools, for the prediction of sorption, partitioning, and natural attenuation processes under flowing conditions in natural porous media. The developed modeling tools were then used to explore potential PFAS transport and fate under representative field conditions, identified in collaboration with the Air Force Civil Engineering Center, and to formulate a decision matrix for use by site managers.

Results and Discussion

Partitioning Studies

A series of interfacial tension (IFT) measurements was undertaken and used to estimate air-water and NAPL-water interfacial accumulation for selected PFAS and PFAS mixtures over a range of environmental conditions. IFT data and associated surface excess estimates suggest that the environmental fate and transport of many PFAS, including PFOA and PFOS, is strongly influenced by accumulation at the air-water interface in unsaturated soils. The magnitude of accumulation is a function of the ionic strength of the solution, with higher total dissolved solids leading to lower IFT and higher interfacial accumulation (Figure 1). Total interfacial accumulation is directly proportional to the specific surface area of the air-water interface, which depends on the degree of water saturation and grain size distribution. For finer-grained sandy-silty media, results indicate that a large percentage of the total PFAS mass in the soil profile will reside at air-water interfaces.

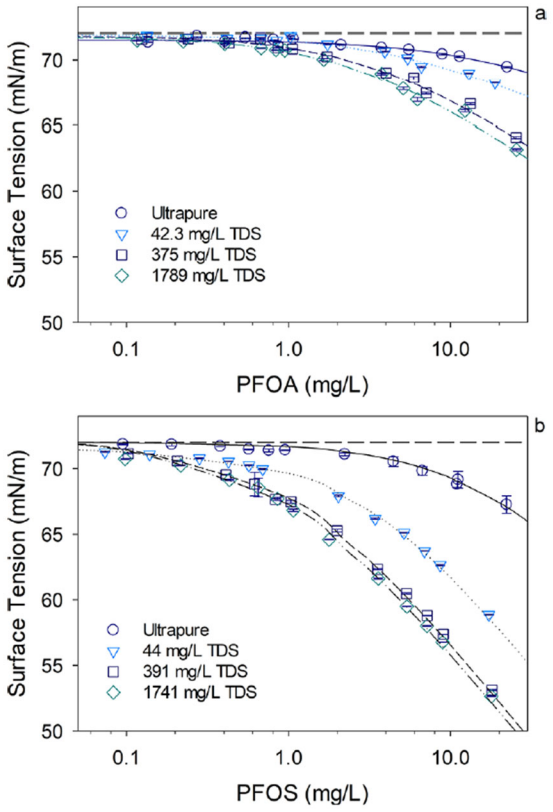


Figure 1. Air-Water surface tension of PFOA(a) and FPOS (b) reported as PFOS in solutions with major cations and anions found in groundwater. Lines are the Szyszkowski equation fit.

Compared to their influence on air-water IFT, larger concentrations of PFOA and PFOS were required for an equivalent decrease in NAPL-water interfacial tension. AFFF formulations, which

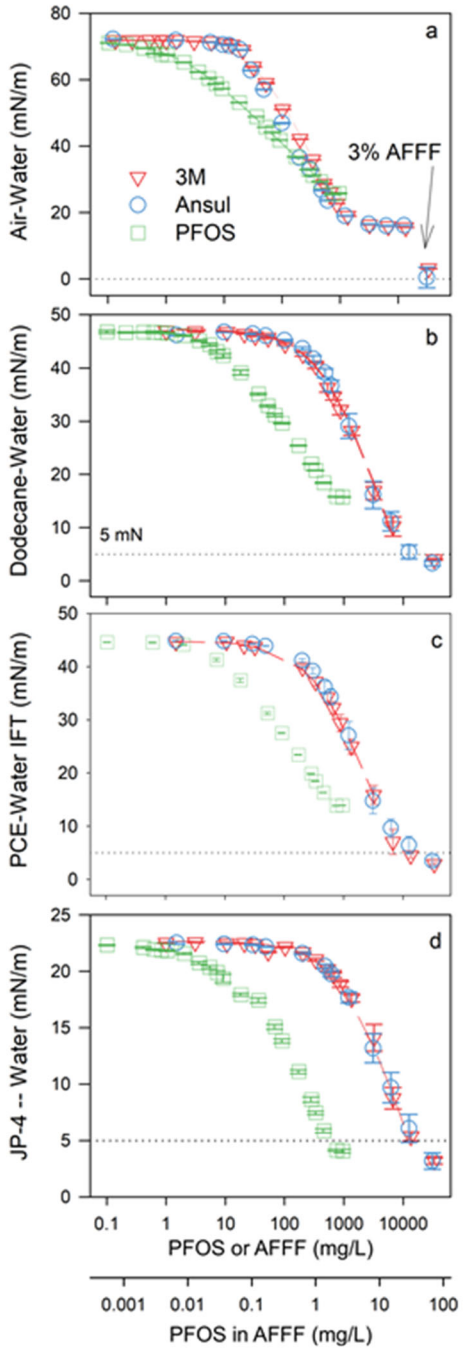


Figure 2. Interfacial tension for 3M AFFF, Ansul AFFF, or PFOS at the air-water (a), dodecane-water (b), PCE-water (c), or JP-4-Water (d) interface. Medium TDS. AFFF concentration is for total mass added. Lower x-axis indicates PFOS concentration in 3M and Ansul formulations.

contain mixtures of water, fluorocarbon and hydrocarbon surfactants, and solvents, were the most effective at reducing both air-water and NAPL-water IFT at concentrations consistent with fire-fighting applications (Figure 2). Surface excess calculations based upon these measurements reveal that, at concentrations below 1 mg/L, the majority of PFAS mass will be associated with the air-water interface, rather than the NAPL-water interface, in typical sandy soils with entrapped NAPL.

In measurements of IFT between PCE-NAPL and aqueous solutions containing individual PFAS and mixtures of PFAS, PFOS displayed the greatest interfacial tension reduction, followed by PFNA, PFOA, PFHxS, PFHpA and PFBS, confirming that both PFAS C-F chain length and functional group govern interfacial accumulation. The IFT curves for the mixture of six PFAS exhibited interfacial tension reductions that were similar to those obtained for solutions containing PFOS and PFNA alone, indicating that the more surface active PFAS controlled the behavior of the mixture. When PFAS concentrations exceeded 0.2 mg/L in the mixture, calculated surface excess decreased compared to that in single solute solutions and nonlinear isotherm behavior was very significant (Figure 3). These results suggest that competitive adsorption can lead to reduced PFAS accumulation and linear partitioning expressions are not appropriate when the total aqueous PFAS concentration is greater than some critical concentration. The critical concentrations observed for the two mixtures were within the range of PFAS concentrations observed at AFFF field sites, indicating that both competitive effects and nonlinear adsorption at the NAPL-water interface should be accounted for when describing PFAS fate and transport in AFFF-impacted source zones.

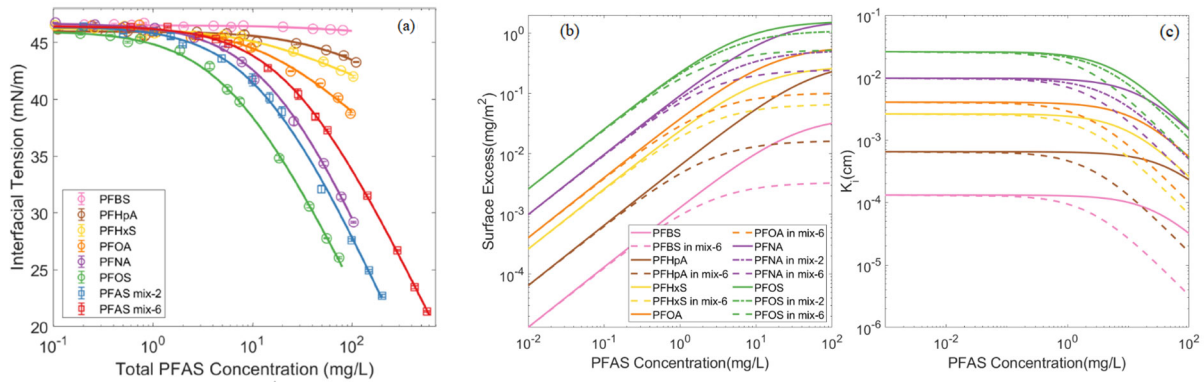


Figure 3. Interfacial tension (a) and corresponding surface excess (b) and interfacial partition coefficient (c) of PCE-NAPL and solutions containing individual PFAS, a 1:1 mixture of PFNA and PFOS (PFAS mix-2), and a mixture of six PFAS (PFAS mix-6).

Microcosm Experiments with AFFF-Impacted Soils

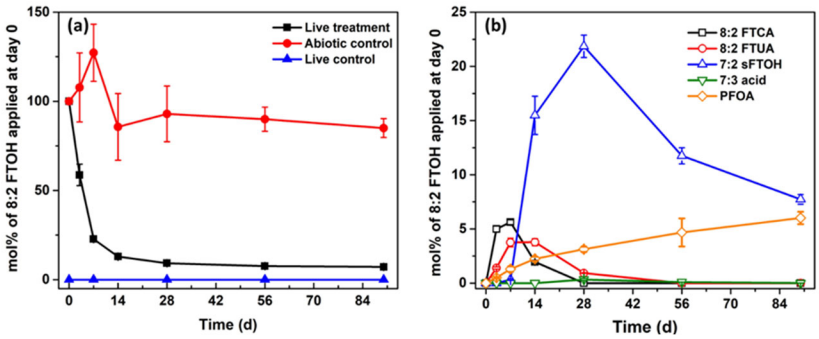


Figure 4. Profiles of 8:2 FTOH (a) and its aerobic biotransformation products (b) from the Robins biotransformation experiment. Error bars represent one standard deviation of triplicate treatments.

Three soils were used for microcosm experiments: two were collected from military sites, Robins Air Force Base (AFB) and the former Loring AFB, which were impacted by PFAS from historical application(s) of AFFF, and the third, not affected by AFFF, was collected from a location close to the Hudson River in Rensselaer County, New York. The biotransformation of three precursors, FOSA, 8:2 FTOH, and 6:2 fluorotelomer sulfonic acid (FTS), as well as constituents of a legacy AFFF, was explored.

Studies of the aerobic transformation in Loring and Hudson microcosms suggested that biotransformation of FOSA in the natural environment was soil/site dependent, with sorption capacity influencing bioavailability and variations in the native microbial community leading to different rates of biotransformation. Experiments in Loring and Robins microcosms demonstrated that 8:2 FTOH can be transformed rapidly by indigenous microbial communities under aerobic conditions. More than 90 mol% of 8:2 FTOH was removed and similar major transformation products were detected during the 90-day incubation period for both soils (Figure 4). In addition to previously documented 8:2 FTOH biotransformation products, 1H-perfluorohexane and perfluoroheptanal were identified as novel products. Results of 16S rRNA gene sequencing suggested that microorganisms in phylum proteobacteria, such as genera *Afipia* and *Sphingomonas*, may be more tolerant of high 8:2 FTOH concentrations. Microorganisms in these

two and other genera, including *Variovorax, Ralstonia, Sphingomonas, Ancylobacter*, and *Methanobacterium*, may be involved as potential degraders. Additional microcosm studies with Loring soil revealed that biotransformation rates and pathways of 8:2 FTOH are highly dependent upon redox conditions. Biotransformation was much slower under sulfate- and iron-reducing than under nitrate-reducing conditions, while the fastest biotransformation was observed under oxic conditions. The PFCAs, which were found as the terminal products of 8:2 FTOH biotransformation under oxic conditions, had less yields under nitrate-reducing conditions, and were not formed under sulfate- and iron-reducing conditions. Biostimulation (e.g., lactate amendment) was shown to increase 8:2 FTOH biotransformation rates and product yields (e.g., PFOA) in the anaerobic microcosms tested (Figure 5), implying that unintended adverse consequences (e.g. PFOA production) could arise when bioremediation is applied to treat other contaminants (e.g., chlorinated solvents) at sites where PFAS are also present.

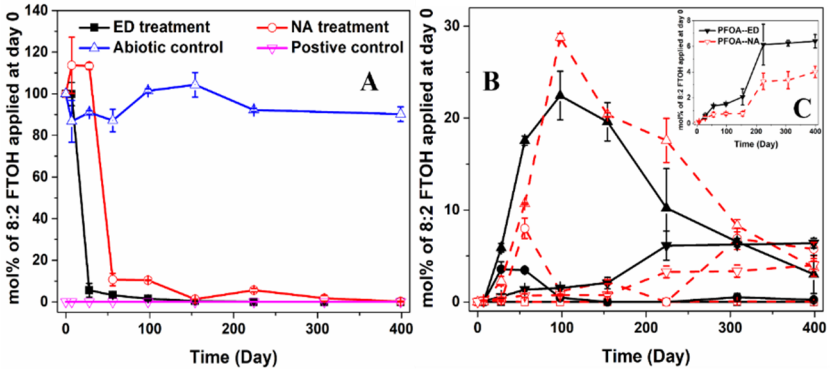


Figure 5. Changes in molar ratios of residual 8:2 FTOH during biotransformation under nitrate-reducing conditions (A). Molar yields of 8:2 FTOH biotransformation products (squares: 8:2 FTCA, circles: 8:2 FTUA, up triangles: 7:2 sFTOH, down triangles: PFOA) in the electron donor (ED) (solid black lines) and natural attenuation (NA) treatments (dash red lines) (B). Panel C is a zoom view of B, showing the time trends of PFOA molar yields.

For the aerobic biotransformation of 6:2 FTS in AFFF-impacted soils, microcosm experiments found that transformation was strongly influenced by environmental factors, such as the availability of sulfur sources and native microbial community composition. The biotransformation of 6:2 FTS was favored by the microbial consortia only after other easily assimilated sulfur sources (e.g., sulfate) were depleted and Desulfobacterota microorganisms likely promoted 6:2 FTS biotransformation via more efficient desulfonation. By identifying additional 6:2 FTS transformation products that were previously undocumented, a novel "fluorotelomer ketone to PFCA" pathway was proposed to account for the formation of PFCAs (Figure 6).

Microcosm experiments were also conducted over a 308-day period to explore the aerobic biotransformation of PFAS mixtures present in a legacy 3M AFFF. Results demonstrated that multiple classes of electrochemical fluorination (ECF)-based precursors are susceptible to abiotic and/or biotic transformation for a wide range of homologues (C_4-C_8), suggesting that these precursors could be sources of PFAAs at historical AFFF-impacted sites. Transformation products include C_3-C_6 and C_8 FASA, C_6 M-AmPr-FASA, C_4 and C_6-C_8 OAmPr-FASA, C_6 N-MeFASAA, C_6 N-EtFASAA, C_5-C_7 OAmPr-FAAd, as well as C_3-C_6 PFSAs and C_4-C_6 PFSAs. Here, "C_n"

represents the number of perfluorinated carbons in each compound. This study provides the first evidence of the biotransformation of AmPr-FASA-PrA/TAmPr-FASA-AA and CEt-AmPr-FAAd. Additionally, the 16S rRNA gene sequencing data from 8:2 FTOH and 6:2 FTS biotransformation studies under various redox conditions was gathered to gain insights into the structure and function of soil microbial communities relevant to fluorotelomerization (FT)-based PFAS biotransformation. Through co-occurrence network analysis, several genera, such as *Variovorax*, *Rhodococcus*, and *Cupriavidus*, were found to likely play important roles in the biotransformation of fluorotelomers. Using a metagenomic prediction approach, functional genes, both previously reported associated with fluorotelomer biotransformation and not yet reported, were identified to be potentially involved in the biotransformation.

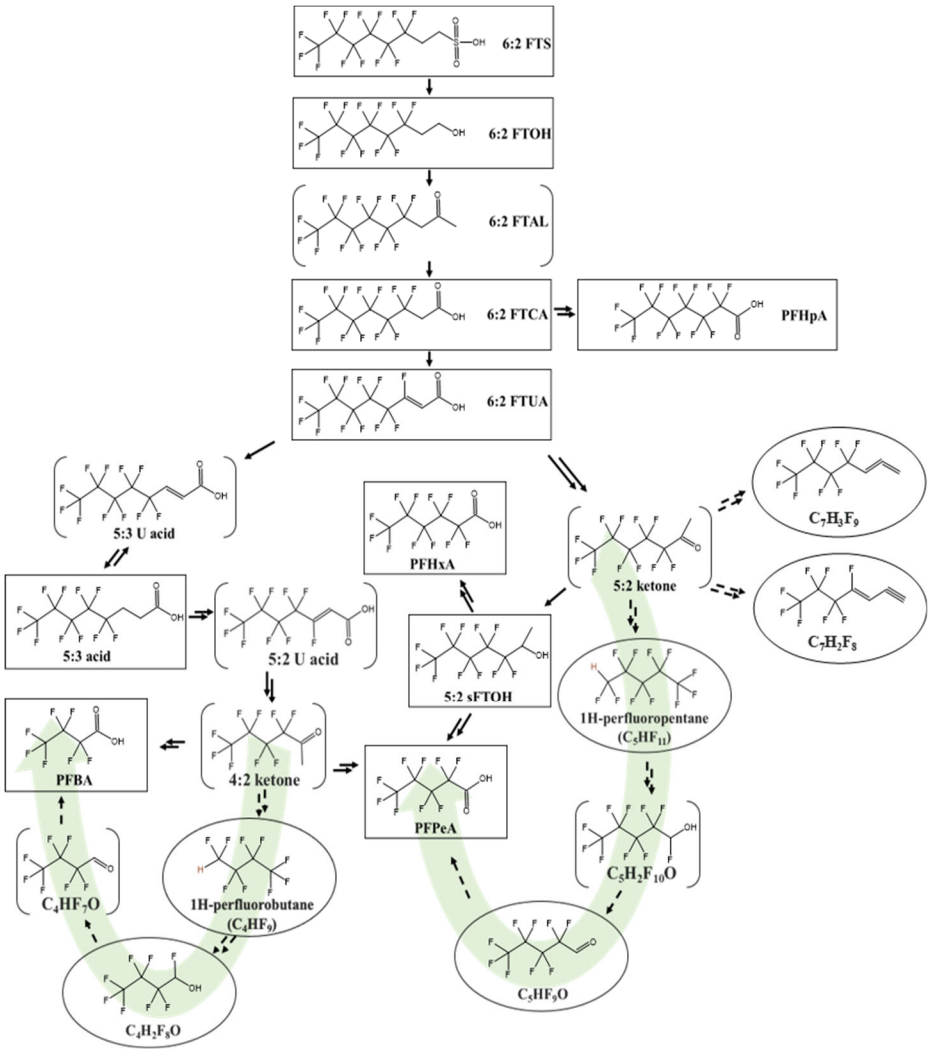


Figure 6. Proposed aerobic biotransformation pathways of 6:2 FTS in AFFF-impacted soils. The Compounds in rectangular and oval boxes were detected by LC-MS/MS and non-targeted LC-HRMS analysis, respectively. Compounds in the brackets are proposed transformation products (not detected in this study). Solid arrows represent the biotransformation steps expected to occur based this and previous studies. Dashed arrows represent the proposed reactions and double arrows represent multiple enzymatic steps. Curved arrows in green illustrate the novel "fluorotelomer ketone to PFCA" pathway proposed.

Column Studies

Experiments were conducted to investigate interactions between AFFF and three representative NAPLs (JP-4, TCE and PCE), and to assess the potential for AFFF to enhance the solubility and mobility of NAPLs in porous media. Batch reactor measurements indicated that the presence of

AFFF was associated with only a minor increase in the aqueous solubility of TCE and PCE at concentrations typical of fire fighting applications, suggesting that AFFF does not form traditional surfactant micelles in aqueous solution over that concentration range. IFT measurements revealed that AFFF accumulates at the NAPL-water interface and can result in IFT reductions below 3 mN/m at a field application concentration of 3 wt %. Column experiments were then conducted to determine if the observed IFT reductions were sufficient to mobilize three NAPLs (JP-4, TCE and PCE) at residual (entrapped) saturation. Partial mobilization of all three NAPLs was observed following the injection of 3 wt% AFFF solution, which resulted in NAPL saturation reductions of 0.7-2.0% and 0.3-1.3% in 20-30 mesh and 60-80 mesh Ottawa sands, respectively. Using the density, viscosity and interfacial tension measurements of the displacing solutions and porous media properties, the total trapping number (N_T) was used to construct NAPL desaturation curves. These results demonstrate that, for a field application concentration of AFFF, partial mobilization and redistribution of NAPLs may occur, and that the total trapping number approach can be used to estimate, *a priori*, the extent of NAPL mobilization based on site specific conditions.

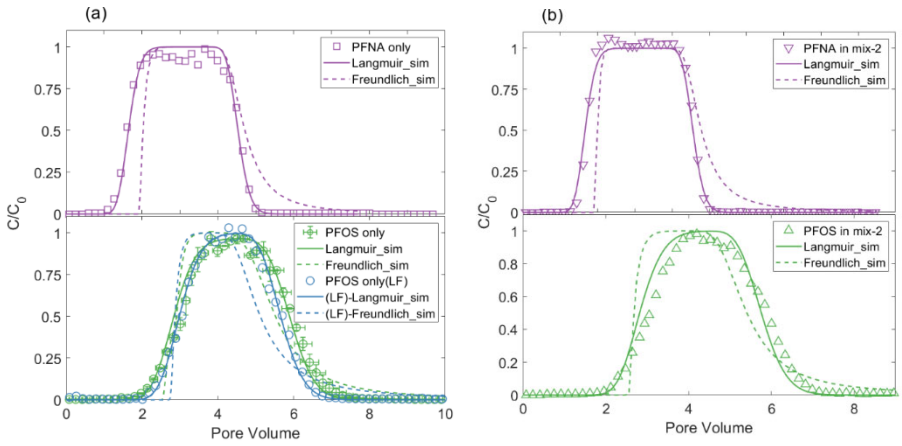


Figure 7. Measured and simulated effluent breakthrough curves obtained for (a) PFNA only and PFOS only columns and (b) 1:1 PFNA and PFOS binary mixture column at residual PCE-NAPL (~16%). Error bar indicates standard deviations in duplicate column for PFOS only.

Additional column experiments were conducted to explore the transport and retention of single PFAS and PFAS mixtures in sandy media in the presence of entrapped PCE-NAPL. Results demonstrated that accumulation of PFNA and PFOS at the NAPL-water interface can strongly influence PFAS transport and retention behavior, whereas partitioning of PFNA and PFOS into the NAPL was of relatively minor importance under the experimental conditions evaluated. The short chain PFAS investigated (i.e., PFBS, PFHpA), PFHxS, and PFOA, however, were highly mobile, even in the presence of residual NAPL. Nearly identical breakthrough curves (BTCs) were observed for PFAS as single solutes or in mixtures, indicating that competitive adsorption effects at the NAPL-water interface are unlikely to impact PFAS transport behavior at most sites where aqueous phase concentrations are below approximately 100 µg/L. A modified version of the HYDRUS-1D model, which accounted for entrapped NAPL and nonlinear and rate-limited adsorption processes for multiple solutes, was able to accurately capture the observed transport behavior for up to six PFAS using a Langmuir-Syzszkowsi isotherm to

model interfacial accumulation. Simulation results also demonstrated that use of a Freundlich isotherm is not suitable for characterization of PFAS NAPL-water interfacial adsorption at lower concentrations (Figure 7). This work furthers our understanding of PFAS transport and retention processes in the presence of NAPLs and provides a mathematical tool for predicting PFAS transport at co-contaminated sites.

The transport and transformation of 6:2 FTS under aerobic conditions was investigated in 305-day column experiments. Here biotransformation was demonstrated to be rate limited, controlled by the flow conditions. By decreasing pore-water velocity from 3.7 to 2.4 cm/day, concentrations of 6:2 FTS in column effluents decreased by 21.7-26.1%. Correspondingly, the yield of late-stage biotransformation products, C_4-C_7 perfluoroalkyl carboxylates, increased (1.0-1.4 mol% vs. 0.3 mol%). Flow interruptions (2- and 7-day durations) were found to enhance the biotransformation of 6:2 FTS over 6-7 pore volumes following the resumption of flow. Additionally, by comparing 6:2 FTS biotransformation in the columns to prior microcosms, the system scale, solid-to-water ratio and/or flow conditions likely impacted the biotransformation rate as well as pathways. These findings highlight the importance of accounting for field conditions (e.g., hydraulic parameters) in the assessment of PFAS fate and transformation in natural environments.

Field-Scale Model Applications and Decision Tool Development

A mathematical model for PFAS transport and retention in multiphase subsurface systems was developed, tested, and refined using the data collected in the partitioning and column experiments described above. This model was implemented through modification of a commercial unsaturated flow and transport simulator (HYDRUS-1D). The enhanced model was then applied to a matrix of PFAS spill scenarios to explore the implications of research findings at the field scale. Scenarios were located at three different USAF installations (two scenarios in Wright-Patterson AFB, OH; one scenario in Tyndall AFB, FL; and two scenarios in Ellsworth AFB, SD) , selected from the Administrative Record as representative of a range of subsurface and climatic conditions across the continental US. Spill conditions, encompassing periodic and one-time AFFF release events, associated with fire training, accidental spills, and emergency applications, were developed based on the variety of actual spills that have occurred at military installations. Site-specific climatic and geological parameters were obtained for actual locations where PFAS contamination had occurred. Simulations were conducted for a 40-year time horizon. AFFF was modeled as a three-component mixture of PFOS, PFOA, and a hydrocarbon surfactant. The simulations incorporated competitive interfacial accumulation effects and associated moisture release. Model outputs included a time series of profiles of moisture content, total PFAS concentrations, and air-water interfacial areas, as well as average mobile-immobile mass ratios and mass fluxes and aqueous concentrations at the water table. A comparison of site-specific model simulations to measured soil concentration data at one fire-training site at Ellsworth AFB revealed that simulated concentrations were generally consistent with ranges of measurements at the same depths. Analyses of model simulations suggest that: (1) interfacial accumulation and soil sorption account for the large

majority of the PFAS mass in the soil profile (i.e., the aqueous phase concentration is not representative of the extent of PFAS contamination); (2) seasonal fluctuations in recharge can lead to oscillations in the distribution between sorbed and interfacial PFAS mass; (3) PFOA is more mobile than PFOS, attributed to differences in sorption and interfacial accumulation properties; (4) under low saturation (dry conditions), interfacial areas are high and PFAS penetration rates are low; (5) the presence of hydrocarbon surfactants in AFFF tends to increase the rate of migration of PFOA and PFOS; and (6) spill conditions (e.g., total mass released and periodicity) have a significant impact on PFAS mobility in the vadose zone, as well as on the maximum concentrations reaching the water table.

Figure 8 presents a meta-analysis in tabular form of model results for PFOS transport in the five soil scenarios within three AFBs mentioned above. Here the degree of correlation of model outputs to model input parameters is indicated for each input-output pairing (a similar figure in the report demonstrates PFOA generally exhibits similar behavior). The degree of correlation shown in this figure may help site managers understand the influence of site parameters on important site characteristics and help guide future remedial site management decision making. For example, sites with a higher variance in permeability are expected to have more PFAS mass in the mobile zone, but the rate of contaminant migration vertically through the vadose zone may be slowed.

OUTPUT / INPUT	Time to Reach Water Table	Max Conc at Water Table	Total Mass/Area at Water Table	Ratio of Mobile to Immobile Mass	Rate of Migration of Center of Mass
Total Mass Spill per Area	0	+	++	+	0
Depth to Water Table	++	-	-	0	- -
Avg Permeability	-	+	+	-	++
Avg Variance in Permeability	-	0	0	++	-
Avg Freundlich Parameter	++	-	- -	-	- -
Avg Net Recharge	- -	++	++	0	++

Figure 8. Meta-analysis of model results for PFOS transport in five soil scenarios within three AFBs. Symbols span from a strong positive correlation (++) through no apparent relationship (0) to a strong negative correlation (--).

Implications for Future Research and Benefits

Research findings from this project revealed that, unlike many other classes of organic contaminants, PFAS migration, retention, and attenuation in the subsurface is strongly influenced by interfacial processes, particularly air-water interfacial accumulation. Futhermore, at the higher PFAS concentrations associated with AFFF releases, the presence of PFAS mixtures, as well as hydrocarbon surfactants, can greatly impact PFAS migration and retention. The research in this project was conducted in laboratory scale, homogeneously packed columns under uniform flow conditions. Therefore, future work should focus on: (1) the development and validation of models for the prediction of interfacial areas from easily measurable soil properties; (2) the collection of data and modeling of sorption and IFT reduction behavior for individual PFAS in PFAS mixtures; (3) the laboratory assessment and modeling of PFAS behavior in the unsaturated zone and capillary

fringe under dynamic recharge conditions; and (4) controlled AFFF release experiments in large-scale heterogeneous formations.

This project has improved our understanding of the potential for biotransformation of FT- and ECF- based precursors in AFFF-impacted soils under various environmental conditions. These results also provide insight into the structure-relevant stability of PFAS and a starting point for screening microbes and functional genes engaged in PFAS biotransformation. Future work in this area should focus on: (1) assessing the prevalence of novel biotranformation products identified in this research at AFFF-impacted sites and on their environmental impacts and fate; (2) isolating individual bacterial strains associated with identified phyla and genera potentially responsible for the biotransformation of PFAA precursors and determining the functional gene(s)/enzymes responsible for defluorination; and (3) assessing PFAS biotransformation in dynamic laboratory experiments of increasing scale and complexity.

1. Objectives

The use of aqueous film forming foam (AFFF) in fire suppression over many decades has resulted in contamination of hundreds of Department of Defense (DoD) fire training areas with per- and polyfluoroalkyl substances (PFASs), often in the presence of chlorinated solvent and fuel hydrocarbon co-contaminants. Although PFAS groundwater contamination source areas typically exist as complex chemical mixtures, as of the commencement of this research, few studies had examined the mechanisms controlling partitioning, interfacial accumulation, or sorption/desorption processes and rates in such mixtures. Furthermore, despite a demonstrated potential for defluorination, the biotransformation of PFASs under conditions representative of natural groundwater systems remained largely unexplored. In addition, there was an absence of PFAS transport and transformation studies in flowing systems, which are necessary for the development and validation of predictive mathematical modeling tools.

The primary objectives of this integrated experimental and modeling research were to: (1) to improve our understanding of sequestration mechanisms (e.g., sorption, interphase partitioning, interfacial accumulation) and abiotic/biotic (aerobic/anaerobic) transformations that control the transport and persistence of selected PFASs (including representative perfluoroalkyl acids, as well as their precursors and transformation products) in natural aquifer materials; and (2) to develop and validate mathematical models and decision tools that describe the key processes governing transformation, transport, and retention of these selected PFASs in complex AFFF source areas.

The research plan was organized around three Tasks, encompassing (1) transport and partitioning experiments; (2) coupled abiotic and biotic transformation experiments; and (3) mathematical modeling and decision tool development. A matrix of batch, column, and aquifer cell experiments of increasing scale and complexity was undertaken with the selected PFASs individually and within mixtures, employing reference media and natural aquifer materials collected from PFAS-impacted sites. These experiments were designed to support the development and calibration/validation of mathematical modeling tools, designed to predict sorption, partitioning, and natural attenuation processes under flowing conditions in natural porous media. The modeling tools were then used to explore potential PFAS transport and fate under representative field conditions, identified in collaboration with the Air Force Civil Engineering Center, and to develop a decision matrix for use by site managers.

2. Background

2.1 PFAS contamination at AFFF source areas

Aqueous film forming foams (AFFFs) were developed in the 1960s as a fire-extinguishing medium for flammable liquid pool fires. In the 1980's, the military sector comprised 75% of the total AFFF product market [1]. Although production of sulfonamide-containing AFFF by 3M ceased in the early 2000s [2], the military continued to use these stockpiled compounds for fire-fighting training until very recently and also began using fluorotelomer-based AFFFs. Commercial AFFF formulations are complex proprietary mixtures typically composed of a solvent, fluorocarbon surfactants, and hydrocarbon-based surfactants [1]. To add to this compositional complexity, AFFFs were usually used in conjunction with flammable liquids, i.e., mixed nonaqueous phase liquids NAPLs (e.g., fuels and chlorinated solvents) Thus, the repeated historic use of AFFF in fire-fighting has resulted in groundwater contamination at hundreds of DoD sites [3], where per- and polyfluoroalkyl substance (PFAS) contamination is often commingled with hydrocarbons and solvents [4, 5].

In May 2016, the U.S. Environmental Protection Agency (USEPA) issued a drinking water health advisory of 0.07 µg/L for two persistent PFASs, the perfluoroalkyl acids (PFAAs) perfluorooctanoic acid (PFOA) and perfluorooctanesulfonic acid (PFOS), both of which are mobile in aquifer formations. Based upon toxicology research in the intervening years since this project began, this EPA advisory has recently been updated (June 15, 2022) to .004 nanograms per liter (ng/L) (PFOA) and 0.02 ng/L (PFOS). At the same time, USEPA also issued final health advisories for perfluorobutane sulfonic acid and its potassium salt (PFBS) and for hexafluoropropylene oxide dimer acid (HFPO-DA), commonly known as GenX Chemicals, which are considered as replacement chemicals for PFOS, and PFOA, respectively. Following this interim advisory, on March 14, 2023, EPA announced a proposed National Primary Drinking Water Regulation (NPDWR) for six PFAS, including the above four (with PFOA and PFOS at 4 ng/L) as well as perfluorononanoic acid (PFNA) and perfluorohexane sulfonic acid (PFHxS).

Given these stringent proposed regulatory levels, it is critical that the transport characteristics of these and related compounds be understood. Several PFASs that are potential degradation precursors to PFOA and PFOS, such as perfluoro-1-octanesulfonamide (FOSA) and 8:2 fluorotelomer alcohol (8:2 FTOH), are also present in AFFFs [6, 7]. A number of studies have suggested that anomalous field observations of PFAA concentrations could be explained by the abiotic or biotic transformation of the nonfluorinated part of the molecule attached to the perfluorinated chain of such precursors (e.g., [5, 8]). Unfortunately, relatively little was known about the sorption, partitioning, and transformation behavior of these precursors in natural groundwater systems [9]. Although considerable progress was made prior to 2019 (when this project was initiated) in advancing our understanding of PFAA occurrence and sorption behavior

(e.g., [5, 10]), very little research focused on the retention and transformation of complex PFAS contaminant mixtures in natural porous media, particularly those that incorporated PFAA precursors. In addition, there was a paucity of laboratory experiments in flowing systems, that could help guide the development and validation of mathematical modeling tools. This research was, thus, designed to address the data gaps associated with the processes that control the transport and transformation (natural attenuation) of complex PFAS mixtures in natural subsurface media and to develop models and decision tools that will aid site managers in the assessment of PFAS mobility and persistence. These goals directly responded to the following four (of five) specific objectives as outlined in the SERDP Statement of Need (ERSON-18-C1):

a) Increase understanding of the key characteristics of AFFF source zone areas (vadose zones and/or saturated zone source areas) that affect the risk that PFASs pose to groundwater quality.
b) Investigate the nature and permanence of PFAS retardation mechanisms, and the potential use of these mechanisms in natural or enhanced attenuation.
c) Fill key data gaps regarding the biotransformation and transport of PFASs in AFFF source zones.
d) Develop analytical or mathematical tools to predict the fate and impacts of PFASs in source zones and the potential for continuing releases to groundwater plumes.

2.2 Interfacial processes and interphase mass transfer

Due to their amphiphilic properties, many PFAS tend to strongly accumulate at fluid-solid and fluid-fluid interfaces in natural subsurface environments. For example, PFOA and PFOS are water soluble substances that exhibit the unique property of spontaneously concentrating at the air-water interface [11]. This rapid transfer of PFOA or PFOS from bulk water to air-water interfaces can be used to remove [12] or degrade [13] these substances, and also has implications for their fate and transport in contaminated source areas. For example, the mass of PFOA concentrated at the air-water interface, rather than adsorbed to solids, was reported to be a major sink for the retention of PFOA in flow-through columns containing quartz sand, with water saturations ranging from 0.68 to 0.86 [14, 15]. Because PFAS typically contaminate surface soils through fire training, equipment maintenance, or emergency response activities [1, 16], they may remain entrained at air-water interfaces in the vadose zone [17-19], serving as a long-term source of contamination to the underlying groundwater.

The surface excess of a surfactant is proportional to the decrease in water cohesion (i.e., surface tension), associated with the increase in bulk water concentration (i.e., Gibbs surface excess). It is well established that the surface tension of PFOA and PFOS depends on the counterions of their respective salt formulations [20]. Given that surface tension is influenced by the counterion of the salt formulation, the dissolved cations and anions present in groundwater could also affect the surface tension and, potentially, the surface excess of PFOA and PFOS [21, 22]. Although experiments employing PFOA or PFOS alone or in combination are important, the results of such

studies may not be applicable to conditions at sites where AFFF was released. This is due to the fact that commercial AFFF formulations consisting of complex proprietary mixtures, typically composed of fluorocarbon (e.g. PFOS) and hydrocarbon surfactants along with solvents [23]. The combination of fluorocarbon and hydrocarbon surfactants in AFFF has a synergistic effect that could increase the concentration of these surfactants at the NAPL-water interface [20]. Research described herein (**Section 4.1.1**) focuses on determining the surface excess for representative PFAS and AFFF at concentrations of environmental relevance in water containing the most common anions and cations found in groundwater. These observations also support the development relationships for estimating/predicting the concentration of these PFAS at the air-water interface (i.e., surface excess) as a function of bulk-water concentration and solution conditions. Such relationships, along with an understanding of the air-water interfacial area, will be required to simulate the fate and transport of these substances in unsaturated subsurface environments and to estimate the potential mass stored in the vadose zone.

In addition to retention at air-water interfaces, NAPL-water interfaces may also play a role in PFAS retention in contaminated source areas. At fire training sites where organic liquid fires were extinguished using AFFF, wastewater containing a mixture of AFFF and residual free fuel along with emulsified fuel was generated and often discharged to surface soils [24-27]. Since the fuel was composed of non-aqueous phase liquids (NAPLs), the release of this wastewater resulted in multi-species, multi-phase contaminated source areas and associated groundwater plumes [1, 25, 26, 28]. Thus, in addition to the air-water interface, there is a potential for PFAS to concentrate at NAPL-water interfaces [10, 29, 30].

When released to the subsurface, NAPLs can be retained in soil pores as immobile droplets or ganglia due to capillary forces and may also accumulate as "pools" above layers of low-permeability porous media [31]. The retained NAPL can slowly dissolve into infiltrating surface water or flowing groundwater, thereby serving as a long-term source of aquifer contamination [32-34]. Traditional surfactants, which have been used to recover NAPLs from the subsurface, have the capacity to increase the aqueous solubility of NAPLs due to micellar solubilization and to mobilize entrapped NAPL due to reductions in the NAPL-water IFT [35-38]. Because AFFF contains a mixture of surfactants, it could reduce NAPL-water interfacial tension (IFT) and enhance NAPL aqueous solubility, potentially mobilizing and redistributing NAPL contaminant mass under field-applied concentrations of AFFF (e.g., 3 or 6% wt.). Potential evidence of this phenomena is described by [39] who observed up to 3 feet of JP-4 jet fuel at Tyndall Air Force Base in Florida associated with firefighting exercises and AFFF use. Here, the distribution of AFFF and JP-4 was found outside the expected zone of influence of the petroleum hydrocarbon plume.

Chen et al. conducted a series of batch reactor experiments with PFOS and soil contaminated with crude oil to investigate PFAS behavior in NAPL-impacted soils [40]. The adsorption of PFOS by oil-contaminated soil was found to be approximately one order-of-magnitude greater than for soil organic matter alone regardless of solution chemistry (i.e., pH and Ca^{2+} concentration), suggesting

oil could be an important sink for PFOS. Guelfo et al. performed batch experiments using TCE-NAPL amended soils and 13 organofluorine compounds commonly found in AFFF formulations [10]. Their results showed that the impact of NAPL on PFAS adsorption was more evident when the soil organic carbon content was low (f_{oc} = 0.017). McKenzie et al. conducted a column experiment to evaluate the effect of residual TCE-NAPL on the transport of a suite of PFAS (each at 2 µg/L) in loamy sand [9]. They reported increased retention of several PFAS (carbon chain length >6) when TCE was present but did not directly investigate specific retention mechanisms (e.g., partitioning and/or interfacial adsorption). To delineate the potential contributions of these two mechanisms on PFAS retardation, Glubt and Brusseau conducted column transport experiments with PFOS and PFOA and two NAPLs (dodecane and TCE) in a quartz sand [41]. Although adsorption at the NAPL-water interface was shown to play an important role in PFOS and PFOA retardation, the aqueous phase concentrations used in these column experiments (10 and 25 mg/L) were substantially higher than those typically observed at most PFAS-contaminated sites, which usually do not exceed 100 µg/L [1, 4, 42]. Since interfacial accumulation of PFAS is known to be a nonlinear, concentration-dependent process [43], evaluation of PFAS-NAPL interactions at environmentally relevant concentrations is needed. Additionally, because PFAS are almost always found as mixtures in contaminated soil and groundwater, it is important to investigate the transport behavior of PFAS mixtures in presence of NAPL.

To assess the contributions of multiple processes to PFAS retention in soils and aquifer materials, Brusseau et al. developed a mathematical model [22, 29] that accounts for PFAS partitioning and interfacial adsorption to NAPL phase. Glubt and Brusseau used this model to obtain retardation factors (R_F) for PFOS and PFOA in the presence of residual NAPL, and reported that most of the predictions matched the R_F values obtained from column effluent BTCs [41]. Although this model provides a method (i.e., retardation factor) to estimate PFAS transport potential, the approach is based on the assumption of linear adsorption at the NAPL-water interface, using a single (applied) concentration to obtain interfacial adsorption coefficient (K_i) values. Thus, there is a need to develop a mathematical model that accounts for the effects of nonlinear interfacial adsorption processes on PFAS transport in the presence of NAPL.

In this research, experiments were undertaken to measure the IFT between representative NAPLs (chlorinated solvents and petroleum hydrocarbons) and PFAS/AFFF solutions under a range of conditions representative of natural groundwater environments, and to explore the potential impact of IFT alteration on the migration and redistribution of NAPLs in packed sand columns. These measurements were also employed to develop equations to predict surface excess concentrations of PFAS and AFFF at NAPL-water interfaces, as well as the onset and extent of NAPL mobilization, which can be used to model the transport and distribution of perfluorooctane mass in subsurface environments. (see **Sections 3.6.1** and **4.1.2**)**.** The mathematical model was then independently validated through a series of detailed column transport studies with emplaced residual NAPL (**Section 4.3.1** and **4.3.2**).

Precursors may exhibit a strong affinity for soil and aquifer solids due to the presence of anionic, cationic, and zwitterionic alkyl moieties, and many are likely to undergo ion exchange processes and/or partition to soil organic matter [9]. In addition, previous research has demonstrated that PFAS sorption is influenced by the presence of co-contaminants, such as NAPLs and non-fluorinated surfactants ([6], [10]). Although some sorption isotherms have been measured for representative PFASs, very few studies have looked at in situ sorption/desorption rates (e.g., [11]). The complexity of the sorption mechanisms and the limited data suggest that simple linear equilibrium distribution coefficients (Kd) based upon soil organic carbon-water partitioning coefficient (Koc) measurements will not capture transport behavior (e.g., [12]).

2.3 Biotransformation

Previous laboratory studies have demonstrated the potential biotransformation products of PFAA precursors found in AFFF under different redox conditions. The majority of these biotransformation studies have been conducted with single compound fluorotelomer precursors under oxic conditions, utilizing bacteria from: activated sludge reactors [44, 45], aerobic surface soils [46-50], aerobic bacterial enrichments [48, 51], and soil from an AFFF site [52]. Additionally, two fluorotelomer precursors were also found to transform under methanogenic conditions utilizing anaerobic digester sludge [53] . Another study with river sediments found that a fluorotelomer precursor was not readily degraded under sulfate-reducing conditions with a terminal sulfonate group (-SO3-), while those with a terminal hydroxyl group (-OH) were transformed [54]. In each of these fluorotelomer precursor studies, perfluorinated carboxylates (including PFOA) were observed as minor products (i.e., <11% of PFAA precursor transformed) with intermediate fluorotelomer products over the two- to three-month duration of the experiment. The biotransformation of sulfonamide-containing precursors with structures similar to those found in AFFF formulations manufactured by 3M has been investigated in limited studies utilizing activated sludge [55, 56] and marine sediments [57]. In these studies, completed under aerobic conditions, PFOS accounted for the transformation of 0.6-40% of the perfluorooctane sulfonamide (FOSA)-containing precursors. These findings indicate that: (1) biotransformation of PFAA precursors under aerobic conditions often results in partial yields of PFAAs, and (2) despite this potential for defluorination [58, 59], the biotransformation of PFAA precursors under anaerobic conditions remains largely unexplored.

To the best of our knowledge, only one microcosm study to date has utilized soils from an AFFF-impacted site [52]. Subsurface microbial communities, however, differ from those found in wastewater treatment plant activated sludge, river sediment, and aerated surface soil. Within an aquifer environment, geochemical conditions, such as redox, pH, ionic strength, and reactive mineral species, also differ from those encountered in high organic sediments, sludges, or surface soils. Hypothesis: Biotransformation of PFAA precursors will differ between experimental systems established with activated sludge or surface soils and aquifer materials, leading to different transformation byproducts, pathways and rates. In addition, co-contaminants such as chlorinated

solvents and petroleum hydrocarbons, typically encountered at AFFF facilities, will likely influence natural attenuation processes. Understanding these abiotic and biotic subsurface processes is crucial because the potential for PFAA bioaccumulation increases with the length of the perfluorinated chain [60]. Microbial defluorination of PFAA precursors, which could reduce the length of the perfluorinated chain could, thus, result in diminished PFAS bioaccumulation potential.

2.4 Transport modeling

Prior to 2018, most PFAS partitioning and transformation experiments focused exclusively on batch systems. The only published packed-column studies were conducted to explore the potential effect of specific treatment technologies (i.e., in situ chemical oxidation) on PFAA mobility and decomposition [9, 61]. In these studies, experiments were conducted with a single porous medium material (loamy sand) and a fixed-composition PFAA mixture under one set of flow conditions. Thus, there were no systematic investigations of PFAS transport in natural porous media under varying flow conditions. In addition, few published studies on PFAS transport prior to 2018 incorporated a mathematical modeling component. Those that did seek to model field or laboratory observations Typically implemented simple linear (equilibrium) sorption [5, 61] and NAPL partitioning [9] expressions, with no attempt to account for nonlinearities, the competitive or synergistic influence of co-constituents, rate-limited mass transfer, or formation heterogeneity.

A number of modeling studies, based upon the solution of coupled aqueous phase flow and PFAS transport equations, have explored the field-scale migration of PFAS in the vadose zone. Guo et al. [62] proposed a 1-D model to simulate the transport of PFOS in two types of media (sand and soil) under two types of climatic conditions (semiarid and humid). They simulated a periodic release of PFOS and predicted a mass retention of >70% at the air-water interface, which resulted in low migration rates. An alternative approach was presented by Silva et al. [63, 64], who modified a commercial simulator (HYDRUS [65]) to include accumulation at the air-water interface and the influence of surface-active substances on moisture retention curves. Their work, which explored the extent of interfacial and solid phase sorption, suggested that accumulation at the air-water interface is less important in media containing solids with high sorption capacity. Later efforts by Zeng et al. [66, 67] considered both 1-D and 3-D models for the flow-transport problem in homogeneous and heterogeneous systems. Their simulations suggested that retention in the vadose zone was correlated with PFAS chain length and demonstrated the critical influence of soil heterogeneity on the migration process. The modeling study of Wallis et al. [68] also highlighted the importance of soil lithology, but their work suggested that net recharge due to precipitation and evaporation is the key process controlling the retention of PFAS in the vadose zone.

Although the research presented above provides a framework for prediction of the transport of PFAS in impacted areas, there is a need for additional modeling efforts that consider the influence of AFFF release conditions on vadose zone transport within realistic soil horizons under natural

climatic conditions. Furthermore, recent studies have shown that surface-active compounds compete for sites at the air-water interface, which can cause anomalous transport behavior in unsaturated porous media [69-72]. Therefore, to produce realistic predictions of PFAS transport in affected areas it will be important to account for simultaneous presence of other surface-active compounds within the AFFF mixture.

Given the complexity of the processes controlling PFAS transport and retention in multiphase source zone mixtures (as highlighted above), it is clear that mathematical models will be indispensable to the interpretation of laboratory experiments and to the development of a conceptual understanding of these systems. In this research, a comprehensive multiphase, multicomponent mathematical model was developed and implemented to predict the migration and retention of PFAS mixtures in natural saturated and unsaturated porous media over a range of environmental conditions. The model was parameterized and partially validated with the batch and column experiments described herein (**Section 3.1**) and then employed to simulate AFFF release scenarios over a range of representative climatic/geologic conditions, representative of DoD AFFF source areas across the US (**Section 3.6.2** and **4.5**). Selected simulations were also compared with available field measurements to qualitatively assess model outputs (**Section 4.5.1.3**). Model simulations then formed the basis for the development of a decision matrix (**Section 4.5.2**) to support in decision-makers in PFAS site prioritization and management.

3. Materials and Methods

3.1 Batch Studies

3.1.1 PFAS Accumulation at the Air-Water Interface

The research described herein focused on determining the surface excess for PFOA and PFOS at concentrations of environmental relevance and in water containing the most common anions and cations found in groundwater. Surface excess was determined by measuring the air-water surface tension for PFOA and PFOS at concentrations ranging from 0.1 to greater than 1,000 mg/L in solutions containing anions and cations at the concentrations and ratios found in the principle aquifers in the United States. The surface tension data were fit to the Szyszkowski equation [73] to describe the surface excess of PFOA and PFOS in bulk water over concentrations ranging from 0.1 to 25 and 0.1 to 90 mg/L, respectively. Equations for estimating the surface excess of PFOA or PFOS as a function of total dissolved solids (TDS) are presented without the need to assume a specific PFAS target concentration.

3.1.1.1 Materials

Aqueous solutions were prepared with ultrapure water [Type 1, ASTM, D1193 - 06(2018)] obtained from a Milli-Q® Reference Water Purification System (Millipore-Sigma, Burlington, MA). The water had resistance of 18.2 MΩ/cm and was dispensed through a LC-Pak™ Point-of-Use Polisher. The ultrapure water was transferred into an 8 L glass carboy and then sealed and placed under vacuum for 12 h to remove dissolved gasses. Before use, the carboy was sanitized using a 10% bleach solution (Ultra bleach with 6% sodium hypochlorite, W.W. Grainger, Lake Forest, IL) and triple rinsed with ultrapure water. Aliquots of the degassed ultrapure water were transferred to 2 L high-density polyethylene (HDPE) bottles (National Plastics, Schaumburg, IL) that had been triple rinsed with ultrapure water. One 2 L bottle was reserved for use in preparing solutions with ultrapure water. For the other three 2 L bottles, a combination of magnesium sulfate, sodium biocarbonate, calcium chloride dihydrate, and potassium chloride (ACS grade from Fisher Scientific, Pittsburg, PA or Macron Fine Chemicals, Center Valley, PA) was added to achieve particular concentration levels of TDS (low, ca. 50 mg/L or 1.25 mM; mid, ca. 500 mg/L or 12.5 mM; and high, ca. 1,500 mg/L or 37.5 mM). The combination of salts was based on the ratios of major cations and anions found in the 60 principle aquifers in the United States between 1991 and 2010 [74].

3.1.1.2 Preparation of PFAS Solutions

PFOA (96% purity, FW 414.07 g/mole, Product No. 171468) and perfluorooctanesulfonic acid potassium salt (KPFOA, 98% purity, FW 538.22 g/mole, Product No. 77282) were obtained from Sigma-Aldrich (Saint Louis, MO). Solutions made from KPFOS contained branched and linear isomers, demonstrated by the existence of two separate elution peaks in the mass spectra

chromatograms. Stock solutions in the concentration range from 50 to 5,000 mg/L were prepared by adding PFOA or KPFOS solids to solutions contained in 100 mL HDPE bottles with HDPE caps (Corning Life Sciences, Corning, NY). Prior to use, each bottle and cap were triple rinsed with ultrapure water and allowed to air-dry. Stock solutions ranging from 5,000 to 50 mg/L were prepared by adding solids to each bottle where the mass of PFOA or KPFOS solids added was determined using a precision analytical balance (XSE105, Mettler-Toledo, Columbus, OH) with readability of 0.01 mg. After adding the solids, the stock solutions were placed in an ultrasonic water bath (Model 3800, Fisher Scientific, Pittsburg, PA), sonicated for 60 min and heated at 40 °C for 12 h. This process was repeated until no dissolved solids were observed in the HDPE bottles and until surface tension measurements produced consistent values. A dilution series in the concentration range from 40 to 0.1 mg/L was prepared from the stock solutions. This process resulted in a series of 100 mL HDPE bottles containing PFOA or KPFOS at concentrations ranging from 0.1 to greater than 1,000 mg/L. The concentration of PFOA or KPFOS in each solution was confirmed using liquid chromatography with tandem mass spectrometry and conductivity probe.

3.1.1.3 Surface Tension Measurements

The surface tension of the aqueous solution in each 100 mL HDPE bottle was automatically determined 10 times using a Sigma 700 precision force tensiometer (Biolin Scientific, Gothenburg, Sweden) equipped with a micro roughened surface platinum Wilhelmy plate (Part No. T107). This system can determine surface tension in the range from 1 to 1,000 mN/m with a resolution of 0.01 mN/m. Each measurement was conducted by wetting the plate to a depth of 6 mm, zeroing the balance, followed by a four second stabilization period and a four second period during which the force required to pull the plate free of the surface was recorded (wetting force). The surface tension is equal to the wetting force assuming a contact angle of 0°. Prior to measuring the surface tension of each solution, the Whilhemy plate was prepared by rinsing with methanol followed by ultrapure water and then flamed to a red color using a 1300 °C butane torch (MT-30 Microtorch, Racine, WI). The balance was periodically checked using a certified mass of 1761.7 mg and the surface tension of freshly dispensed ultrapure water was determined prior to each series of measurements. The temperature of the solutions was determined by placing a calibrated electronic thermometer (H-B Instrument™ SP Scienceware™, Trappe, PA) into a 100 mL HDPE bottle filled with water and co-located with the test solution.

3.1.1.4 Analytical Methods

The concentrations of PFOA and KPFOS in the range from 0.1 to 100 mg/L were determined using a Waters Acquity H-Class ultra-performance liquid chromatograph (UPLC) equipped with a Waters BEH C-18 column with an eluent gradient of ammonium acetate in water or methanol connected to a Waters Xevo TQ-S micro mass spectrometer (MS/MS). The Waters Xevo TQ-S micro was operated in negative electrospray ionization using multiple reaction monitoring mode tuned to unit mass resolution to isolate precursor and product ions (m/z 369 and 169 for PFOA and 80 and 99 m/z for PFOS) for quantitation.

Mobile phases were prepared from LC-MS grade water, methanol, and ammonium acetate purchased from Honeywell Burdick & Jackson (Muskegon, MI). Instrument calibration was performed using 5 concentrations of PFAS using certified calibration standards in the range from 5 to 500 ng/mL obtained from Waters (Cat# 186004624, Milford, MA) and for PFOS using 6 concentrations in the range from 20 to 750 ng/mL prepared from a certified 100 ug/mL analytical standard PFOS (FW 500.13 g/mole) from Sigma-Aldrich (#33607, Saint Louis, MO). Even though the PFOS analytical standard contained both branched and linear isomers, use of this standard led to an overestimation of the concentration for solutions where the PFOS content was known. Additional analytical standards were prepared from the KPFOS solids and when used to calibrate the LC-MS/MS led to agreements that were within 5% of the expected concentrations. To further confirm the concentration of PFOS, 1 mL samples were collected from five separate bottles and transferred to 250 mL of ultrapure water for analysis by a NELAP Accredited Laboratory (Battelle, Norwell Operations, Norwell, MA). These results ranged from ranged from 1 to 11%, average of 6% +/- 0.05.

The concentrations of PFOA and PFOS used in the air-water surface tension experiments were greater than the 5 to 500 µg/L quantitation range of the liquid chromatograph tandem mass spectrometer (LC-MS/MS). Therefore, sample dilution was required to bring these concentrations into the range of quantitation. To determine the dilution which yielded the most accurate and precise results, an experiment was conducted by collecting sample volumes in the range from 10 to 750 µL from a single bottle and into dilution volumes from 10 to 100 mL. The combination of sample and dilution volumes resulted in dilutions ranging from 50 times (750 µL into 50 mL) to 10,000 times (10 µL into 100 mL). Samples were collected from a high-density polyethylene (HDPE) bottle containing 43 mg/L KPFOS that was prepared by addition of KPFOS (98% purity, FW 538.22 g/mole, Product No. 77282) from Sigma-Aldrich (Saint Louis, MO), which contained both branched and linear isomers. The results of this experiment demonstrated that sample volume rather than dilution volume led to poor accuracy. The concentration determined by LC-MS/MS for sample volumes of greater than 250 µL were within 5% of the expected 43 mg/L whereas the concentration for volumes of less than 100 µL were over 20% greater than expected. Based on this, sample volumes of greater than 250 µL were collected for dilution to determine the concentration of PFOA and KPFOS by LC-MS/MS.

The concentration within each 100 mL HDPE bottle was also determined directly without dilution using an analytical grade DuraProbe 4-cell conductivity sensor with automatic temperature compensation connected to an Orion Star A215 pH/conductivity benchtop meter (ThermoFisher Scientific, Waltham, MA). Before each use, the sensor was calibrated using 1413 µS/cm and 12.9 mS/cm certified calibration solutions. For PFOA solutions, the concentration was also confirmed using a Jasco V-730 spectrophotometer (Easton, MD) operated at 213 nm. KPFOS does not exhibit a strong adsorption ban and was not amenable to UV-Vis analysis.

3.1.2 PFAS mixture accumulation at NAPL-water interfaces

Although experiments employing PFOA or PFOS alone or in combination are important, the results of such studies may not be applicable to conditions at sites where AFFF was released. This is due to the fact that commercial AFFF formulations consist of complex proprietary mixtures, typically composed of fluorocarbon (e.g. PFOS) and hydrocarbon surfactants along with solvents [23]. The combination of fluorocarbon and hydrocarbon surfactants in AFFF has a synergistic effect that will likely increase the concentration of these surfactants at the NAPL-water interface [20] and may also decrease the NAPL-water interfacial tension, such that mobilization of entrapped residual NAPL could occur.

These batch studies contribute to the growing body of knowledge on the interfacial concentration of PFOA, PFOS, perfluorooctanesulfonamide (FOSA), and AFFF. Based on measured interfacial tension values, equations are presented to predict surface excess concentrations at the air-water and NAPL-water interfaces and can be used to estimate the phase distribution of PFOA, PFOS, or FOSA mass in subsurface environments.

3.1.2.1 PFOA, PFOS, FOSA, and AFFF Solutions

Aqueous solutions were prepared with ultrapure water and a combination of salts were added to achieve to achieve a concentration of ca. 380 mg/L or 3.7 mM of total dissolved solids (TDS) as described previously. PFOA (96% purity, Product No. 171468) and PFOS (98% purity, Product No. 77282) were obtained from Sigma-Aldrich (Saint Louis, MO). FOSA (95% purity, Code: 459640010) was purchased from Acros Organics (Geel, Belgium). Preparation of PFOA and PFOS solutions were described. Stock solutions of 25, 60, 100, and 170 mg/L were prepared with FOSA solids in 125 mL HDPE bottles (ThermoFisher Scientific, Waltham, MA). Stock solutions were placed in an ultrasonic water bath, sonicated for 60 min and heated at 40 °C for 12 h. This process was repeated until no dissolved solids were observed in each bottle and until surface tension measurements produced consistent values. A dilution series in the concentration range from 80 to 0.1 mg/L was prepared from the FOSA stock solutions. Legacy AFFF formulations included 3M FC-303cf light water AFFF 3% concentrate (provided by Dr. Paul Hatzinger of APTIM) and ANSUL AFFF 3% concentrate (provided by Mr. Naji Akladiss, Maine Department of Environmental Protection). Stock solutions were prepared at the field application concentration of 3% followed by sonication for 30 min to break the foam. A dilution series in the concentration range from 0.12 to 12,000 mg/L was prepared from the 3% stock solutions, with all concentrations determined by weight. This process resulted in a series of individual HDPE bottles containing 50 mL of aqueous solution: 27 with PFOA in the expected range from 0.1 to 3000 mg/L, 22 with PFOS in the expected range from 0.1 to 1000 mg/L PFOS, 18 with FOSA in the expected range from 0.1 to 170 mg/L, and 24 with AFFF in the expected range from 0.1 to 30,000 mg/L. PFAS concentrations were determined following the analytical methods described previously.

3.1.2.2 Interfacial Tension Measurements

The air-water interfacial tension was determined following the methods described previously. The pendant drop method [75] was used to determine the interfacial tensions between the NAPLs and PFAS/AFFF solutions at room temperature (22 ± 1 ºC). Briefly, a drop of JP-4, TCE or PCE was slowly dispensed into a quartz cuvette (Starna Cells, Inc., Atascadero, CA) that contained PFAS/AFFF solution until the maximum drop volume was obtained without dislodging the drop from the stainless-steel needle. The drop shape was then analyzed using a goniometer (Model 190, Ramé-Hart, Succasunna, NJ) and interfacial tension was calculated in triplicate using DROPimage Advanced software (Ramé-Hart). Each NAPL was dispensed from a 2 mL capacity micrometer glass syringe (GS-1200, Gilmont Instruments, IL) through either a straight or inverted 22-gauge stainless steel needle. For low IFT measurements, the pendant drop method is difficult to perform and does not produce reliable results (Lin and Hwang 1994), and thus, interfacial tensions between the NAPLs and 4% wt. AY/OT solution were determined using a force tensiometer (Sigma 700 precision, Biolin Scientific, Gothenburg, Sweden) equipped with a micro roughened surface platinum Wilhelmy plate (Part No. T107). The system can determine interfacial tensions in the range of 1 to 2,000 mN/m with a resolution of 0.001 mN/m. Prior to NAPL-water interfacial tension measurements, the balance was calibrated using a 1761.7 mg certified mass and the interfacial tension of freshly dispensed purified water was determined to verify accuracy.

3.1.2.3 Surface Excess Calculations

The decrease in interfacial tension (γ) with increasing bulk-water concentration (C) was fit using the MatLab (v. R2018a) non-linear regression function fitnlm to the Szyszkowski equation Szyszkowski equation [73]:

$$\gamma = \gamma_0 \left[1 - a\ln\left(\frac{C}{b} + 1\right)\right] \tag{3-1}$$

where γ_o represents the surface tension of ultrapure water and a and b are fitted parameters. The fit was performed for the concentration range from ca. 0.1 mg/L to the maximum concentration in the dilution series or to the point where there was a change in curvature of the interfacial tension versus concentration plot (i.e., inflection point). The fit yielded three parameters: the solute-free air-water interfacial tension (γ_0) and values for a and b. After obtaining the a value, the maximum surface excess concentration (Γ_m) was calculated using:

$$\Gamma_m = \frac{a\gamma_0}{RT} \tag{3-2}$$

with the fitted value obtained for γ_0, the ideal gas constant (R) of 8.314 kJ/mol/K and the absolute temperature (T) of 294 K or 21 °C. The interfacial concentration of a chemical substance can be described using the Langmuir/Szyszkowski equation [76, 77]:

$$\Gamma = \Gamma_m \frac{\mathrm{C}}{\mathrm{C} + b} \tag{3-3}$$

which relates the surface excess concentration (Γ) to C using the fitted parameters from Eq. (3-1) and (3-2).

Scaefer et al. [78] used the Freundlich model to derive an alternative equation for fitting air-water interfacial tension. As discussed in **Appendix A.1**, use of Eq. (3-1) was found to yield a better fit and more physically realistic fitted parameter values. Rather than using the bulk-water concentration, [78] used the mean ionic activity of PFOA or PFOS and the excess salts $\left(C^* = \sqrt{C_{PFOA}(C_{PFOA} + C_{Salt})}\right)$ in fitting measured interfacial tension values. Correcting for mean ionic activity was not appropriate because this correction failed to collapse all the measured interfacial tension values onto a single curve, demonstrating independence of the salt concentration [79, 80]. Traditionally the counterion for anionic surfactants is accounted for by including a factor of ½ in Eq. (3-1) when analyzing the tension data for PFOS, as this was introduced as a potassium salt [81]. However, Schaefer et al. [78] concluded that salts of PFOA behave as pseudo nonionic surfactants at the air-water interface and may be considered as one molecular entity at the air-water interface so that the factor of ½ can be neglected.

3.2 Batch biotransformation studies

3.2.1 Chemicals and Materials

The chemical names, acronyms, molecular structures, and suppliers of PFAS used for microcosm set-up and/or liquid chromatography tandem mass spectrometry (LC-MS/MS) quantitative analysis are listed in Appendix **Table A.4**. The AFFF formulation used in this study is a 1999-era 3M Light Water™ AFFF concentrate (FC-203CF), which was kindly provided by Dr. Paul Hatzinger at APTIM. 1H-perfluorobutane (purity 99%), 1H-perfluoropentane (purity 98%), 1H-perfluorohexane (purity 98%), and 1H-perfluoroheptane (purity 97%) were purchased from Synquest Laboratories (Alachua, FL). Other chemicals used in this study were reagent grade or higher. The LC-MS grade water and methanol (>99.9%) were obtained from Honeywell Burdick & Jackson (Honeywell, Charlotte, NC). Ultrapure deionized water (18.2 MΩ cm) from an Evoqua water purification system (Evoqua Water Technologies, USA) was used for all purposes.

Three soils in total were used in this study for microcosm construction. Two of them are AFFF-impacted soils collected from two military sites; one (referred to hereafter as Robins soil) was collected from an AFFF spray test area with a hand auger down to 1.8m at Robins Air Force Base (AFB) (Houston County, Georgia, USA); and the other (referred to hereafter as Loring soil) was collected by shovel proximate to a crash site and fire station at the former Loring AFB (Aroostook County, Maine, USA). Both locations were impacted by PFAS from historical application(s) of AFFF. Another soil, was collected from a location close to Hudson River in Rensselaer County, New York (Coordinates: 42°29′02″N 73°44′29″W) (referred to hereafter as Hudson soil). Prior to microcosm preparation, the soils were homogenized, ground with a mortar and pestle, passed

through a 2 mm sieve (ASTM E11 # 10 size) and stored at 4 °C. The physical and chemical properties (pH, moisture content, organic matter content, cation exchange capacity (CEC), soil particle size distribution) of Robins, Loring and Hudson soils are provided in Appendix, **Table A.5**.

3.2.2 Microcosm set-up and preparations

3.2.2.1 Microcosms for aerobic biotransformation of FOSA, 8:2 FTOH, 6:2 FTS and AFFF mixture.

As shown in **Table 3.1**, seven sets of microcosms were constructed for the investigation of the aerobic biotransformation of FOSA, 8:2 FTOH, 6:2 FTS and an AFFF mixture. Microcosm was prepared in 60-mL/160-mL Wheaton serum bottles with Robins, Loring or Hudson soil. Each set consisted of triplicate live treatments, duplicate abiotic controls, and duplicate positive controls (except for 8:2 FTOH Loring soil microcosms, see **Table 3.1**). In each 60-mL bottle, 3 g (dry weight) of soil and 30 mL of bicarbonate-buffered growth medium were added (10 g soil and 100 mL medium added in 160-mL bottle). The medium was prepared based on the recipe previously reported [82], with modifications to omit resazurin, L-cysteine, and sodium sulfide due to their potential to serve as carbon sources under oxic conditions. For live treatments, each bottle was spiked with the corresponding PFAS stock solution prepared in diethylene glycol butyl ether (DGBE) to yield an initial targeted concentration (Table 1). DGBE was used to prepare the stock, because it was a primary organic solvent in AFFF formulations and was demonstrated as an electron donor and carbon source in previous aerobic soil microcosms [52, 83] . Abiotic controls were constructed similarly to live treatments, but additional 1 g/L NaN_3 was dosed to inhibit microbial growth (effective concentration determined by preliminary experiments, data not shown). Abiotic controls were used to evaluate potential abiotic transformation of parent PFAS and/or other legacy PFAS present in the soils. In the positive controls, only DGBE (same amount as that added in live treatment and abiotic control) was dosed, and all other procedures were same as the live treatments. The positive controls aimed to monitor background levels of legacy PFAS in the soils, and the associated potential biotransformation products. For 8:2 FTOH Loring soil microcosms, to impose extreme pressure on the soil microbial community, a high-dose treatment was set up in addition to the low-dose treatment, which was same as the live treatment in 8:2 FTOH Robins biotransformation experiment. In the high-dose treatment, 1,700 µg/L of 8:2 FTOH was amended every two weeks. Throughout all microcosm incubations, DGBE was amended into the live treatment and positive control microcosms as needed to support the microbial growth. All bottles were crimp-sealed with rubber septa and aluminum caps (Chemglass; Vineland, NJ). For the bottle in which the headspace sample was planned, one C_{18} cartridge (Maxi-Clean™, Alltech, Deerfield, IL) pre-conditioned with methanol, was connected to an 18G×1″ needle that was pushed through the septum into the headspace of each bottle. The cartridge ensured sufficient aeration, and captured potential volatile transformation products [84]. For the bottle without headspace sampling, a 0.22-µm sterile syringe filter (polyethersulfone (PES), VWR) connected to an 18G×1″

needle was pierced through the septum into the headspace of each bottle to maintain the aeration. All bottles were continuously agitated at 150 rpm on an orbital shaker (Innova 2350, New Brunswick Scientific) at room temperature for certain days until sampling (**Table 3.1**).

Table 3.1 Microcosm set-up examining aerobic biotransformation of FOSA, 8:2 FTOH, 6:2 FTS and AFFF mixture.

Treatment	Soil type	Initially spiked PFAS (μg/L)	Carbon source /electron donor[c]	Electron acceptor	Other[d]	Incubation time (day)
FOSA Loring soil microcosms						
Live treatment	Loring	85	DGBE	Oxygen	/	308
Abiotic control	Loring	85	DGBE	Oxygen	NaN_3	308
Positive control	Loring	N/A	DGBE	Oxygen	/	308
FOSA Hudson soil microcosms						
Live treatment	Hudson	85	DGBE	Oxygen	/	308
Abiotic control	Hudson	85	DGBE	Oxygen	NaN_3	308
Positive control	Hudson	N/A	DGBE	Oxygen	/	308
8:2 FTOH Robins soil microcosms						
Live treatment	Robins	170	DGBE	Oxygen	/	90
Abiotic control	Robins	170	DGBE	Oxygen	NaN_3	90
Positive control	Robins	N/A	DGBE	Oxygen	/	90
8:2 FTOH Loring soil microcosms						
High-dose treatment	Loring	1,700[a]	DGBE	Oxygen	/	90
Low-dose treatment	Loring	170	DGBE	Oxygen	/	90
Positive control	Loring	N/A	DGBE	Oxygen	/	90
6:2 FTS Robins soil microcosms						
Live treatment	Robins	1,700	DGBE	Oxygen	/	224
Abiotic control	Robins	1,700	DGBE	Oxygen	NaN_3	224
Positive control	Robins	N/A	DGBE	Oxygen	/	224
6:2 FTS Loring soil microcosms						
Live treatment	Loring	1,700	DGBE	Oxygen	/	224
Abiotic control	Loring	1,700	DGBE	Oxygen	NaN_3	224
Positive control	Loring	N/A	DGBE	Oxygen	/	224
AFFF Loring soil microcosms						
Live treatment	Loring	0.1%[b]	DGBE	Oxygen	/	308
Abiotic control	Loring	0.1%	DGBE	Oxygen	NaN_3	308
Positive control	Loring	N/A	DGBE	Oxygen	/	308

[a] Amended with additional 1,700 μg/L 8:2 FTOH at day 14, 28, 42, 67, and 82.

[b] Spiked with 0.1% v/v of AFFF concentrate.

[c] DGBE was added into all microcosms with an initial concentration of ca. 5 mM, with the exception of AFFF Loring soil microcosms in which DGBE was not added at day 0 (AFFF formulation contains 20% (v/v) DGBE).

[d] One gram per liter sodium azide was added to inhibit the microbial activity.

3.3 Microcosms for anaerobic biotransformation of 8:2 FTOH

A closed-system using Wheaton serum bottle (60-mL), aluminum crimp-sealed with rubber septum was also adopted for setting up 8:2 FTOH anaerobic microcosms. In each reactor, 30 mL of growth medium [82] and 3 g (dry weight) of Loring soil were added. Microcosms were prepared in the anaerobic glove box (Coy Laboratory Products, Inc., Grass Lake, MI) and an oxygen-free

N_2/CO_2 headspace was maintained in all microcosms throughout the experiments. Sodium nitrate (20 mM), sodium sulfate (20 mM), and goethite (100mM, mineral of Fe(III) oxide-hydroxide) was added in each batch of microcosms as the electron acceptor under nitrate-, sulfate-, and iron-reducing conditions, respectively. Each batch of microcosms included two sets of live-spiked treatments, one set of abiotic control and one set of positive control (see **Table 3.2**). For live-spiked treatments, each bottle was spiked with ~170 μg/L of 8:2 FTOH prepared in DGBE. One set of live-spiked treatment mimicked natural attenuation (NA treatment) where 5 mM DGBE was introduced as the solvent for 8:2 FTOH and as the sole external potential electron donor, while the other set mimicked biostimulation where 20 mM sodium lactate was added as an additional electron donor and carbon source in conjunction with DGBE to enhance the microbial growth (ED treatment). Abiotic controls were prepared similarly to live-spiked treatments, but 1 g/L NaN_3 was added to inhibit the microbial activity. For the positive controls, only DGBE (without 8:2 FTOH) was dosed into the bottles, and all other procedures were identical to the live-spiked treatments. All the microcosms were incubated at room temperature with 150 rpm shaking over ~400 days.

Table 3.2 Experimental set-up of 8:2 FTOH biotransformation microcosms under nitrate-, sulfate-, and iron-reducing conditions

Treatment	Components			
	Spiked 8:2 FTOH[a]	Carbon source & electron donor[b]	Electron acceptor[c]	Other[d]
ED treatment[e]	Yes	Lactate + DGBE	$NO_3^-/SO_4^{2-}/Fe^{3+}$	/
NA treatment[f]	Yes	DGBE	$NO_3^-/SO_4^{2-}/Fe^{3+}$	/
Abiotic control	Yes	Lactate + DGBE	$NO_3^-/SO_4^{2-}/Fe^{3+}$	NaN_3
Positive control	No	Lactate + DGBE	$NO_3^-/SO_4^{2-}/Fe^{3+}$	/

[a] The initial concentration of 8:2 FTOH spiked into the microcosms was ~ 170 μg/L.

[b] The carbon source & electron donor(s) were added into the microcosms with initial concentrations of 20 mM lactate and/or 5 mM DGBE.

[c] Goethite (100mM, mineral of iron (III) oxide-hydroxide), 20 mM of sodium sulfate or 20 mM of sodium nitrate was added as the electron acceptor in iron-reducing, sulfate-reducing, and nitrate-reducing microcosms, respectively.

[d] One gram per liter sodium azide was added to inhibit the microbial activity.

[e] ED represents electron donor.

[f] NA represents natural attenuation.

3.3.1 Microcosm sampling and preparation

The headspace samples were collected from all the above microcosms except FOSA and AFFF aerobic microcosms. For each set of microcosms, at the designated sampling point, triplicate bottles from live treatments (live-spiked treatments for 8:2 FTOH anaerobic microcosms), duplicate bottles from abiotic and positive controls were sacrificed for sampling. The headspace of each bottle (if collected) was purged through a C_{18} cartridge (Maxi-Clean™, Alltech, Deerfield, IL) by flushing N_2 to capture 8:2 FTOH/6:2 FTS and potential volatile transformation products.

Each C_{18} cartridge was eluted with methanol (5mL) for further PFAS analysis. The supernatant (0.5 mL) from each bottle was then collected and immediately mixed with 9.5 mL of methanol to avoid potential loss of volatile PFAS. The diluted sample was filtered with a 0.2-μm Corning® nylon syringe filter (Corning Inc., Corning, NY) into a 15-mL centrifuge tube for PFAS quantification of the microcosm aqueous phase. Subsequently, each bottle was shaken vigorously, and 1 mL of well-mixed slurry was collected for the measurements of geochemical parameters (e.g., dissolved organic carbon (DOC), SO_4^{2-}, NO_3^-, F^-, lactate, etc., details in **Appendix A.2**). All remaining slurry along with the rubber septum were transferred into a 50-mL centrifuge tube. The bottle was rinsed with 5 mL of ultrapure water (18.2 MΩ cm) and the rinse water was combined with the slurry. After centrifugation at 4,000 rpm for 20 min, the supernatant was discarded, and the soil pellet was resuspended in 30 mL methanol and vortexed for 30 min, followed by sonication at 60 °C in a water bath for 30 min. The methanol extract was collected after centrifugation and further filtered with a 0.22-μm Corning® nylon filter for quantification of sorbed PFAS from the septum and microcosm solid phases. The C_{18} cartridge eluent, methanol-diluted aqueous samples, and methanol extracts of soil and septum were stored at -20 °C before PFAS analysis.

3.3.2 Targeted PFAS Analysis

Targeted PFAS analysis of samples collected from FOSA and AFFF aerobic microcosms were conducted in the Mass Spectrometry Center at Auburn University. The analysis was performed on an Vanquish Flex Binary Ultra Performance Liquid Chromatography (UPLC) system (Thermo Scientific) fitted with a PFC-free kit (P/N 80100-62142) coupled to a quadrupole orbitrap mass spectrometer (Orbitrap Exploris 120, Thermo Scientific) with heated electrospray ionization (H-ESI) in negative mode using Xcalibur software (V4.4.16.14). A delay column was placed between the pump and autosampler (HypersilGOLD, 1.9 μm, 175 Å, 3 x 50 mm) to separate any PFAS in the LC system and solvents from the analytes. The standard or sample (10 μL) was injected onto a C18 column (Accucore RP-MS, 2.6 μm, 2.1 x 100 mm) maintained at 40°C, with a 200 μL/min flow rate of mobile phase of solution A (2 mM ammonium acetate in water) and solution B (100% acetonitrile) beginning at 20% B for the first 1.8 min to 95% B at 13.4 min, held at 95% B for 0.5 min, back to 20% B at 14.5 min, and with re-equilibration of 3.5 min. The MS scan range was 100-1000 m/z with resolution of 60,000, standard AGC target, 70% RF lens, maximum injection time auto, with EASY-IC run-start on. The spray voltage was 2200 V, ion transfer tube temperature was 250 °C, and the vaporizer temperature was 175 °C and mild trapping was on. The sheath gas was 30 and aux gas 5 (arbitrary units). A targeted inclusion mass list with retention time windows was used for comparing the standard and sample fragmentation pattern with a 5-ppm mass tolerance as shown in Appendix **Table A.6**. The instrument limits of detection (LODs) and limits of quantification (LOQs) for targeted PFAS are provided in Appendix **Table A.7**.

Targeted LC-MS/MS analysis of samples collected from 8:2 FTOH and 6:2 FTS microcosms were conducted by Pennell lab at Brown University. The analysis was performed using a Waters ACQUITY ultra high-performance liquid chromatograph coupled with a Waters Xevo triple

quadrupole mass spectrometer (UPLC-MS/MS) (Waters Corporation, Milford, MA). PFAAs analysis was performed following established methods [85] . Analysis of 8:2 FTOH, 6:2 FTS and their polyfluorinated biotransformation products was performed following the method reported by Szostek et al. [86] with no ammonium acetate addition in mobile phase, as FTOHs form adducts under negative electrospray ionization. In both methods, analyte separation was achieved using a Waters ACQUITY UPLC BEH C18 Column (130Å, 1.7 µm, 2.1 mm X 50 mm). The solvent gradient and detailed instrumental parameters are specified in Appendix **Table A.8** to **Table A.11**. The detection limits of target analytes are provided in Appendix **Table A.12**.

To quantify 1H-perfluoroheptane in 8:2 FTOH anaerobic microcosm samples, targeted gas chromatography (GC)-HRMS was performed using a high-resolution Thermo Q Exactive Orbitrap MS equipped with a Thermo Trace 1300 GC and a TriPlus RSH Autosampler. Helium (99.9999% purity) and nitrogen (99.999% purity) were used as the carrier and c-trap gases, respectively. Sample extracts (3.5 µL) were injected into a 100ºC split/splitless inlet operated in split-less mode. Analytes were separated on a Restek Rxi-200 column (105 m x 250 µm inner diameter x 0.25 µm film thickness) column with a 1 mL/min carrier gas flow rate. The transfer line was maintained at 200ºC while the oven temperature ramp began at 30ºC for 25 min and increased 30ºC/min to 220ºC, which was held for 1 min, with a 32 min total run time. The source temperature was 150ºC and the MS scan range was 50 to 400 m/z. 1H-Perfluoroheptane eluted at 18.10 min. The instrument was operated in electron ionization (EI) mode (70 eV). Data were collected with 60,000 resolution and 1×10^6 automatic gain control. The extracted ion chromatogram (XIC) was used for quantification using the most abundant peak in the mass spectrum (m/z 68.9947). Analyte identity was confirmed using the two confirming ions ratios and retention time (m/z 130.9915, 118.9915). The detection limit was 1,954 ng L^{-1}.

3.3.3 Non-targeted PFAS Analysis

Non-targeted PFAS analysis was also performed on the aqueous samples and soil methanol extracts collected from each treatment of 8:2 FTOH, 6:2 FTS and AFFF microcosms at select sampling time points. Sampling time points were selected based on targeted LC-MS/MS analysis results to include the samples collected before and after the occurrence of the biotransformation. Samples were injected in triplicate with a 10 µL injection volume on a Thermo QExactive HF-X Orbitrap MS equipped with a Vanquish ultra-high-performance liquid chromatograph (UHPLC-Orbitrap). Sample components were separated on a Thermo Hypersil Gold Vanquish C18 column (50 mm × 2.1 mm × 1.9 µm) at a constant temperature of 60 ºC with a solvent gradient consisting of two mobile phases, A (water) and B (methanol). PFAS were eluted from the column at a constant flow rate of 0.4 mL/min using a mobile phase gradient as follows: equilibration with 10% B for 1 minute, followed by a gradient ramp from 10% B to 100% B over 4 minutes and held for 2 minutes, and back to 10 % B over 1 minute and held for 2 minutes (total run time 11 minutes, data collected from 0.6 to 9 minutes). The MS was operated in full scan dd-MS^2 mode (stepped 15 and 55 NCE) with an inclusion list for 21 PFAS. Ionization was performed in negative mode (operated in both

positive (ESI+) and negative (ESI-) ionization modes for AFFF microcosm samples) with an ionization window of 1.0 *m/z*, sheath gas flow rate of 40, auxiliary gas flow rate of 10, sweep gas flow rate of 2, spray voltage of 2.7 kV, 310 ºC capillary temperature, funnel RF level of 35, and 320 ºC auxiliary gas heater temperature. For the full-scan, the Orbitrap was operated with a resolution of 120,000, automatic gain control (AGC) of $3x10^6$, and maximum dwell time of 100ms. For dd-MS^2, the Orbitrap was operated with a resolution of 15,000, AGC of $2x10^5$, and maximum dwell time of 400ms. MS^2 fragmentation was performed in the HCD collision cell filled with N_2 (produced by a Peak Scientific Nitrogen Generator, Genius NM32LA). The data files were saved in the .RAW file format and analyzed in Thermo Compound Discoverer (CD) 3.2 software. The data processing workflow used in CD 3.2 is displayed in Appendix **Figure A.5**. Spectral libraries and mass lists were used to identify 8:2 FTOH, 6:2 FTS, and transformation byproducts. The libraries included Thermo mzCloud, ChemSpider, and an in-house MS^2 mass spectral library containing 40 PFAS compounds. The mass lists included approximately 200 hypothesized potential transformation products, transformation products predicted by BioTransformer 3.0, and 8,142 fluorinated compounds from the EPA's ToxCast/CompTox database [87, 88].

For each set of microcosms, a final candidate list containing a total of 705-14,000 features was exported to Microsoft Excel after processing the raw data. We developed a R script to facilitate the selection of features of interest based on the peak intensity comparison between samples from an individual treatment over time, and between samples from the live-spiked treatments and abiotic/positive controls at each sampling point. Confidence scores of the features detected were assigned based on the Schymanski Scale to evaluate the certainty of the structure identification [89]. Briefly, the highest confidence level 1 (confirmed structure) represents the proposed structure was confirmed via the comparison of the appropriate measurement of a reference standard. Level 2 (probable structure) was achieved when the MS^2 spectrum and fragmentation have been reported previously for a compound of interest and the spectrum-structure match is unambiguous, or when the structure of the compound could be determined unambiguously by MS^2 fragmentation analysis. Level 3 (tentative candidate) was assigned when the MS^2 spectrum and fragmentation were informative for possible structures, but the information was insufficient for one exact structure only. When the MS^2 fragmentation data was not available while a molecular formula can be assigned unambiguously based on the spectral information, level 4 (unequivocal molecular formula) was assigned.

3.3.4 Microbial Community Analysis

To provide insights on the role of native microbial communities in FOSA, 8:2 FTOH, and 6:2 FTS biotransformation, microbial community analysis was performed on microcosm samples from live or live-spiked treatments and positive controls. Duplicate soil samples were collected at the beginning and the end of incubation, and DNA was extracted using DNeasy PowerSoil Kit (Qiagen, Hilden, Germany) according to the manufacturer's protocols. Amplification and sequencing of soil DNA samples were performed at the Alkek Center for Metagenomics and

Microbiome Research at Baylor College of Medicine. The V4 region of the 16S rRNA gene was amplified by polymerase chain reaction (PCR) using barcoded primer sets (515F/806R) and sequenced on the MiSeq platform (Illumina, San Diego, CA) using a 2 × 250 bp paired-end protocol [90]. The read pairs were demultiplexed based on the unique molecular barcodes, and reads were merged using the USEARCH v7.0.1090 [91]. The 16S rRNA gene sequences were clustered into Operational Taxonomic Units (OTUs) at a similarity cutoff value of 97% using the UPARSE algorithm [92]. The generated sequences were mapped against the latest SILVA Database [93]. The ATIMA (Agile Toolkit for Incisive Microbial Analyses) was used to analyze and visualize trends in taxa abundance, alpha diversity, and beta diversity as they relate to sample metadata.

3.3.5 Microbial co-occurrence network analysis

The raw 16S rRNA gene sequencing data obtained from 8:2 FTOH and 6:2 FTS biotransformation microcosm experiments were also gathered and subjected to downstream analysis using bioinformatics and computational tools. The merged raw sequencing read pairs were demultiplexed, quality-trimmed by removing Illumina adapters and PhiX reads using bbduk, and merged using bbmap. The non-redundant sequences were denoised with Deblur and partitioned into amplicon sequence variants (ASVs). To determine taxonomy assignment, the representative sequences were mapped against an optimized version of the SILVA Database version 138.1.

To explore microbial co-occurrence patterns that are not able to reveal by traditional taxonomic profiling and the microbial taxa that may play crucial roles in fluorotelomer biotransformation but be overlooked due to low relative abundance, a correlation-based network analysis was performed using “igraph” package in R.[94] Briefly, the Spearman rank correlations between ASVs were calculated. Only the robust and significant correlations (Spearman's rank correlation coefficient $\rho > 0.8$ and Benjamin-Hochberg adjusted P-value < 0.01) were used to construct a co-occurrent network associated with fluorotelomer contamination. Network visualization and modularization were achieved using Gephi (version 0.9.2).[95] To describe the pattern of correlations between ASVs, a set of topological properties of this network were calculated and compared to those of 10,000 random networks generated using Erdős-Rényi model with the same number of nodes and edges. Chi-square test along with Cramer's V was performed using “lsr” package[96] in R to determine the correlation between network modules and environmental factors. In addition, two types of potentially important taxa, generalist and keystone taxa in the co-occurrent network were identified based on ecological concepts.

Generalist are species that persist across multiple environments or environmental gradients and contribute to the ecological stability.[97] In this study, the ASVs broadly distributed across different sets of microcosm experiments are regarded as generalists, that is, the ASVs presented independently of soil and contaminant are generalists. Defining taxa in ecological communities as generalists might be somewhat arbitrarily but is useful for providing additional information from those defined by taxonomy.[98, 99] Habitat generalists were thought to be migrating from their

natal habitats by dispersal processes in response to environmental disturbance and signals.[100, 101]

The species in an ecosystem that have strong and disproportionately large impact on the community composition relative to their abundance, are defined as keystone species.[102] Removal of keystone species from a microbial community may have negative impact on the microbiome structure or even result in dysfunction.[103] Two methods based on calculated topological features were used in this study to identify the keystone taxa in the constructed network; one is a centrality-based method and the other is a connectivity-based method. criteria are detailed in **Appendix A.3** and topological features of all nodes are shown in Supplementary Data X1 (**Appendix A.18**).

3.3.6 Functional analysis

To predict functional genes/enzymes in response to the fluorotelomer contamination, a computational tool, phylogenetic investigation of communities by reconstruction of unobserved states (PICRUSt2), was applied with default settings based on normalized 16S rRNA gene abundance levels. According to Kyoto Encyclopedia of Genes and Genomes (KEGG, http://www.kegg.jp/), a KEGG Orthology (KO) identifier (or K number) was assigned to each feature (functional gene/enzyme) predicted by PICRUSt2. The functions of predicted features and potential pathways involving the features were also annotated based on the KO database. Pairwise comparison of predicted gene abundance between treatment (microcosms exposed to fluorotelomer) and control (microcosms without fluorotelomer addition) in each set of microcosm experiment was performed by a differential abundance analysis tool using "edgeR" package in R.[104] The genes with significant changes in abundance (an absolute log2-fold change > 2 and an FDR-adjusted *P*-value < 0.05) were picked as candidates for further investigation. In addition, the genes potentially related to PFAS degradation identified or predicted in previous research were manually picked.[105-107] The genes involved in xenobiotics biodegradation and metabolism according to the KEGG pathway annotation with significantly higher abundance and shared between different microcosm experiments were pooled with the manually picked genes and subjected to subsequent functional analyses.

3.4 Abiotic transport studies

3.4.1 Influence of Aqueous Film Forming Foams on the Solubility and Mobilization of Non-Aqueous Phase Liquid Contaminants

3.4.1.1 Materials

Two size fractions of Ottawa sand (OS) (20-30 mesh and 60-80 mesh) were used as the solid phases in the column studies. The 20-30 mesh and 40-270 mesh (F-65) size fractions were purchased from U.S. Silica (U.S. Silica, TX). The F-65 sand was sieved to obtain the 60-80 mesh size fraction using a programable sieve shaker (Tyler Ro-Tap, W.S. Tyler Industrial Group, OH). The intrinsic permeabilities (ki) of the 20-30 mesh and 60-80 mesh size fractions of Ottawa sand were 1.80 ×

10-11 m2 and 7.05 × 10-12 m2, respectively. Jet Fuel (JP-4), trichloroethylene (TCE) and tetrachloroethylene (PCE) were selected as representative NAPLs. The Jet Fuel (JP-4) was prepared as a 1:1 mixture of unleaded gasoline and kerosene (Reagent grade), TCE (99.6% purity) and PCE (99% purity) were purchased from Acros Organics (Geel, Belgium). The NAPLs were dyed with 2×10-4 M Oil Red O (Fisher Scientific, Pittsburgh, PA) to allow for visualization of the free product migration. Prior studies have demonstrated that Oil Red O at this concentration has negligible effects on interfacial tension and NAPL mobilization [37]. The AFFF solutions were prepared from a legacy 3M FC-783F AFFF 3% concentrate (Lot # 607). The critical micelle concentration (CMC) of the 3M AFFF is approximately 3,000 mg/L based on surface tension measurements [108]. Concentrations of 33 PFAS in the 3% concentrate were measured by SGS AXYS using liquid chromatography quadrupole mass spectrometry (LC-MS/MS) with isotope dilution (Method MLA-110), which has been verified and accredited under Department of Defense (DoD) Quality System Manual (QSM) 3.3 (see **Table 3.3**). The low IFT surfactant solution was prepared as a 4% wt. 1:1 mixture of sodium diamyl sulfosuccinate and sodium dioctyl sulfosuccinate (Aerosol AY/OT, American Cyanamid, NJ). The CMC of the Aerosol AY/OT surfactant formulation is approximately 2,500 mg//L [109]. All aqueous solutions were prepared with 500 mg/L CaCl2 (13.5 mM) as the background electrolyte in ultrapure water (resistance of 18.2 MΩ/cm) that was dispensed through a LC-Pak™ Point-of-Use Polisher from a Milli-Q® System (Millipore-Sigma, Burlington, MA).

Table 3.3 Concentrations of per- and polyfluoroalkyl substances (PFAS) measured in 3M FC-783F 3% wt. concentrate.

	Sample ID:	Drum		Drum	
	Analysis:	PRE[2]		POST OXIDATION[3]	
	Method:	MLA 110		MLA 111	
	Date Collected:	6/17/2019		6/17/2019	
	Units:	ng/g		ng/g	
COMPOUND[1]	CAS_NO	Result	Flag	Result	Flag
PFBA	45048-62-2	21,800	U[4]	762,000	
PFPeA	45167-47-3	27,900		809,000	
PFHxA	92612-52-7	67,400		3,580,000	
PFHpA	120885-29-2	20,100		56,700	
PFOA	45285-51-6	87,800		185,000	
PFNA	72007-68-2	12,000		6,980	U
PFDA	73829-36-4	25,600		6,570	U
PFUnA	196859-54-8	11,000		6,570	U
PFDoA	171978-95-3	11,100		6,570	U
PFTrDA	862374-87-6	8,240		6,570	U
PFTeDA	365971-87-5	6,240		6,570	U
PFBS	45187-15-3	93,400		76,300	
PFPeS	175905-36-9	89,500		76,000	
PFHxS	108427-53-8	574,000		523,000	
PFHpS	146689-46-5	64,700		34,900	
PFOS	45298-90-6	5,330,000		4,920,000	
PFNS	474511-07-4	9,340		8,210	U
PFDS	126105-34-8	5,440	U	8,210	U
PFDoS	343629-43-6	5,440	U	8,210	U

[1]Data are reported as concentration of the anion
[2]"PRE" data are analyses of the neat AFFF product,
[3]"POST OXIDATION" data are analysis of the liquid after oxidative conversion of the neat product per the TOP Assay method [110].
[4]U = not detected above laboratory reporting limit (result is the reporting limit).

3.4.1.2 Density, viscosity, interfacial tension, and NAPL solubility measurements

Liquid densities were determined gravimetrically using a 25-ml borosilicate glass pycnometer (ChemScience Inc, Canada). The viscosity of the 3% wt. AFFF was measured in triplicate using a Brookfield DV-II+ Viscometer (Brookfield Engineering Laboratories Inc., Middleboro, MA) with CPA-40Z cone spindle. All samples were tested as 0.5 mL aliquots and daily calibration checks were performed with purified water to confirm accuracy. Interfacial tensions between NAPLs and AFFF solutions were determined as described in **Section 3.1.2**. The solubilities of PCE and TCE were determined in aqueous solutions of AFFF at six concentrations ranging from 0 to 5 % wt. (50,000 mg/L). Briefly, 1 mL of neat liquid PCE or TCE and 15 mL of AFFF solution were mixed in borosilicate glass centrifuge tubes (Kimble Chase, Rockwood , TN) for 48 h on an oscillating shaker (Fisherbrand, Waltham, MA), after which the liquid phases were separated by

centrifugation at 2,500 rpm for 30 min. Aqueous concentrations of PCE or TCE were measured using a 2010 Model Shimadzu gas chromatograph (GC) equipped with a precolumn trap consisting of a glass insert with an ~3 cm glass wool packing, a Restek, Rxi-624Sil MS fused silica column, and an electron capture detector (ECD). The precolumn trap was installed to prevent fouling of the GC inlet, column and detector. Samples were prepared for analysis by adding approximately 0.04 mL of the aqueous sample to 1.96 ml of isopropanol in glass autosampler vials leaving minimal headspace to avoid volatilization and sealed with Teflon-backed screw caps. A minimum of six standards, prepared using PCE or TCE isopropanol solutions, were analyzed to produce a calibration curve, along with daily single point calibration checks. The limits of detection (LOD) for PCE and TCE were determined to be 6.8 and 1.0 µg/L, respectively, based on the method of Armbruster and Pry (2008).

3.4.1.3 Column mobilization studies

To evaluate the mobilization of residual NAPL by the AFFF and Aerosol AY/OT solutions, a series of multiphase column experiments was conducted following the procedure described by [37]. Briefly, a borosilicate glass column (5 cm dia. × 15 cm length) was packed with air-dried 20-30 mesh or 60-80 mesh Ottawa sand in 1-cm increments under gentle vibration. The packed column was purged with CO_2 gas for at least 2 h to facilitate dissolution of the gas phase during the water imbibition and saturation process. To fully saturate the column with water, at least 5 pore volumes (PVs) of degassed background electrolyte solution (500 mg/L $CaCl_2$) were introduced to the column. The PV of the column was then determined by the difference of column weight before and after water saturation. To establish a uniform residual NAPL saturation, approximately 100 mL of JP-4, PCE, or TCE dyed with Oil-Red-O were injected into the column using a high-pressure syringe pump (Chemyx fusion 100 Stafford, TX) at a flow rate of 10 mL/min in a down-flow mode for JP-4 or an up-flow mode for PCE and TCE to displace water from the pore space. The flow direction was then reversed, and at least 3 PVs of background electrolyte solution were injected at a flow rate of 10 mL/min to displace mobile NAPL or "free product" from the column. A non-reactive tracer (NaBr) test was conducted after establishment of residual NAPL to determine the saturation (see Supplementary Information). The relative water permeabilities (k_{rw}) of the packed columns ranged from 0.37 to 0.43 after establishment of residual NAPL. Following the first non-reactive tracer test, approximately 3 PVs (300 mL) of 3% wt. AFFF solution were introduced into the column at a Darcy velocity of approximately 6.5 cm/h, followed by 3 PVs background electrolyte solution at the same velocity. Column effluent samples were collected continuously in graduated glass centrifuge tubes using a fraction collector (CF-2, Spectrum Laboratories, CA). The volume of NAPL recovered in the effluent was measured and a second non-reactive bromide tracer test was performed to determine the residual saturation of NAPL. The difference in NAPL saturation based on these two measurements was typically less than 10%. In the final phase of the experiment, 3 PVs of the 4% wt. Aerosol AY/OT solution were injected to displace the remaining residual NAPL from the column. The final saturation of NAPL following the 4% wt. Aerosol AY/OT solution flush was determined by a third non-reactive tracer test. Changes in pressure

between the column inlet and outlet were measured using a pressure transducer (Omega PX30-030GV, Norwalk, CT) connected to a digit multimeter (Keithley 2110, Beaverton, OR) and calibrated using five water column heights (0 to 1 m). All column experiments were conducted at room temperature (22 ± 1 °C) in duplicate or triplicate to confirm reproducibility.

3.4.2 Influence of Residual Nonaqueous-Phase Liquids (NAPLs) on the Transport and Retention of Perfluoroalkyl Substances

Here experiments were undertaken to investigate the impact of residual NAPL on the transport and retention behavior of individual PFAS and PFAS mixtures. Six PFAS with C-F chain lengths ranging from four to eight (perfluorobutanesulfonic acid (PFBS), perfluorohexanesulfonic acid (PFHxS), perfluoroheptanoic acid (PFHpA), perfluorooctanoic acid (PFOA), perfluorooctanesulfonic acid (PFOS), perfluorononanoic acid (PFNA)) were selected based on their inclusion in the U.S. Environmental Protection Agency (EPA) Third Unregulated Contaminant Monitoring Rule (UCMR3). PCE was selected as the NAPL due to its frequent occurrence as a separate organic liquid phase in contaminant source zones. Interfacial tension measurements (see **Section 3.4.1**) were conducted with PCE-NAPL and simulated groundwater as a function of PFAS concentration in the aqueous phase to determine PFAS accumulation at the NAPL-water interface. Additional batch reactor experiments were undertaken to assess the extent of PFAS partitioning into PCE-NAPL and adsorption of PFAS by the solid phase. A series of column experiments was then performed for individual PFAS and mixtures of two or six PFAS to explore the influence of residual PCE-NAPL on PFAS transport behavior in a quartz sand. A mathematical model that accounts for PFAS accumulation at the NAPL-water interface, adsorption on the solid phase, and partitioning into NAPL was developed and used to simulate PFAS column effluent BTCs.

3.4.2.1 Materials

PFBS potassium salt (≥98% purity), PFHpA (99% purity), PFHxS potassium salt (≥98% purity), PFOA (96% purity), PFNA (97% purity), and PFOS potassium salt (≥98% purity) were purchased from Sigma-Aldrich (St. Louis, MO) and used for preparation of aqueous PFAS solutions. The 60-80 mesh size fraction of Ottawa sand (OS), which has an intrinsic permeability of 7.05 × 10-12 m2,23 was obtained by sieving U.S Silica F65 Ottawa sand (Seagraves, TX) with a programable sieve shaker (Tyler Ro-Tap, W.S. Tyler Industrial Group, OH). This sand was selected as the solid phase based on its low specific surface area (0.013-0.019 m2/g) and organic carbon content (foc = 0.00025 g OC/g),24, 25 which allowed for detailed investigations of NAPL-water interfacial adsorption and partitioning processes.

3.4.2.2 Batch soil adsorption and phase partitioning experiments

Batch reactors were prepared to evaluate PFAS partitioning into PCE-NAPL and to measure PFAS adsorption on 60-80 OS. To better quantify PFAS adsorption on OS, a liquid to solid ratio of 2 was used. [111] Three types of PFAS solutions were used: PFOS alone, PFNA alone, and equal mass

mixtures of the six PFAS (PFBS, PFHpA, PFHxS, PFOA, PFNA, and PFOS). All batch reactors were prepared in triplicate, including controls containing only PFAS solution (i.e., no NAPL or OS). Reactors and controls were placed onto a rotating shaker and mixed for ~~at least~~ 48-50 hours to reach equilibrium conditions.[112] After mixing, the NAPL-partitioning reactors were allowed to stand for 48 h at room temperature to achieve phase separation. The solid phase sorption reactors were centrifuged at 4,200 rpm for 1 h (Centrifuge 5804R, Eppendorf, Framingham, MA) to separate any suspended solids. Aqueous and solid phase concentrations of PFAS in the batch reactors were determined using LC-MS/MS as described below. In the NAPL partitioning experiments, interfacial adsorption was estimated with fitted parameters from IFT measurements and used to correct for any mass loss to the NAPL-water interface. The concentration of PCE in the aqueous phase of the NAPL-partition reactors was measured using gas chromatography-mass spectrometry (GC-MS) [113].

3.4.2.3 Column experiments

Column experiments were performed to quantify PFAS transport and retention in the absence and presence of residual PCE-NAPL. Following procedures described previously [113], borosilicate glass columns (5 cm i.d. × 15 cm length) were packed with air-dried 60-80 OS and flushed with CO_2 gas. Approximately 10 PVs of SGW (IS = 8.6 mM, pH = 7.5±0.3) were flushed through the vertically oriented column in an upward direction. Following complete water saturation, a non-reactive tracer test (8.6 mM NaBr) was conducted to assess water flow and determine the hydrodynamic dispersivity (0.03 to 0.06 cm for columns with no NAPL and from 0.06 to 0.08 cm for columns with entrapped NAPL). To obtain a residual saturation of PCE-NAPL, 1 PV of PCE-NAPL was introduced into the water-saturated column in an upflow mode (10 mL/min) and then flushed with 3 PVs of background solution in a downflow mode (10 mL/min) to remove "mobile" PCE-NAPL from the column. A second tracer test was then conducted to determine the residual saturation of PCE-NAPL in each column. The PCE-NAPL residual saturation was also confirmed by weighing the column before and after establishing the residual. The difference between these two measurement techniques was typically less than 2 %. After establishing the residual PCE-NAPL (**Figure 3.1**), a 3 PV pulse of PFAS solution was introduced into the column followed by6 to 7 PVs of background solution at a pore-water velocity of approximately 1 m/day. This velocity is in the range of typical groundwater flow velocities in sandy aquifers [114] and is similar to velocities used in other studies [61, 115]. Effluent samples were collected continuously using a fraction collector and analyzed for PFAS concentrations. Four sets of column experiments were conducted using 4 different PFAS solutions: ~100 µg/L PFOS; ~100 µg/L PFNA; ~200 µg/L 1:1 mixture (mass ratio) of PFOS and PFNA (mix-2); and a ~600 µg/L equal mass mixture of the six PFAS (mix-6) (**Table 3.4**). To confirm reproducibility, the PFOS only and six PFAS mixture column experiments were conducted in duplicate. Each set of column experiments contained one control column with no PCE-NAPL and one column containing residual PCE-NAPL. To investigate the effect of flow velocity on PFAS transport in the presence of residual PCE-NAPL,

an additional column experiment was performed with ~100 µg/L PFOS solution at a slower pore-water velocity (0.28 m/day).



Figure 3.1 Photograph of a typical column at residual PCE saturation. Note the PCE-NAPL was distributed uniformly along the column as small globules or ganglia.

Table 3.4 Summary of experimental parameters and results of PCE column studies.

Column identifier	Pore-water velocity (m/day)[3]	Residual PCE-NAPL saturation (%)[4]	Influent (µg/L)[5]	Mass Recovery (%)[6]	Fitted Retardation factor[7]	R^2
PFNA	1.03±0.05	15.0	PFNA (100.62)	92.9	1.64	0.99
PFOS (dup)[1]	1.06±0.04	16.4±0.5	PFOS (108.13±9.87)	94.3±2.9	3.11±0.21	0.97
PFOS (LF)[2]	0.27±0.02	17.1	PFOS (112.23)	92.1	3.09	0.99
PFAS mix-2	1.00±0.05	15.6	PFNA (100.70)	100.5	1.72	0.96
			PFOS (119.24)	95.4	3.14	0.99
PFAS mix-6(dup)	1.01±0.05	16.6±0.6	PFBS (92.54±1.68)	102.5±0.6	1.02±0.02	0.99
			PFHpA (107.03±2.02)	102.9±0.8	1.04±0.02	0.99
			PFHxS (84.02±0.50)	105.3±0.3	1.08±0.03	0.98
			PFOA (101.53±3.26)	104.7±1.6	1.12±0.02	0.98
			PFNA (109.93±0.29)	99.2±2.4	1.67±0.06	0.99
			PFOS (102.32±23.98)	96.0±3.6	2.91±0.24	0.97

Bulk density and porosity for sand columns listed in the table are 1.62 ± 0.01 g/cm^3 and 0.38±0.01, respectively.[1] (dup) indicates duplicate columns. [2] (LF) represents low flow velocity. [3] ± indicates the variation in pore-water velocity. [4-7] ± indicates standard deviations in duplicate columns. [7]retardation factor was calculated by inverse fitting the experimental BTC to the advection- dispersion equation (ADE). [116, 117]

3.5 Abiotic-biotic transport studies

3.5.1 Biotransformation of 6:2 FTS in 1-D flow-through columns

3.5.1.1 Column design and preparation

A total of four borosilicate glass chromatography column (2.5 cm inner diameter, 15 cm length; Kimble-Chase, Vineland, NJ) were used in this study for investigation of 6:2 FTS biotransformation. Each column was customized with three glass sampling ports that are evenly distributed along the column and sealed with rubber septa (Restek, Bellefonte, PA). All column components were either autoclaved (121 ºC, 30 min) or washed in 70% ethanol prior to use. Abiotic and biotic columns were identically packed with mixed Loring soil and Federal Fine sand (1:1, w/w) by alternating the addition of 1-cm porous media with vortexing and manual compression. Federal Fine Ottawa sand (30-140 mesh) was obtained from U.S. Silica Company (Berkeley Spring, WV) with an organic carbon (OC) content of <0.1 mg/g, a mean grain size of 0.32 mm and an intrinsic permeability of 4.2×10^{-11} m^2. Following packing, columns were purged with CO_2 gas to facilitate dissolution of entrapped gas, then saturated with sterile synthetic

groundwater (see below) in an up-flow mode. Non-reactive tracer tests (20 mM bromide, flow rate = 0.04 mL/min) were completed prior to column experiments. The breakthrough curves of bromide were simulated using the Code for Estimating Equilibrium Transport Parameters from Miscible Displacement Experiments (CFITM) as a part of Studio of Analytical Models (STANMOD) Version 2.2 (available through USDA-ARS U.S. Salinity Laboratory; http://www.ars.usda.gov) to determine porosity (n) and aqueous pore volume (PV).

3.5.1.2 Synthetic groundwater preparation

Synthetic groundwater was prepared in 800 mL batches in a 1000-mL PYREX™ media bottle (Corning Inc., Corning, NY), according to the recipe previously reported [82] with modifications to exclude resazurin, L-cysteine, and sodium sulfide which are not required for aerobic microorganisms. After autoclaving at 121 ºC for 30 min, 680 µL of 6:2 FTS stock solution (2,000 mg/L) prepared in diethylene glycol butyl ether (DGBE) was added into the bottle, yielding a starting 6:2 FTS concentration of 1,700 µg/L. DGBE was used to prepare the 6:2 FTS stock, since it is a primary organic solvent in AFFF formulations, and it was shown to serve as electron donor and carbon source for aerobic microorganisms [52, 83]. The synthetic groundwater was then transferred into a 1000-mL PYREX™ Erlenmeyer flask (Corning Inc., Corning, NY) sealed with a rubber stopper, serving as the influent for biotic columns. For preparation of influent for abiotic columns, additional 1 g/L of sodium azide was added into the synthetic groundwater to inhibit microbial growth during column operations [118]. To offset the increase in ionic strength due to sodium azide addition, concentration of sodium bicarbonate in abiotic influent was correspondingly reduced.

3.5.1.3 Column operation and sampling

Column experiments were initiated by introducing the influents described in **Section 3.4** to duplicate abiotic and biotic columns (**Figure 3.2**). The initiation time point was considered as PV = 0. The influent was constantly aerated with sterilized air in the flask, and delivered to the columns via a peristaltic pump (Gilson Miniplus 3, France) in an up-flow mode (**Figure 3.2**). Column experiments were performed in two phases, Phase I and Phase II. In Phase I (0-33.1 PVs), the influent was introduced to the columns at a flow rate of 5.0 ± 0.1 µL/min, equivalent to a pore-water velocity (v_p) of 3.7 ± 0.2 cm/day and a hydraulic residence time (RT) of 4.1 ± 0.2 days. A 2-day flow interruption was conducted at 11.5 PVs. In Phase II (33.1-58.8 PVs), the flow rate was reduced to 3.2 ± 0.1 µL/min (v_p = 2.4 ± 0.1 cm/day, RT = 6.3 ± 0.3 days), and a 7-day flow interruption was conducted at 47.4 PVs. In sum, all columns were operated for a total of 305 days (136 days in Phase I, and 169 days in Phase II).

Throughout the 305-day operation, column effluent dripping out of each effluent tubing was continuously collected in 15-mL centrifuge tubes (**Figure 3.2**). These effluent samples were used to monitor the flow rate and dissolved organic carbon (DOC) concentration (TOC-L CPH, Shimadzu). In addition, 65 µL of column effluent was collected from the 3-way valve (see **Figure**

3.2) every PV (see Appendix **Table A.13** for the overview of sampling events throughout the experiments), and immediately mixed with methanol (1,235 µL) to minimize the potential loss of volatile PFAS. The methanol-diluted sample was then filtered through a 0.2-µm nylon filter (Corning Inc., Corning, NY), and stored at -20 °C prior to PFAS analysis. To investigate the biotransformation of 6:2 FTS along flowing path, additional aqueous samples were withdrawn from the side-ports of biotic columns (Ports 1, 2, and 3, see Fig. 1a) at selected time points (Appendix Table S10), using a Chemyx Fusion 200 syringe pump (Chemyx Inc., Stafford, TX) and 1-mL syringe (BD Luer-Lok) at a 10% of background flow rate (e.g., 0.5 µL/min in Phase I). The withdrawn sample (65 µL) was also mixed with methanol (1,235 µL), filtered, and stored at -20 °C for further PFAS analysis.

To confirm the oxic conditions throughout the biotic columns, 1.5 mL of side-port samples were also withdrawn at selected time points (Appendix **Table A.13**) for measurements of oxidation-reduction potential (ORP) using an ORP meter (Thermo Orion Dual Star) and ORP probe (Thermo Orion 9179 BNMD). Additionally, 1 mL of side-port samples were collected during Phase I and Phase II (Appendix **Table A.13**) for the DNA extraction (See **Section 3.5.1.5**). At the termination of column experiments, biotic columns were destructively sampled to allow for investigation of microbial community in the column solid phases. Each column was divided into several segments, and the solid phase in segments S1-S5 (see **Figure 3.2**) was transferred to a sterile 50-mL centrifuge tube using a flame-sterilized stainless-steel spatula. For the microbial community analysis, approximately 0.25 g of solids in each segment was used for DNA extraction (See **Section 3.5.1.5).**

3.5.1.4 Targeted and Non-Targeted PFAS Analysis

Target analysis of perfluoroalkyl acids (PFAAs) and polyfluorinated compounds were performed as described above (**Section 3.3.2**). Detection was achieved using a Waters ACQUITY ultra high-performance liquid chromatograph coupled with a Waters Xevo triple quadrupole mass spectrometer (UPLC-MS/MS) (Waters Corporation, Milford, MA). The UPLC was equipped with a Waters ACQUITY UPLC BEH C18 Column (130Å, 1.7 µm, 2.1 mm X 50 mm). Details on the solvent gradient, instrumental parameters, and detection limits of target PFAS can be found in **Section 3.3.2**. For non-targeted PFAS analysis, the effluent and side-port samples from duplicate biotic columns at selected sampling points were pooled (Appendix **Table A.13**). Sampling points were selected based on targeted PFAS analysis results, to include representative samples in each subphase of Phase I and Phase II. Four of abiotic column effluent samples were also analyzed (Appendix **Table A.13**). Following the method described above (**Section 3.3.3**), non-targeted LC-HRMS analysis was performed using a Thermo QExactive HF-X Orbitrap MS equipped with a Vanquish UPLC.

3.5.1.5 DNA Extraction and llumina MiSeq Sequencing

DNA extractions of aqueous side-port samples and solid samples from column segments S1-S5 were conducted using DNeasy PowerSoil Pro Kit (Qiagen, Hilden, Germany) according to the manufacturer's protocols. Amplification and sequencing of DNA samples were performed at the Alkek Center for Metagenomics and Microbiome Research at Baylor College of Medicine. Detailed procedures were provided in previous section (**Section 3.3.4**).

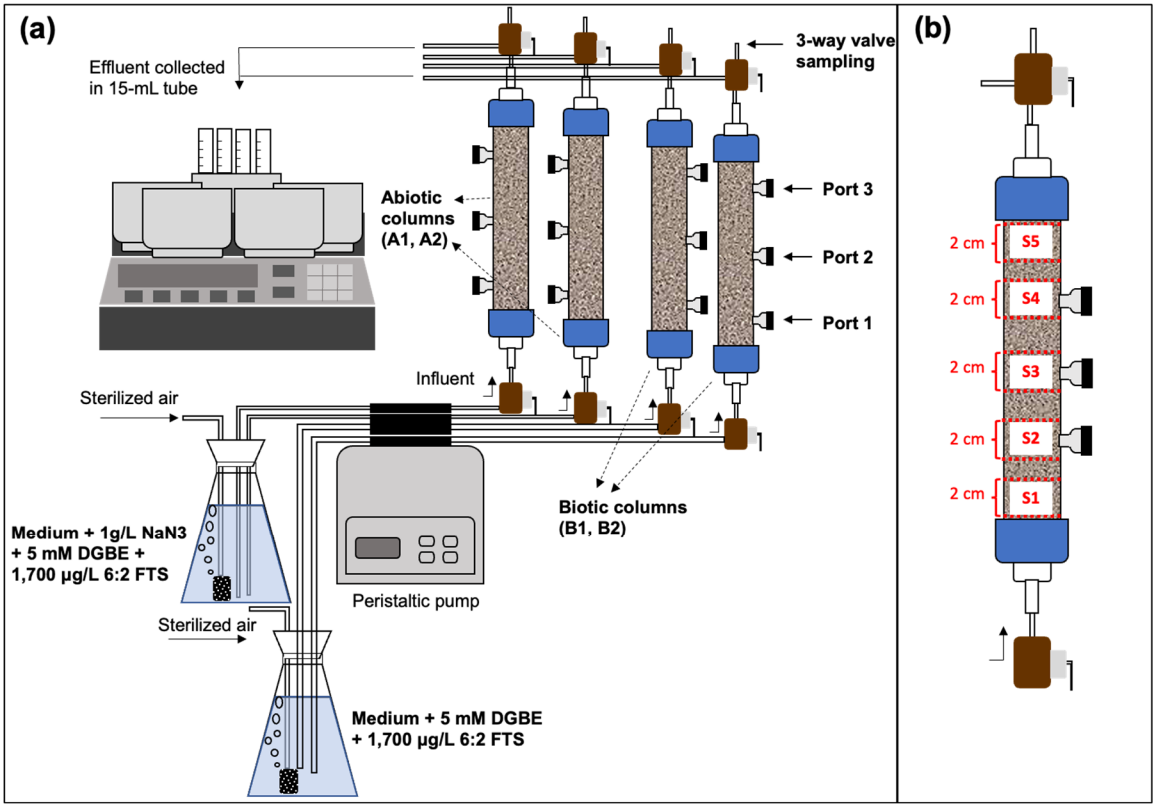


Figure 3.2 Schematic diagrams of (a) column experimental set-up and (b) segments S1-S5 delineated for the dissection of solid phase at the termination of column experiments. Segment S1 was closest to the column inlet, and segment S5 was closest to the column outlet. Ports 1, 2, and 3 were located at the center of segments S2, S3, and S4, respectively.

3.6 Mathematical Modeling of PFAS Transport and Retention

3.6.1 NAPL Column studies

3.6.1.1 Mathematical Model

The soil system was conceptualized as a porous medium containing a mobile aqueous phase and immobile NAPL at residual saturation. PFAS transport in the presence of entrapped NAPL was modeled by an advective-dispersive transport equation which incorporates soil and NAPL-water interfacial sorption as well as NAPL phase partitioning:

$$\theta_w \frac{dC}{dt} + a_{nw} \frac{d\Gamma}{dt} + \rho_b \frac{dS}{dt} + \theta_n K_{nw} \frac{dC}{dt} = \frac{\partial}{\partial x}\left[\theta_w D_H \frac{\partial C}{\partial x}\right] - \frac{\partial qC}{\partial x} \quad (3\text{-}4)$$

here, θ_w is the volumetric water content, C is the PFAS aqueous phase concentration (M/L^3), t is time (t), a_{nw} is NAPL-water specific interfacial area (L^2/L^3), Γ is the PFAS surface excess (M/L^2), $\rho_b$is the soil bulk density (M/L^3), S is the solid-phase sorbed concentration (M/M), θ_n is the volumetric NAPL content, K_{nw} is the NAPL-water partitioning coefficient, D_H is the hydrodynamic dispersion coefficient (L^2/t), x is distance (L), and q is the Darcy velocity (L/t). The HYDRUS-1D code [65] was modified to solve equation (3-4) by incorporating an immobile NAPL phase, PFAS-NAPL partitioning, and PFAS accumulation at NAPL-water interfaces, as described in **Appendix A.5**.

Based on the results of batch experiments, PFAS NAPL partitioning and solid phase sorption were modeled with linear isotherms. Soil partitioning coefficients (K_d) were estimated by fitting simulations to PFAS BTCs from no PCE-NAPL control columns using the Marquardt-Levenberg type parameter optimization algorithm in HYDRUS 1-D [65]. To estimate interfacial surface excess, IFT data for individual PFAS and PFAS mixture solutions were first fit to the Szyszkowski equation (3-1) using a nonlinear least square procedure (Matlab, R2020b) [77, 119]. Individual PFAS equilibrium surface excess (Γ, mg/m^2) was then calculated by combining equation (3-1) with the Gibbs equation [76, 120] to yield the Langmuir equation for surface excess, Langmuir-Szyszkowski equation (3-3) [121, 122].

For mixtures, the equilibrium maximum surface excess was assumed to remain constant for each PFAS and an extended Langmuir model was used to calculate surface excess [123-126]:

$$\Gamma_i = \Gamma_{max,i} \frac{K_{eq,i} C_i}{1 + \sum_i^n K_{eq,i} C_i} \quad (3\text{-}5)$$

Here, i represents the ith component in a PFAS mixture solution, which has n PFAS in total. $\Gamma_{max,i}$ and $K_{eq,i}$ are the fitted parameters for individual PFAS obtained from equation (3-1)**.** This model was recently used by Silva et al. to investigate the air-water interfacial sorption of PFAS mixtures up to 8 components.[125]. To address recent suggestions that the Freundlich isotherm model may better characterize interfacial accumulation[78, 127, 128], the PFOS and PFNA surface excesses were also modeled using a Freundlich isotherm fitted to interfacial tension data. NAPL-water specific interfacial area was estimated from previously developed equations, described in more detail in **Appendix A.4.**

3.6.2 Field-scale transport scenarios

3.6.2.1 Mathematical Model

Field-scale simulations employed a coupled unsaturated flow and transport model that incorporates the influence of the concentration of surface-active solutes on fluid flow. This formulation accounts

for the concentration dependence of surface tension (σ) and its influence on moisture retention and hydraulic conductivity [129-131]. The unsaturated flow is modeled by a mixed form of the Richard's equation [132, 133]:

$$\frac{\partial \theta_w}{\partial t} = \frac{\partial}{\partial x}\left[K\left(\frac{\partial h}{\partial x} + 1\right)\right] \tag{3-6}$$

where θ_w (L^3/L^3) is the volumetric water content, t (T) is time, x (L) is the spatial coordinate (positive upward), K (L/T) is the unsaturated hydraulic conductivity, and h (L) is the water pressure head. Here, van Genuchten-Mualem expressions [134, 135] are used to model moisture content and hydraulic conductivity as functions of σ and h [131]:

$$\theta_w = \begin{cases} \theta_r + \dfrac{\theta_S - \theta_r}{\left[1 + \left(\frac{\sigma}{\sigma_0}\alpha|h|\right)^n\right]^m}, & h < 0 \\ \theta_S, & h \geq 0 \end{cases} \tag{3-7}$$

$$K = K_s S_e^{0.5}\left[1 - \left(1 - S_e^{1/m}\right)^m\right]^2 \tag{3-8}$$

where θ_S and θ_r (L^3/L^3) are the saturated and residual water content, σ and σ_0 (M/T^2) are the surface tension in the presence and absence of AFFF constituents respectively, α (1/L), n (-), and m (-) are fitting parameters, and $S_e = (\theta_w - \theta_r)/(\theta_S - \theta_r)$ (-) is the effective saturation content. The scaling factor for the water pressure (σ/σ_0) is obtained from the Szyszkowski equation for N surface-active species in the mixture [136]:

$$\frac{\sigma}{\sigma_0} = 1 - \frac{\Sigma_i^N a_i C_i/b_i}{\Sigma_i^N C_i/b_i}\ln(1 + \Sigma_i^N C_i/b_i) \tag{3-9}$$

where a_i (-) and b_i (M/L^3) are Langmuir-Szyszkowski parameters obtained from measurements of interfacial tension (IFT) in single-component solutions [76], and C_i (M/L^3) is the aqueous concentration of surface-active species i. Capillary hysteresis is neglected.

Multispecies transport is modeled by an advective-dispersive transport equation which incorporates soil sorption and competitive air-water interfacial adsorption as follows

$$\frac{\partial(C_i\theta_w)}{\partial t} + \frac{\partial(A_{AW}\Gamma_i)}{\partial t} + \rho_b\frac{\partial S_i}{\partial t} = \frac{\partial}{\partial x}\left[\theta_w D_H\frac{\partial C_i}{\partial x} - qC_i\right] \tag{3-10}$$

Here A_{AW} (L^2/L^3) is the air-water specific interfacial area (AWIA), which depends on θ_w, Γ_i (M/L^2) is the surface excess of species i, ρ_b (M/L^3) is the soil bulk density, S_i (M/M) is the solid-phase sorbed concentration, D_H (L^2/T) is the hydrodynamic dispersion coefficient, and q (L/T) is the Darcy velocity. To consider competitive effects, Γ_i is modeled using an extended Langmuir-Szyszkowski isotherm (equation (3-5).

In the absence of experimental data for different porous materials, the Leverett Thermodynamic Model [62, 131, 137] is used to estimate $A_{AW}(\theta_w)$ from moisture retention curves:

$$A_{AW} = \frac{\rho_w g}{\sigma} \int_{\theta_w}^{\theta_s} h(\theta_w) d\theta_w \quad (3\text{-}11)$$

Where ρ_w (M/L^3) is the density of water and g (L/T^2) is the gravitational acceleration. Given the general absence of site-specific data on rate limited and competitive PFAS sorption to the solid phase, soil partitioning is represented in the model by an equilibrium Freundlich isotherm (i.e., $S_i = k_f C_i^n$), where k_f and n are estimated from soil properties (see **Appendix A.6**).

An enhanced version of the HYDRUS 1-D code [65, 138] was developed to solve the system of flow, transport, and constitutive equations presented above. Significant modifications of the simulator included: (1) introduction of interfacial tension dependence on aqueous phase concentration in the flow problem; (2) inclusion of a competitive air-water interfacial sorption in the transport equation (i.e., $\partial_t(A_{AW}\Gamma_i) = A_{AW}\Sigma_k^N \partial_{C_k}\Gamma_i \partial_t C_k + \Gamma_i \partial_t A_{AW}$); and (3) introduction of a finite element chord slope iterative scheme for the evaluation of the nonlinear adsorption isotherm in the accumulation term of the transport equation to improve mass-balance performance [139].

3.6.2.2 Simulation scenario development

To develop a suite of representative scenarios for model application, PFAS contamination information at Air Force bases (AFBs) throughout the continental US was reviewed using the on-line administrative record made available by the Air Force Civil Engineering Center (AFCEC) (https://www.afcec.af.mil/). A detailed description of this review process is given in **Appendices A.7** and **A.8**. Although this research is not intended to model the actual spill conditions at any specific site, using scenarios developed based on real contaminated sites at AFBs ensures that the conclusions drawn from this field-scale modeling effort will be representative of conditions encountered in AFFF source areas. From the candidate AFBs in the database, three locations were selected for simulation scenario development: Wright-Patterson AFB, OH, Tyndall AFB, FL, and Ellsworth AFB, SD. These locations had sufficient site-specific data for soil profile development and were selected as representative of the variety of depositional, climatic, hydrologic, and geochemical environments encountered at DoD AFFF contamination sites throughout the US. **Table 3.5** provides a high-level summary of the important features of each modeled location. Note that two different soil profiles were considered for Wright-Patterson (WP-1 and WP-2) to examine the effect of different soil texture profiles on transport under the same climatic conditions. Inclusion of Ellsworth AFB as one selected location also facilitated a qualitative comparison of model-predicted and field-measured pore water and total soil PFAS concentrations at one AFFF site, where detailed field measurements were undertaken [140].

Table 3.5 High-level summary of site-specific conditions for field-scale simulations.

AFB	Location	Climatic Conditions	Subsurface
Wright-Patterson	Greene County, Southwest Ohio	Medium rainfall (35” per year). Conditions can be humid with warm summers and cold winters. The mean annual temperature is 52 °F.	Alluvial sediments above glacial outwash sediments. Water table fluctuates between 4 and 17 ft BGS.

Tyndall	Bay County, Northwest Florida	High rainfall (61" per year). Coastal location with subtropical conditions. It is a humid region with annual temperatures ranging between 59 and 78 °F.	Highly transmissive, well sorted fine- to medium-grained sands. Shallow water table between 1 and 10 ft BGS.
Ellsworth	Meade County, South Dakota.	Low rainfall (16" per year). Semiarid continental region. Average temperatures in summer and winter are 68 and 26 °F respectively.	Alluvial and colluvial deposits, and Pierre Shale. Water table ranges from 4 to 34 ft BGS.

PFAS spill and usage data in the AFCEC database for the reviewed locations revealed that PFAS contamination was generally associated with fire training areas, real fire extinguishing episodes, vehicle crashes, hangar releases, spray test areas, and fire stations. Thus, for modeling purposes, PFAS source terms were divided into three different categories associated with their contrasting release characteristics: (1) repetitive spills of diluted AFFF, (2) one-time releases of diluted AFFF and (3) one-time accidental releases of AFFF concentrate. Based upon these categories, six release conditions were defined for the simulations (**Table 3.6**). Consistent with fire training and spray test area sources, the first 4 release conditions (Sp1-4) are repetitive spills of a 3% AFFF solution over a 10-year period, each associated with different spill volumes and frequency. Sp5 and Sp6 represent one-time releases of AFFF representative of an emergency crash response (3% solution) and an accidental (concentrate) release, respectively.

Table 3.6 Spill scenario Parameters for field-scale simulations.

Spill	Frequency	Volume[a] (gal)	Area (ft^2)	Spill concentration (C_{sp})	V_c[b] (cm^3/cm^2)
Sp1	4 times per year	100	100 × 100	3% AFFF	1.639
Sp2	4 times per year	40	100 × 100	3% AFFF	0.655
Sp3	4 times per year	25	100 × 100	3% AFFF	0.410
Sp4	biweekly	15	100 × 100	3% AFFF	1.598
Sp5	once	800	100 × 100	3% AFFF	0.328
Sp6	once	400	50 × 50	AFFF concentrate	0.655

[a]Volume of each spill equivalent to AFFF concentrate.

[b]Cumulative equivalent volume of spill (expressed as volume of AFFF concentrate) per unit area released in each scenario.

AFFF formulations are proprietary mixtures containing fluorocarbon and hydrocarbon surfactants. The surface-active properties of AFFF constituents tend to lower the air-water IFT, with a 3% AFFF (3M FC-303cf) solution having a surface tension of ca. 3 mN/m compared with ca. 72 mN/m for pure water (96% reduction) at 25°C [108]. Although PFOS has been documented as the predominant fluorocarbon surfactant in AFFF [8], prior research has revealed that the presence of PFOS alone cannot explain the observed IFT reduction [108]. Thus, accounting for the presence of hydrocarbon surfactants (e.g., short chain alkyl sulfate salts [141]) in AFFF is crucial to predict the IFT reduction associated with AFFF releases. In addition, given the high concentration of hydrocarbon surfactants in AFFF, these compounds would likely compete with PFAS for interfacial accumulation sites, altering the transport and retention of compounds in the unsaturated

soil. Given the proprietary nature and complex composition of commercial AFFF formulations, it was beyond the scope of this work to directly model the influence of the collection of alkyl sulfate salt constituents on IFT. Instead, an alternative approach was used where a model alkyl sulfate salt (MASS) was introduced as a representative component of hydrocarbon surfactants in the solution. In the simulations presented herein, the concentration of MASS in a 3% AFFF solution was set at 1100 mg/L. This concentration is consistent with alkyl sulfate salt levels documented for AFFF formulations (1-5% by weight) [142]. Interfacial adsorption parameters for MASS were estimated from IFT data for AFFF solutions [108] such that the combined influence of PFOS and MASS produced the observed IFT reduction in the referenced study. Here, Equation (3-1) was used for parameter estimation. MASS interfacial adsorption parameters can be found in **Table 3.7**.

In addition to PFOS and MASS, PFOA was selected as a third constituent for the infiltrating AFFF mixture. PFOA is present at significant concentrations in AFFF [143] and is representative of less surface-active PFAS. Use of this mixture facilitates meaningful consideration of the retention in the vadose zone of fluorinated surfactants present in AFFF solutions. A summary of interfacial accumulation parameters used in these simulations for each mixture component is presented in **Table 3.7**.

Table 3.7 Langmuir-Szyszkowski parameters for field-scale simulations.

Compound	b_i (µg/cm3)	Γ_{max} (µg/cm2)	Reference
PFOA	49	0.2095	[108]
PFOS	1.7	0.1530	[108]
MASS	0.75	0.1430	Fitted to AFFF data from [108]

Soil sorption can also play a significant role in the transport and retention of PFAS in the vadose zone. To predict the soil sorption behavior for each compound, separate multilinear regression models were developed to relate sorption isotherm parameters to different soil properties and conditions (such as silt and organic carbon (OC) content, and pH) based on available data in the literature. See **Appendix A.6** for a detailed description of correlation development.

Given that simulations were performed in a 1-D domain, the solution of the coupled flow and transport equations required initial spatial profiles of capillary pressure and concentration, as well as boundary conditions for each dependent variable. To obtain capillary pressure profiles within the modeled soil horizons, the flow problem was solved for a period of one year using a time-dependent water flux as the top boundary condition and a constant pressure head at the bottom boundary. The top water flux was defined based on the actual net recharge (evapotranspiration subtracted from rainfall) for each site (data from AFCEC, see **Appendix A.7.1**), and the constant head at the bottom was defined consistent with the depth to the water table (see **Appendix A.8**). The conditions for the transport problem included initial concentration of zero throughout the domain, defined flux at the ground surface, and zero diffusive-dispersive flux at the lower boundary. The flux at the upper boundary was defined based on the concentration of compounds

in the spill (either 3% or concentrate AFFF, see **Table 3.8**), and the frequency and volume of spill per area (**Table 3.6**) assuming a duration of one day per spill.

Table 3.8 Concentration of PFOA, PFOS, and MASS in mixtures for field-scale simulations.

	Concentration in Mixture (mg/L)	
Compound	**3% AFFF**	**Concentrate AFFF**
PFOA	2.6	87
PFOS	160	5333
MASS	1100	36667

The coupled flow and transport problem was simulated for a period of 40 years for each scenario and suite of spill conditions. Boundary conditions for the flow problem were maintained consistent with the temporally variable evapotranspiration, and a constant water table elevation. Other than during the spill events within the first 10 years of simulations, the top boundary condition for the transport problem was maintained as zero flux for all the species.

4. Results and Discussion

4.1 Batch partitioning studies

4.1.1 PFAS accumulation at the air-water interface

4.1.1.1 Surface Tension Measurements

The surface tension of ultrapure water was determined to be 71.7 ± 0.3 mN/m at 22 °C, consistent with the reference value of 72.3 mN/M for pure water at 20 °C [144]. At concentrations less than 1,000 mg/L in ultrapure water, KPFOS solutions had lower surface tensions than those of PFOA at an equivalent concentration, whereas PFOA solutions had the lowest surface tension (16.7 mN/m vs. 35.3 mN/m for KPFOS) at the highest concentration levels. The decreasing surface tensions associated with KPFOS at concentrations greater than 1,000 mg/L coincided with a visible separate-phase liquid floating on the surface of the solution, which was also observed in solutions with PFOA above 4,000 mg/L (see **Appendix A.9, Figure A.1,** and **Figure A.2**). These concentrations corresponded to the critical micelle concentration (CMC) determined for PFOA (3,460 mg/L) and PFOS (698 mg/L), based on the break in the conductivity versus concentration curve [81]. Comparisons of measured surface tension data for PFOA and PFOS in ultrapure water with previously reported surface tension measurements are shown in **Figure 4.1** and **Figure 4.2**, respectively.

The surface tension decreased for solutions containing the cations and anions (i.e., dissolved solids) commonly found in the ground water of the United States (**Figure 4.3**). For example, the surface tension of ca. 1 mg/L PFOA in solutions with 42.3 mg/L total dissolved solids (TDS) was 0.3 % lower than that measured with ultrapure water, 1.1 % lower in solutions with 375 mg/L TDS, and 1.2 % lower in solutions with 1,789 mg/L TDS. These findings are consistent with those for PFOA in 10 mM NaCl (584 mg/L) reported by [14] (**Figure 4.4**). At approximately 1 mg/L PFOS, the surface tension was 2 % lower in the 44 mg/L TDS solution, 5.5 % lower in 391 mg/L TDS, and 6.4 % lower in the 1,741 mg/L TDS solution. Surface tensions were within 1% of each other for PFOS concentrations up to approximately 50 mg/L in solutions with 391 and 1,741 mg/L TDS.

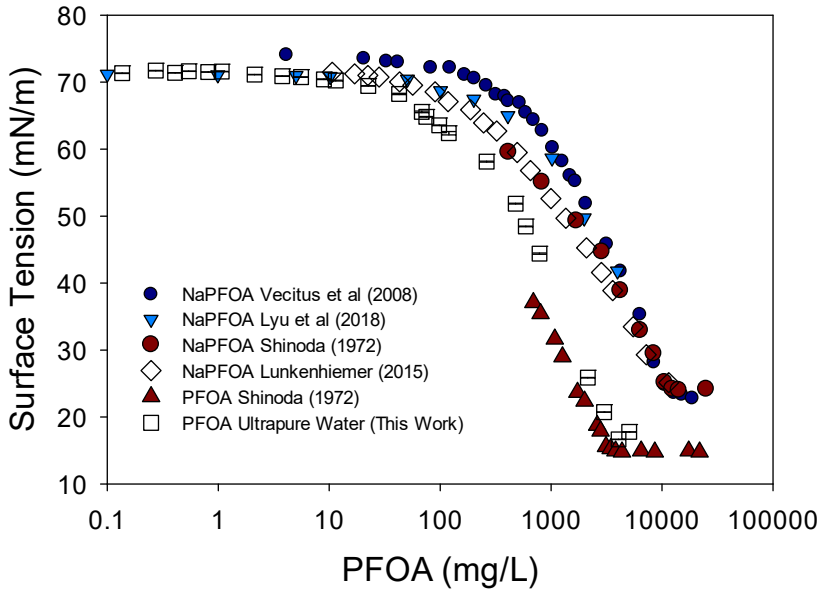


Figure 4.1 Comparison of surface tension data for NaPFOA and PFOA in ultrapure water measured in this work (open boxes) to values obtained from the literature.

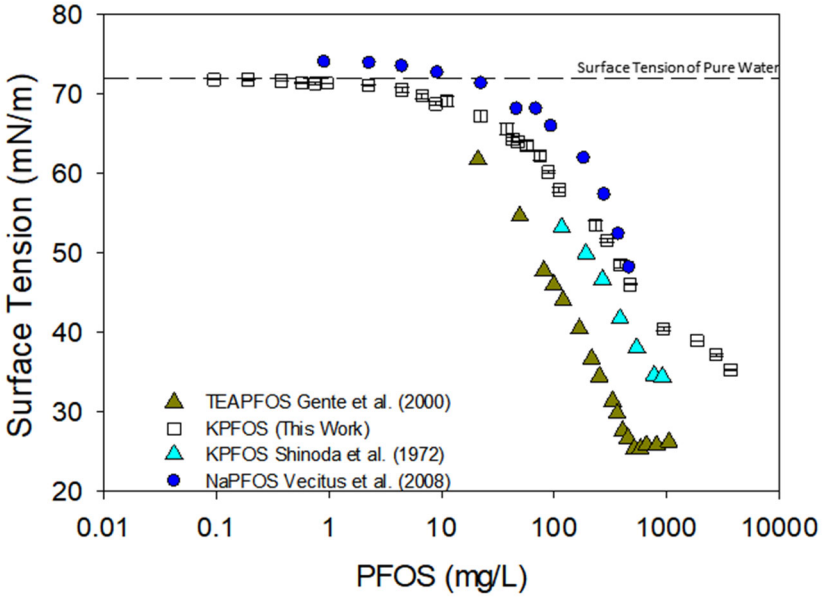


Figure 4.2 Comparison of surface tension data obtained for KPFOS measured in ultrapure water in this work (open boxes) to values for TEAPFOS, KPFOS, and NaPFOS obtained from the literature.

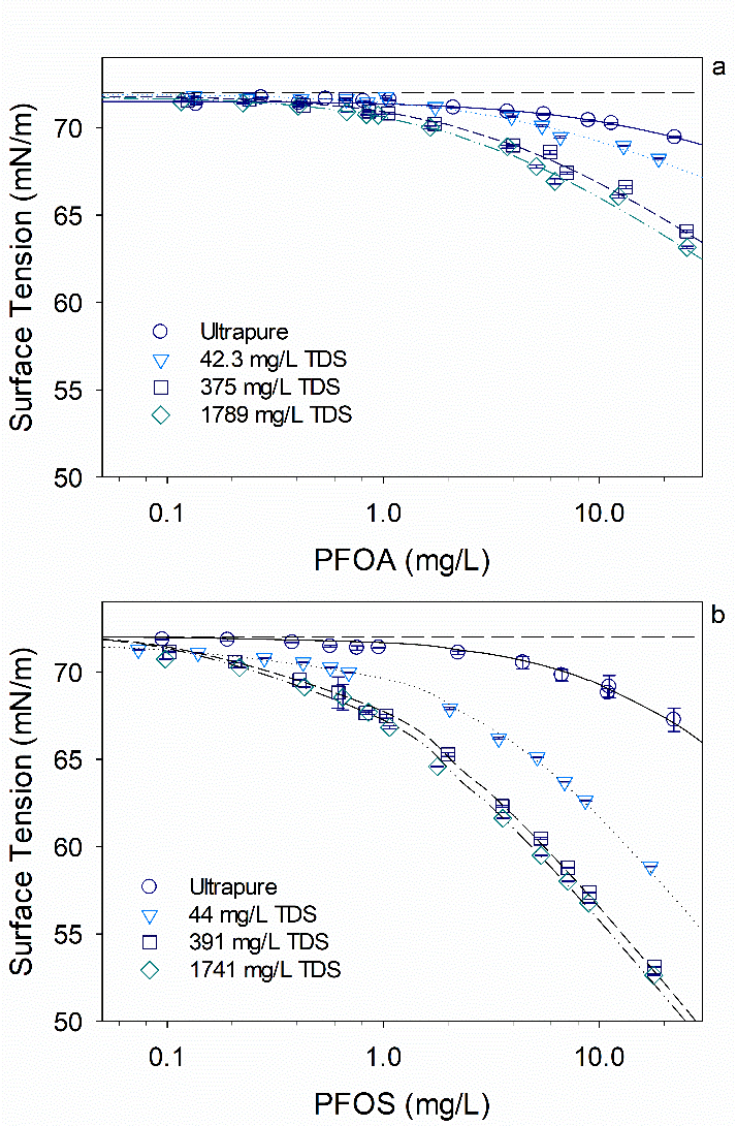


Figure 4.3 Air-Water surface tension of PFOA(a) and FPOS (b) reported as PFOS in solutions with major cations and anions found in groundwater. Lines are the Szyszkowski equation fit.

4.1.1.2 Surface Excess Calculations

The decrease in surface tension at the air-water interface is related to the concentration of surfactant molecules at the air-water interface [145]. By measuring the air-water surface tension over a range of bulk-water concentrations, the surface excess can be determined using the Gibbs equation:

$$\Gamma = -\frac{C}{RT}\left(\frac{\partial \gamma}{\partial C}\right)_T \qquad (4\text{-}1)$$

where Γ is the surface excess or concentration at the air-water interface (mg/m^2), R is the universal gas constant (8.314 J mol/K), T is the absolute temperature (K), γ is the surface tension (mN/m), and C is the bulk-water concentration (mol/L). There is an alternative form for Equation (4-1), known as Millner's equation [146]:

$$\Gamma = -\frac{1}{\mathrm{RT}}\left(\frac{\partial\gamma}{\partial \ln \mathrm{C}}\right)_{\mathrm{T}} \tag{4-2}$$

An air-water interface partitioning coefficient (K_i) relates the surface excess (Γ) to the aqueous phase concentration (C):

$$\Gamma = K_i \mathrm{C} \tag{4-3}$$

Substituting Eq. (4-3) into Eq. (4-1) yields [147]:

$$K_i = -\frac{1}{\mathrm{RT}}\left(\frac{\partial\gamma}{\partial \mathrm{C}}\right)_{\mathrm{T}} \tag{4-4}$$

To calculate K_i using Eq. (4-4) involves determining the slope of the measured surface tension (γ) vs. aqueous concentration (C) (see **Figure 4.4** and **Figure 4.5**) and dividing by R and the temperature at which the measurements were taken. Substituting Eq. (4-3) into Eq. (4-2) yields [14]:

$$K_i = -\frac{1}{\mathrm{RTC}}\left(\frac{\partial\gamma}{\partial \ln(\mathrm{C})}\right)_{\mathrm{T}} \tag{4-5}$$

However, use of Eq. (4-5) requires fitting the slope of the measured surface tension (γ) vs. the natural log of the aqueous concentration (C) (see **Figure 4.5** and **Figure 4.6**) and choosing a 'target concentration' [14, 29, 148]. For example, a target concentration of 1 mg/L was used in Lyu, Brusseau [14].

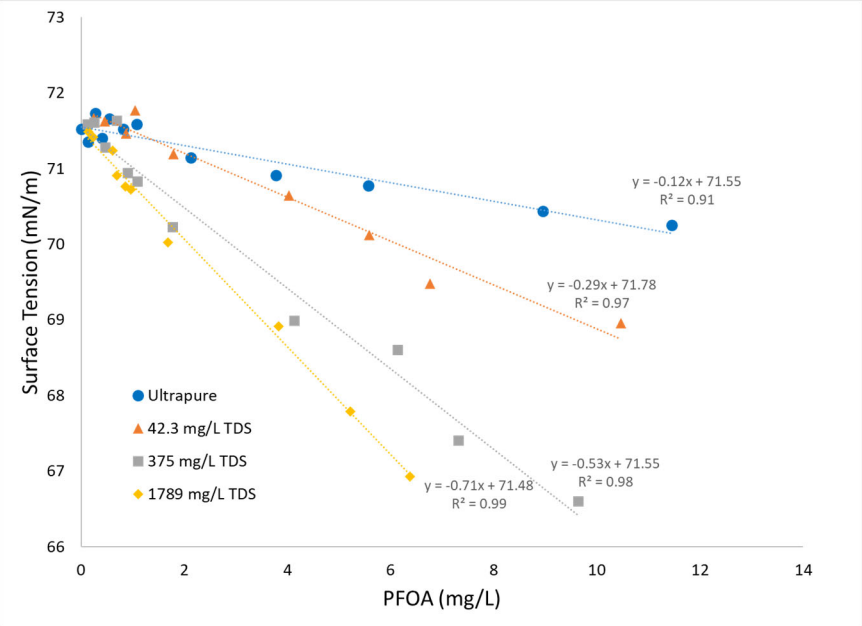


Figure 4.4 Linear fit of surface tension versus PFOA concentration using Eq. (4-4).

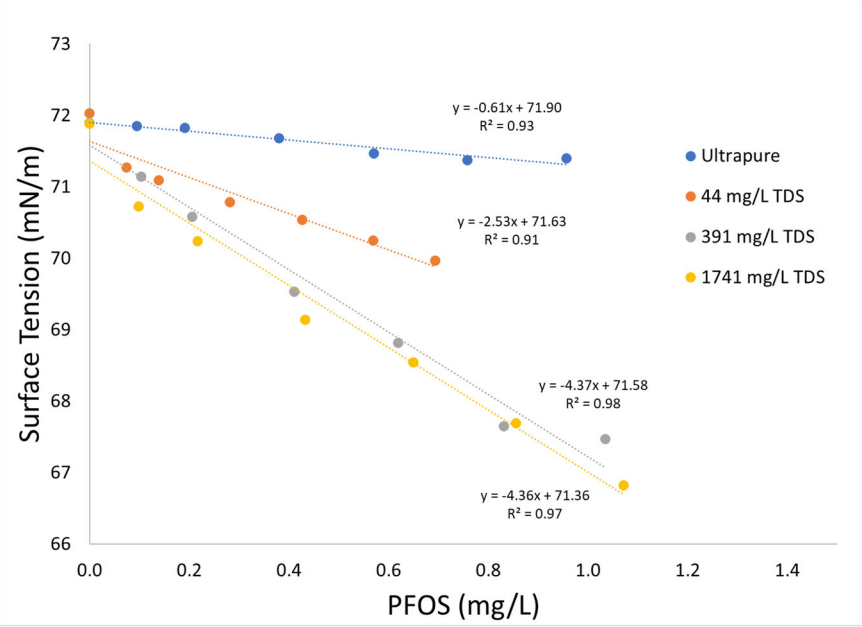


Figure 4.5 Linear fit of surface tension versus PFOS concentrations using Eq. (4-4).

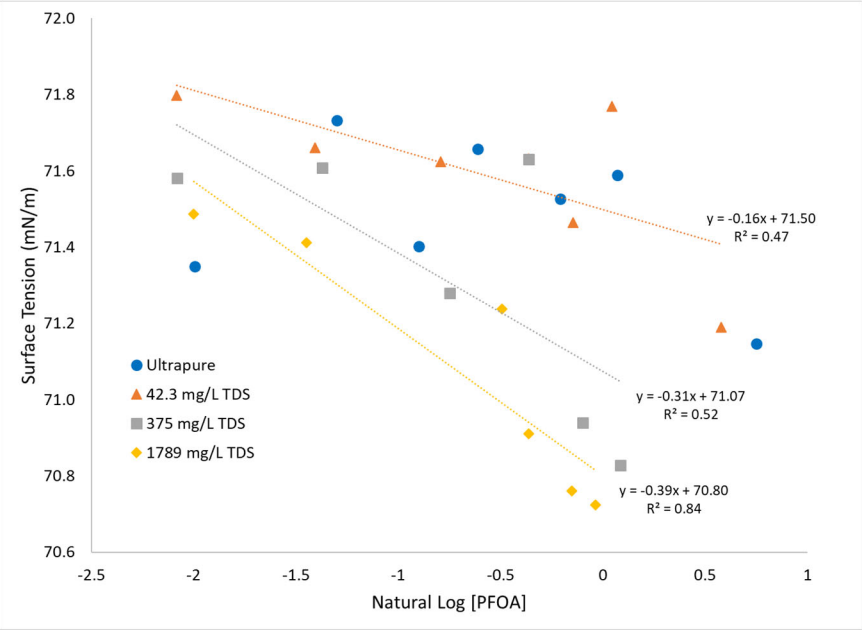


Figure 4.6 Least squares regression fits of surface tension versus the natural log of PFOA concentration using Eq. (4-5).

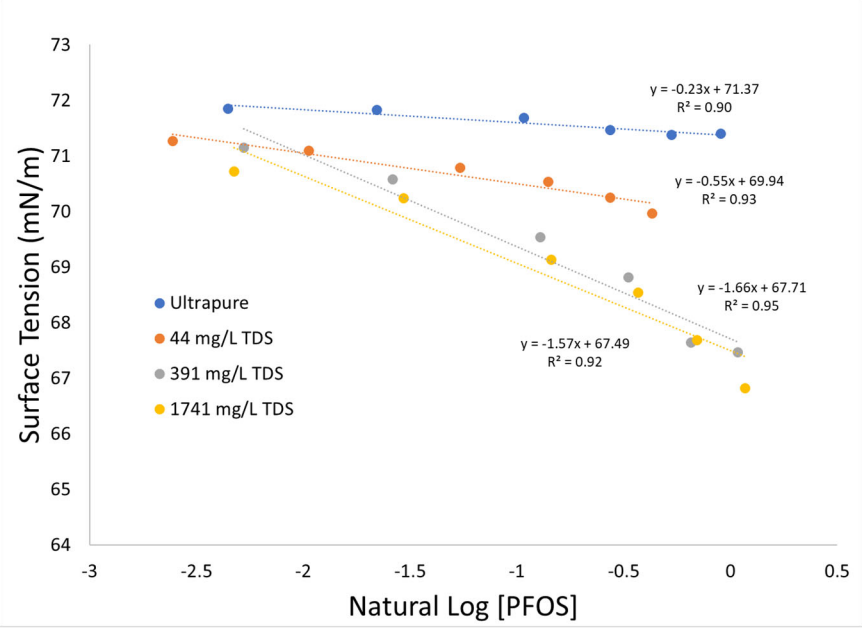


Figure 4.7 Least squares regression fits of surface tension versus the natural log of PFOS concentrations using Eq. (4-5).

An alternative way to fit surface tension data is by using the Szyszkowski equation (3-1). The Syzszkowski equation has been used to fit surface tension measurements ranging from low bulk-water concentrations to those near the CMC [13, 77]. The lines shown in **Figure 4.3** are the fit of Eq. (3-1) to the measured surface tension values, in the range 0.1 mg/L to 25 mg/L and 90 mg/L for PFOA and PFOS, respectively, using the MATLAB® R2018a nonlinear regression model fitnlm. The fitted parameters for the coefficients, a and b, in Eq. (3-1) for PFOA and PFOS are shown in **Table 4.1** and **Table 4.2**, respectively. All fits resulted in a regression coefficient (r^2) of 0.999 or greater, indicating ideal surface behavior of PFOA and PFOS. The Szyszkowski equation fits the entire concentration range (e.g., 0.1 to 5,000 mg/L), however, fitting the entire concentration range does not capture the change in surface tension that occurs for concentrations of less than 100 mg/L. Therefore, the fits were completed using a limited concentration range to best represent the lower concentration ranges that would be expected in the environment.

Table 4.1 Szyszkowski fitted parameters for PFOA concentration range from 0 to 25 mg/L.

Solution	γ_0 (mN/m)*	*a* (estimate ± standard error)	*b* (estimate ± standard error)
Ultrapure	71.52 ± 0.04	0.031 ± 0.015	14.7 ± 9.4
42.3 mg/L TDS	71.92 ± 0.03	0.033 ± 0.006	4.8 ± 1.6
375 mg/L TDS	71.87 ± 0.03	0.052 ± 0.005	3.5 ± 0.7
1789 mg/L TDS	71.80 ± 0.04	0.052 ± 0.003	2.7 ± 0.4

*Measured surface tension of PFOA free solution

Table 4.2 Szyszkowski fitted parameters for PFOS concentration range from 0 to 90 mg/L.

Solution	γ_0 (mN/m)*	*a* (estimate ± standard error)	*b* (estimate ± standard error)
Ultrapure	71.89 ± 0.08	0.087 ± 0.010	18.4 ± 3.8
44 mg/L TDS	72.03 ± 0.02 (71.44 ± 0.01)†	0.100 ± 0.003	3.5 ± 0.3
391 mg/L TDS	71.89 ± 0.04	0.094 ± 0.002	1.1 ± 0.1
1741 mg/L TDS	71.89 ± 0.02	0.093 ± 0.002	1.0 ± 0.1

*Measured surface tension of PFOS free solution
†Value determined to best fit surface tension data

To obtain surface excess values, the first derivative of Eq. (3-1):

$$\gamma_0 \frac{d\left[1 - a \times \ln\left(\frac{C}{b} + 1\right)\right]}{dC} = -\frac{a\gamma_0}{C + b} \tag{4-6}$$

is substituted into Eq. (4-1) to yield:

$$\Gamma = \frac{a\gamma_0}{\mathrm{RT}} \frac{\mathrm{C}}{C + b} \tag{4-7}$$

Equation (4-7) was first presented by Langmuir [149] and is also known as the Langmuir-Szyszkowski equation for describing ideal surface behavior [122]. The term $\frac{a\gamma_0}{\mathrm{RT}}$ represents the maximum surface excess (Γ_{max}) and the b term is the surface activity and relates to the free energy (ΔG) of transfer from the bulk solution to the interface.

Table 4.3 presents the fitted parameters for Eq. (4-7) for solutions containing PFOA or PFOS at bulk-water concentrations between 0.1 and 25 mg/L, and 90 mg/L, respectively, at different concentrations of dissolved solids. In ultrapure water, the maximum surface excess for PFOA was 0.38 ± 0.2 mg/m^2 and was higher for PFOS, reaching 1.28 mg/m^2. The presence of dissolved solids slightly increased the maximum surface excess, from 0.38 ± 0.2 to 0.63 ± 0.04 mg/m^2 for PFOA and 1.28 ± 0.15 to 1.39 ± 0.02 mg/m^2 for PFOS. Most importantly, greater surface excess was obtained at lower PFOA or PFOS concentrations in the presence of dissolved solids. This behavior relates to the b term in Eq. (4-7), which decreased with increasing dissolved solids concentration. Also shown in **Table 4.3** are correlation equations that explicitly incorporate the dependence of b on TDS.

Table 4.3 Fitted Langmuir/Szyszkowski equations for the maximum surface excess (Γ_{max}) of PFOA and PFOS at the air-water interface in solutions as a function of total dissolved solids (TDS)

Fitted Conc. Range	PFOA, 0.1 to 25 mg/L		PFOS, 0.1 to 90 mg/L	
Solution	Maximum Surface Excess, Γ_{max} (**mg/m^2**)	Surface Activity, b (**mg/L**)	Maximum Surface Excess, Γ_{max} (**mg/m^2**)	Surface Activity, b (**mg/L**)
Ultrapure	0.38 ± 0.2	14.7 ± 9.4	1.28 ± 0.15	18.4 ± 3.8
40 mg/L TDS	0.41 ± 0.08	4.8 ± 1.6	1.47 ± 0.04	3.5 ± 0.3
400 mg/L TDS	0.63 ± 0.07	3.5 ± 0.7	1.39 ± 0.02	1.1 ± 0.1
1700 mg/L TDS	0.63 ± 0.04	2.7 ± 0.4	1.36 ± 0.02	1.0 ± 0.1
Average/Correlation	0.51 ± 0.32	$8.58x[TDS]^{-0.15}$	1.37 ± 0.16	$9.07x[TDS]^{-0.32}$

A comparison of the PFOA and PFOS air-water partitioning coefficients (K_i) as determined by the linear and natural log fits of the measured surface tension data for each TDS solution, and the surface excess (Γ) equations determined from the parameters given in **Table 4.1** and **Table 4.2**, is provided in **Table 4.4** and **Table 4.5**, respectively.

Table 4.4 Comparison of air-water partitioning coefficients (K_i) and surface excess (Γ) for PFOA using the Linear, Natural Log and Szyszkowski methods.

Fit Type	Linear	Natural Log	Szyszkowski
Conc. Range (mg/L)	0.1 to 8	0.1 to 1.8	0 to 25
Units	K_i (L/mg)(mg/m^2)	K_i (mg/m^2)	Surface Excess (mg/m^2)
Ultrapure	0.021 ± 0.002	0.011± 0.016	$\Gamma = 0.38 \pm 0.2 \frac{C}{C + (14.7 \pm 9.4)}$
42.3 mg/L TDS	0.049 ± 0.003	0.026 ± 0.013	$\Gamma = 0.41 \pm 0.08 \frac{C}{C + (4.8 \pm 1.6)}$
375 mg/L TDS	0.090 ± 0.005	0.053 ± 0.025	$\Gamma = 0.63 \pm 0.07 \frac{C}{C + (3.5 \pm 0.7)}$
1789 mg/L TDS	0.120 ± 0.004	0.065 ± 0.014	$\Gamma = 0.63 \pm 0.04 \frac{C}{C + (2.7 \pm 0.4)}$
		Summary	$\Gamma = 0.51 \pm 0.32 \frac{C}{C + (8.58x[TDS]^{-0.15})}$

Table 4.5 Comparison of air-water partitioning coefficients (K_i) and surface excess (Γ) for PFOS using the Linear, Natural Log and Szyszkowski methods.

Fit Type	Linear	Natural Log	Szyszkowski
Conc. Range (mg/L)	0.1 to 1	0.1 to 1	0 to 90
Units	K_i (L/mg)(mg/m^2)	K_i (mg/m^2)	Surface Excess (mg/m^2)
Ultrapure	0.125 ± 0.015	0.048 ± 0.008	$\Gamma = 1.28 \pm 0.15 \frac{C}{C + (18.4 \pm 3.8)}$
44 mg/L TDS	0.517 ± 0.071	0.113 ± 0.015	$\Gamma = 1.47 \pm 0.04 \frac{C}{C + (3.5 \pm 0.3)}$
391 mg/L TDS	0.893 ± 0.063	0.340± 0.039	$\Gamma = 1.39 \pm 0.02 \frac{C}{C + (1.1 \pm 0.1)}$
1741 mg/L TDS	0.893 ± 0.065	0.322 ± 0.046	$\Gamma = 1.36 \pm 0.02 \frac{C}{C + (1.0 \pm 0.1)}$
		Summary	$\Gamma = 1.37 \pm 0.16 \frac{C}{C + (9.07x[TDS]^{-0.32})}$

These expressions, along with the average maximum surface excess can be used in Eq. (4-7) to estimate the surface excess for PFOA and PFOS in ground water with TDS concentrations in the typical range of 50 to 1500 mg/L. As shown in **Figure 4.8**, the linear air-water partition coefficients fail to capture the nonlinear plateau indicated by the Langmuir-Szyszkowski equation when the air-water interface is saturated with PFOA or PFOS molecules (i.e., maximum surface excess).

This means that both the linear and natural log approaches should be used with caution, especially at high aqueous phase concentrations.

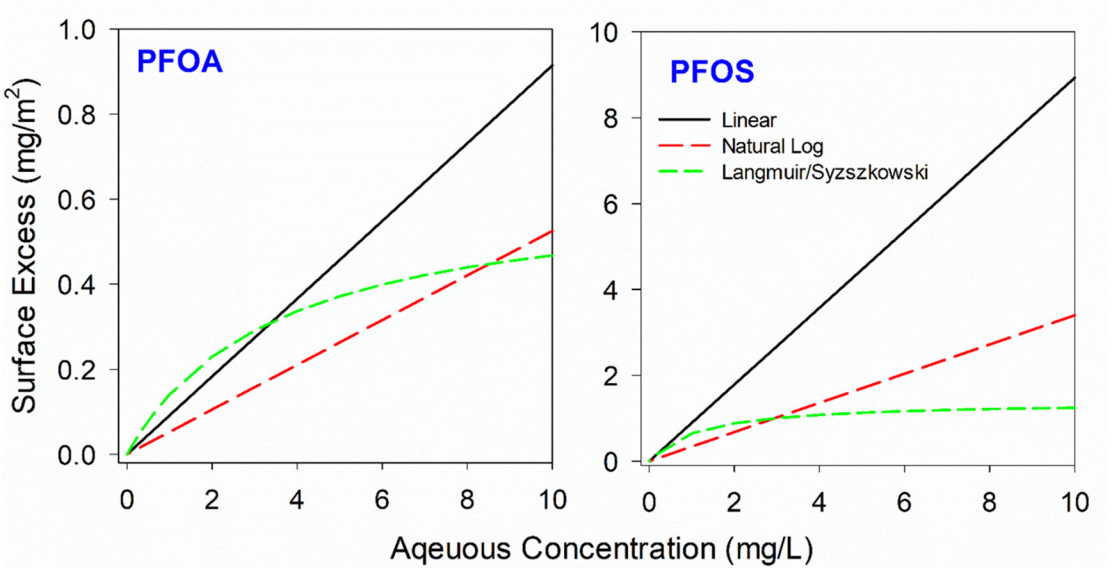


Figure 4.8 Comparison of surface excess values as a function of aqueous phase concentration calculated using the Linear, Natural Log and Langmuir-Szyszkwoski methods.

4.1.1.3 Concluding remarks

The surface excess data presented above indicate that the environmental fate and transport of PFOA and PFOS could be strongly influenced by accumulation at the air-water interface in unsaturated soils. The magnitude of PFOA or PFOS accumulation will be directly proportional to the surface area of the air-water interface. The air-water interfacial area for 1 m^3 volume of soil can range from approximately 80 m^2 up to 10,000 m^2 depending on the degree of water saturation and grain size [147, 150]. For a soil with air-water interfacial area of 80 m^2, the accumulation of PFOA and PFOS, based on the data shown in **Figure 4.9**, is expected to be small relative to the mass present in the aqueous and solid phases. In contrast, accumulation of PFOA and PFOS is expected to be significant in soil with air-water interfacial area of 1,000 m^2 where upwards of 70% of the PFOS mass would be expected to reside at the air-water interface relative to the mass in the bulk water and adsorbed to the soil (**Figure 4.9**). Details of the methods used to calculate the PFOA and PFOS mass distributions are provided in **Appendix A.10**. This analysis indicates that when PFOA and PFOS enter unsaturated soils, they will tend to accumulate at the air-water interface, where they may serve as a long-term sources of subsurface contamination.

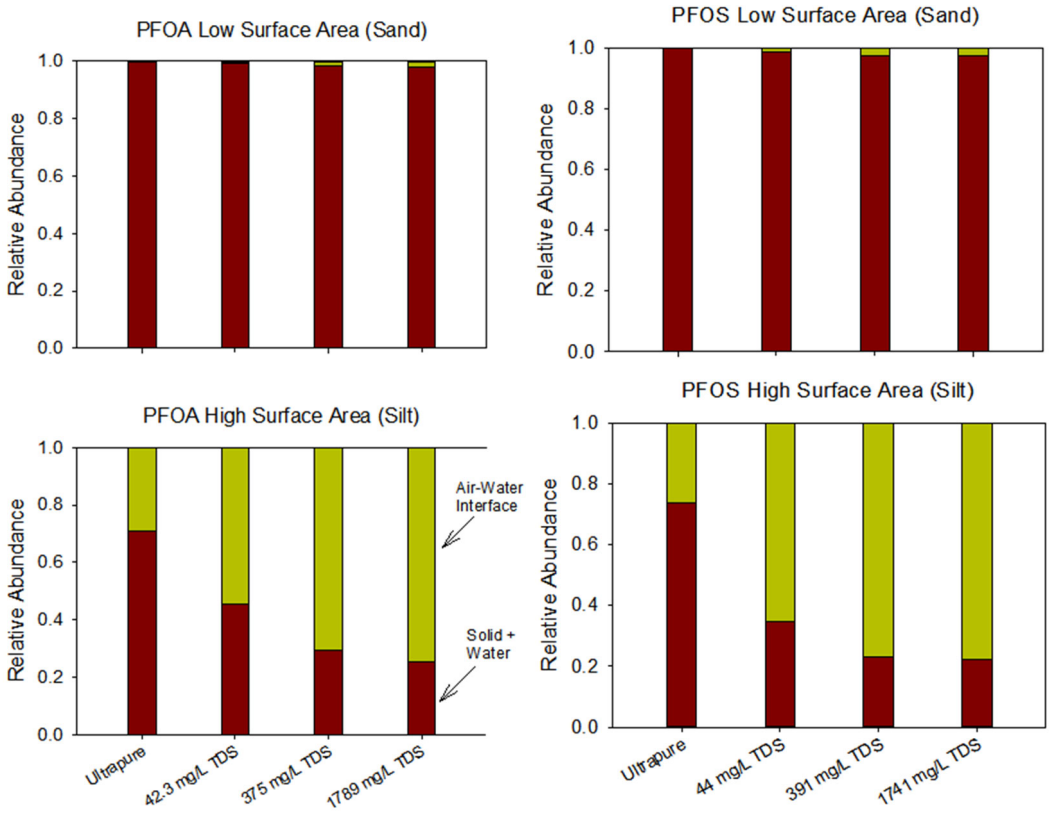


Figure 4.9 Distribution of PFOA or PFOS mass at the air-water interface and the mass dissolved in the aqueous phase and adsorbed onto the solids assuming a 1 mg/L aqueous concentration. It was assumed a water saturation at which surface area is 80 m^2 in 1 m^3 volume of soil.

4.1.2 PFAS mixture accumulation at NAPL-water interfaces

4.1.2.1 Interfacial Tension Measurements

One indicator of surface activity is the concentration required to decrease the interfacial tension by 20 mN/m (i.e., C20), also referred to as efficiency [81]. The C20 for PFOA was 231 mg/L, 18 mg/L for PFOS, and 3.5 mg/L for FOSA, indicating that FOSA was the most efficient at reducing the air-water interfacial tension (**Figure 4.10a-c**). The FOSA air-water interfacial tension decreased to its lowest value of 31 mN/m at 19.4 mg/L with no further decrease up to the maximum measured FOSA concentration of 86.5 mg/L (**Figure 4.10c**). This plateau in interfacial tension with increasing concentration indicates the formation of micelles [81] with 19.4 mg/L representing the critical micelle concentration (CMC) for FOSA in synthetic groundwater. This CMC is significantly greater than the estimated FOSA solubility of 0.008 mg/L [151] or 4.45 mg/L [152] showing that the molecular fragment method based on training datasets and the polarization charge density calculations are not capable of predicting FOSA solubility, pointing to the need to experimentally determine solubility for perfluoroalkyl substances. Although FOSA was the most

efficient based on C20, solutions containing PFOA produced the greatest air-water interfacial tension decrease, to a value of ca. 16 mN/m.

Compared to the decrease in air-water interfacial tension, greater concentrations of PFOA and PFOS were required for an equivalent decrease in NAPL-water interfacial tension. The C20 for PFOA increased from 231 mg/L for the air-water interface to 852 mg/L for the dodecane or PCE-water interface and to 3,091 mg/L for JP-4–water interface (**Figure 4.10a**). Likewise, the C20 for PFOS increased from 18 mg/L for the air-water interface to 170 mg/L for the dodecane-water interface, 90 mg/L for the PCE-water interface, and 448 mg/L for the JP-4–water interface (**Figure 4.10b**). Although FOSA was the most efficient at lowering the air-water interfacial tension, it was the least efficient for the NAPL-water interface. The NAPL-water interfacial tensions only decreased ca. 10 mN/m for dodecane and PCE, and only by 4 mN/m with JP-4 in FOSA solutions, even at concentrations above the CMC. Given that its nonionic amide headgroup is the primary difference between FOSA and PFOA or PFOS, the difference in behavior at the NAPL-water interface can be attributed to the PFOA and PFOS ionic headgroups, indicating that the perfluorocarbon tail plays a less important role at the NAPL-water interface than the headgroup.

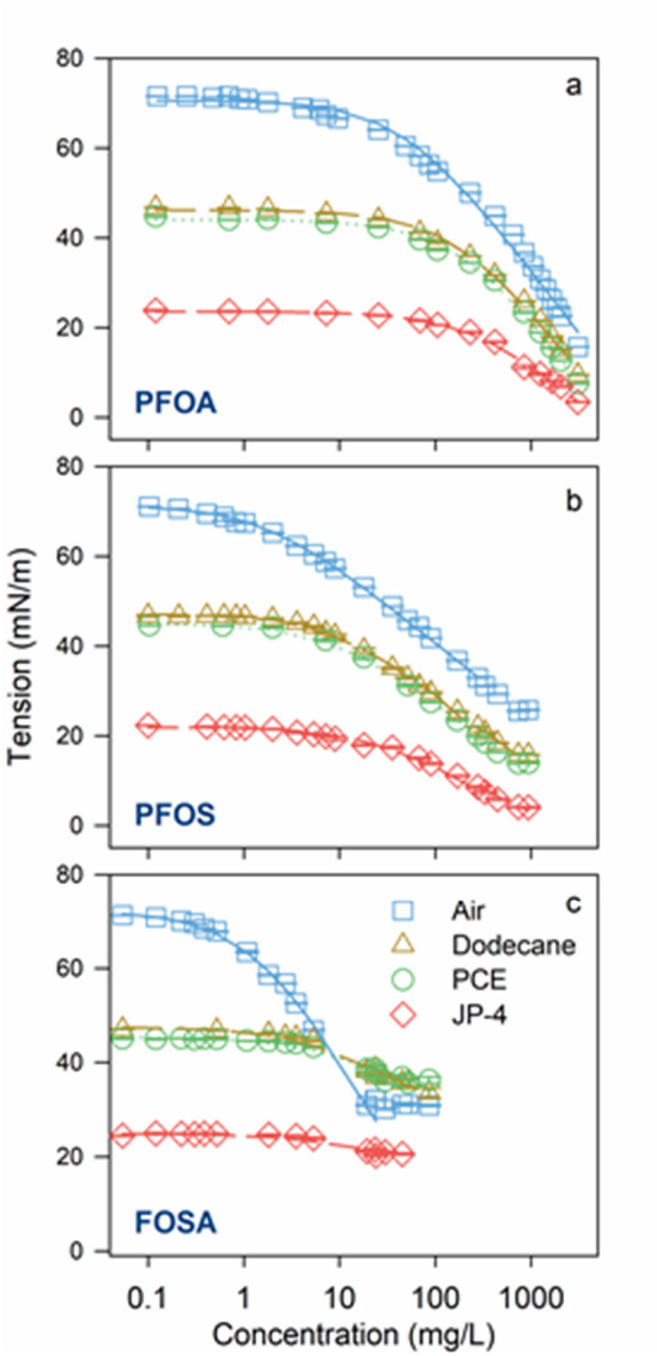


Figure 4.10 Interfacial tension for PFOA (a), PFOS (b), or FOSA (c) in an aqueous solution with approximately 380 mg/L TDS. Air-water interfacial tension results for PFOA and PFOS were previously reported in Costanza et al. (2019). The lines shown in a-c are the fits of the Szyszkowski equation (Eq. (3-1) and (4-1) to (4-5)) to the measured interfacial tension values.

AFFF formulations contain a mixture of water, fluorocarbon and hydrocarbon surfactants, and solvents[153] with average molecular weight of 19 g/mol due to water being between 83 and 87% based on the safety data sheet (SDS) for 3M FC-303cf light water AFFF 3% concentrate. Although the SDS lists amphoteric fluoroalkylamine derivative being present at between 1 and 5%, as noted by Place and FieldPlace and Field [154], these substances were not present in all 3M AFFF formulations. The predominant fluorocarbon surfactant present in the 3M and Ansul AFFF formulations was PFOS at ca. 0.3% based on LC-MS/MS negative ion analysis, which was expected per the SDS listing of between 0.1 to 1 %. The concentration of PFOS in the AFFF solutions is shown on the lower abscissa axis of **Figure 4.11**. No analyses were performed to determine the identity or concentration of hydrocarbon surfactants or solvents present, and thus, the AFFF concentrations reported in **Figure 4.11** are based on the total mass of AFFF added. As shown in **Figure 4.11a**, the AFFF formulations produced interfacial tension curves that differed in shape compared to those obtained for PFOS alone. The air-water interfacial tension for the AFFF formulations deceased by less than 2 mN/m between 0.12 to ca. 20 mg/L, followed by a decrease to ca. 16 mN/m between ca. 20 to 3,000 mg/L. The interfacial tension remained at ca. 16 mN/m between ca. 3,000 and 12,000 mg/L, representing the formation of micelles, and then decreased to 3.1±0.1 mN/m in solutions containing 3M AFFF and to 0.4±3.1 with Ansul AFFF at the field application concentration of 3% (30,000 mg/L). This second decrease likely represents another micelle phase due to the interactions between the fluorocarbon and hydrocarbon surfactants [20].

The air-water C20 for both AFFF formulations was ca. 100 mg/L, showing that, while these AFFF formulations were not as efficient as PFOS, they were clearly more effective in achieving the lowest interfacial tensions (**Figure 4.11a**). The NAPL-water interfacial tension decrease was less than 1 mN/m for AFFF concentrations ranging from 1 to 100 mg/L, followed by a steep decline for concentrations greater than 100 mg/L (**Figure 4.11b-d**). At the highest concentrations considered, the interfacial tension was ca. 3 mN/m for the dodecane-, PCE-, and JP-4, showing that AFFF was also the most effective at reducing NAPL-water interfacial tension. The formation of a hydrocarbon surfactant enriched monolayer at the NAPL surface[20] likely results in the lower NAPL interfacial tension as compared to solutions with PFOS, PFOS, or FOSA alone.

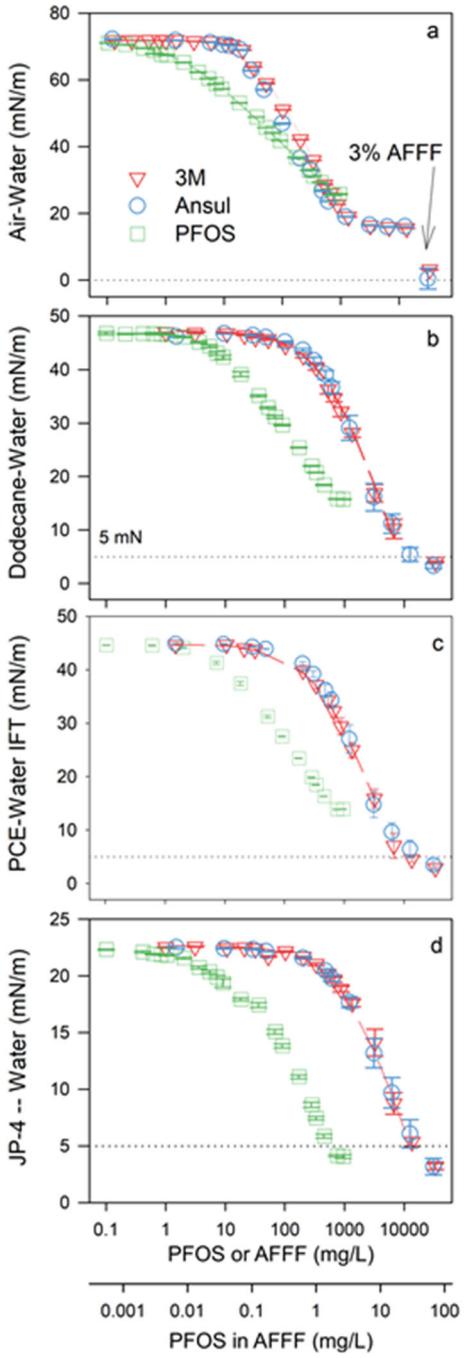


Figure 4.11 Interfacial tension for 3M AFFF in aqueous solution with 371 mg/L TDS, Ansul AFFF in aqueous solution with 379 mg/L TDS, or PFOS (from **Figure 4.2**) at the air-water (a), dodecane-water (b), PCE-water (c), or JP-4—Water (d) interface. AFFF concentration is for total mass added. The lines shown in a-d are the fits of the Szyszkowski equation (Eq (3-1)) to the measured interfacial tension values. Lower x-axis indicates PFOS concentration in 3M and Ansul formulations.

From the extensive work completed to develop surfactant-enhanced remediation for residual dodecane [155] and PCE [156], it was established that NAPL-water interfacial tension has to be lowered to less than ca. 5 mN/m before mobilization of residual NAPL is likely to occur. Based on the total trapping number (N_T) developed by [37] and the data reported in **Figure 4.2**, for vertical downward flow at a Darcy velocity of 2.0 cm/hr in a fine sand (e.g., 100-120 mesh, d_{50} = 0.14 mm), the calculated value of N_T would be ca 2.0 x 10^{-5}, indicating the potential for mobilization of PCE entrapped at residual saturation. For a coarser medium or a higher flow rate, the potential for mobilization would increase, and conversely, for a finer textured soil or a lower flow rate, the potential for mobilization would decrease. It should be noted, however, that for groundwater plumes containing concentrations of PFOA, PFOS, or AFFF below 1,000 mg/L, the measured interfacial tension values would not be low enough to indicate a potential for affecting the stability of entrapped NAPL. Thus, the potential for mobilization of residual NAPL would be most relevant for source zone areas where AFFF was used to extinguish organic liquid fires.

4.1.2.2 Surface Excess Concentration

The lines shown in **Figure 4.10a-c** and **Figure 4.11a-d** are the fits of the Szyszkowski equation (3-1) to the measured interfacial tension values. The root mean square error (RMSE) was less than two and the coefficient of determination (r^2) was greater than 0.98, indicating ideal partitioning between the bulk aqueous phase and the air- or NAPL-water interfaces. The resulting fitted parameters were used to calculate the maximum surface excess concentration (Γ_m) values using Eq. (3-2), which are shown in **Table 4.6**, while the surface activity values (b) are given in **Table 4.7**. The calculated Γ_m at the air-water interface for the salts of PFOA and PFOS were consistent with values reported in the literature of ca. 4 x 10^{-10} mol/cm^2 [81] or 1.7 mg/m^2 for PFOA and 2.0 mg/m^2 for PFOS.

Table 4.6 Calculated maximum surface excess concentrations (Γ_m, mg/m^2)

Interface	Air-Water	Dodecane-Water	PCE-Water	JP-4 – Water
PFOA	2.10 ± 0.10	2.07 ± 0.14	2.25 ± 0.12	1.34 ± 0.09
PFOS	1.53 ± 0.02	1.46 ± 0.03	1.50 ± 0.04	1.00 ± 0.05
FOSA	3.13 ± 0.16	0.97 ± 0.14	0.99 ± 0.20	0.37 ± 0.02
3M AFFF*	3.48 ± 0.21	3.36 ± 0.13	2.74 ± 0.06	1.84 ± 0.15
Ansul AFFF*	3.02 ± 0.29	3.16 ± 0.34	2.93 ± 0.25	1.46 ± 0.13

* assumes molecular weight of 500 g/mol

Table 4.7 Calculated surface activity values (b, mg/L)

Interface	Air-Water	Dodecane-Water	PCE-Water	JP-4 – Water
PFOA	49 ± 8	177 ± 30	217 ± 28	266 ± 42
PFOS	1.7 ± 0.1	8.6 ± 0.6	9.5 ± 1.0	19 ± 3
FOSA	1.4 ± 0.2	4.1 ± 1.7	7.9 ± 3.2	3.6 ± 1
3M AFFF	44.7 ± 7	611 ± 44	420 ± 21	1925 ± 262
Ansul AFFF	21.9 ± 7	585 ± 140	505 ± 101	1181 ± 206

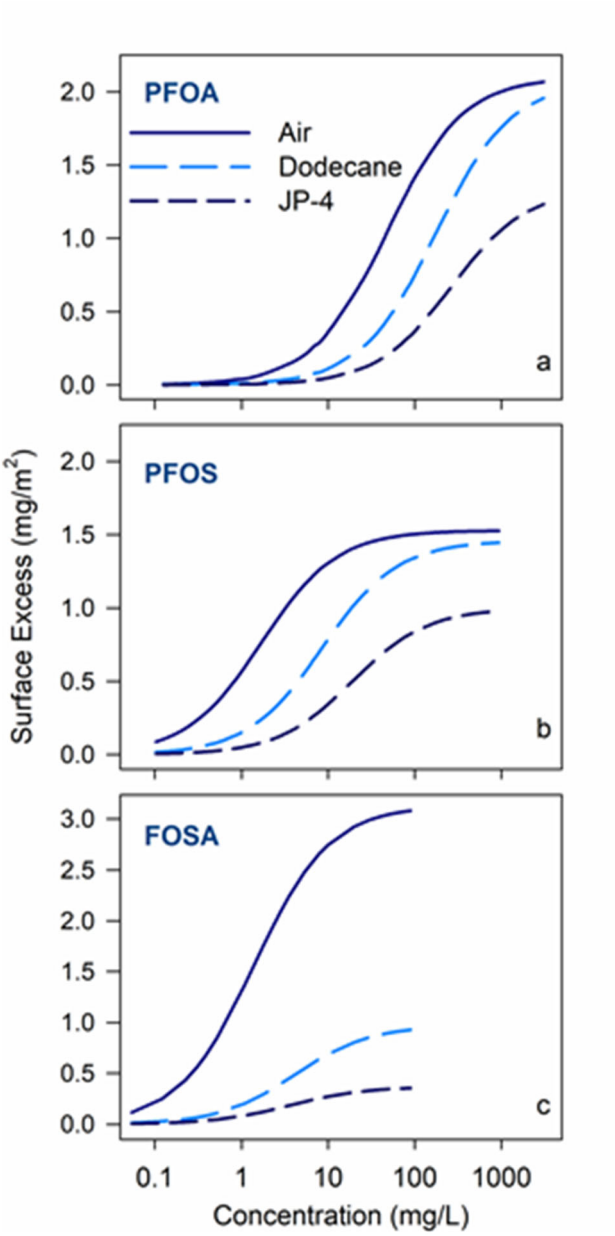


Figure 4.12 Surface excess concentration for PFOA (a), PFOS (b), or FOSA (c) at the air-water, dodecane-water, or JP-4—water interfaces. The lines shown Langmuir/Szyszkowski equation (Eq (3-3) using values from **Table 4.6** and **Table 4.7**. The line for PCE was omitted because it coincided with dodecane.

The fitted parameters were substituted into Eq. (3-3) to estimate the surface excess concentration as a function of bulk-water concentration. **Figure 4.12a** shows that the surface excess of PFOA at the air-water interface was 4 times greater than at the dodecane-water interface up to 9.6 mg/L (same results for PCE). At concentrations greater than 1,200 mg/L, the surface excess for PFOA

was nearly equal at the air-, dodecane-, or PCE-water interfaces. For JP-4, the PFOA surface excess at the air-water interface was 10 times greater than at the JP-4–water interface up to 1 mg/L, and was 2 times greater above 419 mg/L. The preference of PFOA for the air-water interface is related to the surface activity (*b*), where the values increase from air-water to NAPL-water interfaces (**Table 4.7**).

The PFOS surface excess was 4 to 5 times greater at the air-water interface than at the dodecane-water interface up to 1 mg/L and was nearly equal above 100 mg/L (**Figure 4.12b**). The PFOS surface excess was 10 times greater at the air-water interface than at the JP-4–water interface at less than 1 mg/L, and 2 times greater above 36 mg/L. The surface excess of FOSA was 10 times greater at the air-water interface than at the dodecane-water interface at less than 1 mg/L and 3 times greater above 30 mg/L (**Figure 4.12c**).

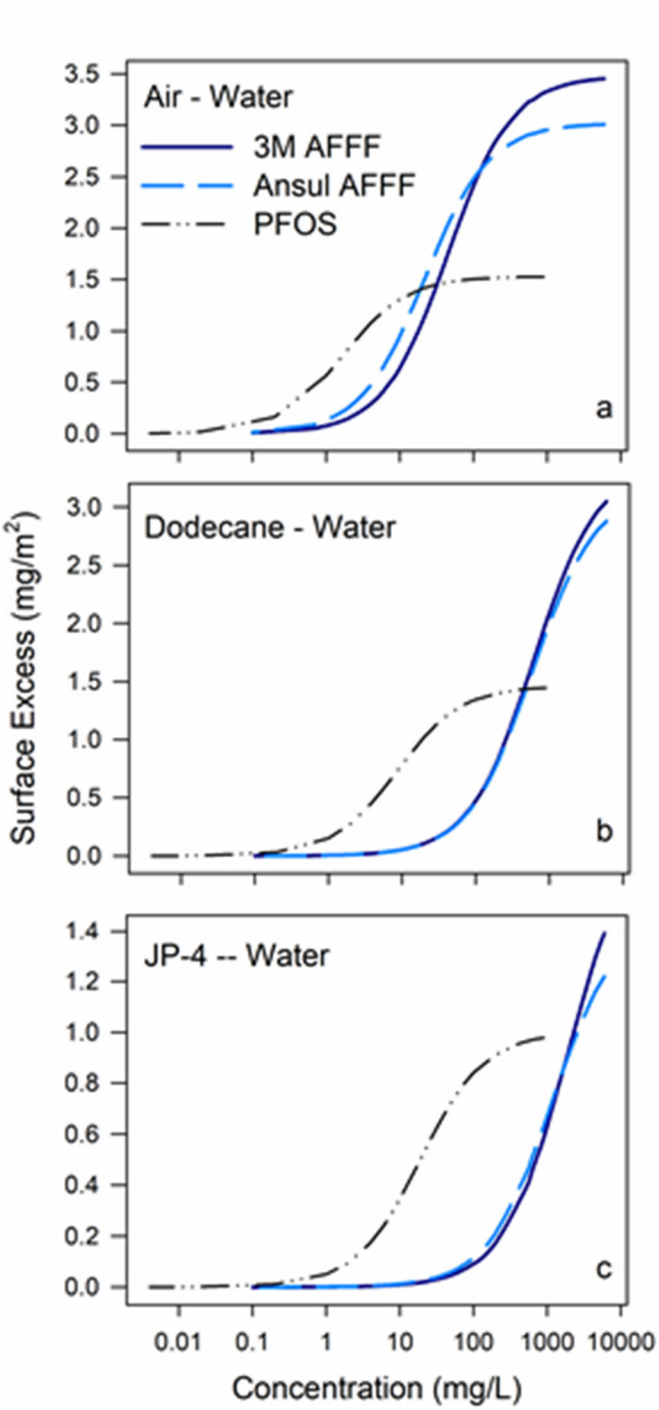


Figure 4.13 Surface excess concentrations for 3M AFFF, Ansul AFFF, or PFOS at the air-water (a), dodecane-water (b), or JP-4—water (c) interfaces. The lines are the Langmuir/Szyszkowski equation (3-3) using values from **Table 4.6** and **Table 4.7**. Lines for PCE not shown because they were similar to those for dodecane.

Overall, the surface excess of the AFFF formulations, at concentrations less than 20 mg/L, were ca. 10 times greater at the air-water interface than at the dodecane-water interface (same results for PCE), and ca. 50 times greater than at the JP-4–water interface. However, at the maximum surface excess (**Table 4.6**), where AFFF formulations were applied to organic liquid fires, the air-water excess was within 10% of the excess at the dodecane- or PCE-water interfaces, and was two times greater than at the JP-4–water interface. The surface excess of PFOS at the air-water interface was ca. 10 times greater than AFFF below 20 mg/L, but was ca. 2 times lower above 20 mg/L (**Figure 4.13a**). While the surface excess of PFOS at the dodecane-water interface was greater than that for AFFF below ca. 500 mg/L (**Figure 4.13b**). Although the NAPL-water surface excess for AFFF was ca. 2 times greater than PFOS, this only occurred for AFFF concentrations beyond the point of maximum PFOS surface excess.

The interfacial tension data presented above have implications for modeling PFOA, PFOS or FOSA retention in source zones. In the absence of measurements, previous work to estimate PFOA and PFOS retention in unsaturated soils containing NAPL assumed that air- and NAPL-water interfacial concentrations were equal [29]. Others have assumed that using interfacial concentrations for PFOS were equivalent to those for AFFF when modelling retention at air-water interfaces [62]. The results presented here, however, indicate that air- and NAPL-water interfacial concentrations for PFOS are not equivalent to AFFF. For example, the results shown in **Figure 4.13** suggest that AFFF surface excess would be ca. two times greater than PFOS alone at concentrations greater than 100 mg/L.

4.1.2.3 Impact of Calculated vs. Measured Concentrations on Surface Excess

Interfacial tension relationships are typically measured for aqueous concentrations ranging from 1,000 down to 0.1 mg/L (i.e., dilution series). The concentration of each serial dilution is typically based on the mass of stock solution added, which assumes no loss of analyte during transfer. The calculated concentration has been used in other studies to derive air-water partitioning coefficients [14, 15, 30, 78]. In the present study, the fitted parameters given in **Table 4.6** and **Table 4.7** were determined using concentrations measured by LC-MS/MS or conductivity analyses. Comparing the calculated concentration of PFOA and PFOS with that determined by LC-MS/MS or conductivity revealed good overall agreement, with PFOA concentrations within 4% of each other for 15 of the 27 bottles and PFOS concentrations within 5% for 12 of the 22 bottles. However, for concentrations less than 100 mg/L, differences were greater than 10% for 9 of the 14 PFOA bottles and 4 of the 16 PFOS bottles.

To illustrate how the difference between the calculated and measured concentrations impacts the fitted parameters, Γ_m and b, the calculated concentrations were used in fitting Eq. (3-1) to the measured interfacial tensions. The difference between the $\Gamma_m$determined by fitting the calculated vs. measured concentrations was less than 5% for PFOA and less than 2% for PFOS. Such close agreement is expected, since the maximum surface excess values represent the fit of concentrations above 100 mg/L, a level at which calculated and measured concentrations were within 5% of each

other. A greater difference was observed in *b* values, which were 18.5% lower for PFOA and 8.1% greater for PFOS when derived using calculated concentrations. The *b* term in Eq. (3-3) relates to the concentration at which the surface excess begins to increase and is sensitive to concentrations below 100 mg/L, where the difference between calculated and measured values was greater than 10%. Consequently, using the *b* value determined from calculated PFOA concentrations results ca. 10% greater surface excess for PFOA in the range from 0.1 to 10 mg/L. Conversely, the *b* value determined from calculated PFOS concentrations results in ca. 5% lower surface excess for PFOS in the 0.1 to 1 mg/L range.

For FOSA, the calculated concentrations were 42 ± 10% greater than the measured concentrations. This large difference occurred even though no solids were observed in the stock solutions up to four days after they were prepared. However, solids and floating structures (i.e., agglomerates) were subsequently observed after preparing the FOSA dilution series indicating that the stock solutions were supersaturated.

4.1.2.4 Mass Distribution in Unsaturated Soil

To provide perspective on the relative importance of surface excess at the interfaces, the mass of PFOA, PFOS and FOSA dissolved in water, adsorbed to soil, and at the air- and dodecane-water interfaces was calculated for a 1 L volume of a low organic carbon content sandy vadose zone soil at water saturation of 0.78. The sandy soil properties were the same as those reported in Brusseau [29], with an organic carbon content of 0.2%, bulk-density of 1.5 kg/L, an air-water interfacial area of 8 m^2 at a volumetric water content of 26%, and a NAPL-water interfacial area of 2 m^2 at a NAPL saturation of 2% [29]. The mass at the air-water and dodecane-water interfaces were calculated using Eq. (3-3) with the parameters given in **Table 4.6** and **Table 4.7**, and adsorption to the sandy soil was calculated using a linear isotherm (see **Appendix A.11** for calculation details).

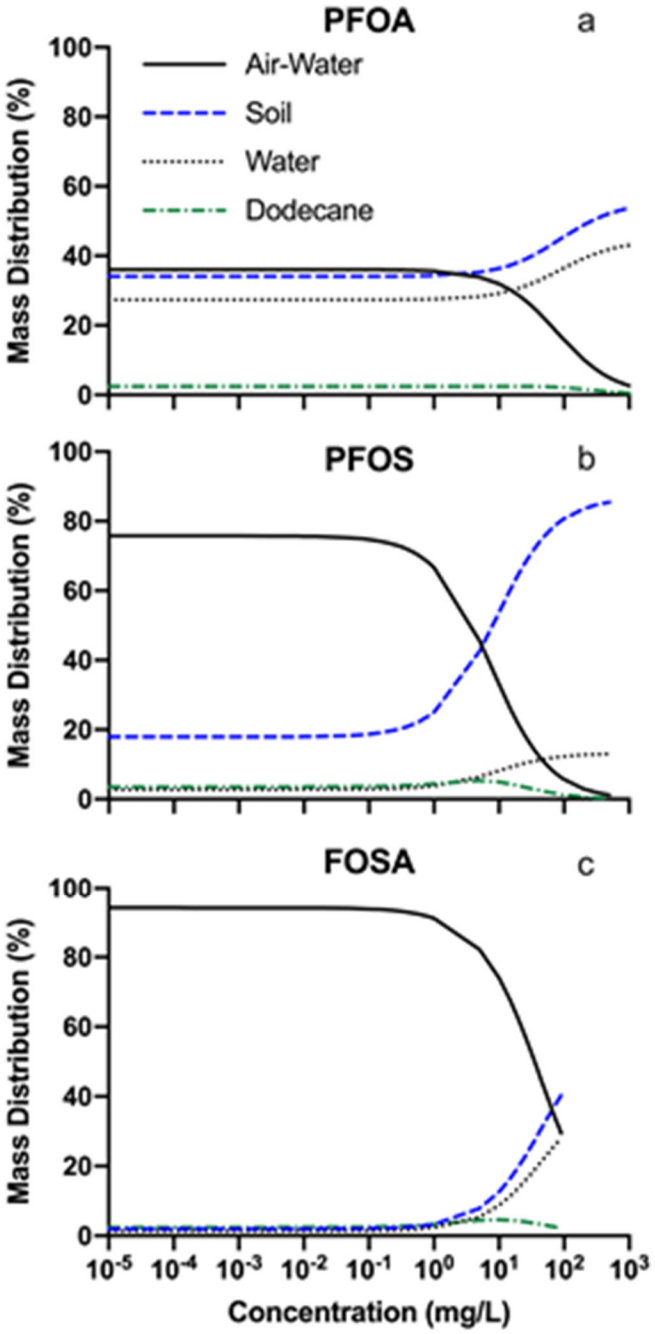


Figure 4.14 Calculated fraction of PFOA (a), PFOS (b), or FOSA (c) mass at the air-water or dodecane-water interface, dissolved in water, and adsorbed to a sandy soil as a function of bulk-water concentration. Soil with water saturation of 0.78, fraction of organic carbon of 0.2%, bulk density of 1.5 kg/L, air-water interfacial area of 8 m^2 at water content of 0.26, NAPL-water interfacial area of 2 m^2 at dodecane residual saturation of 2%. Linear isotherm with PFOA Kd of 0.216 L/kg, PFOS Kd of 1.14 L/kg, and PFOS Kd of 0.25 L/kg.

4.1.2.5 Concluding remarks

The results of these calculations show that, for concentrations below 1 mg/L, greater than 36% of PFOA, 67% of PFOS, or 90% of FOSA is estimated to be at the air-water interface in the sandy soil at a water saturation of 0.78 (**Figure 4.14**). While less than 2.5% of PFOA, 4% of PFOS, or 3% of FOSA is estimated to be at the dodecane-water interface. Although the surface excess at the air- and dodecane-water interfaces reaches maximum values at greater than 10 mg/L (**Figure 4.12**), the relative mass at these interfaces decreases due to adsorption to soil and solubility in water (**Figure 4.14**).

These partitioning calculations show that the majority of the PFOA, PFOS, or FOSA mass would be expected to be associated with the air-water interface below 1 mg/L in the sandy soil. These results also show that relatively little (i.e., less than 4%) mass is estimated to be at the dodecane-water interface in soil with a dodecane saturation of 2%. Thus, these estimates suggest that accumulation at the air-water interface in unsaturated soil could be important in the fate and transport of PFOA, PFOS, and FOSA. This finding is consistent with the modeling simulations by Guo, Zeng [62] who reported that ca. 70% of the PFOS mass was retained at the air-water interface in a vadose zone 40 years after being released at the soil surface. Those simulations assumed releasing PFOS at 1,000 mg/L, whereas the results herein point to the potential for concentrations of less than 1 mg/L to result in significant accumulation at the air-water interface with possible long-term implications.

Calculations for the mass distribution of AFFF were not performed due to lack of soil adsorption isotherms and information on the AFFF composition. Given that the AFFF formulations had larger *b* values compared to those for PFOS (**Table 4.7**), the accumulation at the air-water interface is expected to be lower for AFFF concentrations less than 20 mg/L (**Figure 4.13a**). However, this expectation assumes that AFFF will behave as a mixture in the subsurface when, in fact, the components may separate due to differences in interactions with the air-water interface and soil surfaces.

4.2 Batch biotransformation studies

4.2.1 Aerobic biotransformation of FOSA in Loring and Hudson soil

4.2.1.1 Biotransformation rates.

In the live treatments of Loring soil microcosms, a gradual decrease in the initially spiked FOSA was observed during the 308-day incubation, with 54.7 ± 3.0 mol% of spiked FOSA remaining at the end (**Figure 4.15**). The half-life ($t_{1/2}$) was determined to be 335.1 days by fitting 7 data points using a first-order kinetic model (coefficient of determination R^2 = 0.92). Biotransformation of legacy FOSA was not appreciated in positive controls, where the total mass of FOSA remained constant (0.6-0.8 nmol) during the incubation (Appendix **Table A.14**). The low bioavailability of the small amount of legacy FOSA (>90 mol% of mass partitioned in the solid phase) likely restrained the biotransformation. Surprisingly, a faster biotransformation of FOSA was observed

in the pristine soil (i.e., Hudson soil), with 32.7 ± 5.2 mol% of initially spiked FOSA remaining in live treatments after the 308-day incubation (**Figure 4.15**). The half-life was calculated to be 203.0 days (R^2 = 0.99), indicating the FOSA biotransformation rate in Hudson soil was about 1.7-fold faster than that in Loring soil. One of the reasons contributing to a faster biotransformation in Hudson soil could be the higher bioavailability of FOSA to Hudson soil microbial community than Loring's. Classified as a Loam/Sandy Loam, Loring soil has a higher organic carbon (OC) content of 3.5 ± 0.1% than Hudson soil (1.1 ± 0.0%). The higher OC content likely resulted in a greater partitioning of spiked FOSA into the solid phase of Loring soil microcosms (Appendix **Table A.15**), which reduced the bioavailability of FOSA to the microorganisms. During the 308-day incubation, 88.6-91.8 mol% of FOSA in the Loring soil live treatments was in the solid phase, whereas only 69.6-82.7 mol% of FOSA partitioned into the solid phase of Hudson live treatments (Appendix **Table A.15**). In addition, the differences in microbial community compositions could also lead to the different biotransformation rates, which will be discussed in the later sections.

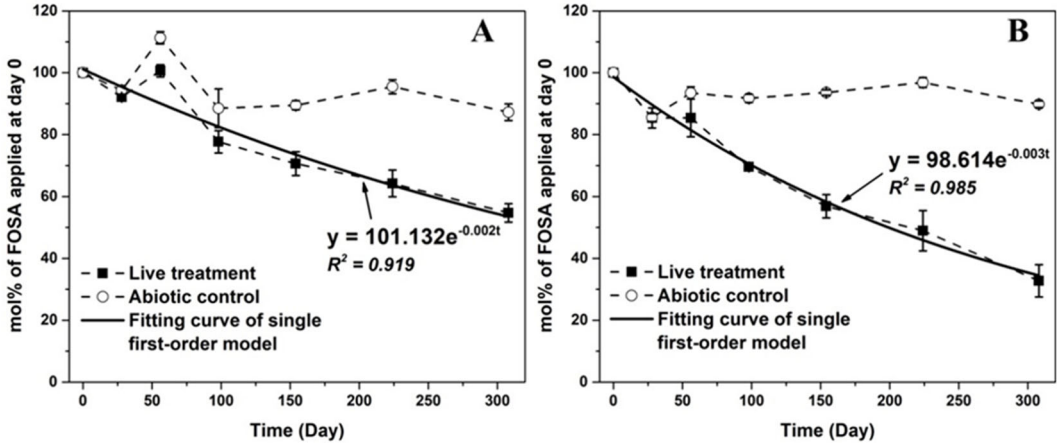


Figure 4.15 Changes in molar ratios of residual FOSA during aerobic biotransformation in Loring (Panel A) and Hudson (Panel B) soil microcosms. Error bars represent the standard deviation of triplicate live treatment microcosms, and of duplicate control microcosms.

4.2.1.2 Quantification of biotransformation products and mass balance.

Analysis of samples collected from Loring and Hudson soil microcosms indicated the production of PFOS which was previously observed as a biotransformation product of FOSA [56, 157-161]. In the live treatments of Hudson soil microcosms, the formation of PFOS was observed at day 28 with a molar yield of 1.7 ± 0.1 mol% (**Figure 4.16**). Then, PFOS was continuously produced, reaching a molar yield of 29.2 ± 7.9 mol% at day 224 (**Figure 4.16**). During day 224 to day 308, PFOS yield stayed relatively constant, and the final yield was 29.5 ± 3.8 mol% (**Figure 4.16**). PFOS was below LODs in the abiotic controls and positive controls throughout the experiment, suggesting that PFOS production only resulted from the biotransformation of FOSA in Hudson soil. Since PFOS was the predominant legacy PFAS in the contaminated Loring soil, high abundance of PFOS was detected in all Loring soil microcosms, with a total mass ranging from

47.0 nmol to 57.9 nmol (Appendix **Table A.14**). Therefore, the production of PFOS by FOSA biotransformation in Loring soil was determined by subtracting the PFOS mass in the positive controls from that in the live treatments (Appendix **Table A.14**). As shown in **Figure 4.16**, the production of PFOS was observed at day 56, then gradually increased to 25.6 ± 3.4 mol% at day 154. The level of PFOS decreased slightly afterwards, and was determined to be 21.6 ± 5.2 mol% by day 308 (**Figure 4.16**). Cautions should be taken regarding these calculated molar yields of PFOS, since the high background level of PFOS in Loring soil and slight variations in PFAS analysis on different batches of samples complicated the assessment of the PFOS yield resulting from the FOSA biotransformation. For example, a 1-nmol variation in PFOS mass would lead to a difference of 4.2 mol% in molar yield, given the total mass of initially spiked FOSA (i.e., 24 nmol). Overall, the PFOS yield in Loring soil was slightly lower than that in Hudson soil (**Figure 4.16**), which is consistent with the observation that less of spiked FOSA was biotransformed in Loring soil than Hudson soil (**Figure 4.16**).

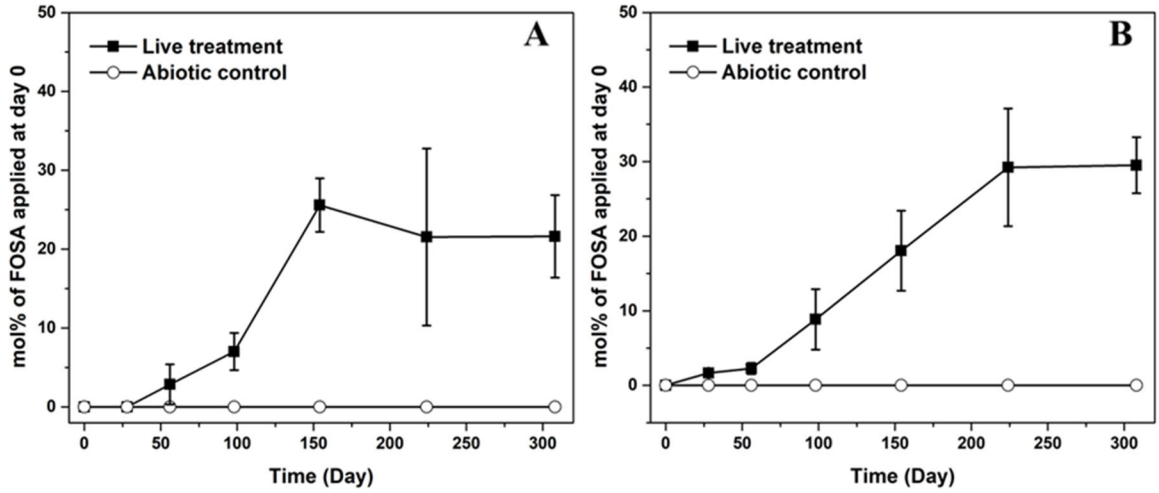


Figure 4.16 The formation of PFOS during FOSA aerobic biotransformation in Loring (Panel A) and Hudson (Panel B) soil microcosms. Error bars represent the standard deviation of triplicate live treatment microcosms, and of duplicate control microcosms.

At the end of the biotransformation experiments, 45.3 ± 3.0 mol% and 67.3 ± 5.2 mol% of spiked FOSA was biotransformed in Loring and Hudson soil microcosms (**Figure 4.15**), whereas PFOS formation only accounted for 21.6 ± 5.2 mol% and 29.5 ± 3.8 mol% of the initially spiked mass (**Figure 4.16**). As good mass recoveries were obtained from Loring and Hudson soil abiotic controls (95.2 ± 7.8 mol% and 93.0 ± 4.3 mol%, respectively) throughout the experiments, the incomplete mass balance in the live treatments was likely caused by the formation of other biotransformation products that were not quantified, or the irreversible bindings of FOSA and/or PFOS to the biomass. Previously studies reported that perfluorooctane sulfinate (PFOSI) was a key intermediate during the biotransformation of FOSA to PFOS [56, 158]. PFOSI was not quantified in the present study due to the unavailability of the authentic chemical standard.

Regardless, PFOSI was likely formed in Loring and Hudson soil microcosms, based on the observed greater mass loss in Hudson soil (37.8 mol% loss) than Loring soil (23.7 mol% loss), which could be explained by the increased extent of FOSA biotransformation (**Figure 4.15**) and the associated greater PFOSI formation in Hudson soil.

4.2.1.3 Biotransformation Comparison of the biotransformation of FOSA and FOSA precursors.

To provide more understandings of the biotransformation kinetics of FOSA and the associated PFOS yields in the environment, prior and current studies investigating the biotransformation of FOSA are summarized (**Table 4.8**) [161, 162]. Given a limited number of studies on direct FOSA biotransformation [161, 162], those previous studies that investigated the biotransformation of other sulfonamide derivatives which were reported as FOSA precursors were also included (**Table 4.8**) [56, 57, 157-160, 163]. Those precursors included EtFOSE, EtFOSA, and perfluorooctane sulfonamido betaine (PFOSB). The half-lives of those precursors and FOSA during the biotransformation, if reported, were listed (**Table 4.8**). Compared to its precursors, FOSA showed a higher microbial stability in activated sludge [56], wetland plants [160], and aerobic soils [157, 163]. The results might explain the frequent detection of FOSA rather than those precursors (i.e., EtFOSE, EtFOSA, PFOSB) in the contaminanted soils [8, 16], surface water [16, 164], and groundwater [8]. Regardless of the potential persistence in the environment, large variations in the biotransformation rate of FOSA are also observed (**Table 4.8**). While shorter half-lives of FOSA ranging from 9.2 to 39 days were reported in three different environmental matrices (i.e., activated sludge [56], aerobic soil [159], and wetland plant microcosm [160]), half-lives up to 712 days [157] and >1000 days [163] were measured or predicted in other aerobic soils. In the present study, a half-life of 203.0-335.1 days which lied in between the low and high values reported in prior studies, was observed in two distinct aerobic soils (i.e., contaminated and pristine soils), further supporting the potential persistence of FOSA in the soil compartment.

PFOS has been always reported as the final biotransformation product of sulfonamide derivatives (e.g., FOSA and FOSA precursors) [56, 57, 158-160, 163]. However, the yields of PFOS from those biotransformation varied (**Table 4.8**). In previous studies, low PFOS yields (0.4-12 mol%) were observed under various incubation conditions (**Table 4.8**), with one exception that 85.1 mol% PFOS was formed during the biotransformation of EtFOSA in wetland plant microcosms [160]. In the present study, relatively high molar yields of PFOS (21.6-29.5 mol%) from FOSA biotransformation were observed in Loring and Hudson soils (**Table 4.8**). The high PFOS yields might be partially attributed to a long-term incubation (i.e., 308 days) performed in this study, confirming that FOSA could serve as a long-term source to PFOS in the environment.

Table 4.8 An overview of the prior and current studies investigating biotransformation of FOSA and FOSA precursors.

Parent compound	Microcosm	Incubation duration	Estimated $t_{1/2}$ of parent compound	Estimated $t_{1/2}$ of FOSA	PFOS yield (mol%)	Reference
EtFOSE	Activated sludge	10 d	0.7 d	9.2 d	N/A	[56]
EtFOSE	Marine sediment	120 d	44 d (25 ºC); 160 d (4 ºC)	N/A	12% (25 ºC); 0.4% (4 ºC)	[57]
EtFOSE	Aerobic soil	180-210 d	25.2-30.8 d	35.6-39 d	1.1-5.5%	[159]
EtFOSE	Aerobic soil	105 d	9.6 d	712 d	7.9%	[157]
EtFOSA	Aerobic soil	182 d	13.9 ± 2.1 d	N/A	4.0 %	[158]
EtFOSA	Wetland plants	91 d	0.5 d	39 d	85.1%	[160]
PFOSB	Aerobic soil	90 d	675 d	>1000 d	1.5%	[163]
FOSA	Groundwater and soil	49 d	/	N/A	0.5-4.9%	[161]
FOSA	Aerobic soil	30 d	/	N/A	N/A	[162]
FOSA	AFFF-impacted soil	308 d	/	335.1 d	21.6 %	This study
FOSA	Aerobic soil	308 d	/	203.0 d	29.5%	This study

N/A: Not available.

4.2.1.4 Microbial communities in Loring and Hudson soil microcosms.

4.2.1.4.1 Diversity and Richness.

The mapped reads of 16S rRNA gene amplicons from Loring and Hudson soil microcosms varied in the range of 4606 to 8298 (Appendix **Table A.16**). To facilitate the comparison of diversity and richness of microbial community, the number of reads in all samples was rarefied to the lowest value within the plateau range of the rarefaction curves. The quality-filtered reads were then clustered into operational taxonomic units (OTUs) at a 97% similarity level. The number of OTUs in all samples ranged from 150 to 687 (Appendix **Table A.16**).

The alpha diversity (i.e., mean diversity of species in a community [165]) and species richness, (i.e., the number of species or OTUs present in a community) of Loring and Hudson soil microbial community was investigated using the Shannon and Simpson, and Chao1 indices, respectively (Appendix **Table A.16**). The overall diversity of the microbial community native to Loring soil is substantially higher than that in Hudson soil, as the Shannon (5.85 ± 0.07 vs. 4.87 ± 0.05), Simpson (0.99 ± 0.00 vs. 0.98 ± 0.00), and Chao1 (1019.8 ± 30.8 vs. 586.6 ± 35.6) indices are much higher in the day 0 samples from Loring soil microcosms than Hudson soil microcosms (Appendix **Table A.16**). The higher diversity in Loring soil might be partially attributed to a more sufficient carbon sources for the microbial growth at the site; the total organic carbon content in Loring soil is about 3.5% which is more than 3-fold greater than that in Hudson soil. After the biostimulation with amendment of DGBE over 308 days, the microbial diversity and richness of both Loring and Hudson soil microbial communities decreased dramatically, as indicated by lower Chao1, Shannon, and Simpson indices at day 154 and day 308 samples relative to day 0 samples

(Appendix **Table A.16**). Such decreases might be due to the biased stimulated growth of certain microbial species over others by the amendment of DGBE.

In Loring or Hudson soil microcosms, significant differences ($p < 0.05$) in Chao1, Shannon, or Simpson indices were not found in day 154 or day 308 samples between the live treatment (85 μg/L FOSA spiked) and the positive control (0 μg/L FOSA spiked) (Appendix **Table A.16**). Results indicate that the presence of spiked FOSA and biotransformation products did not significantly alter the microbial diversity in the present study. Previous studies reported that microbial diversity in river sediment and soil was reduced by the exposure to PFAS compounds (e.g., PFCAs) [166-168]. However, the PFAS concentrations in those studies were much higher (e.g., 15 mg/L) than that in the present study (i.e., 85 μg/L) [166-168]. Principle coordinate analysis (PCoA) was also analyzed on the Weighted Unifrac distance matrices as a measurement of beta diversity to visualize microbial community alteration among the different treatments in Loring and Hudson microcosms. The negligible impact of spiked FOSA on overall diversity is further supported by the obvious grouping of samples from the live treatment and positive controls (Appendix **Figure A.6**). Moreover, a separation of Loring and Hudson soil samples revealed the differences between the microbial community compositions at the two sites (Appendix **Figure A.6**).

4.2.1.4.2 Shifts in microbial community compositions.

The microbial community composition in Loring and Hudson soils was further analyzed on various taxonomic levels. A total of 35 classified phyla in the domain Bacteria and 4 phyla in the domain Archaea were shared. **Figure 4.17** shows the relative abundance of microbial community composition at the phylum level in Loring and Hudson soil microcosms. In general, Proteobacteria was the most dominant phylum in Loring and Hudson soils, especially after the bioaugmentation (relative abundance >40% in day 154 and day 308 samples) (**Figure 4.17**). Prior studies identified Proteobacteria as the predominant phylum in aerobic soils and river sediments that were contaminated by PFAS [168-170]. In addition, an obvious increase (12.5-65.7%) in Proteobacteria was observed previously in wetland slurry and fresh water following exposure to PFAS [171, 172]. Those results indicate that Proteobacteria might be more tolerant to PFAS than other phyla. In the present study, two classes of Proteobacteria, Alpha- and Gamma-proteobacteria, were found in Loring and Hudson soils; microorganisms belonging to the two classes were reported to degrade various hydrocarbon compounds [173, 174], as well as PFAS (e.g., fluorotelomer compounds) [175-178]. In addition, Actinobacteriota, Chloroflexi, Acidobacteriota, and Planctomycetota were observed as primary phyla in Loring and Hudson soil samples (**Figure 4.17**). Some genera from Actinobacteriota were reported as PFAS degraders; for example, *Mycobacterium, Gordonia*, *Rhodococcus*, and *Dietzia* have been shown to biodegrade 6:2 fluorotelomer alcohol or 6:2 fluorotelomer sulfonate [105, 106, 177, 179, 180]. Chloroflexi, Acidobacteriota, and Planctomycetota were previously found to be enriched in the environment where chlorinated solvents or PFAS were present [160, 171]. Taken together with prior work, microorganisms belonging to the aforementioned phyla might play a role in the biotransformation of FOSA observed in this study.

Distinct differences in the relative abundances of phyla discussed above (i.e., Proteobacteria, Actinobacteriota, Chloroflexi, Acidobacteriota, and Planctomycetota) were not observed in day 154/day 308 samples between the live treatment (85 µg/L FOSA spiked) and the positive control (0 µg/L FOSA spiked) (**Figure 4.17**), suggesting that these phyla were not sensitive to the spiked FOSA and associated transformation products. In contrast, a substantially greater relative abundance of Cyanobacteria was found in the live treatments than positive controls in both Loring and Hudson soil microcosms (**Figure 4.17**). In the absence of FOSA, relative abundances of Cyanobacteria were 3.1 ± 0.6% and 2.2 ± 0.3% at day 154 and day 308, respectively; whereas relative abundances increased to 7.3 ± 2.3% and 4.6 ± 2.4%, respectively, in the FOSA-spiked Loring soil microcosms. Similar increase was also observed in Hudson soil microcosms with 0.6 ± 0.1% of Cyanobacteria in day 308 samples from live treatment, compared to 0.1 ± 0.1% from positive control. Another phylum, Bacteroidota was also found with a substantially greater relative abundance in the live treatment than positive control in Hudson soil microcosms (**Figure 4.17**). For example, relative abundances of Bacteroidota were 1.4 ± 0.6% and 0.8 ± 0.2% at day 154 and day 308, respectively in the positive controls while were 3.3 ± 0.8% and 8.0 ± 3.2%, respectively in the live treatments. These results indicate that Cyanobacteria and Bacteroidota were relatively more tolerant to FOSA and/or the associated transformation products. Bacteroidota were reported to be associated with diesel- and PFAS-contaminated soils [166, 174, 181], and Cyanobacteria species were shown to degrade aromatic hydrocarbons and xenobiotics using various enzymes [182].

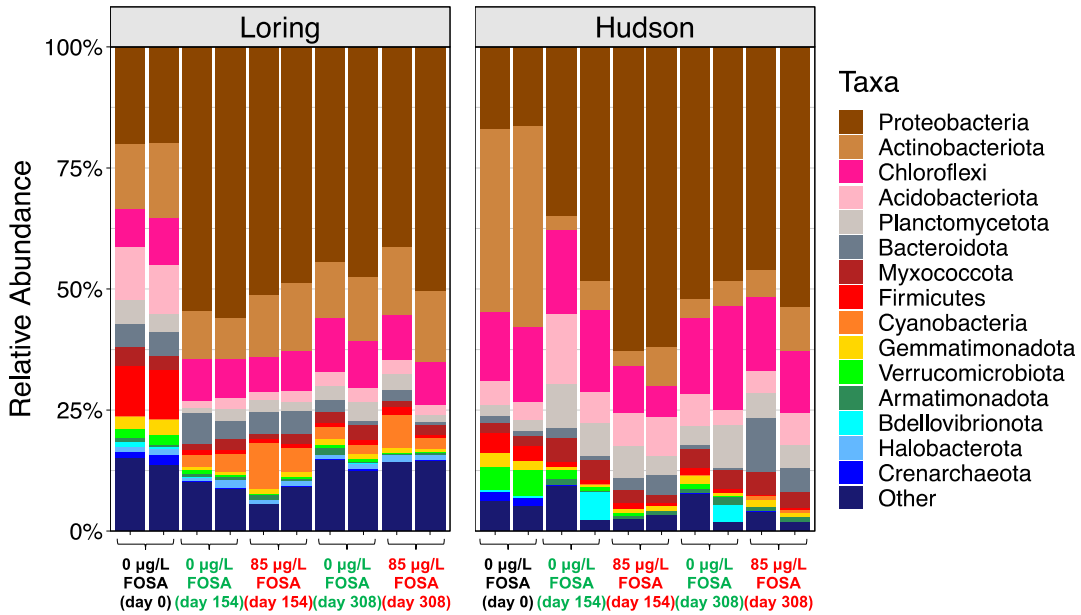


Figure 4.17 The relative abundance of microbial community composition at the phylum level in Loring (left) and Hudson (right) soil microcosms.

On the genus level, a total of 568 genera were identified in the samples from Loring and Hudson microcosms. The relative abundances of predominant 19 genera are shown in Appendix **Figure A.7**. During the incubation, *Afipia* was the most dominant genus in Loring and Hudson soil microcosms, with a relative abundance of 20.7 ± 5.9% in day 154 and day 308 samples (Appendix **Figure A.7**). Previous studies showed that *Afipia* strains were capable of degradation of various environmental contaminants (e.g., 1,4-dioxane, methanesulfonate, and haloacetic acids) [183-185]. Therefore, microorganisms in *Afipia* might be involved in the FOSA biotransformation in Loring and Hudson soils. The Welch t-test with Benjamini-Hochberg false discovery rate (FDR) for multiple test corrections was employed to compare the relative abundance of each genus in the live treatments and positive controls. No genus was found to significantly (adjusted $p < 0.05$) increase in live treatments compared to positive controls in both Loring and Hudson soil microcosm samples (day 154 and day 308). Instead, *Pajaroellobacter* was found to significantly decrease in live treatments compared to positive controls in Loring soil microcosms. At day 154, the relative abundance of *Pajaroellobacter* was 0.0 ± 0.0% in live treatments compared to positive controls (0.2 ± 0.1%); at day 308, the relative abundance was 0.0 ± 0.0% in live treatments compared to positive controls (0.6 ± 0.0%). These results suggest that the relatively low concentration of spiked FOSA and associated biotransformation products may not exert much pressure on the microbial communities in Loring and Hudson soils. Regardless, *Pajaroellobacter* might be more sensitive to FOSA and transformation products such as PFOS.

4.2.1.5 Concluding remarks

This study demonstrates that the biotransformation of FOSA in the natural environment may be soil/site dependent. With a tendency to partition to the solid phase, the bioavailability of FOSA to the native microbial community appears to a critical parameter for the evaluation of FOSA biotransformation in the soil compartment. Thus, soil properties such as organic carbon content that could impact sorption behavior and bioavailability of FOSA need to be assessed. Moreover, differences in microbial community composition could also lead to different rates of biotransformation. Microorganisms belonging to Proteobacteria, Actinobacteriota, Chloroflexi, Acidobacteriota, and Planctomycetota may play a role in the biotransformation of FOSA, while Cyanobacteria and Bacteroidota may be relatively more tolerant to FOSA and/or its associated transformation products. Overall, the findings in the present study suggest that evaluations of site geochemical and biological attributes are important in achieving a better understanding of FOSA biotransformation in the field, as well as gaining insights into the management and remediation of contaminated sites.

4.2.2 Aerobic biotransformation of 8:2 FTOH in Robins and Loring soil

4.2.2.1 Biotransformation of 8:2 FTOH in Robins soil

4.2.2.1.1 Parent compound biotransformation and kinetics

Throughout the 90-day Robins biotransformation experiment, 85–127 mol% of initially spiked 8:2 FTOH was measured in the abiotic controls without significant changes ($p > 0.05$) (**Figure 4.18**). The absence of microbial activity in the abiotic controls was confirmed through organic carbon measurements that did not change significantly (C/C_0 = 106.5 ± 6.0 %, $p > 0.05$); in contrast, decreasing organic carbon in the live treatments and live controls by approximate 90% within 2-3 weeks after each addition of DGBE was indicative of microbial activity in these bottles (Appendix **Figure A.8**). These results confirm the integrity of the experimental systems and the abiotic stability of 8:2 FTOH under the experimental conditions, consistent with prior studies [186-188].

In the live treatment, 8:2 FTOH was transformed rapidly, with 7 mol% of 8:2 FTOH remaining in the systems after 90 days (**Figure 4.18**). The 8:2 FTOH biotransformation in Robins AFB soil was fitted with first-order exponential and first-order double exponential decay models (see Appendix **Table A.17** and **Table 4.9**, respectively). First-order exponential models are frequently used to describe biodegradation kinetics and has been used to depict the biotransformation of 8:2 FTOH under nitrate-reducing conditions and for the biotransformation of other PFAS [118, 189]. However, it was found in this study that a first-order double exponential decay model better fit the data (R^2 of 0.995 vs 0.969); the associated fitted curve is presented in Appendix **Figure A.9**. It was hypothesized that biotransformation of 8:2 FTOH occurs following a two-step mechanism. This assertion is based on previously reported studies examining anaerobic biodegradation of 8:2 FTOH in activated sludge and degradation of other organic compounds in natural environments [190-192]. As shown in Equation (4-8), the molar percentage of 8:2 FTOH remaining in the system (M) at time t is described mathematically as the sum of two first-order kinetic expressions, where M_1 and M_2 are constants representing molar percentages of the initial mass, associated with two differing transformation rate constants of k_1 and k_2, respectively.

$$M(t) = M_1\, e^{-k_1 t} + M_2\, e^{-k_2 t} \qquad (4\text{-}8)$$

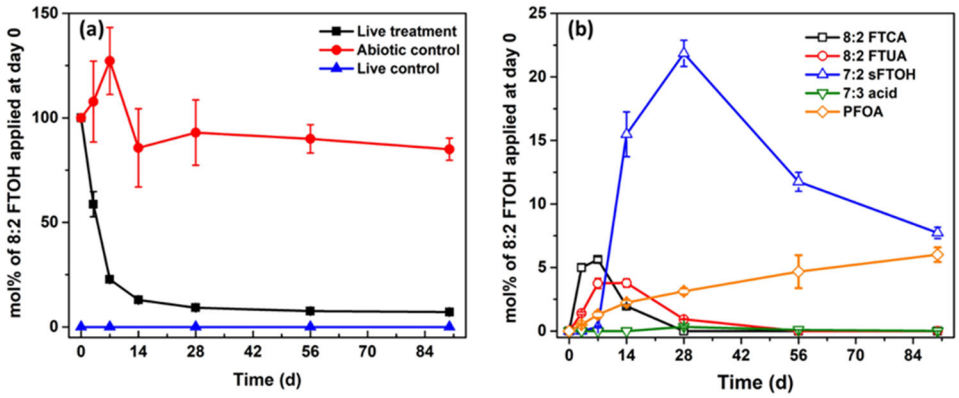


Figure 4.18 Profiles of 8:2 FTOH and its biotransformation products from the Robins biotransformation experiment during 90-day incubation: (a) residual molar percentage of 8:2 FTOH in the live treatment, abiotic control, and live control; error bars represent one standard deviation of triplicate live treatments and duplicate abiotic/live controls; (b) molar yields of quantified biotransformation products in the live treatment; error bars represent one standard deviation of triplicate live treatments.

Table 4.9 Fitting parameters of the first-order double exponential decay model.

Parameter	Value	Standard Error	Statistics	
M_1	92.634	5.042	R^2	0.995
M_2	8.370	4.146	Adjusted R^2	0.991
k_1	0.228	0.028		
k_2	0.002	0.009		

According to the model fits, 92.6 mol% of the initially spiked 8:2 FTOH was rapidly biotransformed with a half-life of about 3 days (first step), while transformation of the remaining 8.4 mol% 8:2 FTOH was much slower, with a half-life of more than 400 days (second step). The rapid biotransformation of the larger 8:2 FTOH fraction in the first step may be attributed to easier access to the compound by microorganisms in the aqueous phase. The lower biotransformation rate associated with the smaller fraction in the second step may be due to the limited bioavailability of 8:2 FTOH that resulted from kinetic limitations associated with desorption of 8:2 FTOH from the soil matrix or microbial biomass [50, 193]. The overall half-life 8:2 FTOH in the present study (~3 days) was similar to the findings for 8:2 FTOH biodegradation in aerobic soils (~5 days) [50], and activated sludge (< 5 days) [188, 190], but considerably shorter than the half-life reported in aerobic landfill leachate-sediment (> 1 year) [186], water-saturated Appling soil (~210 days [194] and anaerobic digestion sludge (~145 days) [53]. The rapid 8:2 FTOH biotransformation observed herein is likely attributed to the prior existence of effective enzymes in the Robins AFB soil microbial community which were either innate or evolved during long term exposure to PFAS in the field.

4.2.2.1.2 Parent compound biotransformation and kinetics.

Four polyfluorinated compounds, 8:2 FTCA [$F(CF_2)_8CH_2COOH$], 8:2 FTUA [$F(CF_2)_7CF{=}CHCOOH$], 7:2 sFTOH [$F(CF_2)_7CHOHCH_3$], and 7:3 acid [$F(CF_2)_7CH_2CH_2COOH$], were detected in the live treatment over the 90-day incubation period, while none of these compounds was detected in control bottles. These data provide further evidence that aerobic biotransformation of 8:2 FTOH occurred in the live treatment.

Among the four polyfluorinated transformation products, 8:2 FTCA and 8:2 FTUA have been widely documented as major polyfluorinated metabolites [51, 53, 176, 186-188, 190, 195]. During the first 14 days, the yields of 8:2 FTCA and 8:2 FTUA increased concurrently with the

consumption of 8:2 FTOH and reached a peak of 5.62% and 3.79% at day 7 and 14, respectively (**Figure 4.18**). The lower yields of 8:2 FTCA and 8:2 FTUA observed in this study compared to those in previous 8:2 FTOH biotransformation studies were likely due to their rapid conversion to downstream transformation products [51, 176, 188, 195].

Although 7:2 sFTOH was the most abundant polyfluorinated biotransformation product after 14 days, it was not detected until day 7 (**Figure 4.18**). As shown in **Figure 4.18**, the molar yield of 7:2 sFTOH reached a peak at 21.85% of initial 8:2 FTOH at day 28 and then gradually decreased to 7.73% at the end of the experiment. A similar trend of 7:2 sFTOH appearance and disappearance was observed during the aerobic biotransformation of 8:2 FTOH in forest and agricultural soils, except that the peak concentration was reached faster (2–7 days) [50]. Similarly, 7:2 sFTOH was found to be the most prevalent product from 8:2 FTOH aerobic biotransformation in a mixed bacterial culture [188]. Furthermore, 7:2 sFTOH was one of the major 8:2 FTOH metabolites produced by native soil microbes and by pure *Pseudomonas* strains under aerobic conditions [176, 187].

Although previously reported as one of the major biotransformation products in aerobic soils [50] and landfill leachate-sediment [186]. 7:3 acid was the least abundant polyfluorinated metabolite in the present study. The molar yield of 7:3 acid at day 28 was only 0.34% of the initial 8:2 FTOH and declined thereafter (**Figure 4.18**). One possible explanation for the low yield of 7:3 acid in this study is due to its rapid β-oxidation and further transformation to PFOA [188, 190, 195]. However, some studies have presented differing observations of 7:3 acid stability. For example, β-oxidation of 7:3 acid to PFOA was not observed in forest and agricultural soils [50]. It was also found that 7:3 acid could accumulate over periods of 90 days to 7 months in soils, digested sludge, and landfill leachate sediment [50, 53, 186].

In addition to polyfluorinated transformation products, PFOA has been widely reported as a major stable 8:2 FTOH transformation product [50, 51, 176, 186-188, 195, 196]. Consistent with prior studies, PFOA was detected as an 8:2 FTOH biotransformation product in live treatments. The molar yield of PFOA was calculated by subtracting the background concentration in the live control samples from the live treatment samples (**Figure 4.18**), as biotransformation of both 8:2 FTOH and other unknown PFOA precursors could have contributed to the formation of PFOA. During the 90-day incubation, PFOA was detected at day 3 and increased continuously to 6.02% of the initial 8:2 FTOH concentration without reaching a steady-state concentration. PFPeA, PFHxA, PFHpA, PFNA, and PFDA were also detected throughout the experiment period in the live treatment, and abiotic and live control groups. The masses of PFPeA, PFHpA, PFNA, and PFDA remained relatively steady at low levels (<1 nmole) and did not change significantly ($p > 0.05$) over time (Appendix **Figure A.10**). Although the mass of PFHxA was measured at slightly over 2 nmole from the initial time point, no significant ($p > 0.05$) increase of PFHxA mass was observed (Appendix **Figure A.10**). These results are not consistent with prior studies that found PFCAs, including PFBA [190, 196], PFPeA [190, 196], PFHxA [50, 53, 176, 186-188, 190, 195,

196], PFHpA [186, 187, 190, 196], and PFNA [196] were formed from 8:2 FTOH biotransformation.

A possible explanation for the observed differences in formation of biotransformation products, including poly- and perfluorinated compounds, between this and earlier studies could be related to differences in microbial communities associated with different environmental matrices. Note that not all PFCAs (C4-C9) that have been identified in earlier studies were identified as biotransformation products in this study. It is possible that those PFCAs were produced as 8:2 FTOH biotransformation products in trace amounts but were masked by background levels of PFAS contaminants in the AFFF-impacted soils.

4.2.2.1.3 Mass balance.

The mass balance was expressed as the % ratio of molar mass recovered at certain timepoints to the total molar mass of initially spiked 8:2 FTOH. The mass balance by day 90 reached 58.5 mol% (Appendix **Figure A.11** and **Table A.18**), which is consistent with previous studies (~40–65%) [51, 176, 186, 190]. There are several possible causes for the incomplete mass balance. First, irreversible sorption to microcosm solids could reduce the extraction efficiencies of 8:2 FTOH and its biotransformation products. Previous studies revealed that up to 35% of 8:2 FTOH was irreversibly bound to soils [50]. Also, some 8:2 FTOH transformation products (e.g., 8:2 FTUA) can covalently bond with biological macromolecules, hindering their extraction and quantification [51, 176, 197]. Second, mass loss could result from mineralization of β- and γ-carbon of 8:2 FTOH [188, 195], masked PFCA generation by background contamination levels, and the potential loss of volatile biotransformation products during sampling. Third, additional unknown products formed during the biotransformation of 8:2 FTOH could account for some mass loss. Therefore, non-targeted PFAS analysis was performed to identify those unknown products, as discussed in **Section 4.2.2.3.1.**

4.2.2.2 Biotransformation of 8:2 FTOH in Loring soil

Native microorganisms in Loring AFB soil also showed effective transformation of 8:2 FTOH, including the treatments with a higher starting concentration of 8:2 FTOH (1,700 μg/L). In the Loring biotransformation experiment, 5.8-10.1 mol% of spiked 8:2 FTOH remained in the system after 90 days, which is comparable to the result in Robins AFB soil (7 mol% of 8:2 FTOH remaining after 90 days).

The polyfluorinated compounds quantified at the end of the Loring biotransformation experiment are shown in Appendix **Table A.19**. Similar to the Robins biotransformation experiment, in the low-dose treatment in the Loring biotransformation experiment, the concentrations of 8:2 FTCA and 8:2 FTUA at day 90 were lower than the limits of detection; the two most abundant transformation products were 7:2 sFTOH and 7:3 acid with yields of 33.0 mol% and 3.0 mol%, respectively. In the high-dose treatment at day 90, 7:2 sFTOH was also the biotransformation compound of measurable abundance (6.9 mol%), while the concentration of 7:3 acid was below

the detection limit. In contrast to the low-dose treatment, 8:2 FTCA and 8:2 FTUA were still detected at day 90 with yields of 0.2 mol% and 1.0 mol%, respectively, in the high-dose treatment. While C_4-C_{10} PFCAs were detected in both low-dose and high-dose treatments, the masses of these PFCAs were significantly higher ($p < 0.05$) in samples from the high-dose treatment at day 90 compared to those from the live control. However, significantly higher mass ($p < 0.05$) of only PFHpA and PFOA were detected in the low-dose treatment (Appendix **Figure A.12**). The total mass recovery by day 90 was 44.7% and 30.3 mol% in the low-dose treatment and high-dose treatment, respectively, which are lower than that of the 8:2 FTOH biotransformation experiment with Robins AFB soil (58.5%).

4.2.2.3 Novel 8:2 FTOH biotransformation products and proposed pathways

4.2.2.3.1 Potential novel transformation products identified by non-targeted analysis.

As shown in Appendix **Table A.20,** ten candidate 8:2 FTOH transformation products were identified and assigned confidence levels 1-4, with 4 indicating the least likely and 1 being the most likely [89]. The change in peak area counts over time for the candidate products are plotted in Appendix **Figure A.13**, **Figure A.14**, and **Figure A.15**.

Three of the ten candidates were classified as level 4 (unequivocal molecular formula) due to lack of MS^2 spectrum data. However, according to their exact mass (m/z = 438.9822, m/z = 356.9785, and m/z = 391.0009) and customized suspect mass list based on prior literature [198], 7:3 U amide, 6:2 FTUA [$F(CF_2)_5CF{=}CHCOOH$], and 6:3 acid [$F(CF_2)_6CH_2CH_2COOH$]) were proposed as the potential transformation products, respectively. Previously, 7:3 U amide was determined as an 8:2 FTOH biotransformation product in activated sludge, although the identification was not confirmed due to the lack of an authentic standard [188]. Neither 6:2 FTUA nor 6:3 acid has been previously reported as 8:2 FTOH transformation products. Longer chain fluorotelomer carboxylic acids have been documented as precursors of shorter chain fluorotelomer carboxylic acids. For example, 5:3 acid [$F(CF_2)_5CH_2CH_2COOH$] could produce 4:3 acid [$F(CF_2)_4CH_2CH_2COOH$] and 3:3 acid [$F(CF_2)_3CH_2CH_2COOH$] with 4:2 FTUA [$F(CF_2)_3CF{=}CHCOOH$] as an intermediate through one-carbon removal pathway [199]. Similarly, it is possible that 6:2 FTUA and 6:3 acid could be generated from the biotransformation of 7:3 acid.

Five of the ten candidates were assigned as level 3 (tentative candidates). The structures of level 3 compounds were based on an exact mass, MS^2 spectrum data, and matching to MetFrag simulations [200]. Based on the results of suspect screening, compounds of m/z = 438.9822 and m/z = 376.9691 were proposed to be 7:3 U acid [$F(CF_2)_7CH{=}CHCOOH$] and 6:2 FTCA [$F(CF_2)_6CH_2COOH$], respectively. Although not quantified due to lack of analytical standard in this study, 7:3 U acid has been identified as an 8:2 FTOH biotransformation product in prior studies and reported as a precursor to 7:3 acid and other polyfluorinated transformation products [53, 176, 186, 188, 190]. The formation of 6:2 FTCA in the present study could be attributed to one-carbon removal pathway as an intermediate from 7:3 acid to 6:3 acid. The compound with m/z = 458.9885 was identified as 3-fluoro-7:3 acid [$F(CF_2)_7CHFCH_2COOH$]. As 3-fluoro-5:3 acid

[$F(CF_2)_5CHFCH_2COOH$] was proposed as 6:2 FTUA biotransformation product, similar reaction could occur to 8:2 FTUA, leading to formation of 3-fluoro-7:3 acid by a reductase [53]. Compounds with m/z = 346.9745 and m/z = 318.9797 were identified as perfluoroalkane-like compounds, perfluoroheptanal [$F(CF_2)_6CH{=}O$] and 1H-perfluorohexane [$F(CF_2)_6H$], respectively. Both were identified as potential 8:2 FTOH biotransformation products for the first time in aerobic 8:2 FTOH biotransformation.

Additionally, one of the ten compounds, 3-OH-7:3 acid [$F(CF_2)_7CHOHCH_2COOH$] with m/z = 456.9930 was assigned as level 2 (probable structure) based on MS^2 fragmentation. 3-OH-7:3 acid is a hypothesized 8:2 FTOH biotransformation product in soils, generating from 7:3 U acid [50]. No reference standards were available for the nine transformation product candidates with confidence level 2-4 discussed above. Only one of the ten compounds (m/z = 368.9764) was classified as level 1, 1H-perfluoroheptane [$F(CF_2)_7H$]). Reference standards were available for 1H-perfluoroheptane and used to confirm the identification (Appendix **Figure A.16**).

All ten candidate products were detected in samples from the high-dose treatment in the Loring biotransformation experiment, while only three of the ten were detected in samples from the low-dose treatment in the Loring biotransformation experiment and four from the Robins biotransformation experiment (Appendix **Table A.20**). The distinct transformation products could be associated with different metabolic pathways or due to lower yields in the low-dose experiments, making it difficult to detect in the non-targeted analysis or distinguish these compounds from the background levels.

4.2.2.3.2 Aerobic biotransformation pathways of 8:2 FTOH.

The proposed 8:2 FTOH biotransformation pathway under aerobic conditions (**Figure 4.19**) is based on biotransformation products detected by LC-MS/MS targeted analysis and by non-targeted HRMS in this study, and on pathways proposed in earlier publications [50, 53, 176, 188, 190, 195]. First, 8:2 FTOH could be oxidized to 8:2 fluorotelomer aldehyde (8:2 FTAL) [$F(CF_2)_8CH_2CHO$] by alcohol dehydrogenase(s), and further oxidized to 8:2 FTCA by aldehyde dehydrogenase(s). Although 8:2 FTAL was commonly recognized as an 8:2 FTOH biotransformation product in aerobic soil and activated sludge [50, 188], it was not identified in this study, consistent with studies using aerobic sludge and digester sludge under anaerobic conditions [53, 190]. It is believed that 8:2 FTAL is unstable and could be rapidly oxidized to 8:2 FTCA, which was detected in this study. Subject to hydrogen fluoride (HF) elimination, 8:2 FTCA could form 8:2 FTUA, which was also detected. Fluoride ion was measured in this study, although no distinguishable increase of fluoride was observed in live treatments from the background levels (discussion on fluoride quantification is detailed in **Appendix A.12**). As speculated in a previous study, 8:2 FTUA could be a key branching point for subsequent biotransformation pathways [188].

There are three potential pathways following 8:2 FTUA formation, including conversion to (I) 3-fluoro-7:3 acid, (II) 7:2 sFTOH, and (III) 7:3 U acid. In branch (I), 8:2 FTUA may undergo a reduction reaction to form 3-fluoro-7:3 acid, which was identified by non-targeted analysis in this

study. Branch (II) involves conversion of 8:2 FTUA to 7:2 sFTOH, which was quantified in this study. However, the intermediates between 8:2 FTUA and 7:2 sFTOH have been a controversial point discussed in prior [50, 176, 188, 190]. For example, 7:2 sFTOH was first identified in 8:2 FTOH biotransformation using aerobic activated sludge where 8:1 olefin [$(CF_3(CF_2)_6CF=CH_2$] and 7:2 olefin [$(CF_3(CF_2)_6CH=CH_2$] were proposed as its precursors [188]. A study investigating anaerobic 8:2 FTOH biotransformation using activated sludge surmised that 7:2 olefin could be a precursor to 7:2 sFTOH, although 7:2 olefin may come from other intermediates (7:3 acid and 7:3 U acid) [190]. As 7:2 ketone rather than olefins was experimentally detected in previous studies using aerobic soil or pure *Pseudomonas* culture [50, 176], 7:2 ketone was assumed as the precursor to 7:2 sFTOH here. Then, 7:2 sFTOH was further catalyzed to form PFCAs (C_4-C_8), possibly by monooxygenases via several oxidation reactions, although the mechanisms have not yet been identified [50, 176, 190].

Branch (III) leads to 7:3 U acid via reductive defluorination by a possible dehalogenase [53]. The reaction pathway after the formation of 7:3 U acid is split into four routes. Route (III-a) converts 7:3 U acid to 7:3 acid by unknown reductase(s) [53]. Route (III-b) and (III-c) produce 7:3 U amide and 3-OH-7:3 acid, respectively [50, 188]. Route (III-d) enters a single carbon removal process to generate 6:3 acid, 6:2 FTCA, 6:2 FTUA as well as short-chain PFCAs (C_4-C_7) by a one-carbon removal process, which is proposed based on the pathways found in a study of 5:3 acid biotransformation [199]. Since 7:2 sFTOH and PFOA were the two major biotransformation products, and 7:3 acid and/or C_4-C_7 PFCAs were minor products, the biotransformation pathway involving 7:2 sFTOH could be a major pathway that soil microbial communities in this study were able to utilize.

The newly identified perfluoroalkane-like compounds might be involved in one pathway after production of 7:2 ketone or 7:3 acid, where perfluoroheptanal is the intermediate between 1H-perfluoroheptane and PFHpA. Through a similar mechanism, 1H-perfluorohaxane, might be produced after 6:3 acid to generate PFHxA. No evidence has been documented that perfluoroalkane-like compounds are precursors to PFCAs. Additional experiments are needed to investigate the formation mechanisms of these novel transformation products.

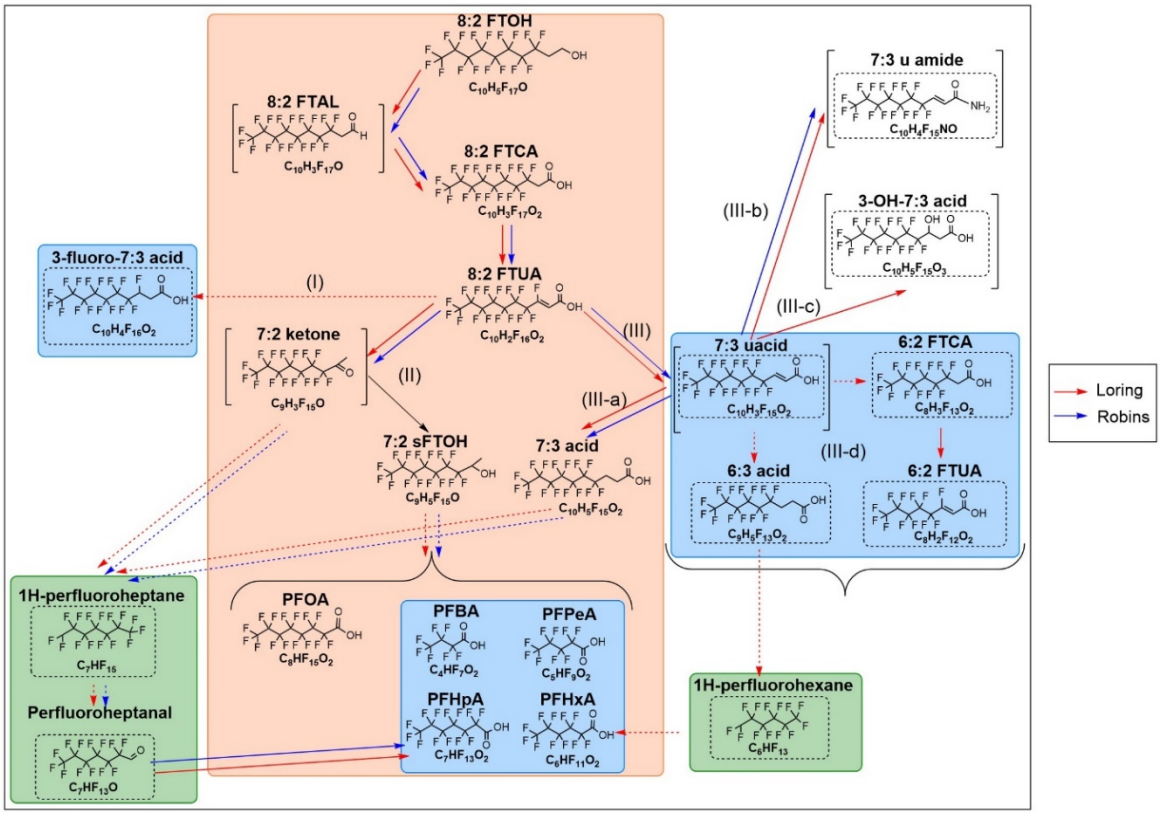


Figure 4.19 Proposed aerobic biotransformation pathways of 8:2 FTOH based on this study and previous studies [50, 53, 176, 188, 190, 195]. Red and blue arrows represent the pathways harbored by microbial communities in Loring and Robins AFB soils, respectively. Compounds in the orange box were directly quantified by LC-MS/MS in this study, except for those with brackets. Compounds in brackets were not detected by LC-MS/MS in this study but have been documented as 8:2 FTOH biotransformation products. Compounds in dashed boxes are tentative biotransformation products identified in non-targeted analysis by LC-HRMS in this study. Compounds/pathway with dashed arrows in blue boxes are proposed based on prior literature. Compounds/pathway in green boxes with dashed arrows are newly identified in this study.

4.2.2.4 Microbial community dynamics during aerobic biotransformation of 8:2 FTOH

4.2.2.4.1 Microbial community richness and diversity.

The mapped reads of 16S rRNA gene amplicons obtained from the Robins and Loring biotransformation experiments varied in the range of 4,753 to 12,647 (Appendix **Table A.21**). To compare diversity and richness of microbial community between different samples, the number of reads was rarefied to an identical sequencing depth (4,753) and clustered into operational taxonomic units (OTUs) ranging from 51 to 312 at a 97% similarity level. Chao 1 and Shannon indices were calculated as microbial richness and diversity estimators, respectively (Appendix **Table A.21**). The original Loring AFB soil had higher Chao 1 index and numbers of OTUs, as well as higher Shannon indices than those of Robins AFB soil. It indicates that the original Loring AFB

soil had both higher microbial richness and diversity than Robins AFB soil. Principal coordinate analysis (PCoA) was also applied to visualize the alteration of microbial community composition across different treatments. Microcosms constructed with Loring AFB soil were clustered together, while all microcosms using Robins AFB soil were clustered together indicating that the microbial community composition was distinct between Loring AFB soil and Robins AFB soil (Appendix **Figure A.17**). Although both sites were highly contaminated with PFAS, the lower microbial richness and diversity in Robins AFB soil are possibly associated with its physical/chemical characteristics, for example, lower organic carbon content (< 0.5%) compared to Loring AFB soil (3.5 %). In addition, based on the Shannon and Chao 1 indices (Appendix **Table A.21**), different 8:2 FTOH doses in the Loring biotransformation experiment led to differences in microbial richness and diversity. Compared with the soil in live controls, soil used in the low-dose treatment had higher microbial richness and diversity, while soil used in the high-dose treatment had lower richness and diversity. This result suggests the possible toxicity of high concentrations of 8:2 FTOH and its biotransformation products and shift of microbial community towards specific microbial taxa during the biotransformation of higher concentration of 8:2 FTOH.

4.2.2.4.2 Microbial community composition shifts in the Robins biotransformation experiment.
As shown in **Figure 4.20**, a total of fifteen phyla were identified in the Robins AFB soil microbial community. Proteobacteria occupied a high proportion (78.90%) in the initial Robins AFB soil after a 7-day incubation with carbon source added. Other major phyla in the initial Robins AFB soil included Myxococcota (8.33%), Firmicutes (7.45%), Bacteroidota (2.88%), and Bdellovibrionota (1.41%). The phylum Proteobacteria dominated over the 90-day period in both live treatment (69.09%) and live control (74.10%). The relative abundance of phyla Firmicutes, Acidobacteriota, Myxococcota, and Desulfobacterota were higher in the live treatment (16.2%, 2.74%, 1.03%, and 1.18%) than those in the live control (10.3%, 0.61%, 0.48%, and 0.42%).

Further analysis at the genus level revealed that obvious shifts towards an uncultured genus belonging to the family Symbiobacteraceae (phylum Firmicutes, 14.75% in the live treatment versus 4.02% in the live control) and genus *Flavisolibacter* in phylum Bacteroidota (7.41% in the live treatment versus 0.08% in the live control). The relative abundance of five genera including *Variovorax*, *Azospirillum*, *Ralstonia*, *Sphingomonas*, and *Ancylobacter* belonging to phylum Proteobacteria (2.42%-8.08%) in the live treatment, were much higher than those in the live control (0.17%-2.12%) after the 90-day incubation (**Figure 4.20**). Species in genera *Variovorax*, *Ralstonia*, *Sphingomonas*, and *Ancylobacter* have been previously found to be responsible for degradation of organic chlorinated compounds [201-204]. indicating they may also be involved in 8:2 FTOH biotransformation.

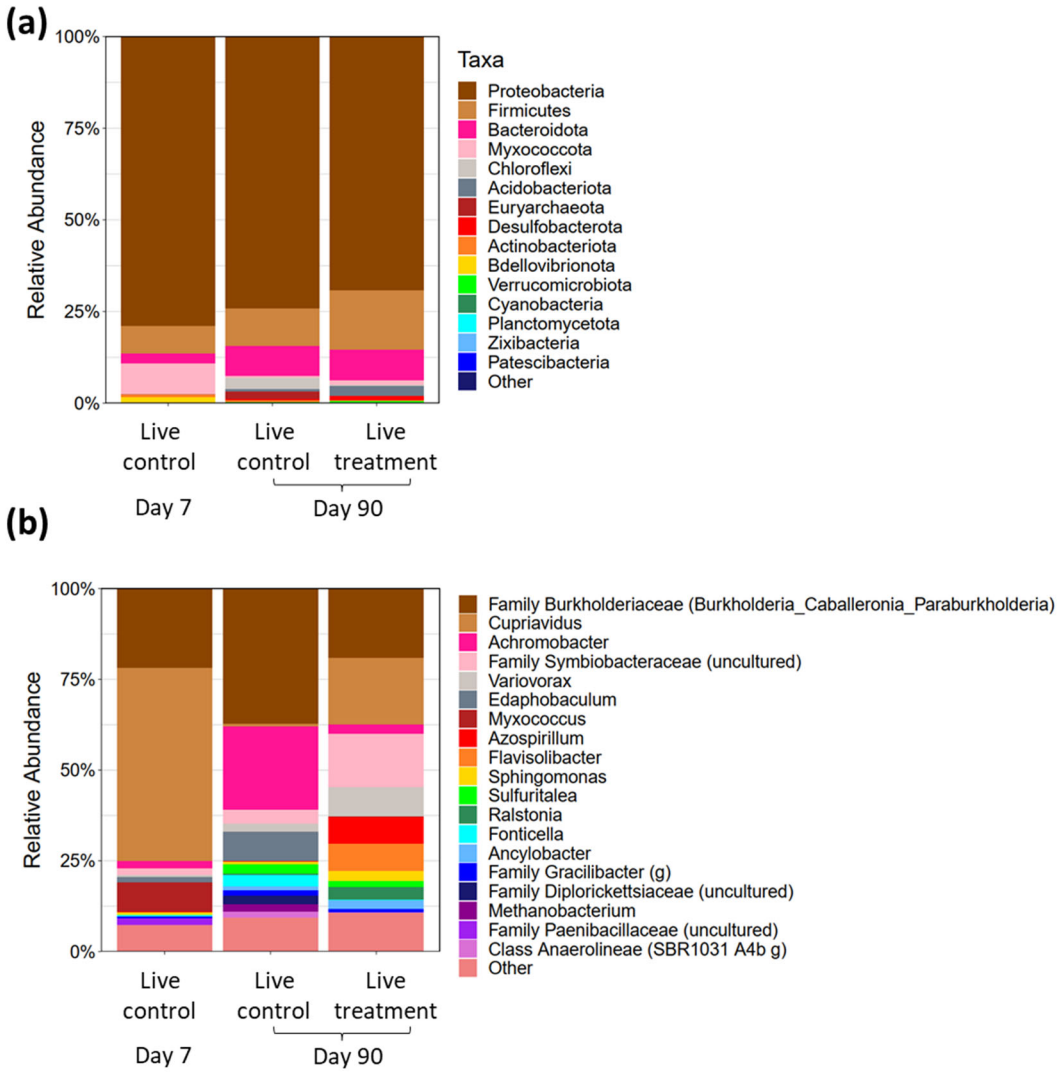


Figure 4.20 Relative abundance of microbial community at the (a) phylum level and (b) genus level in the Robins biotransformation experiment.

4.2.2.4.3 Microbial community composition shifts in the Loring biotransformation experiment. Twenty-seven classified phyla in the domain Bacteria and three in domain Archaea were identified across all treatments over the 90-day Loring biotransformation experiment, though not all phyla were present in all groups. The top fifteen abundant taxa at phylum level are depicted in **Figure 4.21**. In the original Loring AFB soil (day 0), the dominant bacterial phyla included Proteobacteria (35.01%), Bacteroidota (17.04%), Acidobacteriota (14.71%), Chloroflexi (11.66%), and Gemmatimonadota (3.79%). Generally, minor effects of low doses of 8:2 FTOH on microbial community composition in Loring AFB soil were observed after 90 days when compared with the live control. For example, the relative abundance of Proteobacteria and Bacteroidota, were 46.71% and 14.39%, respectively, in the low-dose treatment, which was comparable with the proportions of these phyla in the live control after incubation (44.94% and 14.22%). Conversely, in the high-

dose group, the relative abundance of Proteobacteria was elevated to 56.07%. Proteobacteria, the most prominent phylum in the present study, was also identified by others as the most prominent phylum in surface soil with heavy PFAS pollution [169, 170]. This increase in Proteobacteria abundance is also consistent with observations in river sediments dosed with 6:2 FTOH [166], and in wetland slurry spiked with 6:2 FTS [171]. Additionally, the proportions of Euryarchaeota, an archaeal phylum, as low as 0.19% in the original soil though, enriched in the presence of 8:2 FTOH. The relative abundance of Euryarchaeota increased to 0.74% in the low-dose treatment and 1.24% in the high-dose treatment. These observations suggest the potential tolerance of Proteobacteria and Euryarchaeota to specific PFAS, including 8:2 FTOH.

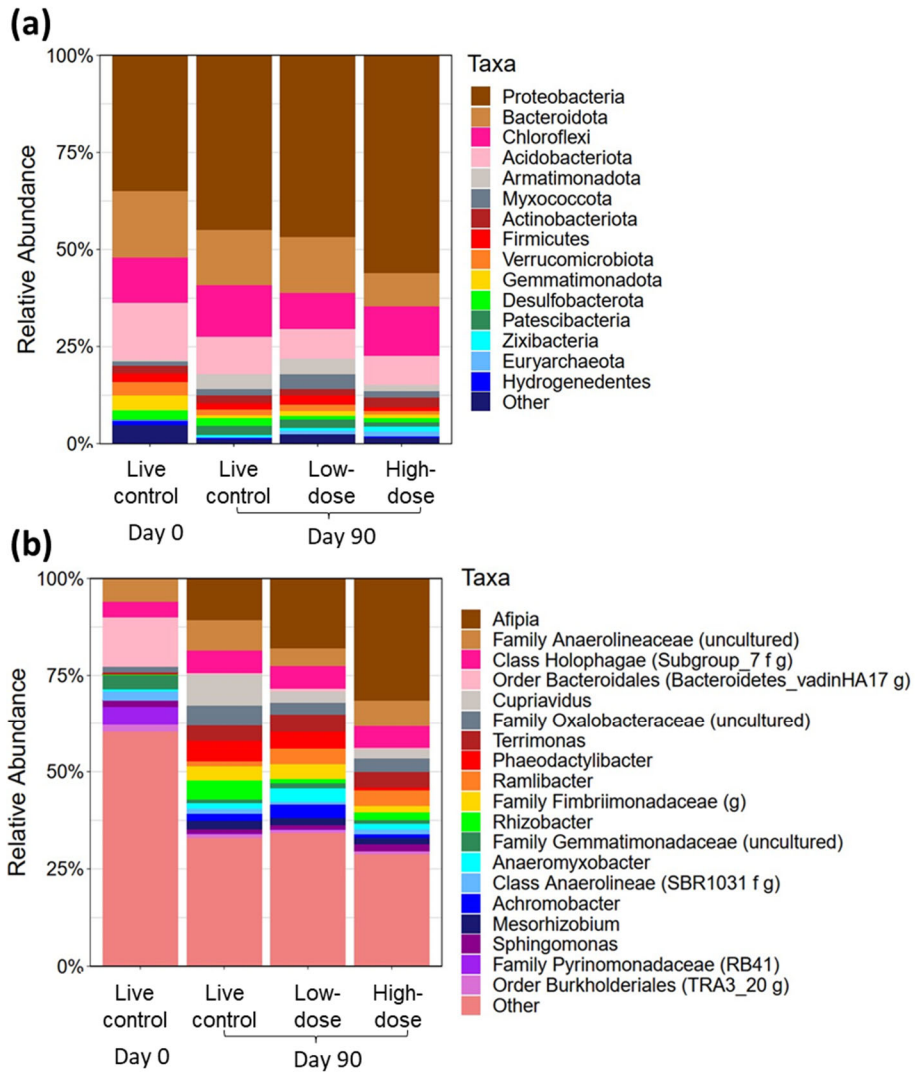


Figure 4.21 Relative abundance of microbial community at the (a) phylum level and (b) genus level in the Loring biotransformation experiment.

To identify subtler shifts in the microbial community, analysis of microbial genera was performed. A sum of 246 genera was shared among day 90 samples of all three treatments. The predominant 19 genera are shown in **Figure 4.21**. The abundance of *Afipia* and *Sphingomonas*, both affiliated with phylum Alphaproteobacteria were positively correlated with the concentration of 8:2 FTOH. After the 90-day incubation, the relative abundance of *Afipia* increased from non-detectable levels to 10.58% in the live control. The relative abundance of *Afipia* was further enriched to 17.95% and 31.37% in the low-dose treatment and high-dose treatment, respectively. *Afipia* strains exist widely in freshwater, river sediments, Antarctic habitats, and soil [183, 205]. Previous studies showed that isolated *Afipia* strains had the ability to degrade 1,4-dioxane and methanesulfonate [183, 184]. Interestingly, some *Afipia* spp. are capable of degrading different haloacetic acids as α-halocarboxylic acid dehalogenase genes are present in their genomes [185]. Similarly, the relative abundance of *Sphingomonas* was imperceptibly higher in the low-dose treatment (1.18%) at day 90 compared to that in the live treatment (1.14%), while it was noticeably higher in the high-dose treatment (1.81%). *Sphingomonas* spp. are also widespread in soil and aquatic systems [206, 207], and are known to be metabolically versatile in degrading organic pollutants, including polycyclic aromatic hydrocarbons and highly chlorinated pesticides using dehalogenases [201, 208]. The relative abundance of *Methanobacterium* (Euryarchaeota) followed a similar trajectory with elevated 8:2 FTOH concentrations as *Afipia* and *Sphingomonas* and increased to 1.24% in the high-dosed treatment after incubation, although they accounted for less than 0.20% in the original soil. Members of *Methanobacterium* were also reported to have the ability to tolerate and degrade halogenated compounds [209, 210]. The existence of *Afipia*, *Sphingomonas*, and *Methanobacterium* in AFFF-impacted soil and their increasing abundance after 8:2 FTOH exposure, particularly under the high-dose condition, indicated that species in these genera could be potential 8:2 FTOH degraders and tolerant towards 8:2 FTOH and its biotransformation products.

Despite the difference in microbial community composition, the occurrences of 8:2 FTOH biotransformation of 8:2 FTOH in both soils in the present study and in other environmental matrices from prior studies [50, 188, 190] suggest that microorganisms capable of transforming 8:2 FTOH are not rare in the environment. The similar major 8:2 FTOH transformation products detected in Loring AFB soil and Robins AFB soil incubations, indicate that these two soils may share key 8:2 FTOH degraders.

4.2.2.5 Concluding remarks

This study demonstrated that 8:2 FTOH can be transformed rapidly by indigenous microbial communities from two different AFFF-impacted surface soils under aerobic conditions. More than 90 mol% of 8:2 FTOH was removed, and similar major transformation products were detected during the 90-day incubation period, irrespective of the amount of 8:2 FTOH spiked initially and the microbial communities present in the soil. Previously documented 8:2 FTOH biotransformation products, including polyfluorinated substances, like 8:2 FTCA, 8:2 FTUA, 7:2

sFTOH, and 7:3 acid, as well as perfluorinated compounds like PFOA were identified and quantified. Importantly, perfluoroalkane-like compounds, including 1H-perfluoroheptane, 1H-perfluorohexande, and perfluoroheptanal were identified as novel transformation products that have not been previously reported.

This work also documented that the microbial community composition shifted over the 90-day incubation period after exposure to two dosages of 8:2 FTOH (one-time addition of 170 µg/L and repeated additions of 1,700 µg/L). By imposing selective pressure, exposure to the higher concentration of 8:2 FTOH facilitated not only the detection of novel transformation products, but also the identification of microbes that may be more tolerant of 8:2 FTOH and its biotransformation products. Results suggest that microorganisms in phylum proteobacteria, such as genera *Afipia* and *Sphingomonas* may be more tolerant of high 8:2 FTOH concentrations. Microorganisms in these two and other genera, including *Variovorax*, *Ralstonia*, *Sphingomonas*, *Ancylobacter*, and *Methanobacterium,* may be involved as potential degraders. Our findings provide insights on 8:2 FTOH biotransformation potential and a starting point for screening microbes engaged in fluorotelomer degradation in the future.

4.2.3 Biotransformation of 8:2 FTOH under nitrate-, sulfate-, and iron-reducing conditions

Throughout the experiments, nitrate-, sulfate-, and iron-reducing activities were confirmed in the respective microcosms by monitoring the consumption of electron donor (i.e., lactate and/or DGBE) and electron acceptor (i.e., NO_3^-, SO_4^{2-}, or Fe(III)/Fe(II)) (Appendix **Figure A.18**, **Figure A.19**, and **Figure A.20**). Additional information related to the establishment of nitrate-, sulfate-, and iron-reducing microcosms is provided in **Appendix A.13**. Some PFAS were detected in the day 0 samples, thus the background levels of legacy PFAS in Loring soil were determined (Appendix **Table A.22**). Additional discussion on the measurement of legacy PFAS in Loring soil is provided in **Appendix A.14**. As shown in **Figure 4.22** and **Figure 4.23**, 94.9 ± 7.8 mol%, 88.1 ± 7.4 mol% and 90.7 ± 8.0 mol% of the initially spiked 8:2 FTOH remained in the abiotic controls of nitrate-, sulfate-, and iron-reducing microcosms, respectively, without significant changes ($p > 0.05$) throughout the experiments. These stable 8:2 FTOH concentrations under various abiotic experimental conditions verify the integrity of the experimental system and the efficiency of the extraction method applied in the present study.

4.2.3.1 Biotransformation of 8:2 FTOH under nitrate-reducing conditions

4.2.3.1.1 Biotransformation rates.

In the live-spiked treatments (i.e., ED and NA treatments), dramatic decreases in the spiked 8:2 FTOH were observed under nitrate-reducing conditions in the first 56-day incubations (**Figure 4.22**). The half-life of 8:2 FTOH biotransformation in the NA treatment was calculated as ~36.5 days as determined by fitting 9 data points into a single first-order kinetic model (coefficient of determination R^2 = 0.847, Appendix **Figure A.21**). Amendment of 20 mM lactate (i.e., ED

treatment) greatly enhanced the biotransformation rate by reducing the half-life of 8:2 FTOH to ~12.5 days (R^2 = 0.931, Appendix **Figure A.21**). Thus, the biostimulation of nitrate-reducing microorganisms with lactate as a supplemental and/or favorable electron donor and carbon source could promote more efficient biotransformation of 8:2 FTOH. Specifically, in the ED treatment, the residual 8:2 FTOH fraction decreased sharply from 99.9 ± 5.6 mol% at day 7 to 5.6 ± 3.3 mol% at day 28 and was further reduced to 0.4 ± 0.2 mol% by day 154 (**Figure 4.22**). The residual 8:2 FTOH in the NA treatment, by comparison, did not decrease in the first 28 days. However, a rapid decrease was observed in the following 28 days with only 10.7 ± 3.0 mol% remaining by day 56, which was then gradually decreased to 0.2 ± 0.2 mol% by the end of incubation (**Figure 4.22**). The relatively fast biotransformation of 8:2 FTOH under nitrate-reducing conditions in Loring soil, especially with lactate amendment, was comparable with those observed in aerobic soils (half-lives ranging from one to four weeks [50, 211], and was much faster than previously documented in digester sludge under methanogenic conditions (half-life of ca. 145 days) [53].

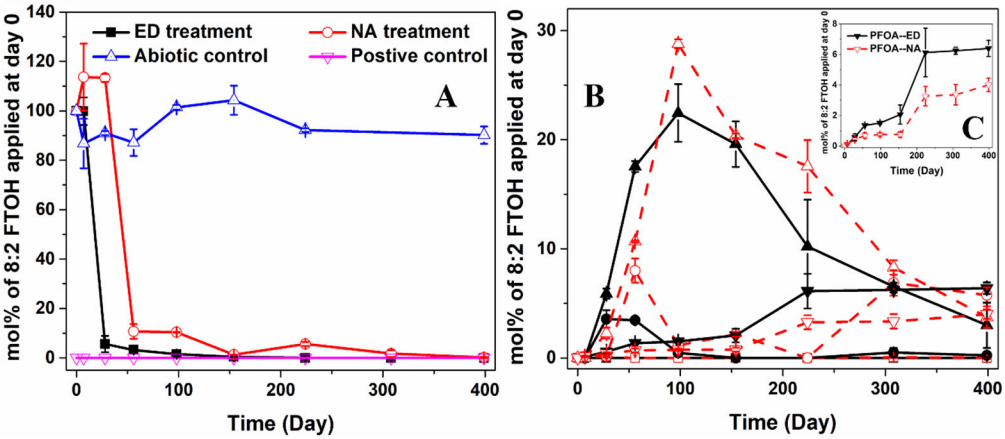


Figure 4.22 Changes in molar ratios of residual 8:2 FTOH during biotransformation under nitrate-reducing conditions in the electron-donor (ED) treatment, natural attenuation (NA) treatment, abiotic controls, and positive controls microcosms (Panel A). Molar yields of 8:2 FTOH biotransformation products (squares: 8:2 FTCA, circles: 8:2 FTUA, up triangles: 7:2 sFTOH, down triangles: PFOA) in the ED (solid black lines and solid symbols) and NA treatments (dash red lines and open symbols) (Panel B). Panel C is a zoom view of B, showing the time course trends of PFOA molar yields.

4.2.3.1.2 Biotransformation products quantified by LC-MS/MS targeted analysis.

As shown in **Figure 4.22**, 8:2 fluorotelomer saturated carboxylic acid (8:2 FTCA), 8:2 fluorotelomer unsaturated carboxylic acid (8:2 FTUA), and 7:2 secondary fluorotelomer alcohol (7:2 sFTOH), which were previously reported as polyfluorinated intermediates of 8:2 FTOH [50, 190, 195], were quantified in both ED and NA treatments during 8:2 FTOH biotransformation under nitrate-reducing conditions. None of these compounds were above the limits of detection (LOD) in abiotic and positive controls. The most abundant transformation product was 7:2 sFTOH,

which reached peak molar yields of 22.5 ± 2.6 mol% and 28.8 ± 0.4 mol% of the initially applied 8:2 FTOH by day 98 in ED and NA treatments, respectively. Concentrations of 7:2 sFTOH then decreased to 10.2 ± 4.3 mol% and 17.6 ± 2.4 mol% at day 224, further to 3.0 ± 2.1 mol% and 3.7 ± 1.0 mol% at the end of incubation, respectively (**Figure 4.22**). In contrast, 8:2 FTCA was only detected sporadically in the NA treatment (< 0.2 mol% of initially applied 8:2 FTOH) and was below the LOD in the ED treatment (**Figure 4.22**), likely due to its rapid conversion to other products (e.g., 8:2 FTUA). In the ED treatment, 8:2 FTUA was produced with a peak molar yield of 3.6 ± 0.8 mol% by day 28, then later decreased to low levels (< 0.5 mol%). While in the NA treatment, 8:2 FTUA reached a peak molar yield of 8.0 ± 1.1 mol% by day 56 followed by some fluctuations and settled at 5.8 ± 0.7 mol% by the termination of the experiment (**Figure 4.22**). The molar yields and time trends of these three polyfluorinated intermediates in the present study were consistent with 8:2 FTOH biotransformation reported in aerobic soils [50]. Another previously reported major polyfluorinated product of 8:2 FTOH was 7:3 acid [50, 53, 190]; however, it was not measured as a product in this study. Although 7:3 acid was detected in ED and NA treatments, it was also detected in abiotic and positive controls without significant differences ($p > 0.05$) throughout the incubations (Appendix **Figure A.22**). This finding is in contrast to most previous studies on aerobic and anaerobic 8:2 FTOH biotransformation where 7:3 acid was a major stable transformation product [50, 53, 186]. Only one study found that 7:3 acid and its known direct precursor, 7:3 U acid (7:3 unsaturated acid, $F(CF_2)_7CH{=}CHCOOH$), were absent in the biotransformation of 8:2 FTOH by an alkane-degrading strain, *Pseudomonas oleovorans* [176]. The researchers assumed that *P. oleovorans* might lack microbial enzymes capable of defluorinating 8:2 FTUA to 7:3 U acid and then reducing the latter to 7:3 acid. Therefore, the formation of 7:3 acid was absent or extremely minimal during 8:2 FTOH biotransformation under nitrate-reducing conditions could be interpreted by the lack of those enzymes responsible for 7:3 acid formation in the nitrate-reducers in Loring soil.

As potential perfluorinated transformation products of 8:2 FTOH [50, 190], C4 to C9 perfluoroalkyl carboxylates (PFCAs) were detected in all treatments, indicating that these legacy PFAS were present in Loring soil (Appendix **Figure A.22**). However, a significant increase ($p < 0.05$) was only observed for PFOA after comparing the concentrations of these PFCAs in ED and NA treatments to positive controls (Appendix **Figure A.22**), demonstrating that PFOA was formed during 8:2 FTOH biotransformation under nitrate-reducing conditions. Although the concentrations of other PFCAs including perfluorobutanoic acid (PFBA), perfluoropentanoic acid (PFPeA), perfluorohexanoic acid (PFHxA), and perfluoroheptanoic acid (PFHpA) in live-spiked treatments were not significantly different from those in positive controls, some PFCAs might be biotransformation products as reported previously under both oxic [186, 187] and anoxic conditions [190, 212], but with yields that were too low to be distinguished from the background levels in Loring soil. After subtracting the PFOA mass in positive controls at each sampling point, the molar yields of PFOA in both ED and NA treatments continued to increase during the incubations, reaching to 6.4 ± 0.5 mol% and 4.0 ± 0.4 mol% of the initially applied 8:2 FTOH at

the end of incubation, respectively (**Figure 4.22**). The PFOA yields measured here are much less than those previously reported in aerobic soils over ca.7 months incubation [50], but substantially higher than yields measured in digester sludge under methanogenic conditions over the 181-day study [53]. In addition, higher molar yield of PFOA observed in the ED treatment compared to the NA treatment implies that the presence or amendment of additional and/or favorable electron donor and carbon source (e.g., lactate) at AFFF-impacted sites will likely result in more extensive and/or more rapid release of PFCAs to the environmental matrices under nitrate-reducing conditions.

4.2.3.1.3 Biotransformation products identified by LC-HRMS.

In ED and NA treatments under nitrate-reducing conditions, total mass recovery of 8:2 FTOH and the transformation products quantified by LC-MS/MS decreased sharply during the periods when 8:2 FTOH was rapidly transformed (**Figure 4.22** and Appendix **Figure A.23**). Total mass recovery then further gradually decreased to only ca.10.0 mol% of the initially applied 8:2 FTOH by the end of incubation. Such a decrease was not observed in the abiotic controls (Appendix **Figure A.23**). The irreversible binding of 8:2 FTOH and/or biotransformation products in the soil, which has been reported in previous 8:2 FTOH studies in soils, resulted in those compounds not being recovered [50, 187, 213]. This binding process, moreover, was likely catalyzed by microbial enzymatic activities [189], which explains the overall satisfactory molar recovery (86.8-104.3 mol%) in abiotic controls. In addition, the formation of unknown 8:2 FTOH biotransformation products could contribute to the low mass recovery. Therefore, non-targeted LC-HRMS analysis was performed on the samples from each treatment under nitrate-reducing conditions, and a total of four potential biotransformation products of 8:2 FTOH were identified (Appendix **Table A.23**).

Tentatively identified as a biotransformation product of 8:2 FTOH at confidence level 3 (assigned based on the Schymanski Scale [89]), based on MS^2 spectrum (Appendix **Figure A.24**), 7:3 U acid (*m/z* 438.9822) accumulated to a similar amount in ED and NA treatments after a 32-week incubation, but remained at a very low level in abiotic and positive controls under nitrate-reducing conditions (Appendix **Figure A.24**). In previous studies, 7:3 U acid has been recognized as a precursor to 7:3 acid under oxic and methanogenic conditions [50, 53, 176, 195], and the absence of 7:3 U acid was attributed to the fast biotransformation to 7:3 acid [50, 53]. In this study, however, the formation of 7:3 acid was not observed in either ED or NA treatments under nitrate-reducing conditions, in spite of the gradual accumulation of 7:3 U acid. This finding was likely due to a lack of microbial enzymes (e.g., reductase) capable of converting 7:3 U acid to 7:3 acid by the microorganisms in Loring soil under nitrate-reducing conditions.

In nitrate-reducing microcosms, 3-OH-7:3 acid ($F(CF_2)_7CHOHCH_2COOH$, *m/z* 456.9930) was identified as another biotransformation product of 8:2 FTOH (confidence level 2, based on MS^2 (Appendix **Figure A.24**). The authentic standard of 3-OH-7:3 acid was not available for further structure verification. This product gradually accumulated in only ED and NA treatments under nitrate-reducing conditions, as indicated by the increase in peak area over time (Appendix **Figure A.26**). Only one previous study identified 3-OH-7:3 acid as a product during 8:2 FTOH

biotransformation, and it was reported to form by the conversion of 7:3 U acid in aerobic soils [50]. This study represents the first reported identification of 3-OH-7:3 acid as a product during 8:2 FTOH biotransformation under nitrate-reducing conditions. During biotransformation, 3-OH-7:3 acid may be formed by the oxidation of 7:3 U acid by a hydratase type enzyme.

Non-targeted analysis also suggested the presence of a biotransformation product with potential structure as 7:3 U amide ($F(CF_2)_7CH{=}CHCONH_2$, *m/z* 437.9975). However, the MS^2 fragmentation data of this product was not available, resulting in the identification at confidence level 4. It was reported that 7:3 U amide was a potential product during 8:2 FTOH aerobic biotransformation [195], but this compound was not observed in subsequent aerobic or anaerobic 8:2 FTOH biotransformation studies [50, 53, 187, 190]. In the present study, increases in the peak area of 7:3 U amide were observed only in ED and NA treatments under nitrate-reducing conditions (Appendix **Figure A.27**), indicating its formation during 8:2 FTOH biotransformation under nitrate-reducing conditions. The maximum peak area of 7:3 U amide was much larger in the NA treatment than the ED treatment, peaking at week 22 (Appendix **Figure A.27**). The formation of 7:3 U amide may result from the conversion of 7:3 U acid by a transaminase under nitrate-reducing conditions, and this reaction may be reversible [195]. In addition, decreases of 7:3 U amide in ED and NA treatments after week 22 indicated that it was likely an intermediate and was converted to downstream biotransformation products, such as PFHxA or PFOA as proposed previously [195].

A novel biotransformation product, 1H-perfluoroheptane ($F(CF_2)_6\ CF_2H$, *m/z* 368.9764), was identified during 8:2 FTOH biotransformation (confidence level 1 with a verified reference standard). Fragmentation analysis using MS^2 spectrum indicated the presence of characteristic moieties, including the deprotonated molecule ion (*m/z* 368.9764) and several fragment ions (*m/z* 218.9860, *m/z* 168.9893, and *m/z* 118.9929) with one or multiple losses of $-CF_2$ groups (50 Da) (Appendix **Figure A.28**). The identification of this product as 1H-perfluoroheptane was further confirmed by the comparison with the compound standard (Appendix **Figure A.28**). The quantification of 1H-perfluoroheptane was then conducted using a GC-HRMS. As shown in Appendix **Figure A.29**, 1H-perfluoroheptane was formed rapidly in ED and NA treatments, with a molar yield of 56.1-81.1 mol% at day 28. Then, 1H-perfluoroheptane gradually decreased to below the LOD (1,954 ng/L) by day 399 in the ED treatment; while in the NA treatment, its molar yield increased to 76.4 mol% at day 154 then decreased to below the LOD at day 399 (Appendix **Figure A.29**). In the abiotic and positive controls, 1H-perfluoroheptane was below the LOD during the incubation. As the concentration of 1H-perfluoroheptane measured in some solid and headspace samples were close to the LOD, caution should be taken regarding the quantification results, for example, the total mass of 1H-perfluoroheptane formed may be overestimated. Regardless, the substantial formation in the early incubation followed by the gradual decrease indicated that 1H-perfluoroheptane is a major intermediate during 8:2 FTOH biotransformation under nitrate-reducing conditions.

4.2.3.2 Biotransformation of 8:2 FTOH under sulfate-reducing and iron-reducing conditions

4.2.3.2.1 Biotransformation rates and products quantified by LC-MS/MS targeted analysis.

The biotransformation of 8:2 FTOH under sulfate-reducing and iron-reducing conditions was also observed in live-spiked microcosms based on the detections of known biotransformation products (**Figure 4.23**). The biotransformation under both redox conditions, however, was less complete and much slower than that under nitrate-reducing conditions. At the end of the incubation (> 400 days), 64.4 ± 13.3 mol% and 75.2 ± 8.4 mol% of the initially applied 8:2 FTOH remained in ED and NA treatments, respectively, under sulfate-reducing conditions (**Figure 4.23**). Similarly, under iron-reducing conditions, 71.8 ± 20.6 mol% and 90.0 ± 1.1 mol% remained in ED and NA treatments, respectively (**Figure 4.23**). Among the known 8:2 FTOH biotransformation products reported previously [50, 186] and those under nitrate-reducing conditions, only 8:2 FTCA and 8:2 FTUA were measured as transformation products in the sulfate-reducing and iron-reducing live-spiked microcosms (**Figure 4.23**). No significant differences ($p > 0.05$) in 7:2 sFTOH, 7:3 acid or C4-C9 PFCAs were observed among all treatments at each sampling event (Appendix **Figure A.30** and **Figure A.31**). Specifically, low concentrations of 8:2 FTCA and/or 8:2 FTUA were measured starting at day 56 in ED and NA treatment under sulfate-reducing conditions (**Figure 4.23**). Both transformation products peaked at day 154 in the ED treatment with 3.5 ± 1.7 mol% of 8:2 FTCA and 0.2 ± 0.1 mol% of 8:2 FTUA, and then subsequently decreased (**Figure 4.23**). In the NA treatment, however, 8:2 FTCA and 8:2 FTUA increased continuously to the molar yields of 6.5 ± 1.8 mol% and 1.1 ± 0.8 mol% at the end of incubation (**Figure 4.23**D). The slower biotransformation rate of 8:2 FTOH under iron-reducing conditions resulted in later detection of transformation products, which was not detected until day 154 (**Figure 4.23**D). Only trace amounts of 8:2 FTCA and 8:2 FTUA (< 0.1 mol%) were quantified throughout the incubation in the NA treatment (**Figure 4.23**D). Relatively more of 8:2 FTCA and 8:2 FTUA were formed in the ED treatment, continuously increasing to 4.2 ± 1.5 mol% and 0.2 ± 0.1 mol% by day 450 (**Figure 4.23**D). Based on the residual fractions of 8:2 FTOH and the amounts of quantified transformation products (i.e., 8:2 FTCA and 8:2 FTUA) in ED and NA treatments during biotransformation under sulfate- and iron-reducing conditions (**Figure 4.23**B), it is likely that the lactate amendment resulted in the faster biotransformation of 8:2 FTOH, similar to observations under nitrate-reducing conditions.

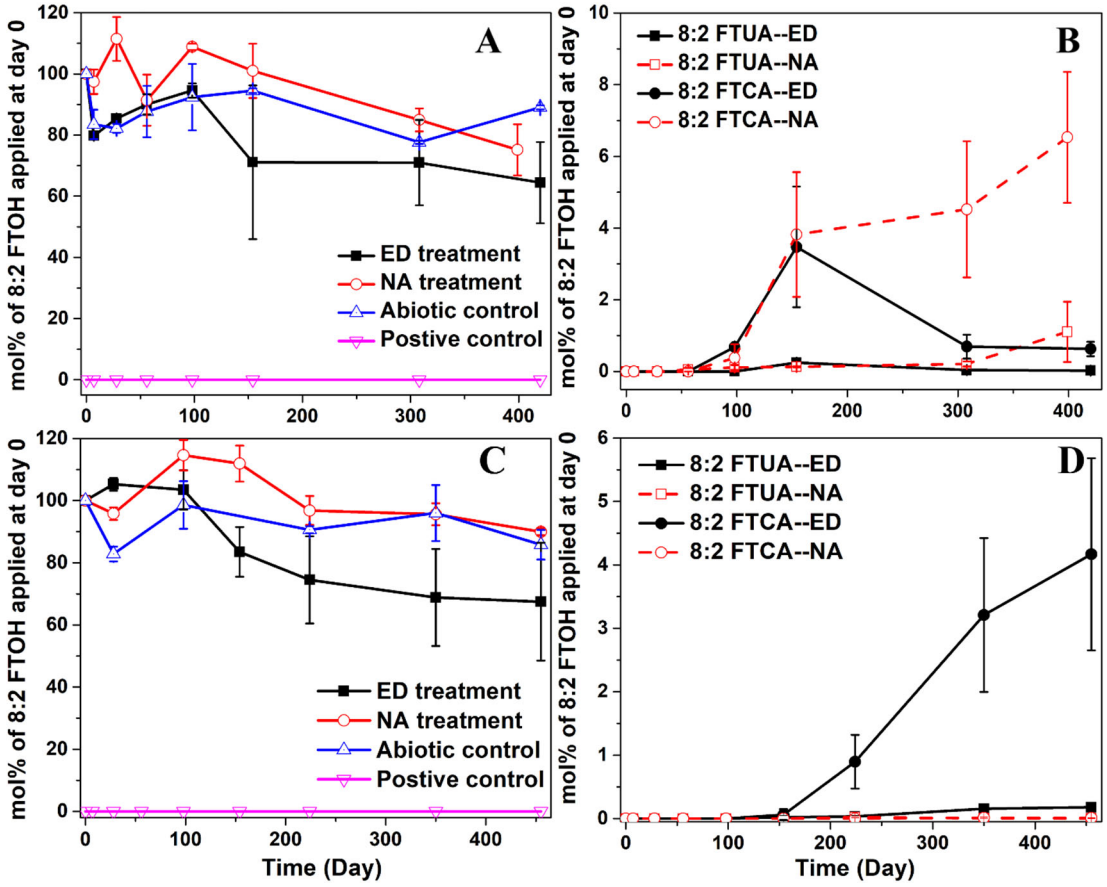


Figure 4.23 Changes in concentrations of targeted PFAS during 8:2 FTOH biotransformation under sulfate-reducing (Panels A and B), and iron-reducing conditions (Panels C and D). Panels A and C show 8:2 FTOH in the electron-donor (ED) treatment, natural attenuation (NA) treatment, abiotic control, and positive control. Panels B and D show the biotransformation products of 8:2 FTOH in ED and NA treatments. Note that the y-axis scale in Panel B is larger than the scale in Panel D.

4.2.3.2.2 Biotransformation product identified by LC-HRMS analysis.

The molar recoveries were relatively higher in live-spiked treatments under sulfate- and iron-reducing conditions with 65.1 to 82.8 mol% and 71.8 to 90.0 mol% at the termination of the experiment, respectively. These higher molar recoveries were likely due to the decreased extent of 8:2 FTOH biotransformation (**Figure 4.23** and Appendix **Figure A.23**) relative to the nitrate-reducing conditions. Non-targeted LC-HRMS analysis was also performed on the samples from each treatment under sulfate- and iron-reducing conditions, and a novel biotransformation product of 8:2 FTOH, 3-F-7:3 acid ($F(CF_2)_7CFHCH_2COOH$, *m/z* 458.9885), was tentatively identified (confidence level 3, based on MS^2 (Appendix **Figure A.24**) under both conditions (Appendix **Table A.23**). The obvious increases in the peak area were observed in ED and/or NA treatments under sulfate- and iron-reducing conditions, but not in abiotic and positive controls (Appendix

Figure A.32). One analogue of 3-F-7:3 acid, 3-F-5:3 acid ($F(CF_2)_5CFHCH_2COOH$) was previously identified as a product during 6:2 FTOH biotransformation in digester sludge, and 3-F-7:3 acid was proposed as a product of 8:2 FTOH in the same system [53]. In this study, 3-F-7:3 acid was likely formed by the reduction of 8:2 FTUA with a reductase under sulfate- and iron-reducing conditions. In the ED treatment under sulfate-reducing condition, 3-F-7:3 acid increased at week 22 and then decreased at week 44 (Appendix **Figure A.32**), indicating further biotransformation to other byproducts, or the possible conversion back to 8:2 FTUA as proposed previously [53]. The reverse reaction from 3-F-7:3 acid to 8:2 FTUA was less likely as the increase of 8:2 FTUA was not observed at week 44 in the ED treatment under sulfate-reducing condition.

4.2.3.3 Distinct 8:2 FTOH biotransformation pathways under different redox conditions

4.2.3.3.1 Comparison of biotransformation under sulfate- and iron-reducing conditions with that under nitrate-reducing conditions.

The biotransformation of 8:2 FTOH observed in the sulfate- and iron-reducing microcosms was distinctly different from that in nitrate-reducing microcosms, and also from those previously reported under oxic [50, 187] and methanogenic conditions [53, 190]. It has been proposed in prior studies that 8:2 FTOH was oxidized to 8:2 FTCA, which was further dehydrohalogenated to 8:2 FTUA [53, 187]. Transformation from 8:2 FTOH to 8:2 FTUA was shown to occur readily under nitrate-reducing conditions, as well as under oxic and methanogenic conditions [53, 187]. However, in the present study, 8:2 FTUA formation remained low (< 1.1 mol%) during incubation under sulfate- and iron-reducing conditions. These results suggest that the conversion of 8:2 FTCA to 8:2 FTUA may be the rate-limiting step for 8:2 FTOH biotransformation under sulfate-reducing and iron-reducing conditions, likely associated with the lack of (unknown) microbial enzymes involved in the dehydrohalogenation reaction.

Moreover, the conversion of 8:2 FTUA to either 7:2 sFTOH or 7:3 U acid, which has been previously reported [50, 176] and was also observed under nitrate-reducing conditions, did not occur under sulfate- and iron-reducing conditions. Instead, 3-F-7:3 acid was identified to be the likely transformation product of 8:2 FTUA under both conditions. Thus, under sulfate- and iron-reducing conditions, the hydrogenation pathway for 8:2 FTUA leading to 3-F-7:3 acid formation was preferred over the reductive defluorination pathway, which is required for the formation of 7:2 sFTOH or 7:3 U acid. This observation resonates with a recent study [214] that reported reductive defluorination of fluorinated carboxylic acids with one fluorine substitution on the unsaturated carbon (e.g., 6:2 FTUA) was much less favorable than hydrogenation by an anaerobic microbial enrichment culture (82.9% and 17.1% of 6:2 FTUA underwent hydrogenation and reductive defluorination pathways, respectively). The preference of the hydrogenation pathway under sulfate- and iron-reducing conditions observed herein could also be associated with a lack/inefficiency of relevant enzymes responsible for defluorinating 8:2 FTUA to 7:3 U acid and decarboxylating 8:2 FTUA to 7:2 sFTOH. The similar enzymatic inefficiency has been reported in aerobic and methanogenic microorganisms [53, 176].

4.2.3.3.2 Comparison of microbial communities under different redox conditions.

Microbial community analysis of the samples collected from nitrate-, sulfate-, and iron-reducing microcosms provided further insight into the effect of redox condition on the biotransformation of 8:2 FTOH. Principal coordinate analysis (PCoA), an ordination technique used to visualize microbial community alternation [215], revealed distinct clustering of microbial communities in Loring soil on day 0 compared to those at the end of ca. 400 days incubation under each redox condition (Appendix **Figure A.33**). At the end of incubation, microbial communities in the nitrate-reducing microcosms substantially separated from those in sulfate- and iron-reducing microcosms, while separation between communities from the sulfate- and iron-reducing microcosms was not apparent (Appendix **Figure A.33**). These results indicate that the distinct biotransformation of 8:2 FTOH observed under sulfate- and iron-reducing conditions from that under nitrate-reducing condition was very likely due to the different microbial community compositions. As many sulfate-reducing bacteria are capable of using sulfate and iron (III) interchangeably as electron acceptors [216, 217], the relatively close microbial community structures may explain the similar 8:2 FTOH biotransformation observed under sulfate- and iron-reducing conditions.

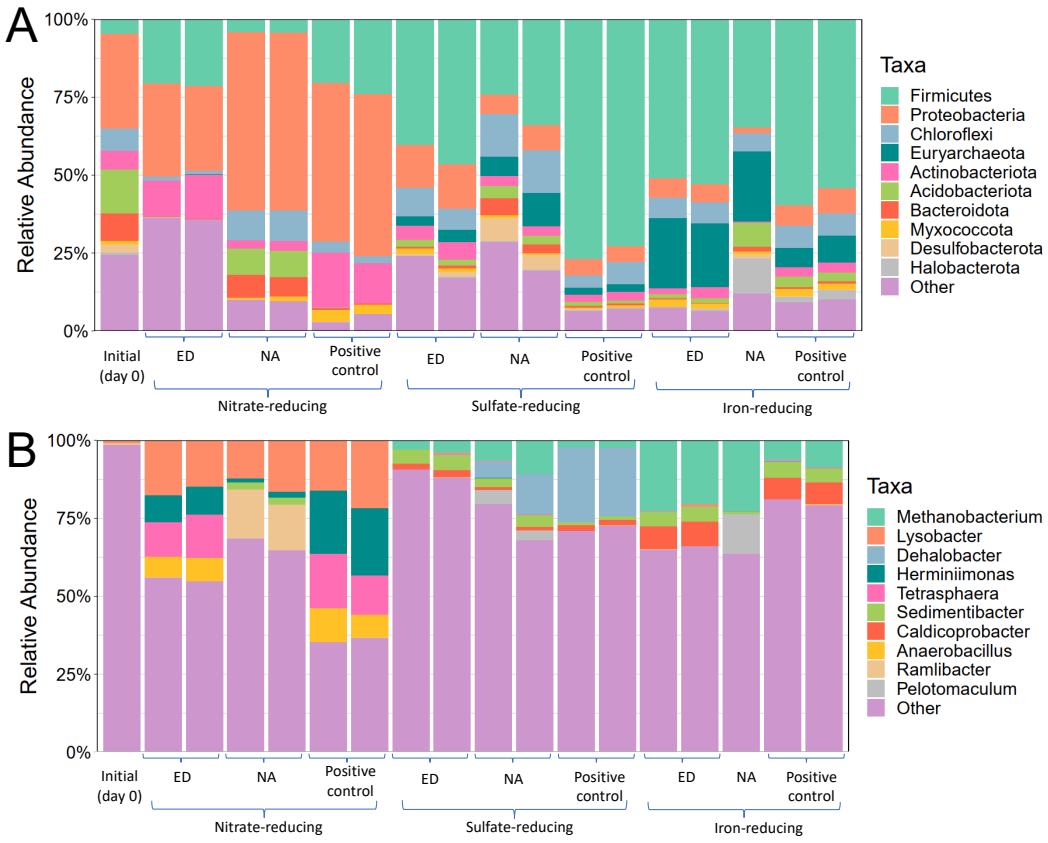


Figure 4.24 The relative abundance of microbial community composition at the phylum level (Panel A) and genus level (Panel B) in the initial Loring soil (Day 0), and in the nitrate-, sulfate-, and iron-reducing microcosms at the end of ca. 400 days incubation. Microcosms are classified as electron-donor (ED) treatment, natural attenuation (NA) treatment and positive control.

The microbial community composition in nitrate-, sulfate- and iron-reducing microcosms was further analyzed at the taxonomic level by evaluating the OTUs and making comparisons to the SILVA database [92, 93]. This additional analysis provided further support that distinctly different microbial communities were present under nitrate-reducing conditions compared to those under sulfate- and iron-reducing conditions (**Figure 4.24**). Proteobacteria was the most dominant phylum (relative abundance of 46.2 ± 12.2 %) in nitrate-reducing microcosms, whereas it only accounted for 8.8 ± 3.7 % and 5.4 ± 2.2 % in sulfate- and iron-reducing microcosms, respectively (**Figure 4.24**A). Microorganisms belonging to Proteobacteria have been reported to degrade various hydrocarbon compounds [173, 174], as well as PFAS (e.g., FTOHs) [175-178]. In this study, three genera in the Proteobacteria phylum, *Lysobacter*, *Herminiimonas*, and *Ramlibacter*, were exclusively found to be abundant in the ED and/or NA treatments under nitrate-reducing conditions (**Figure 4.24**B). Species in these genera may be responsible for the relatively rapid 8:2 FTOH biotransformation and transformation pathways observed under nitrate-reducing conditions. In sulfate- and iron-reducing microcosms, Firmicutes was the predominant phylum with relative abundances of 48.4 ± 19.1% and 51.0 ± 8.7%, respectively (**Figure 4.24**A). Firmicutes was previously found as a dominant phylum in PFAS-contaminated soils [167, 170], and are also capable of biotransformation of chlorinated solvents [218, 219]. In the present study, two genera in the Firmicutes phylum, *Caldicoprobacter* and *Sedimentibacter,* were found to be exclusively abundant at 1.6 ± 0.5% and 6.1 ± 3.0% in sulfate-reducing microcosms, respectively, and 3.0 ± 1.6% and 3.9 ± 1.7% in iron-reducing microcosms, respectively (**Figure 4.24**B). This prevalence suggests that the two genera may have contributed to the 8:2 FTOH biotransformation. However, the relevant enzymes for the transformation of 8:2 FTCA to 8:2 FTUA and further conversion of 8:2 FTUA to 7:2 sFTOH or 7:3 U acid may be absent in these genera.

Substantial differences between microbial communities under nitrate-reducing conditions and those under sulfate- and iron-reducing conditions described above likely resulted in the distinct 8:2 FTOH biotransformation (e.g., rate and pathways) observed in this study (**Figure 4.25**).

4.2.3.4 Comprehensive biotransformation pathways of 8:2 FTOH

Based on the biotransformation products detected by LC-MS/MS targeted analysis and by non-targeted HRMS under nitrate-, sulfate-, and iron-reducing conditions in this study, as well as the pathways proposed in previous studies on 8:2 FTOH biotransformation under oxic [50, 176, 220] and methanogenic conditions [53, 190], comprehensive biotransformation pathways for 8:2 FTOH were proposed under various redox conditions representative of most of natural environments (**Figure 4.25**). Although the pathways under oxic [50, 176, 220] and methanogenic conditions [53, 190] were observed in various environmental matrices (e.g., aerobic soil, activated sludge, digester sludge), which likely possessed different microbial communities from those in Loring soil (i.e., a historically AFFF-contaminated soil), they were compiled here to compare with the pathways observed in Loring soil under nitrate-, sulfate-, and iron-reducing conditions to: (1) provide the insights into the role of redox condition and/or microbial community in 8:2 FTOH

biotransformation; (2) give a holistic understanding of the 8:2 FTOH biotransformation pathways that have been observed to-date.

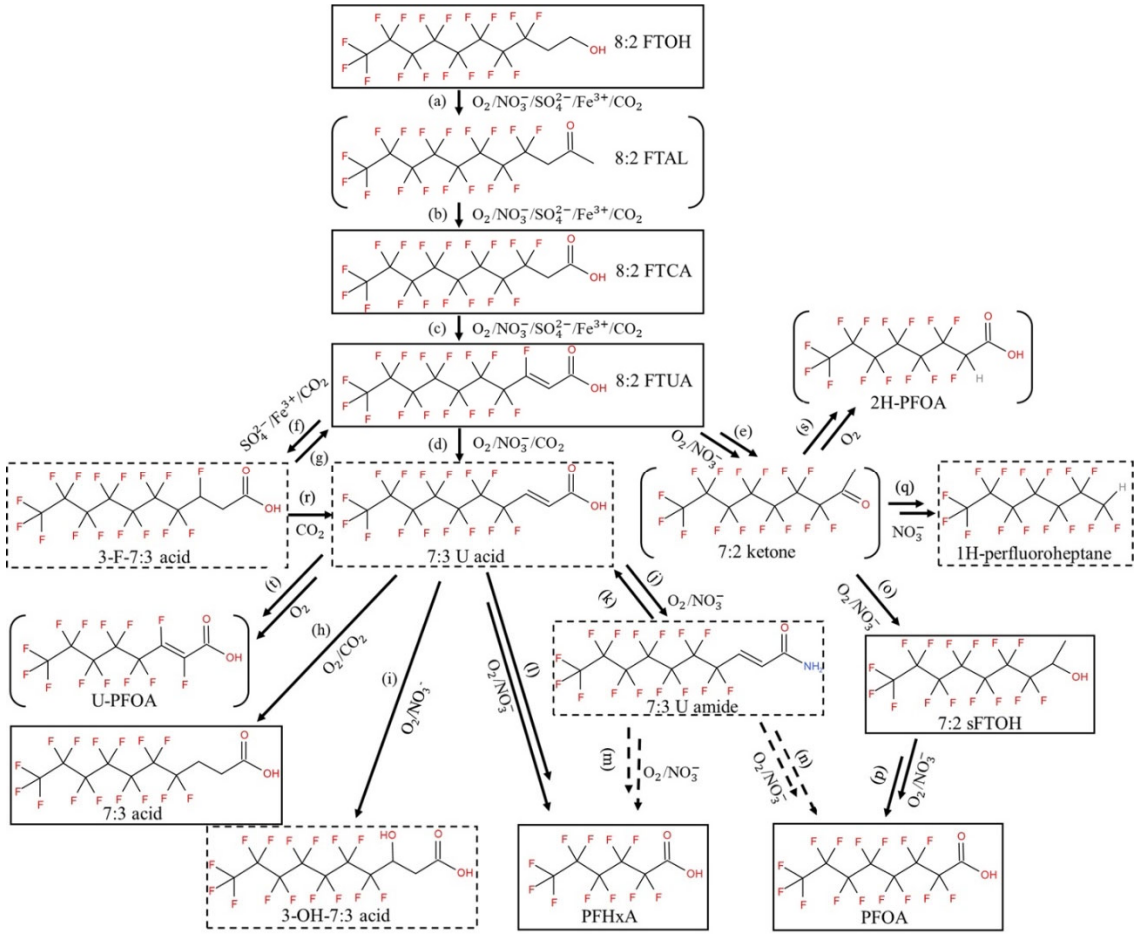


Figure 4.25 Proposed comprehensive biotransformation pathways of 8:2 FTOH under various redox conditions. O_2, NO_3^-, SO_4^{2-}, Fe^{3+}, and CO_2 represent oxic, nitrate-reducing, sulfate-reducing, iron-reducing, and methanogenic conditions, respectively. The pathways under oxic and methanogenic conditions were proposed in previous studies [50, 53, 176, 190, 220], and they were observed in various environmental matrices (e.g., aerobic soil, activated sludge, digester sludge), which likely possessed different microbial communities from those in Loring soil (i.e., a historically AFFF-contaminated soil). The compounds in the solid rectangular boxes were quantitatively analyzed by LC-MS/MS, and the compounds in the dashed rectangular boxes were identified using non-targeted HRMS in the present study. The compounds in the brackets are the aerobic biotransformation products proposed and/or detected in previous studies whereas not detected in this study. The solid arrows indicate the biotransformation steps that would be expected to occur based on the current and/or previous studies. The dashed arrows indicate the

potential reactions that may or may not occur. The double arrows indicate multiple enzymatic steps.

Under all redox conditions, 8:2 FTOH biotransformation pathways shared the first three biotransformation steps before diverging into different paths. The first step was the oxidization of 8:2 FTOH aerobically or anaerobically to 8:2 fluorotelomer aldehyde (8:2 FTAL) by an alcohol dehydrogenase as described previously (pathway "a"; refers to **Figure 4.25**) [50, 53]. Next, 8:2 FTAL was oxidized aerobically or anaerobically to 8:2 FTCA catalyzed by an aldehyde dehydrogenase (pathway "b"). Further, 8:2 FTCA was dehydrohalogenated to 8:2 FTUA with hydrogen fluoride (HF) elimination involved (pathway "c"). In the present study, 8:2 FTAL was not quantified by LC-MS/MS analysis due to the unavailability of an authentic standard and was not identified by HRMS analysis, indicating that this product was either unstable or rapidly oxidized under the tested conditions, as previously reported in 8:2 FTOH biotransformation under oxic [188, 195] and methanogenic [190] conditions.

A key branch point for further biotransformation under the various redox conditions was 8:2 FTUA, after which the pathways diverged (i.e., pathways "d", "e", and "f"). On pathway "d", 8:2 FTUA was converted to 7:3 U acid possibly via reductive defluorination, which was demonstrated for unsaturated PFAS by a commercially available microbial culture [221]. This step has been commonly reported in the studies on 8:2 FTOH biotransformation under oxic and methanogenic conditions [50, 53, 176, 186, 190, 195]; however, it was only observed in the nitrate-reducing microcosms in the present study. Although previous studies showed that 7:3 U acid could be further transformed to 7:3 acid by reductases under oxic or methanogenic conditions (pathway "h") [50, 53, 176, 190, 195], transformation to 7:3 acid was not observed in the nitrate-reducing microcosms. Instead, 7:3 U acid was likely transformed to 3-OH-7:3 acid (pathway "i") and 7:3 U amide (pathway "j") by a hydratase and a transaminase, respectively, under nitrate-reducing conditions, and the latter reaction might be reversible (pathway "k"). The conversion of 7:3 U acid to PFHxA (pathways "l"), and 7:3 U amide to PFHxA/PFOA (pathways "m" and "n") were proposed and/or demonstrated previously under oxic conditions [50, 176, 195]. The reactions may also happen under nitrate-reducing conditions, and the rate of PFHxA production might be too slow to be appreciated.

Biotransformation of 8:2 FTUA to 7:2 ketone proceeded via multiple enzymatic steps involving defluorination and decarboxylation (pathway "e") [50, 176]. Then, 7:2 ketone was converted to 7:2 sFTOH (pathway "o"), which was further transformed to PFOA through some unknown enzymatic steps (pathway "p"). The sequence of pathways "e" to "o" and "p" have been reported as a major aerobic biotransformation pathway for 8:2 FTOH in the soil [50], landfill leachate [186], and mixed bacterial cultures [176]. In this study, 7:2 ketone was not targeted in LC-MS/MS analysis due to the lack of an authentic standard, and was not detected in non-targeted analysis possibly due to its rapid conversion to downstream products. However, the substantial formations of 7:2 sFTOH and PFOA indicate that the pathways "e", "o", and "p" were likely prevailing during

the 8:2 FTOH biotransformation under nitrate-reducing conditions. Moreover, 7:2 ketone might also be metabolized via multiple enzymatic reactions to form 1H-perfluoroheptane (pathway "q"), a major intermediate product during 8:2 FTOH biotransformation under nitrate-reducing conditions, though the transformation products of 1H-perfluoroheptane are unknown at this point.

Under sulfate- and iron-reducing conditions, 8:2 FTUA was potentially converted to 3-F-7:3 acid by a reductase (pathway "f"), which could be converted back to 8:2 FTUA (pathway "g"). These reactions were proposed previously in digester sludge (i.e., under methanogenic conditions) [53], where 3-F-7:3 acid was also proposed to be transformed to 7:3 U acid via dehydrohalogenation (pathway "r"). Two other biotransformation products identified in previous aerobic biotransformation studies of 8:2 FTOH [50, 220], 2H-PFOA ($F(CF_2)_6CFHCOOH$) and unsaturated PFOA (U-PFOA, $F(CF_2)_5CF{=}CFCOOH$) through pathways "s" and "t", respectively, were not detected in non-targeted HRMS analysis under tested conditions in the present study.

4.2.3.5 Concluding remarks

This study demonstrates that the biotransformation rates and pathways of 8:2 FTOH are highly dependent upon redox conditions. Biotransformation was much slower under sulfate- and iron-reducing conditions than under nitrate-reducing conditions, while the fastest biotransformation was reported under oxic conditions. The PFCAs, which were found as the terminal products of 8:2 FTOH biotransformation under oxic conditions, were produced with less yield under nitrate-reducing conditions, and were not formed under sulfate- and iron-reducing conditions. The production of two polyfluorinated acids (i.e., 8:2 FTCA and 8:2 FTUA), however, was observed under all redox conditions investigated in this and previous studies. Biostimulation (e.g., lactate amendment) was shown to increase 8:2 FTOH biotransformation rates and product yields (e.g., PFOA) in the anaerobic microcosms tested, implying that unintended adverse consequences (e.g. PFOA production) could arise when bioremediation is applied to treat other contaminants (e.g., chlorinated solvents) at sites where PFAS are also present.

The environmental fate of some newly identified products such as 1H-perfluoroheptane and 3-F-7:3 acid is not yet understood; therefore, future research is needed to elucidate the potential biotransformation and pathways of these compounds. In addition, genera potentially responsible for 8:2 FTOH biotransformation under each redox condition were identified including *Lysobacter*, *Herminiimonas*, and *Ramlibacter* under nitrate-reducing conditions, and *Caldicoprobacter* and *Sedimentibacter* under sulfate- and iron-reducing conditions. Future studies with isolated pure cultures would help to better assess the biotransformation of 8:2 FTOH with species from these genera. Overall, these research findings provide an improved understanding of the role of microbial communities in 8:2 FTOH biotransformation rates and pathways under various redox conditions, which impact its fate in different environmental matrices.

4.2.4 Aerobic biotransformation of 6:2 FTS in Robins and Loring soil

4.2.4.1 Experimental system

Throughout the experiments, the consumption of DGBE was monitored in Loring and Robins soil bioactive microcosms (i.e., live treatments and positive controls), which were amended 4-5 times of 10 mM DGBE (Appendix **Figure A.34**). No change in DOC concentration was detected in abiotic controls (Appendix **Figure A.34**). These results indicated aeration was sufficient to support DGBE biodegradation by the aerobic microorganisms in both soils. In addition, no differences in the consumption rates of DGBE were observed between live treatments and positive controls (Appendix **Figure A.34**), suggesting that the addition of 6:2 FTS did not negatively impact substrate consumption by the native microbial community.

The background levels of 6:2 FTS and potential transformation products [45, 54] in Loring and Robins soils were determined from the day 0 positive control samples (Appendix **Table A.24**). Additional discussion on the occurrence of legacy PFAS in the two AFFF-impacted soils is provided in **Appendix A.15**. The total mass of 6:2 FTS initially spiked into live treatments and abiotic controls was approximately180-fold and 22-fold greater than the legacy 6:2 FTS in Loring and Robins soils, respectively (Appendix **Table A.25** and **Table A.26**). Such spiked amounts allowed for the identification and quantification of 6:2 FTS transformation products. As shown in **Figure 4.26**, 102.9 ± 5.5 mol% and 95.9 ± 6.6 mol% of the initially spiked 6:2 FTS remained in Loring and Robins abiotic controls, respectively, with no significant changes ($p > 0.05$) over the 224-day incubation period, indicating the integrity of the experimental system and the efficiency of extraction methods used in this study, and that 6:2 FTS was stable under abiotic experimental conditions.

4.2.4.2 Biotransformation of 6:2 FTS in Loring and Robins soil microcosms

4.2.4.2.1 Biotransformation rates.

In the live treatments of Loring soil microcosms, rapid 6:2 FTS biotransformation was observed with only 0.2 mol% of the initially spiked 6:2 FTS remaining after 154 days (**Figure 4.26**A). The half-life was determined to be 43.3 days by fitting 7 data points using a first-order kinetic model (R^2 = 0.98). Biotransformation of legacy 6:2 FTS was also observed in positive controls, where the total mass of 6:2 FTS decreased from 0.8 ± 0.2 nmol at day 0 to 0.0 ± 0.0 nmol at day 28 (Appendix **Table A.25**). In contrast, much slower 6:2 FTS biotransformation was observed in Robins soil, with 63.7 ± 6.0 mol% of initially spiked 6:2 FTS remaining in live treatments after the 224-day incubation (**Figure 4.26**B). Similarly, legacy 6:2 FTS in positive controls was biotransformed slowly, with 7.0 ± 2.0 nmol remaining at day 98 (8.3 ± 0.3 nmol at day 0, Appendix **Table A.26**). The presence of legacy 6:2 FTS biotransformation in Loring and Robins soils suggests that the lack of electron donor, carbon source or nutrients limited natural attenuation of 6:2 FTS at the field sites.

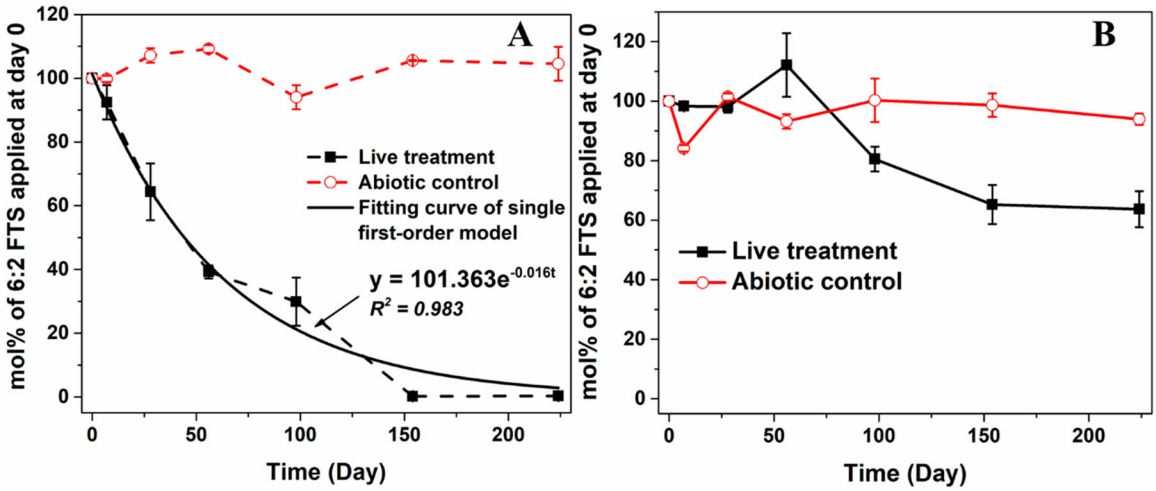


Figure 4.26 Changes in molar ratios of residual 6:2 FTS during aerobic biotransformation in Loring (Panel A) and Robins (Panel B) soil microcosms. Error bars represent the standard deviation of triplicate live treatments and duplicate abiotic controls.

4.2.4.2.2 Biotransformation products quantified by LC-MS/MS targeted analysis.

Four polyfluorinated compounds including 6:2 fluorotelomer saturated carboxylic acid (6:2 FTCA), 6:2 fluorotelomer unsaturated carboxylic acid (6:2 FTUA), 5:2 secondary fluorotelomer alcohol (5:2 sFTOH) and 5:3 acid, and four perfluorinated compounds (perfluorobutanoic acid-PFBA, PFPeA, PFHxA, and perfluoroheptanoic acid-PFHpA) were identified as biotransformation products of 6:2 FTS in Loring soil using LC-MS/MS analysis. Significant increases ($p < 0.05$) in the mass of these compounds were detected in live treatments compared to abiotic and positive controls (Appendix **Table A.25**). Formation of 6:2 FTUA and 5:2 sFTOH in positive controls confirmed the occurrence of legacy 6:2 FTS biotransformation in Loring soil (Appendix **Table A.25**). An initial intermediate of 6:2 FTS biotransformation reported previously [54], 6:2 FTOH, was below the limit of detection (LOD), suggesting that it was rapidly converted to downstream products. This finding is consistent with observations in activated sludge [45] and river sediment [54] where 6:2 FTOH was absent or detected at low levels (<2.5 mol%). Similarly, low levels of 6:2 FTCA (<0.5 mol%) were detected over the 224-day incubation likely due to its rapid biotransformation to 6:2 FTUA, which peaked at day 28 (3.7 ± 0.5 mol%) and decreased to less than 0.5 mol% by day 224 (**Figure 4.27**A). As a major intermediate product [54], 5:2 sFTOH concentrations increased throughout the incubation period, reaching a peak molar yield of 13.3 ± 5.1 mol% by day 224 (**Figure 4.27**A). Higher production rates from upstream products (e.g., 6:2 FTUA) relative to conversion to downstream products likely resulted in this accumulation of 5:2 sFTOH. The slower accumulation rate observed in the later stage of the incubation (i.e., day 56 to day 224) (**Figure 4.27**A) may be attributed to increasing conversion to downstream products (e.g., PFPeA, PFHxA, etc.). Another major transformation product of 6:2 FTS [45, 54], 5:3 acid reached its peak molar yield at 8.9 ± 1.2 mol% by day 154 then decreased to 0.2 ± 0.1 mol% at day 224

(**Figure 4.27**A). The biotransformation of 5:3 acid was reported previously in activated sludge via "one-carbon removal pathways", leading to the formation of two major products (4:3 acid and PFPeA) and two minor products (3:3 acid and PFBA) [199]. In the present study, the occurrence of a substantial decrease in 5:3 acid and increases in PFPeA and PFBA between day 154 and day 224 indicated that reactions in "one-carbon removal pathways" likely occurred in the later stage of incubation (**Figure 4.27**A). However, 4:3 acid could not be quantified due to the absence of an authentic standard, while the formation of 3:3 acid was not found to be significant ($p > 0.05$) in live treatments (Appendix **Table A.25**). Neither 4:3 acid nor 3:3 acid was identified in subsequent non-targeted PFAS analysis, suggesting that both compounds might be formed with an extremely low molar yield that cannot be distinguished from the background levels. PFBA, PFPeA, and PFHxA were the major stable transformation products in Loring soil with molar yields of 1.3 ± 0.5 mol%, 7.0 ± 2.7 mol%, and 5.3 ± 0.7 mol% by day 224, respectively (**Figure 4.27**B). Low amounts of PFHpA (0.2 ± 0.1 mol%) were also formed. The detection of PFPeA and PFHxA as the most abundant terminal products is consistent with previous studies of 6:2 FTS biotransformation in mixed microbial cultures (i.e., activated sludge [45], sediment [54], wetland slurry [222], landfill leachate [186]).

Figure 4.27 C and D show the molar yields of 6:2 FTS biotransformation products in the live treatments of Robins soil microcosms. Also, 6:2 FTUA, 6:2 FTCA, and 5:2 sFTOH were detected in positive controls but not in abiotic controls, indicating that biotransformation of legacy 6:2 FTS occurred in Robins soil (Appendix **Table A.26**). In live treatments, trace amounts of 6:2 FTOH were detected at day 98, which increased to 0.1 ± 0.0 mol% by day 154, while other transformation products were below the LODs until day 154 (**Figure 4.27** C and D). At day 224, 6:2 FTS biotransformation in Robins soil yielded 6:2 FTUA (2.1 ± 1.0 mol%), 6:2 FTCA (0.3 ± 0.2 mol%), 5:2 sFTOH (2.0 ± 0.1 mol%), 5:3 acid (2.3 ± 1.9 mol%), PFBA (0.3 ± 0.1 mol%), PFPeA (0.1 ± 0.0 mol%), and PFHxA (0.8 ± 0.7 mol%). Taken together, the total molar yield of all quantified transformation products in Robins soil by day 224 was ca. 8.0 mol%, while it was ca. 27.1 mol% in Loring soil. These results illustrate that 6:2 FTS was biotransformed in Robins soil at a much slower rate and to a lesser extent than in Loring soil.

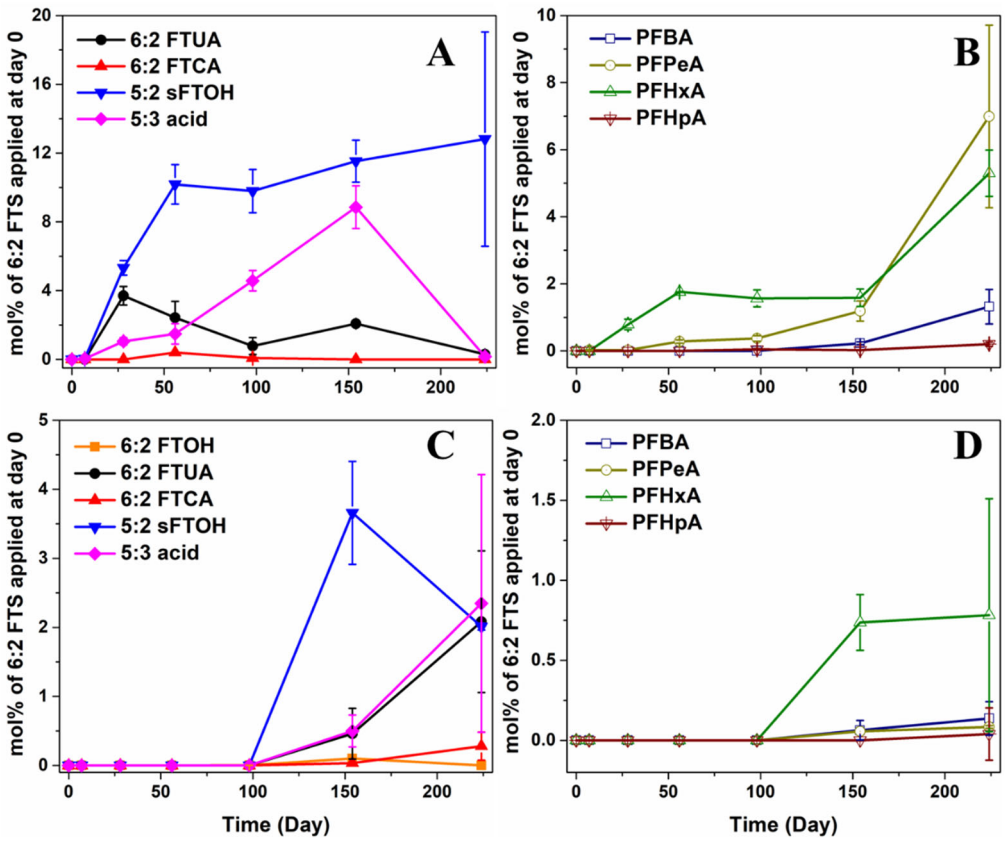


Figure 4.27 Changes in concentrations of poly- (Panels A and C) and perfluorinated (Panels B and D) biotransformation products during 6:2 FTS aerobic biotransformation in Loring (Panels A and B) and Robins (Panels C and D) soil microcosms. Error bars represent the standard deviation of triplicate live treatments. Note that different y-axis scales were used in Panels A-D.

4.2.4.2.3 Comparison of 6:2 FTS biotransformation.

To compare 6:2 FTS transformation rates and product formation in different environmental matrices and pure cultures, previous and current studies investigating aerobic biotransformation of 6:2 FTS are summarized in Appendix **Table A.27**. Unlike the biotransformation of FTOHs that has been widely investigated and reported to consistently occur in various environmental matrices [48, 50, 84, 212, 223], relatively limited data are available on 6:2 FTS biotransformation. Furthermore, conflicting results have been obtained from these studies [45, 54, 179, 222]. Rapid biotransformation of 6:2 FTS was generally achieved by pure bacterial cultures (i.e., *Gordonia* sp. strain NB4-1Y, *Rhodococcus jostii* RHA1, and *Dietzia aurantiaca* J3), with a substantial decrease (i.e., 44-100 mol%) in 6:2 FTS during short incubation periods (<10 days) [105, 106, 179, 180]. In contrast, relatively slow 6:2 FTS biotransformation was observed in various environmental matrices including activated sludge [45], wetland slurry [222], landfill leachate [186, 224], and AFFF-impacted soils (the present study), with the exception of a river sediment where a half-life of <5 days was reported [54]. 6:2 FTS biotransformation in Robins soil (63.7 mol% remaining

after 224 days) was comparable to that in activated sludge (63.7 mol% remaining after 90 days) and constructed wetlands (91.1 mol% remaining after 142 days) [45, 222], and was lower than that in landfill leachate (50 mol% remaining after 90 days; half-life = 86 days) [186, 224]. The biotransformation in Loring soil (half-life = 43.3 days), however, was approximately 2-fold faster than in landfill leachate (Appendix **Table A.27**).

In addition to biotransformation rates, large variations in 6:2 FTS transformation products and yields are observed in prior studies (Appendix **Table A.27**). The biotransformation of 6:2 FTS by pure bacterial cultures yielded minimal or negligible amounts of perfluoroalkyl carboxylic acids (PFCAs), whereas 6:2 FTS biotransformation by microbial communities in environmental media consistently resulted in PFCAs formation. Although the molar yields of PFCAs varied among the experimental systems, PFPeA and PFHxA were the most abundant (Appendix **Table A.27**), and PFBA and PFHpA were not consistently detected as 6:2 FTS biotransformation products. Small amounts of PFHpA were only detected in the studies using river sediment [54], pure strain *Rhodococcus jostii* RHA [106], and in the present study. Polyfluorinated products including 6:2 FTOH, 6:2 FTCA, 6:2 FTUA, 5:2 sFTOH, 5:2 ketone and 5:3 acid were commonly reported during 6:2 FTS biotransformation. However, the detection frequency and molar yield of each product varied across these studies (Appendix **Table A.27**). Taken together, these results suggest that 6:2 FTS biotransformation in different environments and/or by different microbial communities is likely to undergo different pathways.

4.2.4.2.4 Factors impacting 6:2 FTS biotransformation.

Sulfur Source. The presence of more easily assimilated sulfur sources (e.g., sulfate) was reported to potentially inhibit enzymatic desulfonation of 6:2 FTS, the initial step of 6:2 FTS biotransformation [175]. It was shown that rapid 6:2 FTS biotransformation was achieved by pure microbial cultures under sulfur-limiting conditions [105, 106, 179, 180], while the presence of sulfate (10 mM) suppressed the desulfonation process [106]. The sulfate present in activated sludge (0.21-0.52 mM) [45], landfill leachate (0.32 mM) [186], and wetland slurry (8 mM) [222] was also assumed by researchers to cause the observed slow 6:2 FTS biotransformation (i.e., ≥ 50 mol% remaining after more than 90 days). There was one exception where 6:2 FTS was biotransformed readily (half-life <5 days) in sediment in the presence of 0.3 mM sulfate [54]. However, all the aforementioned studies only reported the background levels (i.e., initial concentration) of sulfate in the environmental media, and did not track the sulfate throughout the experiments. In the present study, sulfate concentrations in Loring and Robins soil microcosms were monitored throughout incubation (Appendix **Figure A.35**). The background levels of sulfate in both soils (<0.12 mM at day 0) were lower than those in previous environmental media studies [45, 54, 186, 222]. The initial concentration was 3 to 5 times higher in Robins soil than Loring soil (0.10 ± 0.00 mM and 0.02 ± 0.01 mM, respectively). Sulfate in bioactive Loring soil microcosms was rapidly and completely consumed by day 7, whereas sulfate was not nearly depleted (<0.01 mM) until day 98 in Robins soil (Appendix **Figure A.35**). The time point of the initiation of 6:2 FTS biotransformation (e.g., formation of biotransformation products) appeared to coincide with the

time point of sulfate depletion in both microcosms (**Figure 4.26** and **Figure 4.27**, and Appendix **Figure A.35**; day 7 and day 98 for Loring and Robins microcosms, respectively), indicating that 6:2 FTS biotransformation was favored by the microbial consortium in both soils once sulfur sources were depleted. Therefore, differences in the initial sulfate concentrations and depletion over the incubation period was likely a critical factor resulting in the distinct 6:2 FTS biotransformation behaviors observed between Loring and Robins soil microcosms. Likewise, the rapid 6:2 FTS biotransformation observed in river sediment even in the presence of 0.3 mM sulfate could be explained by rapid sulfate assimilation by the native microbes [54]. These findings suggest that the availability of alternate sulfur sources in the environment may inhibit the desulfonation of 6:2 FTS, and could be a limiting step for 6:2 FTS biotransformation.

Microbial community. The diversity and richness of Loring and Robins soil microbial community was investigated, and differences between the two soils were expressed using the Shannon and Simpson, and Chao1 indices, respectively (Appendix **Table A.28**). Principle coordinate analysis (PCoA) also revealed the distinct differences between the two soil microbial communities (Appendix **Figure A.36**). However, a significant impact of spiked 6:2 FTS and its biotransformation products on the diversity and richness of the two soil microbial communities was not observed ($p > 0.05$, Appendix **Table A.28**). Detailed results and discussion on diversity and richness are described in **Appendix A.16**.

The microbial community composition in Loring and Robins soils was further analyzed on various taxonomic levels. A total of 36 classified phyla in the domain Bacteria and 5 phyla in the domain Archaea were shared. Appendix **Figure A.37** shows Proteobacteria was the most dominant phylum in Loring and Robins soils (relative abundance >35%). These results corroborate previous studies that identified Proteobacteria as the predominant phylum in surface soils and river sediments that were heavily contaminated by PFAS [168-170]. Additionally, prior studies have observed an obvious increase (12.5-65.7%) in Proteobacteria in wetland slurry and fresh water following exposure to PFAS [172, 222]. These results suggest that Proteobacteria is likely more tolerant of PFAS than other phyla. In this study, two classes of Proteobacteria, Alpha- and Gamma-proteobacteria, were observed in Loring and Robins soils; these microorganisms have been reported to degrade various hydrocarbon compounds [173, 174], as well as PFAS (e.g., FTOHs, 6:2 FTS) [175-178]. Another phylum, Actinobacteriota was also observed in all of Loring and Robins soil samples (Appendix **Figure A.37**). Some genera from Actinobacteriota are known as PFAS degraders; for example, *Mycobacterium* is known to degrade 6:2 FTOH [177], and *Gordonia*, *Rhodococcus*, and *Dietzia* have been shown to transform 6:2 FTS [105, 106, 179, 180]. In the current study, *Rhodococcus* was present in Loring and Robins soils (Appendix **Figure A.38**). Taken together with prior work, *Rhodococcus* and/or other strains belonging to the Proteobacteria and Actinobacteriota likely played a role in the 6:2 FTS biotransformation observed in this study.

Desulfobacterota was present in Loring soil at a relative abundance of 1.7-6.5% whereas it was absent in Robins soil (Appendix **Figure A.37**). Many genera in Desulfobacterota have been

reported to desulfonate the organosulfonates [225]. Since the desulfonation is a critical and often a rate-limiting step in 6:2 FTS biotransformation [45, 186], the distinct difference in the abundance of Desulfobacterota could have contributed to the observed differences in biotransformation rates of 6:2 FTS in Loring and Robins soils. In addition, higher abundances of Bacteroidota (12.7 ± 3.4% vs. 0.9 ± 1.3%), Zixibacteria (3.0 ± 2.5% vs. 0%), Cyanobacteria (2.1 ± 1.5% vs. 0%), Patescibacteria (1.6 ± 0.8% vs. 0%), as well as Archaea (1.2 ± 0.5% vs. 0%), in Loring soil than Robins soil may partially account for the observed differences in 6:2 FTS biotransformation (Appendix **Figure A.37**). Bacteroidota and Archaea were shown to be associated with diesel- and PFAS-contaminated soils [166, 174, 181]. Cyanobacteria species were reported to degrade aromatic hydrocarbons and xenobiotics using various enzymes [182]. Patescibacteria was widely detected at sites with organic and metal pollutants [226], and was linked to the remediation of aromatic hydrocarbons and heavy metals [227]. Zixibacteria was recently proposed as a new bacterial phylum, and the representative organism in the phylum was reported to be metabolically versatile [228].

The impacts of 6:2 FTS and its biotransformation products on microbial community composition were also investigated by comparing the day 224 samples from live treatments (~1,700 μg/L 6:2 FTS spiked) and from positive controls (0 μg/L 6:2 FTS spiked). At the phylum level, the increase in Myxococcota and Firmicutes were found in both Loring AFB and Robins AFB soil after being exposed to 6:2 FTS (Appendix **Figure A.37**). More discussion about the findings on phylum level is described in **Appendix A.17**. At the genus level, a total of 320 genera were shared, and the Welch t-test with Benjamini-Hochberg false discovery rate (FDR) for multiple test corrections was applied to compare the relative abundance of each genus in live treatments and positive controls. It was found that *Sphingomonas* was the only genus that increased significantly (adjusted $p < 0.05$) in live treatments compared to positive controls in both Loring and Robins soil microcosms. In Loring soil, the relative abundance of *Sphingomonas* was 0.3 ± 0.0% in live treatments compared to positive controls (0.2 ± 0.0%); in Robins soil, the relative abundance was 12.0 ± 3.8% in live treatments compared to positive controls (5.7 ± 1.1%) (Appendix **Figure A.38**). These results suggest that the genus of *Sphingomonas* likely has higher tolerance to the elevated concentrations of 6:2 FTS and its biotransformation products. Moreover, some species in *Sphingomonas* might play a role in 6:2 FTS biotransformation. Species in *Sphingomonas* are present in various natural environments, and widely known to degrade many kinds of environmental pollutants (e.g., polycyclic aromatic hydrocarbons, chlorinated pesticides) [201, 208, 229-231]. Recent studies reported that the relative abundance of *Sphingomonas* increased under PFAS-spiked (e.g., PFOS, 6:2 FTS) conditions [167, 222].

4.2.4.3 Identification of novel biotransformation products by LC-HRMS analysis

In the live treatments of Loring and Robins soil microcosms, total mass recovery of 6:2 FTS and transformation products generally decreased with incubation time. For Loring soil, mass recovery decreased from 92.5 ± 5.4 mol% at day 7 to 55.8 ± 4.8 mol% at day 56, then further to 25.7 ± 3.2

mol% at day 154), and for Robins soil, recovery decreased from 98.3 ± 1.1 mol% at day 7 to 71.1 ± 8.1 mol% at day 154 (Appendix **Figure A.39**). However, a similar decrease was not observed in the abiotic controls (Appendix **Figure A.39**). The relatively lower mass recovery observed in live treatments of Loring soil compared with Robins soil can be attributed to the increased extent of 6:2 FTS biotransformation and the associated formation of unknown transformation products. By performing non-targeted LC-HRMS analysis, seven additional compounds were identified as potential biotransformation products of 6:2 FTS (Appendix **Table A.29**). The abundances of these seven products (based on peak areas of extracted ion chromatograms) were substantially higher (> 6-fold) in live treatments than the abiotic and positive controls of Loring and Robins soil microcosms during 6:2 FTS biotransformation (Appendix **Figure A.40**, **Figure A.41**, and **Figure A.42**).

As a novel transformation product, 1H-perfluoropentane (C_5HF_{11}, *m/z* 268.98271) was identified at a highest confidence level 1 (confirmed structure, assigned based on the Schymanski Scale [89]). Fragmentation analysis on the MS^2 spectrum (Appendix **Figure A.43**) demonstrated the presence of its characteristic moieties, including the deprotonated molecule ion (*m/z* 268.9861) and related ions (e.g., C_2F_5, *m/z* 118.9926). The identification was further confirmed by comparison to the chemical standard (Appendix **Figure A.43**). Another 1H-perfluoroalkane with a shorter carbon chain, 1H-perfluorobutane (C_4HF_9, *m/z* 218.98587) was also identified at confidence level 1 by comparison of the MS^2 spectra and fragmentations from microcosm samples and the reference standard (Appendix **Figure A.44**). In addition, ions at *m/z* 216.98912 and 236.99543 were identified as 1,2,2,3,3,4,4,4-octafluorobutan-1-ol ($C_4H_2F_8O$) at confidence level 2 (probable structure) and $C_7H_2F_8$ (structure shown in Appendix **Figure A.45**) at confidence level 3 (tentative candidate) based on the MS^2 spectra and fragmentation analysis (Appendix **Figure A.45**). Chemical standards were not commercially available to allow for further structure confirmation.

4.2.4.4 Biotransformation pathways of 6:2 FTS in AFFF-impacted soil

The proposed biotransformation pathways of 6:2 FTS in Loring and Robins soils, based on the transformation products detected by targeted LC-MS/MS (**Figure 4.27**) and non-targeted LC-HRMS analyses (Appendix **Table A.29**) are presented in **Figure 4.28**. The detection of products in LC-MS/MS analysis such as 5:2 sFTOH, 5:3 acid, and PFCAs indicated that pathways reported previously in activated sludge [45], river sediment [54], and landfill leachate [186], also occurred during 6:2 FTS biotransformation by native microbial communities in AFFF-impacted soils. The biotransformation initiated by the microbial desulfonation of 6:2 FTS catalyzed by monooxygenases [106, 180], resulted in the formation of 6:2 FTOH. Then, 6:2 FTOH was oxidized to 6:2 fluorotelomer aldehyde (6:2 FTAL) by an alcohol dehydrogenase, which was further oxidized to 6:2 FTCA catalyzed by an aldehyde dehydrogenase. Through a dehydrohalogenation reaction, 6:2 FTCA was converted to 6:2 FTUA involving elimination of a hydrogen fluoride (HF). Similar to those previously reported [48, 106, 189], the biotransformation of 6:2 FTOH to 6:2 FTAL, to 6:2 FTCA, and then to 6:2 FTUA was likely a rapid process, so that accumulation of 6:2

FTCA (<0.5 mol%) was minimal (**Figure 4.28**). The low level of PFHpA formation (**Figure 4.28**, Appendix **Table A.25** and **Table A.26**) observed in this study suggests that α-oxidation of 6:2 FTCA might be a minor pathway during 6:2 FTS biotransformation. Although microbial α-oxidation of fluorotelomer compounds (e.g., 6:2 FTOH, 8:2 FTOH) was not previously observed in studies conducted with bacterial culture, activated sludge or soil [45, 48, 50, 187, 189], the detection of PFHpA in recent 6:2 FTS and 6:2 polyfluoroalkyl phosphates (PAPs) biotransformation studies supports the possibility that microbial α-oxidation of 6:2 FTS to PFHpA occurred [44, 54, 106].

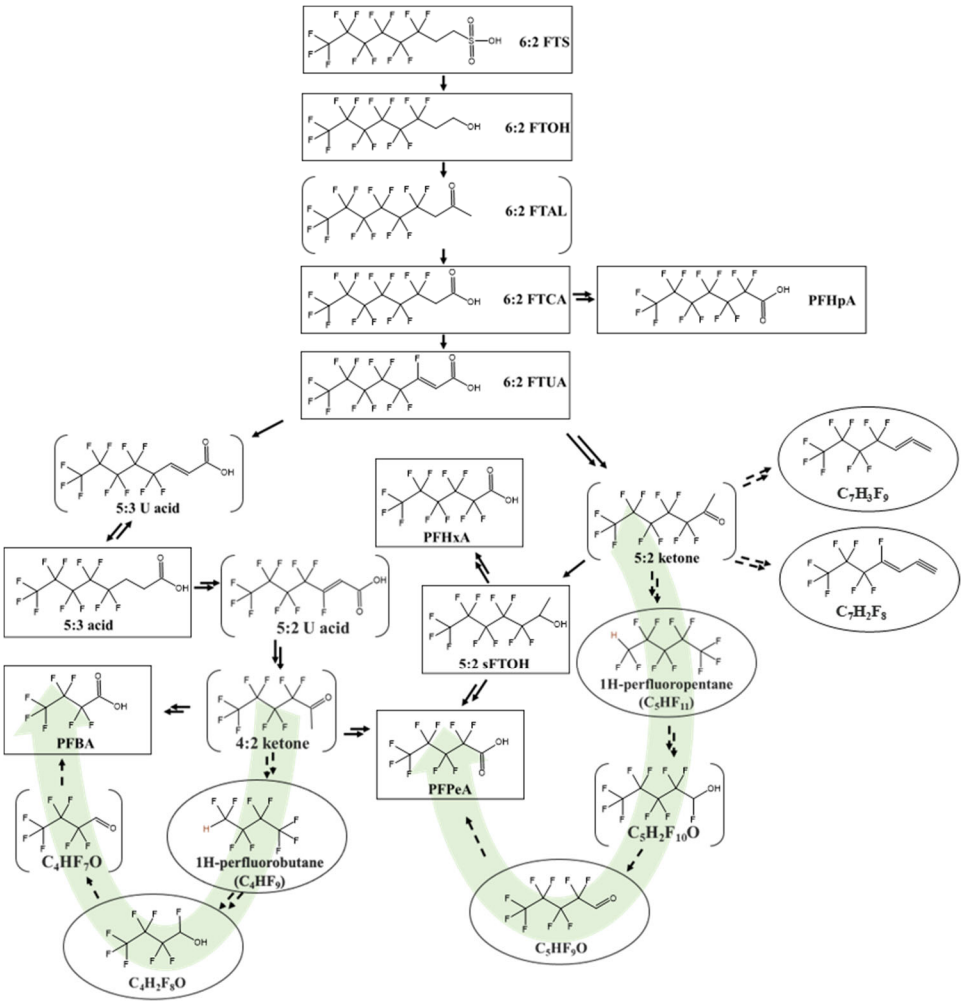


Figure 4.28 Proposed aerobic biotransformation pathways of 6:2 FTS in AFFF-impacted soils. The compounds in the rectangular boxes were detected by LC-MS/MS analysis, and the compounds in the oval boxes were identified using non-targeted LC-HRMS analysis. The compounds in the brackets are proposed transformation products and were not detected in this study. The solid arrows represent the biotransformation steps expected to occur based on the present and previous studies [45, 54, 179]. The dashed arrows represent the proposed reactions that may occur. The double arrows represent multiple enzymatic steps involved. The two large,

curved arrows in green illustrate the novel "fluorotelomer ketone to PFCA" pathway proposed in this study which elucidate the formation process of PFCAs.

A key branching point for further biotransformation was 6:2 FTUA, after which the pathways diverged. Through multiple enzymatic steps (e.g., defluorination and decarboxylation) [45, 179], 6:2 FTUA can be metabolized to 5:2 ketone. Then, the ketone was converted to 5:2 sFTOH, which is the precursor to PFPeA and PFHxA via multiple unknown reactions involving the removal of fluorine and carbon atoms [45, 48]. The other transformation pathway for 6:2 FTUA leads to the formation of 5:3 U acid possibly via reductive defluorination [48, 177, 186]. Very recently, Yu et al., demonstrated the microbial reductive defluorination of unsaturated PFAS by a mixed microbial culture [221]. Further, 5:3 U acid was converted to 5:3 acid through a reduction step facilitated by nicotinamide-adenine dinucleotide phosphate (NADPH), and 5:3 acid could then enter into the "one-carbon removal pathways", leading to the formation of 5:2 U acid and 4:2 ketone, which are the precursors to PFBA and PFPeA [180, 186, 199].

Although PFCAs have been widely reported as the terminal biotransformation products of fluorotelomer precursors, the specific formation steps have not been elucidated [45, 50, 186, 187]. Based on the transformation products detected using non-targeted LC-HRMS analysis (Appendix **Table A.29**), and the associated abundances over time during 6:2 FTS biotransformation (Appendix **Figure A.40**, **Figure A.41**, and **Figure A.42**), a novel "fluorotelomer ketone to PFCA" pathway is proposed (**Figure 4.28**). It is hypothesized that the fluorotelomer ketones (i.e., 5:2 ketone and 4:2 ketone) are converted to 1H-perfluoroalkanes (i.e., 1H-perfluoropentane and 1H-perfluorobutane) through multiple enzymatic steps. The structures of both 1H-perfluoroalkanes were confirmed (confidence level 1), and both compounds were formed at a substantially high abundance in the live treatments based on the greater than 6-fold change in peak areas (Appendix **Figure A.40**). The 1H-perfluoroalkanes are then biotransformed to alcohols (i.e., $C_4H_2F_8O$ and $C_5H_2F_{10}O$) with a fluoride atom replaced by a hydroxyl group (**Figure 4.28**). The probable structure of 1,2,2,3,3,4,4,4-octafluorobutan-1-ol (confidence level 2) was identified for $C_4H_2F_8O$ in this study. In addition, this compound was confirmed as an intermediate transformation product, based on a 48-fold increase in the peak area at week 14 (relative to day 0) that was followed by a decrease in the abundance at week 32 in Loring soil live treatments (Appendix **Figure A.41**). Subsequently, the two alcohols (i.e., $C_4H_2F_8O$ and $C_5H_2F_{10}O$) are oxidized by an alcohol dehydrogenase to the corresponding aldehydes (i.e., C_4HF_7O and C_5HF_9O), respectively. With relatively low abundances (peak areas < 3.0E+4) detected (Appendix **Figure A.41**), the C_4HF_7O and C_5HF_9O aldehydes are transient intermediates that are rapidly oxidized by an aldehyde dehydrogenase to PFBA and PFPeA, respectively. Three other products identified in LC-HRMS analysis, $C_7H_2F_8$, $C_7H_3F_9$, and ion at *m/z* 292.98316, are suspected to be formed from 5:2 ketone through unknown reduction reactions (**Figure 4.28**). Based on peak area trends over the incubation, these compounds are further biotransformed to additional downstream products that are not known at this point (Appendix **Figure A.42**).

4.2.4.5 Concluding remarks

This study demonstrates that the biotransformation of 6:2 FTS in AFFF-impacted soils is strongly influenced by environmental factors, such as the availability of sulfur sources and native microbial community composition. The biotransformation of 6:2 FTS was favored by the microbial consortia only after other easily assimilated sulfur sources (e.g., sulfate) were depleted. Desulfobacterota microorganisms likely promoted 6:2 FTS biotransformation via more efficient desulfonation. Species in the genus *Sphingomonas,* which exhibited higher tolerance to the elevated concentrations of 6:2 FTS and its biotransformation products, are likely to have contributed to 6:2 FTS biotransformation. These results suggest that evaluations of site geochemical and biological attributes are critical in achieving a better understanding of 6:2 FTS transformation in the field, as well as gaining insights into the management and remediation of AFFF-impacted sites.

By identifying additional 6:2 FTS transformation products that were previously undocumented, a novel "fluorotelomer ketone to PFCA" pathway was proposed to account for the formation of PFCAs from fluorotelomer precursors. Additional studies should address novel compounds such as 1H-perfluoroalkanes (e.g., 1H-perfluoropentane and 1H-perfluorobutane), since the analogues (i.e., 1H-perfluorohexane and 1H-perfluoroheptane) to these compounds were also identified in this work examining biotransformation of a C_8-fluorotelomer precursor. These 1H-perfluoroalkanes are likely unique transformation products that could be present at sites contaminated by fluorotelomer precursors. Future research is needed to assess the prevalence of these compounds at AFFF-impacted sites and to evaluate their potential impacts on ecosystems and human health.

4.2.5 Aerobic biotransformation of PFAS mixtures in AFFF formulation

4.2.5.1 PFAS identified by LC-HRMS in AFFF-amended microcosms

A total of 16 classes of PFAS were identified and semi-quantified throughout the 308-day microcosm experiment, using the non-targeted LC-HRMS analysis. The full name and corresponding acronym of each PFAS class is provided in Appendix **Table A.30**. The acronym was adopted from recent publications [232, 233], and an explanation of the naming conventions was provided by Choi et al. [234]. Further, detailed information on the PFAS identification in LC-HRMS analysis (e.g., mass error, retention time, confidence level [235]) is provided in Appendix **Table A.31**.

Figure 4.29 illustrates the chemical structures of the 16 PFAS classes, all identified homologues within each class, and the general trend of peak area which represents the mass change of each PFAS over the microcosm incubation. Among the 16 PFAS classes, 10 of them were categorized as AFFF components, and 8 other classes were categorized as transformation products (**Figure 4.29**). Two classes, PFCAs and PFSAs, were categorized as both AFFF components and transformation products (**Figure 4.29**). The homologues in each class were semi-quantified by

nontargeted LC-HRMS analysis and the complete profiles of peak area during the 308-day incubation were plotted in Appendix **Figure A.46** to **Figure A.60**. The LFCs in the peak area were also calculated and shown in **Figure 4.30** and Appendix **Table A.32**.

Thirteen individual PFAS whose analytical standards are commercially available, including AmPr-FHxSA, FHxSA, FOSA, and some PFCAs and PFSAs, were also quantified by targeted LC-MS analysis. The changes in total mass of these compounds over 308-day period are shown in Appendix **Figure A.61** and **Figure A.62**, which are accorded with the semi-quantification results by non-targeted LC-HRMS analysis (i.e., trends of peak area, see Appendix **Figure A.47**, **Figure A.53**, **Figure A.54** and **Figure A.55**), confirming that the semi-quantification in the present study could well represent the temporal changes of identified PFAS classes.

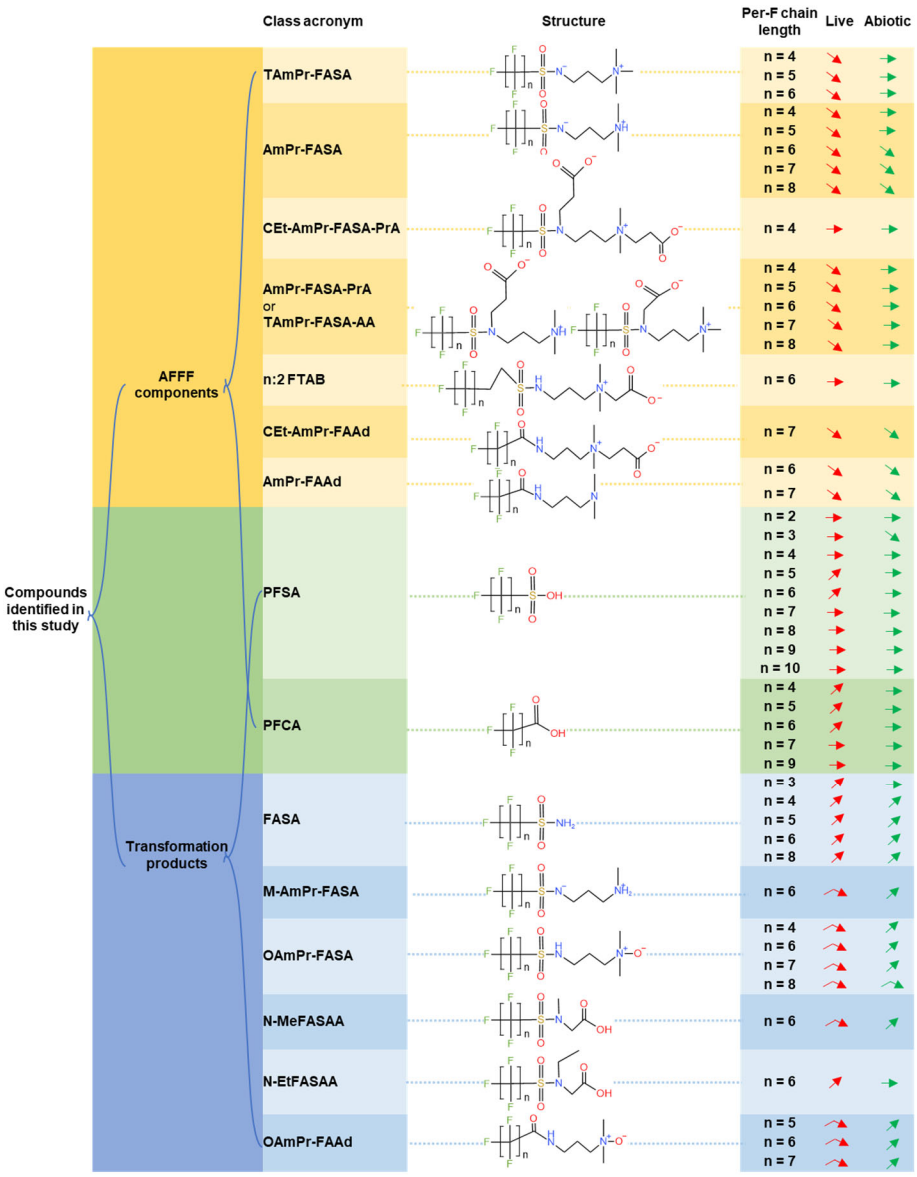


Figure 4.29 Sixteen classes of PFAS identified by LC-HRMS in AFFF-amended microcosms, including 10 classes categorized as AFFF components (shaded in yellow), 8classes categorized as transformation products (shaded in blue), and 2 classes as both AFFF components and transformation products (shaded in green). The chemical structures of the PFAS classes, and general trends of peak area in live treatment and abiotic control over the 308-day incubation of each homologue within each class were also illustrated.

4.2.5.1.1 PFAS identified as AFFF components and associated transformation potential

TAmPr-FASA. This PFAS class is characteristics of perfluoroalkyl sulfonamide base structure with propyl trimethylammonium (**Figure 4.29**). Homologues with C_4-C_6 perfluoroalkyl chain were detected in ESI+ in this study. Recent studies also reported the occurrence of this class in

both historical AFFFs [236] and AFFF-impacted soils [232, 233]. In the present study, peak areas of C_4-C_6 homologues within TAmPr-FASA class gradually decreased by >99.5%, 60.1%, and 31.0% in average in live treatments during the 308-day incubation (Appendix **Figure A.46**). In contrast, peak areas of these homologues stayed relatively constant in abiotic controls. These results suggest that TAmPr-FASA could be biotransformed by the native microbes in Loring soil but were stable under abiotic condition. The observed susceptibility of TAmPr-FASA to biotransformation corroborate the previous study that reported the soil biotransformation of C_8 homologue of TAmPr-FASA [237].

AmPr-FASA. This class (C_4-C_8 homologues identified in both ESI+ and ESI- modes) shares the same base structure with TAmPr-FASA with one methyl group in trimethylammonium replaced by hydrogen (**Figure 4.29**). Multiple homologues in AmPr-FASA class were previously identified in several AFFF formulations [238], while they were only sporadically detected in AFFF-impacted soils and groundwater [4, 232, 233]. The infrequent detection of AmPr-FASA in AFFF-impacted sites was likely attributed to the associated transformation potential [8]. In this study, biotic transformation of C_4-C_8 AmPr-FASA homologues were observed; in the live treatment, the peak areas of C_4-C_8 homologues decreased by 47.4-93.6% after 308 days (Appendix **Figure A.47**). Possible abiotic transformation of was also observed, but only for the long-chain C_6-C_8 homologues and with a slower rate (10.6-53.7% decrease in peak areas) in abiotic controls (Appendix **Figure A.47**).

CEt-AmPr-FASA-PrA. This class (C_4 homologue identified in ESI+ mode) comprises the base structure of TAmPr-FASA and two additional propionate groups on the tertiary sulfonamide nitrogen and the quaternary ammonium terminal (**Figure 4.29**). Homologues in this class were previously detected in various AFFF formulations [6, 154, 238], whereas the environmental stability of this class has not yet been investigated. In the present study, no obvious decrease in peak areas of CEt-AmPr-FASA-PrA (C_4 homologue) was observed during 308-day incubation (Appendix **Figure A.48**), suggesting it was stable under abiotic and biotic conditions on the timescale of this study.

AmPr-FASA-PrA *or* ***TAmPr-FASA-AA***. AmPr-FASA-PrA features a propionate group linked to the sulfonamide nitrogen in AmPr-FASA, while TAmPr-FASA-AA contains an acetate branch on the sulfonamide nitrogen in TAmPr-FASA (**Figure 4.29**). LC-HRMS analysis suggested possible presence of either or both isomeric classes with C_4-C_8 homologues in this study, and available evidence obtained cannot readily distinguish between them. Previous studies reported the occurrence of AmPr-FASA-PrA homologues in AFFF formulations [4, 154, 238], and AFFF-impacted sites [4, 232, 233]. TAmPr-FASA-AA class has not yet been reported in the AFFF formulation or environmental samples. Furthermore, the environmental stability of either class has not been studied. In this study, the peak areas of C_4-C_8 homologues within AmPr-FASA-PrA or TAmPr-FASA-AA class decreased by 43.3-84.6% in the live treatments after 308-day incubation (Appendix **Figure A.49**). In contrast, such decreases were not observed in the abiotic controls

(Appendix **Figure A.49**). These results suggested that either (or both) PFAS class was readily susceptible to biotic transformation but was abiotically stable under present conditions.

n:2 FTAB. The identification of this FT-based PFAS class (**Figure 4.29**) was unexpected, given the 3M AFFF formulation used in this study should contain only ECF-based precursors based on previous studies [4, 154, 236, 238]. The occurrence of n:2 FTAB in the present AFFF formulation was likely due to the cross-contamination during the historical storage. Although the biotransformation of 6:2 FTAB was previously reported with variations in the rate [179, 239, 240], in this study, no decrease in the peak areas of 6:2 FTAB was observed in the live treatments or abiotic controls (Appendix **Figure A.50**). The results indicated the high stability of 6:2 FTAB in the present soil microcosms.

AmPr-FAAd. This PFAS class (C_6-C_7 homologues identified in ESI+ mode) is a group of analogues to AmPr-FASA with the sulfonamide group replaced by a carboxamide group (**Figure 4.29**). Previously, AmPr-FAAd class was detected in some AFFF formulations and a commercial surfactant [238]. In the present study, a rapid abiotic transformation of AmPr-FAAd was observed in the microcosms, with the peak areas of C_6 and C_7 homologues decreasing by 81.9-82.3% in the abiotic control after 308-day incubation (Appendix **Figure A.51**). The biotransformation of AmPr-FAAd was also found, as greater decreases (90.2-91.3%) in the peak areas of C_6 and C_7 homologues were observed in the live treatment (Appendix **Figure A.51**). These findings are consistent with results in previous studies that the C_8 homologue of AmPr-FAAd could be transformed through abiotic and biotic processes [163, 237, 241]. Taken together, the AmPr-FAAd class was likely not persistent in the environment, and readily transformed after the release.

CEt-AmPr-FAAd. This class (C_7 homologue identified in ESI+ mode) has the same base structure of AmPr-FAAd and an additional carboxylethyl branch on the tertiary amine to make it a quaternary ammonium (**Figure 4.29**). Neither the occurrence in AFFF formulations nor the biotransformation potential of CEt-AmPr-FAAd has been reported previously. In this study, gradual decreases (45.2 ± 7.6 %) in the peak areas of CEt-AmPr-FAAd were observed in both live treatment and abiotic control during the 308-day incubation (Appendix **Figure A.52**). Also, the peak areas decreased similarly in live treatment and abiotic control, suggesting that CEt-AmPr-FAAd could be transformed abiotically in the microcosms, while the associated biotransformation might be minimal.

PFCA *and* ***PFSA***. These two commonly investigated PFAS classes were also identified in the present AFFF formulation, with C_4-C_7 and C_9 homologues within PFCAs and C_2-C_{10} homologues within PFSAs detected in ESI- mode (**Figure 4.29**). The detection of PFCAs and PFSAs were in agreement with previous studies that reported PFCAs (e.g., 0-170 mg/L for C_4-C_9 PFCAs) and PFSAs (e.g., 6,700-15,000 mg/L for PFOS) as minor and major PFAS components of ECF-based AFFF formulations, respectively [4]. The environmental persistence of PFCAs and PFSAs has been widely acknowledged [8, 242]. Due to their high persistence, PFCAs and PFSAs were widely detected in AFFF-impacted soils and groundwater [4, 154]. In this study, no decrease in the peak

areas of any homologue within PFCAs and PFSAs was observed (Appendix **Figure A.53** and **Figure A.54**), indicating their high stability in the microcosms. In addition, the increases in the peak areas of certain homologues (e.g., PFHxS) were observed (Appendix **Figure A.53**), likely due to the formations during the transformation of aforementioned precursors (discussed in **Section 3.3.5.1.2**).

4.2.5.1.2 PFAS identified as transformation products and associated potential of further transformation

FASA. FASA class (C_3-C_6 and C_8 homologues detected in ESI- mode) was identified as biotransformation products in the microcosms (**Figure 4.29**). As shown in Appendix **Figure A.55**, the peak areas of FASAs increased by a factor of 5.8-410.8 in live treatments over 308 days. The abiotic formation of FASAs was also observed, with the peak areas of C_4-C_6 and C_8 homologues increasing in the abiotic control, but by a smaller factor of 1.4-5.0 (Appendix **Figure A.55**). These results indicated that FASA homologues were substantially formed during the transformation of precursors in the AFFF formulation spiked in the microcosms, especially through the biotic process. The findings could explain why FASAs have been widely detected in AFFF-impacted soil and groundwater samples, though FASAs were not ingredients of AFFF formulations [8, 232, 236]. Previous studies also reported the biotransformation potential of FASAs to PFSAs (C_8 homologue, FOSA to PFOS), with a wide range in the biotransformation rate (half-lives of 9.2-712 days) [56, 157, 159, 160]. In the present study, a further biotransformation of FASAs likely also occurred, as suggested by a slower increase in the peak areas of FASAs after between day 98 and day 154 (Appendix **Figure A.55**). Regardless, the overall formation rate was much higher than the transformation rate of FASAs, resulting in a substantial accumulation over the incubation period.

M-AmPr-FASA. This class (C_6 homologue identified in ESI+ and ESI- modes) shares the same base structure of AmPr-FASA with one methyl terminus substituted by a hydrogen atom (**Figure 4.29**). The peak areas of C_6 M-AmPr-FASA increased substantially in the first 98 days incubation (by a factor of 82.1 and 34.5 in ESI+ and ESI- modes, respectively), and decreased afterwards in the live treatments (Appendix **Figure A.56**). In the abiotic controls, the peak areas kept increasing over 308 days (by a factor of 10.3-18.2), indicating that the formation of M-AmPr-FASA was much slower by abiotic process than biotic process. The formation of M-AmPr-FASA was likely from the transformation of TAmPr-FASA and AmPr-FASA, the two PFAS classes that were previously reported to be potential precursors to M-AmPr-FASA [163, 237, 241], and were also detected in the present study (see **Section 3.3.5.1.1**). Further biotransformation of M-AmPr-FASA was also reported previously [163, 237, 241], which was consistent with the decreasing trends observed in the live treatments after day 98 in this study (Appendix **Figure A.56**). In addition, only C_6 homologue of M-AmPr-FASA was detected in the present microcosms despite the detections of C_4-C_6 TAmPr-FASA and C_4-C_8 AmPr-FASA (see **Section 3.3.5.1.1**). The absence of other homologues in M-AmPr-FASA was likely due to the rapid conversion to downstream products [163, 237, 241].

OAmPr-FASA. This class (C_4 and C_6-C_8 homologues identified in ESI+ and ESI- modes) shares the same base structure of TAmPr-FASA where trimethylammonium was replaced by a dimethylamine oxide (**Figure 4.29**). Previously, C_6-C_9 homologues of OAmPr-FASA were detected in AFFF formulations [238], and C_4-C_6 homologues were detected in AFFF-impacted groundwater and soil samples [232, 236]. In the present study, OAmPr-FASA was determined as intermediate transformation products rather than AFFF components (Appendix **Figure A.57**). The peak areas of C_4 and C_6 homologues in the live treatments continuously increased from day 0 to day 98 (by a factor of 7.1-34.0), then sharply decreased until day 154 (Appendix **Figure A.57**); afterwards, the peak areas increased again from day 154 until day 224 (by a factor of 9.8-13.5), followed by a second decrease (Appendix **Figure A.57**). Similar trends of peak area were observed for C_7 and C_8 homologues in the live treatments, but with 1 to 2 order of magnitude lower peak area counts (Appendix **Figure A.57**). In addition, a substantial accumulation of C_4 and C_6-C_8 homologues was observed in the abiotic controls (by a factor of 5.5-60.6), and a further decrease of C_8 homologue was observed after day 154 (Appendix **Figure A.57**). These results indicated that OAmPr-FASA was readily formed from AFFF components (see **Section 3.3.5.1.1**) through biotic and abiotic transformation. Moreover, the further biotic transformation of OAmPr-FASA was more rapid than abiotic transformation under the present conditions.

N-MeFASAA and ***N-EtFASAA***. These two classes (C_6 homologues identified in ESI- mode) share a perfluoroalkane sulfonamido acetate chain. N-MeFASAA has a methyl group on the sulfonamide nitrogen, while N-EtFASAA has an ethyl group (**Figure 4.29**). Although the two classes were not previously found in AFFF formulations, their occurrence was reported in AFFF-impacted soil and groundwater samples [232, 236], suggesting that those PFAS might be formed in situ during the transformation of AFFF components. In the present study, the peak areas of C_6 N-MeFASAA increased greatly by a factor of 15.3 in the first 98 days, then decreased by half at the end of the incubation in the live treatments (Appendix **Figure A.58**), suggesting its initial formation from AFFF components followed by the further biotransformation. In the abiotic controls, the peak area of C_6 N-MeFASAA gradually increased by a factor of 2.6 during the incubation (Appendix **Figure A.58**), indicating that C_6 N-MeFASAA can also be formed by abiotic processes with a slower rate. For C_6 N-EtFASAA, a rapid and substantial increase in the peak areas (171.8 times increase) was observed in the live treatments, while no distinguishable change was found in the abiotic controls over 308-day incubation (Appendix **Figure A.59**). This indicated that the formation of N-EtFASAA was primarily from biotransformation of its precursor(s).

OAmPr-FAAd. This class (C_5-C_7 homologues identified in ESI+ mode) is structural analogue to OAmPr-FASA, but the sulfonamide functional group was substituted by a carboxamide group (**Figure 4.29**). In the live treatment, the peak areas of C_5-C_7 homologues increased by a factor of 13.0-29.5 at day 98 compared to day 0, and decreased to nearly 0 at day 154, then increased again (Appendix **Figure A.60**). In contrast, continuous increase in OAmPr-FAAd was observed in the abiotic controls; at the end of incubation, the peak area increased by a factor of 28.8-48.2 (Appendix **Figure A.60**). These results indicated that OAmPr-FAAd was readily formed under

both biotic and abiotic conditions, and the further transformation of OAmPr-FAAd was also rapid under biotic conditions but slow/infeasible under abiotic conditions. The rapid biotransformation of OAmPr-FAAd observed here is quite consistent with the prior study that reported 50% of C_8 homologue of OAmPr-FAAd was biotransformed within 3-7 days in soil microcosms [241]. Also, the findings resonated with the rare detection of OAmPr-FAAd in AFFF-impacted environment.

PFCA and PFSA. Under biotic conditions, increases in PFSAs (C_3-C_6 homologues, by a factor of 1.6-2.7) and PFCAs (C_4-C_6 homologues, by a factor of 1.5-1.6) were observed in this study (Appendix **Figure A.53** and **Figure A.54**), due to the biotransformation of certain AFFF components and intermediate products (discussed in **Section 3.3.5.1.1 and Section 3.3.5.1.2**). Under abiotic conditions, only C_4 $C_{6\text{-}7}$ PFSAs were found to be formed, and with a slower rate (peak areas increased by a factor of 1.2-1.5) (Appendix **Figure A.53**), indicating the possibly higher abundance of C_4 and $C_{6\text{-}7}$ homologues PFSA-precursors and associated abiotic transformation potential. The formations of PFCAs and PFSAs are in agreement with previous studies in which the two PFAS classes were widely documented as stable transformation products from FT- and ECF-based precursors [163, 237, 241].

4.2.5.2 Structurally relevant factors impacting the stability of identified AFFF-derived PFAS

As discussed in **Section 3.3.5.1**, the environmental stability (i.e., transformation rate) of AFFF-derived PFAS identified in the present study varied widely, which resulted from the PFAS structural differences. To facilitate the evaluation of the influences of structural differences on the environmental stability, LFCs in the peak areas of identified PFAS between certain sampling points during the 308-day microcosm experiments were calculated to approximately assess the PFAS transformation potential and rate (Appendix **Table A.32**).

The chemical structure of PFAS identified in this study comprised of a perfluorinated moiety linked to a nonfluorinated moiety (**Figure 4.29**). Within one PFAS class, the carbon chain length of perfluorinated moiety was found to likely influence the stability of the homologues, especially under the biotic conditions (**Figure 4.30**). LFCs of homologues in TAmPr-FASA, AmPr-FASA, and AmPr-FASA-PrA/TAmPr-FASA-AA in the live treatments increased with the elongation of perfluorinated carbon chain (**Figure 4.30**a), suggesting a longer perfluorinated carbon chain could render a higher microbial stability. Specifically, LFCs for C_4, C_5, and C_6 homologues of TAmPr-FASA in the live treatment were -7.78 ± 0.56, -1.33 ± 0.09, and -0.54 ± 0.25, respectively (**Figure 4.30**a). LFCs for C_5-C_8 homologues of AmPr-FASA increased from -3.98 ± 0.08 to -2.58 ± 0.65, and C_5-C_7 homologues of AmPr-FASAA-PrA/TAmPr-FASA-AA increased from -2.53 ± 0.21 to -2.04 ± 0.58 (**Figure 4.30**a). Unexpectedly, LFCs for C_4 homologues of AmPr-FASA and AmPr-FASAA-PrA/TAmPr-FASA-AA were greater than those C_5 homologues (**Figure 4.30**); the reason might be the potentially more rapid formation from their precursors, resulting in a less overall decrease extent than other homologues. In contrast to biotic conditions, the influence of perfluorinated carbon chain length on abiotic transformation rate of PFAS classes (e.g., AmPr-FASA) was not observed (**Figure 4.30**). These results implied that the impact of perfluorinated

carbon chain length on PFAS biotransformation is likely due to increased hydrophobicity with elongation of the perfluorinated carbon chain. Enhancing hydrophobicity could increase the affinity of PFAS to soil particles in the microcosms, thereby reducing the bioavailability to microorganisms.

Among the identified ECF-based precursors, some classes (e.g., AmPr-FASA) harbor a sulfonamide group (-SO_2-N(H)-) while some (e.g., AmPr-FAAd) contain a carboxamide group (-C(O)-N(H)-), both of which link the perfluorinated moiety with nonfluorinated moiety (**Figure 4.29**). These two functional groups were found to potentially impact the PFAS stability under biotic and abiotic conditions. Compared to AmPr-FASA, much more rapid transformation of AmPr-FAAd was observed in abiotic controls (Appendix **Figure A.47** and **Figure A.51**), as indicated by lower LFCs for C_6 and C_7 AmPr-FAAd (-2.51 ± 0.27 and -2.47 ± 0.03) than the AmPr-FASA analogues (-0.52 ± 0.33 and -0.64 ± 0.08) (**Figure 4.30**). The results indicated that carboxamide-based PFAS might be less stable than sulfonamide-based analogues under abiotic conditions, which was likely due to the lower resistance of carboxamides to abiotic hydrolysis [243]. The abiotic transformation of another carboxamide-based PFAS class, CEt-AmPr-FAAd observed in this study also evidenced the abiotic lability of carboxamides (Appendix **Figure A.52**). Under biotic conditions, rapid transformation of both AmPr-FASA and AmPr-FAAd were observed in live treatment (Appendix **Figure A.47** and **Figure A.51**), as indicated by close LFCs (ca. -3.5) for both PFAS classes (**Figure 4.30**a). Similar rapid transformation was also observed for OAmPr-FASA and OAmPr-FAAd after both classes were initially produced (e.g., from day 98 to 154 in live treatment), as shown in Appendix **Figure A.57** and **Figure A.60**. This observation contradicts previous findings that sulfonamide-based PFAS were more microbially stable than their carboxamide counterparts [163]. The discrepancy might be explained by the hypothesis that the sulfonamide- and carboxamide-based PFAS classes compared in this study were both readily biotransformed, masking the potentially slight enhancement of microbial stability by the sulfonamide group. This hypothesis would be confirmed by more comparisons between sulfonamide- and carboxamide-based analogues with higher microbial stability, e.g., between TAmPr-FASA (Appendix **Figure A.46**) and TAmPr-FAAd (not detected in this study).

Most of ECF-based precursors identified in the present study, for example, AmPr-FASA and TAmPr-FASA, contain a second nitrogen atom (another amine group) in addition to the first nitrogen in the sulfonamide/carboxamide group (**Figure 4.29**). The structural differences on the second nitrogen atom influenced the PFAS transformation potential. With three methyl groups on the second nitrogen atom (quaternary ammonium), the PFAS microbial stability appeared to be higher than that with two methyl groups on the nitrogen atom (tertiary amine); for example, LFCs of C_5 and C_6 TAmPr-FASA homologues (-1.33 ± 0.09 and -0.54 ± 0.25) are greater than those of their AmPr-FASA counterparts (-3.98 ± 0.08 and -3.52 ± 0.25) in the live treatment (**Figure 4.30**a). Similarly, the microbial stability of PFAS with one or no methyl group on the second nitrogen atom (secondary or primary amine) was hypothesized to be further lower. M-AmPr-FASA (with a secondary amine head group, as shown in **Figure 4.29**) was detected in this study as an

intermediate, and a rapid transformation following initial formation was observed in the live treatment (Appendix **Figure A.56**). In addition, an oxygen atom on the tertiary amine head group, e.g., OAmPr-FASA and OAmPr-FAAd (**Figure 4.29**), led to low microbial stability for the PFAS classes, as evidenced by their rapid biotransformation following the production (Appendix **Figure A.57** and **Figure A.60**). On the contrary, adding a carboxyalkyl group on the tertiary amine head group could potentially enhance the resistance of PFAS to both biotic and abiotic transformation. With an addition of a carboxyethyl group on the second nitrogen atom, CEt-AmPr-FAAd exhibited higher stability than AmPr-FAAd in the live treatment and abiotic controls (**Figure 4.30**); LFCs of C_7 homologue of CEt-AmPr-FAAd were -0.69 ± 0.48 and -1.08 ± 0.33 in the live treatment and abiotic controls, respectively, which were much greater than that for C_7 AmPr-FAAd (-3.36 ± 0.13 and -2.47 ± 0.03, respectively). The above findings on the impact of structural differences in second amine group on PFAS stability are in accord with a previous study that showed PFAS containing quaternary ammonium or a carboxyalkyl group on tertiary amine groups was more stable than those with tertiary amine or an oxygen atom on tertiary amine groups [163].

Beyond the second nitrogen atom, it was found that adding a carboxyalkyl group on the first nitrogen atom (i.e., sulfonamide/carboxamide group) further enhanced the PFAS stability. For example, with a carboxyalkyl group on both nitrogen atoms, CEt-AmPr-FASA-PrA (**Figure 4.29**) exhibited high persistence in the microcosms without abiotic or biotic transformation observed during 308-day incubation (Appendix **Figure A.48**). Comparatively, if only one carboxyalkyl group is attached on either of nitrogen atom, e.g., AmPr-FASA-PrA/TAmPr-FASA-AA and CEt-AmPr-FAAd (**Figure 4.29**), the PFAS compounds were not persistent (**Figure 4.30**, Appendix **Figure A.49** and **Figure A.52**) and the transformation likely started at the nitrogen atom without the carboxyalkyl group. Previous studies documented the increased stability resulting from adding a carboxyalkyl group to the sulfonamide group. For example, N-ethyl perfluorooctane sulfonamide (EtFOSA) was readily transformed in soil (half-life of 11.2-26.8 days), while N-ethyl perfluorooctane sulfonamido acetic acid (EtFOSAA) with an additional carboxymethyl group on the sulfonamide group was more resistant to biotransformation (half-life of 287-653 days) [157, 159]. Also, after the ethyl branch on sulfonamide group of EtFOSA was oxidized to carboxymethyl, the compound (perfluorooctane sulfonamido acetic acid (FOSAA) became more microbially stable (half-life of 96.2-334 days) [157, 159]. Taken together, these findings suggested that adding a carboxyalkyl group to the nitrogen atom(s) in ECF-based precursors likely hinders N-decarboxylation and N-dealkylation (when a alkyl group is present on the same nitrogen), leading to the increased stability.

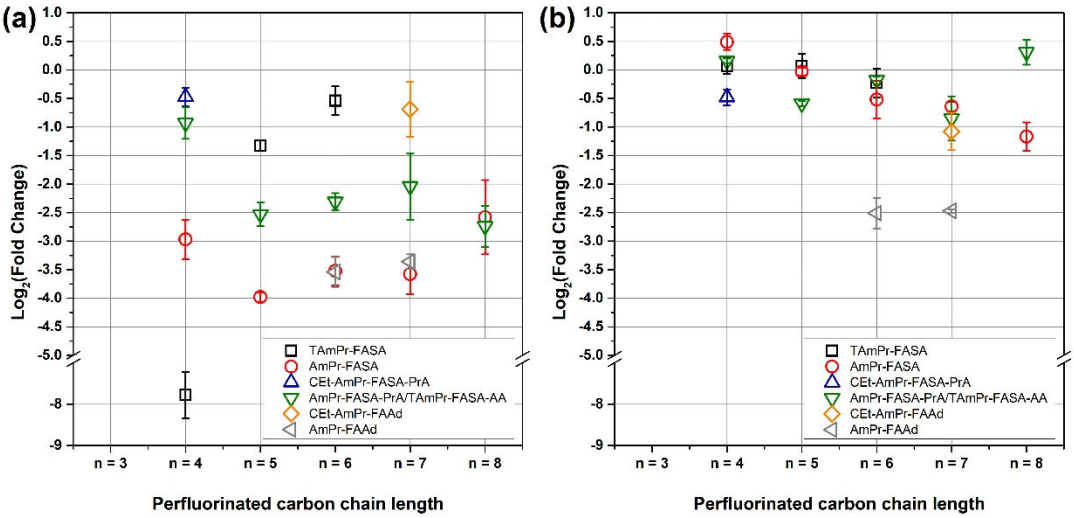


Figure 4.30 Log_2-fold changes (LFCs) in peak areas of different PFAS between day 308 and day 0. (a) and (b) show LFCs for the AFFF components detected live treatment and abiotic control, respectively. Error bars represent one standard deviation among replicate microcosms.

4.2.5.3 Transformation pathways of identified AFFF-derived PFAS

Based on the AFFF components and transformation products identified by LC-HRMS and their associated transformation potentials as discussed in **Sections 3.3.5.1** and **3.3.5.2**, transformation pathways of sulfonamide-based and carboxamide-based PFAS in aerobic soil involving 15 AFFF-derived PFAS classes (n:2 FTAB was not included) were proposed, as illustrated in **Figure 4.31**.

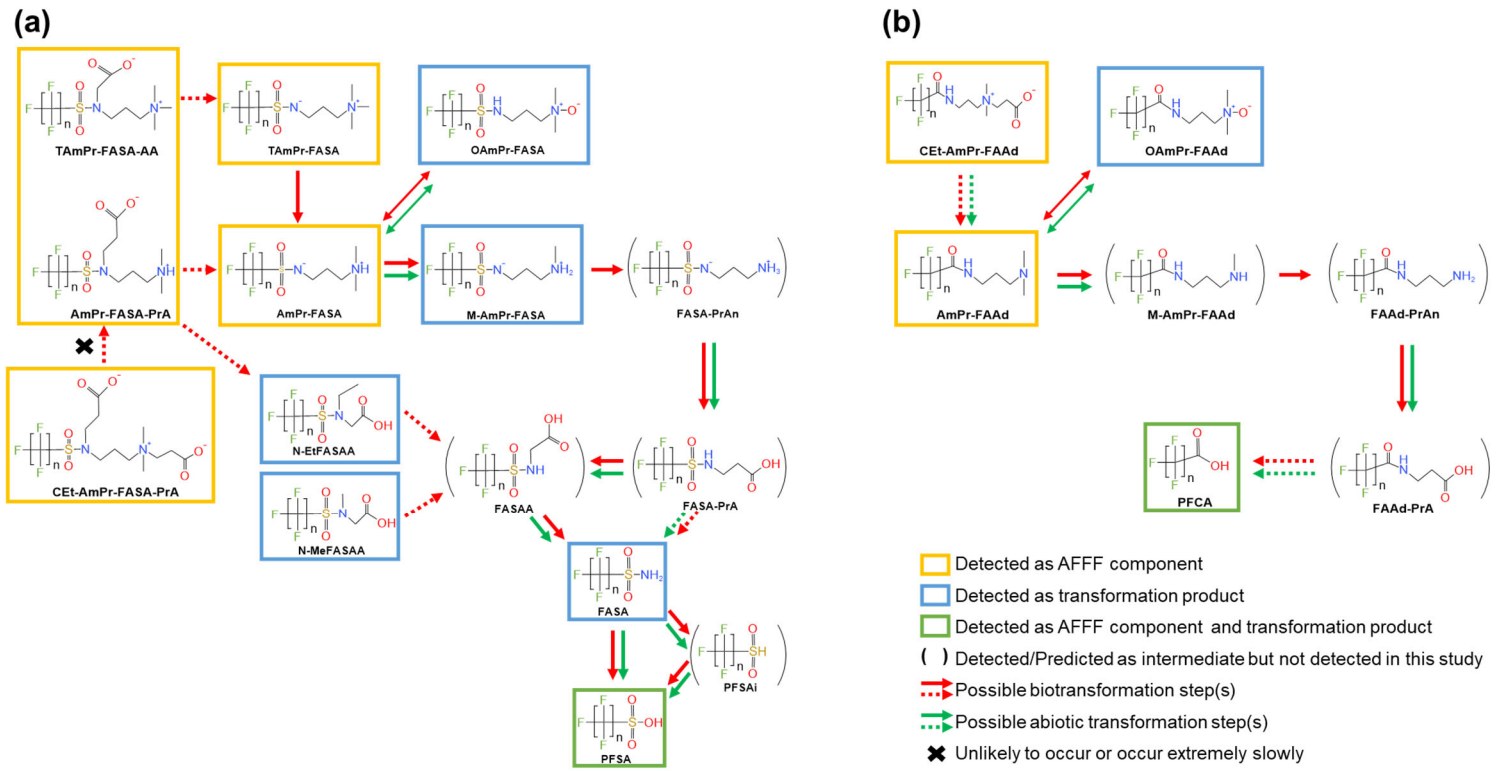


Figure 4.31 Proposed transformation pathways of (a) sulfonamide-based and (b) carboxamide-based PFAS identified by LC-HRMS in AFFF-amended soil microcosms. Compounds in yellow and blue boxes were identified in this study as AFFF components and transformation products, respectively. Compounds in green box were identified in this study as both AFFF components and transformation products. Compounds in parentheses were not detected in this study, but detected or predicted as intermediates in previous studies [163, 237, 241]. Red and green arrows represent possible biotransformation and abiotic transformation steps, respectively. Dashed arrows indicate hypothetical multiple steps.

The abiotic and biotic transformation potentials of CEt-AmPr-FASA-PrA, TAmPr-FASA-AA or AmPr-FASA-PrA were for the first time investigated in the present study. With a carboxyalkyl group on each nitrogen atom, CEt-AmPr-FASA-PrA showed high stability in the soil microcosms (Appendix **Figure A.48**). Transformation of CEt-AmPr-FASA-PrA in this study was less likely or occurred at an extremely slow rate (**Figure 4.31**a). As for TAmPr-FASA-AA/AmPr-FASA-PrA, they remained stable under abiotic conditions, while their biotransformation might proceed via two different pathways. One pathway involved decarboxylation and N-dealkylation of the carboxyalkyl branch on the first nitrogen atom, converting TAmPr-FASA-AA or AmPr-FASA-PrA to TAmPr-FASA or AmPr-FASA, respectively (**Figure 4.31**a). The other pathway involved multiple N-dealkylation of the tertiary/secondary amine head groups on the second nitrogen atom and deamination reaction, converting TAmPr-FASA-AA or AmPr-FASA-PrA to N-MeFASAA and N-EtFASAA (**Figure 4.31**a). The transformation of TAmPr-FASA-AA or AmPr-FASA-PrA may mainly proceed through the latter pathways to form N-MeFASAA and N-EtFASAA, given the absence of carboxyalkyl group on the second nitrogen atom but presence on the first nitrogen.

As an AFFF component and a potentially minor product of TAmPr-FASA-AA, TAmPr-FASA was persistent under abiotic conditions, but was susceptible to microbial transformation (Appendix **Figure A.46**). One of the methyl groups on the quaternary ammonium head group of TAmPr-FASA could be replaced by a hydrogen, leading to the formation of a tertiary amine (i.e., AmPr-FASA) (**Figure 4.31**a). AmPr-FASA further lost the two methyl groups from the tertiary amines successively through N-dealkylation, forming products with secondary amines (M-AmPr-FASA) and primary amines (FASA-PrAn), respectively (**Figure 4.31**a). Through deamination and oxidation, FASA-PrAn was then transformed to FASA-PrA, which was potentially converted to either FASAA via decarboxylation and oxidation, or to FASA via further decarboxylation and N-dealkylation. These transformation pathways from TAmPr-FASA to FASA were also proposed in previous studies using the C_8 homologue of each PFAS class [163, 237].

The substantial formation of OAmPr-FASA was observed in this study under both abiotic and biotic conditions (Appendix **Figure A.57**), possibly from the oxidation of AmPr-FASA (**Figure 4.31**a), as proposed recently [244]. In addition, substantial abiotic formation of C_4 OAmPr-FASA was found (Appendix **Figure A.57**) despite no obvious abiotic transformation of C_4 homologue of AmPr-FASA (Appendix **Figure A.47**), the presence of other unknown precursors of OAmPr-FASA in the AFFF formulation cannot be ruled out. The amine oxide in OAmPr-FASA can also be reduced back to tertiary amine as reported previously [241], resulting in the reversible reactions between OAmPr-FASA and AmPr-FASA.

This study for the first time reported the formation of N-MeFASAA and N-EtFASAA during the transformation of AFFF-derived PFAS. As mentioned above, N-MeFASAA and N-EtFASAA might be the transformation products of TAmPr-FASA-AA/AmPr-FASA-PrA via multiple steps (**Figure 4.31**a). N-MeFASAA and N-EtFASAA were then converted to FASAA through N-dealkylation or a decarboxylation followed by multiple steps of alkyl oxidation (**Figure 4.31**a)

[56, 158, 159]. FASAA could be further transformed to FASA via decarboxylation and N-dealkylation (**Figure 4.31**a) [56, 157, 159]. The increases of FASA peak areas were observed in both live treatment and abiotic control (Appendix **Figure A.55**), suggesting that FASA can be formed under both biotic and abiotic conditions. FASA was eventually transformed to PFSA (**Figure 4.31**a). The transformation of FASA to PFSA might be a direct process as reported previously [158, 241], or the transformation may occur through an intermediate PFSAi as detected in some studies [56, 163, 244].

Transformation pathways of carboxamide-based PFAS in AFFF formulation is illustrated in **Figure 4.31**b. The reactions leading AmPr-FAAd to PFCA were similar to its sulfonamide counterpart (**Figure 4.31**a). First, successive N-dealkylation occurred to the methyl groups on the second nitrogen of AmPr-FAAd, resulting in the production of M-AmPr-FAAd and FAAd-PrAn (**Figure 4.31**b). Then, N-deamination and following oxidation processes converted FAAd-PrAn to FAAd-PrA (**Figure 4.31**b). FAAd-PrA was further transformed to PFCA through decarboxylation, multiple steps of alkyl oxidation, and amide hydrolysis (**Figure 4.31**b). Similar reactions involving carboxamide-based PFAS (i.e., from AmPr-FAAd to PFCA) were also predicted in previous studies [163, 237, 241]. The occurrence of CEt-AmPr-FAAd in the AFFF formulation and associated transformation potential were for the first time reported in the present study. It is hypothesized that CEt-AmPr-FAAd could be biotically and abiotically transformed to AmPr-FAAd through decarboxylation and N-dealkylation (**Figure 4.31**b). Similar to AmPr-FASA and OAmPr-FASA, the reactions between AmPr-FAAd and OAmPr-FAAd might be reversible and able to occur biotically and abiotically (**Figure 4.31**a).

4.2.5.4 Concluding remarks

This study identified 16 classes of PFAS in a historically used 3M AFFF formulation and demonstrated that multiple classes of ECF-based precursors are susceptible to abiotic and/or biotic transformation under biotic and/or abiotic conditions based on LC-HRMS and LC-MS analysis results. The transformation of ECF-based precursors in this study suggests that these precursors could be sources of PFAAs at historical AFFF-impacted sites. Although biotransformation of some classes of precursors, for example, AmPr-FASA, has been documented in previous studies for specific homologues (C_6 and C_8), this study included a wider range of homologues (C_4-C_8) and found that all of them could be biotransformed. Despite detection in AFFF formulations or contaminated sites, AmPr-FASA-PrA/TAmPr-FASA-AA and CEt-AmPr-FAAd have not been reported to be transformed before. This study provides, for the first time, evidence of the biotransformation of AmPr-FASA-PrA/TAmPr-FASA-AA and CEt-AmPr-FAAd. CEt-AmPr-FASA-PrA was found to be stable during the 308-day incubation, suggesting a lack of degraders in the soil used in this study or that this class of PFAS is persistent in the environment. Considering the timeframe of this study and the transformation extent observed, AFFF release into soils will likely have long-term impacts on the PFAS emminating from a source zone. The detection of many similar precursors in environmental samples from aged contaminated sites provides further

evidence that the transformation rates in the field may be even slower than under laboratory conditions.

The addition of AFFF as the parent compounds provided this study with a broader view on the stability of different classes of precursors and different homologues in individual classes. It was found that the functional groups of the nonfluorinated moiety and the carbon chain length of the perfluorinated moiety influenced the stability of these precursors. The presence of an additional methyl group at the end of the nonfluorinated moiety and carboxyalkyl group(s) on one or both nitrogen atoms, and a longer perfluorinated carbon chain may enhance the stability of the precursors. The structural-relevant results obtained in this study provide important information to PFAS manufacturers regarding producing and using more stable PFAS in their products and supply chains. However, due to the complex composition and transformation pathways of the AFFF, the transformation kinetics of individual precursors could not be determined in the present study. Further studies are needed to better understand these transformation mechanisms.

4.2.6 Potential Microbial Taxa in Soil Microbial Communities and Functional Genes Related to Fluorotelomer Biotransformation

4.2.6.1 Microbial co-occurrence network

4.2.6.1.1 Microbial community compositions, topological properties, and modules

The network generated using identified microbial taxa in treatment groups (with addition of fluorotelomers) is called constructed network hereafter and shown in **Figure 4.32**a. The constructed network consisted of 269 nodes (ASVs) and 1,627 edges (correlations). The ASVs were distributed primarily into ten major phyla accounting for over 90% of all nodes, in which the most abundant phylum was Firmucutes (31.60%), followed by Proteobacteria (25.65%), Chloroflexi (11.52%), Bacteroidota (6.69%), Acidobacteriota (6.32%), Actinobacteriota (2.97%), Myxococcota (1.86%), Halobacterota (1.86%), Desulfobacterota (1.49%), and Verrucomicrobiota (1.49%).

The nodes in the constructed network were highly connected (approximately 12 edges per node). The average path length (i.e., average network distance between all pairs of nodes) was 3.474 edges with a diameter (longest distance) of 10 edges. Compared with the identically sized Erdős-Rényi random networks, the modularity and clustering coefficient (the degree of the nodes tend to cluster together) of the constructed network were both greater (Appendix **Table A.33**), suggesting the nodes in the constructed network tended to co-occur more and form a significantly clustered topology than expected by chance. The taxa detected in control groups (without addition of fluorotelomers) were also used to construct a network (called the control network hereafter). Although the topological properties of the constructed network were similar to the control network (Appendix **Table A.33** and **Supplementary Data X2** in Appendix S8), these two networks shared

less than 50% nodes (ASVs). This study focused on the constructed network associated with fluorotelomer contamination.

As shown in **Figure 4.32**b all nodes of the constructed network were modularized into 7 major modules (containing more than 10 nodes) that were comprised of different taxonomic profiles. Module 1 and 2 were the two largest modules with 57 and 52 nodes, representing 21.2% and 19.3% of the nodes in the entire constructed network, respectively. Module 1 was dominated by Firmicutes, while module 2 was dominated by Proteobacteria and Chloroflexi. Module 3 (26 nodes) and 7 (15 nodes) contained a variety of taxa dominated by Proteobacteria and Firmicutes, respectively. The taxonomic composition of Module 4, 5, and 6 were relatively simple. Module 4 (19 nodes) contained ASVs from Chloroflexi, Firmicutes, and Proteobacteria, and mostly belonged to Proteobacteria. Nodes in both Module 5 (18 nodes) and 6 (16 nodes) were mostly Firmicutes. Module 5 also contained a few nodes from Chloroflexi and Module 6 contained some nodes from Actinobacteriota.

The formation of modules in microbial networks have been reported to be driven by environmental factors, such as soil properties and water depth [245, 246]. In the constructed network, environmental factors, including contaminant added externally, soil type, and redox conditions all showed strong correlations (Cramer's $V > 0.6$ and Chi-square $P < 0.001$) with modules (Appendix **Table A.34**). To better visualize the environmental factors associated with the modules in the constructed network, the nodes of the constructed network were colored according to different conditions, including the contaminant added externally (8:2 FTOH or 6:2 FTS), soil (Loring soil or Robins soil), and redox conditions (aerobic, nitrate-, sulfate-, or iron-reducing conditions) (Appendix **Figure A.63**). Most ASVs in Module 1, 5, and 7 existed in Loring soil under sulfate-reducing conditions. Module 2 and 3 represented the most aerobic microorganisms presented in Loring soil and Robins soil, respectively. Module 4 and 6 contained ASVs mostly from Loring soil under nitrate-, and iron-reducing conditions, respectively. The diverging modules associated with various soil types and redox conditions indicate the modules in microbial networks may represent different niches.

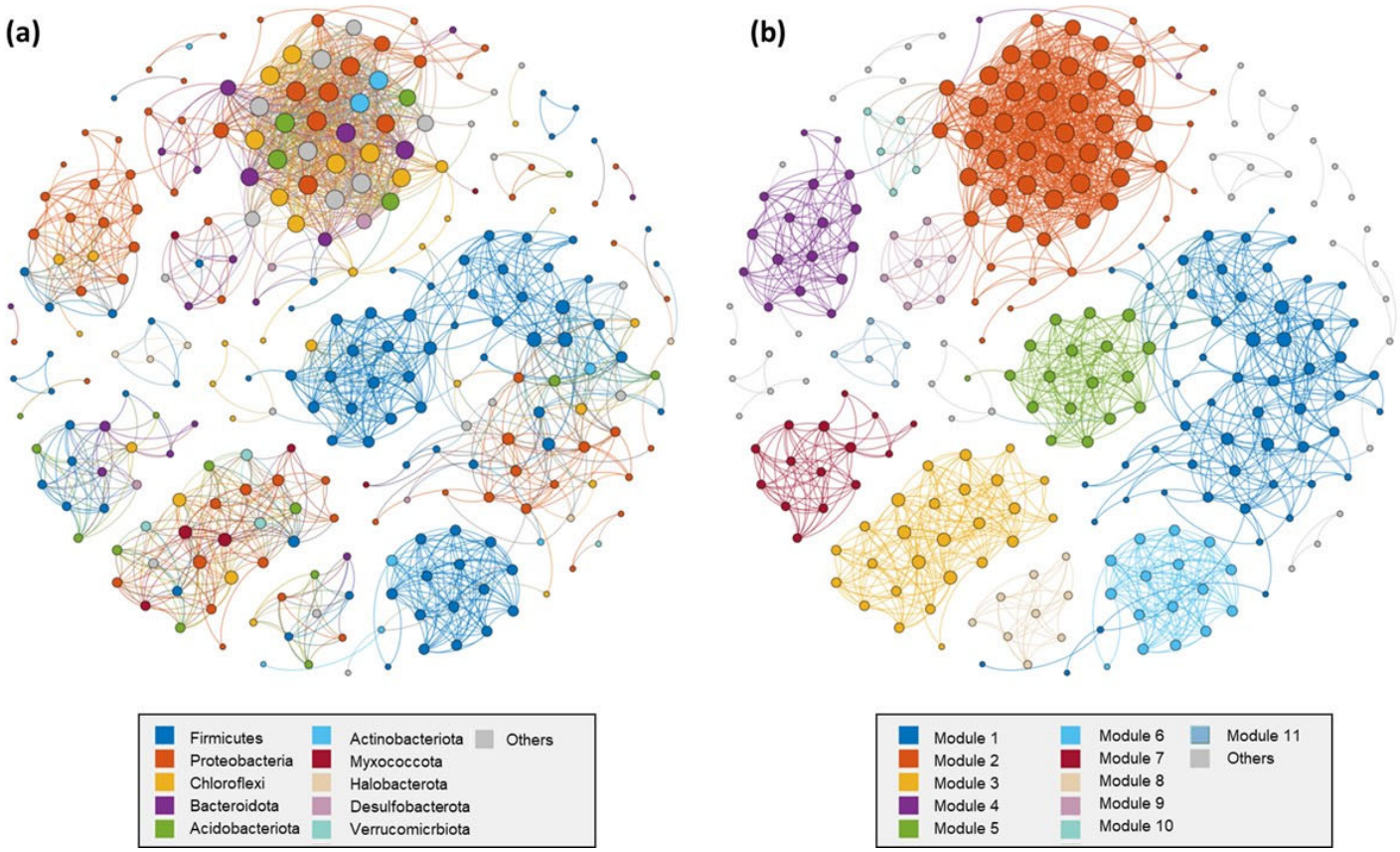


Figure 4.32 Microbial co-occurrence networks in fluorotelomer contaminated soils under different redox conditions (constructed networks). An edge (connection) between nodes (ASVs) indicates a strong and significant correlation between two nodes. The size of each node is proportional to the number of connections (degree). The nodes are colored according to (a) phylum taxa and (b) module assigned.

4.2.6.1.2 Generalist taxa and co-occurrent microbes

The generalist ASVs and their co-occurrent ASVs with significant correlations (Spearman's correlation coefficient $\rho > 0.8$ and adjusted *P*-value < 0.01) are shown in **Table 4.10**. A total of five ASVs were found in both Loring and Robins soils and both 8:2 FTOH and 6:2 FTS microcosm experiments. One of them (ASV0242) is a member in genus *Candidatus* Solibacter (phylum Acidobacteriota) associated with chlorocyclohexane and chlorobenzene biodegradation [247] and decomposition of plant residues [248]. Two of these five generalists belong to phylum Proteobacteria (Alphaproteobacteria subclass): ASV0606 and ASV 0944 are affiliated to genera *Rhodoplanes* and *Variovorax*. Some microbes in the former genus are linked to biodegradation of PAHs and polybrominated diphenyl ethers (PBDEs) [249, 250]. Species in the latter genus possess diverse catabolic abilities, including removing chloride ions from aromatic rings [251], degrading benzene [252], chlorinated triazine [253], as well as trichloroethylene (TCE) [202]. Another two generalists are unclassified genera in phylum Chloroflexi: ASV1016 is a member in order SJA-15 widely identified in wastewater treatment plant activated sludge [254]; ASV0614 is in class KD4-96, previously reported as a keystone taxon in rhizosphere microbial community [255] and involved in the biodegradation of halosulfuron methyl [256]. Although these generalists are not highly connected with other microbes in the community, they are believed to be well adapted to a variety of conditions and might be playing a role during fluorotelomer biotransformation.

Similar to the degree (number of connections with other nodes) of soil generalists identified in soil samples collected across spatial or temporal gradient (< 20) [257], the generalists identified in this study also have small degrees (1, 2, and 13). The co-occurrent ASVs of generalists are also shown in **Table 4.10**. Both ASV0654 and ASV2000 are affiliated to genus *Anaeromyxobacter* (phylum Myxococcota). Some *Anaeromyxobacter dehalogenans* strains were recognized to use halogenated compounds as terminal electron acceptor [219]. ASV0257 and ASV1604 are members in genus *Pseudolabrys* (phylum Proteobacteria) with great potential functional activity in degradation of chloroalkanes and chloroalkenes [258]. ASV1309 (genus *Ancylobacter*), ASV0204 (genus *Cupriavidus*), and ASV1805 (genus *Mesorhizobium*), all belonging to phylum Proteobacteria. Some species in these three genera were documented to encode haloalkane dehalogenases and be responsible for degradation of halogenated aliphatic compounds [203, 259, 260]. The co-occurrent ASVs with generalists may also play a role during fluorotelomer biotransformation.

Table 4.10 Taxonomy of generalists ASVs and their significant (*P*-value < 0.01) co-occurrent ASVs

Generalist	Phylum	Genus	Co-occurrent ASV	Spearman's ρ	Phylum	Genus
ASV0242	Acidobacteriota	*Candidatus* Solibacter	ASV0117	0.809	Acidobacteriota	Unassigned
			ASV0104	0.809	Chloroflexi	Unassigned
			ASV0939	0.809	Chloroflexi	*Anaerolinea*
			ASV2084	0.804	Firmicutes	Uncultured
			ASV0654	0.811	Myxococcota	*Anaeromyxobacter*
			ASV2000	0.809	Myxococcota	*Anaeromyxobacter*
			ASV1309	0.804	Proteobacteria	*Ancylobacter*
			ASV1652	0.802	Proteobacteria	*Azospirillum*
			ASV0257	0.811	Proteobacteria	*Pseudolabrys*
			ASV0204	0.804	Proteobacteria	*Cupriavidus*
			ASV1653	0.804	Proteobacteria	*Burkholderia_Caballeronia_Paraburkholderia*
			ASV0202	0.809	Verrucomicrobiota	*ADurb_Bin063_1*
			ASV1491	0.809	Verrucomicrobiota	Unassigned
ASV0606	Proteobacteria	*Rhodoplanes*	ASV0849	0.837	Proteobacteria	Uncultured
			ASV0955	0.842	Firmicutes	Unassigned
ASV0944	Proteobacteria	*Variovorax*	ASV1665	0.810	Actinobacteriota	*Rhodococcus*
			ASV1805	0.805	Proteobacteria	*Mesorhizobium*
ASV1016	Chloroflexi	Unassigned	ASV0274	0.816	Firmicutes	*Clostridium_sensu_stricto_13*
ASV0614	Chloroflexi	Unassigned	ASV1604	0.915	Proteobacteria	*Pseudolabrys*

4.2.6.1.3 Keystone taxa

With the centrality-based method, 11 ASVs were identified as keystone taxa listed in **Supplementary Data X3** (**Appendix A.18**). Three out of them (ASV0242, ASV2086, and ASV2157) belong to phylum Acidobacteriota. ASV0242 within genus *Candidatus* Solibacter was also identified as a generalist presented in both Loring and Robins soils and thrived with both 8:2 FTOH and 6:2 FTS contaminants. ASV2086 affiliated to genus Bryobacter was reported to be involved in carbon cycle and energy cycle [261]. ASV 2157 is an uncultured family member in order Vicinamibacterales, which might be related to 1,4-dioxine biodegradation [262]. Two of these 11 keystone taxa (ASV2084 and ASV2091) belong to phylum Firmicutes. ASV2084 is an unculture genus in family Symbiobacteraceae, which was reported to have contribution to syntrophic acetate oxidation [263], while ASV2091 is an unclassified member in order Hydrogenispora. Species in Hydrogenispora can ferment sugars and fulvic acid [264, 265]. Another two ASVs (ASV2000 and ASV0917) among the keystone taxa are from phylum Myxococcota. ASV2000 is also identified as a generalist. ASV0917 belongs to the genus *Pajaroellobacter*. Species in this genus were found to be involved in sulfadiazine biodegradation [266] and correlated with higher pH, nitrate, nitrite, phosphorus and ammonia [267]. Other keystone taxa included microbes in phylum Actinobacteriota (ASV0924), Bacteroidota (ASV1644), Gemmatimonadota (ASV2193), and Proteobacteria (ASV1652). ASV0924 is affiliated to order OPB41 and linked to sugar catabolism [268]. ASV1644 within family BSV40 (order Ignavibacteriales) may be able to break down ethylene glycol [269]. ASV2193, an uncultured group in family Gemmatimonadaceae, could be relevant to degradation of chlorinated organophosphate flame retardants [270] and PAHs [271]. ASV1652, affiliated to genus Azospirillum, in which strains were found to have capability to degrade benzoate and phenol [272].

Based on the connectivity-based method, 29 ASVs identified as key taxa are shown in **Supplementary Data X4** (**Appendix A.18**). Among them, two ASVs (ASV1532 and ASV0610) were classified as network hubs, which might be important for the coherence of the global network. ASV 1532 is an unculture class belonging to phylum Armatimonadota, which has been reported to degradation of organic matters [273] and antibiotics [274], and support anammox process [275]. ASV0610 belongs to genus *Christensenellaceae* R-7 group within phylum Firmicutes. Little is known about the functions of microorganisms in this genus, although commonly detected as fermentative bacteria in rumen [276].

Rest keystone taxa identified by the connectivity-based method were classified as modular hubs, which are primarily distributed in Module 1, 2, as well as 3, and likely played important roles in their local modules in the network. In Module 1, several ASVs belonging to genera *Sedimentibacter* (ASV0604, ASV1391, and ASV1121), *Christensenellaceae* R-7 group (ASV0575), *Clostridium sensu stricto 13* (ASV0274), an unclassified genus group in family SRB2 (ASV1714) within phylum Firmicutes, *Rhodomicrobium* (ASV0941), *Methylocystis* (ASV1222), and an uncultured group in family Beijerinckiaceae (ASV0530) of phylum Proteobacteria, were identified as keystone taxa. Species in genus *Sedimentibacter* were broadly reported involved in biodegradation of organic pollutants, including polychlorinated biphenyls [277],

pentachlorophenol [278], hexachlorocyclohexane [279], and polyacrylamide [280]. *Clostridium sensu stricto 13* was identified as atrazine-degrading strains [281]. Species in genus *Rhodomicrobium* were documented to harbor genes required for solvent resistance and degradation of aromatic compounds [282]. Members in genus *Methylocystis* were found to be capable of degrading a variety of halogenated compounds including chlorinated aromatic compounds [283], and chlorinated ethenes, alkanes, as well as alkenes [284]. Moreover, an uncultured genus from family Anaerolineaceae with in phylum Chloroflexi (ASV1118), unclassified suborder OPB41 within phylum Actinobacteriota (ASV0884), and order Subgroup 7 of phylum Acidobacteriota (ASV2019) were also keystone taxa in Module 1. Members in family Anaerolineaceae were evident in crude oil degradation [285], whereas functions of microorganisms belonging to order OPB41 and Subgroup 7 were poorly studied.

In Module 2, multiple genera *Legionella* (ASV1718), *Achromobacter* (ASV2151), and an uncultured group in family Oxalobacteraceae (ASV1298) within phylum Proteobacteria, unclassified groups in class Holophagae order Subgroup 7 within phylum Acidobacteriota (ASV0777), family A4b within phylum Chloroflexi (ASV04115), class Sericytochromatia within phylum Cyanobacteria (ASV2068), and unassigned class in phylum Zixibacteria (ASV0491) behaved as modular hubs. Some species in genus *Legionella* have been recognized as pathogens of legionellosis [286], but some were also classified as anthracene degrader [287]. Members in genus *Achromobacter* were widely documented playing roles during degradation of organic compounds, including polychlorinated biphenyls [288] and hydrocarbons [289]. Lineages in family Oxalobacteraceae were found to be responsible for PAHs and polyacrylamide biodegradation [290, 291], and showed strong negative correlations with PFAS [292]. Little information if available on family A4b, which was hypothesized to contribute to PAHs and carbohydrate degradation [250, 293].

In Module 3, genus *Anaerolinea* (ASV0939) and a group in family A4b (ASV0104) both within phylum Chloroflexi, genus *Anaeromyxobacter* of phylum Myxococcota (ASV 0654 and ASV2000), as well as genus *Pseudolabrys* in phylum Proteobacteria (ASV0257) acted as module hubs. *Anaerolinea* species were characterized as carbohydrate and PAH degraders [294, 295]. Other keystone taxa that were not within Module 1, 2, and 3 included unclassified genera in family BSV40 in phylum Bacteroidota (ASV1644) and order SBR1031 in phylum Chloroflexi (ASV1379). Members in order SBR1031 appeared to play a crucial role in degradation of biodegradable plastics and PAHs [296]. The only keystone ASV belonging to domain Archaea other than Bacteria (ASV1149) was an uncultured group in order Methanomicrobiales of phylum Halobacterota, which was likely a major player in hydrocarbon degradation [297].

The keystone taxa played an important role in maintaining the stability of the network, especially the shared ASVs in different modules and identified as keystone taxa by both methods. For example, species in order Subgroup 7 of phylum Acidobacteriota and family A4b within phylum Chloroflexi were found in different modules; species in family BSV40 in phylum Bacteroidota and genus *Anaeromyxobacter* belonging to phylum Myxococcota; their functions in fluorotelomer transformation need further investigation.

4.2.6.2 Microbial functional profiles

PICRUSt2 predicted nearly 7,000 genes across all samples in this study. The count of genes with significant changes in abundance (absolute log2-fold change > 2 and an FDR-adjusted *P*-value < 0.05) during biotransformation of fluorotelomers in each set of microcosm experiment is shown in Appendix **Table A.35**. The genes with significantly higher abundance (log2-fold change > 2 and FDR-adjusted *P*-value < 0.05) in the treatment exposed to fluorotelomer compared to the control without fluorotelomer might be functional genes associated with fluorotelomer biotransformation. The count of these genes in each set of microcosm experiment (A-F) varied greatly from 36 (6:2 FTS microcosms with Loring soil under aerobic conditions) to 1,266 (8:2 FTOH microcosm with Loring soil under nitrate-reducing conditions) (**Figure 4.33**). Overall, most of these functional genes were not shared at all. There was relatively little overlap between microcosm experiments (from 1 to 94) (**Figure 4.33**).

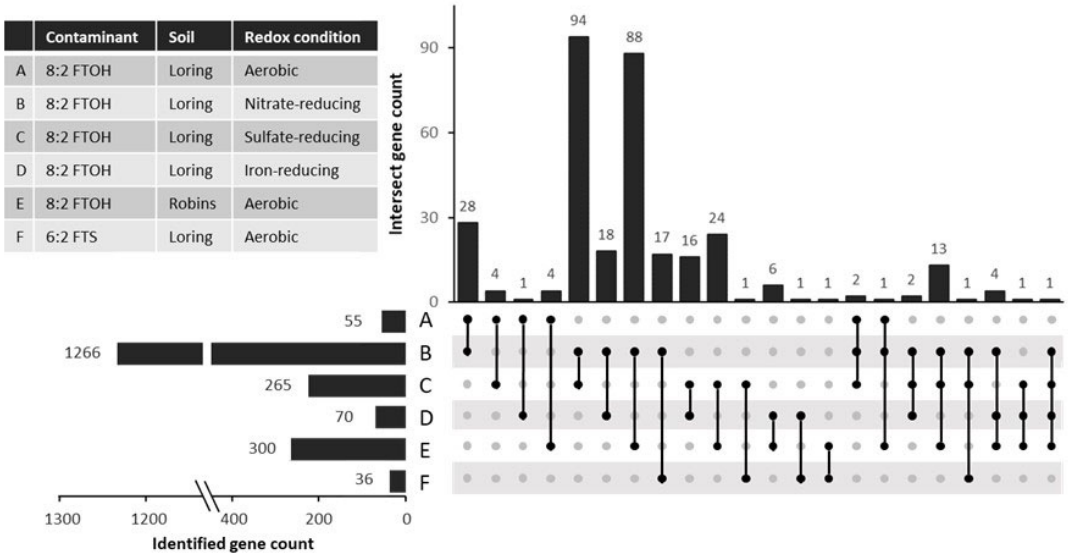


Figure 4.33 UpSet plot for genes shared among different sets of microcosm experiments. The table (top, left panel) shows the contaminant, soil type, and redox condition in each set of microcosms. The horizontal bar plot (bottom, left panel) exhibits the total number of genes with significantly higher abundance in each set of microcosms. The vertical bar plot (top, right panel) depicts the number of genes shared by two or more of sets of microcosms. The matrix (bottom, right panel) indicates which sets of genes are represented by each bar.

4.2.6.2.1 Functional genes that may be involved in fluorotelomer biotransformation

The substantial variations without consistent functional genes across microcosm experiments made it difficult to identify universal functional gene(s) related to fluorotelomer biotransformation. To avoid missing any possible potential functional genes capable of fluorotelomer biotransformation, all the functional genes with significantly higher abundance shared by at least two sets of microcosm experiments were selected for further screening. The selected 258 functional genes belong to 12 KEGG level 2 pathways, including nucleotide metabolism, carbohydrate metabolism, lipid metabolism, amino acid metabolism, energy metabolism,

xenobiotics biodegradation and metabolism, genetic information processing, and signaling and cellular processes (**Supplementary Data X5** in **Appendix A.18**). Specifically, we targeted genes associated with xenobiotics biodegradation and metabolism, which are probably responsible for some steps in fluorotelomer biotransformation. As shown in **Supplementary Data X5** (**Appendix A.18**), 26 out of the 258 selected functional genes encoding different classes of enzymes, including oxidoreductases, hydrolases, and lyases are related to xenobiotics biodegradation pathways. The relative abundance of these 26 functional genes in different sets of microcosm experiments was illustrated in Appendix **Figure A.66**.

Common oxidoreductases are dehydrogenases and reductases that catalyze oxidation-reduction reactions on different bonds, such as the CH-OH group, aldehyde, or CH-CH group. Eight genes among the 26 identified function genes were found to encode dehydrogenases or reductases. The potential functions of these genes reported in prior literature were summarized in Appendix **Table A.36**. Most of them contribute to biodegradation of aromatic compounds. For example, K07538, the gene (*had*) encoding 6-hydroxycyclohex-1-ene-1-carbonyl-CoA dehydrogenase was reported to oxidize the secondary alcohol to ketone and likely involved in anaerobic degradation of benzoate and its derivatives in denitrifying bacteria, like *Magnetospirillum* sp. strain pMbN1 and *Thauera aromatica* [298, 299]. Interestingly, K00217, encodes a maleylacetate reductase, which has been reported as an important enzyme for dechlorination of chloroaromatics in multiple bacterial strains, such as *Pseudomonas sp* [300], *Cupriavidus necator* JMP134 [260], and *Rhodococcus opacus* [301].

Another subclass of oxidoreductases is oxygenase, which plays key roles in breaking down numerous compounds [302]. They are widely documented to be essential in aerobic degradation of aromatic compounds by ring hydroxylation or cleavage of the inert aromatic structure. They can also function in dehalogenation. For example, 2, 2-fluoro-1,3-benzodioxole and its derivatives can undergo defluorination by dioxygenases in *Pseudomonas* strains [303]. *Arthrobacter* strain IF1 was found to harbor a pathway to degrade 4-fluorophenol that involves immediate defluorination by a monooxygenase was the one responsible for defluorination [304]. In present study, six genes among the 26 identified function genes are oxygenases and listed in Appendix **Table A.37**. Similar to the above dehydrogenases, these oxygenases are generally involved in degradation of PAHs by breaking aromatic rings. It is worth noting that K04098, encoding hydroxyquinol 1,2-dioxygenase, have been documented to be responsible for removal of chlorines from chlorinated phenols and cleavage of chlorohydroquinone in multiple genera of microorganism such as *Azotobacter* and *Burkholderia* [305, 306].

Other identified functional genes, encoding enzymes in classes of hydrolases, lyases, transferase, isomerase, and ligase are presented in Appendix **Table A.38**. Enzymes encoded by these genes can participate in catabolic processes of organic compounds and a few of them are associated with halogenated compounds degradation. K07539, 6-oxocyclohex-1-ene-carbonyl-CoA hydrolase encoded by *oah*, which was considered to be capable of defluorination of 2-F-1,5-dienoyl-CoA, its isomers, and 2-F-6-OH-1-enoyl-CoA [307]. This hydrolase, and cyclohexa-1,5-dienecarbonyl-CoA hydratase encoded by *dch* (K07537), were both reported to initiate defluorination of the 2-F-

1,5-dienoyl-CoA intermediate by 1,4-hydration. In addition, K03382, hydroxydechloroatrazine ethylaminohydrolase encoded by *atzB*, which can break carbon-nitrogen bonds in a chlorinated triazine systemic herbicide [308], was identified as a functional gene in this study. Although this hydrolase itself is not directly acting on chlorine, another component in the same gene cluster, *atzA* encodes atrazine chlorohydrolase, which can remove chloride [308].

4.2.6.2.2 Other interesting functional genes

Apart from the above discussed functional genes/enzymes, some other interesting enzymes (summarized in Appendix **Table A.39**) predicted in this study were selected and discussed below. Despite showing no significant abundance according to the PICRUSt2 prediction results in this study, they were documented in previous or emerging studies, and having capacity to degrade halogenated compounds including fluoroaliphatics and fluorotelomers. For example, haloacetate dehalogenase (K01561), was found to be responsible for microbial defluorination of fluoroacetate [309]. With significant similarity to haloacetate dehalogenase in terms of encoding gene sequence, haloalkane dehalogenase (K01563), purified from multiple bacterial strains, such as *Rhodococcus rhodochrous*, *Sphingomonas paucimobilis*, and *Xanthobacter autotrophicus* were found to degrade a variety of chlorinated, brominated, and iodinated compounds [310-312]. Recently, a study examining genes involved in 6:2 FTS biotransformation by *Rhodococcus jostii* RHA1, found that alkanesulfonate monooxygenase is associated with desulfonation of 6:2 FTS, while haloacid dehalogenase (K01560), alkane monooxygenase (K00496), and cytochrome P450 (K16389) are linked to defluorination [106]. Another recent study reported that a gene cluster in *Dietzia aurantiaca* J3 encoding an FMN reductase (*ssuE*, K00299), an alkanesulfonate monooxygenase component B (*ssuD*, K04091), an alkanesulfonate permease protein (*ssuC*, K15554), an ABC transporter (*ssuB*, K15555), and an alkanesulfonate-binding protein (*ssuA*, K15553) are involved in 6:2 FTS biotranformation [105]. Although defluorination was observed the 6:2 FTS biotransformation, the potential role of this gene cluster was thought to be alkanesulfonate utilization rather than defluorination. Additionally, to mitigate fluoride toxicity, Wackett speculated the existence of a fluoride-proton antiporter to expel fluoride from the cell in polyfluorinated compounds degraders [107]. One common fluoride-specific riboswitch encoding by *crcB* (K06199) that can serve as a fluoride-proton antiporter was also predicted in this study. The relative abundance of these interesting functional genes in different sets of microcosm experiments was illustrated in Appendix **Figure A.66**.

4.2.6.3 Association between functional genes/enzymes and microorganisms

PICRUSt2 was also used to link the functional genes/enzymes discussed above, including 26 of them associated with xenobiotics biodegradation and metabolism, and the interesting genes/enzymes reported previously, to the microbial taxa (**Supplementary Data X6** in **Appendix A.18**). Some genes are widely distributed in numerous genera of microorganisms. For example, K04098 and K00217, both responsible for dechlorination, were possessed by genera *Rhodococcus*, *Bradyrhizobium*, *Burkholderia_Caballeronia_Paraburkholderia*, *Cupriavidus* (**Figure 4.34**a). K07537 and K07539, which can initiate defluorination, both showed a high contribution from

Azoarcus and *Desulatiglans* (**Figure 4.34**a). It suggests that more than one strain of bacteria in the soils may contribute to defluorination and fluorotelomer biotransformation.

It is not surprising that some generalists and their co-occurrent microorganisms identified in the network analysis are found to harbor multiple functional genes that may associate with fluorotelomer biotransformation. ASV0944, a generalist belonging to genus *Variovorax*, and co-occurrent ASVs, including species within the genera *Cupriavidus* (ASV0204), *Burkholderia_Caballeronia_Paraburkholderia* (ASV1653), *Rhodococcus* (ASV1665), *Pseudolabrys* (ASV1604), *Mesorhizobium* (ASV1805), and *Ancylobacter* (ASV1309), are all predicted to contain the components (K00299 and K15553-15555) in a gene cluster reported to be responsible for 6:2 FTS biotransformation in another bacterial strain [105], a haloacid dehalogenase gene (K01560), and a fluoride exporter gene (K06199) (**Figure 4.34**b). This again evidences these microorganisms are potential fluorotelomer degraders.

Moreover, most keystone taxa identified in the network analysis are predicted to carry at least one functional gene related to fluorotelomer biotransformation. ASV2151, a species within the genus *Achromobacter* contains the 6:2 FTS biotransformation gene cluster (K00299 and K15553-15555), a haloacid dehalogenase gene (K01560), a haloacetate dehalogenase (K01560), and a fluoride exporter gene (K06199) (**Figure 4.34**b). ASV2000 belonging to genus *Anaeromyxobacter* likely have a haloacid dehalogenase gene (K01560), a haloalkane dehalogenase gene (K01563), and a fluoride exporter gene (K06199) in its genome (**Supplementary Data X6** in **Appendix A.18**). This also indicates that the keystone taxa are possibly able to contribute to fluorotelomer transformation.

4.2.6.4 Concluding remarks

This work highlights the modular structure of soil microbial communities formed after exposure to fluorotelomers. Through network modeling, we were able to identify keystone taxa including genera *Variovorax*, *Rhodococcus*, and *Cupriavidus*. In addition, using metagenomic prediction, a wide range of genes involved in the biotransformation, such as 6-oxocyclohex-1-ene-carbonyl-CoA hydrolase gene and cyclohexa-1,5-dienecarbonyl-CoA hydratase gene were predicted to be associated with fluorotelomer biotransformation. The functional potential was found widely distributed in the keystone taxa. It is tempting to speculate whether the functional genes/enzymes identified in this work are also relevant during transformation of PFOA and PFOS, as well as many others PFAS. This study provides good candidates for microbial taxa and functional genes to test for other PFAS transformation and defluorination; the data generated in this study have the potential to be incorporated into other PFAS biotransformation studies for assessing biotransformation potential in soils and other environmental matrices.

An expansion of the study with more diverse PFAS transformation experiments and a larger size of sequencing samples should be considered as a future step to further elucidate the mechanism of PFAS microbial transformation. Advances in next-generation sequencing and -omics technologies, coupled with more powerful computational tools will allow for better prediction of microbial participation in biotransformation and defluorination, and of assessing how these organisms might

potentially be harnessed to serve as biomarkers to indicate PFAS fate in the environment or to develop function-based microbial consortia for PFAS bioremediation at contaminated sites.

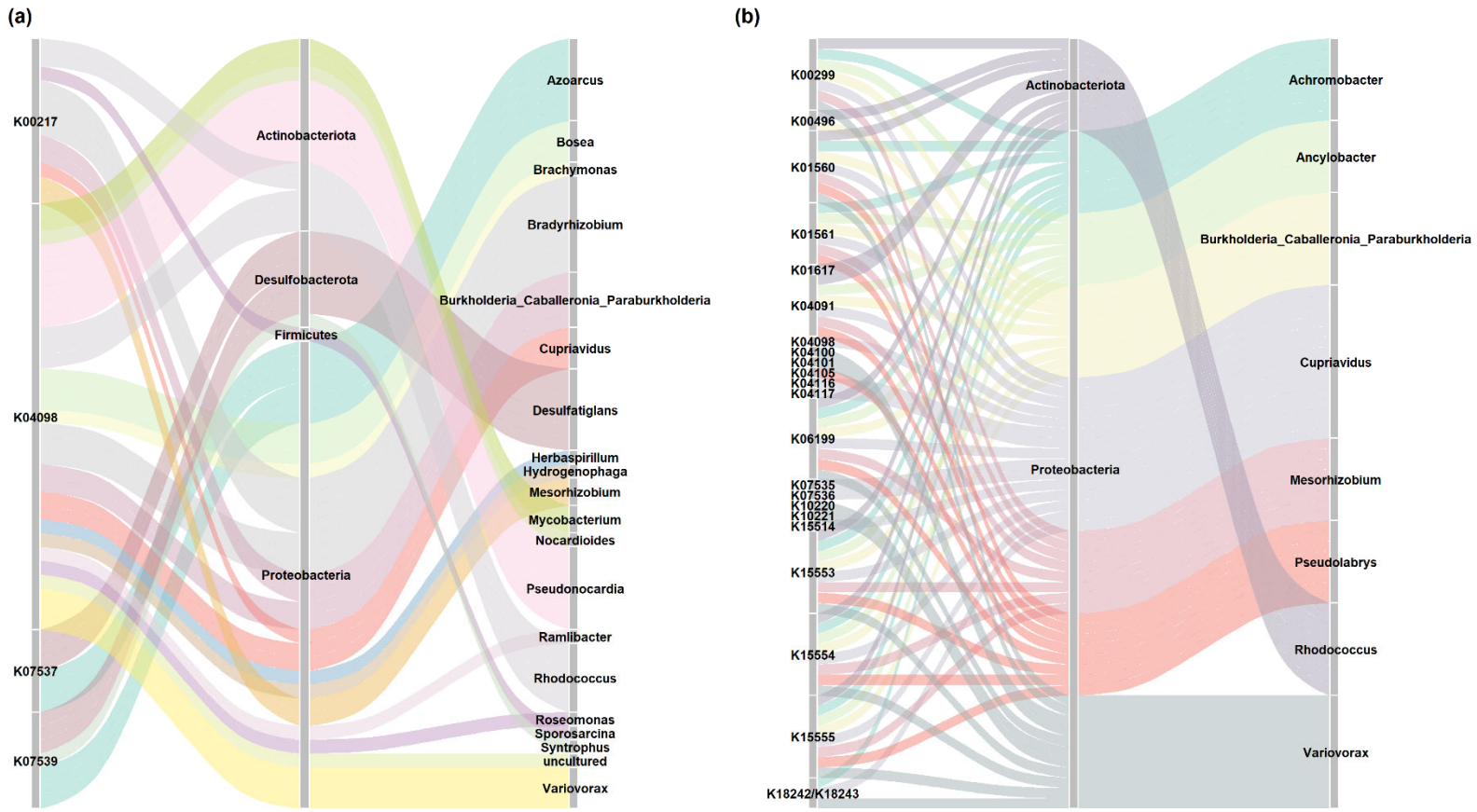


Figure 4.34 Sankey diagrams indicating the contribution of predicted functional genes by bacterial taxa across all microcosm experiments. Noted that the vertical nodes are not proportional to the size of relative abundance. The left column represents functional genes (a) that may be related to defluorination and (b) that were also identified as important functional genes in this study. The middle and right columns are taxonomic groups at phylum level and taxonomic groups at genus level, respectively. The colors are assigned based on the taxonomy at genus level.

4.3 Abiotic Transport Studies

4.3.1 Influence of Aqueous Film Forming Foams on the Solubility and Mobilization of Non-Aqueous Phase Liquid Contaminants

The objectives of this study were to assess the potential for AFFF solutions to alter the aqueous solubility and migration of three representative NAPLs (JP-4, TCE and PCE) in two well-characterized quartz sands. Batch reactor experiments were conducted to (a) measure NAPL-water IFT reductions as a function of AFFF concentration, (b) determine relevant solution properties (i.e., density and viscosity), and (c) assess the effect of AFFF on the aqueous solubility of the NAPLs. Column experiments were then performed to establish residual NAPL saturations and measure the extent of NAPL mobilization in 20-30 mesh and 60-80 mesh Ottawa sand by a 3% wt. AFFF solution. For comparison purposes, a low-IFT anionic surfactant formulation commonly used in enhanced oil recovery (4% wt. Aerosol AY/OT) was also used as a displacing fluid. The observed NAPL desaturation curves were expressed as a function of the total trapping number (NT), which accounts for the effects of viscous and density forces on entrapped NAPLs and were used to obtain critical NT values corresponding to onset and complete NAPL mobilization.

4.3.1.1 NAPL Solubility

The solubilities of PCE and TCE in aqueous solutions of AFFF over a concentration range of 0 to 5% wt. (0 to 50,000 mg/L) are shown in **Figure 4.35**. In the case of PCE, the aqueous solubility in the absence of AFFF was 177 mg/L, which is consistent with reported values ranging from 150 to 200 mg/L at room temperature (21-25ºC) [313, 314]. When the AFFF concentration was increased up to 5% wt. (50,000 mg/L or 50 g/L), the measured PCE solubilities never exceeded 260 mg/L (**Figure 4.35b**), clearly demonstrating that AFFF has a minimal effect on the aqueous solubility of PCE over a wide concentration range. Similarly, the aqueous solubility of TCE in the background solution without AFFF was 1,191 mg/L and increased to only 1,401 mg/L at 5% wt. AFFF. For comparison purposes, previously measured solubilities of PCE and TCE in aqueous solutions of a common nonionic surfactant, Tween® 80 (polyoxyethylene (20) sorbitan monooleate), are also plotted in **Figure 4.35a**. The solubilities of PCE and TCE increased linearly above the critical micelle concentration (CMC) of Tween® 80, consistent with a micellar solubilization process, and yielded weight solubilization ratios (WSRs) of 0.91 and 1.74, respectively [38, 315]. For a Tween® 80 concentration of 5% wt., the aqueous solubilities of PCE and TCE were 45,500 mg/L and 85,800 mg/L, respectively, which are approximately 175 and 60 times greater than the concentrations of PCE and TCE measured in 5% wt. AFFF. These comparisons suggest that AFFF does not exhibit traditional surfactant micelle formation and solubilization of hydrophobic organic compounds (HOCs) over the concentration range considered. The relatively small increases in solubility observed for PCE and TCE, which have been reported for other HOCs at surfactant concentrations below the CMC [316], are likely due to associations between the dissolved organic species and surfactant monomers or disorganized aggregates.

4.3.1.2 NAPL-water interfacial tension

NAPL-water interfacial tensions measured for ten AFFF concentrations ranging from 0.0001% wt. (1 mg/L) to 10% wt. (100,000 mg/L) are shown in **Figure 4.36**. As the AFFF concentration was increased, NAPL-water IFT values decreased steadily to less than 1.5 mN/m for all three NAPLs, showing that the AFFF formulation was effective at reducing the NAPL-water interfacial tension. This observation is consistent with other studies which found that dissolved PFAS accumulate at

NAPL-water interface and thereby decreases the NAPL-water IFT [29, 30]. At an AFFF field application concentration of 3% wt. (30,000 mg/L), the IFTs for JP-4, PCE and TCE were 3.10, 3.00 and 1.98 mN/m, respectively. These values are below a critical IFT value of 5 mN/m that can potentially lead to mobilization of residual dodecane and PCE in unconsolidated porous media [37, 156]. The NAPL-water IFT data as a function of AFFF aqueous concentration (C) were fit to the Szyszkowski equation (3-1) using a nonlinear least square procedure (MATLAB, R2020a). The fit was performed over an AFFF concentration range of 1 mg/L to the inflection point (~10,000 mg/L), above which the change in IFT with increasing AFFF concentration was minimal. The fitted parameters, including NAPL-water interfacial tension (γ), component specific constant (a) and surface activity (b), are presented in **Table 4.11.** The maximum surface excess concentration (Γ_m) was then calculated using Equation (3-2). The surface concentration of AFFF at the NAPL-water interface as a function of the aqueous AFFF concentration was computed using the Langmuir-Szyszkowski equation (3-3).

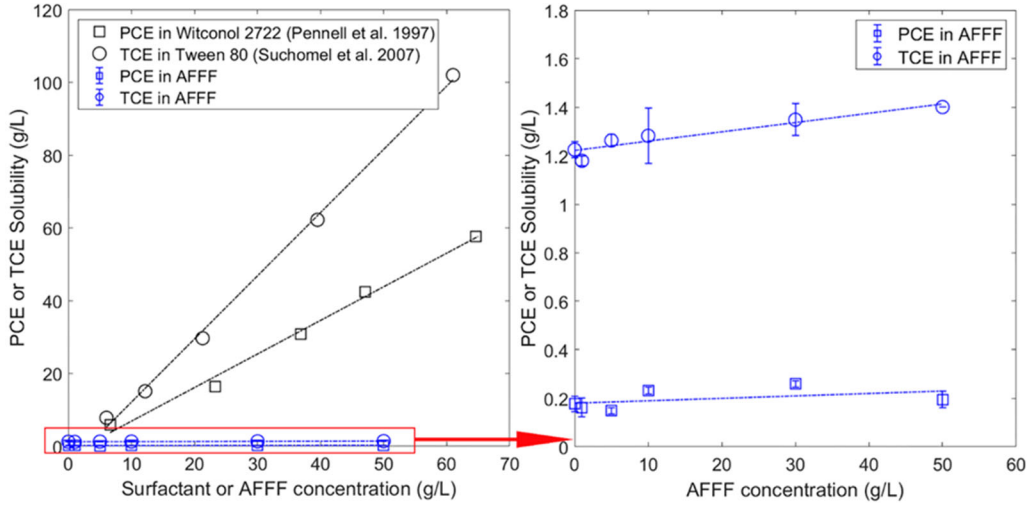


Figure 4.35 Equilibrium solubilities of PCE and TCE in aqueous solutions of AFFF over a concentration range of 0 to 50 g/L (5 % wt.). For comparison purposes, previously reported solubilities of PCE and TCE in aqueous solutions of a nonionic surfactant, Tween® 80, over a similar concentration range are also presented. Errors bars represent standard error of duplicate measurements.

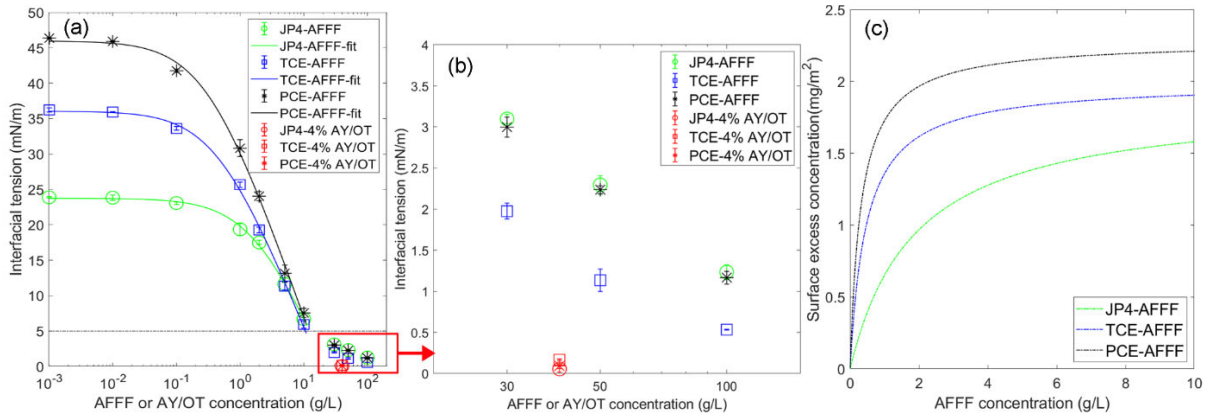


Figure 4.36 NAPL-water interfacial tensions for (a) JP4, TCE and PCE as a function of AFFF concentration; data fit to Szyszkowski equation (solid lines), (b) enlarged graph of interfacial tension data below 4 mN/m, and (c) corresponding surface excess concentrations at the NAPL-water interface obtained using Langmuir/Szyszkowski equation.

Table 4.11 Szyszkowski equation fitted parameters for NAPL-water interfacial tension data in the presence of AFFF.

	γ_0(mN/m)	*a*	*b* (mg/L)
JP4	23.7 (23.2,24.3)	0.3892 (0.2832,0.4952)	1874.6 (869.0, 2880.1)
TCE	36.0 (34.9, 37.2)	0.2723 (0.2182,0.3265)	467.0 (211.6,722.4)
PCE	46.0 (44.1,47.8)	0.2444 (0.1870,0.3018)	320.3 (93.9,546.7)

*assumes an average molecular weight of 500 g/mole for AFFF, based on the formula weight of PFOS, which is the predominant PFAS in the AFFF formulation. † The values in parentheses indicate 95% confidence interval of fitted parameters.

The resulting surface excess concentration (Γ) as a function of AFFF concentration is shown in **Figure 4.36c**. The maximum surface excess of AFFF at the NAPL-water interface, which ranges from approximately 1.7 to 2.3 mg/m^2, was reached at an AFFF concentration of approximately 1 % wt. (10,000 mg/L) for all three NAPLs. Accumulation of AFFF at the PCE-water interface was 1.2 and 1.3 times greater than that of TCE and JP4, respectively.

4.3.1.3 NAPL mobilization

Column experiments were conducted with two size fractions of Ottawa sand (20-30 mesh and 60-80 mesh) to evaluate the potential of AFFF to mobilize residual (entrapped) NAPLs at a field application concentration of 3 % wt. The columns were flushed with a sequence of three aqueous solutions; a background electrolyte (500 mg/L $CaCl_2$) to establish the initial residual saturation, followed by 3% wt. AFFF solution to assess mobilization of the residual NAPL, and finally 4% wt. 1:1 Aerosol AY/OT to achieve near complete mobilization of any remaining NAPL. The density, viscosity and IFT values for each displacing solution are provided in **Table 4.12**.

* values in parentheses represent standard error of three replicates. Measurements were conducted at room temperature (22 ± 1 ºC). † Pennell et al. [37] at 22 ºC

Following NAPL imbibition and displacement of free product with the 500 mg/L $CaCl_2$ solution, the entrapped NAPLs were observed visually as discrete droplets or 'globules' in the pore space, distributed uniformly along the length of column (**Figure 4.37**). In 20-30 mesh OS, the non-reactive tracer tests yielded initial saturations for JP-4, TCE and PCE of 13.0%,12.9% and 11.4% respectively, which are consistent with residual saturation values reported previously [37]. The relative water permeabilities (k_{rw}) of the packed columns ranged from 0.37 to 0.43 after establishment of residual NAPL. Upon the injection of 3 PVs of 3% wt. AFFF solution, all three NAPLs were partially mobilized and a separate organic liquid phase was observed in the column effluent. Macroemulsion formation was not observed in any of the effluent samples collected during the 3% wt. AFFF flush (**Figure 4.38**) and the pressure remained relatively constant during NAPL displacement. A second non-reactive tracer test (**Figure 4.39**) indicated that the residual saturations were reduced by 0.7% for JP4, 1% for PCE and 2% for TCE following the injection of 3% wt. AFFF. TCE exhibited the greatest reduction in saturation after the AFFF flush, which was attributed to lower interfacial tension (1.98 mN/m) compared to JP-4 and PCE (~3 mN/m). For the 60-80 mesh OS, the initial NAPL saturations were 14.9%, 16.4%, 17.6% for JP-4, PCE and TCE, respectively. These larger values are attributed to the finer grain size of the sand.

Table 4.12 Properties of the displacing fluids and porous media used in the NAPL mobilization column studies

Displacing fluids						Porous media	
	ρ (g/cm^3)	μ (cP)	IFT (mN/m)				k_i(m^2)
			JP-4	TCE	PCE		
500 mg/L $CaCl_2$	1.000 (0.001) *	0.98 (0.01)	24.15 (0.04)	35.75 (0.04)	46.35 (0.05)	20-30 mesh Ottawa Sand	1.80×10^{-11}
3% wt. AFFF	1.030 (0.002)	1.20 (0.02)	3.10 (0.06)	1.98 (0.10)	3.00 (0.12)		
4% wt. 1:1 Aerosol AY/OT	1.027† (0.005)	1.19† (0.04)	0.05 (0.04)	0.17 (0.01)	0.09 (0.03)	60-80 mesh Ottawa sand	7.05×10^{-12}

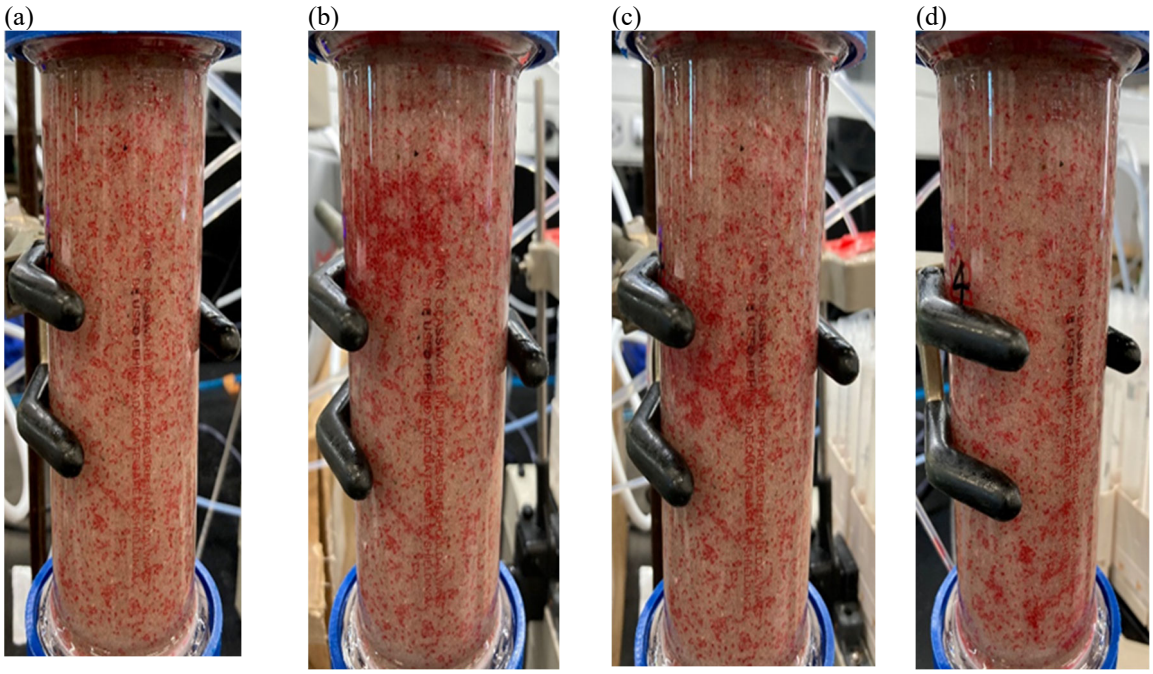


Figure 4.37 Vertical (downward) mobilization of TCE in 20-30 mesh Ottawa sand with 3% wt. AFFF as the displacing fluid: (a) prior to AFFF flush; (b) after injection of 0.8 PVs of 3 wt. % AFFF solution (TCE moved downward and formed a bank); (c) after injection of 1.5 PVs of 3 wt. % AFFF solution, (TCE continued to migrate downward); (d) after injection of 3 PVs of 3% wt. AFFF solution.

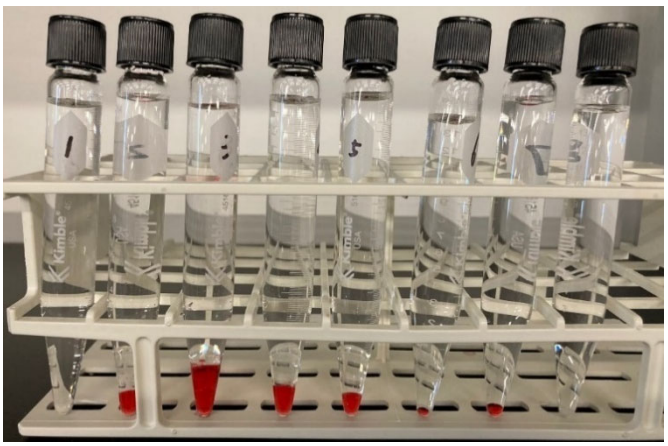


Figure 4.38 Effluent samples showing TCE-DNAPL displaced by 3% wt. AFFT from column shown in Figure S1. Collection time (pore volumes) for each tube (left to right): 0.74, 0.89, 1.05, 1.17, 1.32, 1.47, 1.62, 1.77 PV.

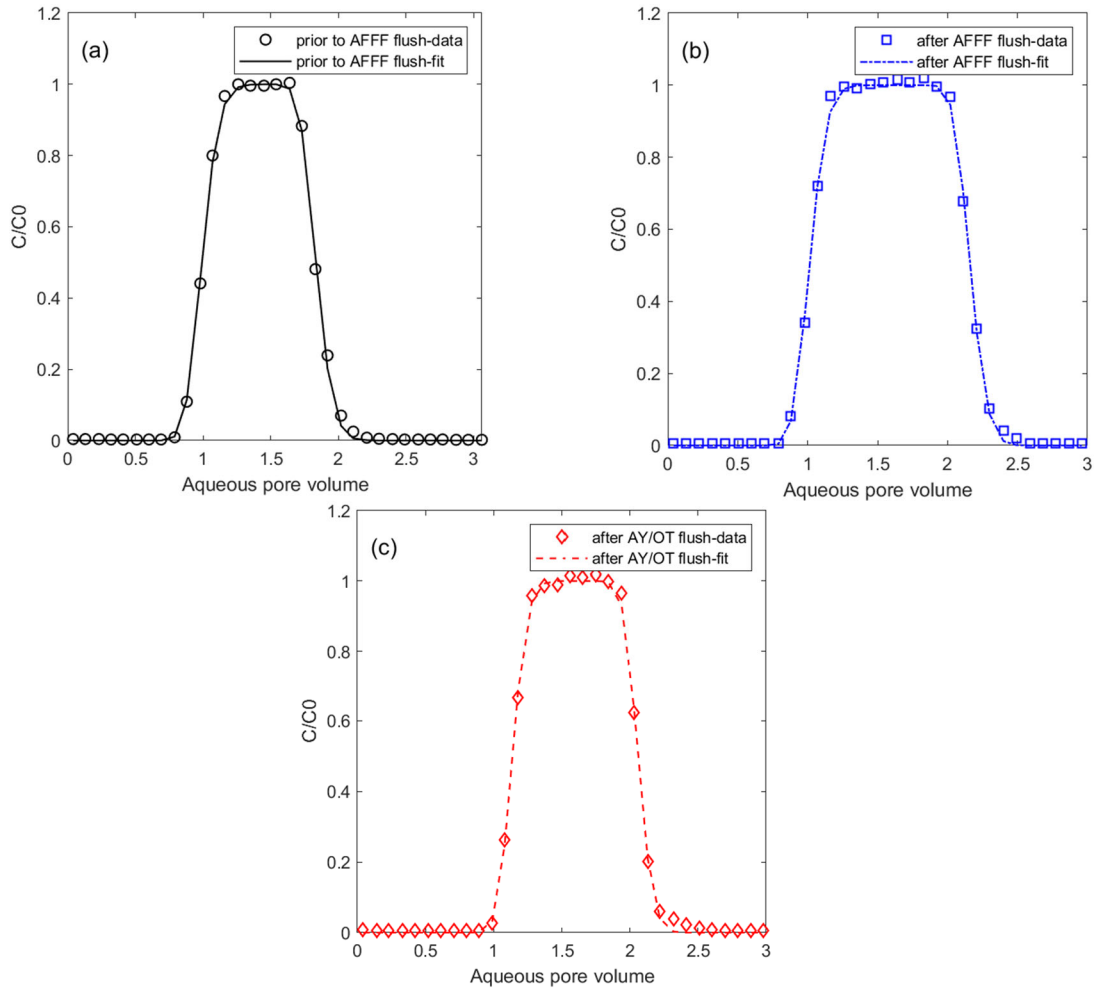


Figure 4.39 Representative non-reactive tracer test showing effluent breakthrough curves obtained for bromide before and after flushing with a displacing fluid: (a) after 500mg/L CaCl2 flush, prior to AFFF flush, (b) after AFFF flush and (c) after AY/OT flush. Note the delayed tracer breakthrough after the AFFF flush(b) and AY/OT flush(c) since NAPL was displaced from the column and water pore volume was increased.

Following injection of 3% wt. AFFF, the saturations of JP-4, PCE and TCE were reduced by 0.3%, 1.3% and 1.2%, respectively. The observed partial displacement of residual NAPL by 3% AFFF is not consistent with the findings of [317], who reported the formation of viscous emulsions and column plugging after injecting a 3% wt. AFFF-1 solution into OK -75 sand columns containing Jet A fuel at residual saturations of 23.8 and 31.5%. This disparity in results could be attributed to several factors, including differences in the AFFF formulation, which had a much lower CMC in the study (60 mg/L versus 3,000 mg/L), higher residual NAPL saturations, and used a lower permeability sand [317].

In the final phase of each experiment, the columns were flushed with 3 to 4 PVs of the low-IFT surfactant solution, 4% Aerosol AY/OT, which has been shown to achieve nearly complete mobilization of PCE from quartz sands [37]. Consistent with prior experiments, the 4% Aerosol AY/OT flush displaced most of the remaining NAPL from both the 20-30 mesh and 60-80 mesh

OS columns (**Figure 4.40** and **Figure 4.41**), with final NAPL saturations below 1.2% for all cases based on the third and final non-reactive tracer test results (**Figure 4.39)**. During NAPL displacement with 4% Aerosol AY/OT, the pressure increased only slightly (< 9 mbar). The initial residual saturation of JP-4, TCE and PCE, and changes after each sequential solution injection, are summarized in **Table 4.13**.

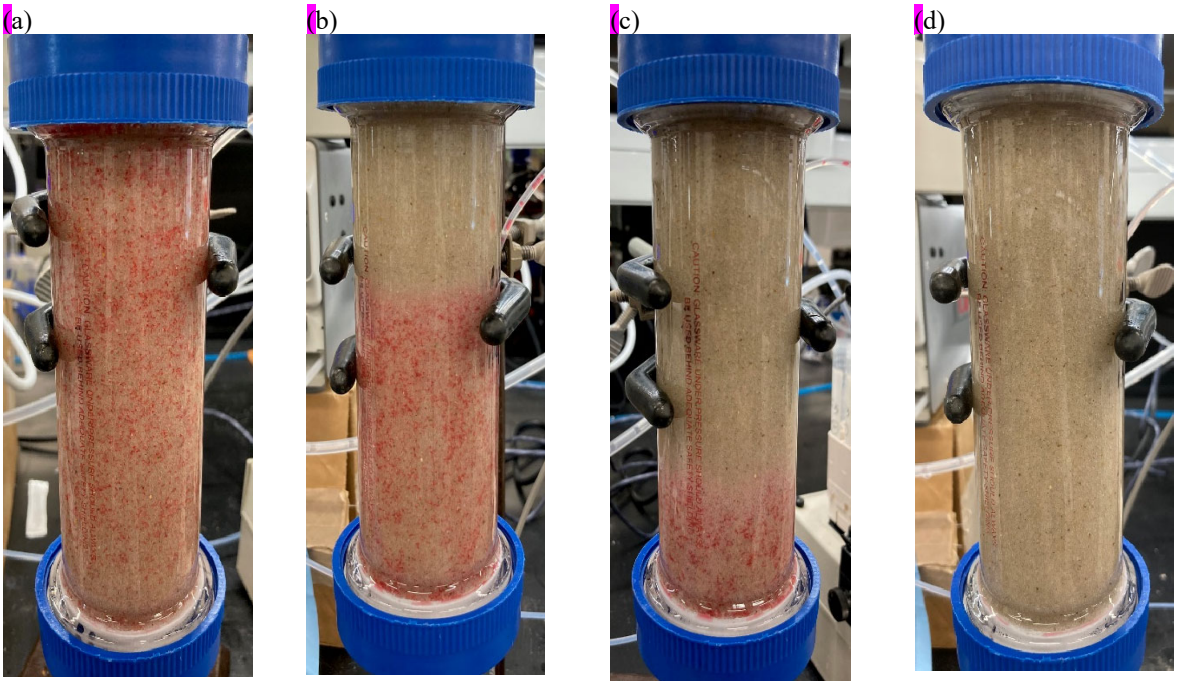


Figure 4.40 Vertical (downward) mobilization of TCE-DNAPL in 20-30 mesh Ottawa sand with 4% wt. Aerosol AY/OT solution as the displacing fluid: (a) prior to Aerosol AY/OT flush; (b) after injection of 0.5 PVs of 4% wt. Aerosol AY/OT solution (TCE moved downward and formed a bank); (c) after injection of 0.9 PVs of 4% wt. Aerosol AY/OT, (TCE continued to migrate downward); (d) after injection of 1.5 PVs of 4% wt. Aerosol AY/OT solution.

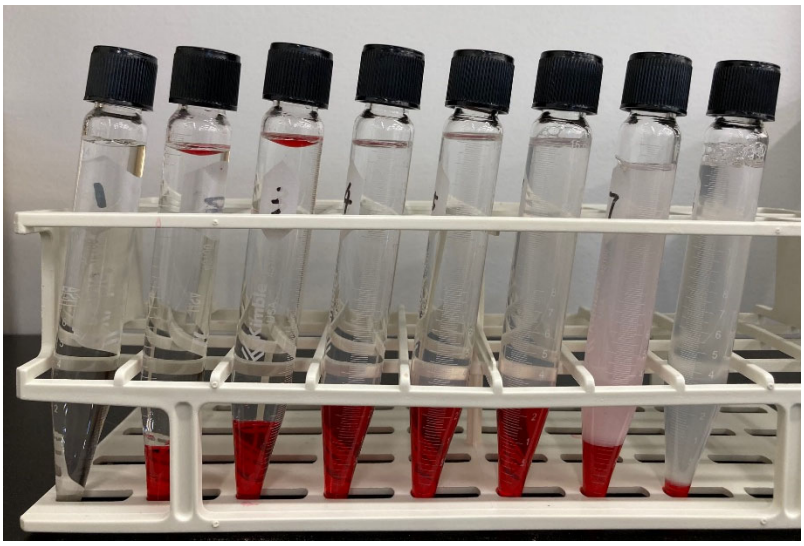


Figure 4.41 Effluent samples showing TCE-DNAPL displaced by 4% wt. Aerosol AY/OT solution from column shown in Figure S3. Collection time (pore volumes) for each tube (left to right): 0.33, 0.48, 0.63, 0.79, 0.94, 1.09, 1.24, 1.39 PV.

Table 4.13 Residual saturations of JP-4, TCE and PCE in 20-30 mesh and 60-80 mesh Ottawa sand following sequential injection of background electrolyte (500 mg/L $CaCl_2$), 3% wt. AFFF, and 4% wt. 1:1 Aerosol AY/OT solutions.

	Porous Media	NAPL saturation after 500 mg/L $CaCl_2$ solution (%)	NAPL saturation after 3% wt. AFFF (%)	NAPL saturation after 4% wt. AY/OT (%)
JP4	OS 20-30 mesh	13.0 (0.7) *	12.3 (0.5)	0.4 (0.0)
	OS 60-80 mesh	14.9 (0.2)	14.6 (0.4)	0.7 (0.3)
TCE	OS 20-30 mesh	13.0 (0.2)	11.1 (0.4)	0.8 (0.2)
	OS 60-80 mesh	17.6 (0.0)	16.4 (0.4)	1.2 (0.1)
PCE	OS 20-30 mesh	12.1 (0.6)	11.2 (0.5)	0.7 (0.2)
	OS 60-80 mesh	16.4 (0.2)	15.1 (0.4)	0.4 (0.0)

* values in parenthesis represent the standard error of duplicate or triplicate column experiments.

4.3.1.4 NAPL desaturation curves

In order for mobilization of residual NAPL to occur, the viscous and buoyancy forces must exceed the capillary forces acting to retain the NAPL droplet in the pore space. This balance of forces can be described using the total trapping number (N_T) [37]:

$$N_T = \sqrt{N_{Ca}^2 + 2N_{Ca}N_B \sin\alpha + N_B^2} \quad (4\text{-}9)$$

where α is the angle of aqueous-phase flow relative to the horizontal axis. Here, the capillary number (N_{Ca}) and Bond number (N_B) are defined as:

$$N_{Ca} = \frac{q_w \mu_w}{\gamma \cos\theta}, N_B = \frac{\Delta\rho g k k_{rw}}{\gamma \cos\theta} \quad (4\text{-}10)$$

where q_w is the Darcy velocity of the aqueous phase (upward direction is taken as positive), μ_w is the dynamic viscosity of the aqueous phase, γ is the interfacial tension between the organic and aqueous phases, θ is the contact angle between the aqueous and solid phases, $\Delta\rho$ is the difference between the aqueous and organic phase densities ($\rho_w - \rho_o$), g is the gravitational constant, k is the intrinsic permeability of the porous medium, and k_{rw} is the relative permeability of the aqueous phase. For the case of vertical flow (α = 90º) in the direction of the buoyancy (gravity) force, Equation (4-9) reduces to:

$$N_T = |N_{Ca} + N_B| \quad (4\text{-}11)$$

Total trapping number (N_T) values were computed for JP-4, TCE and PCE using the measured properties of displacing fluids (**Table 4.12**) and porous media (here the contact angel θ was assumed to be 0). The NAPL desaturation curves were then expressed in terms of total trapping number as shown in **Figure 4.42.** NAPL residual saturation data as a function of the total trapping number were fit to the van Genuchten equation [134] using MATLAB nonlinear regression function *nlinfit:*

$$s = s_r + \frac{s_i - s_r}{[1 + (\alpha N_T)^n]^{1-1/n}} \quad (4\text{-}12)$$

Here, s is the NAPL saturation, s_i is the NAPL residual saturation prior to any surfactant flush, s_r is the residual saturation after AY/OT flush. N_T is the total trapping number. α and n are fitting parameters. This approach is derived from previously reported estimation methods of NAPL retention in porous medium [318, 319].

For JP-4, mobilization of residual NAPL occurred at an N_T value of approximately 2×10^{-5} for both 20-30 mesh and 60-80 mesh OS, with nearly complete mobilization observed at a value of 1×10^{-3}. Similar results were obtained for TCE and PCE desaturation curves. In the case of PCE, the desaturation curves are consistent with earlier findings in the same porous media, which showed that the threshold value of N_T required for the onset of PCE mobilization was approximately 2×10^{-5}, while nearly complete displacement of PCE was observed when N_T exceeded 1×10^{-4}. Note that, consistent with multiphase fluid flow theory, if NAPL and AFFF are co-released to the subsurface, the consequent reduction in NAPL-water IFT (capillary forces) would not only reduce entrapped saturations, but would be expected to increase the propensity for NAPL spreading, since capillary forces act to counteract the onset of gravity and textural fingering [320, 321], reduce spreading at the water table [322], and limit penetration into lower permeability lenses [322, 323]. Enhancement of penetration into finer textured media, could be particularly concerning in the context of aquifer remediation. For example, based on the approach of [324], the thickness of a TCE-DNAPL pool necessary for entry into a layer of porous media with a hydraulic conductivity (K_{sat}) of 0.001 cm/s and a porosity (n) of 0.3 would be reduced from approximately 100 to 6 cm for an interfacial tension reduction of 35 (water) to 2 mN/m (3% wt. AFFF) (**Figure 4.36**).

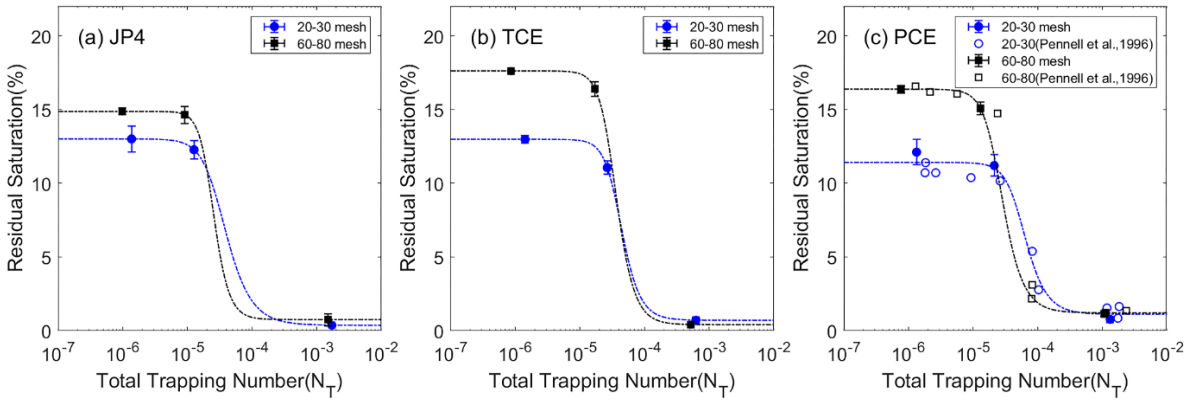


Figure 4.42 NAPL desaturation curves for (a) JP-4, (b) TCE and (c) PCE in 20-30 mesh and 60-80 mesh Ottawa sand expressed in terms of the total trapping number (N_T). The solid data points represent measured NAPL saturations obtained for the three displacing solutions: 500 mg/L $CaCl_2$, 3% wt. AFFF and 4% wt. Aerosol® AY/OT solutions. The open data points shown in (c) are results from previous study using 4% Tween® 80 and Aerosol® surfactants [37]. Errors bars represent standard error of duplicate or triplicate column experiments.

4.3.1.5 Concluding remarks

This study was designed to investigate interactions between AFFF and three representative NAPLs (JP-4, TCE and PCE), and to assess the potential for AFFF to enhance the solubility and mobility of NAPLs in porous media. In this work, relatively high concentrations of AFFF were employed to simulate conditions at or near a fire training facility or fire response, where operational concentrations of 3 to 6% wt. AFFF were typically applied. Batch reactor tests indicated that presence of AFFF increased the solubility of TCE and PCE by no more than 50% at concentrations up to 5% wt. (50,000 mg/L). When compared to a representative nonionic surfactant (Tween® 80), which yielded PCE and TCE solubilities of 45,500 mg/L and 85,800 mg/L in 5% wt., the effects of AFFF on solubility are relatively minor. These findings also suggest that AFFF does not form traditional surfactant micelles (i.e., oil in water microemulsions) in aqueous solution over the concentration range investigated. Interfacial tension measurements revealed that AFFF accumulates at the NAPL-water interface and can result in IFT reductions below 3 mN/m at a field application concentration of 3% wt. AFFF. Column experiments were then conducted to determine if the observed IFT reductions were sufficient to mobilize three NAPLs (JP-4, TCE and PCE) at residual (entrapped) saturation. Partial mobilization of all three NAPLs was observed following the injection of 3% wt. AFFF solution, which resulted in NAPL saturation reductions of 0.7-2.0% and 0.3-1.3% in 20-30 mesh and 60-80 mesh Ottawa sands, respectively. Using the density, viscosity and interfacial tension measurements of the displacing solutions and porous media properties, the total trapping number (N_T) was used to construct NAPL desaturation curves, which showed that the onset of NAPL mobilization occurred when the value N_T exceeded approximately 1×10^{-5} and that nearly complete mobilization corresponded to N_T values greater than 1×10^{-4}. These results demonstrate that, for a field application concentration of AFFF (3% wt.), partial mobilization and redistribution of NAPLs may occur, and that the total trapping number approach can be used to estimate, *a priori*, the extent of NAPL mobilization that may occur based on site specific conditions. Given the importance of capillary forces in the migration of NAPLs, these IFT reductions in the presence of AFFF would also be expected to alter the accumulation and

distribution of NAPL free product, increasing penetration into low permeability media.

4.3.2 Influence of Residual Nonaqueous-Phase Liquids (NAPLs) on the Transport and Retention of Perfluoroalkyl Substances

4.3.2.1 PFAS accumulation at the PCE-NAPL water interface.

The IFT between PCE-NAPL and aqueous solutions containing individual PFAS and mixtures of PFAS are shown in **Figure 4.43a** as a function of PFAS concentration. Among the six individual PFAS, PFOS displayed the greatest interfacial tension reduction, followed by PFNA, PFOA, PFHxS, PFHpA and PFBS, consistent with previous findings and further confirming that both PFAS C-F chain length and functional group govern interfacial accumulation.[78, 325, 326] The IFT curves for the mixture of six PFAS exhibited interfacial tension reductions that were similar to those obtained for solutions containing PFOS and PFNA alone, indicating that the more surface active PFAS controlled the behavior of the mixture. Fitted IFT parameters (3-1) are listed in **Table 4.14** and calculated surface excess data (3-3) are plotted in **Figure 4.43b**.

A NAPL-water interfacial partition coefficient (K_i, cm) for individual PFAS can be defined as:

$$\mathrm{K}_i = \frac{\Gamma}{C} \tag{4-13}$$

Computed K_i values for the PFAS are presented in **Figure 4.43c**. For individual PFAS over the concentration range of 0 to 1 mg/L, K_i was nearly constant for all 6 PFAS compounds investigated, and PFAS accumulation increased linearly as a function of the PFAS aqueous phase concentration (**Figure 4.43b**). Here, PFOS exhibited greatest surface excess, approximately 2, 5, and more than 10 times greater than the surface excess obtained for PFNA, PFOA, PFHxS and the short C-F chain length PFAS (i.e., PFHpA, PFBS), respectively.

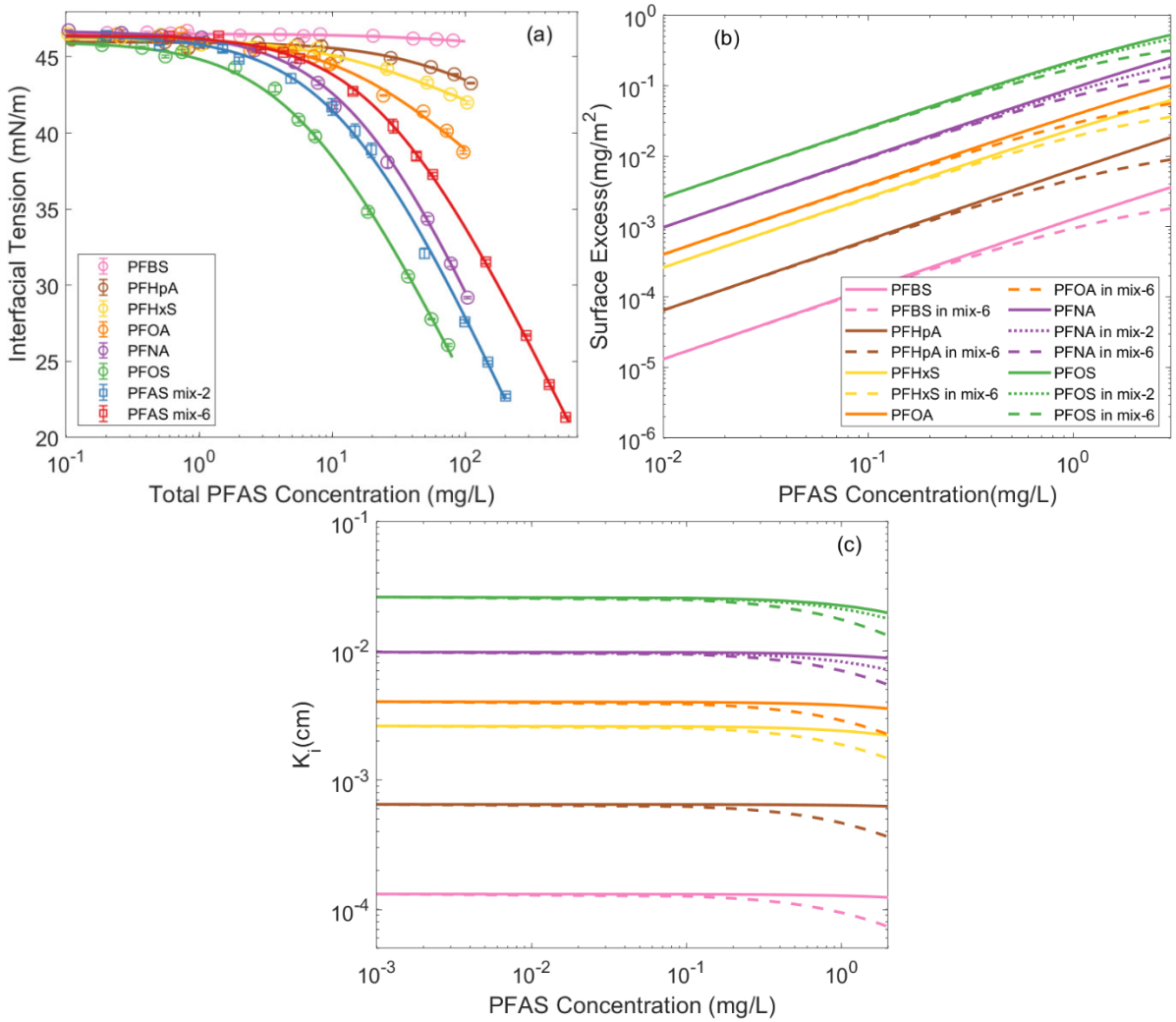


Figure 4.43 Interfacial tension (a) and corresponding surface excess (b) and interfacial partition coefficient (K_i) (c) of PCE-NAPL and solutions containing individual PFAS, a 1:1 mixture of PFNA and PFOS (PFAS mix-2), and a mixture of six PFAS (PFAS mix-6). Error bars in (a) indicate standard deviations in triplicate measurements.

The calculated surface excess and K_i values for each PFAS in the mixture solutions are also presented in **Figure 4.43 b** and **c** (dashed lines, 0-1 mg/L concentration range) and **Figure 4.44** (0-100 mg/L concentration range). When PFAS aqueous concentrations are less than 0.2 mg/L and 0.5 mg/L, the surface excess curves and K_i values of PFAS in single-solute solutions are nearly identical to those in the mix-6 and mix-2 solutions, respectively, suggesting that competitive interfacial adsorption effects among PFAS are minimal at these concentrations. Similar findings were reported by Silva et al,[125] who found calculated air-water interfacial concentrations of PFAS in a mixture were similar to corresponding single component values at low concentrations. However, when PFAS concentrations exceeded 0.2 mg/L in mix-6 or 0.5 mg/L in mix-2, PFAS calculated surface excess decreased compared to that in single solute solutions. For example, based on Equations (3-3) and (3-5), the surface excess of PFOS decreased from 0.22 mg/m^2 to 0.21 mg/m^2 in mix-2, and further decreased to 0.17 mg/m^2 in mix-6 even though the PFOS concentrations were the same in these solutions (1 mg/L, **Figure 4.43b**). These findings suggest

that competitive adsorption can lead to reduced PFAS accumulation at the NAPL-water interface when the total aqueous PFAS concentration of the mixture is greater than some critical concentration. As shown in **Figure 4.43c**, nonlinear interfacial adsorption behavior of PFAS in mixed solutions also becomes apparent (i.e., decreasing K_i) as PFAS aqueous concentrations increase. The critical concentration obtained for mix-2 and mix-6 are within the range of PFAS concentrations observed at AFFF field sites,[4, 42] indicating that both competitive effects and nonlinear adsorption at the NAPL-water interface should be accounted for when describing PFAS fate and transport in AFFF-impacted source zones.

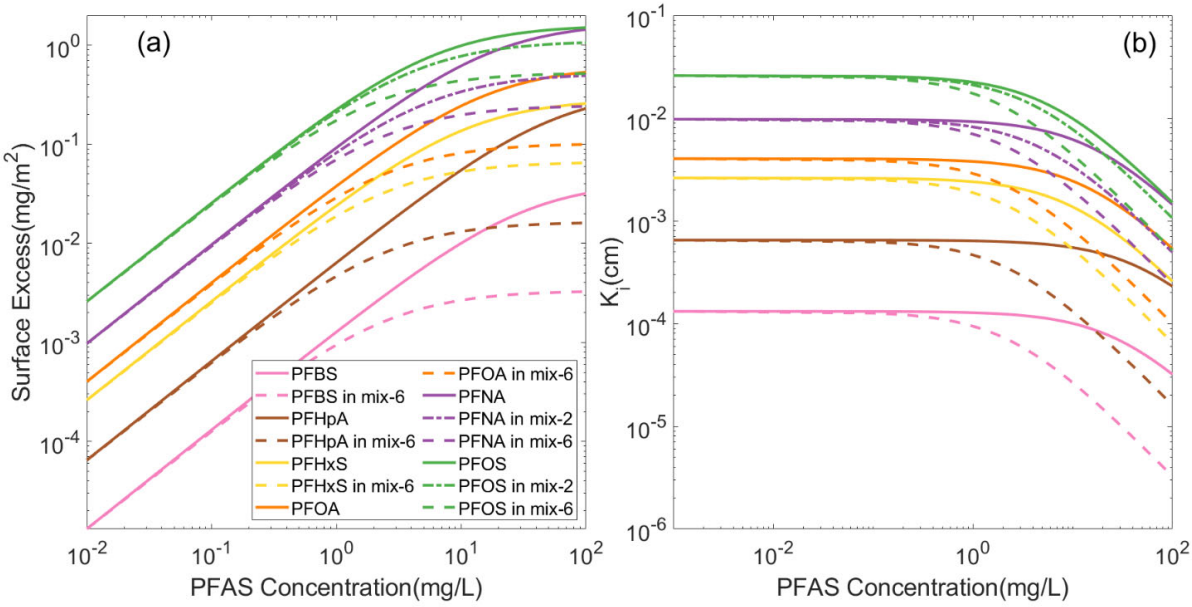


Figure 4.44 (a) Surface excess (Γ) and (b) interfacial partition coefficient (K_i) of PFAS as single solute and in the PFAS mixtures over a concentration range of 0-100 mg/L.

4.3.2.2 PFAS Partitioning into PCE-NAPL

Measured PFAS distributions between the aqueous and PCE-NAPL phases are presented in **Figure 4.45**. PFAS uptake by PCE-NAPL was linear with increasing aqueous PFAS concentration, consistent with a partitioning process. PFOS exhibited a NAPL-water partition coefficient K_{nw} of 0.098, which is approximately twice as large as the value obtained for PFNA (K_{nw} = 0.048). The K_{nw} values obtained for PFOA, PFHpA, PFHxS, and PFBS in mix-6 ranged from 0.028 to 0.034. Notably, the partitioning isotherms obtained for PFOS and PFNA alone and those from mix-6 were similar, suggesting that the presence of other PFAS compounds had minimal effect on PFOS and PFNA partitioning behavior, consistent with a phase partitioning process. McKenzie et al.[9] and Guelfo et al.[10] measured K_{nw} for a suite of PFAS with TCE or decane using a single concentration (2 µg/L and 500 µg/L, respectively). Their reported K_{nw} values for PFOA and PFOS were generally one order of magnitude greater than those measured in this study. However, all of their K_{nw} values have large 95% confidence intervals (CI) that overlap with those obtained here (**Table 4.14**). For example, their reported K_{nw} value for PFOS in TCE-NAPL was 0.95 (CI, -0.72 to 2.6), while the

measured K_{nw} for PFOS in PCE-NAPL in this work was 0.098 (CI, 0.091 to 0.104). Several additional factors can impact PFAS partitioning into NAPL, such as solution pH, water/NAPL ratio, and NAPL source. Glubt and Brusseau also investigated the partitioning of PFOA and PFOS into decane and TCE. [41] Their K_{nw} values (0.022-0.19) are in close agreement with the K_{nw} values reported herein, as both studies were conducted using synthetic groundwater with similar composition (ionic strength ~10 mM and pH ~7.5). These K_{nw} magnitudes indicate that partitioning of these PFAS into PCE-NAPL is likely to be minimal under most environmentally relevant conditions.

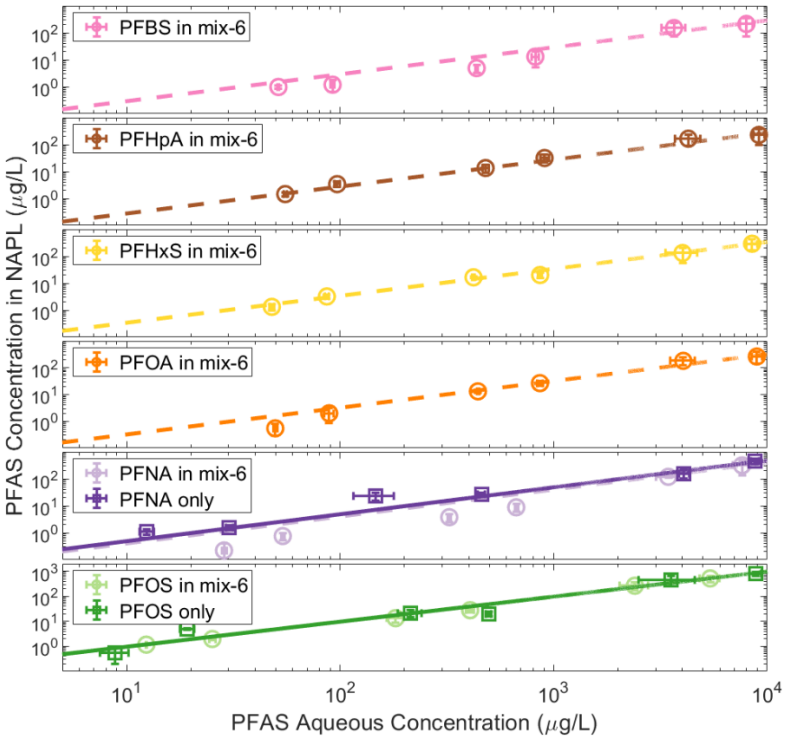


Figure 4.45 PFAS partitioning isotherms into PCE-NAPL. The dashed lines indicate PFAS partitioning isotherm in mix-6, the solid lines are PFNA only and PFOS only partitioning isotherms. Error bar indicates standard deviations in triplicate measurements.

Table 4.14 Fitted NAPL-water partitioning coefficients (K_{nw}) for PFNA, PFOS and 6 PFAS compounds in the mixture.

Compound	K_{nw}	R^2
PFNA only	0.0487 (0.0428,0.0546)	0.9436
PFOS only	0.0966 (0.0830,0.1103)	0.9414
PFBS in PFAS mix-6	0.0291 (0.0226,0.0356)	0.9983
PFHpA in PFAS mix-6	0.0276 (0.0215,0.0336)	0.9492
PFHxS in PFAS mix-6	0.0340 (0.0327,0.0353)	0.9893
PFOA in PFAS mix-6	0.0321 (0.0255,0.0388)	0.9947
PFNA in PFAS mix-6	0.0402 (0.0362,0.0443)	0.9839
PFOS in PFAS mix-6	0.0976 (0.0909,0.1043)	0.9778

*The values in parenthesis are the 95% confidence interval for the fitted parameters.

4.3.2.3 PFAS Adsorption on Ottawa sand

Sorption results for PFAS on 60-80 OS are presented in **Figure 4.46** and **Figure 4.47**. Due to the limited surface area (2×10^{-3} m^2/g) and low organic carbon content (f_{oc} = 0.00025 g OC/g) of the sand, sorption of PFAS was minimal. The sorption of short chain length PFAS (i.e., PFBS, PFHpA), PFHxS and PFOA was so small that analytical variability resulted in poor model fits (**Figure 4.47a-d**). For PFNA and PFOS sorption (**Figures Figure 4.46, Figure 4.47e-f**), both the linear and Freundlich isotherm models provided good fits to the measured data (adjusted R^2 > 0.85). Since the concentrations used in the column studies were in the linear range (≤ 100 ug/L), a linear isotherm was employed in the numerical model. As single solutes, PFOS exhibited a greater affinity for the solid phase than PFNA, with K_d values of 5.8×10^{-5} and 2.7×10^{-5} L/g, respectively (**Table 4.15**). For the PFAS mixture, the adsorption of PFBS, PFHpA, PFHxS and PFOA was minimal and K_d values ranged from 2.3×10^{-6} to 6.7×10^{-6} L/g (**Table 4.15**). K_d values obtained for PFOS and PFNA from the PFAS mixture were similar (5.2×10^{-5} and 2.8×10^{-5} L/g) to those obtained for the single solute experiments (**Table 4.15**), indicating other PFAS had minimal impact on PFNA and PFOS sorption over the concentration range investigated. Taken in concert, these data indicate that 60-80 OS has a low sorption capacity for PFAS, and that competitive effects are minimal under these experimental conditions (synthetic ground water, PFAS concentration range of 0 – 1,000 µg/L).

Model simulations of control column experiments for PFNA and PFOS transport in the absence of PCE-NAPL (**Figure 4.48, Figure 4.49,Figure 4.50e-f**) revealed that fitted K_d values were approximately 2-3 times smaller than batch-fitted K_d values. Guelfo et al.[115] reported a similar discrepancy between batch and column derived K_d values for long chain PFAS, including PFNA and PFOS, and suggested that non-equilibrium adsorption could account for the observed differences. Based upon the higher uncertainty associated with batch sorption measurements (**Figure 4.46** and **Figure 4.47**) and evidence of non-equilibrium sorption for PFOS in mixtures (**Figure 4.49b, Figure 4.50f**), column-fitted sorption parameters were employed herein for prediction of PFAS BTCs in the presence of PCE-NAPL.

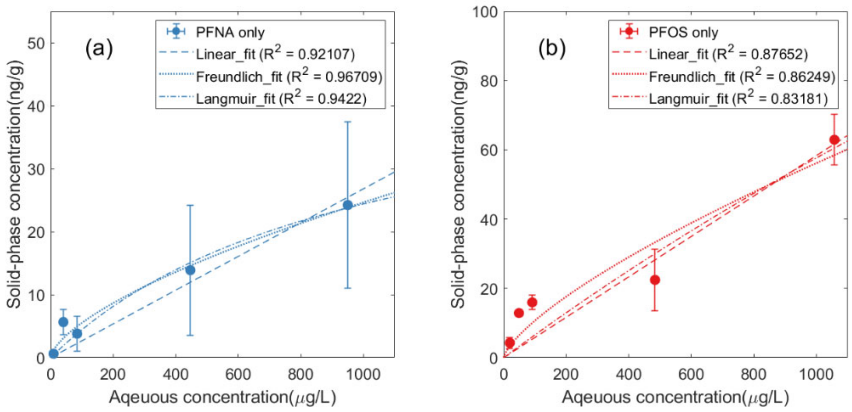


Figure 4.46 Single component (a) PFNA and (b) PFOS adsorption data for 60-80 mesh OS. Data were fit with the linear, Freundlich and Langmuir isotherm models.

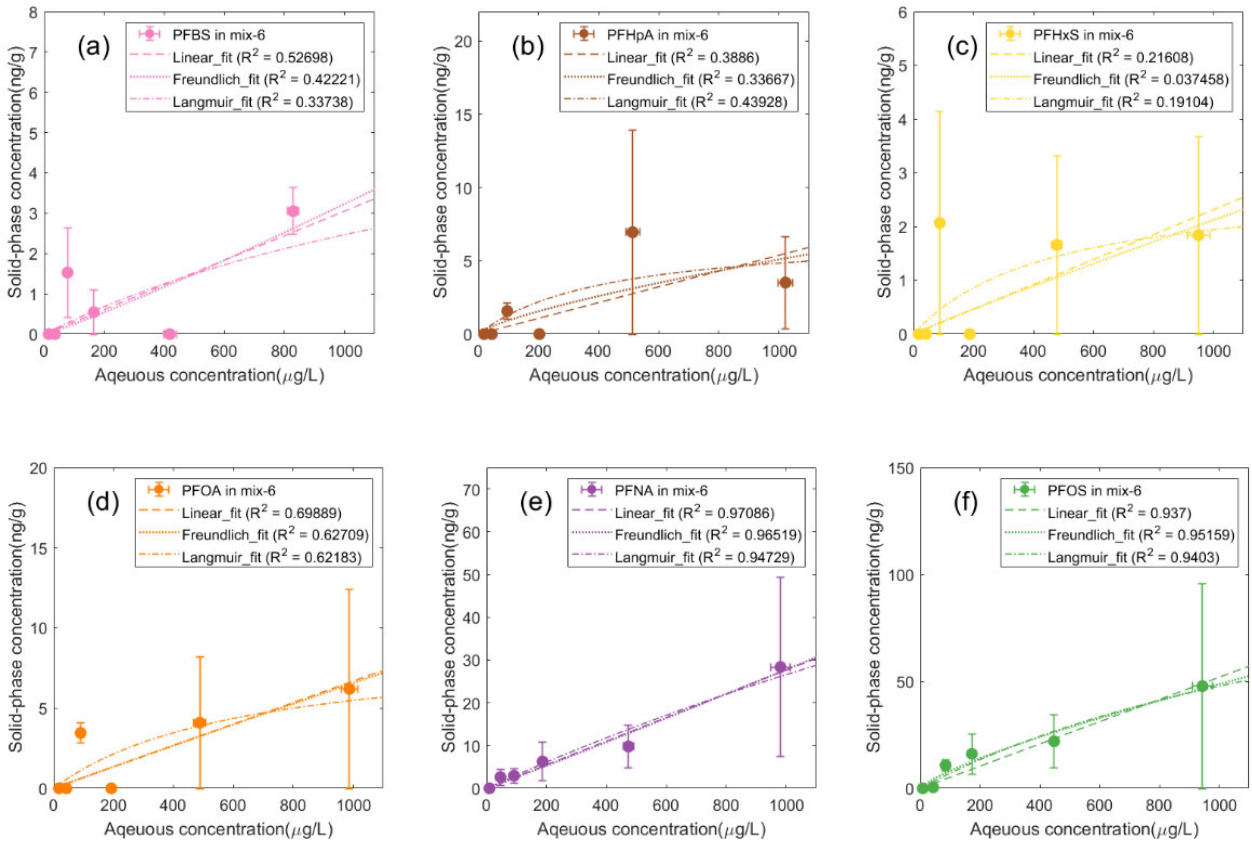


Figure 4.47 Solid phase adsorption data for (a) PFBS, (b) PFHpA, (c) PFHxS, (d)PFOA, (e) PFNA and (f) PFOS in solutions containing mixtures of 6 PFAS. Data were fit with the linear, Freundlich and Langmuir isotherm models.

Table 4.15 Fitted *Kd* values obtained from batch reactor and control column experiments.

		Batch fitted Kd(L/g)			[2]Eq-Column fitted Kd(L/g) (Column fitted Kd assuming equilibrium sorption)			[3]Neq-Column fitted Kd(L/g) (Column fitted Kd assuming non-equilibrium/rate-limited sorption)			Batch-vs Eq-column fitted Kd	Batch-vs Neq-column fitted Kd
		mean	lower 95%	upper 95%	mean	lower 95%	upper 95%	mean	lower 95%	upper 95%	Z-test[327] p-value	Z-test p-value
PFNA only	PFNA	2.68E-05	1.98E-05	3.38E-05	1.10E-05	8.40E-06	1.50E-05				0.00	
PFOS only	PFOS	5.83E-05	3.92E-05	7.74E-05	4.30E-05	3.90E-05	4.60E-05				0.03	
PFAS mix-2	PFNA	NA1	NA	NA	2.80E-05	2.40E-05	3.10E-05				NA	
	PFOS	NA	NA	NA	6.90E-05	6.60E-05	7.30E-05	7.60E-05	7.10E-05	8.10E-05	NA	NA
PFAS mix-6	PFBS	3.05E-06	7.57E-07	5.35E-06	4.10E-6	3.46E-07	7.84E-06				0.61	
	PFHpA	5.38E-06	5.63E-07	1.02E-05	3.48E-06	0	7.08E-06				0.46	
	PFHxS	2.31E-06	1.64E-07	4.46E-06	3.82E-06	1.60E-07	7.48E-06				0.45	
	PFOA	6.68E-06	3.33E-06	1.00E-05	4.86E-06	1.35E-06	8.37E-06				0.40	
	PFNA	2.76E-05	2.35E-05	3.17E-05	9.90E-06	6.20E-06	1.40E-05				0.00	
	PFOS	5.19E-05	4.11E-05	6.27E-05	4.60E-05	4.30E-05	5.00E-05	4.20E-05	3.40E-05	5.00E-05	0.19	0.08

[1]NA: not applicable. [2] All R2 values for equilibrium model-fitted columns are greater than 0.96. [3]All R2 values for non-equilibrium model-fitted columns are greater than 0.99.

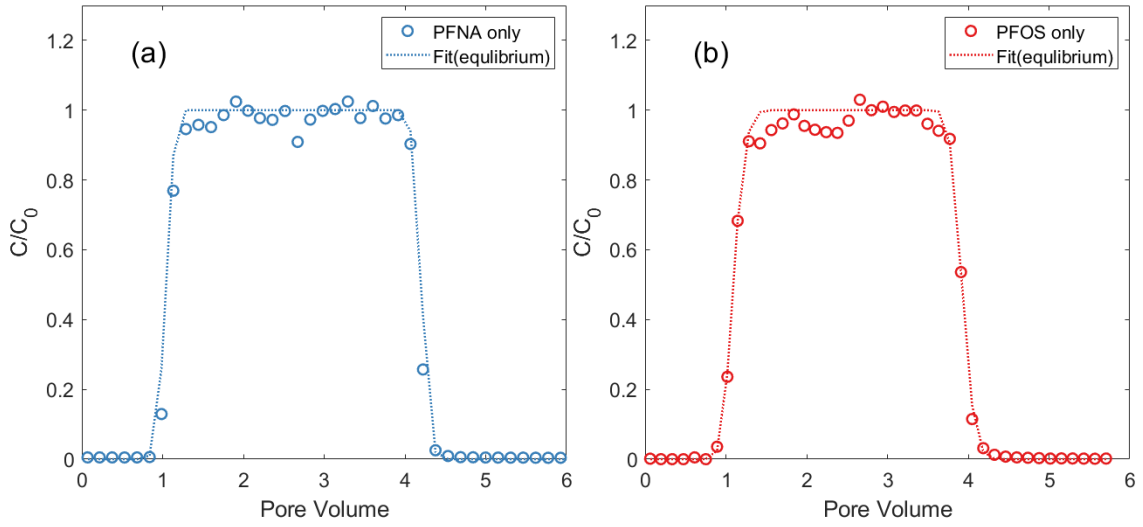


Figure 4.48 Breakthrough curves obtained for (a) PFNA only and (b) PFOS only in control columns (no PCE-NAPL). Data were fit with either the linear/equilibrium or linear/non-equilibrium solid phase adsorption models.

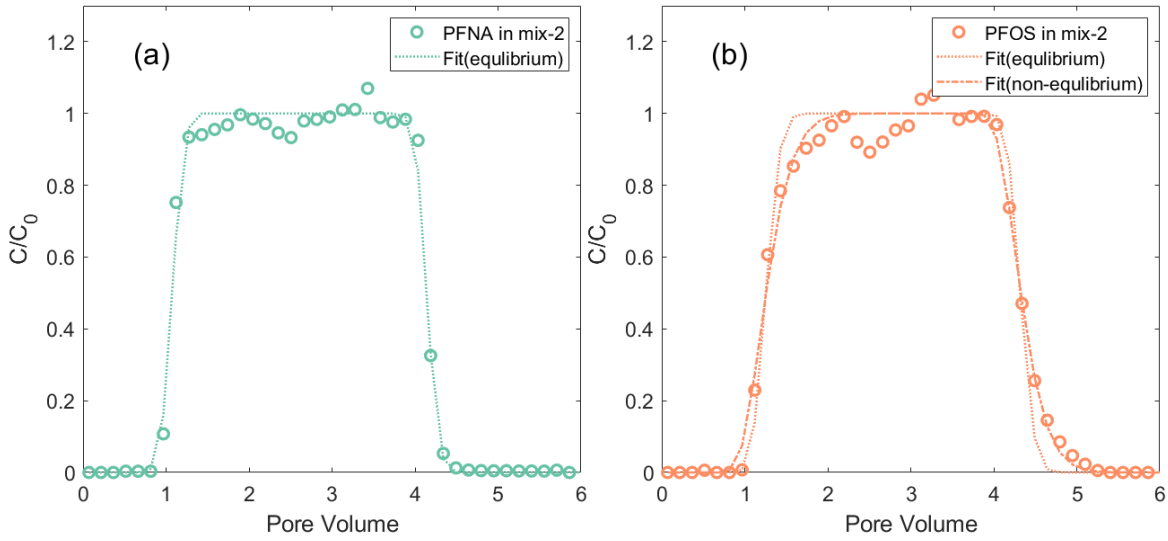


Figure 4.49 Breakthrough curves obtained for (a) PFNA and (b) PFOS in a control column (no PCE-NAPL) for a 1:1 PFNA:PFOS mixture. Data were fit with either the linear/equilibrium or linear/non-equilibrium solid phase adsorption models.

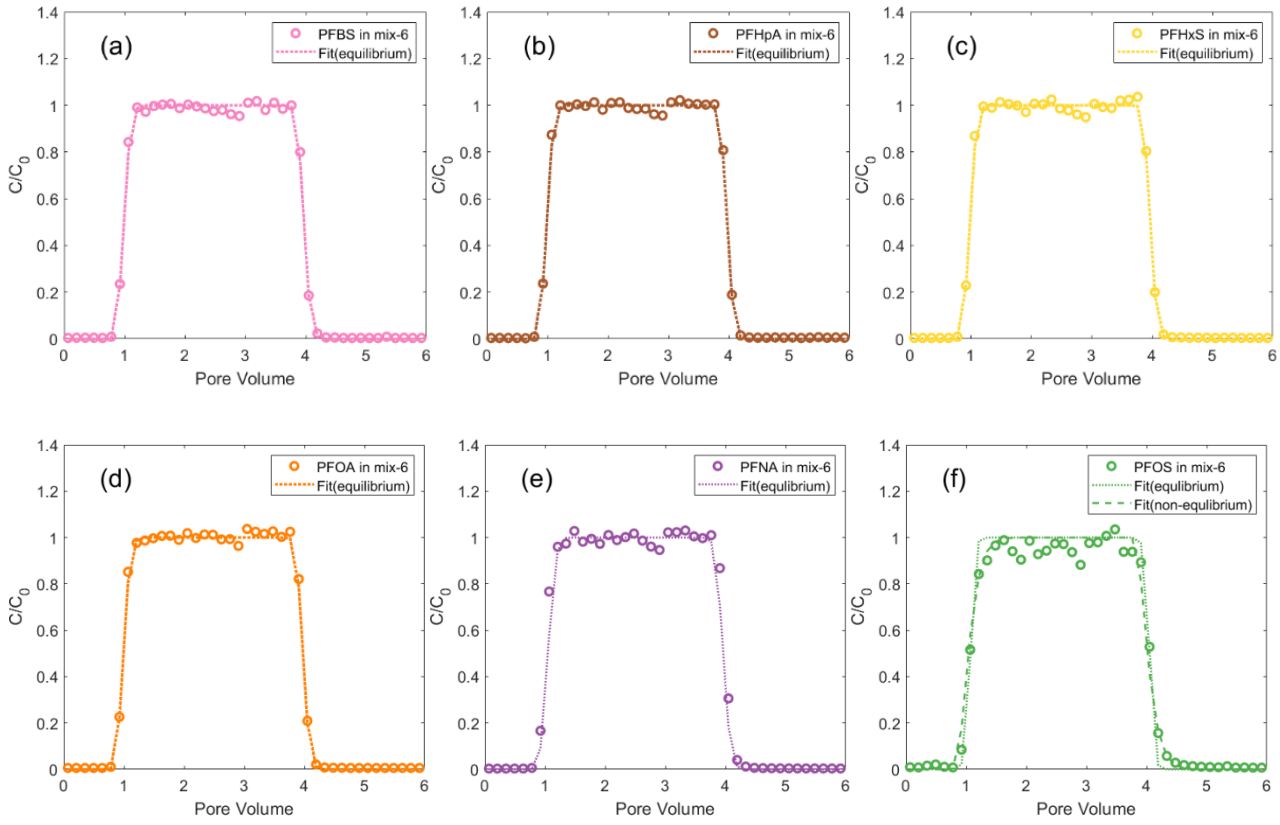


Figure 4.50 Breakthrough curves obtained for (a) PFBS, (b) PFHpA, (c) PFHxS, (d) PFOA, (e) PFNA and (f) PFOS in a control column (no PCE-NAPL) for a mixture of 6 PFAS. Data were fit using either a linear/equilibrium or linear/non-equilibrium solid phase adsorption model.

4.3.2.4 Effect of residual PCE-NAPL on PFOS and PFNA transport

The effect of residual PCE-NAPL on PFAS transport was first evaluated using single solute solutions containing PFNA or PFOS at an environmentally relevant concentration (~ 100 µg/L). BTCs for columns with ~16% residual PCE-NAPL saturation are shown in **Figure 4.51**. In the control columns (**Figure 4.48**), PFNA or PFOS was detected in the column effluent after approximately 1 PV, increased rapidly to the influent concentration, and then decreased rapidly to background levels after the pulse injection ceased. These results are indicative of limited PFNA and PFOS sorption on 60-80 OS (3.6 ng/g and 4.1 ng/g) and are consistent with the batch reactor results.

In the presence of residual PCE-NAPL, however, PFNA and PFOS were not detected in the column effluent until 1.2 and 2 PVs, respectively, and concentrations gradually increased to the influent value (i.e., $C/C_0 = 1$) (**Figure 4.51**). The variations in peak PFAS concentrations observed here and in other column experiments were attributed to slight changes in flow velocity ($\leq \pm 5\%$) and experimental error introduced by the need to dilute the peak effluent samples by a factor of 10 prior to analysis. The differences in PFNA and PFOS arrival times between the control columns and the columns containing PCE-NAPL clearly demonstrate that the presence of residual NAPL substantially delayed PFNA and PFOS transport. Since PFAS sorption to 60-80 OS occurred in both sets of columns (estimated to be 0.8 µg and 1.7µg for PFNA and PFOS, respectively, based on batch adsorption results), the observed delay could be attributed to PFAS partitioning into residual NAPL and/or accumulation at NAPL-water interfaces. Based on the K_{nw} values obtained from batch studies and the PCE-NAPL saturation of ~16%, the NAPL phase partitioning capacities were calculated as 0.09 µg and 0.18 µg for PFNA and PFOS, respectively. Total PFNA and PFOS retarded during transport through the column, however, was 5.2 µg and 16.4 µg, respectively, demonstrating that NAPL-water interfacial accumulation accounted for approximately 83% and 88% of the observed PFNA and PFOS retardation. This finding is consistent with a recent column study[41] which reported that adsorption at the NAPL-water interface contributed up to 75% of the total retardation of PFOS or PFOA for an applied concentration of 10 mg/L.

Following the pulse injection of PFAS-free background solution, the relative concentrations of PFNA and PFOS rapidly decreased to 0, suggesting PFNA and PFOS readily desorbed from the NAPL-water interface. Further, the overall BTCs were symmetrical in shape, indicating that the interfacial adsorption-desorption of PFNA and PFOS was not rate-limited. This finding was supported by an additional PFOS column experiment conducted at a lower pore-water velocity (0.28 m/day versus 1.0 m/day), which yielded nearly identical BTCs (**Figure 4.51**, bottom panel).

Simulated BTCs for PFNA or PFOS in columns containing residual PCE using Langmuir (solid lines) or Freundlich (dashed lines) isotherms to model interfacial accumulation are presented in **Figure 4.51.** Here, the fraction of interfacial area in contact with the mobile aqueous phase, f (eq. S1), was fit to data in simulations of the first PFOS column experiment and then used as a constant in predictions of the effluent concentration in subsequent simulations. These results demonstrate that the Langmuir isotherm predictions closely matched the experimental data. The calibrated f value associated with the Langmuir isotherm (0.53) and the associated effective NAPL-water interfacial area (23-25 cm^2/cm^3) are also consistent with previously reported values for sands.[328-330] In contrast, the Freundlich isotherm model fails to accurately capture observed trends; it predicts significant tailing that was not evident in the experimental data. Furthermore, the calibrated f value (0.19) and associated effective NAPL-water interfacial area (8-9 cm^2/cm^3) were notably lower than physically realistic values for sand.[328-330] These fitted parameters are

compensating for a large retardation (an overestimation of surface excess) (**Figure 4.52** and **Figure 4.53**) at lower concentrations, a known theoretical limitation of the Freundlich isotherm, which predicts unbounded PFAS interfacial accumulation at lower concentrations.[127] Similar limitations of the Freundlich isotherm were recently reported for modeling air-water interfacial accumulation.[331]

The PFOS BTCs presented herein exhibited minimal tailing because the applied concentrations were relatively low (100 µg/L). In contrast, the PFOS BTCs reported by Van Glubt and Brusseau[41] exhibited substantial tailing at relatively high PFOS concentrations (i.e., 10 and 25 mg/L), which was attributed to nonlinearity of the interfacial adsorption isotherm. It is important to note that at typical field concentrations (<100 µg/L), our column data indicate that PFOS and PFNA concentrations exhibited no tailing, indicating that a linear interfacial adsorption model could be used to predict PFOS and PFNA transport under most environmentally relevant concentrations. However, for sites with higher PFAS concentrations (e.g., >1 mg/L), nonlinear interfacial adsorption models will be necessary to accurately predict PFAS transport behavior in the presence of NAPLs.

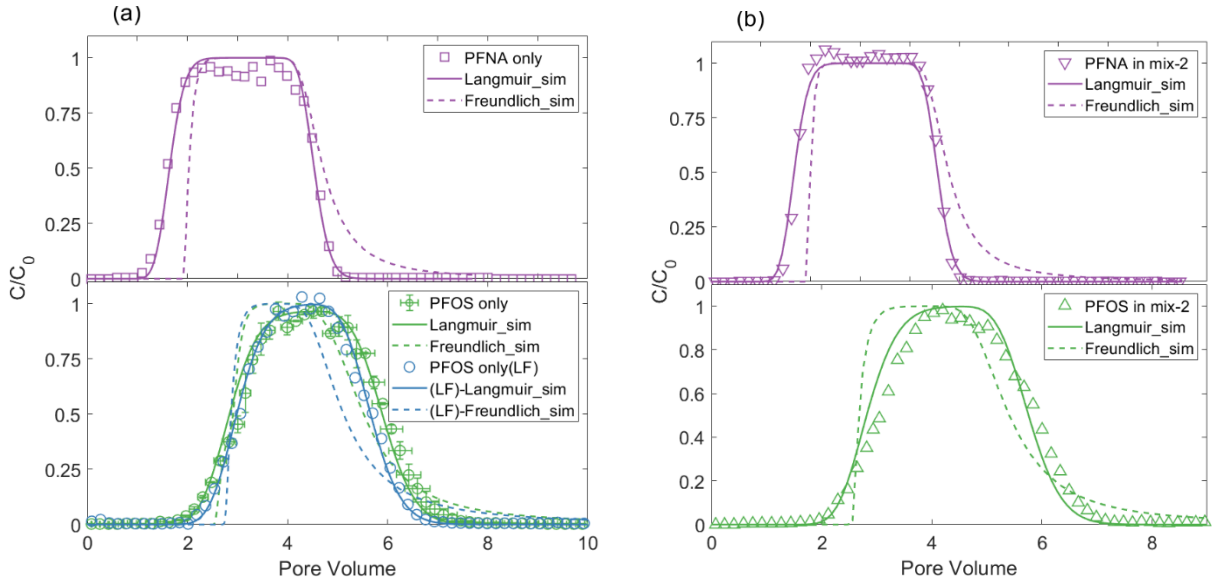


Figure 4.51 Measured and simulated effluent breakthrough curves obtained for (a) PFNA only and PFOS only columns and (b) 1:1 PFNA and PFOS binary mixture column at residual PCE-NAPL (~16%). Error bar indicates standard deviations in duplicate columns.

4.3.2.5 Effect of residual PCE-NAPL on the transport of PFAS mixtures

To evaluate the impact of residual PCE-NAPL on the transport of PFAS mixtures, column experiments were conducted with mix-2 and mix-6 solutions. Effluent concentration data for PFAS mixtures in control columns and columns containing residual PCE-NAPL are shown in **Figure 4.49** and **Figure 4.50**, and **Figure 4.51** and **Figure 4.54**, respectively. In the control columns, BTCs of short chain PFAS (PFBS, PFHpA), PFHxS and PFOA (**Figure 4.50a-d**) exhibited tracer-like behavior, consistent with low batch adsorption measurements (**Figure 4.47a-d**). PFOS exhibited delayed breakthrough compared to the other PFAS in the mixture, followed by PFNA, also consistent with batch adsorption data (**Figure 4.47e-f**). The tailing and asymmetrical shape of

PFOS BTCs in these experiments (**Figure 4.49b and Figure 4.50f**) suggest that PFOS solid-phase sorption in the control columns was rate-limited in the mixture, whereas equilibrium behavior (symmetry/no tailing) was observed in the PFOS alone control column (**Figure 4.48b**). Here, the non-equilibrium sorption model (equation S6) was able to accurately capture the observed tailing in the PFOS BTC data (**Figure 4.49b** and **Figure 4.50f**). The fitted first-order adsorption rate coefficients (α) for PFOS in the mixture control experiments were similar (i.e., 0.073 min^{-1} for PFOS-PFNA mixture and 0.067 min^{-1} for 6 PFAS mixture). The ability of the nonlinear Freundlich model to fit PFOS BTCs in mixtures was also examined. As shown in **Figure 4.54**, the nonlinear model was unable to reproduce the extended tailing, indicating that rate-limited mass transfer, rather than nonlinearity, was responsible for the observed transport behavior of PFOS. Based upon the symmetrical BTCs (i.e., no tailing), the equilibrium sorption model was used for all other PFAS (including PFOS alone).

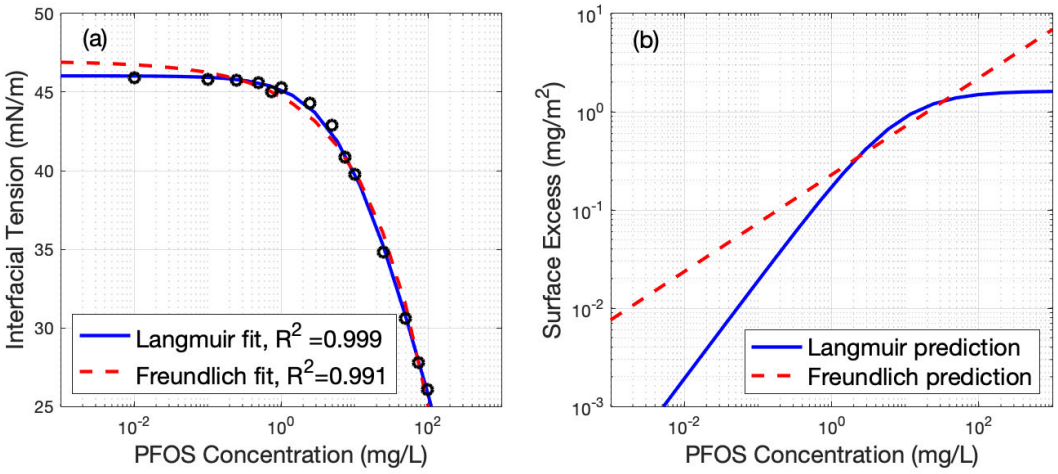


Figure 4.52 Comparison of Langmuir and Freundlich isotherms fits for NAPL-water Interfacial tension (a) and corresponding estimation of surface excess (b) for PFOS solutions. The Freundlich fitted parameters for PFOS surface excess are: $k_f^{IA} = 0.228\ (\mathrm{mg/m^2})(\mathrm{L/mg})^{n_{IA}}$, $n_{IA} = 0.493$.

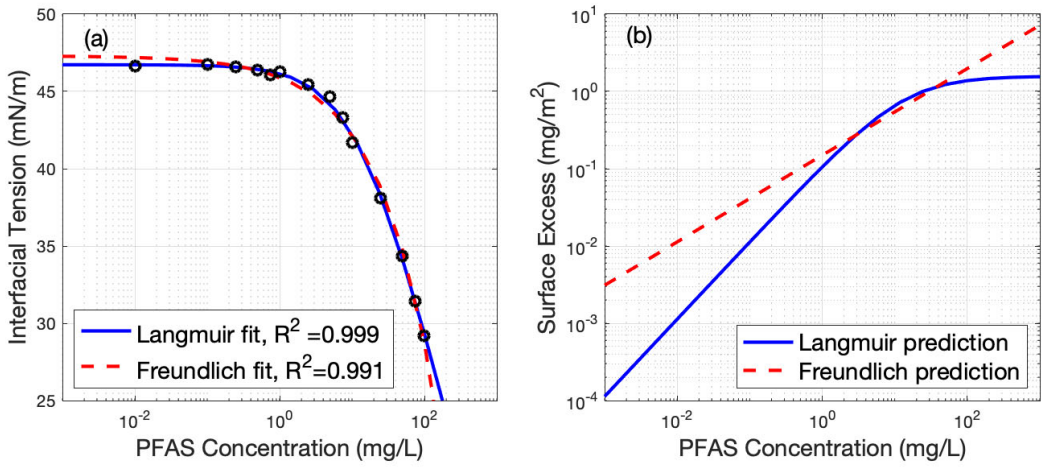


Figure 4.53 Comparison of Langmuir and Freundlich isotherms fits for NAPL-water Interfacial tension (a) and corresponding surface excess (b) for PFNA solutions. The Freundlich fitted parameters for PFOS surface excess are: $k_f^{IA} = 0.149\ (\mathrm{mg/m^2})(\mathrm{L/mg})^{n_{IA}}$, $n_{IA} = 0.561$.

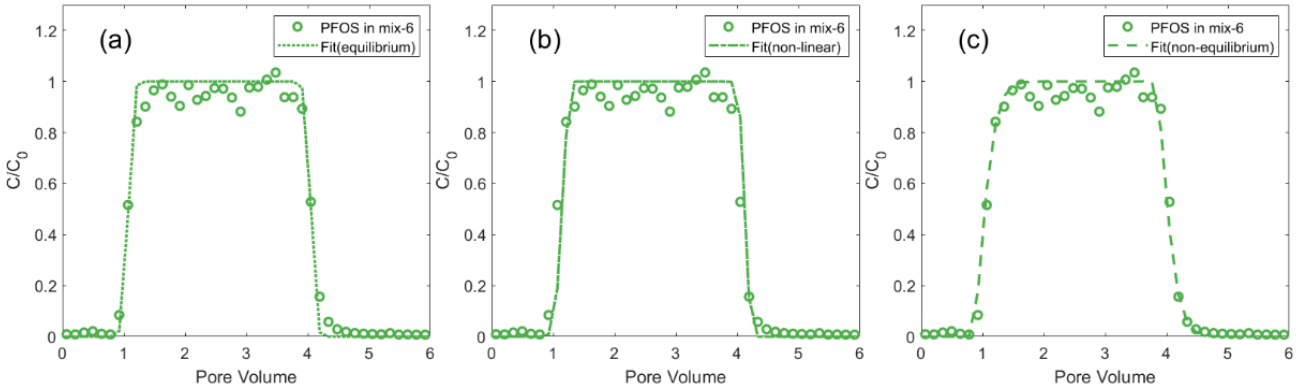


Figure 4.54 Breakthrough curves for PFOS in a control column (no PCE-NAPL) using a mixture of 6 PFAS mixture that were fit with (a) linear/equilibrium model, (b) nonlinear/equilibrium model, and (c) linear/non-equilibrium model.

For the mix-2 application to columns containing residual PCE-NAPL (**Figure 4.51b**), PFNA was detected in the column effluent after 1.2 PVs, while PFOS was observed after 2 PVs. Following breakthrough, both the PFNA and PFOS concentrations gradually increased to the applied concentration and decreased to zero after the pulse injection. BTCs obtained for PFNA and PFOS were nearly identical to the single solute PFNA and PFOS BTCs (**Figure 4.51a** vs **Figure 4.51b**), indicating that competitive adsorption of PFNA and PFOS at the NAPL-water interface was minimal under these experimental conditions. The PFOS tailing observed in the PFAS mixture control columns was less pronounced in the presence of residual PCE-NAPL, which was attributed to the far greater magnitude of NAPL-water interfacial adsorption versus solid phase sorption. Simulation results shown in **Figure 4.51b** indicate that the BTCs predicted using an extended

Langmuir model (solid line) for surface excess matched experimental data much more closely than Freundlich model predictions (dashed line).

For the mix-6 experiment, PFAS, PFBS, PFHpA, PFHxS, and PFOA exhibited only slightly delayed breakthrough (**Figure 4.54**), consistent with the relatively small interfacial accumulation of these PFAS (**Figure 4.43**). Using the fitted parameters (**Table 4.16**) from the batch IFT data, along with the non-equilibrium (for PFOS) and equilibrium solid phase sorption parameters fitted to the NAPL-free control columns, model predictions using an extended Langmuir isotherm to describe interfacial adsorption closely matched measured BTC data (**Figure 4.54**). In addition, the BTCs for PFNA and PFOS exhibited shapes similar to those measured in columns using single PFAS and mix-2 solutions, indicating that adsorption of PFNA and PFOS at the NAPL-water interface was not impacted by the presence of the other four PFAS at relatively low concentrations (~100 μg/L each). This finding is consistent with surface excess calculations **(Figure 4.43b**), which indicated nearly identical single solute mixture behavior at PFAS concentrations below ~200 μg/L.

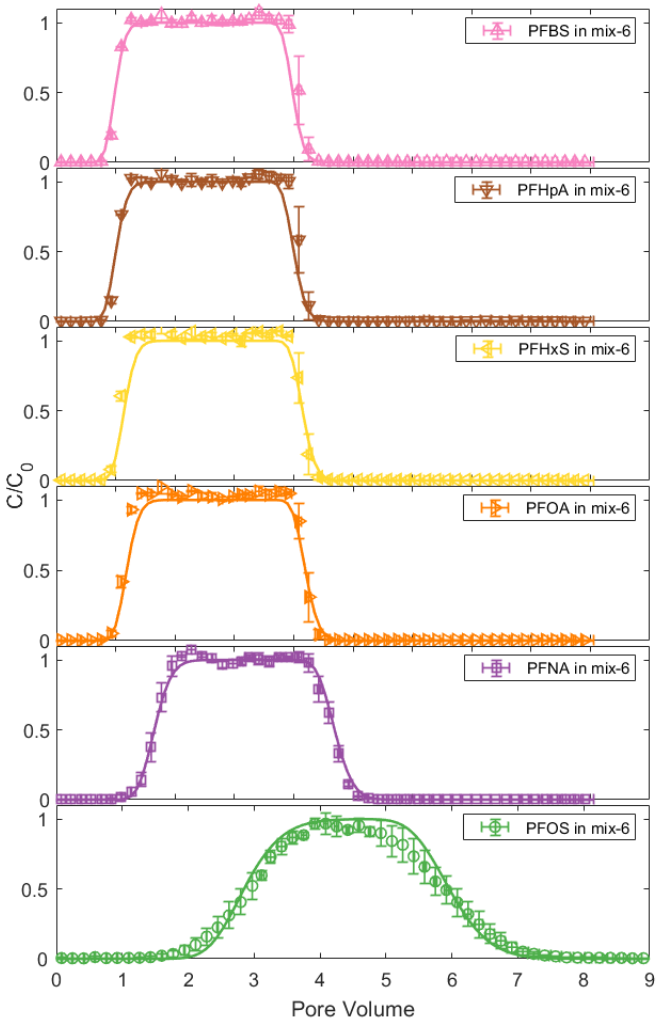


Figure 4.55 Measured and simulated effluent breakthrough curves for injected solutions containing a mixture of six PFAS (~70-100 µg/L each) in columns containing residual PCE-NAPL (~16%). Error bar indicates standard deviations in duplicate columns.

Table 4.16 Fitted parameters (equilibrium interfacial adsorption constant K_{eq} and maximum surface excess Γ_{max}) for mixtures of 6 PFAS and 2 PFAS at PCE-water interface.

	K_{eq}(L/mg)	Γ_{max}(mmol/m2)	R2
PFBS	0.0311 (0, 0.1803)	1.4214e-4 (0, 5.5293e-4)	0.7829
PFHpA	0.0182 (0, 0.0465)	9.8709e-4 (8.6839e-6, 1.9655e-3)	0.9821
PFHxS	0.0916 (0, 0.2050)	7.2203e-4 (3.4588e-4, 1.0982e-3)	0.9692
PFOA	0.0652 (0.0014, 0.1291)	1.5068e-3 (8.1044e-4, 2.2032e-3)	0.9819
PFNA	0.0578 (0.0454,0.0702)	3.6768e-3 (3.2952e-3, 4.0584e-3)	0.9996
PFOS	0.1625 (0.1262,0.1988)	3.2272e-3 (2.9364e-3, 3.5179e-3)	0.9991
PFAS mix-2	0.0798 (0.0603,0.0992)	3.4736e-3 (3.1287e-3, 3.8235e-3)	0.9986
PFAS mix-6	0.0397 (0.0358,0.0436)	3.2561e-3 (3.1328e-3, 3.3802e-3)	0.9998

*The values in parenthesis represent the 95% confidence interval for the fitted parameters

4.3.2.6 Concluding remarks

Results obtained from these experimental and mathematical modeling studies demonstrate that accumulation of PFNA and PFOS at the NAPL-water interface can strongly influence PFAS transport and retention behavior, whereas partitioning of PFNA and PFOS into the organic liquid phase (NAPL) is of relatively minor importance under the experimental conditions evaluated. For example, based on BTC data, accumulation of PFOS or PFNA at the NAPL-water interface accounted for up to ~90% of the PFAS retardation observed at a residual PCE-NAPL saturation of ~16%. The short chain PFAS investigated (i.e., PFBS, PFHpA), PFHxS and PFOA, however, were highly mobile, even in the presence of residual NAPL, due to minimal partitioning into PCE-NAPL or accumulation at the NAPL-water interface. These findings demonstrate that the impact of residual NAPL on PFAS transport is strongly dependent upon PFAS properties. For example, the phase distribution and persistence of long chain PFAS, such as PFOS and PFNA, at contaminated sites could be influenced by residual NAPL via interfacial adsorption and partitioning processes. In contrast, the presence of residual NAPL is likely to have minimal effects on the mobility of short chain length PFAS, such as PFBS. This information can be used to support informed decisions regarding site management, risk assessment and remediation strategies at PFAS-impacted sites. Nearly identical BTCs were observed for PFAS as single solutes or in mixtures, indicating that competitive adsorption effects at the NAPL-water interface are unlikely to impact PFAS transport behavior at most sites where aqueous phase concentrations are below approximately 100 µg/L. A modified version of the HYDRUS model, which accounted for nonlinear and rate-limited adsorption processes for multiple solutes was able to accurately capture the observed transport behavior for up to six PFAS using a Langmuir isotherm to model interfacial accumulation. The simulation results also demonstrate that the Freundlich isotherm is not suitable for characterization of PFAS NAPL-water interfacial adsorption at lower concentrations. This work furthers our understanding of PFAS transport and retention processes in the presence of NAPLs and provides a mathematical tool for predicting PFAS transport at co-contaminated sites. Additional experimental and modeling studies are underway to investigate the competitive adsorption of PFAS mixtures at the NAPL-water interface at higher concentrations, and to further explore the relative contributions of solid-phase and NAPL-water interfacial adsorption processes in soils with higher organic carbon content.

4.4 Abiotic-biotic transport studies

4.4.1 Biotransformation of 6:2 FTS in 1-D flow-through columns

Results from non-reactive tracer tests revealed that four columns were packed almost identically, with a PV of 28.9 ± 0.3 mL and a porosity of 0.35 ± 0.00 cm^3/cm^3 (Appendix **Table A.40**). For simplicity, the average PV was used for all columns in subsequent results and discussion, and no relative standard deviation of PV was noted for duplicate abiotic and biotic columns. During the experiments, the consumption of DGBE in both biotic and abiotic columns was monitored by measuring effluent DOC concentrations (Appendix **Figure A.67**). Lower DOC concentrations were constantly observed in the effluents from biotic columns than abiotic ones (Appendix **Figure A.67**). In addition, ORPs of biotic column samples collected from influent, effluent, and side-ports during the experiments were all greater than 450 mV (values reported relative to standard hydrogen electrode) (Appendix **Table A.41**). These results indicated that oxic conditions were maintained in biotic columns throughout the experiments, and DGBE was consumed by the aerobic microorganisms in biotic columns.

4.4.1.1 Biotransformation of 6:2 FTS under dynamic flow conditions

Throughout the 305-day experiments, 6:2 FTS in abiotic column effluents remained relatively constant (98.8 ± 10.5 mol% of spiked 6:2 FTS in the influent) after the breakthrough (i.e., increased from 1.2 ± 0.0 mol% at 0.5 PVs to 103.8 ± 9.3 mol% at 2.5 PVs), indicating that 6:2 FTS was stable under the abiotic column conditions (**Figure 4.56**). In contrast, obvious decrease in 6:2 FTS was observed in biotic column effluents (**Figure 4.56**). Targeted PFAS analysis also revealed the production of eight compounds only in biotic columns (**Figure 4.57**), confirming the occurrence of 6:2 FTS biotransformation under the biotic column conditions. The biotransformation products quantified by LC-MS/MS targeted analysis include 6:2 fluorotelomer saturated carboxylic acid (6:2 FTCA), 6:2 fluorotelomer unsaturated carboxylic acid (6:2 FTUA), 5:2 secondary fluorotelomer alcohol (5:2 sFTOH), 5:3 fluorotelomer carboxylic acid (5:3 acid), perfluorobutanoic acid (PFBA), perfluoropentanoic acid (PFPeA), perfluorohexanoic acid (PFHxA), and perfluoroheptanoic acid (PFHpA), which were also observed in the previous microcosm study [332]. To better depict and understand the biotransformation of 6:2 FTS in the present column experiments, the eight products were categorized into three classes: early intermediates (6:2 FTCA and 6:2 FTUA), middle intermediates (5:2 sFTOH and 5:3 acid), and terminal products (PFBA, PFPeA, PFHxA, and PFHpA), based on the pathways proposed previously [332] (Appendix **Figure A.68**).

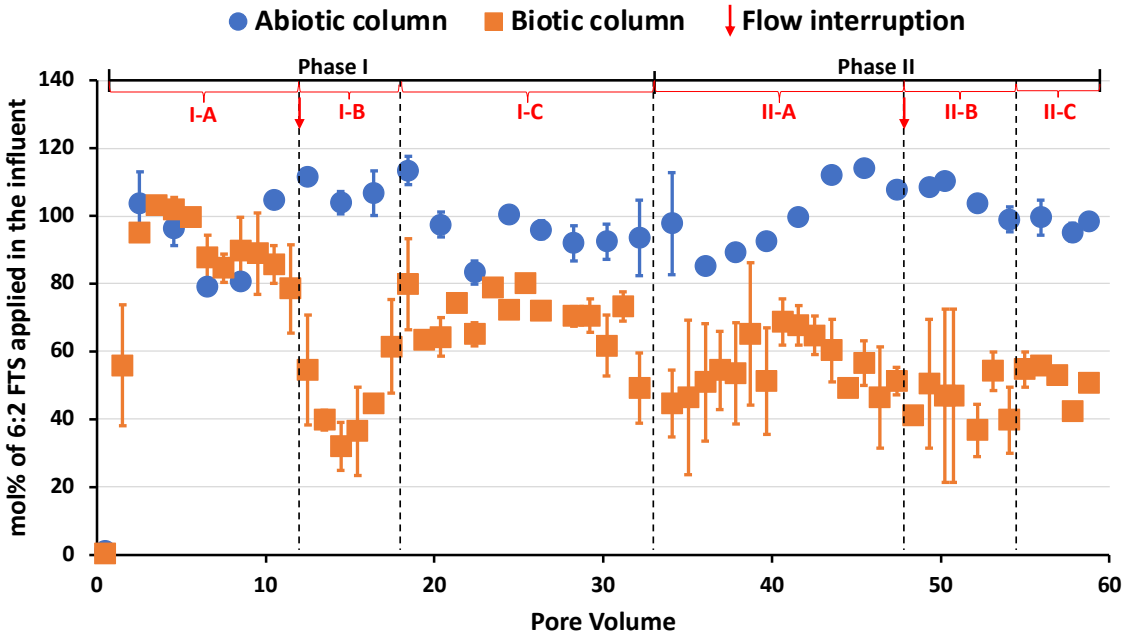


Figure 4.56 Time-course of 6:2 FTS concentration in the effluents from abiotic and biotic columns. Error bars represent the standard deviation of duplicate abiotic and biotic columns.

4.4.1.1.1 Profiles of 6:2 FTS and LC-MS/MS quantified biotransformation products in biotic column effluents

Based on the biotransformation of 6:2 FTS observed in biotic columns, the column operations in Phase I and Phase II were further divided into three subphases (Phases I-A, I-B, and I-C, and Phase II-A, II-B, and II-C; **Figure 4.56** and **Figure 4.57**). In Phase I-A (0.5-11.5 PVs), the breakthrough of 6:2 FTS was first observed (0.5-2.5 PVs), followed by a slow decrease in 6:2 FTS (**Figure 4.56**), as well as an increasing formation of biotransformation products especially early intermediates during 2.5-11.5 PVs (**Figure 4.57**). Specifically, 6:2 FTS decreased from 95.0 ± 0.7 mol% at 2.5 PVs to 84.6 ± 4.2 mol% at 7.5 PVs, further to 78.5 ± 13.0 mol% at 11.5 PVs (**Figure 4.56**). Correspondingly, the combined molar yields of 6:2 FTCA and 6:2 FTUA increased from 1.9 ± 1.5 mol% at 2.5 PVs to 6.6 ± 5.0 mol% at 7.5 PVs, further to 18.1 ± 4.3 mol% at 11.5 PVs (**Figure 4.57**). The formation of terminal products during this subphase was minimal, except PFHxA which was produced with 0.3 ± 0.1 mol% at 11.5 PVs (**Figure 4.57**). Taken together, these results indicated that 6:2 FTS biotransformation was initiated in Phase I-A, and the extent of biotransformation was gradually increasing, which might be attributed to the acclimation of native soil microorganisms under tested column conditions.

At 11.5 PVs, a 2-day flow interruption was conducted to all columns. After resuming flow, a sharp decrease in 6:2 FTS was observed (only 32.0 ± 7.1 mol% of 6:2 FTS at 14.5 PVs), followed by a bounce-back (61.4 ± 13.8 mol% at 17.5 PVs) in biotic columns (**Figure 4.56**). Similar decrease was not found in abiotic column effluents (**Figure 4.56**), indicating that no rate-limited adsorption of 6:2 FTS was present under studied column conditions. During Phase I-B (11.5-17.5 PVs), a greater formation of terminal products, and less production of early intermediates were observed than that prior to flow interruption (**Figure 4.57**), suggesting that a greater extent of 6:2 FTS biotransformation likely occurred in Phase I-B following the 2-day flow interruption. For example,

PFBA and PFHpA that were not produced in Phase I-A, were both formed with an average molar yield of 0.1 ± 0.1 mol% during Phase I-B (**Figure 4.57**).

During 17.5-33.1 PVs (Phase I-C), relatively constant concentration of 6:2 FTS was observed in biotic column effluents (**Figure 4.56**). Also, the formation of 6:2 FTS biotransformation products appeared to be stable, though some fluctuation was observed (**Figure 4.57**). Therefore, 6:2 FTS biotransformation likely reached a steady-state in Phase I-C under the tested conditions (i.e., RT = 4.1 ± 0.2 days). Under this steady-state, an average concentration of 70.8 ± 11.9 mol% for 6:2 FTS remained in biotic column effluents, along with average molar yields of 5.2 ± 3.8 mol% for 6:2 FTCA, 5.1 ± 2.5 mol% for 6:2 FTUA, 3.8 ± 3.2 mol% for 5:2 sFTOH, 2.0 ± 1.9 mol% for 5:3 acid, 0.0 ± 0.1 mol% for PFBA, 0.1 ± 0.1 mol% for PFPeA, 0.2 ± 0.2 mol% for PFHxA, and 0.0 ± 0.1 mol% for PFHpA, respectively (**Figure 4.57**).

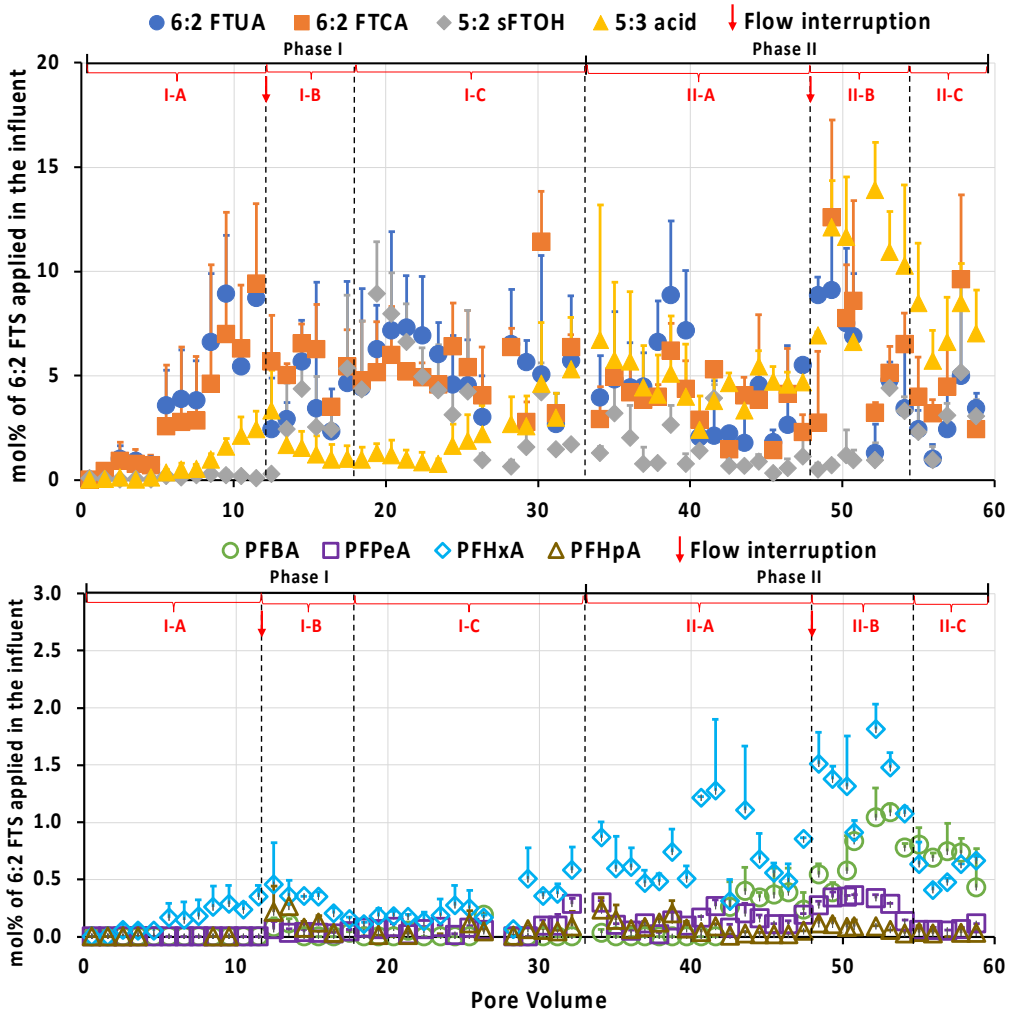


Figure 4.57 Time-courses of 6:2 FTS biotransformation products quantified by LC-MS/MS analysis in biotic columns effluents. Error bars represent the standard deviation of duplicate biotic columns. Note that different y-axis scales were used in top and bottom plots.

Column operation entered Phase II-A at 33.1 PVs, where the flow rate for influent delivery to all columns was reduced to 3.2 ± 0.1 µL/min. Overall, lower concentrations of 6:2 FTS were observed

in Phase II-A (33.1-47.4 PVs) than Phase I-C (**Figure 4.56**). In average, 55.4 ± 15.0 mol% and 70.8 ± 11.9 mol% of 6:2 FTS remained in the effluents during Phase II-A and Phase I-C, respectively. As for the biotransformation products, less early intermediates but greater amounts of terminal products were formed in Phase II-A compared to Phase I-C (**Figure 4.57**). For instance, the average molar yield of PFHxA during Phase II-A (0.7 ± 0.4 mol%) was more than tripled compared to Phase I-C (0.2 ± 0.2 mol%). These results indicated a greater extent of 6:2 FTS biotransformation occurred in Phase II-A than Phase I-C. The longer residence time in Phase II-A provided soil microorganisms more time to achieve a more complete biotransformation of 6:2 FTS. For the two middle intermediates, the average molar yield of 5:2 sFTOH decreased from 3.8 ± 3.2 mol% in Phase I-C to 1.4 ± 1.4 mol% in Phase II-A; while 5:3 acid increased from 2.0 ± 1.9 mol% in Phase I-C to 4.7 ± 2.7 mol% in Phase II-A (**Figure 4.57**). The different trends observed between two middle intermediates was likely due to an earlier formation of 5:2 sFTOH and earlier conversion to downstream products, compared to 5:3 acid (Appendix **Figure A.68**).

At 47.4 PVs, a longer flow interruption of 7 days was performed to all columns. Immediately after resuming the flow, ORPs measurements of the samples collected from biotic column side-ports confirmed that oxic conditions were maintained during the flow interruption (Appendix **Table A.41**). In Phase II-B (47.4-54.1 PVs) following the flow resumption, a substantial increase in the production of 6:2 FTS biotransformation products was observed (**Figure 4.57**), along with the decrease in average 6:2 FTS concentration from 55.4 ± 15.0 mol% in Phase II-A to 45.1 ± 17.3 mol% in Phase II-B (**Figure 4.56**). Average molar yields of 5:3 acid (10.4 ± 3.4 mol%), PFBA (0.7 ± 0.3 mol%), PFPeA (0.3 ± 0.1 mol%) and PFHxA (1.4 ± 0.4 mol%) in Phase II-B were all more than doubled compared to Phase II-A (**Figure 4.57**). Even for early intermediates, both 6:2 FTCA and 6:2 FTUA were also formed with higher molar yields (6.6 ± 4.0 and 6.0 ± 4.1mol%, respectively) in Phase II-B compared to Phase II-A (**Figure 4.57**). Taken together, the biotransformation of 6:2 FTS was greatly promoted by the 7-day flow interruption, resulting in a greater production of all targeted 6:2 FTS transformation products in Phase II-B.

The promoting effect from flow interruption appeared to be minimal after 54.1 PVs, as the production of biotransformation products in Phase II-C (54.1-58.8 PVs) returned to a similar level observed in Phase II-A (**Figure 4.57**). The combined average molar yield of early intermediates was 7.9 ± 5.2 mol% in Phase II-A, and 7.6 ± 6.0 mol% in Phase II-C. Also, the combined average molar yield of terminal products was 1.0 ± 0.8 mol% in Phase II-A, and 1.4 ± 0.3 mol% in Phase II-C. Moreover, similar concentrations of 6:2 FTS, 55.4 ± 15.0 and 52.3 ± 5.8 mol% were observed in Phase II-A and Phase II-C, respectively (**Figure 4.56**). These findings suggested that Phase II-A and Phase II-C may represent the steady-state of 6:2 FTS biotransformation under the slower tested flowing conditions (i.e., RT = 6.3 ± 0.3 days).

The average molar yields of 6:2 FTS and biotransformation products at each subphase discussed above were summarized in Appendix **Table A.42**. Overall, a greater extent of 6:2 FTS biotransformation was achieved in Phase II compared to Phase I. By reducing the flow rate from approximately 5.0 to 3.2 μL/min (36% reduction), 22-26% lower concentrations of 6:2 FTS were measured in Phases II-A and II-C than Phase I-C (Appendix **Table A.42**). Correspondingly, less early intermediates but more terminal products were produced in Phases II-A and II-C than Phase I-C (Appendix **Table A.42**). A substantial promoting effect of flow interruption on 6:2 FTS biotransformation was demonstrated in Phases I-B and II-B, and the effects of both 2-day and 7-day flow interruptions could last approximately 6-7 PVs after the flow resumption (**Figure 4.56** and **Figure 4.57**). The reasons for the promoting effect might include but are not limited to growing

abundances of soil microbial communities during the flow interruption. Overall, these findings demonstrated that the 6:2 FTS biotransformation under the investigated column conditions was rate limited by the dynamic flow conditions.

4.4.1.1.2 Biotransformation of 6:2 FTS along flowing path

Throughout the 305-day column experiments, a total of 14 sets of side-port samples were collected during different subphases for the investigation of 6:2 FTS biotransformation along flowing path. The flowing path started from influent 3-way valve to Port 1, then to Port 2 and Port 3, and finally to effluent 3-way valve (see **Figure 3.2**). To better depict the biotransformation along flowing path, concentrations of 6:2 FTS and LC-MS/MS quantified biotransformation products in respective side-port samples collected from each subphase were averaged and compared to the effluent samples (**Figure 4.58**).

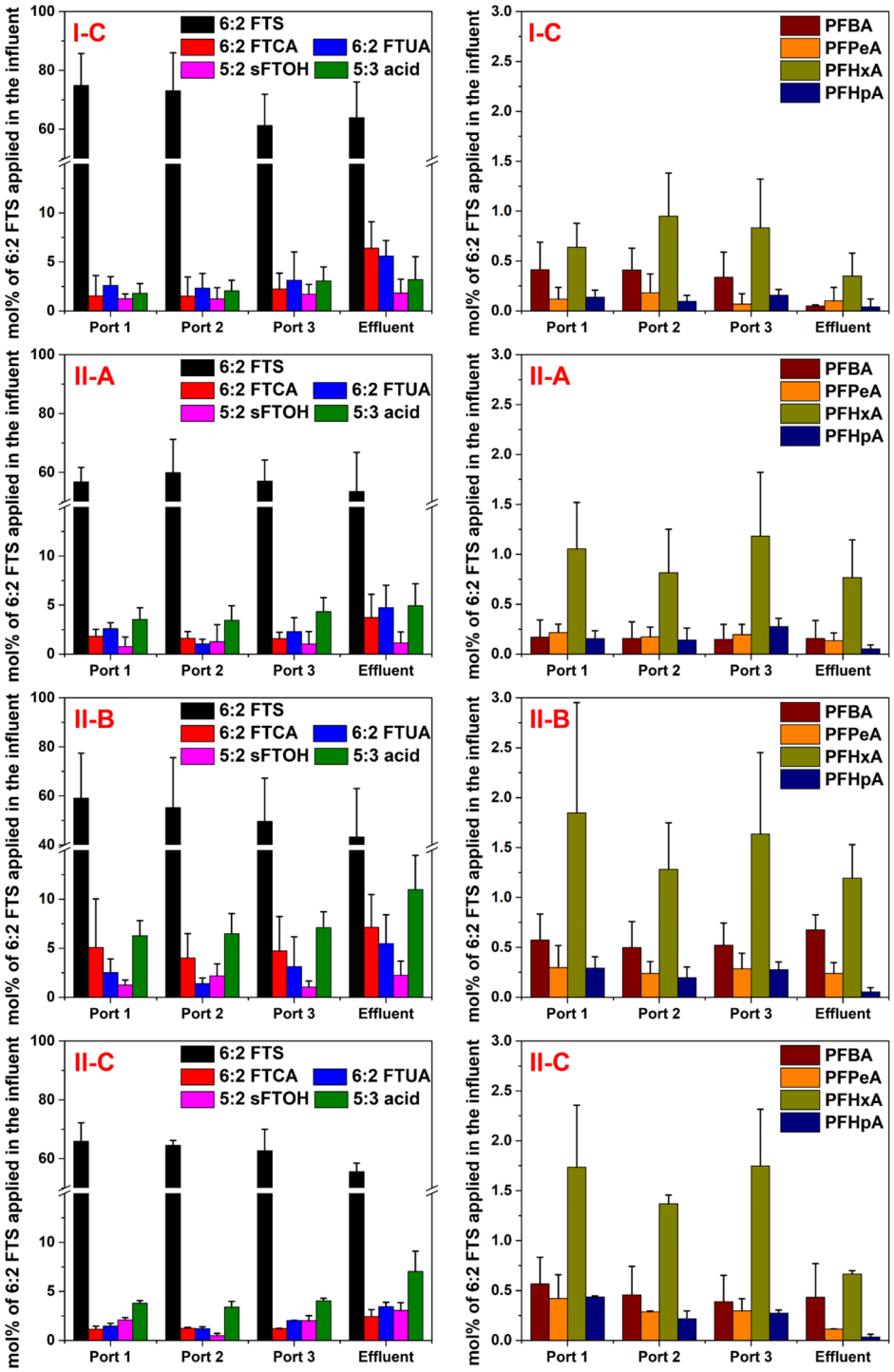


Figure 4.58 The average molar yields of 6:2 FTS and LC-MS/MS quantified biotransformation products along flowing path (i.e., Port 1, Port 2, Port 3, and Effluent, See Fig. 1) in different subphases. Phases I-A and I-B were not included because an incorrect sampling technique was used initially for side-port sampling, which resulted in the collected samples were mostly from the side-port itself (i.e., a "dead zone") instead of the flowing stream.

In general, a decreasing trend in 6:2 FTS concentration along flowing path was observed in each subphase. During Phase I-C, 6:2 FTS decreased from 74.9 ± 10.9 mol% at Port 1 to 73.1 ± 12.8 mol% at Port 2, and further decreased to 61.3 ± 10.6 mol% at Port 3. Likewise, average molar yields of 6:2 FTS in Ports 1-3 and effluent samples during Phase II-C were 65.9 ± 6.3, 64.6 ± 1.7, 62.7 ± 7.3, and 55.6 ± 2.9 mol%, respectively (**Figure 4.58**). Correspondingly, increasing trends in early and middle intermediates along flowing path were observed. For example, during Phase I-C, 6:2 FTCA and 6:2 FTUA gradually increased from 1.5 ± 2.1 and 2.6 ± 0.9 mol% at Port 1, to 6.4 ± 2.7 and 5.6 ± 1.6 mol% in the effluent, respectively. Similarly, 5:2 sFTOH and 5:3 acid gradually increased from 1.3 ± 0.5 and 1.8 ± 1.0 mol% at Port 1, to 1.8 ± 1.4 and 3.2 ± 2.3 mol% in the effluent, respectively. Overall, a decrease of 14.6%, 5.9%, 26.7%, and 15.6% in 6:2 FTS concentration was found in the effluent relative to Port 1 in Phases I-C, II-A, II-B, and II-C, respectively. Correspondingly, the formations of 6:2 FTCA, 6:2 FTUA, 5:2 sFTOH, and 5:3 acid in these four subphases were increased by 40.3-320.3%, 82.1-136.5%, 45.7-81.1%, and 39.5-85.3%, respectively, in the effluent relative to Port 1. These findings demonstrated that the biotransformation of 6:2 FTS was gradually proceeding along flowing path under tested column conditions.

Surprisingly, an increasing formation of terminal products was not observed along flowing path (**Figure 4.58**). During Phase II-A, for example, average molar yields of PFHxA in Ports 1-3 and effluent samples were 1.1 ± 0.5, 0.8 ± 0.4, 1.2 ± 0.6, and 0.8 ± 0.4 mol%, respectively. Meanwhile, PFBA, PFPeA, and PFHpA remained at 0.1-0.3 mol% among Ports 1-3 and effluent samples. The relatively stable terminal products along flowing path might be attributed to the short RTs used in the column experiments. Despite the increase to 6.3 days in Phase II, the RT was likely still much shorter than that needed for a substantial production of terminal products. In the prior microcosm study [332], molar yields of terminal products from day 28 to day 154 (e.g., 0.8-1.8 mol% of PFHxA) were also low and comparable to those in the present column experiments. Substantial increase in terminal products was not observed in the microcosms until day 224; for example, PFHxA increased from 1.6 mol% at day 154 to 5.3 mol% by day 224 [332]. Therefore, in the present study, pathways leading to the formation of terminal products might not be able to be completed given such short RTs (4.1-6.3 days).

Another surprising finding was that 6:2 FTS biotransformation occurring in the first quarter of the column (i.e., from influent 3-way valve to Port 1) seemed to represent a significant portion of the overall biotransformation throughout the column (**Figure 4.58**). In Phases I-C, II-A, II-B, and II-C, concentration of 6:2 FTS decreased by 25.1-43.2 mol% at Port 1 compared to the influent, while only 5.9-26.7% more decrease in 6:2 FTS concentration was found in the effluent compared to Port 1. However, the flowing distance from Port 1 to the column outlet was 3-fold longer than that from the inlet to Port 1. In addition, most of the quantified biotransformation products were increased by less than 100% in the effluent relative to Port 1. These results suggested that the first several biotransformation steps of 6:2 FTS leading to the formation of 6:2 FTCA, 6:2 FTUA, 5:2 sFTOH, or 5:3 acid could be completed in the first quarter of flowing path within 1-2 days (1/4 of RTs). Since then, the biotransformation might occur relatively slowly, resulting in a slower decrease in 6:2 FTS from Port 1 to the outlet. The potential higher toxic effects of 6:2 FTCA and 6:2 FTUA produced in the first quarter of flowing path on microorganisms [333, 334] might cause the slower biotransformation of 6:2 FTS afterwards. In addition, further transformation of 6:2 FTCA, 6:2 FTUA, 5:2 sFTOH, and 5:3 acid to downstream products may contribute to their lower-than-expected increases from Port 1 to the outlet.

4.4.1.1.3 Biotransformation products of 6:2 FTS identified by LC-HRMS in effluent and side-port samples.

Non-targeted LC-HRMS analysis was performed on the selected effluent and side-port samples (Appendix **Table A.13**) to identify potential unknown 6:2 FTS biotransformation products formed throughout the column experiments. One compound, C_7HF_{11} (*m/z* 292.98325), was tentatively identified as biotransformation product of 6:2 FTS (Appendix **Table A.43**). The obvious increases in the peak area were observed in the effluent samples collected from biotic columns compared to abiotic column (Appendix **Figure A.69**). A higher production of C_7HF_{11} was observed in the Phase I than Phase II, for example, the average peak area was approximately 5.0E+05 in Phase I-C and 3.0E+05 in Phase II-A (Appendix **Figure A.69**), indicating that C_7HF_{11} was likely formed in the early- or middle-stage of 6:2 FTS biotransformation. In addition, a general increasing trend in C_7HF_{11} formation was observed along flowing path (Appendix **Figure A.69**), further confirming C_7HF_{11} to be an early or middle intermediate. These findings are in agreement with the previous 224-day microcosm study in which the peak area of C_7HF_{11}, one of tentatively identified 6:2 FTS biotransformation products, peaked at day 28 then decreased [332]. Other biotransformation products identified previously were not found to be significantly formed in the present column experiments (Table S6), which was likely due to the limited extent of 6:2 FTS biotransformation occurring throughout the columns given the short RTs (4.1-6.3 days).

4.4.1.1.4 Comparison of 6:2 FTS biotransformation between microcosm and column experiments.

To provide more insights into the effects of dynamic flow conditions on the biotransformation 6:2 FTS, concentrations of 6:2 FTS and biotransformation products in different phases of the present column study were compared to those during the previous microcosm experiment (Appendix **Table A.43** and **Table A.44**). In prior microcosm study [332], the 6:2 FTS biotransformation was minimal in the first 7 days, while substantial biotransformation was observed at day 28 with 64.4 ± 8.9 mol% of 6:2 FTS remaining (Appendix **Table A.44**). Throughout the 224-day incubation, a gradual decrease in the total mass recovery was observed due to the increasing formations of biotransformation products that were not quantified by LC-MS/MS analysis (Appendix **Table A.44**). In the present column experiments, the extent of 6:2 FTS biotransformation in different phases can be approximately corresponded to that at a certain incubation time in the microcosms, based on the comparisons of molar yields of 6:2 FTS and quantified biotransformation products, as well as the total mass recovery (Appendix **Table A.42** and **Table A.44**). Specifically, 6:2 FTS biotransformation during the steady-state under the faster flow rate (i.e., Phase I-C, RT = 4.1 ± 0.2 days) might be close to that occurred between day 7 to day 28 in the microcosms, considering the slightly higher 6:2 FTS concentration and mass recovery in Phase I-C than those at day 28 microcosms (Appendix **Table A.42** and **Table A.44**). Similarly, 6:2 FTS biotransformation during the steady-state under the slower flow rate (Phases II-A and II-C, RT = 6.3 ± 0.3 days) might be close to that occurred between day 28 to 56 in the microcosms study, since the 6:2 FTS concentration and mass recovery in Phases II-A and II-C were higher than those at day 56 microcosms but lower than day 28 microcosms (Appendix **Table A.42** and **Table A.44**). The comparison between the extent of 6:2 FTS biotransformation occurring in the columns and microcosms was further supported by the formation of products identified by LC-HRMS analysis (Appendix **Table A.43**). Among the products identified in prior microcosms (Appendix **Table A.43**), only C_7HF_{11} was formed substantially at day 28 while others were not substantially formed until day 98 [332]. In the present column experiments, as discussed in Section 3.1.3, only C_7HF_{11} was identified to be the 6:2 FTS biotransformation product by LC-HRMS analysis. Therefore, the

extent of 6:2 FTS biotransformation in the columns likely reached to that at day 28 microcosms, but did not reach to that at day 98 microcosms.

The above results demonstrated that RTs in the present column experiments were much shorter than the incubation time needed in the microcosms to achieve an approximately same extent of 6:2 FTS biotransformation. Therefore, the flow conditions likely promoted the biotransformation of 6:2 FTS. Promoting effects of continuous flow on microbial dechlorination activity was previously reported, with >200-fold greater dechlorination rates in columns than those in batch reactors [335]. In addition to the rate, biotransformation pathways of 6:2 FTS might also be impacted by flow conditions. First, a greater production of early intermediates was observed in the columns than microcosms (Appendix **Table A.42** and **Table A.44**). The combined molar yield of 6:2 FTCA and 6:2 FTUA in column experiments was 7.6-12.6 mol%, which was much higher than that in the microcosms (<3.7 mol%). Second, further biotransformation of 6:2 FTUA to 5:2 sFTOH was preferred over the conversion to 5:3 acid in the microcosms [332], with a much greater molar yield of 5:2 sFTOH than 5:3 acid during the incubation, especially in first 56 days (Appendix **Table A.44**). However, such preference was not observed in the column experiments (**Figure 4.57**); instead, the reverse preference of conversion to 5:3 acid over 5:2 sFTOH was found in Phase II (**Figure 4.57**, Appendix **Table A.42**). Last, PFPeA and PFHxA were the two primary terminal products of 6:2 FTS biotransformation in the microcosms (Appendix **Table A.44**). However, PFPeA was not a main terminal product in the columns (<0.3 ml%); instead, PFBA was found to be more abundant (ca. 0.7 mol% in Phases II-B and II-C) (**Figure 4.57**, Appendix **Table A.42**). Taken together, these findings suggested that the flow conditions likely impact the preferred pathways of 6:2 FTS in addition to promoting the biotransformation. Therefore, the results from batch reactor experiments might not be enough to accurately evaluate the biotransformation of 6:2 FTS at a site where dynamic flow is present.

4.4.1.2 Dynamics of microbial communities throughout the column experiments

4.4.1.2.1 Diversity of microbial communities

The microbial communities present in aqueous side-port samples collected during Phase I and Phase II, and solid samples from column segments S1-S5 upon the termination of experiments, are referred to hereafter as free-living (FL) and porous media-attached (PMA) microbial communities, respectively. Diversity and richness of these microbial communities were evaluated by the Shannon index and Chao1 index, respectively (Appendix **Table A.45**). No significant difference ($p > 0.05$) in Shannon indices was found among side-port samples collected in Phase I or II (Appendix **Table A.45**), indicating that the diversity of FL microbial communities throughout the columns remained stable during the 305-day experimental period. However, higher Chao1 indices were observed in Port 3 samples than Ports 1 and 2 samples (Appendix **Table A.45**), which suggested that the number of FL microbial species tended to be greater at the location closer to column outlet. Moreover, no significant differences ($p > 0.05$) in Shannon and Chao 1 indices were found among samples from segments S1-S5 (Appendix **Table A.45**), indicating that the diversity and richness of PMA microbial communities were not significantly influenced along flowing path. The overall richness and diversity of FL microbial communities (Chao 1 and Shannon indices of 97.4 ± 30.6 and 2.4 ± 0.3, respectively) were significantly lower than those of PMA microbial communities (Chao 1 and Shannon indices of 324.0 ± 48.9 and 4.6 ± 0.3, respectively) (Appendix **Table A.45**). The higher richness and diversity of PMA microbial communities than its FL counterparts implied that the majority of native microorganisms derived from Loring soil were attached onto the porous media throughout the column experiments. In addition, the micro-

compartments around porous media particles may protect the attached microbes from the adverse ambient environment (e.g., high PFAS concentration in the flow), which assisted in maintaining PMA microbial community diversity.

Principal coordinate analysis (PCoA) further revealed the distinct separation between the clusters of aqueous side-port samples and solid samples from segments S1-S5 (**Figure 4.59**). Thus, the composition between FL and PMA microbial communities in the present column experiments were highly different. In addition, FL microbial communities in different side-port samples showed convergence along axis PC1 which contributed 80.6% of the total variation, whereas PMA microbial communities in S1-S5 exhibited high variability (**Figure 4.59**). The results suggested that dissimilarities within FL microbial communities were much smaller than those within PMA microbial communities throughout the columns.

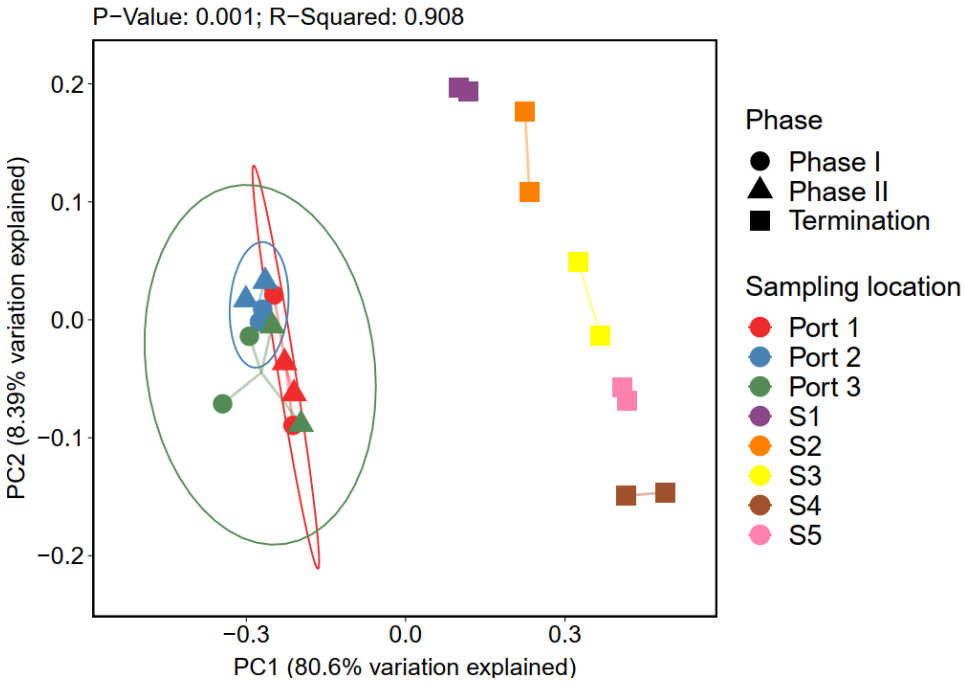


Figure 4.59 Principal coordinate analysis (PCoA) plot based on microbial communities in aqueous side-port and solid samples from segments S1-S5. Each data point represents an individual sample. PCoA was calculated using weighted UniFrac distances. Samples collected at three side-ports and five segments along the column in Phase I, Phase II, and at the termination of the experiments are differentiated by color and shape. The ellipses represent 95% confidence interval around the cluster centroid.

4.4.1.2.2 Dynamics of FL microbial communities

In Phase I and Phase II of column experiments, FL microbial communities were dominated by phylum Proteobacteria (85.8 ± 3.5%), followed by Firmicutes (7.3 ± 1.7%) (**Figure 4.60**). Genus *Pseudomonas* (belonging to Proteobacteria) in which almost all species are aerobic microorganisms was the predominant genus across Ports 1-3 samples from Phases I and II without significant differences ($p > 0.05$) (**Figure 4.61**). These results confirmed that oxic conditions were maintained in the flow throughout the experiments. In addition to phyla Proteobacteria and

Firmicutes, Actinobacteriota (1.5 ± 0.5%) and Desulfobacterota (7.3 ± 1.6%) were observed in FL microbial communities. Species in Proteobacteria such as *Pseudomonas*, *Brevundimonas*, *Afipia*, and *Herminiimonas* were reported to be involved in the biotransformation of halogenated aromatic compounds, fluorinated alkanes or PFAS compounds [118, 176, 177, 336-338]. In this study, these genera, *Pseudomonas*, *Brevundimonas, Afipia*, and *Herminiimonas* were detected in Ports 1-3 samples with average relative abundances of 38.1 ± 7.6%, 1.2 ± 1.0%, 9.1 ± 5.4%, and 4.5 ± 3.1%, respectively. Moreover, Species in Actinobacteriota and Desulfobacterota were identified to be potentially responsible for 6:2 FTS biotransformation in the previous microcosm study [332]. Taken together, these results indicated that FL microbial communities likely contribute to the 6:2 FTS biotransformation while flowing through the columns, though the extent of the contribution is not clear at this point.

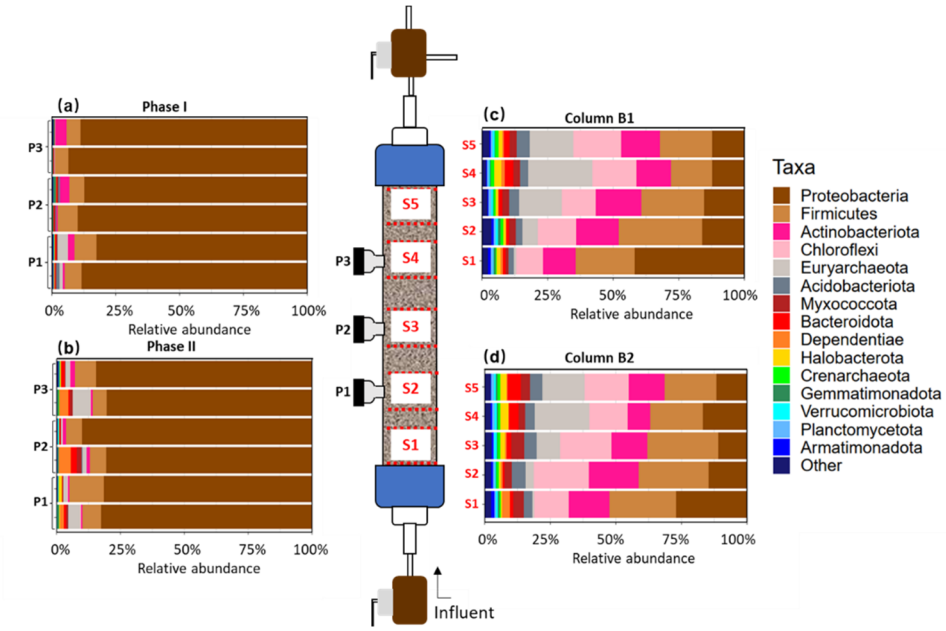


Figure 4.60 Phylum-level microbial composition of free-living (FL) microbial communities in aqueous side-port samples collected during Phase I (a) and Phase II (b), and porous media-attached (PMA) microbial communities in solid samples from segments S1-S5 of two biotic columns (c) (d).

In general, structures of FL microbial communities remained relatively stable in this study either among the Ports 1-3 or between two phases (**Figure 4.60** and **Figure 4.61**). Slight shifts in certain taxa were observed. For example, the average relative abundance of Actinobacteriota in Ports 1-2 was 1.7 ± 0.4% but decreased to 1.1 ± 0.5% in Port 3. Genus *Pseudomonas* had a higher average abundance in Phase I (43.7 ± 6.5%) than Phase II (32.6 ± 3.4%). The shifts along flowing path or between two phases might be related to the associated sensitivity/tolerance to 6:2 FTS and biotransformation products. Compared to Phase I, FL microbial communities were exposed to a lower level of 6:2 FTS but higher levels of transformation products in Phase II. However, some of the transformation products (e.g., 6:2 FTCA and 6:2 FTUA) might be more toxic to certain species [333, 334], resulting in the associated decrease in the relative abundance.

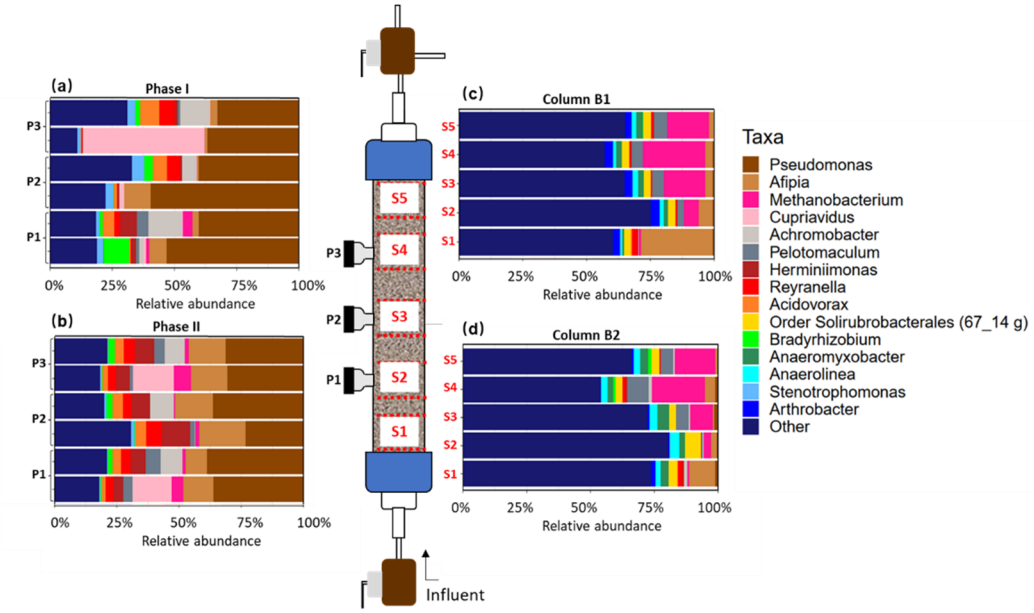


Figure 4.61 Genus-level microbial composition of free-living (FL) microbial communities in aqueous side-port samples collected during Phase I (a) and Phase II (b), and porous media-attached (PMA) microbial communities in solid samples from segments S1-S5 of two biotic columns (c) (d).

4.4.1.2.3 Spatial distribution of PMA microbial communities

After the 305-day experiments, the dominant microbial taxa in column segments S1-S5 included four bacterial phyla, Firmicutes (23.3 ± 4.1%), Proteobacteria (17.8 ± 8.3%), Chloroflexi (15.8 ± 2.2%), Actinobacteriota (14.4 ± 2.2%), and one archaeal phylum Euryarchaeota (11.4 ± 7.9%). These five phyla combined accounted for a significant proportion (79.8–84.8%) of the PMA microbial communities (**Figure 4.60**c,d). Some species in phyla Proteobacteria and Actinobacteriota are known to be PFAS degraders [106, 176, 177, 180]. Firmicutes and Chloroflexi were found capable of the biotransformation of chlorinated solvents and organohalides [218, 339]. In addition, all five phyla were previously reported to be dominant or abundant in the PFAS-contaminanted soils [340]. Therefore, the dominance of these phyla throughout the columns was likely due to their higher tolerance to 6:2 FTS and biotransformation products, as well as the potential capabilities of 6:2 FTS biotransformation.

Differences in microbial community composition among segments S1-S5 were further investigated to provide insights into how PMA microbial communities shifted along flowing path. As illustrated in **Figure 4.60**, the relative abundances of Firmicutes and Proteobacteria tended to decrease from the column inlet (23.9 ± 1.3% and 34.4 ± 7.3% in S1, respectively) to the outlet (19.9 ± 0.1% and 11.9 ± 0.2% in S5, respectively). On the contrary, phyla such as Euryarchaeota (0.9 ± 0.2% and 16.3 ± 0.2% in S1 and S5, respectively) and Halobacterota (1.0 ± 0.4% and 2.0 ± 0.5% in S1 and S5, respectively) were more abundant at the locations close to the outlet than the inlet (**Figure 4.60**). Looking at PMA microbial communities more closely on genus level, the relative abundance of genus *Methanobacterium* increased significantly from the inlet (0.9 ± 0.2% in S1) to the outlet (16.3 ± 0.2% in S5). Also, genus *Pelotomaculum* became dramatically more abundant in the segment closer to the outlet (5.0 ± 0.1% in S5) than the segment closer to the inlet (<0.1% in S1). Increasing trends in relative abundance from segments S1 to S5 were also observed

for genera *Levilinea* (0.3 ± 0.1% in S1, and 1.0 ± 0.0% in S5) and *Methanospirillum* (0% in S1, and 0.3 ± 0.2% in S5). In contrast, decreasing trends from segments S1 to S5 were observed for genera such as *Rhodococcus* (0.7 ± 0.2% in S1, and <0.1% in S5) and *Actinotalea* (0.4 ± 0.0% in S1, and 0% in S5).

The shifts in PMA microbial communities along flowing path could be attributed to the following factors. First, although oxic conditions were maintained throughout the column experiment, the gradual decrease in the availability of oxygen to PMA microbial communities from segments S1 to S5 might lead to the increase in facultative and anaerobic microorganisms (e.g., *Methanobacterium* and *Methanospirillum*, as discussed above) at the latter part of flowing path (**Figure 4.61**). Second, with the biotransformation of 6:2 FTS occurring along flowing path, PMA microbial communities in segments S1-S5 were, in a long-term period (i.e., 305 days), exposed to different levels of various PFAS compounds. For example, the microbial communities in segments S1-S2 might be exposed to higher level of 6:2 FTS than those in segments S3-S5, while the microbial communities in segments S4-S5 might be exposed to higher levels of biotransformation products of 6:2 FTS than those in segments S1-S3. Therefore, the extent of tolerance of species in PMA microbial communities to those various PFAS played a role in the associated spatial distribution. Genus *Levilinea* was previously reported to increase in river sediment after the exposure to 6: 2 fluorotelomer alcohol [159], an intermediate of 6:2 FTS biotransformation. The tolerance of *Levilinea* to 6:2 FTS biotransformation products could explain the increasing trend of its relative abundance observed from segments S1 to S5. Last, the shifts in some genera along flowing path might be due to their involvement in a specific biotransformation pathway of 6:2 FTS. For example, the decrease in genus *Rhodococcus* from segments S1 to S5 indicated that species in the genus might be more involved in the early stage of 6:2 FTS biotransformation [106]. On the contrary, the increase in genus *Pelotomaculum* along flowing path might be because the associated species could potentially involve in the later stage of 6:2 FTS biotransformation [341].

4.4.1.3 Concluding remarks

This study, for the first time, investigated the biotransformation of 6:2 FTS under continuous flow conditions during 305-day column experiments. The biotransformation was demonstrated to be rate limited, controlled by the flow conditions. Under a slower flow rate, more time was provided to soil microorganisms for a more complete 6:2 FTS biotransformation, resulting in less formation of early intermediates (i.e., 6:2 FTCA and 6:2 FTUA) but greater formation of terminal products (i.e., C_4-C_7 PFCAs). In addition, flow interruption (2-7 days) was found to promote the biotransformation of 6:2 FTS after the resumption of flow, and this transformation enhancement was demonstrated to persist for approximately 6-7 PVs. The analysis of samples collected from the side-ports on columns confirmed that 6:2 FTS biotransformation proceeded along the flow path, with a generally decreasing trend in 6:2 FTS concentration and increasing trends in biotransformation products over the path length. These findings indicate that flow rate is a critical parameter for the assessment of the fate and transformation of 6:2 FTS in the natural environment.

By a comparison of 6:2 FTS biotransformation in the column experiments to that in microcosm experiments, a continuous flow condition was demonstrated to promote biotransformation. In other words, the environmental stability of 6:2 FTS under flowing conditions is likely substantially lower than that observed in batch reactor experiments using the same microbial community. Correspondingly, substantially greater production of 6:2 FTS biotransformation products is expected under flowing conditions than would be predicted by batch reactor experiments during a specific time period. Moreover, the biotransformation pathways of 6:2 FTS in column experiments

differed from those observed in batch experiments. Thus, caution may need to be taken when applying knowledge gained from batch reactor experiments for the biotransformation of one PFAS compound to the evaluation of its fate in the natural environment under dynamic flowing conditions. Given that almost all previous studies of PFAS biotransformation have been conducted in batch reactor experiments, these findings highlight the importance and underscore the urgent need to develop and implement more representative experimental systems for the investigation of PFAS biotransformation.

4.5 Field-Scale Mathematical Modeling

4.5.1 Field-scale transport simulations

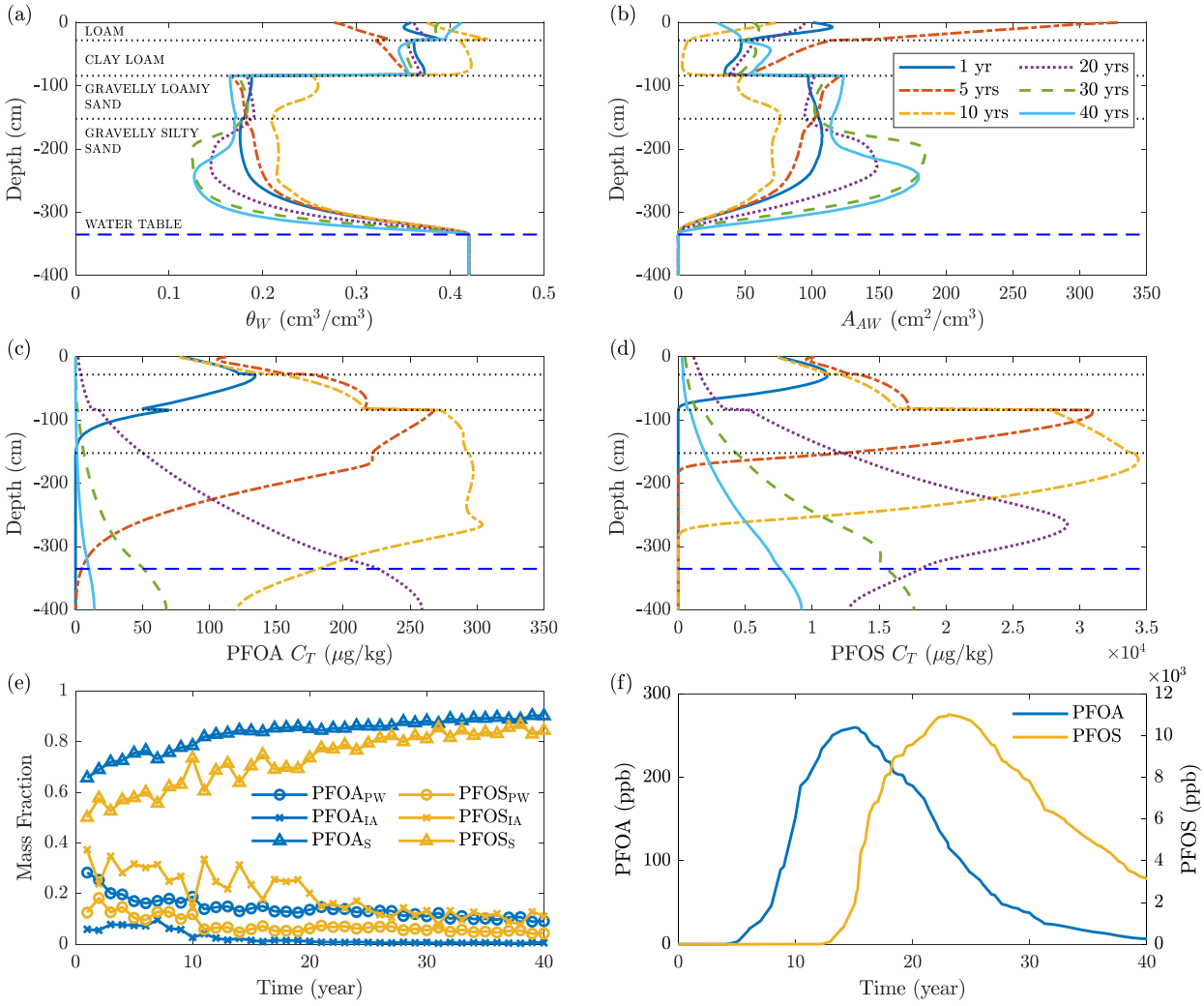


Figure 4.62 Simulation results for the first soil profile at Wright-Patterson AFB (WP-1) with four spills per year equivalent to 100 gal of AFFF concentrate (conditions Sp1). (a) Water content profiles (horizontal lines indicate the soil layers and water table); (b) AWIA profiles; (c) and (d) PFOA and PFOS total soil concentration profiles; (e) average mass fraction in each phase (PW = pore water, IA = AWIA, S = solids) in the vadose zone; and (f) breakthrough curves at the water table.

The model described in Section 3.6.2.1 was employed to simulate the selected field scale AFFF release scenarios as described in Section 3.6.2.2 to develop insight in to the properties and processes that control PFAS migration within the soil profile at AFFF-impacted sites. As an example, **Figure 4.62** shows the simulation results for the first scenario at Wright-Patterson AFB with spills of 3333 gal of 3% AFFF solution (equivalent to 100 gal of AFFF concentrate) every 3 months for a period of 10 years (conditions Sp1 in **Table 3.6**). Panel (a) presents the simulated water content profiles at selected times after the first release. These predicted profiles within the 40-year simulation period do not show marked differences in moisture content over time. However, since the simulations consider discrete soil horizons, the profiles do exhibit sharp discontinuities. For example, the model predicts a drastic drop in moisture content from the clay loam to the gravelly loam sand around 90 cm BGS, which is the result of horizon differences in hydraulic conductivity and moisture-retention capacity. The predicted AWIA, at different times is presented in panel (b). Here AWIA is based upon the moisture retention curve of the soil horizon through the thermodynamic model (equation **(3-11)**). Inspection of the curves reveals that an increase in AWIA is associated with a decrease in moisture content in the same horizon. The profiles also show the influence of soil texture on the AWIA. As an example, consider the profile at 5 years. Note that AWIA is much larger for the loam (top horizon) than for the sand (bottom horizons) even when the former has a higher moisture content. The wider range of AWIA exhibited by the loam is associated with the high capillary pressure exhibited at low moisture contents that correlate with the small pores.

The central panels (c and d) present the total soil concentration (C_T) profiles for PFOA and PFOS at different times. C_T is defined here as the sum of mass in the aqueous (pore water), sorbed (solid), and interfacial (air-water) phases per unit mass of total soil and is a commonly measured parameter in site investigations. Examination of the figure reveals that the magnitude and depth of penetration of C_T increase with time during the first 10 years, as a result of the periodic spills. Because of the AFFF composition, PFOS C_T values are approximately two orders of magnitude larger than those of PFOA. However, the C_T of PFOA exhibits a larger spatial spread with time compared to PFOS, which is a consequence of the different partitioning behavior of these compounds. PFOS is more hydrophobic with higher affinity to solids, and more surface-active, which increases its accumulation at the air-water interface. As a result, the mobility of PFOS in pore water is more limited, and it propagates more slowly. This greater retention is evident in **Figure 4.62** (e), which shows that the mobile mass fraction of PFOS (pore water fraction) is smaller than that of PFOA. Even though PFOS' partitioning to the solid phase is stronger than PFOA's, panel (e) also reveals that the PFOA mass fraction (% of the total PFOA mass) in the solids is larger than that of PFOS. This behavior is attributed to: (1) PFOS having a significant fraction at the AWIA that decreases the fraction in the solids, and (2) PFOA being outcompeted at the interface, which shifts its mass to the solids.

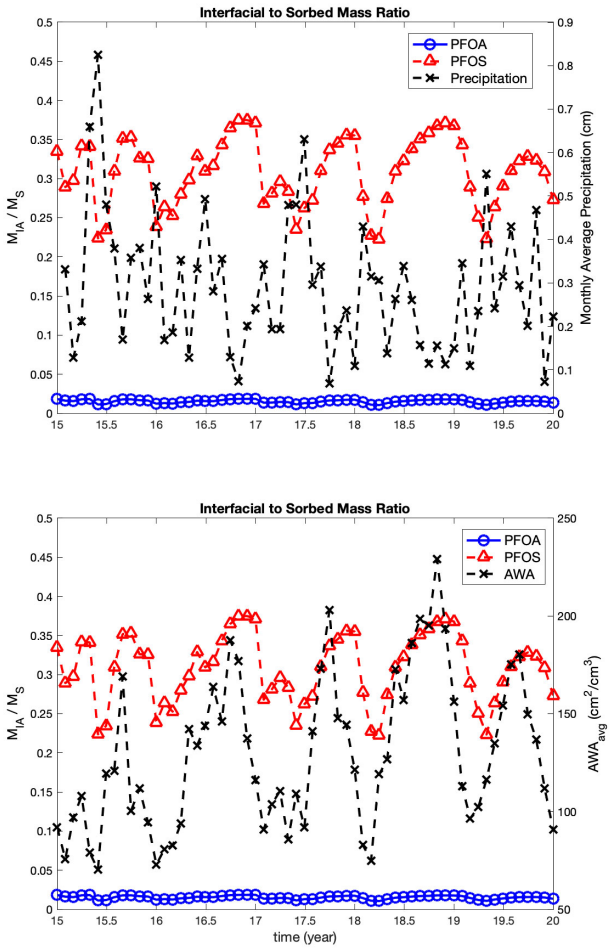


Figure 4.63 Close inspection of precipitation, average AWIA, and ratio of mass accumulated at the AWIA and sorbed mass in solid phase over the period from 15 to 20 years at WP-1. Interfacial to sorbed mass ratio varies with the change in available interfacial area, increasing in drier months and decreasing in wetter seasons

A close inspection of panel (e) suggests that retained mass fractions tend to oscillate somewhat, while temporal variations in pore water mass fraction (the mobile phase) are not as pronounced. A more detailed examination of mass fraction fluctuations on a finer time scale (**Figure 4.63**) reveals that oscillations are more pronounced seasonally and are correlated with precipitation. As net recharge increases, moisture content increases and the specific interfacial area decreases considerably. This results in a shift of sorbed mass from the interface to the solids. The fraction of the mass within pore water, however, is not greatly affected because of the high affinity of PFAS for the immobile phases. The last panel in **Figure 4.62** shows PFAS breakthrough curves at the water table resulting from the migration through the unsaturated zone. Based upon the physicochemical differences between the compounds, there is a chromatographic separation in the vadose zone. The earlier arrival of PFOA is a consequence of its lower affinity to the solids and its smaller accumulation at the interface.

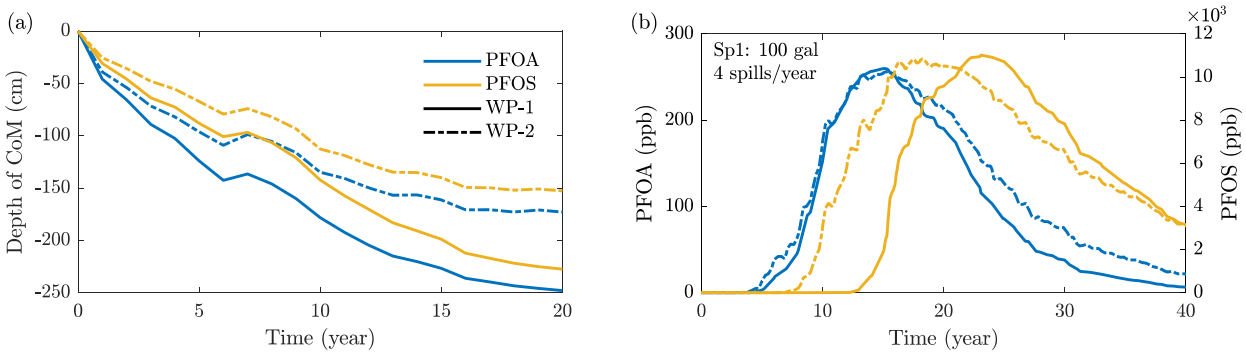


Figure 4.64 Comparison between the two soil profiles at Wright-Patterson AFB (WP-1 and WP-2) with spill conditions Sp1. (a) Position of the center of total mass in the vadose zone during the first 20 years, and (b) breakthrough of PFOA and PFOS at the water table.

To illustrate the effect of soil texture horizons on the retention and mobility of PFAS, **Figure 4.64** presents a comparison of the migration rates of PFAS within two profiles at Wright-Patterson (WP-1 and WP-2). Here, release and net recharge conditions are the same for both simulations. The soil horizons in the vadose zone at WP-2 consist of loam and clay loam followed by silty clay at the bottom (see **Figure A.70** and **Figure A.71**). Compared to WP-1, the top loam layer at WP-2 is thicker (60 vs 28 cm), WP-2 has a higher average organic carbon content (ca. 60% more) and is associated with a shallower depth to the water table (ca. 20% less deep). In terms of average hydraulic conductivity, the harmonic means for the layers at both sites are similar (18.2 and 17.5 cm/d for WP-1 and WP-2 respectively).

Since WP-2 has a larger organic carbon content, the sorption model (see **Table A.53** and **Table A.54**) predicts a higher PFAS affinity for the solid phase. This increased partitioning to the immobile phase retards the migration in the vadose zone, as is evident by comparing the evolving position of the center of (total) mass (**Figure 4.64** (a)). At first glance, it is surprising that the arrival of PFOA at the water table does not seem to be affected by the soil profile, and the arrival of PFOS occurs first in WP-2 (**Figure 4.64** (b)). This prediction, however, is just a consequence of WP-2 having a thinner vadose zone. Also note that there is a smaller chromatographic separation between PFOA and PFOS at WP-2, which is also a direct consequence of the smaller traveled distance in this profile.

4.5.1.1 Influence of climatic conditions

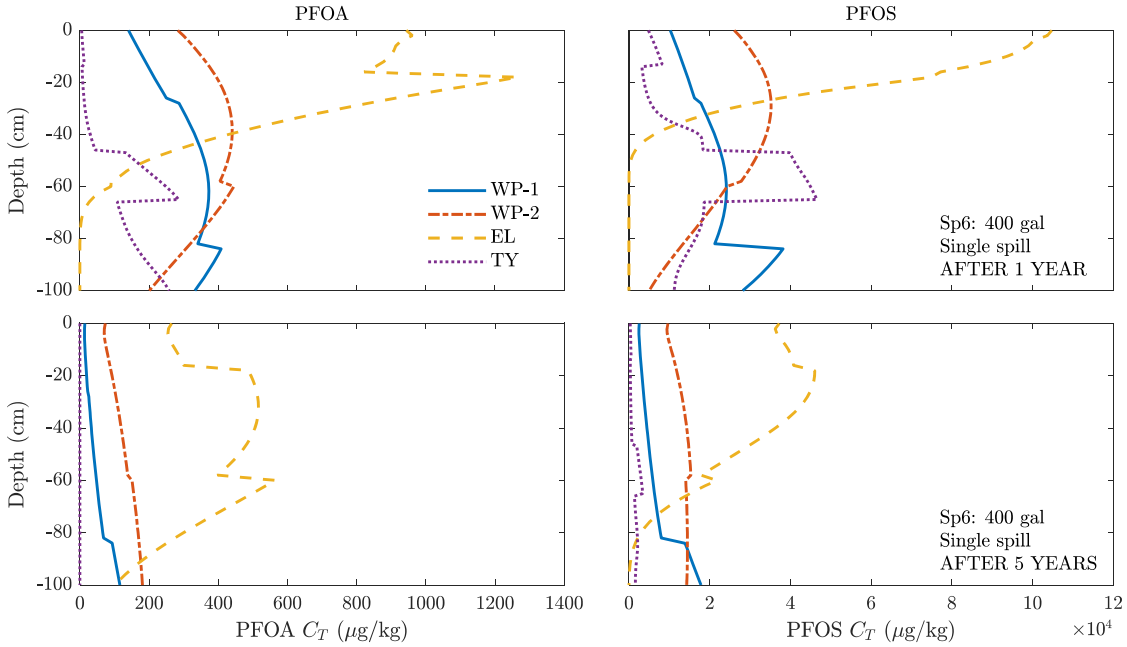


Figure 4.65 Total soil concentration of PFOA (left) and PFOS (right) at the four soil scenarios on the top 100 cm after 1 year (top) and 5 years (bottom) from a single spill of 400 gal of AFFF concentrate (Sp6).

In addition to soil characteristics (sorption and hydraulic properties), climatic conditions have a significant influence on the migration of PFAS in the vadose zone. This section illustrates these factors through comparisons of predicted concentration profiles across three geographic locations (Wright-Patterson, Ellsworth, and Tyndall) after a spill of AFFF concentrate (single pulse release, Sp6 in table 2). **Figure 4.65** plots total soil concentration of PFOA and PFOS in the top 100 cm of soil at 1 and 5 years after the spill.

Climatic conditions in the two scenarios at Wright-Patterson are identical. Thus, the observed differences between WP-1 and WP-2 are the result of differences in the soil profiles. A comparison between locations shows that PFOA and PFOS propagate faster in WP-1 than in WP-2, which is consistent with the discussion presented above for this site. Since WP-2 has a thicker loam layer with more organic carbon in the near surface, the migration of compounds is more retarded by sorption effects.

The simulations at Ellsworth AFB (EL) illustrate the combined effects of low rainfall, low moisture content, and highly sorptive materials on the retention of PFAS in the vadose zone. Here the hydraulic conductivity is very similar to that in Wright-Patterson (harmonic mean of 17.3 cm/d), however, sorption coefficients in the soil horizons can be up to an order of magnitude higher (see **Table A.56**). Since precipitation is sparse and there is substantial evapotranspiration, the soil remains at a low moisture content. Consequently, the model predicts a large AWIA. The overall result is a large retained mass fraction (mass associated with the soil and air-water interfaces). The large fraction of immobile mass along with the slow movement of pore water creates a scenario where compounds are likely to persist in the vadose zone. This is evident in the total concentration profiles, which indicate notably higher concentrations and less penetration for EL.

Compared with the other scenarios, Tyndall AFB (TY) is a location with a high net recharge rate and a more transmissive (sandy) soil (harmonic mean of hydraulic conductivity is 827 cm/d). In addition, the developed sorption correlation indicates that there is a low Freundlich partitioning capactity coefficient for PFOS compared to the other scenarios (see **Table A.55**). The consequence of higher recharge rates and lower partitioning to the solid phase is a faster migration of compounds to the water table. This is evident in the profiles, which exhibit lower total concentration levels in the upper meter of the profile. The concentration profiles also exhibit a marked difference between concentrations within the 47 and 66 cm BGS interval and the other sections of the profile, especially in the first year. The larger concentration in this interval results from a soil horizon which has a higher organic carbon content that retains a significant fraction of mass on the solid phase. As such, PFOS exhibits a more pronounced change at this depth than PFOA because of its greater hydrophobicity. Despite the highly sorptive layer, the profiles at TY indicate more mass penetration and dissipation after 5 years than at the other sites, which is a consequence of the large net recharge.

4.5.1.2 Effect of spill conditions on transport of AFFF constituents

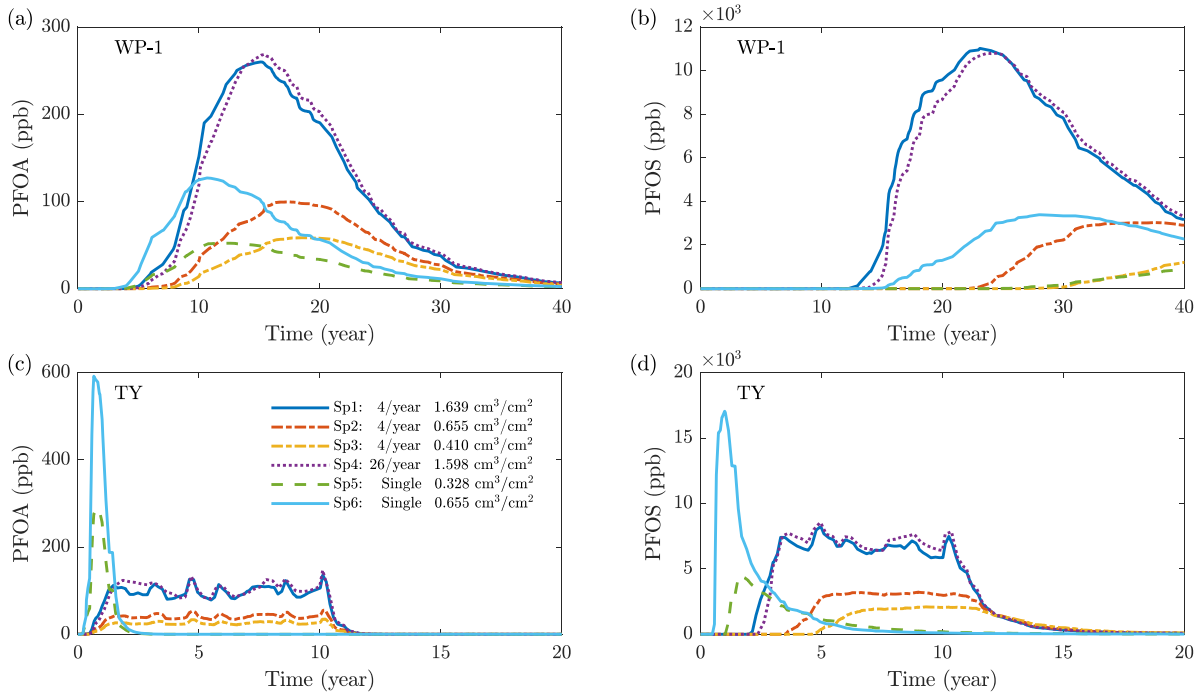


Figure 4.66 Breakthrough curves of PFOA (left) and PFOS (right) at the water table at Wright-Patterson, scenario 1 (top) and Tyndall (bottom) as a function of spill conditions. For each condtion, the legend indicates the spill frequency in a 10-year period and the cumulative volume of concentrate AFFF released per unit area.

The model simulations undertaken for this investigation considered realistic spills that varied in frequency, volume, and concentration (see **Table 3.6**). To illustrate the effect of spill conditions on the migration of PFAS in the vadose zone, **Figure 4.66** compares the PFAS (aqueous) concentration at the water table as a function of time at Wright-Patterson (WP-1) and Tyndall AFBs.

The first three spill conditions (Sp1-Sp3) consist of quarterly releases of 3% diluted AFFF over a 10-year period. The only difference between them is the total mass released, which can be quantified as the volume of equivalent AFFF concentrate per unit area (V_c, in cm^3/cm^2). Inspection of the figure suggests that, for these three spill scenarios, the maximum concentration at the water table is proportional to V_c regardless of the site (e.g., the ratio of maximum concentration at the WT for PFOA between Sp3 and Sp1 is around ~0.25 for both sites, which is also the ratio of V_c between these two spill cases) Since release frequencies are identical, this proportionality is expected given the direct relationship between the magnitude of the mass pulse in each spill and the concentration in the system. A further observation in Sp1-Sp3 is that the time to breakthrough at the water table increases as V_c decreases, which becomes more evident in the case of PFOS. This behavior would not be expected for a simple linear partitioning model, where the effective retardation factor is a function of the soil properties, not the mass released. The differences in breakthrough behavior exhibited in **Figure 4.66** for these three scenarios is a direct consequence of the nonlinear sorption and interfacial accumulation models employed here. Both the Freundlich and Langmuir-Szyszkowski models predict partition coefficients between phases that tend to decrease as concentration increases. In the case of interfacial accumulation, the Langmuir-Szyszkowski model actually predicts a maximum capacity, beyond which no further accumulation can occur. Thus, as concentration increases in proportion to V_c, the retention decreases and transport is less retarded. The effect is more pronounced for PFOS since this compound has a higher concentration in 3% AFFF than PFOA and its Freundlich parameters indicate a larger deviation from linear partitioning (see **Tables Table A.53** through **Table A.57**.

Simulations show that breakthrough curves for Sp4 (biweekly spills) are close to those for Sp1 (quarterly spills). Since V_c in Sp1 and Sp4 are similar, this similitude suggests that the released mass per unit area is the controlling factor in scenarios with periodic spills. This behavior is likely the result of a damping effect caused by the slowness of transport processes when infiltrating volumes are small. In this case, dissipation of a quarterly pulse of 100 gal (Sp1) is roughly identical to that for a biweekly pulse of 15 gal (Sp4). As a result, the effective input to the system in Sp1 and Sp4 is a 10-year mass pulse of similar size.

The last two conditions (Sp5 and Sp6) illustrate PFAS transport behavior for one-time spills of larger AFFF volumes. At both sites, simulations of single releases are associated with earlier arrival times and larger peak concentrations even when compared with simulations involving the same total mass released per area (e.g., Sp2 vs Sp6). This behavior is likely due to the strong influence of the released volume on the flow field, and the differences in mass input rate. First, the sudden infiltration of a large volume of liquid raises the soil saturation that in turn increases the hydraulic conductivity. As a result, the infiltrated volume flows downwards and the advective transport of dissolved species is augmented. Second, the introduction of a large amount of mass helps maintain a high concentration. Consequently, soil and interfacial area approach sorption capacities, thus reducing partitioning of compounds to immobile phases and decreasing retention. The overall effect of these processes is an enhanced transport of PFAS in the vadose zone. This enhancement is more noticeable in Tyndall given the larger net recharge and the high soil transmissivity in this scenario.

4.5.1.3 Qualitative comparison of simulations with field data

A recent publication reported measurements of PFAS in co-located soil and pore water samples from Ellsworth AFB [140]. The sampled site is a former fire-training area, where AFFF was released periodically from 1970 to 1990. The reported set of data includes PFAS measurements in

surface (~1 m BGS) and subsurface (~4m BGS) soils, which could allow a meaningful comparison with simulation results considered herein.

For these simulations, two soil profiles were considered within the affected area. The first one (SC01) corresponds to the Ellsworth scenario discussed above (see **Table 3.5**), and the second one (SC02) was developed based on the soil profiles provided in the aforementioned publication [138]. Details are presented in **Appendix A.8.3**. Given that the actual volume of AFFF released in the site is unknown, model inputs encompassed two scenarios: applications of 25 and 100 gal of 3% AFFF with a frequency of 4 times per year (consistent with similar sites; see **Appendix A.7**) for a period of 20 years (duration of fire-training activities in the sampled site [140]). Climatic conditions for all scenarios were identical (see **Appendix A.7**). **Table 4.17** summarizes a comparison of the ranges of field measurements and simulated values after 50 years (from the beginning of training activities to the sampling time) at two depths in the profiles.

Table 4.17 Modeling predictions and measurements of PFAS in soil and pore water at Ellsworth AFB.

	Soil (ug/kg)	**PW (ppb)**	**Soil (ug/kg)**	**PW (ppb)**
PFOA	**Shallow (1 m)**		**Deep (4 m)**	
Simulation: SC01	360-950	190-450	30-90	40-100
Simulation: SC02	10-30	10-20	80-300	60-280
Measured	418 (0.35-2200)	598 (0-4900)	62 (0.35-270)	94 (0-590)
PFOS	**Shallow (1 m)**		**Deep (4 m)**	
Simulation: SC01	2e4-9e04	6e3-1.9e4	0	0
Simulation: SC02	7e3-1.3e4	700-4e3	0-1.3e4	0-9e3
Measured	1516 (0.66-1.1e4)	494 (0-8e3)	53 (0.53-310)	44 (0-400)

Results presented in **Table 4.17** show that simulations in general overlap with reported measurements. However, given that measurements range up to five orders of magnitude at the same depth, there is a clear indication of lateral heterogeneity, which our modeling approach cannot capture. In the case of PFOA, simulations are in line with average measurements for both shallow and deep portions of the soil profiles. Additionally, predicted and observed ratios between soil and pore water concentrations are similar (~1 L/kg), which validates our approach to predict soil-water partitioning for PFOA. On the other hand, simulated PFOS concentrations are in general above the solid and liquid measurements in the shallow section of the soil. Since average PFOA measurements are within simulations, the overprediction of PFOS values could indicate that our simulated mixture has a higher ratio PFOS/PFOA than the actual AFFF used at the site, or that PFOS penetrated deeper that our predictions indicate. The latter hypothesis is consistent with the field measurements, which indicate deeper penetration of PFOS; only our simulation scenarios with the largest spill volume predicted PFOS at the 4 m depth. The higher mobility of PFOS compared to our model suggests that partitioning to immobile phases was lower than predicted by the assumed corrrelations, or it could indicate the presence of kinetic-limited retention, which our approach does not consider.

4.5.1.4 *Influence of interfacial accumulation processes on transport predictions*

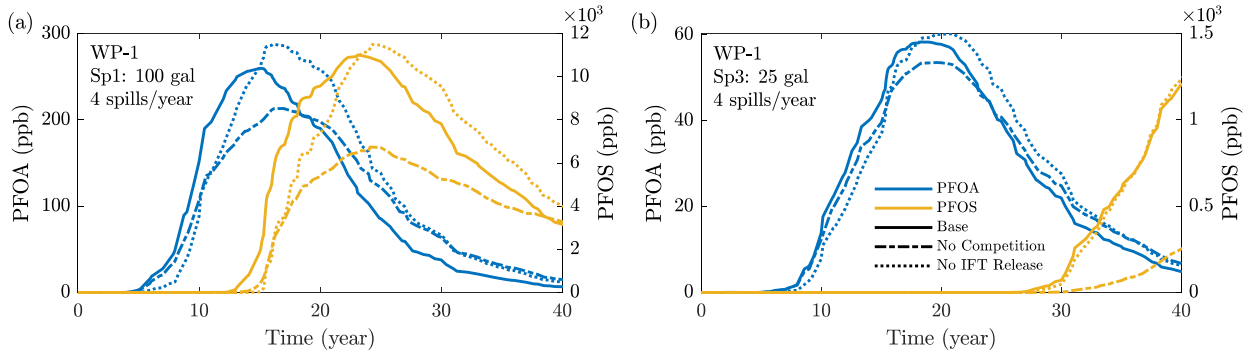


Figure 4.67 Predicted breakthrough of PFOA and PFOS at the water table after periodic spills equivalent to (a) 100 gal and (b) 25 gal of 3% AFFF solution at Wright-Patterson considering (i) the base model of this manuscript, (ii) no competition at the air-water interface, and (iii) no moisture release from interfacial tension (IFT) reduction.

Current modeling approaches in literature ignore competition effects at the air-water interface, and some studies suggest moisture release from surface tension reduction can be neglected under certain circumstances [63, 331]. To illustrate the effect of these phenomena on predictions of PFAS migration under realistic field conditions, **Figure 4.67** presents an example comparison of predicted water table breakthrough curves associated with different modeling assumptions. These plots are for the WP-1 scenario at the Wright-Patterson AFB under periodic release conditions (SP1 and SP3).

Recall that the AFFF release scenarios were modeled as the transport of a three-component mixture: PFOA, PFOS, and MASS. Competitive interfacial tension/accumulation expressions (equations (3-5) and (3-9)) were used to predict the influence of co-contaminants on interfacial processes. The form of these expressions has been verified with laboratory measurements of organic liquid-water interfacial tension for a range of six PFAS [126]. For the simulation presented herein, model parameters were obtained from laboratory measurements of single PFAS air-water IFT (see **Table 3.7**). Based upon these parameters, both MASS and PFOS will out-compete PFOA for surface sites, with MASS also displacing PFOS.

Inspection of **Figure 4.67** reveals that, if competition for sites at the air-water interface is ignored, both PFOA and PFOS exhibit a later breakthrough and lower concentration levels at the water table. This effect is more noticeable in the scenario with the largest spill volume. When competition is neglected, each surface-active compound (PFOA, PFOS and MASS) has access to the full interfacial area for accumulation. Thus, the model predicts that more mass will accumulate at the air-water interface, enhancing retardation and creating a later arrival at the water table. Also, as interfacial accumulation increases, the apparent dispersion in the breakthrough curve increases and concentration levels decrease. As shown in the simulations, this effect is less important at low concentrations (smaller spill scenario). In this case, the capacity of the air-water interface is large enough to allow for the equilibration of compounds with less competition for sorption sites. Given that PFOS is more surface-active and is present at a larger concentration, the competition effect is more pronounced in the breakthrough of this compound in comparison to PFOA. Overall, the differences in predictions with and without competition effects highlight the potential for additional surface-active compounds in AFFF to have a significant impact on the retention and transport of PFAS in the vadose zone.

A number of modeling and experimental studies have indicated that IFT reduction created by the presence of PFAS can decrease the amount of water held by capillarity in the soil pores [129-131]. The simulations plotted in **Figure 4.67** with and without considering the potential influence of IFT on water flow suggest that effects of IFT reduction are more marked in the spill scenario Sp1, which is associated with a higher total mass release (and, consequently, higher IFT reductions). **Figure 4.67** also reveals that IFT reduction causes an earlier arrival at the water table and leads to slightly lower peak concentrations. These effects are associated with moisture release that enhances the advective flux and dilutes the PFAS at the front.

4.5.2 Decision matrix

To facilitate transfer of the knowledge gained through this study, the modeling results were interrogated to identify insights and characterize relationships between identifying factors of PFAS spill sites and expected PFAS fate and transport behavior. The results of these findings are summarized in a decision-matrix that may be used by site managers to better understand the behavior expected for a given spill and site characterization scenario.

The modeling results employed six alternative spill scenarios simulated at sites located at three different USAF installations spread across the continental US. The spill scenarios were developed based on the variety of actual spills that have occurred at military installations. The sites at which the spills were simulated were selected from the Administrative Record as representative of a range of subsurface and climatic conditions that could be expected. The sites included Tyndall AFB (TY) in Florida, Wright-Patterson AFB in Ohio (WP), and Ellsworth AFB in South Dakota (EL). The data selected for the simulations were collected from the Administrative Record for actual locations where PFAS contamination occurred (see **Appendix A.7)**. Although the intent was to investigate a broad spectrum of behavior by selecting geographically diverse sites, many of the simulation parameters were not as variable as initially anticipated. For example, the average permeability at the Wright Patterson sites was quite similar to the average permeability at one of the Ellsworth sites (i.e., only a 5% difference). This makes it more challenging to draw broader conclusions. However, there still was enough variability in several model factors to help intuit observations that will prove informative to PFAS site managers.

To facilitate development of the decision matrix, each simulation was characterized according to general input parameters selected due to their likelihood for characterization by site managers. Input parameters investigated included: depth to water table, average profile moisture content, net recharge computed from precipitation and temperature data, and PFAS release characteristics including the PFAS composition, release concentration, release volume, and release periodicity (e.g., one-time (i.e., crash response), or quarterly (e.g., fire training area (FTA)), as well as soil properties, which included porosity, permeability, uniformity index (e.g., grain size distribution), organic carbon content, pH, and degree of subsurface heterogeneity. These input parameters were characterized for each simulation to provide the independent parameters for data analysis. To limit the size of the matrix, a select subset of input parameters was chosen based upon potential accessibility to remedial site managers: Total Mass Spilled per Area, Depth to Water Table, Average Permeability, Variance of log(K), Freundlich Partitioning Parameter, and Average Net Recharge.

Output parameters were characterized for each of the simulations. These output parameters were selected based on recent experience with EPA and state regulators and their likely influence on site manager decision making. Output parameters interrogated as part of this analysis included Time

to Reach the Water Table, the Maximum PFAS Concentration at the Water Table, Average Mass Flux to the Water Table, the Ratio of Mobile to Immobile Mass in the Soil Column, and the Rate of Migration of the Center of Mass. These parameters served as the dependent variables in the subsequent data analysis.

Plotting the outputs as a function of inputs led to a robust investigation that allowed the team to interrogate and identify those parameters that had the most influence on the outputs of interest. Based on this data analysis, qualitative relationships were developed to facilitate a better understanding of how certain site characteristics may influence PFAS spill behavior. The intent of this analysis, founded on the rigor of complex quantitative simulations, is to provide site managers and program managers with the information necessary to make well-informed decisions about how best to dedicate limited resources to address and remediate PFAS contaminated sites. The following sections outline each of the relationships investigated. The results are summarized in tabular form in **Table 4.18**. This matrix summary table depicts the relationship of outputs to inputs, along with qualitative observations of the strength of the relationships.

4.5.2.1 Peak Concentration at the Water Table

A key factor of interest to remedial site managers is the expected contaminant concentration at the water table and the site and spill conditions impacting that concentration. To investigate the influence of input parameters on the peak concentration at the water table the maximum concentration was plotted as a function of the input parameters identified in the previous section.

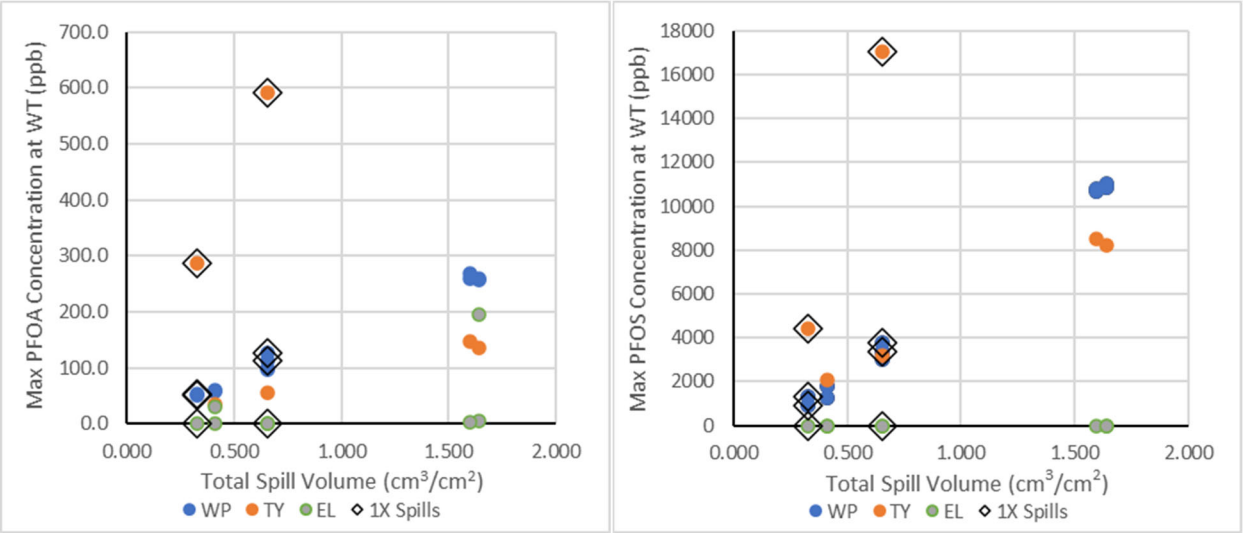


Figure 4.68 Maximum concentration at the water table as a function of the Equivalent Total Volume of AFFF Concentrate released per area for both (a) PFOA and (b) PFOS. Symbols enclosed by diamonds represent one-time spills.

Figure 4.68 shows that the peak concentration at the water table is a strong function of the equivalent concentrate mass (or, here, plotted as volume) spilled per unit area. As the spilled mass increases, the maximum concentration at the water table is shown to increase. This is true for periodic spills and one-time spills at all three sites.

Interestingly, the maximum concentration at the water table appears to decrease with an increase in water table depth for both PFOA and PFOS, regardless of the site (see **Figure 4.69**,). This

observation may be expected as the larger vadose zone has more volume to retain contaminant, decreasing the amount of contaminant that reaches the water table.

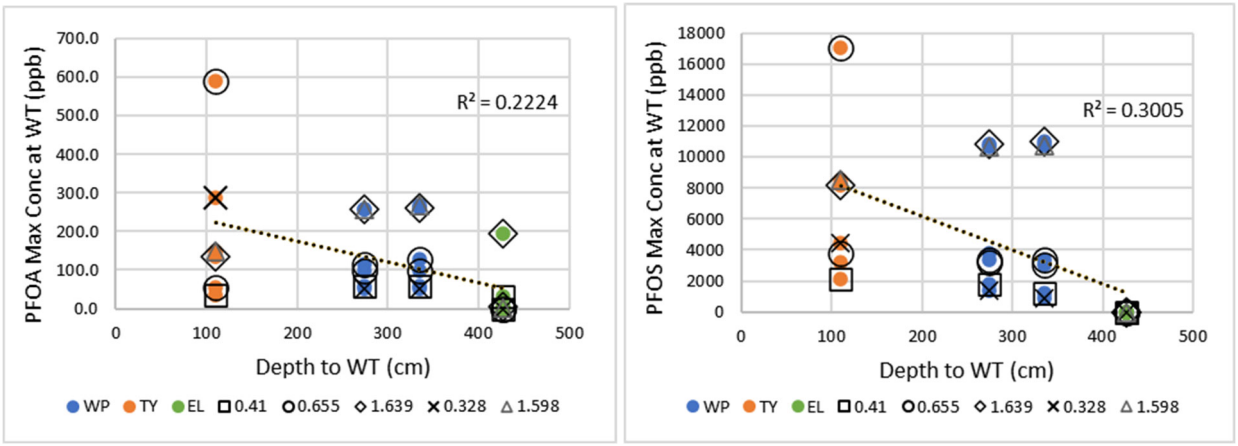


Figure 4.69 Maximum concentration at the water table as a function of the water table depth for (a) PFOA and (b) PFOS.

By contrast, as the average net recharge rate increases, the maximum concentration at the water table increases (see **Figure 4.70**). Note that here and in **Figure 4.68** some points are pinned to the x-axis, since, for these scenarios, the contaminant did not reach the water table in the 40 year simulation period. Although one might expect that a higher net recharge would result in more dilution and lower max concentrations, it appears that the maximum concentration instead increases with recharge. This behavior is likely attributed to the higher moisture content in the vadose zone, associated with the higher recharge rate, which decreases the interfacial area available for retention, resulting in more spilled contaminant reaching the water table.

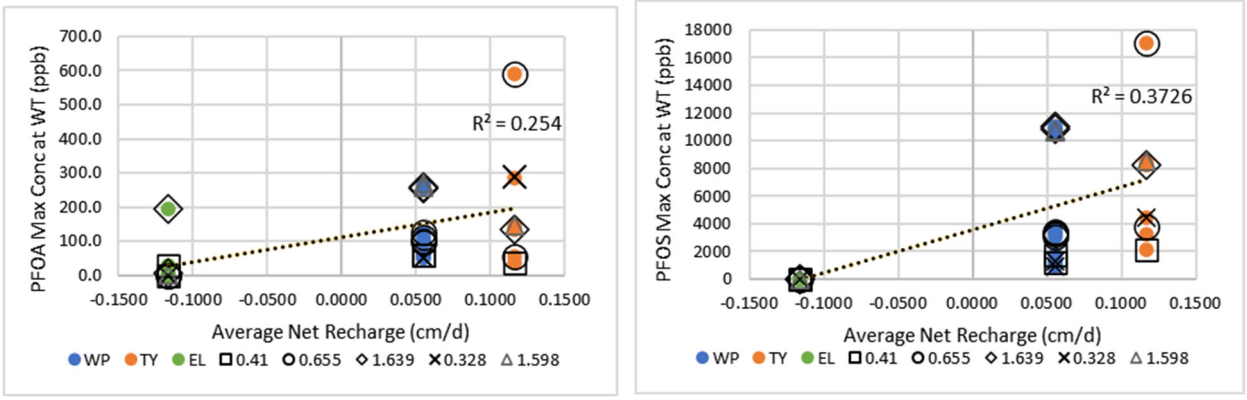


Figure 4.70 Maximum concentration at the water table as a function of average net recharge for both (a) PFOA and (b) PFOS.

The team evaluated the potential relationship of maximum concentration at the water table and other input parameters (e.g., average permeability and variance log(K)) but there were no observable trends.

4.5.2.2 Rate of Contaminant Migration

The time expected for PFOA or PFOS to reach the water table at the 4 ppt concentration level is expected to be a function of water table depth. Hence, to facilitate investigation of the rate of

contaminant migration, a parameter representing contaminant front propagation – Depth to Water Table/Time to Reach the Water Table (4 ppt concentration) – was plotted against Average (harmonic mean) Permeability (input) for both PFOA and PFOS (**Figure 4.71**). Here different colored symbols represent different sites.

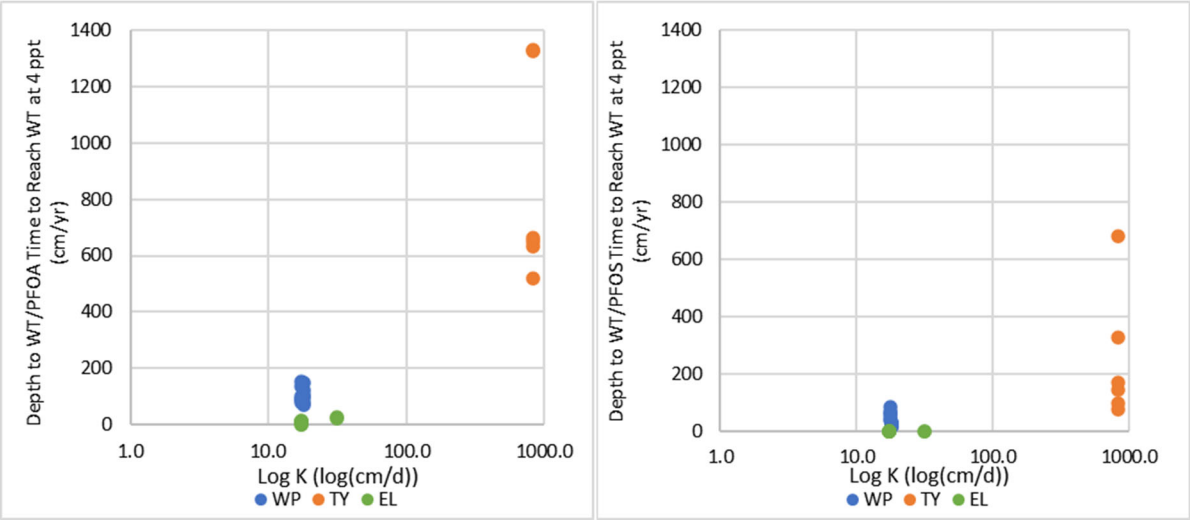


Figure 4.71 Depth to Water Table/Time to Reach Water Table plotted as a function of Average Permeability (log K) for both (a) PFOA and (b) PFOS.

PFOS breakthrough tends to be slower than that for PFOA for the same average permeabilities and recharge, attributed to the higher propensity for PFOS to accumulate at air-water interfaces. As would be expected, for sites with higher average permeability the time to reach breakthrough at the water table decreases, meaning more PFAS may reach and contaminate the saturated zone. Note, however that there is a large variability in the rate of breakthrough of PFAS at Tyndall AFB. This large variability suggests that other factors, in addition to permeability, such as release concentration and released volume/area, are affecting the migration rate. For more permeable soils, less concentration dilution within the profile is anticipated and the nonlinear relationship between concentration and both soil sorption and interfacial accumulation likely enhances PFAS propagation as source concentrations increase. Note here that data for PFOS at Ellsworth AFB are pinned to the x axis, since PFOS did not reach the water table during the simulation period.

This trend with permeability is likewise true, although harder to differentiate, for the Rate of Migration of the Center of Mass. **Figure 4.72** plots the Rate of Migration of the Center of Mass over the first 10 years against the log permeability for the Wright-Patterson and Ellsworth sites. Here Tyndall AFB was excluded from the analysis due to its shallow water table depth (approximately 1 meter). At this site, mass rapidly reaches the water table and migrates out of the model domain. Even after reducing the time over which the rate of migration was calculated to one year, too much mass was lost from the system, leading to an erroneous interpretation of the results. Hence, the team focused on the two locations with deeper water tables. For these sites, we see that there is generally an increase in the rate of migration as the log(K) increases (see for example, Ellsworth PFOA data). It is also important to note the significant variability in the rate of migration for the different spill volumes and spill scenarios, as revealed by examining the symbols associated with each data point. This variability demonstrates that spill frequency and volume (mass) per unit area can influence the rate of migration of the contaminant center of mass. A close inspection of the figure suggests, however, that spill volume is more influential than the

spill frequency. Comparing symbols enclosed by diamonds and triangles, which represent approximately the same spill volume, we see that the rate of migration between these two scenarios is quite similar for each of the sites modeled. This observation suggests remedial site managers may need to dedicate effort toward identifying the cumulative volume of contaminant spilled and not necessarily the pattern or frequency of the spill(s).

It is also important to note that there does not seem to be a large difference in the rate of migration between PFOA and PFOS. PFOA is generally considered to be more mobile. However, in the simulations considered here, the PFOA rate of migration was only approximately 50% greater than that of the PFOS. This may be partially attributed to the competition by hydrocarbon surfactants present in AFFF for interfacial retention sites and the (order of magnitude) difference between PFOS and PFOA concentrations in typical AFFF formulations like those simulated here. As noted above, it may also be associated with the decreasing effective partitioning coefficient (slope of the interfacial accumulation curve) of PFOS at higher concentrations (isotherm nonlinearity).

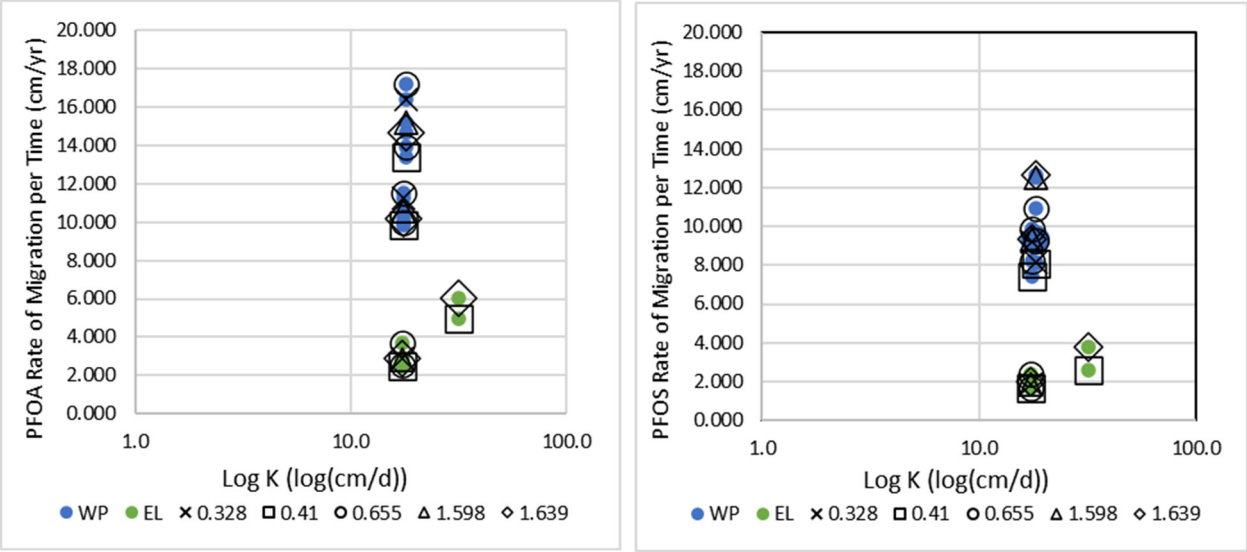


Figure 4.72 Rate of Migration of Center of Mass for the first 10 years of simulation plotted as a function of Log(K) for both (a) PFOA and (b) PFOS.

Net recharge is another factor expected to impact the rate of front propagation to the water table. Net recharge for each site was investigated for a 1-year timeframe and for the full 40-year simulation window. This resulted in net recharge rates ranging from -0.148 cm/d to 0.116 cm/d. Interestingly, the negative recharge occurred at Ellsworth AFB – a location that is an arid, desert-like climate. The highest recharge occurred at Tyndal AFB in FL, which is expected. Regardless of whether the 1-year or 40-year average net recharge was considered, the simulation results indicate that, as the average net recharge increases, the time to reach the max concentration at the water table decreases (see **Figure 4.73**).

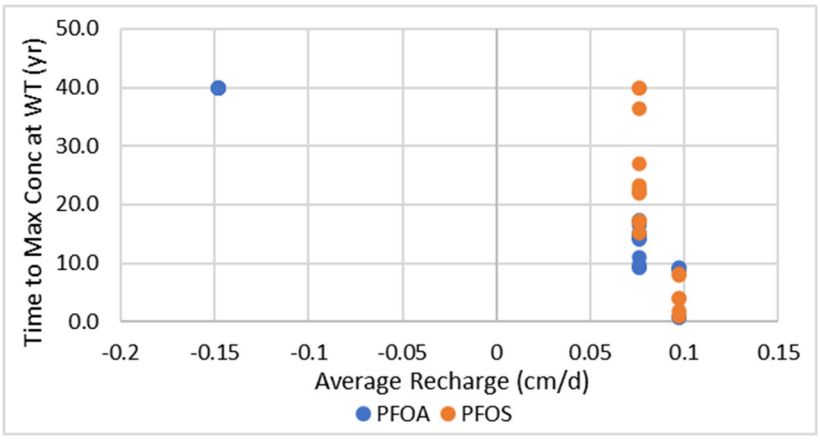


Figure 4.73 Time to reach max concentration at the water table as a function of the net recharge averaged over one (1) year for both PFOA (blue symbols) and PFOS (orange symbols).

The trends depicted in the above figure are consistent with contaminant transport expectations. The negative recharge values, however, suggest that future work may should focus on how best to model evapotranspiration in very arid climates. This also could be a factor of our changing climate with some regions becoming more arid with lower precipitation.

4.5.2.3 Mass Distribution in the Contaminant Source Zone

In addition to the rate of migration, simulations were interrogated to determine how the mass is distributed within the source zone directly below the spilled area. As described in previous sections, a significant amount of PFAS mass is expected to be retained in the vadose zone due to sorption on the soil surface and partitioning to the air-water interface. To investigate these retention mechanisms, simulations were investigated to determine those factors influencing the ratio of mobile to immobile contaminant mass as a function of input parameters.

Figure 4.74 depicts the mobile/immobile ratio for both PFOA and PFOS as a function of the equivalent total volume of AFFF concentrate per area. These data suggest that, as the equivalent total volume of AFFF concentrate increases, the percentage of mass in the mobile zone likewise increases (i.e., percentage of retained mass decreases). This effect is likely attributed to the nonlinearity of the sorption and interfacial partitioning isotherms; partition coefficients tend to decrease with concentration. These results are also likely impacted by the relative differences in PFOA and PFOS concentrations in typical AFFF formulations. PFOS concentrations in the AFFF formulation simulated here were 60 times greater than PFOA concentrations leading to the counterintuitive result that more PFOS can be found in the mobile zone as the total volume per spill area increases. Note that the PFOA data for Tyndall do not show the same trend. This is due to the shallow water table, resulting in most of the contaminant mass leaving the system within the simulated period (40 years). If we examine the PFOA results for the Tyndall simulations at 10 years (rather than 40 years) the data follow the same general trends as those depicted in **Figure 4.74**.

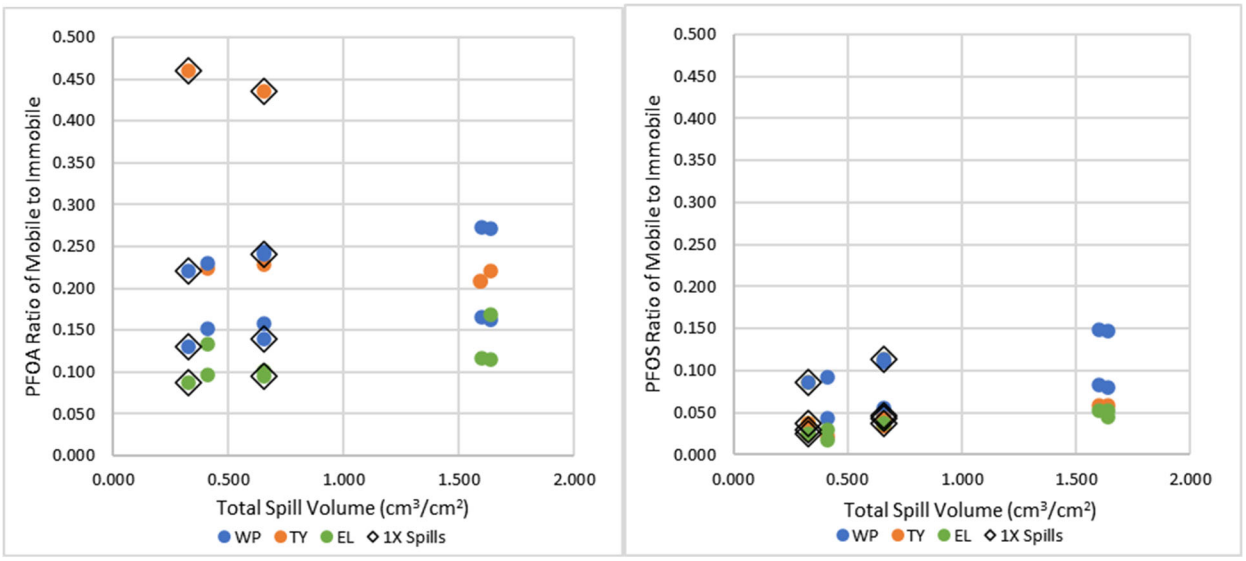


Figure 4.74 Ratio of mobile to immobile mass as a function of Equivalent Total Volume of AFFF Concentrate per area for both (a) PFOA and (b) PFOS. The colors of the symbols represent the different locations and the symbols enclosed by diamonds represent single-spill scenarios.

The fraction of mobile to immobile mass is also likely to be a function of site parameters. The team examined this ratio as a function of log(K) with an expectation that log(K) is a simple surrogate for the air-water interfacial area. **Figure 4.75** shows that as log(K) increases the ratio of mobile to immobile mass increases. This could be a function of the potential for higher permeability soils to have lower interfacial area, resulting in less mass retained at interfaces. However, this observation does not hold true for PFOS. It appears that as log(K) increases the PFOS ratio of mobile to immobile mass decreases. This trend contradicts the trend observed for PFOA and suggests other factors may have a more significant influence on retained mass.

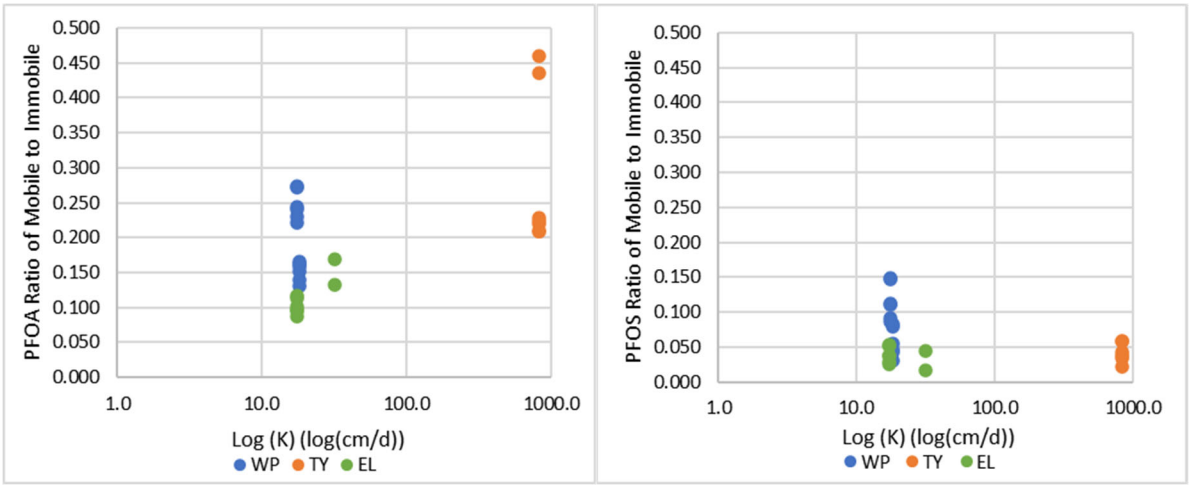


Figure 4.75 Ratio of mobile to immobile mass as a function of log(K) for (a) PFOA and (b) PFOS. Note the colors represent the different contaminant sites. All data are plotted after a 40-year simulation except Tyndall, which are plotted at the end of 10 years.

The team also examined the ratio of mobile to immobile mass as a function of the variance in Log(K). As depicted in the summary table, the variance in Log(K) didn't appear to correlate well

with many of the output parameters except the ratio of mobile to immobile mass for PFOS. This likely reflects the expectation that a larger variance indicates more higher permeability zones exist in the formation. As described previously, the higher permeability zones result in lower specific interfacial area and less PFOS mass retained at the interface. Hence, as the variance in Log(K) increases the ratio of mobile to immobile PFAS mass increases. The same is not observed for PFOA, likely due to the lower affinity of PFOA for the interface – it behaves more like a traditional advective-dispersive contaminant and is not as significantly influenced by the presence of air-water interfaces.

Clearly, one might expect the ratio of mobile to immobile contaminant mass to be a function of the Freundlich parameter (k_f, see **Appendix A.6**). **Figure 4.76** Ratio of mobile to immobile mass as a function of the average Freundlich parameter for (a) PFOA and (b) PFOS. Note Tyndall is excluded. depicts this ratio as a function of the average Freundlich parameter for both PFOA and PFOS at Wright Patterson ABF and Ellsworth AFB. Tyndall AFB data were excluded here for similar reasons as discussed for **Figure 4.76**. Regardless of the simulated location, it appears that, as the Freundlich parameter increases, the ratio of mobile to immobile mass for PFOA decreases. This is expected; higher sorption results in higher retained mass. This same observation is generally true for PFOS although the effect is not nearly as strong as that for PFOA. This indicates that other factors, such as retention on the air-water interface, play a stronger role in the retention of PFOS in the vadose zone.

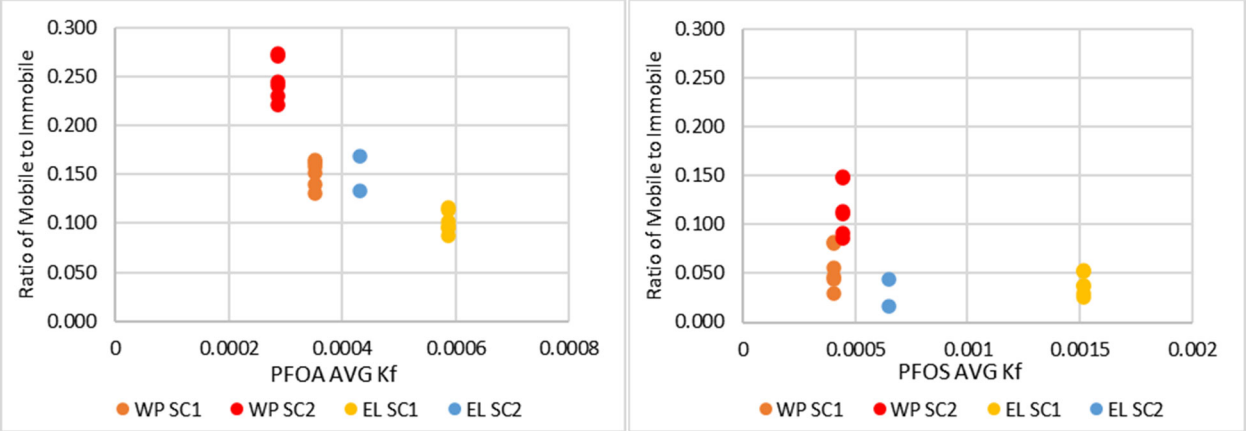


Figure 4.76 Ratio of mobile to immobile mass as a function of the average Freundlich parameter for (a) PFOA and (b) PFOS. Note Tyndall is excluded.

In addition to the retained mass it is interesting to investigate the influence of the sorption parameters on other output values. For example, **Figure 4.77** demonstrates that the rate of migration of the center of mass decreases and the time to reach the water table increases for PFOA as the Freundlich parameter increases. These trends were generally true for PFOS as well, though not quite as marked (not shown). This is to be expected; as sorption becomes stronger, more mass is retained in the vadose zone, decreasing the rate of migration of the center of mass and the time to reach the water table.

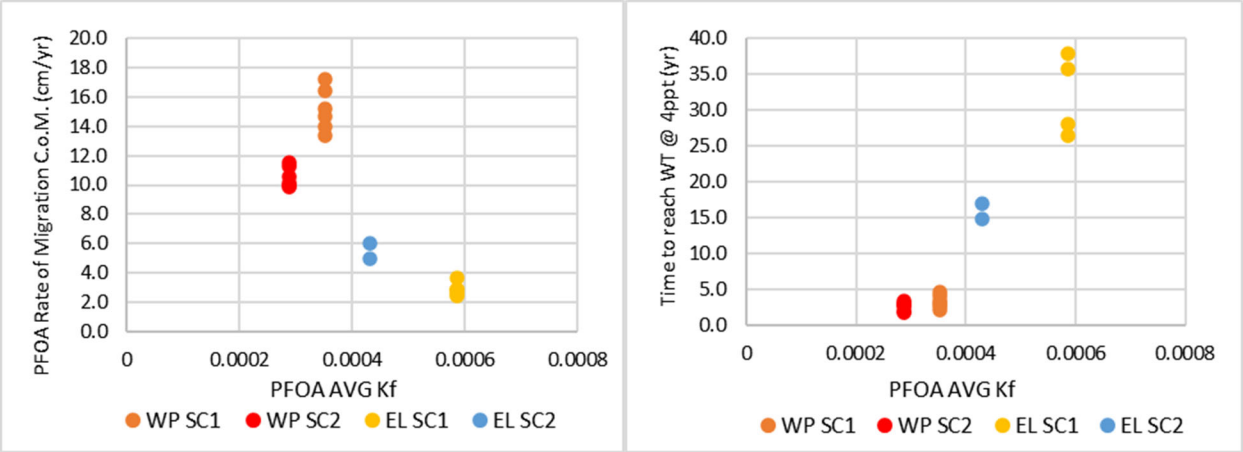


Figure 4.77 (a) PFOA rate of migration of the center of mass and (b) time to reach the water table as a function of the Freundlich parameter.

Table 4.18 Meta-analysis of model results to show correlation between inputs and outputs for PFOA and PFOS transport.

PFOA

INPUT \ OUTPUT	Time to Reach Water Table (yr)	Max Conc at Water Table (ug/L)	Total Mass/Area at Water Table (ug/cm^2)	Ratio of Mobile to Immobile Mass	Rate of Migration of Center of Mass (cm/yr)
Total Mass Spill per Area (ug/cm^3)	0	+	++	0	0
Depth to Water Table (cm)	++	-	-	- -	- -
Avg Permeability (cm/d)	-	+	0	++	++
Avg VAR (log(K) (log(cm/d))	-	0	+	+	-
Avg Freundlich Parameter	++	-	-	-	0
Avg Net Recharge (cm/d)	- -	+	++	++	++

PFOS

INPUT \ OUTPUT	Time to Reach Water Table (yr)	Max Conc at Water Table (ug/L)	Total Mass/Area at Water Table (ug/cm^2)	Ratio of Mobile to Immobile Mass	Rate of Migration of Center of Mass (cm/yr)
Total Mass Spill per Area (ug/cm^3)	0	+	++	+	0
Depth to Water Table (cm)	++	-	-	0	- -
Avg Permeability (cm/d)	-	+	+	-	++
Avg VAR (log(K) (log(cm/d))	-	0	0	++	-
Avg Freundlich Parameter	++	-	- -	-	- -
Avg Net Recharge (cm/d)	- -	++	++	0	++

LEGEND

++	Strong Positive Relationship	- -	Strong Negative Relationship
+	Weak Positive Relationship	-	Weak Negative Relationship
0	No Apparent Relationship		

4.5.2.4 Concluding remarks

The above data can be readily summarized in tabular form to give a general idea of what remedial site managers may expect for a given set of input parameters. The summary **Table 4.18** provided for PFOA and PFOS provides several important observations that can be used to aid remedial site managers and program managers as they work to allocate scarce resources and funding. These tables suggest:

- The higher the equivalent spilled mass per area – perhaps considered the strength of the spill - the more likely the site will have higher concentrations of both PFOS and PFOA at the water table. However, the magnitude of the spill strength is not necessarily linked with an earlier arrival at the water table nor a faster rate of transport through the vadose zone.
- A larger depth to water table generally results in a longer time for PFOA and PFOS to reach the water table but all other output parameters considered appeared to have a negative relationship with water table depth (i.e., the deeper the water table, the lower the maximum concentration to reach the water table, the slower the rate of migration, etc.)
- The average permeability and the variance of log(K) did not appear to have as important an influence on the output parameters as one might expect. There was either no apparent relationship or a weak relationship with most output parameters. However, there might be a stronger dependence on log(K) variance if spatial variability were present in the horizontal direction, such that lateral flow could occur.
- Output parameters appear to be correlated with the Freundlich parameter for both PFOA and PFOS, although the strength of the relationships appeared to be greater for PFOA suggesting retention at the air-water interface may play a more important role in the migration and retention of PFOS.
- Average net recharge generally resulted in higher ratios of mobile to immobile mass, maximum concentrations at the water table and rates of contaminant migration. However, the relationships weren't always consistent between PFOS and PFOA

5. Conclusions and Implications for Future Research/Implementation

5.1 Conclusions

5.1.1 Interfacial Processes

Many PFAS accumulate at air-water and NAPL-water interfaces and exhibit surfactant-like properties:

- Ionic strength strongly influences interfacial accumulation, with higher concentrations leading to more PFAS accumulation
- PFAS sorption and interfacial accumulation are nonlinear functions of concentration, well-characterized by Freundlich isotherms and a Langmuir-Szyszkowski equation, respectively
- AFFF has the capacity to mobilize entrapped NAPLs at field application concentrations (e.g., 3% solution); the onset of mobilization can be quantified using a 'trapping number' concept.
- More surface-active PFAS, such as PFOS and PFNA, can out-compete other PFAS for surface sites when introduced as a mixture; this competition is more pronounced at high concentrations (ppm range).
- Air-water interfacial accumulation can significantly reduce PFAS transport, leading to substantial mass retention in unsaturated soils
- NAPL-water interfacial accumulation is likely a less important retardation mechanism than air-water interfacial accumulation in unsaturated soils.

5.1.2 Biotransformation

Batch and column studies demonstrated the biotic transformation of selected PFAA precursors in AFFF impacted soils. These experiments support the following conclusions.

- The extent and rate of biotransformation of FOSA in the natural environment may be soil/site dependent.
  - With its tendency to partition to the solid phase, the bioavailability of FOSA to the native microbial community appears to a critical parameter in the evaluation of FOSA biotransformation in soils.
  - Microorganisms belonging to Proteobacteria, Actinobacteriota, Chloroflexi, Acidobacteriota, and Planctomycetota may play a role in the biotransformation of FOSA, while Cyanobacteria and Bacteroidota may be relatively more tolerant to FOSA and/or its associated transformation products.
  - Evaluation of site geochemical and biological attributes will, thus, be important in achieving a better understanding of FOSA biotransformation in the field and support insights into the management and remediation of contaminated sites.
- 8:2 FTOH can be transformed rapidly by indigenous microbial communities from AFFF-impacted surface soils under aerobic conditions. More than 90 mol% of initially spiked 8:2 FTOH was removed within 90-day incubation.
  - Previously documented 8:2 FTOH biotransformation products, including polyfluorinated substances, like 8:2 FTCA, 8:2 FTUA, 7:2 sFTOH, and 7:3 acid, as

well as perfluorinated compounds such as PFOA, were identified as biotransformation products.
    - Although rarely documented, 7:3 U amide, 3-OH-7:3 acid, and 6:3 acid were also identified as biotransformation products in this study. Perfluoroalkane-like compounds, including 1H-perfluoroheptane, 1H-perfluorohexane, and perfluoroheptanal were identified as novel transformation products that have not been previously reported.
    - Microorganisms in phylum Proteobacteria, such as genera *Afipia* and *Sphingomonas* may be more tolerant of high 8:2 FTOH concentrations and may be involved as potential degraders.

- The biotransformation rates and pathways of 8:2 FTOH are highly dependent upon redox conditions.
    - Biotransformation was much slower under sulfate and iron-reducing conditions than under nitrate-reducing conditions, while the fastest biotransformation occurred under oxic conditions.
    - The yield of the PFCAs, identified as terminal products of 8:2 FTOH biotransformation, were higher for oxic than nitrate-reducing conditions and these compounds were not present under sulfate- and iron-reducing conditions.
    - The production of two polyfluorinated acids (i.e., 8:2 FTCA and 8:2 FTUA) was observed under all redox conditions.
    - Biostimulation was shown to increase 8:2 FTOH biotransformation rates and product yields (e.g., PFOA) in anaerobic microcosms.
    - Genera potentially responsible for 8:2 FTOH biotransformation were identified including *Lysobacter, Herminiimonas*, and *Ramlibacter* under nitrate-reducing conditions and *Caldicoprobacter* and *Sedimentibacter* under sulfate- and iron-reducing conditions.
- Biotransformation of 6:2 FTS is strongly influenced by environmental factors such as the availability of sulfur sources and native microbial community composition.
    - The biotransformation of 6:2 FTS was favored by the microbial consortia only after other easily assimilated sulfur sources (e.g., sulfate) were depleted.
    - *Desulfobacterota* microorganisms likely promoted 6:2 FTS biotransformation via more efficient desulfonation, while species in the genus *Sphingomonas,* which exhibited higher tolerance to elevated 6:2 FTS concentrations and transformation products, likely also contributed to its biotransformation.
    - By identifying additional 6:2 FTS transformation products that were previously undocumented, novel "fluorotelomer ketone to PFCA" pathways were proposed to account for formation of PFCAs from fluorotelomer precursors.

- Sixteen classes of PFAS in a historically used 3M AFFF formulation were identified, and multiple classes of ECF-based precursors and a wider range of homologues, in comparison to previous studies (e.g., C_4-C_8 AmPr-FASA), were demonstrated to be transformed under biotic and/or abiotic conditions.
    - For the first time, experimental results provided evidence for the biotransformation of AmPr-FASA-PrA/TAmPr-FASA-AA and CEt-AmPr-FAAd, while CEt-AmPr-FASA-PrA was found to be persistent during the 308-day incubation.

- Functional groups (e.g., sulfonamide group, methyl group, and carboxyalkyl group) in the nonfluorinated moiety and the carbon chain of the perfluorinated moiety influenced the stability of ECF-based precursors.

- Soil microbial communities tended to form specific modular structures after exposure to fluorotelomers.
  - Genera *Variovorax*, *Rhodococcus*, and *Cupriavidus* were found to be keystone taxa during fluorotelomer biotransformation.
  - A wide range of genes, such as 6-oxocyclohex-1-ene-carbonyl-CoA hydrolase gene and cyclohexa-1,5-dienecarbonyl-CoA hydratase gene, were predicted to be associated with fluorotelomer biotransformation.

- The biotransformation of 6:2 FTS was demonstrated to be rate limited under flowing conditions in one-dimensional column experiments.
  - Slower flow conditions (longer residence times) were associated with more complete 6:2 FTS biotransformation, resulting in less formation of early intermediates (i.e., 6:2 FTCA and 6:2 FTUA) but greater formation of terminal products (i.e., C_4-C_7 PFCAs).
  - Flow interruption (2-7 days) was found to promote the biotransformation of 6:2 FTS after the resumption of flow. This enhancement of biotransformation could last approximately 6-7 PVs.
  - Biotransformation of 6:2 FTS proceeded along the flow path, with a generally decreasing trend in 6:2 FTS concentration and increasing trend in biotransformation products over the path.
  - Continuous flow conditions were demonstrated to promote a more complete biotransformation of 6:2 FTS.

5.1.3 Field Scale Modeling

Mathematical model simulations for model AFFF (3-component mixture of PFOS, PFOA and a hydrocarbon surfactant) field scale release scenarios reveal:

- Under unsaturated conditions, interfacial accumulation and soil sorption account for the large majority of the PFAS mass in the soil profile; the aqueous phase concentration is not representative of the extent of PFAS contamination.

- Climatic conditions and soil properties have a significant influence on the migration of PFAS in the vadose zone.
  - High recharge is associated with more rapid penetration, particularly in sandy soils.
  - Seasonal fluctuations in recharge can lead to oscillations in the distribution between sorbed and interfacial PFAS mass.
  - Under low saturation (dry conditions), interfacial areas are high and PFAS penetration rates are low.
  - PFOA is more mobile than PFOS in the soil profile, attributed to differences in sorption and interfacial accumulation properties.
  - PFOA and PFOS migration rates increase as Freundlich sorption capacity coefficients decrease. This trend is more pronounced for PFOA, consistent with the greater importance of interfacial accumulation for PFOS.

- Spill conditions have a significant impact on PFAS mobility in the vadose zone, as well as on the maximum concentrations reaching the water table.

    - For periodic releases (i.e., fire-training scenarios), maximum concentrations at the water table are proportional to the released mass/area, regardless of soil profile and climate conditions.
    - For periodic releases, time for breakthrough at the water table decreases with an increase in released mass/area, a consequence of nonlinear partitioning behavior.
    - Single release events are associated with earlier breakthroughs and higher concentrations at the water table, in comparison with periodic spills with the same mass/area released.

- The presence of hydrocarbon surfactants in AFFF tends to increase the rate of migration of PFOA and PFOS in the soil profile. This effect will be very important for higher mass release rates.

5.2 Implications for Future Research

5.2.1 Interfacial Processes

This project has improved our understanding of the multiphase (NAPL-water and air-water) migration and retention of PFAS and PFAS mixtures in natural soils. In particular, the research points to the potential importance of interfacial processes (e.g., air-water interfacial accumulation) and of competitive effects on contaminant transport rates and mobile/immobile mass ratios in AFFF-impacted soil profiles. As a necessary first step, the research described herein focused on transport measurements under steady flow conditions in homogeneous porous media. Modeling results in realistic soil profiles, however, suggest that dynamic flow conditions and porous media textural and chemical variations will play a significant role in determining the extent of PFAS migration. Based upon this work, the following future research directions are suggested:

- In this research, modeling revealed the critical importance of accurate interfacial area estimates to the prediction of interfacial mass retention. Future research should therefore be directed towards the development and validation of constitutive models for interfacial area (that of relevance to PFAS retention) as a function of easily measured soil properties.
- Although the transport behavior of a number of single PFAS and PFAS mixtures was examined in this research, future transport and fate predictions and risk assessment should collect data on the sorption and IFT reduction behavior for additional individual PFAS and PFAS mixtures over a wide range of environmental (chemical and mineralogical) conditions. These data will be needed to support the development and validation of competitive sorption and interfacial reduction models appropriate to the prediction of PFAS behavior in realistic field conditions.
- In natural systems under dynamic recharge conditions, it is likely that the capillary fringe will play an important role in the retention of PFAS at or above the water table. Future work should focus on the laboratory assessment, through larger-scale experiments, of PFAS behavior in the soil profile and capillary fringe under dynamic flow conditions. These experiments will support mathematical model enhancement to incorporate the influence of capillary hysteresis on PFAS retention
- Future research should focus on conducting controlled AFFF release experiments in larger scale, multi-dimensional, heterogeneously-packed unsaturated porous media in laboratory and, if possible, field settings. Such experiments will support an improved understanding of the influence of dimensionality and heterogeneity on PFAS transport and retention and support the validation of multi-dimensional transport models.

5.2.2 PFAS Biotransformation

This project has improved our understanding of the transformation of different PFAS, including FT- and ECF- based precursors, in AFFF-impacted soils in terms of the capability and extent of biotic/abiotic transformation under various environmental conditions. These results also provide insight into the structure-relevant stability of PFAS and a starting point for screening microbes and functional genes engaged in PFAS biotransformation. Based on the findings, the following future research directions are suggested:

- Novel compounds including 1H-perfluoroalkanes (e.g., 1H-perfluorobutane, 1H-perfluoropentane, and 1H-perfluoroheptane) were identified as the biotransformation products of 8:2 FTOH or 6:2 FTS under various redox conditions. These 1H-perfluoroalkanes are likely unique transformation products that could be present at sites contaminated by fluorotelomer precursors. Future research is needed to assess the prevalence of these compounds at AFFF-impacted sites and to evaluate their potential impacts on ecosystems and human health. Moreover, the environmental fate of these newly identified compounds is not yet understood. Therefore, future research should seek to elucidate the biotransformation rates and reaction pathways of these compounds.
- Multiple phyla and genera were identified to be potentially responsible for the biotransformation of FOSA, 8:2 FTOH, 6:2 FTS, and AFFF-derived precursors under oxic or anoxic conditions. Future studies are needed to isolate individual bacterial strain(s) and/or develop enrichment culture, which can be used to better assess the function of those potential degrader(s) using more advanced-omics technologies and additional analyses, e.g., metatranscriptomics and quantitative PCR. The most essential step will be determining the functional gene(s) and enzymes that are responsible for defluorination and will eventually facilitate development of PFAS bioremediation technology.
- PFAS stability related to chemical structures was investigated. However, because AFFF, a PFAS mixture, was used in place of individual PFAS as the parent compound(s) it was difficult to elucidate the transformation mechanisms. To better predict fate of different PFAS, including both legacy and emerging PFAS, further studies are needed to evaluate biotransformation of individual PFAS with different chemical structures and to develop quantitative structure–biotransformation relationship models. These studies will support better predictions of the environmental fate of PFAS and be beneficial for the management of the PFAS-impacted sites.
- This project demonstrates that the biotransformation rates and pathways of 6:2 FTS in flow-through one-dimensional columns differed from those observed in batch experiments. The findings highlight the importance of incorporation of system conditions such as hydraulic parameters into experimental systems in the investigation of PFAS biotransformation. Given that almost all PFAS biotransformation studies reported to date were conducted in batch reactor experiments, future research is needed to assess the biotransformation of PFAS in dynamic laboratory experiments of increasing scale and complexity. (e.g., in one-dimensional saturated/unsaturated columns and multi-dimensional systems incorporating unsaturated and saturated zones). Further, field-scale studies will be needed to provide a more detailed understanding of PFAS fate and transformation in natural systems.

6. Literature Cited

1. Moody, C.A. and J.A. Field, *Perfluorinated Surfactants and the Environmental Implications of Their Use in Fire-Fighting Foams.* Environmental Science & Technology, 2000. **34**(18): p. 3864-3870.
2. Darwin, R., *Estimated quantities of aqueous film forming foam (AFFF) in the United States.* Baltimore, MD: Aug, 2004. **2004**.
3. SERDP-ESTCP. *SERDP Core FY 2018 Solicitation: Improved Understanding of Per- and Polyfluoroalkyl Substance Source Zones*. 2018 (Accessed on 5/22/23); Available from: https://serdp-estcp.org/workingwithus/callforproposal?id=e9783b3b-0222-45ab-91cb-0d6c04ae152e.
4. Backe, W.J., T.C. Day, and J.A. Field, *Zwitterionic, cationic, and anionic fluorinated chemicals in aqueous film forming foam formulations and groundwater from US military bases by nonaqueous large-volume injection HPLC-MS/MS.* Environmental Science & Technology, 2013. **47**(10): p. 5226-5234.
5. McGuire, M.E., et al., *Evidence of Remediation-Induced Alteration of Subsurface Poly- and Perfluoroalkyl Substance Distribution at a Former Firefighter Training Area.* Environmental Science & Technology, 2014. **48**(12): p. 6644-6652.
6. Favreau, P., et al., *Multianalyte profiling of per-and polyfluoroalkyl substances (PFASs) in liquid commercial products.* Chemosphere, 2017. **171**: p. 491-501.
7. Herzke, D., E. Olsson, and S. Posner, *Perfluoroalkyl and polyfluoroalkyl substances (PFASs) in consumer products in Norway – A pilot study.* Chemosphere, 2012. **88**(8): p. 980-987.
8. Houtz, E.F., et al., *Persistence of Perfluoroalkyl Acid Precursors in AFFF-Impacted Groundwater and Soil.* Environmental Science & Technology, 2013. **47**(15): p. 8187-8195.
9. McKenzie, E.R., et al., *The influence of a non-aqueous phase liquid (NAPL) and chemical oxidant application on perfluoroalkyl acid (PFAA) fate and transport.* Water Research, 2016. **92**: p. 199-207.
10. Guelfo, J.L. and C.P. Higgins, *Subsurface transport potential of perfluoroalkyl acids at aqueous film-forming foam (AFFF)-impacted sites.* Environmental Science & Technology, 2013. **47**(9): p. 4164-4171.
11. Cao, Y., et al., *1000-fold preconcentration of per-and polyfluorinated alkyl substances within 10 minutes via electrochemical aerosol formation.* Analytical chemistry, 2019. **91**(22): p. 14352-14358.
12. Meng, P., et al., *Role of the air-water interface in removing perfluoroalkyl acids from drinking water by activated carbon treatment.* Journal of Hazardous Materials, 2020. **386**: p. 121981.
13. Vecitis, C., et al., *Enhancement of perfluorooctanoate and perfluorooctanesulfonate activity at acoustic cavitation bubble interfaces.* The Journal of Physical Chemistry C, 2008. **112**(43): p. 16850-16857.
14. Lyu, Y., et al., *Adsorption of PFOA at the air–water interface during transport in unsaturated porous media.* Environmental Science & Technology, 2018. **52**(14): p. 7745-7753.
15. Lyu, Y. and M.L. Brusseau, *The influence of solution chemistry on air-water interfacial adsorption and transport of PFOA in unsaturated porous media.* Science of the Total Environment, 2020. **713**: p. 136744.

16. Anderson, R.H., et al., *Occurrence of select perfluoroalkyl substances at US Air Force aqueous film-forming foam release sites other than fire-training areas: Field-validation of critical fate and transport properties.* Chemosphere, 2016. **150**: p. 678-685.
17. Xiao, F., et al., *Perfluorooctane sulfonate (PFOS) and perfluorooctanoate (PFOA) in soils and groundwater of a US metropolitan area: migration and implications for human exposure.* Water Research, 2015. **72**: p. 64-74.
18. Anderson, R.H., D.T. Adamson, and H.F. Stroo, *Partitioning of poly-and perfluoroalkyl substances from soil to groundwater within aqueous film-forming foam source zones.* Journal of Contaminant Hydrology, 2019. **220**: p. 59-65.
19. Høisæter, Å., A. Pfaff, and G.D. Breedveld, *Leaching and transport of PFAS from aqueous film-forming foam (AFFF) in the unsaturated soil at a firefighting training facility under cold climatic conditions.* Journal of Contaminant Hydrology, 2019. **222**: p. 112-122.
20. Shinoda, K. and T. Nomura, *Miscibility of fluorocarbon and hydrocarbon surfactants in micelles and liquid mixtures. Basic studies of oil repellent and fire extinguishing agents.* The Journal of Physical Chemistry, 1980. **84**(4): p. 365-369.
21. Downes, N., G. Ottewill, and R. Ottewill, *An investigation of the behaviour of ammonium perfluoro-octanoate at the air/water interface in the absence and presence of salts.* Colloids and Surfaces A: Physicochemical and Engineering Aspects, 1995. **102**: p. 203-211.
22. Brusseau, M.L., et al., *Comprehensive retention model for PFAS transport in subsurface systems.* Water Research, 2019. **148**: p. 41-50.
23. Hill, C., et al., *Surface and bulk properties of surfactants used in fire-fighting.* Journal of Colloid and Interface Science, 2018. **530**: p. 686-694.
24. Chan, D.B. and E.S. Chian, *Economics of membrane treatment of wastewaters containing firefighting foam.* Environmental Progress, 1986. **5**(2): p. 104-109.
25. Moody, C.A., et al., *Occurrence and persistence of perfluorooctanesulfonate and other perfluorinated surfactants in groundwater at a fire-training area at Wurtsmith Air Force Base, Michigan, USA.* Journal of Environmental Monitoring, 2003. **5**(2): p. 341-345.
26. Baduel, C., C.J. Paxman, and J.F. Mueller, *Perfluoroalkyl substances in a firefighting training ground (FTG), distribution and potential future release.* Journal of Hazardous Materials, 2015. **296**: p. 46-53.
27. Hale, S.E., et al., *Sorbent amendment as a remediation strategy to reduce PFAS mobility and leaching in a contaminated sandy soil from a Norwegian firefighting training facility.* Chemosphere, 2017. **171**: p. 9-18.
28. Filipovic, M., et al., *Historical usage of aqueous film forming foam: A case study of the widespread distribution of perfluoroalkyl acids from a military airport to groundwater, lakes, soils and fish.* Chemosphere, 2015. **129**: p. 39-45.
29. Brusseau, M.L., *Assessing the potential contributions of additional retention processes to PFAS retardation in the subsurface.* Science of the Total Environment, 2018. **613**: p. 176-185.
30. Silva, J.A., et al., *Evaluating air-water and NAPL-water interfacial adsorption and retention of Perfluorocarboxylic acids within the Vadose zone.* Journal of Contaminant Hydrology, 2019. **223**: p. 103472.
31. Soga, K., J. Page, and T. Illangasekare, *A review of NAPL source zone remediation efficiency and the mass flux approach.* Journal of Hazardous Materials, 2004. **110**(1-3): p. 13-27.

32. Fortin, J., W.A. Jury, and M.A. Anderson, *Enhanced removal of trapped non-aqueous phase liquids from saturated soil using surfactant solutions.* Journal of Contaminant Hydrology, 1997. **24**(3-4): p. 247-267.
33. Longino, B.L. and B.H. Kueper, *Effects of capillary pressure and use of polymer solutions on dense, non-aqueous-phase liquid retention and mobilization in a rough-walled fracture.* Environmental Science & Technology, 1999. **33**(14): p. 2447-2455.
34. Singh, K., et al., *Remobilization of residual non-aqueous phase liquid in porous media by freeze− thaw cycles.* Environmental Science & Technology, 2011. **45**(8): p. 3473-3478.
35. Martel, R. and P.J. Gélinas, *Surfactant solutions developed for NAPL recovery in contaminated aquifers.* Groundwater, 1996. **34**(1): p. 143-154.
36. Oostrom, M., et al., *Movement and remediation of trichloroethylene in a saturated, heterogeneous porous medium: 2. Pump-and-treat and surfactant flushing.* Journal of Contaminant Hydrology, 1999. **37**(1-2): p. 179-197.
37. Pennell, K.D., G.A. Pope, and L.M. Abriola, *Influence of viscous and buoyancy forces on the mobilization of residual tetrachloroethylene during surfactant flushing.* Environmental Science & Technology, 1996. **30**(4): p. 1328-1335.
38. Rathfelder, K.M., et al., *Surfactant enhanced recovery of tetrachloroethylene from a porous medium containing low permeability lenses: 2. Numerical simulation.* Journal of Contaminant Hydrology, 2001. **48**(3-4): p. 351-374.
39. Levine, A., et al., *Biogeochemical assessment of natural attenuation of JP-4-contaminated ground water in the presence of fluorinated surfactants.* Science of the Total Environment, 1997. **208**(3): p. 179-195.
40. Chen, H., et al., *Sorption of perfluorooctane sulfonate (PFOS) on oil and oil-derived black carbon: influence of solution pH and [Ca2+].* Chemosphere, 2009. **77**(10): p. 1406-1411.
41. Van Glubt, S. and M.L. Brusseau, *Contribution of nonaqueous-phase liquids to the retention and transport of per and polyfluoroalkyl substances (PFAS) in porous media.* Environmental Science & Technology, 2021. **55**(6): p. 3706-3715.
42. Moody, C.A. and J.A. Field, *Determination of perfluorocarboxylates in groundwater impacted by fire-fighting activity.* Environmental science & technology, 1999. **33**(16): p. 2800-2806.
43. Brusseau, M.L., *Simulating PFAS transport influenced by rate-limited multi-process retention.* Water Research, 2020. **168**: p. 115179.
44. Lee, H., J. D'eon, and S.A. Mabury, *Biodegradation of polyfluoroalkyl phosphates as a source of perfluorinated acids to the environment.* Environmental Science & Technology, 2010. **44**(9): p. 3305-3310.
45. Wang, N., et al., *6: 2 Fluorotelomer sulfonate aerobic biotransformation in activated sludge of waste water treatment plants.* Chemosphere, 2011. **82**(6): p. 853-858.
46. Dasu, K., J. Liu, and L.S. Lee, *Aerobic soil biodegradation of 8: 2 fluorotelomer stearate monoester.* Environmental Science & Technology, 2012. **46**(7): p. 3831-3836.
47. Liou, J.-C., et al., *Investigating the biodegradability of perfluorooctanoic acid.* Chemosphere, 2010. **80**(2): p. 176-183.
48. Liu, J., et al., *6-2 Fluorotelomer alcohol aerobic biodegradation in soil and mixed bacterial culture.* Chemosphere, 2010. **78**(4): p. 437-444.
49. Royer, L.A., et al., *Microbial transformation of 8: 2 fluorotelomer acrylate and methacrylate in aerobic soils.* Chemosphere, 2015. **129**: p. 54-61.

50. Wang, N., et al., *8-2 Fluorotelomer alcohol aerobic soil biodegradation: Pathways, metabolites, and metabolite yields.* Chemosphere, 2009. **75**(8): p. 1089-1096.
51. Dinglasan, M.J.A., et al., *Fluorotelomer Alcohol Biodegradation Yields Poly- and Perfluorinated Acids.* Environmental Science & Technology, 2004. **38**(10): p. 2857-2864.
52. Harding-Marjanovic, K.C., et al., *Aerobic biotransformation of fluorotelomer thioether amido sulfonate (Lodyne) in AFFF-amended microcosms.* Environmental Science & Technology, 2015. **49**(13): p. 7666-7674.
53. Zhang, S., et al., *6:2 and 8:2 Fluorotelomer Alcohol Anaerobic Biotransformation in Digester Sludge from a WWTP under Methanogenic Conditions.* Environmental Science & Technology, 2013. **47**(9): p. 4227-4235.
54. Zhang, S., et al., *Biotransformation potential of 6: 2 fluorotelomer sulfonate (6: 2 FTSA) in aerobic and anaerobic sediment.* Chemosphere, 2016. **154**: p. 224-230.
55. Lange, C., *The aerobic biodegradation of N-EtFOSE alcohol by the microbial activity present in municipal wastewater treatment sludge.* For 3M Company, 2000.
56. Rhoads, K.R., et al., *Aerobic biotransformation and fate of N-ethyl perfluorooctane sulfonamidoethanol (N-EtFOSE) in activated sludge.* Environmental Science & Technology, 2008. **42**(8): p. 2873-2878.
57. Benskin, J.P., et al., *Biodegradation of N -Ethyl Perfluorooctane Sulfonamido Ethanol (EtFOSE) and EtFOSE-Based Phosphate Diester (SAmPAP Diester) in Marine Sediments.* Environmental Science & Technology, 2013. **47**(3): p. 1381-1389.
58. Im, J., et al., *Environmental fate of the next generation refrigerant 2, 3, 3, 3-tetrafluoropropene (HFO-1234yf).* Environmental Science & Technology, 2014. **48**(22): p. 13181-13187.
59. Loeffler, F.E., *Microbial Transformation of Fluorinated Environmental Pollutants.* 2005. Prepared by
60. Conder, J.M., et al., *Are PFCAs bioaccumulative? A critical review and comparison with regulatory criteria and persistent lipophilic compounds.* Environmental Science & Technology, 2008. **42**(4): p. 995-1003.
61. McKenzie, E.R., et al., *Effects of Chemical Oxidants on Perfluoroalkyl Acid Transport in One-Dimensional Porous Media Columns.* Environmental Science & Technology, 2015. **49**(3): p. 1681-1689.
62. Guo, B., J. Zeng, and M.L. Brusseau, *A mathematical model for the release, transport, and retention of per-and polyfluoroalkyl substances (PFAS) in the vadose zone.* Water Resources Research, 2020. **56**(2): p. e2019WR026667.
63. Silva, J.A.K., J. Šimůnek, and J.E. McCray, *A modified HYDRUS model for simulating PFAS transport in the vadose zone.* Water, 2020. **12**(10): p. 2758.
64. Silva, J.A., et al., *Simulated leaching of PFAS from land-applied municipal biosolids at agricultural sites.* Journal of Contaminant Hydrology, 2022. **251**: p. 104089.
65. Šimůnek, J., M.T. Van Genuchten, and M. Šejna, *Recent developments and applications of the HYDRUS computer software packages.* Vadose Zone Journal, 2016. **15**(7).
66. Zeng, J., M.L. Brusseau, and B. Guo, *Model validation and analyses of parameter sensitivity and uncertainty for modeling long-term retention and leaching of PFAS in the vadose zone.* Journal of Hydrology, 2021. **603**: p. 127172.
67. Zeng, J. and B. Guo, *Multidimensional simulation of PFAS transport and leaching in the vadose zone: Impact of surfactant-induced flow and subsurface heterogeneities.* Advances in Water Resources, 2021. **155**: p. 104015.

68. Wallis, I., et al., *Model-based identification of vadose zone controls on PFAS mobility under semi-arid climate conditions.* Water Research, 2022. **225**: p. 119096.
69. Lyu, X., et al., *Transport of perfluorooctanoic acid in unsaturated porous media mediated by SDBS.* Journal of Hydrology, 2022. **607**: p. 127479.
70. Abraham, J.E., et al., *Retention of PFOS and PFOA mixtures by trapped gas bubbles in porous media.* Environmental Science & Technology, 2022. **56**(22): p. 15489-15498.
71. Gao, Y., et al., *A fundamental model for calculating interfacial adsorption of complex ionic and nonionic PFAS mixtures in the presence of mixed salts.* Environmental Science: Processes & Impacts, 2023.
72. Le, S.-T., et al., *Predicting the impact of salt mixtures on the air-water interfacial behavior of PFAS.* Science of the Total Environment, 2022. **819**: p. 151987.
73. Szyszkowski, B.v., *Experimentelle Studien über kapillare Eigenschaften der wässerigen Lösungen von Fettsäuren.* Zeitschrift für physikalische Chemie, 1908. **64**(1): p. 385-414.
74. DeSimone, L., P. McMahon, and M. Rosen, *The Quality of Our Nation's Waters: Water Quality in Principal Aquifers of the United States, 1991-2010.(Circular 1360).* US Geological Survey, 2015.
75. Berry, J.D., et al., *Measurement of surface and interfacial tension using pendant drop tensiometry.* Journal of Colloid and Interface Science, 2015. **454**: p. 226-237.
76. Costanza, J., et al., *Accumulation of PFOA and PFOS at the air–water interface.* Environmental Science & Technology Letters, 2019. **6**(8): p. 487-491.
77. Lunkenheimer, K., K. Geggel, and D. Prescher, *Role of Counterion in the Adsorption Behavior of 1: 1 Ionic Surfactants at Fluid Interfaces · Adsorption Properties of Alkali Perfluoro-n-octanoates at the Air/Water Interface.* Langmuir, 2017. **33**(39): p. 10216-10224.
78. Schaefer, C.E., et al., *Uptake of poly-and perfluoroalkyl substances at the air–water interface.* Environmental Science & Technology, 2019. **53**(21): p. 12442-12448.
79. Fainerman, V. and E. Lucassen-Reynders, *Adsorption of single and mixed ionic surfactants at fluid interfaces.* Advances in Colloid and Interface Science, 2002. **96**(1-3): p. 295-323.
80. Lucassen-Reynders, E., *Surface equation of state for ionized surfactants.* The Journal of Physical Chemistry, 1966. **70**(6): p. 1777-1785.
81. Rosen, M.J. and J.T. Kunjappu, *Surfactants and interfacial phenomena*. 2012: John Wiley & Sons.
82. Löffler, F.E., R.A. Sanford, and K.M. Ritalahti, *Enrichment, Cultivation, and Detection of Reductively Dechlorinating Bacteria*, in *Methods in Enzymology*. 2005, Academic Press. p. 77-111.
83. Yi, S., et al., *Biotransformation of AFFF Component 6:2 Fluorotelomer Thioether Amido Sulfonate Generates 6:2 Fluorotelomer Thioether Carboxylate under Sulfate-Reducing Conditions.* Environmental Science & Technology Letters, 2018. **5**(5): p. 283-288.
84. Zhao, L., et al., *6:2 Fluorotelomer alcohol biotransformation in an aerobic river sediment system.* Chemosphere, 2013. **90**(2): p. 203-209.
85. McCord, J., S. Newton, and M. Strynar, *Validation of quantitative measurements and semi-quantitative estimates of emerging perfluoroethercarboxylic acids (PFECAs) and hexfluoroprolyene oxide acids (HFPOAs).* Journal of Chromatography A, 2018. **1551**: p. 52-58.

86. Szostek, B., K.B. Prickett, and R.C. Buck, *Determination of fluorotelomer alcohols by liquid chromatography/tandem mass spectrometry in water.* Rapid Communications in Mass Spectrometry, 2006. **20**(19): p. 2837-2844.
87. Williams, A.J., et al., *The CompTox Chemistry Dashboard: a community data resource for environmental chemistry.* Journal of Cheminformatics, 2017. **9**(1): p. 61.
88. Wishart, D.S., et al., *BioTransformer 3.0—a web server for accurately predicting metabolic transformation products.* Nucleic Acids Research, 2022: p. gkac313.
89. Schymanski, E.L., et al., *Identifying Small Molecules via High Resolution Mass Spectrometry: Communicating Confidence.* Environmental Science & Technology, 2014. **48**(4): p. 2097-2098.
90. Thompson, L.R., et al., *A communal catalogue reveals Earth's multiscale microbial diversity.* Nature, 2017. **551**(7681): p. 457-463.
91. Edgar, R.C., *Search and clustering orders of magnitude faster than BLAST.* Bioinformatics, 2010. **26**(19): p. 2460-2461.
92. Edgar, R.C., *UPARSE: highly accurate OTU sequences from microbial amplicon reads.* Nature Methods, 2013. **10**(10): p. 996-998.
93. Quast, C., et al., *The SILVA ribosomal RNA gene database project: improved data processing and web-based tools.* Nucleic Acids Research, 2013. **41**(Database issue): p. D590-596.
94. Csardi, G. and T. Nepusz, *The igraph software package for complex network research.* InterJournal, complex systems, 2006. **1695**(5): p. 1-9.
95. Bastian, M., S. Heymann, and M. Jacomy. *Gephi: an open source software for exploring and manipulating networks*. in *Proceedings of the international AAAI conference on web and social media*. 2009.
96. Navarro, D., *Learning statistics with R: A tutorial for psychology students and other beginners: Version 0.5*. 2013: University of Adelaide Adelaide, Australia.
97. Kokou, F., et al., *Core gut microbial communities are maintained by beneficial interactions and strain variability in fish.* Nature microbiology, 2019. **4**(12): p. 2456-2465.
98. Magurran, A.E. and P.A. Henderson, *Explaining the excess of rare species in natural species abundance distributions.* Nature, 2003. **422**(6933): p. 714-716.
99. Pandit, S.N., J. Kolasa, and K. Cottenie, *Contrasts between habitat generalists and specialists: an empirical extension to the basic metacommunity framework.* Ecology, 2009. **90**(8): p. 2253-2262.
100. Shen, D., S. Langenheder, and K. Jürgens, *Dispersal modifies the diversity and composition of active bacterial communities in response to a salinity disturbance.* Frontiers in microbiology, 2018. **9**: p. 2188.
101. Klausen, M., et al., *Dynamics of development and dispersal in sessile microbial communities: examples from Pseudomonas aeruginosa and Pseudomonas putida model biofilms.* FEMS microbiology letters, 2006. **261**(1): p. 1-11.
102. Power, M.E., et al., *Challenges in the quest for keystones: identifying keystone species is difficult—but essential to understanding how loss of species will affect ecosystems.* BioScience, 1996. **46**(8): p. 609-620.
103. Banerjee, S., K. Schlaeppi, and M.G. van der Heijden, *Keystone taxa as drivers of microbiome structure and functioning.* Nature Reviews Microbiology, 2018. **16**(9): p. 567-576.

104. Yu, X., et al., *Dorsal root ganglion macrophages contribute to both the initiation and persistence of neuropathic pain.* Nature communications, 2020. **11**(1): p. 1-12.
105. Méndez, V., et al., *Aerobic biotransformation of 6:2 fluorotelomer sulfonate by Dietzia aurantiaca J3 under sulfur-limiting conditions.* Science of the Total Environment, 2022. **829**: p. 154587.
106. Yang, S.-H., et al., *Desulfonation and defluorination of 6: 2 fluorotelomer sulfonic acid (6: 2 FTSA) by Rhodococcus jostii RHA1: Carbon and sulfur sources, enzymes, and pathways.* Journal of Hazardous Materials, 2022. **423**: p. 127052.
107. Wackett, L.P., *Why is the biodegradation of polyfluorinated compounds so rare?* Msphere, 2021. **6**(5): p. e00721-21.
108. Costanza, J., L.M. Abriola, and K.D. Pennell, *Aqueous film-forming foams exhibit greater interfacial activity than PFOA, PFOS, or FOSA.* Environmental Science & Technology, 2020. **54**(21): p. 13590-13597.
109. Brown, C., et al., *Demonstration of surfactant flooding of an alluvial aquifer contaminated with dense nonaqueous phase liquid*. 1999, ACS Publications.
110. Houtz, E.F. and D.L. Sedlak, *Oxidative Conversion as a Means of Detecting Precursors to Perfluoroalkyl Acids in Urban Runoff.* Environmental Science & Technology, 2012. **46**(17): p. 9342-9349.
111. Van Glubt, S., et al., *Column versus batch methods for measuring PFOS and PFOA sorption to geomedia.* Environmental Pollution, 2021. **268**(Pt B): p. 115917.
112. Johnson, R.L., et al., *The adsorption of perfluorooctane sulfonate onto sand, clay, and iron oxide surfaces.* Journal of Chemical & Engineering Data, 2007. **52**(4): p. 1165-1170.
113. Liao, S., et al., *Influence of aqueous film forming foams on the solubility and mobilization of non-aqueous phase liquid contaminants in quartz sands.* Water Research, 2021. **195**: p. 116975.
114. Harter, T., *Basic concepts of groundwater hydrology*. 2003: UCANR Publications.
115. Guelfo, J.L., et al., *Subsurface transport potential of perfluoroalkyl acids (PFAAs): Column experiments and modeling.* Journal of Contaminant Hydrology, 2020. **233**: p. 103661.
116. Ogata, A. and R.B. Banks, *A solution of the differential equation of longitudinal dispersion in porous media: fluid movement in earth materials*. 1961: US Government Printing Office.
117. Markhali, S. and M. Ehteshami, *Environmental assessment of leachate transport in saturated homogeneous media using finite element modeling.* Environmental Earth Sciences, 2016. **75**(16): p. 1-10.
118. Yan, P.-F., et al., *Biotransformation of 8: 2 Fluorotelomer Alcohol in Soil from Aqueous Film-Forming Foams (AFFFs)-Impacted Sites under Nitrate-, Sulfate-, and Iron-Reducing Conditions.* Environmental Science & Technology, 2022. **56**(19): p. 13728-13739.
119. Dharmawardana, U.R., et al., *A surface tension method for determining binding constants for cyclodextrin inclusion complexes of ionic surfactants.* Langmuir, 1993. **9**(9): p. 2258-2263.
120. Milner, S., *IV. On surface concentration, and the formation of liquid films.* The London, Edinburgh, and Dublin Philosophical Magazine and Journal of Science, 1907. **13**(73): p. 96-110.
121. Langmuir, I., *The constitution and fundamental properties of solids and liquids. II. Liquids.* Journal of the American chemical society, 1917. **39**(9): p. 1848-1906.

122. Lunkenheimer, K., et al., *Adsorption properties of surface chemically pure sodium perfluoro-n-alkanoates at the air/water interface: counterion effects within homologous series of 1: 1 ionic surfactants.* Langmuir, 2015. **31**(3): p. 970-981.
123. Markham, E. and A.F. Benton, *The adsorption of gas mixtures by silica.* Journal of the American Chemical Society, 1931. **53**(2): p. 497-507.
124. Fritz, W. and E.-U. Schluender, *Simultaneous adsorption equilibria of organic solutes in dilute aqueous solutions on activated carbon.* Chemical Engineering Science, 1974. **29**(5): p. 1279-1282.
125. Silva, J.A., W.A. Martin, and J.E. McCray, *Air-water interfacial adsorption coefficients for PFAS when present as a multi-component mixture.* Journal of Contaminant Hydrology, 2021. **236**: p. 103731.
126. Liao, S., et al., *Influence of residual nonaqueous-phase liquids (NAPLs) on the transport and retention of perfluoroalkyl substances.* Environmental Science & Technology, 2022.
127. Arshadi, M., et al., *Comment on "Uptake of Poly- and Perfluoroalkyl Substances at the Air-Water Interface".* Environ Sci Technol, 2020. **54**(11): p. 7019-7020.
128. Schaefer, C.E., D. Nguyen, and J. Field, *Response to the Comment on "Uptake of Poly- and Perfluoroalkyl Substances at the Air-Water Interface".* Environ Sci Technol, 2020. **54**(11): p. 7021-7022.
129. Smith, J.E. and R.W. Gillham, *Effects of solute concentration–dependent surface tension on unsaturated flow: Laboratory sand column experiments.* Water Resources Research, 1999. **35**(4): p. 973-982.
130. Karagunduz, A., M.H. Young, and K.D. Pennell, *Influence of surfactants on unsaturated water flow and solute transport.* Water Resources Research, 2015. **51**(4): p. 1977-1988.
131. Leverett, M., *Capillary behavior in porous solids.* Transactions of the AIME, 1941. **142**(01): p. 152-169.
132. Šimůnek, J., M.T. van Genuchten, and O. Wendroth, *Parameter estimation analysis of the evaporation method for determining soil hydraulic properties.* Soil Science Society of America Journal, 1998. **62**(4): p. 894-905.
133. Richards, L.A., *Capillary conduction of liquids through porous mediums.* Physics, 1931. **1**(5): p. 318-333.
134. van Genuchten, M.T., *A closed-form equation for predicting the hydraulic conductivity of unsaturated soils.* Soil Science Society of America Journal, 1980. **44**(5): p. 892-898.
135. Mualem, Y., *A new model for predicting the hydraulic conductivity of unsaturated porous media.* Water Resources Research, 1976. **12**(3): p. 513-522.
136. Lee, J.Y. and L.M. Hildemann, *Surface tensions of solutions containing dicarboxylic acid mixtures.* Atmospheric environment, 2014. **89**: p. 260-267.
137. Bradford, S.A. and F.J. Leij, *Estimating interfacial areas for multi-fluid soil systems.* Journal of Contaminant Hydrology, 1997. **27**(1-2): p. 83-105.
138. Simunek, J., M.T. van Genuchten, and M. Sejna, *Development and applications of the HYDRUS and STANMOD software packages and related codes.* Vadose zone journal, 2008. **7**(2): p. 587-600.
139. Rathfelder, K. and L.M. Abriola, *Mass conservative numerical solutions of the head-based Richards equation.* Water Resources Research, 1994. **30**(9): p. 2579-2586.
140. Anderson, R.H., et al., *Assessment of PFAS in collocated soil and porewater samples at an AFFF-impacted source zone: Field-scale validation of suction lysimeters.* Chemosphere, 2022. **308**: p. 136247.

141. Alm, R.R. and R.M. Stern, *US Patent US5085786A: Aqueous film-forming foamable solution useful as fire extinguishing concentrate*. 1992.
142. 3M. *MSDS: FC-203CF Light Water(TM) AFFF 3%*. 2005 (Accessed on 04/07/2023); Available from: https://safety365.sevron.co.uk/substances/accessSDS/SDS-13203-582efc750a7865.35052437.
143. Kärrman, A., et al., *Environmental levels and distribution of structural isomers of perfluoroalkyl acids after aqueous fire-fighting foam (AFFF) contamination.* Environmental Chemistry, 2011. **8**(4): p. 372-380.
144. Vargaftik, N.B., B.N. Volkov, and L.D. Voljak, *International Tables of the Surface-Tension of Water.* Journal of Physical and Chemical Reference Data, 1983. **12**(3): p. 817-820.
145. Matubayasi, N., *Surface Tension and Related Thermodynamic Quantities of Aqueous Electrolyte Solutions*. 2013, Boca Raton, FL: CRC Press. 223.
146. Milner, S.R., *On surface concentration and the formation of liquid films.* Philosophical Magazine, 1907. **13**(73-78): p. 96-110.
147. Kim, H., M.D. Annable, and P.S.C. Rao, *Influence of air-water interfacial adsorption and gas-phase partitioning on the transport of organic chemicals in unsaturated porous media.* Environmental Science & Technology, 1998. **32**(9): p. 1253-1259.
148. Brusseau, M.L. and S. Van Glubt, *The influence of surfactant and solution composition on PFAS adsorption at fluid-fluid interfaces.* Water Research, 2019. **161**: p. 17-26.
149. Langmuir, I., *The constitution and fundamental properties of solids and liquids. II. Liquids.* Journal of the American Chemical Society, 1917. **39**: p. 1848-1906.
150. Costanza-Robinson, M.S. and M.L. Brusseau, *Air-water interfacial areas in unsaturated soils: Evaluation of interfacial domains.* Water Resources Research, 2002. **38**(10).
151. National Center for Biotechnology Information. *PubChem Database. Perfluorooctanesulfonamide, CID=69785*. (Accessed on April 4); Available from: https://pubchem.ncbi.nlm.nih.gov/compound/69785#section=Solubility&fullscreen=true.
152. Wang, Z.Y., et al., *Using COSMOtherm to predict physicochemical properties of poly- and perfluorinated alkyl substances (PFASs).* Environmental Chemistry, 2011. **8**(4): p. 389-398.
153. Hill, C., et al., *Surface and bulk properties of surfactants used in fire-fighting.* Journal of Colloid and Interface Science, 2018. **530**: p. 686-694.
154. Place, B.J. and J.A. Field, *Identification of novel fluorochemicals in aqueous film-forming foams used by the US military.* Environmental Science & Technology, 2012. **46**(13): p. 7120-7127.
155. Pennell, K.D., L.M. Abriola, and W.J. Weber, *Surfactant-Enhanced Solubilization of Residual Dodecane in Soil Columns .1. Experimental Investigation.* Environmental Science & Technology, 1993. **27**(12): p. 2332-2340.
156. Pennell, K.D., et al., *Surfactant Enhanced Remediation of Soil Columns Contaminated by Residual Tetrachloroethylene.* Journal of Contaminant Hydrology, 1994. **16**(1): p. 35-53.
157. Liu, J., et al., *Isomer-specific biotransformation of perfluoroalkyl sulfonamide compounds in aerobic soil.* Science of the Total Environment, 2019. **651**: p. 766-774.
158. Mejia Avendaño, S. and J. Liu, *Production of PFOS from aerobic soil biotransformation of two perfluoroalkyl sulfonamide derivatives.* Chemosphere, 2015. **119**: p. 1084-1090.
159. Zhang, L., et al., *Kinetic analysis of aerobic biotransformation pathways of a perfluorooctane sulfonate (PFOS) precursor in distinctly different soils.* Environmental Pollution, 2017. **229**: p. 159-167.

160. Yin, T., et al., *Biotransformation of Sulfluramid (N-ethyl perfluorooctane sulfonamide) and dynamics of associated rhizospheric microbial community in microcosms of wetland plants.* Chemosphere, 2018. **211**: p. 379-389.
161. Murakami, M., et al., *Formation of perfluorinated surfactants from precursors by indigenous microorganisms in groundwater.* Chemosphere, 2013. **93**(1): p. 140-145.
162. Zhao, S., et al., *Different biotransformation behaviors of perfluorooctane sulfonamide in wheat (Triticum aestivum L.) from earthworms (Eisenia fetida).* Journal of Hazardous Materials, 2018. **346**: p. 191-198.
163. Liu, M., et al., *Stability of nitrogen-containing polyfluoroalkyl substances in aerobic soils.* Environmental Science & Technology, 2021. **55**(8): p. 4698-4708.
164. Awad, E., et al., *Long-Term Environmental Fate of Perfluorinated Compounds after Accidental Release at Toronto Airport.* Environmental Science & Technology, 2011. **45**(19): p. 8081-8089.
165. Whittaker, R.H., *Evolution and Measurement of Species Diversity.* TAXON, 1972. **21**(2-3): p. 213-251.
166. Zhang, S., et al., *Impact of 6:2 fluorotelomer alcohol aerobic biotransformation on a sediment microbial community.* Science of the Total Environment, 2017. **575**: p. 1361-1368.
167. Qiao, W., et al., *Perfluoroalkyl substances (PFASs) influence the structure and function of soil bacterial community: Greenhouse experiment.* Science of the Total Environment, 2018. **642**: p. 1118-1126.
168. Sun, Y., et al., *Bacterial community compositions in sediment polluted by perfluoroalkyl acids (PFAAs) using Illumina high-throughput sequencing.* Environmental Science and Pollution Research, 2016. **23**(11): p. 10556-10565.
169. Bao, Y., et al., *Vertical profiles of microbial communities in perfluoroalkyl substance-contaminated soils.* Annals of Microbiology, 2018. **68**: p. 399-408.
170. Li, B., et al., *Vertical distribution of microbial communities in soils contaminated by chromium and perfluoroalkyl substances.* Science of the Total Environment, 2017. **599-600**: p. 156-164.
171. Yin, T., et al., *Biotransformation of polyfluoroalkyl substances by microbial consortia from constructed wetlands under aerobic and anoxic conditions.* Chemosphere, 2019. **233**: p. 101-109.
172. Zhang, D., W. Zhang, and Y. Liang, *Bacterial community in a freshwater pond responding to the presence of perfluorooctanoic acid (PFOA).* Environmental Technology, 2020. **41**(27): p. 3646-3656.
173. van Beilen, J.B. and E.G. Funhoff, *Alkane hydroxylases involved in microbial alkane degradation.* Applied Microbiology and Biotechnology, 2007. **74**(1): p. 13-21.
174. Sutton, N.B., et al., *Impact of Long-Term Diesel Contamination on Soil Microbial Community Structure.* Applied and Environmental Microbiology, 2013. **79**(2): p. 619-630.
175. Key, B.D., R.D. Howell, and C.S. Criddle, *Defluorination of Organofluorine Sulfur Compounds by Pseudomonas Sp. Strain D2.* Environmental Science & Technology, 1998. **32**(15): p. 2283-2287.
176. Kim, M.H., et al., *Biodefluorination and biotransformation of fluorotelomer alcohols by two alkane-degrading Pseudomonas strains.* Biotechnology and Bioengineering, 2012. **109**(12): p. 3041-3048.

177. Kim, M.H., N. Wang, and K.H. Chu, *6:2 Fluorotelomer alcohol (6:2 FTOH) biodegradation by multiple microbial species under different physiological conditions.* Applied Microbiology and Biotechnology, 2014. **98**(4): p. 1831-1840.
178. Lewis, M., et al., *Engineering artificial communities for enhanced FTOH degradation.* Science of the Total Environment, 2016. **572**: p. 935-942.
179. Shaw, D.M.J., et al., *Degradation and defluorination of 6:2 fluorotelomer sulfonamidoalkyl betaine and 6:2 fluorotelomer sulfonate by Gordonia sp. strain NB4-1Y under sulfur-limiting conditions.* Science of the Total Environment, 2019. **647**: p. 690-698.
180. Van Hamme, J.D., et al., *Genomic and proteomic characterization of Gordonia sp. NB4-1Y in relation to 6 : 2 fluorotelomer sulfonate biodegradation.* Microbiology, 2013. **159**(Pt_8): p. 1618-1628.
181. Yu, X., F. Nishimura, and T. Hidaka, *Effects of microbial activity on perfluorinated carboxylic acids (PFCAs) generation during aerobic biotransformation of fluorotelomer alcohols in activated sludge.* Science of the Total Environment, 2018. **610-611**: p. 776-785.
182. Touliabah, H.E.-S., et al., *A Review of Microalgae- and Cyanobacteria-Based Biodegradation of Organic Pollutants.* Molecules, 2022. **27**(3): p. 1141.
183. Sei, K., et al., *Isolation and characterization of bacterial strains that have high ability to degrade 1, 4-dioxane as a sole carbon and energy source.* Biodegradation, 2013. **24**(5): p. 665-674.
184. Moosvi, S.A., et al., *Isolation and properties of methanesulfonate-degrading Afipia felis from Antarctica and comparison with other strains of A. felis.* Environmental Microbiology, 2005. **7**(1): p. 22-33.
185. Zhang, P., et al., *Isolation and characterization of haloacetic acid-degrading Afipia spp. from drinking water.* FEMS microbiology letters, 2009. **297**(2): p. 203-208.
186. Hamid, H., L.Y. Li, and J.R. Grace, *Aerobic biotransformation of fluorotelomer compounds in landfill leachate-sediment.* Science of the Total Environment, 2020. **713**: p. 136547.
187. Liu, J., et al., *Biotransformation of 8:2 Fluorotelomer Alcohol in Soil and by Soil Bacteria Isolates.* Environmental Science & Technology, 2007. **41**: p. 8024-8030.
188. Wang, N., et al., *Aerobic Biotransformation of 14 C-Labeled 8-2 Telomer B Alcohol by Activated Sludge from a Domestic Sewage Treatment Plant.* Environmental Science & Technology, 2005. **39**: p. 531-538.
189. Liu, J., et al., *Aerobic biodegradation of [14C] 6: 2 fluorotelomer alcohol in a flow-through soil incubation system.* Chemosphere, 2010. **80**(7): p. 716-723.
190. Li, F., et al., *Anaerobic biodegradation of 8:2 fluorotelomer alcohol in anaerobic activated sludge: Metabolic products and pathways.* Chemosphere, 2018. **200**: p. 124-132.
191. Scherr, F.F., et al., *Modeling degradation and metabolite formation kinetics of estrone-3-sulfate in agricultural soils.* Environmental Science & Technology, 2008. **42**(22): p. 8388-8394.
192. Torabi, E., et al., *Diazinon dissipation in pesticide-contaminated paddy soil: kinetic modeling and isolation of a degrading mixed bacterial culture.* Environmental Science and Pollution Research, 2017. **24**(4): p. 4117-4133.
193. Milinovic, J., et al., *Sorption behaviour of perfluoroalkyl substances in soils.* Science of the Total Environment, 2015. **511**: p. 63-71.
194. Washington, J.W., et al., *Decades-scale degradation of commercial, side-chain, fluorotelomer-based polymers in soils and water.* Environmental science & technology, 2015. **49**(2): p. 915-923.

195. Wang, N., et al., *Fluorotelomer Alcohol Biodegradation-Direct Evidence that Perfluorinated Carbon Chains Breakdown.* Environmental Science & Technology, 2005. **39**: p. 7516-7528.
196. Yu, X., F. Nishimura, and T. Hidaka, *Enhanced generation of perfluoroalkyl carboxylic acids (PFCAs) from fluorotelomer alcohols (FTOHs) via ammonia-oxidation process.* Chemosphere, 2018. **198**: p. 311-319.
197. Russell, M.H., et al., *Investigation of the biodegradation potential of a fluoroacrylate polymer product in aerobic soils.* Environmental Science & Technology, 2008. **42**: p. 800-807.
198. Williams, A.J., et al., *The CompTox Chemistry Dashboard: a community data resource for environmental chemistry.* Journal of cheminformatics, 2017. **9**: p. 1-27.
199. Wang, N., et al., *5:3 Polyfluorinated acid aerobic biotransformation in activated sludge via novel "one-carbon removal pathways".* Chemosphere, 2012. **87**(5): p. 527-34.
200. Ruttkies, C., et al., *MetFrag relaunched: incorporating strategies beyond in silico fragmentation.* Journal of Cheminformatics, 2016. **8**(1): p. 3.
201. Premnath, N., et al., *A crucial review on polycyclic aromatic Hydrocarbons-Environmental occurrence and strategies for microbial degradation.* Chemosphere, 2021: p. 130608.
202. Futamata, H., et al., *Unique kinetic properties of phenol-degrading Variovorax strains responsible for efficient trichloroethylene degradation in a chemostat enrichment culture.* Applied and Environmental Microbiology, 2005. **71**(2): p. 904-911.
203. van den Wijngaard, A.J., et al., *Degradation of 1, 2-dichloroethane by Ancylobacter aquaticus and other facultative methylotrophs.* Applied and Environmental Microbiology, 1992. **58**(3): p. 976-983.
204. Plumeier, I., et al., *Importance of different tfd genes for degradation of chloroaromatics by Ralstonia eutropha JMP134.* Journal of Bacteriology, 2002. **184**(15): p. 4054-4064.
205. Glöckner, F.O., et al., *Comparative 16S rRNA analysis of lake bacterioplankton reveals globally distributed phylogenetic clusters including an abundant group of actinobacteria.* Applied and Environmental Microbiology, 2000. **66**(11): p. 5053-5065.
206. Tabata, K., et al., *Poly (Aspartic Acid) Degradation by aSphingomonas sp. Isolated from Freshwater.* Applied and Environmental Microbiology, 1999. **65**(9): p. 4268-4270.
207. Xia, Y., et al., *Isolation and characterization of phenanthrene-degrading Sphingomonas paucimobilis strain ZX4.* Biodegradation, 2005. **16**(5): p. 393-402.
208. Nagata, Y., K. Miyauchi, and M. Takagi, *Complete analysis of genes and enzymes for γ-hexachlorocyclohexane degradation in Sphingomonas paucimobilis UT26.* Journal of Industrial Microbiology and Biotechnology, 1999. **23**(4): p. 380-390.
209. Kim, E.-J., et al., *Mineralization and transformation of monofluorophenols by Pseudonocardia benzenivorans.* Applied microbiology and biotechnology, 2010. **87**(4): p. 1569-1577.
210. Kotelnikova, S., A.J. Macario, and K. Pedersen, *Methanobacterium subterraneum sp. nov., a new alkaliphilic, eurythermic and halotolerant methanogen isolated from deep granitic groundwater.* International journal of systematic and evolutionary microbiology, 1998. **48**(2): p. 357-367.
211. Koch, V., et al., *Biodegradation kinetic and estimated half-life of a Clariant fluorotelomer-based acrylate polymer—Results from a test on aerobic transformation in soil.* Reproductive Toxicology, 2009. **3-4**(27): p. 420-421.

212. Yu, X., et al., *Biodegradation Property of 8:2 Fluorotelomer Alcohol (8:2 FTOH) under Aerobic/Anoxic/Anaerobic Conditions.* Journal of Water and Environment Technology, 2016. **14**(3): p. 177-190.
213. Liu, J. and L.S. Lee, *Solubility and Sorption by Soils of 8:2 Fluorotelomer Alcohol in Water and Cosolvent Systems.* Environmental Science & Technology, 2005. **39**(19): p. 7535-7540.
214. Yu, Y., et al., *Microbial Defluorination of Unsaturated Per- and Polyfluorinated Carboxylic Acids under Anaerobic and Aerobic Conditions: A Structure Specificity Study %U https://doi.org/10.1021/acs.est.1c05509.* Environmental Science & Technology, 2022.
215. Ramette, A., *Multivariate analyses in microbial ecology: Multivariate analyses in microbial ecology.* FEMS Microbiology Ecology, 2007. **62**(2): p. 142-160.
216. Lovley, D.R., et al., *Enzymatic iron and uranium reduction by sulfate-reducing bacteria.* Marine Geology, 1993. **113**(1): p. 41-53.
217. Tebo, B.M. and A.Y. Obraztsova, *Sulfate-reducing bacterium grows with Cr(VI), U(VI), Mn(IV), and Fe(III) as electron acceptors.* FEMS Microbiology Letters, 1998. **162**(1): p. 193-199.
218. Krzmarzick, M.J., et al., *Novel Firmicutes Group Implicated in the Dechlorination of Two Chlorinated Xanthones, Analogues of Natural Organochlorines.* Applied and Environmental Microbiology, 2014. **80**(3): p. 1210-1218.
219. Sanford, R.A., J.R. Cole, and J.M. Tiedje, *Characterization and description of Anaeromyxobacter dehalogenans gen. nov., sp. nov., an aryl-halorespiring facultative anaerobic myxobacterium.* Applied and environmental microbiology, 2002. **68**(2): p. 893-900.
220. Washington, J.W., T.M. Jenkins, and E.J. Weber, *Identification of Unsaturated and 2H Polyfluorocarboxylate Homologous Series and Their Detection in Environmental Samples and as Polymer Degradation Products.* Environmental Science & Technology, 2015. **49**(22): p. 13256-13263.
221. Yu, Y., et al., *Microbial Cleavage of C–F Bonds in Two C 6 Per- and Polyfluorinated Compounds via Reductive Defluorination.* Environmental Science & Technology, 2020. **54**(22): p. 14393-14402.
222. Yin, T., et al., *Biotransformation of polyfluoroalkyl substances by microbial consortia from constructed wetlands under aerobic and anoxic conditions.* Chemosphere, 2019. **233**: p. 101-109.
223. Zhao, L., et al., *6:2 Fluorotelomer alcohol aerobic biotransformation in activated sludge from two domestic wastewater treatment plants.* Chemosphere, 2013. **92**(4): p. 464-470.
224. Hamid, H., L.Y. Li, and J.R. Grace, *Formation of perfluorocarboxylic acids from 6:2 fluorotelomer sulfonate (6:2 FTS) in landfill leachate: Role of microbial communities.* Environmental Pollution, 2020. **259**: p. 113835.
225. Cook, A.M., H. Laue, and F. Junker, *Microbial desulfonation.* FEMS Microbiology Reviews, 1998. **22**(5): p. 399-419.
226. Tripathi, S., et al., *Microbial community dynamics and their relationships with organic and metal pollutants of sugarcane molasses-based distillery wastewater sludge.* Environmental Pollution, 2022. **292**: p. 118267.
227. Cao, X., et al., *Amendments and bioaugmentation enhanced phytoremediation and micro-ecology for PAHs and heavy metals co-contaminated soils.* Journal of Hazardous Materials, 2022. **426**: p. 128096.

228. Castelle, C.J., et al., *Extraordinary phylogenetic diversity and metabolic versatility in aquifer sediment.* Nature Communications, 2013. **4**: p. 2120.
229. Bhatt, P., et al., *Mechanism of allethrin biodegradation by a newly isolated Sphingomonas trueperi strain CW3 from wastewater sludge.* Bioresource Technology, 2020. **305**: p. 123074.
230. Zhang, J., et al., *Chloramphenicol biodegradation by enriched bacterial consortia and isolated strain Sphingomonas sp. CL5.1: The reconstruction of a novel biodegradation pathway.* Water Research, 2020. **187**: p. 116397.
231. Zhou, L., et al., *Sphingomonas from petroleum-contaminated soils in Shenfu, China and their PAHs degradation abilities.* Brazilian Journal of Microbiology, 2016. **47**(2): p. 271-278.
232. Maizel, A.C., et al., *Release of per-and polyfluoroalkyl substances from aqueous film-forming foam impacted soils.* Environmental Science & Technology, 2021. **55**(21): p. 14617-14627.
233. Nickerson, A., et al., *Enhanced extraction of AFFF-associated PFASs from source zone soils.* Environmental Science & Technology, 2020. **54**(8): p. 4952-4962.
234. Choi, Y.J., et al., *Microbial biotransformation of aqueous film-forming foam derived polyfluoroalkyl substances.* Science of the Total Environment, 2022: p. 153711.
235. Charbonnet, J.A., et al., *Communicating confidence of per-and polyfluoroalkyl substance identification via high-resolution mass spectrometry.* Environmental Science & Technology letters, 2022. **9**(6): p. 473-481.
236. Barzen-Hanson, K.A., et al., *Discovery of 40 Classes of Per- and Polyfluoroalkyl Substances in Historical Aqueous Film-Forming Foams (AFFFs) and AFFF-Impacted Groundwater.* Environmental Science & Technology, 2017. **51**: p. 2047-2057.
237. Mejia-Avendaño, S., et al., *Generation of Perfluoroalkyl Acids from Aerobic Biotransformation of Quaternary Ammonium Polyfluoroalkyl Surfactants.* Environmental Science & Technology, 2016. **50**: p. 9923-9932.
238. D'Agostino, L.A. and S.A. Mabury, *Identification of novel fluorinated surfactants in aqueous film forming foams and commercial surfactant concentrates.* Environmental Science & Technology, 2014. **48**(1): p. 121-129.
239. D'Agostino, L.A. and S.A. Mabury, *Aerobic biodegradation of 2 fluorotelomer sulfonamide–based aqueous film–forming foam components produces perfluoroalkyl carboxylates.* Environmental Toxicology and Chemistry, 2017. **36**: p. 2012-2021.
240. Li, R., et al., *Transformation of novel polyfluoroalkyl substances (PFASs) as co-contaminants during biopile remediation of petroleum hydrocarbons.* Journal of Hazardous Materials, 2019. **362**: p. 140-147.
241. Chen, H., et al., *Fast generation of perfluoroalkyl acids from polyfluoroalkyl amine oxides in aerobic soils.* Environmental Science & Technology Letters, 2020. **7**(10): p. 714-720.
242. Ochoa-Herrera, V., et al., *Microbial toxicity and biodegradability of perfluorooctane sulfonate (PFOS) and shorter chain perfluoroalkyl and polyfluoroalkyl substances (PFASs).* Environmental Science: Processes & Impacts, 2016. **18**(9): p. 1236-1246.
243. Chen, H., et al., *Synthesis and characterization of fluoropoly (amide–sulfonamide) s via polycondensation.* Polymer, 2009. **50**(18): p. 4317-4324.
244. Cook, E.K., et al., *Biological and Chemical Transformation of the Six-Carbon Polyfluoroalkyl Substance N-Dimethyl Ammonio Propyl Perfluorohexane Sulfonamide (AmPr-FHxSA).* Environmental Science & Technology, 2022. **56**(22): p. 15478-15488.

245. Jiang, Y., et al., *Aggregate-related changes in network patterns of nematodes and ammonia oxidizers in an acidic soil.* Soil Biology and Biochemistry, 2015. **88**: p. 101-109.
246. Cram, J.A., et al., *Cross-depth analysis of marine bacterial networks suggests downward propagation of temporal changes.* The ISME journal, 2015. **9**(12): p. 2573-2586.
247. Thelusmond, J.-R., T.J. Strathmann, and A.M. Cupples, *Carbamazepine, triclocarban and triclosan biodegradation and the phylotypes and functional genes associated with xenobiotic degradation in four agricultural soils.* Science of the Total Environment, 2019. **657**: p. 1138-1149.
248. Zhang, X., et al., *Effects of composted bamboo residue amendments on soil microbial communities in an intensively managed bamboo (Phyllostachys praecox) plantation.* Applied Soil Ecology, 2019. **136**: p. 178-183.
249. Li, J., et al., *Autochthonous bioaugmentation-modified bacterial diversity of phenanthrene degraders in PAH-contaminated wastewater as revealed by DNA-stable isotope probing.* Environmental Science & Technology, 2018. **52**(5): p. 2934-2944.
250. Wu, Y., et al., *Field study on the soil bacterial associations to combined contamination with heavy metals and organic contaminants.* Science of the Total Environment, 2021. **778**: p. 146282.
251. Dejonghe, W., et al., *Synergistic degradation of linuron by a bacterial consortium and isolation of a single linuron-degrading Variovorax strain.* Applied and Environmental Microbiology, 2003. **69**(3): p. 1532-1541.
252. Posman, K.M., C.M. DeRito, and E.L. Madsen, *Benzene degradation by a Variovorax species within a coal tar-contaminated groundwater microbial community.* Applied and Environmental Microbiology, 2017. **83**(4): p. e02658-16.
253. Sørensen, S.R., C.N. Albers, and J. Aamand, *Rapid mineralization of the phenylurea herbicide diuron by Variovorax sp. strain SRS16 in pure culture and within a two-member consortium.* Applied and Environmental Microbiology, 2008. **74**(8): p. 2332-2340.
254. Nierychlo, M., et al., *The morphology and metabolic potential of the Chloroflexi in full-scale activated sludge wastewater treatment plants.* FEMS microbiology ecology, 2019. **95**(2): p. fiy228.
255. Lewin, S., et al., *Crop host signatures reflected by co-association patterns of keystone Bacteria in the rhizosphere microbiota.* Environmental microbiome, 2021. **16**(1): p. 1-18.
256. Wang, Y., et al., *Halosulfuron methyl did not have a significant effect on diversity and community of sugarcane rhizosphere microflora.* Journal of Hazardous Materials, 2020. **399**: p. 123040.
257. Barberán, A., et al., *Using network analysis to explore co-occurrence patterns in soil microbial communities.* The ISME journal, 2012. **6**(2): p. 343-351.
258. Manucharova, N., et al., *Microbial degraders of petroleum and polycyclic aromatic hydrocarbons from sod-podzolic soil.* Microbiology, 2021. **90**(6): p. 743-753.
259. Sato, Y., et al., *Two rhizobial strains, Mesorhizobium loti MAFF303099 and Bradyrhizobium japonicum USDA110, encode haloalkane dehalogenases with novel structures and substrate specificities.* Applied and Environmental Microbiology, 2005. **71**(8): p. 4372-4379.
260. Sánchez, M. and B. González, *Genetic characterization of 2, 4, 6-trichlorophenol degradation in Cupriavidus necator JMP134.* Applied and Environmental Microbiology, 2007. **73**(9): p. 2769-2776.

261. Wang, W., et al., *Tobacco-associated with Methylophilus sp. FP-6 enhances phytoremediation of benzophenone-3 through regulating soil microbial community, increasing photosynthetic capacity and maintaining redox homeostasis of plant.* Journal of Hazardous Materials, 2022. **431**: p. 128588.
262. Dang, H. and A.M. Cupples, *Identification of the phylotypes involved in cis-dichloroethene and 1, 4-dioxane biodegradation in soil microcosms.* Science of the Total Environment, 2021. **794**: p. 148690.
263. Hao, L., et al., *Gradual development of ammonia-induced syntrophic acetate-oxidizing activities under mesophilic and thermophilic conditions quantitatively tracked using multiple isotopic approaches.* Water Research, 2021. **204**: p. 117586.
264. Yin, M. and H. Chen, *Unveiling the dual faces of chitosan in anaerobic digestion of waste activated sludge.* Bioresource Technology, 2022. **344**: p. 126182.
265. Yi, X.-Y., et al., *Coupling metabolisms of arsenic and iron with humic substances through microorganisms in paddy soil.* Journal of Hazardous Materials, 2019. **373**: p. 591-599.
266. Zheng, J., et al., *Efficient elimination of sulfadiazine in an anaerobic denitrifying circumstance: biodegradation characteristics, biotoxicity removal and microbial community analysis.* Chemosphere, 2020. **252**: p. 126472.
267. Foysal, M., et al., *Biological ball filters regulate bacterial communities in marron (Cherax cainii) culture system.* Letters in applied microbiology, 2019. **68**(5): p. 455-463.
268. Bird, J.T., et al., *Uncultured microbial phyla suggest mechanisms for multi-thousand-year subsistence in Baltic Sea sediments.* MBio, 2019. **10**(2): p. e02376-18.
269. Mumford, A.C., et al., *Common hydraulic fracturing fluid additives alter the structure and function of anaerobic microbial communities.* Applied and Environmental Microbiology, 2018. **84**(8): p. e02729-17.
270. Fang, Y., et al., *Influence of terminal electron-accepting conditions on the soil microbial community and degradation of organic contaminants of emerging concern.* Science of the Total Environment, 2020. **706**: p. 135327.
271. Jiao, S., W. Chen, and G. Wei, *Resilience and assemblage of soil microbiome in response to chemical contamination combined with plant growth.* Applied and Environmental Microbiology, 2019. **85**(6): p. e02523-18.
272. Barkovskii, A.L., V.E. Korshunova, and L.I. Pozdnyacova, *Catabolism of phenol and benzoate by Azospirillum strains.* Applied Soil Ecology, 1995. **2**(1): p. 17-24.
273. Cheng, C., et al., *Effects of side-stream ratio on sludge reduction and microbial structures of anaerobic side-stream reactor coupled membrane bioreactors.* Bioresource technology, 2017. **234**: p. 380-388.
274. Qin, K., et al., *Removal trend of amoxicillin and tetracycline during groundwater recharging reusing: Redox sensitivity and microbial community response.* Chemosphere, 2021. **282**: p. 131011.
275. Ismail, S., et al., *Fatigue of anammox consortia under long-term 1, 4-dioxane exposure and recovery potential: N-kinetics and microbial dynamics.* Journal of Hazardous Materials, 2021. **414**: p. 125533.
276. Zhang, K., et al., *Characterization of growth phenotypes and gastrointestinal tract microbiota in sheep fed with caragana.* Journal of Applied Microbiology, 2021. **131**(6): p. 2763-2779.

277. Gomes, B.C., et al., *Analysis of a microbial community associated with polychlorinated biphenyl degradation in anaerobic batch reactors.* Biodegradation, 2014. **25**(6): p. 797-810.
278. Zhu, M., et al., *Synchronous response in methanogenesis and anaerobic degradation of pentachlorophenol in flooded soil.* Journal of Hazardous Materials, 2019. **374**: p. 258-266.
279. van Doesburg, W., et al., *Reductive dechlorination of β-hexachlorocyclohexane (β-HCH) by a Dehalobacter species in coculture with a Sedimentibacter sp.* FEMS Microbiology Ecology, 2005. **54**(1): p. 87-95.
280. Liu, X., et al., *Alkaline pre-fermentation for anaerobic digestion of polyacrylamide flocculated sludge: Simultaneously enhancing methane production and polyacrylamide degradation.* Chemical Engineering Journal, 2021. **425**: p. 131407.
281. Qu, M., et al., *Fate of atrazine and its relationship with environmental factors in distinctly different lake sediments associated with hydrophytes.* Environmental Pollution, 2020. **256**: p. 113371.
282. Tushar, L., C. Sasikala, and C.V. Ramana, *Draft genome sequence of Rhodomicrobium udaipurense JA643T with special reference to hopanoid biosynthesis.* DNA research, 2014. **21**(6): p. 639-647.
283. Jechorek, M., K.-D. Wendlandt, and M. Beck, *Cometabolic degradation of chlorinated aromatic compounds.* Journal of Biotechnology, 2003. **102**(1): p. 93-98.
284. Im, J. and J.D. Semrau, *Pollutant degradation by a Methylocystis strain SB2 grown on ethanol: bioremediation via facultative methanotrophy.* FEMS microbiology letters, 2011. **318**(2): p. 137-142.
285. Sherry, A., et al., *Anaerobic biodegradation of crude oil under sulphate-reducing conditions leads to only modest enrichment of recognized sulphate-reducing taxa.* International Biodeterioration & Biodegradation, 2013. **81**: p. 105-113.
286. Fields, B.S., R.F. Benson, and R.E. Besser, *Legionella and Legionnaires' disease: 25 years of investigation.* Clinical microbiology reviews, 2002. **15**(3): p. 506-526.
287. Zhang, S., Q. Wang, and S. Xie, *Stable isotope probing identifies anthracene degraders under methanogenic conditions.* Biodegradation, 2012. **23**(2): p. 221-230.
288. Ahmed, M. and D. Focht, *Degradation of polychlorinated biphenyls by two species of Achromobacter.* Canadian Journal of Microbiology, 1973. **19**(1): p. 47-52.
289. Nielsen, D.R., P.J. McLellan, and A.J. Daugulis, *Direct estimation of the oxygen requirements of Achromobacter xylosoxidans for aerobic degradation of monoaromatic hydrocarbons (BTEX) in a bioscrubber.* Biotechnology letters, 2006. **28**(16): p. 1293-1298.
290. Remizovschi, A., et al., *Mud volcanoes and the presence of PAHs.* Scientific Reports, 2020. **10**(1): p. 1-9.
291. Li, C.-Y., et al., *The biofilm property and its correlationship with high-molecular-weight polyacrylamide degradation in a water injection pipeline of Daqing oilfield.* Journal of Hazardous Materials, 2016. **304**: p. 388-399.
292. O'Carroll, D.M., et al., *Developing a roadmap to determine per-and polyfluoroalkyl substances-microbial population interactions.* Science of the Total Environment, 2020. **712**: p. 135994.
293. Timm, C.M., et al., *Abiotic stresses shift belowground Populus-associated bacteria toward a core stress microbiome.* MSystems, 2018. **3**(1): p. e00070-17.

294. Narihiro, T., et al., *Quantitative detection of previously characterized syntrophic bacteria in anaerobic wastewater treatment systems by sequence-specific rRNA cleavage method.* Water Research, 2012. **46**(7): p. 2167-2175.
295. Júlio, A.D.L., et al., *Metataxonomic analyses reveal differences in aquifer bacterial community as a function of creosote contamination and its potential for contaminant remediation.* Scientific reports, 2019. **9**(1): p. 1-14.
296. Wu, Y., et al., *Influence of bacterial community diversity, functionality, and soil factors on polycyclic aromatic hydrocarbons under various vegetation types in mangrove wetlands.* Environmental Pollution, 2022. **308**: p. 119622.
297. Siddique, T., et al., *Microbial communities involved in methane production from hydrocarbons in oil sands tailings.* Environmental Science & Technology, 2012. **46**(17): p. 9802-9810.
298. Lahme, S., et al., *Anaerobic degradation of 4-methylbenzoate via a specific 4-methylbenzoyl-CoA pathway.* Environmental Microbiology, 2012. **14**(5): p. 1118-1132.
299. Laempe, D., M. Jahn, and G. Fuchs, *6-Hydroxycyclohex-1-ene-1-carbonyl-CoA dehydrogenase and 6-oxocyclohex-1-ene-1-carbonyl-CoA hydrolase, enzymes of the benzoyl-CoA pathway of anaerobic aromatic metabolism in the denitrifying bacterium Thauera aromatica.* European Journal of Biochemistry, 1999. **263**(2): p. 420-429.
300. Kaschabek, S.R. and W. Reineke, *Maleylacetate reductase of Pseudomonas sp. strain B13: dechlorination of chloromaleylacetates, metabolites in the degradation of chloroaromatic compounds.* Archives of microbiology, 1992. **158**(6): p. 412-417.
301. Seibert, V., et al., *Characterization of the maleylacetate reductase MacA of Rhodococcus opacus 1CP and evidence for the presence of an isofunctional enzyme.* Journal of Bacteriology, 1998. **180**(14): p. 3503-3508.
302. Mampel, J., M.A. Providenti, and A.M. Cook, *Protocatechuate 4, 5-dioxygenase from Comamonas testosteroni T-2: biochemical and molecular properties of a new subgroup within class III of extradiol dioxygenases.* Archives of microbiology, 2005. **183**(2): p. 130-139.
303. Bygd, M.D., et al., *Unexpected Mechanism of Biodegradation and Defluorination of 2, 2-Difluoro-1, 3-Benzodioxole by Pseudomonas putida F1.* Mbio, 2021. **12**(6): p. e03001-21.
304. Ferreira, M.I.M., et al., *Analysis of two gene clusters involved in the degradation of 4-fluorophenol by Arthrobacter sp. strain IF1.* Applied and Environmental Microbiology, 2009. **75**(24): p. 7767-7773.
305. Latus, M., et al., *Purification and characterization of hydroxyquinol 1, 2-dioxygenase from Azotobacter sp. strain GP1.* Applied and Environmental Microbiology, 1995. **61**(7): p. 2453-2460.
306. Daubaras, D.L., K. Saido, and A. Chakrabarty, *Purification of hydroxyquinol 1, 2-dioxygenase and maleylacetate reductase: the lower pathway of 2, 4, 5-trichlorophenoxyacetic acid metabolism by Burkholderia cepacia AC1100.* Applied and Environmental Microbiology, 1996. **62**(11): p. 4276-4279.
307. Tiedt, O., et al., *Promiscuous defluorinating enoyl-CoA hydratases/hydrolases allow for complete anaerobic degradation of 2-fluorobenzoate.* Frontiers in microbiology, 2017. **8**: p. 2579.
308. Boundy-Mills, K.L., et al., *The atzB gene of Pseudomonas sp. strain ADP encodes the second enzyme of a novel atrazine degradation pathway.* Applied and Environmental Microbiology, 1997. **63**(3): p. 916-923.

309. Kurihara, T., et al., *Purification, characterization, and gene cloning of a novel fluoroacetate dehalogenase from Burkholderia sp. FA1.* Journal of Molecular Catalysis B: Enzymatic, 2003. **23**(2-6): p. 347-355.
310. Keuning, S., D.B. Janssen, and B. Witholt, *Purification and characterization of hydrolytic haloalkane dehalogenase from Xanthobacter autotrophicus GJ10.* Journal of Bacteriology, 1985. **163**(2): p. 635-639.
311. Kulakova, A.N., M.J. Larkin, and L.A. Kulakov, *The plasmid-located haloalkane dehalogenase gene from Rhodococcus rhodochrous NCIMB 13064.* Microbiology, 1997. **143**(1): p. 109-115.
312. Marek, J., et al., *Crystal structure of the haloalkane dehalogenase from Sphingomonas paucimobilis UT26.* Biochemistry, 2000. **39**(46): p. 14082-14086.
313. Broholm, K. and S. Feenstra, *Laboratory measurements of the aqueous solubility of mixtures of chlorinated solvents.* Environmental Toxicology and Chemistry: An International Journal, 1995. **14**(1): p. 9-15.
314. Ladaa, T.I., et al., *Cosolvent effects of alcohols on the Henry's law constant and aqueous solubility of tetrachloroethylene (PCE).* Chemosphere, 2001. **44**(5): p. 1137-1143.
315. Suchomel, E.J., C.A. Ramsburg, and K.D. Pennell, *Evaluation of trichloroethene recovery processes in heterogeneous aquifer cells flushed with biodegradable surfactants.* Journal of contaminant hydrology, 2007. **94**(3-4): p. 195-214.
316. Kile, D.E. and C.T. Chiou, *Water solubility enhancements of DDT and trichlorobenzene by some surfactants below and above the critical micelle concentration.* Environmental Science & Technology, 1989. **23**(7): p. 832-838.
317. Kostarelos, K., et al., *Viscous microemulsions of aqueous film-forming foam (AFFF) and jet fuel a inhibit infiltration and subsurface transport.* Environmental Science & Technology Letters, 2020. **8**(2): p. 142-147.
318. Powers, S.E., W.H. Anckner, and T.F. Seacord, *Wettability of NAPL-contaminated sands.* Journal of Environmental Engineering-Asce, 1996. **122**(10): p. 889-896.
319. Fagerlund, F., A. Niemi, and T.H. Illangasekare, *Modeling of nonaqueous phase liquid (NAPL) migration in heterogeneous saturated media: Effects of hysteresis and fluid immobility in constitutive relations.* Water Resources Research, 2008. **44**(3).
320. Glass, R. and M. Nicholl, *Physics of gravity fingering of immiscible fluids within porous media: An overview of current understanding and selected complicating factors.* Geoderma, 1996. **70**(2-4): p. 133-163.
321. Held, R.J. and T.H. Illangasekare, *Fingering of dense nonaqueous phase liquids in porous media: 1. Experimental investigation.* Water Resources Research, 1995. **31**(5): p. 1213-1222.
322. Miller, C., D. Durnford, and A. Fowler, *Equilibrium nonaqueous phase liquid pool geometry in coarse soils with discrete textural interfaces.* Journal of contaminant hydrology, 2004. **71**(1-4): p. 239-260.
323. Rathfelder, K.M., et al., *Influence of surfactant-facilitated interfacial tension reduction on chlorinated solvent migration in porous media: Observations and numerical simulation.* Journal of Contaminant Hydrology, 2003. **64**(3-4): p. 227-252.
324. McWhorter, D. and B. Kueper, *Mechanics and mathematics of the movement of dense non-aqueous phase liquids (DNAPLs) in porous media.* Dense chlorinated solvents and other DNAPLs in groundwater, 1996: p. 89-128.

325. Brusseau, M.L., *The influence of molecular structure on the adsorption of PFAS to fluid-fluid interfaces: Using QSPR to predict interfacial adsorption coefficients.* Water Res, 2019. **152**: p. 148-158.
326. Brusseau, M.L. and S. Van Glubt, *The influence of molecular structure on PFAS adsorption at air-water interfaces in electrolyte solutions.* Chemosphere, 2021. **281**: p. 130829.
327. Paternoster, R., et al., *Using the correct statistical test for the equality of regression coefficients.* Criminology, 1998. **36**(4): p. 859-866.
328. Powers, S.E., et al., *Phenomenological models for transient NAPL-water mass-transfer processes.* Journal of Contaminant Hydrology, 1994. **16**(1): p. 1-33.
329. Schaefer, C.E., D.A. DiCarlo, and M.J. Blunt, *Determination of Water-Oil Interfacial Area during 3-Phase Gravity Drainage in Porous Media.* J Colloid Interface Sci, 2000. **221**(2): p. 308-312.
330. Brusseau, M.L. and H. Taghap, *NAPL-water interfacial area as a function of fluid saturation measured with the interfacial partitioning tracer test method.* Chemosphere, 2020. **260**: p. 127562.
331. Brusseau, M.L., et al., *Ideal versus nonideal transport of PFAS in unsaturated porous media.* Water Research, 2021. **202**: p. 117405.
332. Yan, P.-F., et al., *Aerobic Biotransformation of 6:2 Fluorotelomer Sulfonate in Soils from Two Aqueous Film-Forming Foam (AFFF)-Impacted Sites.* Environmental Science & Technology, 2022.
333. Mitchell, R.J., et al., *Toxicity of fluorotelomer carboxylic acids to the algae Pseudokirchneriella subcapitata and Chlorella vulgaris, and the amphipod Hyalella azteca.* Ecotoxicology and Environmental Safety, 2011. **74**(8): p. 2260-2267.
334. Phillips, M.M., et al., *Fluorotelomer Acids are More Toxic than Perfluorinated Acids.* Environmental Science & Technology, 2007. **41**(20): p. 7159-7163.
335. Schaefer, C.E., et al., *Bioaugmentation for chlorinated ethenes using Dehalococcoides sp.: Comparison between batch and column experiments.* Chemosphere, 2009. **75**(2): p. 141-148.
336. Lewis, M., et al., *Biotransformation of 6:2 polyfluoroalkyl phosphates (6:2 PAPs): Effects of degradative bacteria and co-substrates.* Journal of Hazardous Materials, 2016. **320**: p. 479-486.
337. Li, Y.-J., et al., *A metagenomics study of hexabromocyclododecane degradation with a soil microbial community.* Journal of Hazardous Materials, 2022. **430**: p. 128465.
338. Xie, Y., et al., *Pseudomonas sp. Strain 273 Degrades Fluorinated Alkanes.* Environmental Science & Technology, 2020. **54**(23): p. 14994-15003.
339. Krzmarzick, M.J., et al., *Natural Niche for Organohalide-Respiring Chloroflexi.* Applied and Environmental Microbiology, 2012. **78**(2): p. 393-401.
340. Li, L., et al., *Identify biosorption effects of Thiobacillus towards perfluorooctanoic acid (PFOA): Pilot study from field to laboratory.* Chemosphere, 2017. **171**: p. 31-39.
341. Dong, X., et al., *Reconstructing metabolic pathways of a member of the genus Pelotomaculum suggesting its potential to oxidize benzene to carbon dioxide with direct reduction of sulfate.* FEMS Microbiology Ecology, 2017. **93**(3): p. fiw254.
342. Costanza, J., *Degradation of tetrachloroethylene and trichloroethylene under thermal remediation conditions*. 2005, Georgia Institute of Technology.
343. Berry, D. and S. Widder, *Deciphering microbial interactions and detecting keystone species with co-occurrence networks.* Frontiers in microbiology, 2014. **5**: p. 219.

344. Sievert, C., *Interactive web-based data visualization with R, plotly, and shiny*. 2020: CRC Press.
345. Guimera, R. and L.A. Nunes Amaral, *Functional cartography of complex metabolic networks.* Nature, 2005. **433**(7028): p. 895-900.
346. Bradford, S.A. and L.M. Abriola, *Dissolution of residual tetrachloroethylene in fractional wettability porous media: Incorporation of interfacial area estimates.* Water Resources Research, 2001. **37**(5): p. 1183-1195.
347. O'Carroll, D.M., et al., *Prediction of two-phase capillary pressure–saturation relationships in fractional wettability systems.* Journal of contaminant hydrology, 2005. **77**(4): p. 247-270.
348. Simunek, J., M.T. Van Genuchten, and M. Sejna, *The HYDRUS-1D software package for simulating the one-dimensional movement of water, heat, and multiple solutes in variably-saturated media.* University of California-Riverside Research Reports, 2005. **3**: p. 1-240.
349. Abriola, L.M. and K. Rathfelder, *Mass balance errors in modeling two-phase immiscible flows: causes and remedies.* Advances in Water resources, 1993. **16**(4): p. 223-239.
350. Chen, H., et al., *Sorption of perfluorooctane sulfonate (PFOS) on marine sediments.* Marine Pollution Bulletin, 2012. **64**(5): p. 902-906.
351. Brusseau, M.L., et al., *Nonideal transport and extended elution tailing of PFOS in soil.* Environmental science & technology, 2019. **53**(18): p. 10654-10664.
352. You, C., C. Jia, and G. Pan, *Effect of salinity and sediment characteristics on the sorption and desorption of perfluorooctane sulfonate at sediment-water interface.* Environmental pollution, 2010. **158**(5): p. 1343-1347.
353. Mejia-Avendaño, S., et al., *Sorption of Polyfluoroalkyl Surfactants on Surface Soils: Effect of Molecular Structures, Soil Properties, and Solution Chemistry.* Environmental Science & Technology, 2020. **54**(3): p. 1513-1521.
354. Liu, Y., et al., *The effects of soil properties and co-contaminants on sorption of perfluorooctane sulfonate (PFOS) in contrasting soils.* Environmental Technology & Innovation, 2020. **19**: p. 100965.
355. Rodriguez-Cruz, M., M. Sanchez-Martin, and M. Sanchez-Camazano, *A comparative study of adsorption of an anionic and a non-ionic surfactant by soils based on physicochemical and mineralogical properties of soils.* Chemosphere, 2005. **61**(1): p. 56-64.
356. Fabregat-Palau, J., M. Vidal, and A. Rigol, *Modelling the sorption behaviour of perfluoroalkyl carboxylates and perfluoroalkane sulfonates in soils.* Science of the Total Environment, 2021. **801**: p. 149343.
357. USDA-NRC. *Web Soil Survey*. 2023 (Accessed on; Available from: https://websoilsurvey.nrcs.usda.gov/app/.
358. Blake, G.R. and K. Hartge, *Particle density.* Methods of soil analysis: Part 1 physical and mineralogical methods, 1986. **5**: p. 377-382.
359. Schaap, M.G., F.J. Leij, and M.T. Van Genuchten, *Rosetta: A computer program for estimating soil hydraulic parameters with hierarchical pedotransfer functions.* Journal of hydrology, 2001. **251**(3-4): p. 163-176.
360. Air Force Civil Engineer Center (AFCEC), *Final Preliminary Assessment Report for Perfluorinated Compounds at Wright-Patterson Air Force Base Ohio.* 2015. Prepared by C.M. HILL. September 2015.
361. US Air Force (USAF), *Integrated Natural Resources Management Plan (INRMP) 2012-2016.* 2012. Prepared by USAF. May 2012.

362. Air Force Civil Engineer Center (AFCEC), *Final Site Inspection Report of Aqueous Film Forming Foam Areas at Wright-Patterson Air Force Base Montgomery and Greene Counties, Ohio.* 2018. Prepared by A.S. LLC. June 2018.
363. Air Force Civil Engineer Center (AFCEC), *Final Site Inspections Report of Fire Fighting Foam Usage at Tyndall Air Force Base Bay County, Florida.* 2018. Prepared by A.S. LLC. September 2018.
364. US Army Corps of Engineers (USACE), *Project Management Plan – Remedial actions and associated activities for AETC and Tyndall Air Force Base – Panama City, Florida.* 2006. Prepared by I. Weston Solutions. October 2006.
365. Air Force Civil Engineer Center (AFCEC), *Final Site Inspection Report of Aqueous Film Forming Foam Areas at Ellsworth Air Force Base Meade and Pennington Counties, South Dakota.* 2019. Prepared by A.S. LLC. March 2019.
366. Air Force Civil Engineer Center (AFCEC), *Final Site Investigation Report for Site Investigations of Fire Fighting Foam Usage at Various Air Force Bases in the United States for Ellsworth Air Force Base, Meade and Pennington Counties, South Dakota.* 2015. Prepared by S.C.a.F.S. LLC. January 2015.
367. Air Force Civil Engineer Center (AFCEC), *Update to the Final Basewide Quality Assurance Project Plan for Performance- Based Remediation at Ellsworth Air Force Base, South Dakota.* 2020. Prepared by A.L.J.a.G. Federal. February 2020.
368. US Army Corps of Engineers (USACE), *Draft Remedial Investigation Report for Per- and Polyfluoroalkyl Substances at Area of Concern Perfluorinated Compound-1 Ellsworth Air Force Base, South Dakota.* 2018. Prepared by A.P.J. Venture. November 2018.
369. Stumm, W. and G.F. Lee, *Oxygenation of Ferrous Iron.* Industrial & Engineering Chemistry, 1961. **53**(2): p. 143-146.
370. Sepulvado, J.G., et al., *Occurrence and Fate of Perfluorochemicals in Soil Following the Land Application of Municipal Biosolids.* Environmental Science & Technology, 2011. **45**(19): p. 8106-8112.
371. Rankin, K., et al., *A North American and global survey of perfluoroalkyl substances in surface soils: Distribution patterns and mode of occurrence.* Chemosphere, 2016. **161**: p. 333-341.
372. Schultz, M.M., D.F. Barofsky, and J.A. Field, *Quantitative Determination of Fluorotelomer Sulfonates in Groundwater by LC MS/MS.* Environmental Science & Technology, 2004. **38**(6): p. 1828-1835.
373. Perrotta, J.A. and C.S. Harwood, *Anaerobic metabolism of cyclohex-1-ene-1-carboxylate, a proposed intermediate of benzoate degradation, by Rhodopseudomonas palustris.* Applied and Environmental Microbiology, 1994. **60**(6): p. 1775-1782.
374. Gescher, J., et al., *Aerobic benzoyl-coenzyme A (CoA) catabolic pathway in Azoarcus evansii: conversion of ring cleavage product by 3, 4-dehydroadipyl-CoA semialdehyde dehydrogenase.* Journal of Bacteriology, 2006. **188**(8): p. 2919-2927.
375. Boll, M., *Key enzymes in the anaerobic aromatic metabolism catalysing Birch-like reductions.* Biochimica et Biophysica Acta (BBA)-Bioenergetics, 2005. **1707**(1): p. 34-50.
376. Brackmann, R. and G. Fuchs, *Enzymes of anaerobic metabolism of phenolic compounds: 4-Hydroxybenzoyl-CoA reductase (dehydroxylating) from a denitrifying Pseudomonas species.* European Journal of Biochemistry, 1993. **213**(1): p. 563-571.

377. Atashgahi, S., et al., *A benzene-degrading nitrate-reducing microbial consortium displays aerobic and anaerobic benzene degradation pathways.* Scientific reports, 2018. **8**(1): p. 1-12.
378. Schürmann, M., et al., *A novel 3-sulfinopropionyl coenzyme A (3SP-CoA) desulfinase from Advenella mimigardefordensis strain DPN7T acting as a key enzyme during catabolism of 3, 3'-dithiodipropionic acid is a member of the acyl-CoA dehydrogenase superfamily.* Journal of Bacteriology, 2013. **195**(7): p. 1538-1551.
379. Sanz, D. and E. Díaz, *Genetic characterization of the cyclohexane carboxylate degradation pathway in the denitrifying bacterium Aromatoleum sp. CIB.* Environmental Microbiology, 2022.
380. Chen, Y.-F., H. Chao, and N.-Y. Zhou, *The catabolism of 2, 4-xylenol and p-cresol share the enzymes for the oxidation of para-methyl group in Pseudomonas putida NCIMB 9866.* Applied microbiology and biotechnology, 2014. **98**(3): p. 1349-1356.
381. Kasai, D., et al., *Characterization of the gallate dioxygenase gene: three distinct ring cleavage dioxygenases are involved in syringate degradation by Sphingomonas paucimobilis SYK-6.* Journal of Bacteriology, 2005. **187**(15): p. 5067-5074.
382. Sugimoto, K., et al., *Crystal structure of an aromatic ring opening dioxygenase LigAB, a protocatechuate 4, 5-dioxygenase, under aerobic conditions.* Structure, 1999. **7**(8): p. 953-965.
383. Grund, E., B. Denecke, and R. Eichenlaub, *Naphthalene degradation via salicylate and gentisate by Rhodococcus sp. strain B4.* Applied and Environmental Microbiology, 1992. **58**(6): p. 1874-1877.
384. Izmalkova, T.Y., et al., *The organization of naphthalene degradation genes in Pseudomonas putida strain AK5.* Research in microbiology, 2013. **164**(3): p. 244-253.
385. Leutwein, C. and J. Heider, *Succinyl-CoA:(R)-benzylsuccinate CoA-transferase: an enzyme of the anaerobic toluene catabolic pathway in denitrifying bacteria.* Journal of Bacteriology, 2001. **183**(14): p. 4288-4295.
386. Hobbs, M.E., et al., *Structure and catalytic mechanism of LigI: insight into the amidohydrolase enzymes of cog3618 and lignin degradation.* Biochemistry, 2012. **51**(16): p. 3497-3507.
387. Zhao, L.N., et al., *Histidine protonation states are key in the LigI catalytic reaction mechanism.* Proteins: Structure, Function, and Bioinformatics, 2022. **90**(1): p. 123-130.
388. Eberhard, E.D. and J.A. Gerlt, *Evolution of function in the crotonase superfamily: the stereochemical course of the reaction catalyzed by 2-ketocyclohexanecarboxyl-CoA hydrolase.* Journal of the American Chemical Society, 2004. **126**(23): p. 7188-7189.
389. Egland, P.G., et al., *A cluster of bacterial genes for anaerobic benzene ring biodegradation.* Proceedings of the National Academy of Sciences, 1997. **94**(12): p. 6484-6489.
390. Kuntze, K., et al., *6-Oxocyclohex-1-ene-1-carbonyl-coenzyme A hydrolases from obligately anaerobic bacteria: characterization and identification of its gene as a functional marker for aromatic compounds degrading anaerobes.* Environmental Microbiology, 2008. **10**(6): p. 1547-1556.
391. Kujur, R.R.A. and S.K. Das, *Pseudomonas phenolilytica sp. nov., a novel phenol-degrading bacterium.* Archives of Microbiology, 2022. **204**(6): p. 1-10.
392. Hara, H., et al., *The 4-oxalomesaconate hydratase gene, involved in the protocatechuate 4, 5-cleavage pathway, is essential to vanillate and syringate degradation in Sphingomonas paucimobilis SYK-6.* Journal of Bacteriology, 2000. **182**(24): p. 6950-6957.

393. Wu, J.-H., et al., *Community and proteomic analysis of methanogenic consortia degrading terephthalate.* Applied and Environmental Microbiology, 2013. **79**(1): p. 105-112.
394. Nogales, J., et al., *Unravelling the gallic acid degradation pathway in bacteria: the gal cluster from Pseudomonas putida.* Molecular microbiology, 2011. **79**(2): p. 359-374.
395. Nishino, S.F. and J. Spain, *Degradation of nitrobenzene by a Pseudomonas pseudoalcaligenes.* Applied and Environmental Microbiology, 1993. **59**(8): p. 2520-2525.
396. Samanta, S.K. and C.S. Harwood, *Use of the Rhodopseudomonas palustris genome sequence to identify a single amino acid that contributes to the activity of a coenzyme A ligase with chlorinated substrates.* Molecular microbiology, 2005. **55**(4): p. 1151-1159.
397. Biegert, T., et al., *Enzymes of anaerobic metabolism of phenolic compounds: 4-Hydroxybenzoate-CoA ligase from a denitrifying Pseudomonas species.* European Journal of Biochemistry, 1993. **213**(1): p. 555-561.
398. Gibson, J., et al., *4-Hydroxybenzoate-coenzyme A ligase from Rhodopseudomonas palustris: purification, gene sequence, and role in anaerobic degradation.* Journal of Bacteriology, 1994. **176**(3): p. 634-641.
399. Baker, J.L., et al., *Widespread genetic switches and toxicity resistance proteins for fluoride.* Science, 2012. **335**(6065): p. 233-235.
400. Air Force Civil Engineer Center (AFCEC), *Final Site Inspection for Aqueous Film Forming Foam Areas at Altus Air Force Base Oklahoma.* 2017. Prepared by OTIE. August 2017.
401. Air Force Civil Engineer Center (AFCEC), *Final Site Inspection for Aqueous Film Forming Foam Areas at Joint Base San Antonio (JBSA) Lackland, Texas.* 2017. Prepared by OTIE. June 2017.
402. Air Force Civil Engineer Center (AFCEC), *Site Inspection for Aqueous Film Forming Foam Areas at Edwards Air Force Base, California.* 2018. Prepared by OTIE. August 2018.
403. Air Force Civil Engineer Center (AFCEC), *Site Inspection for Aqueous Film Forming Foam Areas at Travis Air Force Base, California.* 2018. Prepared by OTIE. July 2018.

Appendix A: Supporting Data

A.1 Appropriateness of using the Freundlich Equation to Fit Surface Tension

Schaefer, Culina [78] used a Freundlich model for surface excess to derive the following equation for fitting air-water surface tension (γ) with increasing bulk-water concentration (C):

$$\gamma = \gamma_o - RTk\frac{C^n}{n} \tag{A-1}$$

where the ideal gas constant (R) and the absolute temperature (T) are constants, and the solute-free air-water interfacial tension (γ_0), pre-exponential (k), and exponential (n) are fitted. To evaluate the ability of this equation to represent surface tension measurements in this study, measured air-water surface tensions for PFOS at concentrations from 1.5 x 10^{-4} to 1.51 mol/m^3 (or mM) in a 42 mM TDS solution were fit to Eq. S1 using the MatLab (v. R2018a) non-linear regression function fitnlm. One approach is to fit the three parameters γ_0, k, and n (see solid line in **Figure A.3a** and the fitted values given in **Table A.2**. This approach results in an overestimated (physically unrealistic) γ_o value of 78.46 mN/m as well as an overestimation of surface tension values in the concentration range from 1.5 x 10^{-4} to 10 x 10^{-4} mM and an underestimation for concentrations ranging from 10 x 10^{-4} to 0.1 mM. An alternative approach to fit Eq. A-1 is to fix γ_o at 72 mN/m, however, this results in a poorer overall fit to the data (r^2=0.55) with an underestimation of surface tensions between 1.5 x 10^{-4} and 0.07 mM and an overestimation at concentrations from 0.07 to 0.5 mM (**Figure A.3b**).

The approached adopted by [76] was to fit the air-water surface tension (γ) with increasing bulk-water concentration (C) using the Szyszkowski Eq. 1-6. A fit of Eq. A-1 was performed using the MatLab (v. R2018a) non-linear regression function fitnlm for PFOS concentrations from 1.5 x 10^{-4} to 1.51 mM and yielded three parameters including the solute-free air-water interfacial tension (γ_0), and values for a and b. As shown in **Figure A.3c**, Eq. A-1 captures the shape of the surface tension curve without under or over prediction of surface tension values and yields a physically realistic γ_o of 71.35 mN/m.

Another way the Freundlich model fails to match system behavior is related to the maximum surface excess (Γ_m), which occurs in the aqueous concentration range over which the interfacial tension is concentration independent [81]. This range is from 0.007 to 1.51 mM for the measured tension values shown in **Figure A.3** and can be fit with a straight line over this concentration range using Milner's equation:

$$\Gamma_m = -\frac{1}{RT}\left(\frac{\partial\gamma}{\partial lnC}\right)_T \tag{A-2}$$

This fit yields a maximum surface excess of 1.52 mg/m^2 which is the same value obtained from using Eq. (3-2). By contrast, the Freundlich model does not have a plateau or maximum surface excess, as the excess concentration increases with bulk-water concentration according to:

$$\Gamma = kC^n \tag{A-3}$$

Figure A.4 compares the estimated surface excess curves for the Freundlich or Langmuir-Szyszkowski models (Eq. (3-3)) for this system over a large concentration range, highlighting the fact that the Freundlich surface excess provides physically unrealistic estimates, with increasing concentration.

A.2 Organic and inorganic content analysis

The consumption of DGBE was determined by measuring the dissolved organic carbon concentration using a total organic carbon (TOC) analyzer (TOC-L CPH, Shimadzu). Ions including SO_4^{2-}, NO_3^-, and F^- were analyzed using a Thermo Scientific™ Dionex™ Aquion™ ion chromatography (IC) system equipped with an IonPac™ AS22 column (4 × 250 mm) and IonPac™ AG22 guard column (4 × 50 mm). The eluent was 4.5 mM sodium carbonate and 1.4 mM sodium bicarbonate at a flow rate of 1.2 mL/min. Conversion of Fe(III) to Fe(II) was determined by the ferrozine assay in iron-reducing microcosms [342]. Briefly, 100 μL of well-mixed slurry collected from the bottle was immediately mixed with 900 μL of 0.1 M HCl in a 1.7-mL microcentrifuge tube, to extract Fe(II) from the solid phase and stabilize Fe(II) in the sample (pH < 2). After equilibrating for 1 h, the sample was centrifuged and analyzed by the ferrozine colorimetric assay using a UV-Vis spectrophotometer at 562 nm. The collected well-mixed slurry was centrifuged at 15,000 rpm for 10 min, and the supernatant was used for other analyses. Specifically, the concentrations of lactate, propionate, and acetate in the aqueous phase were analyzed by a high-performance liquid chromatography (HPLC, Agilent Technologies 1260 Infinity series, CA), equipped with a Bio-Rad Aminex HPX-87H column (300 mm × 7.8 mm). The mobile phase was 5 mM sulfuric acid at a flow rate of 1.0 mL/min, and the column was maintained at 35 ºC.

A.3 Criteria for identification of potential important taxa in network analysis

A centrality-based method was used for identification of keystone taxa that have a large impact on the community composition. It was documented that keystone taxa tend to have high degree, high closeness centrality, and low betweenness centrality [343]. Degree, closeness centrality, and betweenness centrality of each node were calculated using Gephi (version 0.9.2) [95]. Visualization in a 3D scatter plot using "plotly" package in R was used to assist keystone taxa identification and a snapshot of the 3D plot was shown in **Figure A.62** and **Figure A.64** [344].

The modular structure of complex networks also plays an important role in their functionality. A connectivity-based method developed to determine the role of a node in a highly modular network was modified and used to identify critical taxa in the observed network [345]. All nodes in the observed network were classified into four "universal roles" based on their within-module degree, z, and participation coefficient, P: (a) approximate 90% nodes in the network are defined as peripheral nodes, or non-hubs, ($z < 0.9$); (b) modular hubs, the nodes with the vast majority (at least 80%) of edges within their module ($z \geq 0.9$, $P \leq 0.30$); (c) connector hubs, the nodes with many (at least 50%) edges to most of the other modules ($z \geq 0.9$, $0.30 < P \leq 0.75$); and (d) network hubs, the nodes with links homogeneously distributed among all modules ($z \geq 0.9$, $P > 0.75$). The node positions and regions of roles in the z–P parameter space were shown in **Figure A.63**.

A.4 Calculation of NAPL-Water Interfacial Area

To estimate the PCE NAPL-water specific interfacial area (a_{nw}), the NAPL geometry is conceptualized as a fixed number of spherical ganglia within each computational element. [38, 137, 346] The specific interfacial area, calculated as the ratio of ganglia surface area to volume of porous medium, is a function of NAPL saturation (s_n) and characteristic NAPL ganglia radius (r_n):

$$a_{nw} = \frac{3f\emptyset s_n}{r_n} \tag{A-4}$$

where ∅ is porosity and, *f* is a calibration factor that accounts for discrepancies between actual blob shape and the assumed spherical geometry and for the fraction of interfacial area in contact with mobile aqueous phase.

Following the method demonstrated by Bradford and Abriola [346], r_n was estimated from NAPL-water capillary pressure (P_{nw})–water saturation (s_w) data using the Laplace equation for capillarity and assuming that the ganglia are entrapped in the largest portions of the pore space (i.e., in the saturation range $1\text{-}s_n<s_w<1$) [137]

$$r_n = \frac{2\sigma_{nw}\cos\omega_{nw}}{P_{nw}(s_w^*)} \tag{A-5}$$

Here, σ_{nw} is NAPL-water interfacial tension, ω_{nw} is solid-NAPL-water contact angle and s_w^* is calculated as $1\text{-}\ s_n/2$ assuming that residual NAPL blobs are entrapped in the largest portions of the pore space.

The capillary pressure curve for 60-80 Ottawa sand was approximated by employing Leverett scaling [347] using imbibition capillary pressure data for a water wet (i.e. $\omega_{nw} \approx 0$) 70-110 Ottawa sand.

The parameter *f* is unknown, and therefore, it was calibrated by fitting the BTC data for the first (i.e. one among duplicate) PFOS column experiment. This calibrated *f* value was then used to predict the BTC data for the rest of the PCE-NAPL column experiments.

A.5 Modifications to the HYDRUS 1-D Code

PFAS transport in the presence of entrapped NAPL was modeled using an enhanced version of the Hydrus 1-D model, modified to include an immobile NAPL phase as well as nonlinear PFAS interfacial accumulation and linear NAPL partitioning. Through this modification, an immobile NAPL phase was added to the Hydrus code. Based upon its low solubility, PCE-NAPL dissolution was assumed to be minimal over the time frame of the column experiments, and therefore, the residual NAPL saturation (s_n) was kept constant. The specific NAPL-water interfacial area (a_{nw}) was estimated from s_n and NAPL-water capillary pressure curve using Eqs. (**A-4**) and (**A-5**). The retardation factor (R) in the Hydrus code was modified to account for the retardation processes caused by NAPL-water interfacial accumulation and NAPL partitioning (i.e., $R = 1 + \left(\rho_b \frac{dS}{dC} + a_{nw}\frac{d\Gamma}{dC} + +\theta_n K_{nw}\right)/\theta_w$). The nonlinear PFAS NAPL-water interfacial accumulation term (i.e., $\frac{d\Gamma}{dt} = \frac{d\Gamma}{dC}\frac{dC}{dt}$) was incorporated in the current Hydrus iterative solution scheme [348] for solving the nonlinear transport equation (Eq. (3-4)). Through this iterative scheme, at each time-step the nonlinear coefficient in the interfacial accumulation term (i.e., $\frac{d\Gamma}{dC}$) is re-evaluated at each iteration, and the new equation is solved using results of the previous iteration. The iterative process continues until a satisfactory degree of convergence is obtained between concentrations in two successive iterations [348]. To obtain mass-conservative results [139, 349], a finite element chord slope iterative scheme, rather than an analytical derivative, was used for evaluation of the nonlinear adsorption isotherm slope in the mass-term of the transport equation (i.e., $\frac{d\Gamma}{dC}$).

A.6 Estimation of Sorption Isotherms for Field-Scale Simulations

To predict solid-water partition of PFAS as a function of soils properties, available data in literature [10, 111, 350-354] were used to estimate isotherm parameters through a multilinear regression. For the MASS compound, the regression was conducted using data presented in [355] assuming sorption properties similar to those of sodium dodecyl sulphate (SDS). Except

for the K_f of PFOA, Freundlich coefficients were fitted as a function of soil properties according to the following equations

$$K_f = a_0 + a_1 f_{oc} + a_2 f_{SC} + a_3 \mathrm{pH} + a_4 f_{oc} f_{SC} + a_5 f_{oc} \mathrm{pH} + a_6 f_{SC} \mathrm{pH} + a_7 f_{oc} f_{SC} \mathrm{pH} \quad \text{(A-6)}$$

$$n = b_0 + b_1 f_{oc} + b_2 f_{SC} + b_3 \mathrm{pH} + b_4 f_{oc} f_{SC} + b_5 f_{oc} \mathrm{pH} + b_6 f_{SC} \mathrm{pH} + b_7 f_{oc} f_{SC} \mathrm{pH} \quad \text{(A-7)}$$

where K_f and n are the Freundlich coefficients, f_{oc} and f_{SC} correspond to the percentage of organic carbon and silt-clay content respectively, pH is the potential hydrogen, and terms a_i and b_i are the regression coefficients. The fitted regression coefficients employed in these expressions are presented in **Table A.46**.

Given the narrow range of soil parameters and conditions for PFOA sorption in the reviewed literature, K_f for this compound was scaled from PFOS using the scaling model presented in [356].

A.7 Development of Spill Scenarios for Field-Scale Modeling

A.7.1 AFCEC Database

PFAS contamination at Air Force bases throughout the continental U.S. was investigated using the on-line administrative record made available by the Air Force Civil Engineering Center (AFCEC). This administrative record contains a significant amount of data on the many contaminated sites on USAF bases, which were assumed to be representative of the PFAS sites distributed across the DoD. Eight AFB locations were initially examined in this study: Altus, Edwards, Ellsworth, Lackland, Moody, Travis, Tyndall and Wright-Patterson. These sites were chosen based upon their known areas of AFFF contamination and available information pertaining to spill characteristics. Following the initial selection, the AFCEC database was mined for information about each of these sites.

In order to find relevant files, the full document search tool available on the website was used with keywords AFFF, PFAS, PFOA and PFOS. The resulting files (approximately 300) were downloaded, reviewed, and organized according to their data availability. Following this 'deep dive' into the data, the information was compiled and grouped into three broad categories:

- Subsurface characteristics: depth to water table, moisture content, groundwater temperature, hydraulic conductivity, soil content, average hydraulic gradient, annual rainfall, recharge rate, fraction of organic carbon or TOC, dissolved oxygen (DO), pH, presence of metals, and oxidation reduction potential (ORP).
- Spill characteristics: type of spill (e.g., fire training sessions, spray tests, hangar releases, real fire extinguish, WTP/drainage/outfall, vehicle crashes and fire station spills) and volume spilled.

A.7.2 Site selection

The initial eight sites were narrowed down to three sites that had the most complete data and spanned the diversity of AFB PFAS release characteristics and environments. Wright-Patterson, Tyndall, and Ellsworth were selected as representative of hydrogeologic environments across the United States. These sites have the most information that can be used to create realistic and diverse simulation scenarios to inform the decision matrix. Brief descriptions of the rationale used for choosing each of the sites are summarized below.

- Wright-Patterson (WP) AFB: it is located in an area of medium rainfall (35" per year) and the water table in the AFFF inspection areas fluctuates between 4 and 17 ft bgs. The subsurface is formed by alluvial sediments above glacial outwash sediments and

glacial till which makes this site stand out. The base has several known AFFF contamination locations, such as fire training sessions, spray tests, real fires, vehicle crashes, and fire station and hangar releases. The many spills at this site provide a variety of contamination scenarios.

- Tyndall (TY) AFB: it is located in a region of high rainfall (61" per year) which makes this site relatively unique. The water table is shallow, ranging from 1 foot to 10 feet bgs, with sandy subsurface material. The main documented AFFF contamination at the site is due to real fires and vehicle crashes. There are several co-contaminants present and a number of completed studies and reports, providing ample information about the contaminants present in the subsurface.
- Ellsworth (EL) AFB: it has an average 18" of rainfall per year. The water table in the AFFF inspection areas ranges from 4 to 34 ft bgs and the subsurface consists of alluvial deposits and shale. The main documented spills are in vehicle crash and fire station area. The high volume of available information along with its northwestern location in South Dakota make an interesting addition to the group.

The sites were selected with the goal of being representative of a variety of depositional, climatic, hydrologic, and biogeochemical conditions. It was desired that the selected sites capture the range of contamination scenarios encountered on DoD installations, encompassing diverse physical and chemical characteristics. Field-scale simulations performed for scenarios based on these sites will be used to explore the diversity and complexity of PFAS contamination under realistic field conditions.

A.7.3 Spill selection

The collected data showed that the main types of spills are associated with fire training areas, real fire extinguishing episodes, vehicle crashes, hangar releases, spray test areas and fire stations. For modeling purposes, these spills can be organized into three different categories, based upon release characteristics: repetitive spills, one-time fast releases and one-time concentrated AFFF releases. After creating a matrix of data from the air force base contaminated sites, three types of spills were chosen as representative. These spills are presented in **Table A.47** with the corresponding sites and descriptions. Based on these data, the following release scenarios were developed:

1. Fire training areas
    - Description: repetitive (ranging from weekly to 4 times a year) release that occur during fire training sessions.
    - Frequency: biweekly or four sessions per year over a 10-years period.
    - Volume: 25-100 gallons of AFFF concentrate per session (diluted to 3%).
2. Fire station
    - Description: one-time spill that usually presents a concentrated AFFF release, such as spills from fire engines and AFFF tanks.
    - Volume: 400 gallons of AFFF concentrate.
3. Vehicle crash
    - Description: one-time spill that results from emergency response, such as airplane and drone crashes.
    - Volume: 800 gallons of AFFF concentrate.

A.7.4 Soil profile and parameters

To develop the scenarios, data from the AFCEC database was combined with information from the Web Soil Survey (WSS, [357]). In the WSS website, data is available only for the first/top

layers (i.e., 5 to 7 ft bgs) of soil. For the deeper layers, information was obtained from the AFCEC documents.

The WSS website was used to gather information about hydraulic conductivity, bulk density, organic matter, pH and particle size distribution. Soil porosity values were calculated from bulk density, using

$$porosity\ (\%) = \left(1 - \frac{bulk\ density}{particle\ density}\right) \times 100 \quad \text{(A-8)}$$

where the particle density was assumed as 2.65 g/cm3 for all soils [358]. Total organic carbon (TOC) values were calculated by dividing the soil organic matter by 1.724 [357]. The AFCEC documents provided information about boring logs, particle size distribution, percentage of solids, pH and TOC.

The capillary-pressure curve parameters for each soil layer were estimated using the ROSSETA model [359] provided in Hydrus 1-D package based on the available particle size distribution for each soil.

A.8 Selected Sites for Field-Scale Simulations

A.8.1 Wright-Patterson AFB

Located in Greene County, Ohio, the principal water-bearing zones in the surficial aquifer beneath Wright-Patterson are in a highly transmissive glacial outwash sediments. Generally, the base is a recharge area. Groundwater recharge happens by direct infiltration of rainfall and from surface streams, including the Mad River and its tributaries. To increase recharge near the Dayton drinking water well field immediately downgradient of the AFB, artificial ponds have been maintained [360]. The aquifer is located approximately from 20 to 30 feet bgs and yields between 1,500 and 2,000 gallons per minute [361]. However, depth to the water table can vary from 3 feet bgs to 100 feet bgs. The site has 26 AFFF inspection areas, where groundwater levels range from approximately 4 to 17 feet bgs. The climate of the region around the Wright-Patterson AFB is temperate and humid, with a mean annual temperature of 51.9 degrees Fahrenheit. The mean annual rainfall is 34.71 inches.

Based on the WSS database, the AFB is mainly occupied by Warsaw and Sloan soils.[357]. According to the Official Soil Series Descriptions and Series Classification, the Warsaw series consists of well drained soils formed in loamy sediments and in the underlying gravelly outwash on outwash plains. The Sloan series consists of very poorly drained soils formed in loamy alluvium on flood plains. Two different scenarios were developed, one in the Warsaw soil (i.e., AFFF Area 8) and the other in the Sloan soil (i.e., AFFF Area 22). **Table A.48** and **Table A.49** show the soil layer properties for Area 8 and 22 based on WSS and AFCEC documents [362]. Estimated sorption properties according to relationship presented in **Appendix A.6** are reported in **Table A.53** and **Table A.54**. The resulting soil profiles are shown in **Figure A.70** and **Figure A.71** respectively.

A.8.2 Tyndall AFB

Tyndall AFB is in eastern Bay County in the panhandle region of northwest Florida. This area has a humid subtropical climate with average annual temperatures ranging from 59 to 78.3 degrees Fahrenheit. The mean annual rainfall is 61.1 inches. Due to the coastal location, Tyndall AFB is exposed to severe tropical storms, which results in extremely high winds, heavy rainfall, and tidal surges [363]. The surficial aquifer in the Tyndall AFB consists of highly transmissive, well sorted, fine- to medium-grained sands, which extends up to 110 feet deep, where there is a clayey-sand strata. The shallow aquifer is unconfined and encountered at

depths ranging from less than 1 foot to 10 feet bgs. The water table is relatively flat but can fluctuate up to 5 feet as a result of the seasonal rainfall and tidal cycles. The hydraulic gradient ranges from 0.004 to 0.008 [364]. Tyndall AFB has 15 AFFF inspection areas.

The majority of the Tyndall AFFF areas is in the Arents, which are soils that have been deeply mixed by human activities and, therefore, have no diagnostic horizons [357]. For this reason, no scenario was developed for this area. The only scenario developed in Tyndall is in the Leon sand (map unit 13), which consists of very deep, very poorly and poorly drained, moderately rapid to moderately slowly permeable soils formed in sandy marine sediments (see **Table A.50** and **Figure A.72**). Estimated sorption properties according to relationship presented in **Appendix A.6** are reported in **Table A.55**.In the WSS website, information for the Tyndall AFB area is available for the first 80 inches of soil. Since the water table is encountered before 80 inches (approximately 42 and btoc), the scenario for Tyndall AFB was developed only with information from the WSS website.

A.8.3 Ellsworth

Ellsworth AFB is located approximately 10 miles from Rapid City, South Dakota, in a semi-arid continental region with the Black Hills to the west influencing the climate. The average summer temperature is 68 degrees Fahrenheit and the average winter temperature is 26 degrees Fahrenheit. Average annual rainfall is 16.3 inches [365]. At Ellsworth AFB, there is one shallow unconfined aquifer and three deep confined aquifers. The upper shallow aquifer consists of alluvial and colluvial deposits and fractured Pierre Shale. In some areas, the aquifer depth extends from only a few feet below the surface to 60 feet. In the southern region of the base, the monitoring wells in the alluvial sand and gravel beds and shallow fracture zones typically produce less than 2 gallons per minute [366]. The base of the shallow aquifer is defined by the unfractured shale at a depth of approximately 50 feet or less. The deep confined aquifers are not connected to the overlying unconfined aquifer [367]. The base has 12 AFFF inspection areas, where groundwater levels range from approximately 4 to 34 feet btoc.

The predominant soil type in upper five feet of material underlying the surface is a clay loam with permeability rates varying from 0.2 to 2.0 inches per hour [368]. The area is mostly occupied by the Nunn series, which consists of very deep, well drained soils that formed in loess and mixed alluvium. For this reason, only one scenario was developed for Ellsworth AFB. The scenario is located at AFFF Area 1 where the soil is Nunn clay loam (NcA).

In the WSS website, information for the Ellsworth AFB area is available for the first 79 inches of soil. **Table A.51** shows the NcA horizons, texture, classification, parameters, and particle size distribution. For the soil layers deeper than 79 inches, information was obtained from the AFCEC documents. After 79 inches, there are five layers of clay soil (CL) above the water table. The AFCEC document does not provide the particle size distribution and TOC for the CL soils. By combining the horizons from the WSS with the boring log from the AFCEC document, the resulting soil profile is shown in **Figure A.73**.

Finally, the additional scenario at Ellsworth that was used to compare simulations with field data was developed from soil data presented in [140]. This scenario consisted of two horizons whose properties correspond to location LY210109 (S and D) within the former fire-training area OU1. A summary of the soil horizons is presented in **Table A.52**. Estimated sorption properties according to relationship presented in **Appendix A.6** are reported in**Table A.56** and **Table A.57**.

A.9 Observations of PFOA and PFOS Separate Phase Formation

A separate phase was observed at the surface of a solution containing 5,000 mg/L PFOA in ultrapure water (**Figure A-1**). **Figure A-2** shows a photograph where a separate phase floating

on a solution containing 500 mg/L KPFOS in water with 1741 mg/L total dissolved solids. These observations clearly demonstrate that PFOA and KPFOS will form separate phases at relatively low concentrations, which is lowered in the presence of salts.

A.10 Calculation of PFOA and PFOS Mass Distribution in an Unsaturated Soil

The distribution of PFOA or PFOS in 1 L of soil was calculated using the following parameters.:

Soil Water Fraction:

Volumetric water content = 0.26

Volume of water in 1L volume = 0.26 L

Solids Fraction:

Fraction of organic matter (f_{oc}) = 0.002

K_{oc} for PFOA = 108

K_{oc} for PFOS = 568

Bulk density (g/mL) = 1.5

Mass solids in 1L = 1.5 kg

Air-Water Interface Fraction:

Air-water interfacial area (area of air-water interface/total system volume)

Low interfacial area in 1L total = $\frac{80m^2\ surface\ area}{m^3 air\ volume}\frac{m^3}{1000\ L}1L = 0.08m^2$

High interfacial area in 1L total = $\frac{1000m^2\ surface\ area}{m^3 air\ volume}\frac{m^3}{1000\ L}1L = 1m^2$

Phase Distribution Calculation:

Assuming an aqueous concentration of 1 mg/L leads to the following:

Mass in aqueous phase = 0.26 L x 1 mg/L = 0.26 mg

Mass of PFOA on solid phase = 1 mg/L x 108 x 0.002 L/kg x 1.5 kg/L x 1L = 0.324 mg

Mass of PFOS on solid phase = 1 mg/L x 568 x 0.002 L/kg x 1.5 kg/L x 1L = 1.704 mg

Mass accumulated at the air-water interface was calculated using the following Syzszkowski surface excess values obtained using the Szyszkowski fits from **Table 4.4** and **Table 4.5** with an aqueous concentration of 1 mg/L are presented in **Table A.1.**

A.11 PFAS Phase Distribution Calculations

Total Mass = mass in water + mass at air-water interface + mass at NAPL-water interface + mass adsorbed to soil

$$M_t = V_t(C_w\theta_w + \Gamma_{aw}A_{aw} + \Gamma_{Nw}A_{Nw} + C_s\rho_b) \quad \text{(A-9)}$$

where:

- $V_t = total\ volume(L\ total)$
- $C_w = water\ concentration\ \left(\frac{mg}{L\ water}\right)$

- $\theta_w = volumetric\ water\ content\ \left(\frac{L\ water}{L\ total}\right)$
- $\Gamma_{aw} = air\ water\ excess\ \left(\frac{mg}{m^2 airwater\ area}\right)$
- $A_{aw} = air\ water\ interfacial\ area\ \left(\frac{m^2 airwater\ area}{L\ total}\right)$
- $\Gamma_{Nw} = NAPL\ water\ excess\ \left(\frac{mg}{m^2 airwater\ area}\right)$
- $A_{Nw} = NAPL\ water\ interfacial\ area\ \left(\frac{m^2 NAPLwater\ area}{L\ total}\right)$
- $C_s = soil\ concentration\ \left(\frac{mg}{kg\ soil}\right)$
- $\rho_b = soil\ bulk\ density\ \left(\frac{kg\ soil}{L\ total}\right)$

Linear Sorption to Sandy Soil

Sandy vadose-zone subsoil composed primarily of quartz with moderately low organic carbon content and properties given in **Table A.3** [29].

Water Fraction: Volumetric water content = 0.26 and Volume of water in 1L volume = 0.26 L

Interfacial Areas: Air-water and NAPL-water interfacial areas of 80 cm^2/cm^3 and 20 cm^2/cm^3 based on values measured for sandy soil with S_w of 0.78 and S_{NAPL} of 0.02 [29].

Air-water interfacial area in 1 L total:

$$80\frac{cm^2\ surface\ area}{cm^3\ total\ volume} \times \frac{1000\ cm^3}{L} \times \frac{1\ L\ total}{} \times \frac{m^2}{(100cm)^2} = 8\ m^2$$

NAPL-water interfacial area

$$20\frac{cm^2\ surface\ area}{cm^3\ total\ volume} \times \frac{1000\ cm^3}{L} \times \frac{1\ L\ total}{} \times \frac{m^2}{(100cm)^2} = 2\ m^2$$

Solids Fraction:

$$C_s = K_d C_w$$

Fraction of organic carbon: foc = 0.002

PFOA K_{oc} = 108 (Table 2 of Brusseau, 2018)

K_d = 108*0.002 = 0.216 L/kg

PFOS K_{oc} = 568 (Table 2 of Brusseau, 2018 taken from Milinovic et al. 2015)

K_d = 568*0.002 = 1.14 L/kg

K_d FOSA = 0.25 L/kg (determined for 20-30 mesh Ottawa sand)

Surface Excess: Parameters from **Table 4.6** and **Table 4.7** of this work for 380 mg/L TDS and C_w with units of mg/L.

	Air-water	Dodecane-water
PFOA	$\Gamma_{aw} = 2.10\frac{mg}{m^2} \times \frac{C_w}{C_w + 49}$	$\Gamma_{NW} = 2.07\frac{mg}{m^2} \times \frac{C_w}{C_w + 177}$

PFOS $\Gamma_{aw} = 1.53 \frac{mg}{m^2} \times \frac{C_w}{C_w + 1.7}$ $\Gamma_{NW} = 1.46 \frac{mg}{m^2} \times \frac{C_w}{C_w + 8.6}$

FOSA $\Gamma_{aw} = 3.13 \frac{mg}{m^2} \times \frac{C_w}{C_w + 1.4}$ $\Gamma_{NW} = 0.97 \frac{mg}{m^2} \times \frac{C_w}{C_w + 4.1}$

A.12 Fluoride detection

The measurement of fluoride ion using IC is detailed in **S1**. If all the initially spiked 8:2 FTOH (170 μg/L) was completely defluorinated, the resulting fluoride concentration would be about 118.32 μg/L. However, the actual fluoride concentration is expected to be much lower because the major transformation products in this study, 7:2 sFTOH and PFOA, were largely removed by headspace sampling or were not amenable to further defluorination. If 170 μg/L of 8:2 FTOH underwent the hypothesized pathway to generate 7:2 sFTOH and PFOA, the theoretically yield of fluoride ions would be approximately 13.92 μg/L, which was one order of magnitude lower than the average background fluoride concentration in the microcosms (192.6 ± 51.9 μg/L). Also, samples measured by ion chromatography had to be diluted ten-times due to the high concentration of chloride ion presented in the mineral medium (> 5 mg/L), which prevented the detection of fluoride. All these factors made it difficult to discern fluoride derived from 8:2 FTOH from background levels.

A.13 Establishment of nitrate-, sulfate-, and iron-reducing microcosms

Throughout the experiments, anaerobic conditions were strictly maintained in all microcosms, as demonstrated by the colorless appearance of the resazurin indicator. In the microcosms under each redox condition, carbon sources and electron donors (i.e., lactate and/or DGBE), and electron acceptors (i.e., NO_3^-, SO_4^{2-}, or Fe(III)/Fe(II)) were monitored to confirm the corresponding microbial activity during incubation period (**Figure A.16** to **Figure A.18**). At certain time points, the amendment of nitrate, sulfate, lactate, or DGBE was made to appropriate microcosms to ensure the presence of sufficient electron acceptor, electron donor, or carbon source (**Figure A.16** to **Figure A.18**).

The establishment of nitrate-, sulfate-, or iron(III)-reducing conditions in the corresponding biologically-active microcosms (i.e., all treatments except abiotic control) were confirmed by the following observations: (1) the decrease in NO_3^- or SO_4^{2-} in nitrate- or sulfate-reducing microcosms; (2) the increase in Fe(II) in iron-reducing microcosms; (3) the conversion of lactate to acetate and propionate, followed by the consumption of latter byproducts in ED treatments and positive controls; (4) the consumption of DGBE, as indicated by decrease in TOC in NA treatments. None of the observations (1) to (4) was found in the abiotic controls, indicating the abiotic conditions were maintained throughout the incubation period in each batch of experiment. Greater extents of carbon source, electron donor and acceptor consumption were measured in ED treatment and positive control under nitrate-reducing conditions than that in all other biologically-active microcosms (i.e., NA treatment under nitrate-reducing, and sulfate-, iron-reducing microcosms). A total of 11 amendments of 40 mM nitrate and 8 amendments of 20 mM lactate were made to ED treatment or positive control under nitrate-reducing conditions, whereas no more than 2 amendments of electron donor or acceptor were made to others. These indicated that the amendment of lactate, additional electron donor and carbon source greatly increased the growth rate of nitrate-reducing microorganisms, however, only slight or no enhancement of the growth was observed in sulfate-, and iron-reducing microorganisms. Although the continuously steady increase in Fe(II) was not observed in biologically-active microcosms, compared to abiotic controls, the formation of Fe(II) from Fe(III) reduction was apparent, and the consumption of lactate and/or DGBE in the situation of sufficient supply of electron acceptor (i.e., 100 mM goethite) was

observed (**Figure A.18**). The active iron-reducing activities were thus confirmed. Fe(II) did not continuously increase, likely due to the pH of the aqueous phase in the microcosms (>7.5 during the most of incubation period, **Figure A.18**), and the precipitation of ferrous hydroxide (solubility product K_{sp} = 8.0E-16, ferrous hydroxide started to precipitate at pH = 7.5 in 10 mM Fe(II) solution) occurred [369]. The well-mixed slurry sample was used in the present study to extract Fe(II) from the solid phase, however, the ferrous hydroxide precipitates might not be evenly and/or efficiently extracted.

A.14 Background levels of legacy PFAS in Loring AFB soil

Table A.22 shows the background levels of legacy PFAS in Loring soils according to the measurements of day 0 samples from all microcosms (8:2 FTOH background levels only from positive control microcosms). None of 8:2 FTOH, 8:2 FTUA, 8:2 FTCA, 7:2 sFTOH was detected in day 0 samples, indicating that AFFF-contaminated Loring AFB soil did not contain a detectable concentration of these polyfluorinated compounds. However, 7:3 acid was detected in the Loring AFB soil (0.034 ± 0.011 nmole/g dw). Since 7:3 acid is not known to be manufactured but is almost exclusively formed by the biotransformation of fluorotelomer compounds (e.g., 8:2 FTOH etc.) [186], its presence in day 0 samples indicated the *in-situ* biotransformation of AFFF-based fluorotelomer precursors likely occurred in the Loring AFB soil before the soil was collected and transported to the lab. PFOS was present at higher concentration in Loring AFB soil than any other PFAAs targeted in this study, with around 3.4 nmole/g dw. PFHxS was also detected with a concentration of 0.018 ± 0.002 nmole/g dw while the other PFSAs were below the detection limits (**Table A.22**). The contamination of PFOS and PFHxS is consistent with the historical applications of 3M AFFF formulation at the Loring AFB [4]. Among PFCAs, short-chain congeners (i.e., PFBA, PFPeA, PFHxA) were detected with higher concentrations than longer-chain congeners including PFOA, a preponderance of which was found in previous soil surveys [370, 371]. The plausible explanation is that certain amounts of fluorotelomer-based AFFFs (e.g., Ansul and National Foam AFFF) were also used in the Loring AFB [8]. It was further supported by the detection of one fluorotelomer precursor, 6:2 fluorotelomer sulfonate in Loring AFB soil (unpublished work). The higher abundance of short-chain PFCAs likely resulted from the transformation of those fluorotelomer-based precursors [8, 52].

A.15 Background levels of 6:2 FTS and its potential transformation products in Loring and Robins soils.

Based on previous 6:2 FTS biotransformation studies [45, 54, 222] and the commercial availability of authentic standards, a total of 11 PFAS compounds including 6:2 FTS and its potential transformation products were quantitatively analyzed throughout the experiments. **Table A.24** shows the background levels of these compounds in Loring and Robins soils based on the measurements of day 0 samples from all microcosms (6:2 FTS background levels only from positive control microcosms). 6:2 FTS, which has been widely detected in soil and groundwater samples at AFFF-impacted sites [154, 372], was detected in both soils, with about 10-fold higher concentrations in Robins soil than Loring soil. Since 6:2 FTS was reported as a transformation product of the major ingredients (e.g., fluorotelomer thioamido sulfonates, fluorotelomer sulfonamide betains and amines) in several AFFF formulations (e.g., Ansul and National Foam AFFF) [8, 52], the higher background levels of 6:2 FTS detected in Robins soil were likely due to more historical applications of these fluorotelomer-based AFFFs at the sites.

Two polyfluorinated compounds, 5:3 acid and 3:3 acid, were also detected in the Loring and Robins soils (**Table A.24**). However, both compounds are not known to be manufactured but

are almost exclusively formed by the biotransformation of fluorotelomer compounds (e.g., 6:2 FTS and 6:2 FTOH) [186]. The presence of these compounds implied that the on-site biotransformation of AFFF-derived fluorotelomer precursors was likely occurring in the two AFFF-impacted sites where the soils were sampled. Among the C4-C7 PFCAs, PFHxA was detected in Robins soil with the highest concentration (0.291 ± 0.039 nmole/g dw), which was around 8-fold higher than PFHxA in Loring soil (0.036 ± 0.005 nmole/g dw) (**Table A.24**). The concentration of each target PFCA in Loring soil was lower than that in Robins soil, which might be due to more and/or greater extent of on-site biotransformation of fluorotelomer-based precursors in Robins soil that partially resulted in the formation of PFCAs [52, 179].

A.16 Diversity and richness of microbial community.

The mapped reads of 16S rRNA gene amplicons from Loring and Robins soil microcosms varied in the range of 1,878 to 18,059 (**Table A.28**). To facilitate the comparison of diversity and richness of microbial community, the number of reads in all samples was rarefied to an identical sequencing depth (1,878), which was within the plateau range of the rarefaction curves, indicating that the sequencing depth was reasonable. The quality-filtered reads were clustered into operational taxonomic units (OTUs) at a 97% similarity level. The number of OTUs in all the samples ranged from 25 to 554 (**Table A.28**).

Alpha diversity, defined as the mean diversity of species in a community [165] was estimated using the Shannon and Simpson indices. Species richness, the number of species or OTUs present in a community, was estimated using richness index Chao1. These indices of the microbial communities in Loring and Robins soil samples were shown in **Table A.28**. The overall diversity of the microbial community native to Robins soil is substantially lower than that in Loring soil, as the Shannon (2.00 ± 0.06 vs. 5.64 ± 0.12), Simpson (0.81 ± 0.01 vs. 0.99 ± 0.00), and Chao1 (27.6 ± 2.5 vs. 726.6 ± 80.2) indices are much less in the day 7 samples from Robins soil microcosms than that in the day 0 samples from Loring soil microcosms (**Table A.28**). The lower diversity in Robins soil might be partially due to the heavier PFAS contamination detected in this site (**Table A.24**), as it has been reported that high concentrations of PFAS (e.g., 1 μg PFOS/g soil, 0.5 μg PFOA/g sediment) reduced the microbial community diversity and caused a shift in microbial community composition [166-168]. The other reason may be the lack of sufficient carbon sources for the microbial growth at the site; the total organic carbon content in Robins AFB soil is as low as 0.5% while it is about 3.5% in Loring AFB soil. After the biostimulation with amendment of DGBE over 224 days, the microbial diversity in Robins AFB soil increased dramatically; the Chao1 and Shannon indices increased from 27.6 and 2.0 at day 7 samples to 123.9 and to 3.6 at day 224 samples, respectively (**Table A.28**). Conversely, the diversity and richness of Loring AFB soil microbial community decreased after a 224-day incubation with DGBE, as indicated by lower Chao1, Shannon, and Simpson indices at day 224 samples compared to day 0 samples (**Table A.28**). The decrease possibly resulted from the biased stimulated growth of certain species over others in original Loring soil by the DGBE amendment.

In both Loring or Robins soil microcosms, the significant difference ($p < 0.05$) in Chao1, Shannon, or Simpson indices was not found between day 224 samples from the live treatment (~1700 μg/L 6:2 FTS spiked) and the positive control (0 μg/L 6:2 FTS spiked) (**Table A.28**), suggesting that the presences of spiked 6:2 FTS and its biotransformation products did not significantly change the microbial diversity in this study. Although the results are not in agreement with the previous studies that microbial diversity in river sediment and soil was reduced by the exposure to PFCAs or 6:2 FTS biotransformation products, the concentrations of PFAS detected or applied in those studies were much higher (e.g., 15 mg/L) than that in the

present study [166-168]. Principle coordinate analysis (PCoA) was also analyzed on the Weighted Unifrac distance matrices as a measurement of beta diversity to visualize microbial community alteration among the different treatments in Loring and Robins microcosms. The minimal impact of spiked 6:2 FTS on overall diversity is further supported by the clear grouping of day 224 samples from the live treatment and positive controls (**Table A.35**). In addition, the apparent separation of Loring and Robins soil samples revealed the distinct differences between the microbial community compositions at the two sites (**Table A.35**).

A.17 The impacts of 6:2 FTS and its biotransformation products on the microbial community compositions

At the phylum level, the increase in Myxococcota and Firmicutes were found in both Loring AFB and Robins AFB soil after being exposed to 6:2 FTS (**Table A.36**). Specifically, the relative abundance of Myxococcota was 2.2 ± 0.7% and 1.1 ± 0.4% in non-spiked Loring AFB and Robins AFB soils, respectively; while it increased to 3.5 ± 1.9% and 3.5 ± 0.3% in the 6:2 FTS spiked soils, respectively. Likewise, Firmicutes increased from 1.3 ± 0.1% and 4.3 ± 0.2% in non-spiked soils, to 2.7 ± 0.5% and 7.5 ± 1.1% in the 6:2 FTS spiked Loring AFB and Robins AFB soil soils, respectively. The results suggest that Myxococcota and Firmicutes were relatively more tolerant to 6:2 FTS and/or its transformation products. Both of phyla were found capable of biotransformation of chlorinated solvents [218, 219], and Firmicutes is a dominant phylum in the PFAS-contaminated soils [167, 170].

A.18 Supplementary files

The supplementary data file (.xlsx) can be found and downloaded in the link: https://github.com/SD610/AU-Dissertation/blob/3ad4be091b66b6901f7f4b3a85f06b0631190401/Chapter%205_Supplementary%20data.xlsx

It contains 6 spreadsheets listed below:

- **Supplementary Data X1**: Taxa assignment and topological features of each ASV in the constructed network
- **Supplementary Data X2**: Taxa assignment and topological features of each ASV in the control network
- **Supplementary Data X3**: ASVs that were identified as keystone taxa by the centrality-based method
- **Supplementary Data X4**: ASVs that were identified as keystone taxa by the connectivity-based method.
- **Supplementary Data X5**: genes and corresponding pathways identified by differential analysis
- **Supplementary Data X6**: contribution of predicted functional genes/enzymes by bacterial taxa across all microcosm experiments

A.19 Supplementary tables

Table A.1 Surface excess values obtained for a concentration of 1 mg/L.

Aqueous Solution	PFOA Surface Excess (mg/m^2)	PFOS Surface Excess (mg/m^2)
Ultrapure	0.024	0.07
ca. 40 mg/L TDS	0.070	0.37
ca. 400 mg/L TDS	0.140	0.65
ca. 1700 mg/L TDS	0.171	0.69

Table A.2 Fitted parameters obtained using Eq. A-1.

Approach	γ_0	RTk	n	RMSE	r^2
Fit	78.5 ± 1.4	10.55 ± 0.51	0.239 ± 0.017	1.08	0.994
Fixed	72	12.71 ± 0.78	0.333 ± 0.015	0.215	0.55

Table A.3 Properties of representative porous medium

Property	Value
Bulk density (g/cm^3)	1.5
Porosity	0.333
Fraction of soil organic carbon	0.002
Water saturation	0.78
Air saturation	0.2
NAPL saturation	0.02
Volumetric water content	0.26
Volumetric air content	0.067
Volumetric NAPL content	0.0067
Air-water interfacial area (cm^{-1})	80
NAPL-water interfacial area (cm^{-1})	20

Table A.4 Chemical names, acronyms, molecular structures, and suppliers of target poly- and perfluoroalkyl substances (PFAS) for LC-MS/MS quantitative analysis.

Chemical name	Acronym	Molecular structure	Supplier
8:2 fluorotelomer alcohol	8:2 FTOH	$F(CF_2)_8CH_2CH_2OH$	Sigma-Aldrich (St. Louis, USA); Wellington Laboratories (Ontario, Canada)
6:2 fluorotelomer sulfonate	6:2 FTS	$F(CF_2)_6CH_2CH_2SO_3^-$	
Perfluorooctane sulfonamide	FOSA	$F(CF_2)_8SO_2NH_2$	
8:2 fluorotelomer saturated carboxylic acid	8:2 FTCA	$F(CF_2)_8CH_2COOH$	
8:2 fluorotelomer unsaturated carboxylic acid	8:2 FTUA	$F(CF_2)_7CF{=}CHCOOH$	
7:2 secondary fluorotelomer alcohol	7:2 sFTOH	$F(CF_2)_7CH(OH)CH_3$	
7:3 fluorotelomer carboxylic acid	7:3 acid	$F(CF_2)_7CH_2CH_2COOH$	
6:2 fluorotelomer alcohol	6:2 FTOH	$F(CF_2)_6CH_2CH_2OH$	
6:2 fluorotelomer saturated carboxylic acid	6:2 FTCA	$F(CF_2)_6CH_2COOH$	Wellington Laboratories
6:2 fluorotelomer unsaturated carboxylic acid	6:2 FTUA	$F(CF_2)_5CF{=}CHCOOH$	
5:2 secondary fluorotelomer alcohol	5:2 sFTOH	$F(CF_2)_5CH(OH)CH_3$	
5:3 fluorotelomer carboxylic acid	5:3 acid	$F(CF_2)_5CH_2CH_2COOH$	
3:3 fluorotelomer carboxylic acid	3:3 acid	$F(CF_2)_3CH_2CH_2COOH$	
Perfluorohexane sulfonamide	FHxSA	$F(CF_2)_6SO_2NH_2$	
N-dimethyl ammonio propyl perfluoroalkane sulfonamide	AmPr-FHxSA	$F(CF_2)_6SO_2NH(CH_2)_3N(CH_3)_2$	
Perfluorobutanoic acid	PFBA	$F(CF_2)_3COOH$	
Perfluoropentanoic acid	PFPeA	$F(CF_2)_4COOH$	
Perfluorohexanoic acid	PFHxA	$F(CF_2)_5COOH$	
Perfluoroheptanoic acid	PFHpA	$F(CF_2)_6COOH$	
Perfluorooctanoic acid	PFOA	$F(CF_2)_7COOH$	
Perfluorononanoic acid	PFNA	$F(CF_2)_8COOH$	PFAC-MXC stock, Wellington Laboratories
Perfluorodecanoic acid	PFDA	$F(CF_2)_9COOH$	
Perfluoroundecanoic acid	PFUnA	$F(CF_2)_{10}COOH$	
Perfluorododecanoic acid	PFDoA	$F(CF_2)_{11}COOH$	
Perfluorobutanesulfonic acid	PFBS	$F(CF_2)_4SO_3H$	
Perfluoropentanesulfonic acid	PFPeS	$F(CF_2)_5SO_3H$	
Perfluorohexanesulfonic acid	PFHxS	$F(CF_2)_6SO_3H$	
Perfluoroheptanesulfonic acid	PFHpS	$F(CF_2)_7SO_3H$	
Perfluorooctanesulfonic acid	PFOS	$F(CF_2)_8SO_3H$	

Table A.5 Physical and chemical properties of Robins, Loring, and Hudson soils.

	Robins soil	Loring soil	Hudson soil
Sand, Silt, Clay (%)	77.5 ± 1.3, 5.6 ± 1.0, 16.9 ± 0.3	53.1 ± 3.1, 32.7 ± 2.3, 14.2 ± 0.8	15.6 ± 3.1, 68.3 ± 1.7, 16.1 ± 1.4
USDA Textual Class	Sandy Loam	Loam/Sandy Loam	Silt Loam
CEC (meq/100 grams)	2.8 ± 0.5	18.7 ± 0.0	14.7 ± 1.1
Organic Carbon (%)	0.6 ± 0.1	3.5 ± 0.1	1.1 ± 0.0
Moisture Content (%)	7.0 ± 0.1	24.1 ± 1.1	13.8 ± 0.6
pH (1-part soil: 1-part deionized water)	5.1 ± 0.1	7.2 ± 0.2	6.5 ± 0.0

Table A.6 Targeted mass inclusion list used in LC-MS analysis.

Compound	Formula	m/z	RT (min)	Window (min)	HCD Collision Energy (%)
AmPr-FHxSA	C11H13F13N2O2S	483.0417	11.25	2	40
FOSA	C8HF17NO2S	497.9462	12.4	1	40
FHxSA	C6HF13NO2S	397.9526	10.59	1	40
PFOS	C8F17SO3	498.9302	10.3	2	50
PFHpS	C7F15SO3	448.9334	9.8	2	60
PFHxS	C6F13SO3	398.9366	9.2	2	40
PFPeS	C5F11SO3	348.9398	8.39	1	50
PFBS	C4F9SO3	298.943	6.7	1.5	50
PFBA	C4HF7O2	212.9792	1.6	0.5	30
PFPeA	C5F9O2	262.976	2.9	1	14
PFHxA	C6F11O2	312.9728	7	1	14
PFHpA	C7F13O2	362.9696	8.3	1	14
PFOA	C8F15O2	412.9664	9.04	2	14

Table A.7 Limits of detection (LODs) and limits of quantification (LOQs) of targeted PFAS.

Analytes	LOD[a] (ng/mL)	LOQ (ng/mL)
PFBA	0.01	0.01
PFPeA	0.01	0.03
PFHxA	0.01	0.04
PFHpA	0.01	0.01
PFOA	0.01	0.01
PFBS	0.02	0.07
PFPeS	0.01	0.01
PFHxS	0.01	0.01
PFHpS	0.01	0.01
PFOS	0.01	0.01
FHxSA	0.01	0.01
FOSA	0.01	0.01
AmPr-FHxSA	0.01	0.01

[a]LODs and LOQs were calculated based on the signal-to-noise ratio (S/N), with a S/N of 3 for LOD and 10 for LOQ, respectively.

Table A.8 Instrument conditions and LC gradient used for the detection and quantification of 8:2 FTOH, 6:2 FTS and their polyfluorinated transformation products by UPLC-MS/MS.

LC conditions			
LC system:	Waters ACQUITY UPLC I-Class fitted with PFC kit		
Column:	Waters BEH C-18 column (1.7 μm dia., 2.1 × 50 mm)		
Column temp:	30 °C		
Sample temp:	4 °C		
Injection volume:	50 μL		
Mobile phase A:	Water		
Mobile phase B:	Methanol		
LC gradient			
Time (min)	Flow rate (mL/min)	%A	%B
0	0.25	50	50
2	0.25	10	90
4	0.25	0	100
6	0.25	0	100
7	0.25	50	50
10	0.25	50	50
MS conditions			
MS system:	Waters Xevo TQ-S		
Ionization mode:	ESI-		
Capilary voltage:	5 kV		
Desolvation temp:	350 °C		
Desolvation gas flow:	750 L/hr		
Source temp:	120 °C		
Cone gas flow:	50 L/hr		

Table A.9 Multiple reaction monitoring (MRM) parameters used for the detection and quantification of 8:2 FTOH, 6:2 FTS and their polyfluorinated transformation products by UPLC-MS/MS.

Compound	Molecular Ion (m/z)	Cone Voltage (V)	Collision Energy (V)	Quant. Ion (m/z)	Cone Voltage (V)	Collision Energy (V)	Confirmation Ion (m/z)
8:2 FTOH	462.97	14	12	402.99	18	18	354.97
8:2 FTUA	456.97	30	8	393.08	30	44	119.04
8:2 FTCA	476.90	36	6	413.50	26	14	393.18
7:2 sFTOH	393.03	40	14	219.07			
7:3 Acid	440.97	44	12	337.13	44	20	317.09
6:2 FTS	427.10	25	18	407.09	25	34	80.84
6:2 FTOH	363.00	18	8	303.00			
6:2 FTCA	377.03	20	20	293.05	20	8	63.03
6:2 FTUA	357.00	30	14	293.00			
5:2 sFTOH	293.10	50	18	119.04			
5:3 Acid	340.97	32	14	237.1	32	20	217.06
3:3 Acid	241.00	10	10	177.00	10	20	219

Table A.10 Instrument conditions and LC gradient used for the detection and quantification of PFAAs by UPLC-MS/MS.

LC conditions			
LC system:	Waters ACQUITY UPLC I-Class fitted with PFC kit		
Column:	Waters BEH C-18 column (1.7 µm dia., 2.1 × 50 mm)		
Column temp:	50 °C		
Sample temp:	4 °C		
Injection volume:	10 µL		
Mobile phase A:	95:5 Water:methanol + 2 mM ammonium acetate		
Mobile phase B:	Methanol + 2 mM ammonium acetate		
LC gradient			
Time (min)	Flow rate (mL/min)	%A	%B
0	0.4	85	15
1.2	0.4	85	15
17	0.4	15	85
17.5	0.4	0	100
18	0.4	85	15
20	0.4	85	15
MS conditions			
MS system:	Waters Xevo TQ-S Micro		
Ionization mode:	ESI-		
Capilary voltage:	0.50 kV		
Desolvation temp:	350 °C		
Desolvation gas flow:	650 L/hr		
Source temp:	150 °C		
Cone gas flow:	20 L/hr		

Table A.11 Multiple reaction monitoring (MRM) parameters used for the detection and quantification of PFAAs by UPLC-MS/MS.

Compound	Molecular Ion (m/z)	Cone Voltage (V)	Collision Energy (V)	Quant. Ion (m/z)	Cone Voltage (V)	Collision Energy (V)	Confirmation Ion (m/z)
PFBA	212.93	12	5	169.09			
PFPeA	262.95	4	4	219.09			
PFBS	298.95	6	28	98.99	6	32	79.99
PFHxA	312.94	4	4	269.12	4	20	119.02
PFPeS	349.00	15	32	99.00	15	32	80
PFHpA	362.90	12	8	319.14	12	16	169.08
PFHxS	398.90	68	32	98.99	68	36	79.98
PFOA	412.93	2	8	369.12	2	16	169.03
PFNA	462.89	6	9	419.16	6	15	219.1
PFOS	498.83	30	40	99.01	30	44	80
PFDA	512.85	6	10	469.00	6	16	219
PFNS	549.00	10	43	99.00	10	43	80
PFUnA	563.03	8	8	519.08	8	14	269
PFDS	599.03	2	48	99.02	2	55	79.97

Table A.12 Limits of detection (LODs) and limits of quantification (LOQs) of target PFAS.

Analytes	LOD[a] (ng/mL)	LOQ[b] (ng/mL)
8:2 FTOH[c]	0.56	6.10
8:2 FTCA	0.02	0.09
8:2 FTUA	0.02	0.03
7:2 sFTOH[c]	0.17	1.20
7:3 acid	0.02	0.03
6:2 FTS	0.02	0.06
6:2 FTOH[c]	0.63	11.10
6:2 FTCA	0.02	0.10
6:2 FTUA	0.02	0.03
5:2 sFTOH[c]	0.26	4.20
5:3 acid	0.01	0.02
3:3 acid	0.03	0.13
PFBA	0.01	0.05
PFPeA	0.01	0.05
PFHxA	0.01	0.05
PFHpA	0.01	0.05
PFOA	0.01	0.05
PFNA	0.01	0.05
PFDA	0.01	0.05
PFUnA	0.01	0.05
PFDoA	0.01	0.05
PFBS	0.01	0.05
PFPeS	0.01	0.05
PFHxS	0.01	0.05
PFHpS	0.01	0.05
PFOS	0.01	0.05

[a]LODs are determined based on EPA Method 537.1

[b]LOQs are determined with the Lowest Concentration Minimum Reporting Level (LCMRL) Calculator distributed by EPA.

[c]The LODs and LOQs for 8:2 FTOH, 6:2 FTOH, 7:2 sFTOH, 5:2 sFTOH were run-dependent, and the values reported here were the highest levels during the analysis of all microcosm samples.

Table A.13 The number and the time points of the effluent and side-port samples collected from biotic columns for targeted and non-targeted PFAS analysis, ORP measurement, and DNA extraction throughout the experiments.

Note: effluent samples were collected from abiotic columns at the same time as the biotic columns, but only half of samples were subject to targeted PFAS analysis and only 4 samples (at 14.5, 28.3, 47.4, 58.8 PVs) were subject to non-targeted PFAS analysis. No side-port samples were collected from abiotic columns.

Experimental stage	Number of effluent samples collected (at which PV sample was collected)		Number of sets of side-ports 1-3 samples collected (at/during which PV sample was collected)			
	For targeted PFAS analysis	For non-targeted PFAS analysis	For targeted PFAS analysis	For non-targeted PFAS analysis	For ORP measurement	For DNA extraction
Phase I-A (0-11.5 PVs)	12 (Each PV)	1 (0.5 PVs)	1 (8.0 PVs*)	0	0	0
Phase I-B (11.5-17.5 PVs)	6 (Each PV)	3 (14.5, 15.4, 17.5 PVs)	2 (12.5*, 16.4 PVs*)	0	0	0
Phase I-C (17.5-33.1 PVs)	14 (Each PV)	3 (24.4, 28.3, 31.2 PVs)	4 (20.4*, 24.4, 28.3, 32.2 PVs)	2 (24.4, 28.3 PVs)	1 (25.5-27.5 PVs)	1 (25.5-27.5 PVs)
Phase II-A (33.1-47.4 PVs)	15 (Each PV)	4 (35.0, 39.7, 43.5, 47.4 PVs)	4 (36.0, 39.7, 43.5, 47.4 PVs)	2 (39.7, 47.4 PVs)	1 (40.6-42.0 PVs)	0
Phase II-B (47.4-54.1 PVs)	7 (Each PV)	2 (50.3, 54.1 PVs)	2 (50.3, 54.1 PVs)	2 (50.3, 54.1 PVs)	1 (47.4-48.4 PVs)	0
Phase II-C (54.1-58.8 PVs)	5 (Each PV)	2 (56.9, 58.8 PVs)	1 (58.8 PVs)	1 (58.8 PVs)	0	1 (57.8-58.8 PVs)

*An incorrect sampling technique was used initially for side-port sampling, which resulted in the collected samples were mostly from the side-port itself (i.e., a “dead zone”) instead of the flowing stream. Therefore, those side-port samples were not included in this study (Fig. 4).

Table A.14 Changes in the mass (nmole) of FOSA and PFOS in Loring soil microcosms.

Time	FOSA			PFOS		
	Live treatment	Abiotic control	Positive control	Live treatment	Abiotic control	Positive control
Day 0	24.2 ± 1.2	17.0 ± 0.1	0.6 ± 0.0	47.1 ± 0.4	47.3 ± 0.1	47.5 ± 1.4
Day 28	22.4 ± 0.2	16.1 ± 0.3	0.6 ± 0.0	52.1 ± 0.4	53.7 ± 0.8	57.2 ± 0.4
Day 56	24.5 ± 0.5	19.0 ± 0.3	0.8 ± 0.1	57.9 ± 0.6	57.5 ± 2.2	57.2 ± 0.1
Day 98	18.9 ± 0.9	15.1 ± 1.1	0.6 ± 0.0	55.0 ± 0.6	54.1 ± 2.7	53.3 ± 1.6
Day 154	17.2 ± 0.9	15.2 ± 0.2	0.7 ± 0.1	52.5 ± 0.8	47.0 ± 0.0	46.3 ± 0.2
Day 224	15.6 ± 1.1	16.3 ± 0.4	0.6 ± 0.0	55.9 ± 2.7	49.7 ± 1.1	50.7 ± 0.4
Day 308	13.3 ± 0.7	14.9 ± 0.5	0.6 ± 0.1	51.5 ± 1.3	47.5 ± 1.2	46.3 ± 1.5

Table A.15 Partitioning of FOSA and PFOS in aqueous and solid phases of Loring and Hudson live treatments (percentage (%) of mass in each phase relative to the total mass).

Time (day)	Loring-live treatments				Hudson-live treatments			
	FOSA		PFOS		FOSA		PFOS	
	Aqueous	Solid	Aqueous	Solid	Aqueous	Solid	Aqueous	Solid
28	9.4 ± 0.6	90.6 ± 0.6	30.4 ± 3.0	69.6 ± 3.0	30.4 ± 1.3	69.6 ± 1.3	60.5 ± 1.2	39.5 ± 1.2
56	8.6 ± 0.2	91.4 ± 0.2	26.2 ± 3.2	73.8 ± 3.2	23.5 ± 1.0	76.5 ± 1.0	53.9 ± 2.4	46.1 ± 2.4
98	11.4 ± 0.5	88.6 ± 0.5	29.4 ± 0.9	70.6 ± 0.9	28.4 ± 1.8	71.6 ± 1.8	51.8 ± 6.3	48.2 ± 6.3
154	9.5 ± 1.2	90.5 ± 1.2	26.4 ± 2.0	73.6 ± 2.0	28.9 ± 1.5	71.1 ± 1.5	49.6 ± 2.7	50.4 ± 2.7
224	9.4 ± 0.5	90.6 ± 0.5	25.1 ± 1.5	74.9 ± 1.5	21.2 ± 4.1	78.8 ± 4.1	44.9 ± 1.5	55.1 ± 1.5
308	8.2 ± 0.5	91.8 ± 0.5	21.3 ± 1.6	78.7 ± 1.6	17.3 ± 7.5	82.7 ± 7.5	43.6 ± 5.3	56.4 ± 5.3

Table A.16 Microbial richness and diversity in Loring and Hudson soils.

Soil type	FOSA (μg/L)	Sampling time	Mapped reads	OTUs	Chao1	Shannon	Simpson
Loring AFB soil	0	Day 0	6490	687	1019.8 ± 30.8	5.85 ± 0.07	0.99 ± 0.00
	0	Day 0	6403	651			
	0	Day 154	6945	267	422.8 ± 0.5	3.67 ± 0.01	0.91 ± 0.01
	0	Day 154	7194	283			
	85	Day 154	6742	267	524.5 ± 95.1	3.69 ± 0.14	0.92 ± 0.01
	85	Day 154	6283	280			
	0	Day 308	5300	280	419.9 ± 6.3	3.98 ± 0.14	0.92 ± 0.02
	0	Day 308	6354	276			
	85	Day 308	6430	251	408.9 ± 34.6	3.75 ± 0.18	0.92 ± 0.02
	85	Day 308	6272	233			
Hudson AFB soil	0	Day 0	4606	393	586.6 ± 35.6	4.87 ± 0.05	0.98 ± 0.00
	0	Day 0	5254	388			
	0	Day 154	6230	206	256.6 ± 54.6	3.65 ± 0.08	0.94 ± 0.00
	0	Day 154	8298	150			
	85	Day 154	6111	161	254.2 ± 1.3	3.34 ± 0.04	0.91 ± 0.01
	85	Day 154	6225	171			
	0	Day 308	6073	226	297.6 ± 25.5	3.66 ± 0.12	0.93 ± 0.01
	0	Day 308	6590	162			
	85	Day 308	6649	158	219.1 ± 2.9	3.54 ± 0.08	0.92 ± 0.02
	85	Day 308	5761	166			

Table A.17 Fitting parameters of the first-order exponential decay model[a].

Parameter	Value	Standard Error	Statistics	
M	99.840	6.604	R2	0.969
k	0.184	0.028	Adjusted R2	0.962

The model can be mathematically expressed as equation $M(t) = M e^{-kt}$

Table A.18 Molar percentage of 8:2 FTOH and 7:2 sFTOH being removed by headspace sampling over the initially spiked 8:2 FTOH in Robins biotransformation experiment during 90-day incubation.

Compound	Sampling time	Mol%
8:2 FTOH	Day 3	14.54 ± 0.01
	Day 7	1.54 ± 0.23
	Day 14	0.07 ± 0.07
	Day 28	0.03 ± 0.01
	Day 56	0.01 ± 0.00
	Day 90	ND[a]
7:2 sFTOH	Day 3	ND[a]
	Day 7	0.34 ± 0.07
	Day 14	4.59 ± 0.86
	Day 28	9.49 ± 4.80
	Day 56	7.07 ± 1.50
	Day 90	7.69 ± 0.81

[a] ND = not detected

Table A.19 Molar percentage (mol%) of 8:2 FTOH and its biotransformation products over the initially spiked 8:2 FTOH at the end of 90-day Loring biotransformation experiment.

	Day 90-Low	Day 90-High
8:2 FTOH	5.8 ± 2.3	10.1 ± 1.4
8:2 FTCA	0.0 ± 0.0	0.2 ± 0.0
8:2 FTUA	0.0 ± 0.0	1.0 ± 0.2
7:2 sFTOH	33.0 ± 1.1	15.8 ± 0.0
7:3 acid	1.5 ± 1.0	0.9 ± 0.2
PFBA	0.1 ± 0.1	0.0 ± 0.0
PFPeA	0.3 ± 0.0	0.1 ± 0.0
PFHxA	0.5 ± 0.4	0.3 ± 0.0
PFHpA	0.5 ± 0.0	0.3 ± 0.0
PFOA	3.0 ± 0.2	1.7 ± 0.3

Table A.20 Identification confidence level of potential 8:2 FTOH transformation products.

Tentative name	Identification confidence level	Tentative formula	Mass error [ppm]	Retention time [min]	Theoretical m/z	Observed m/z	Identified in the experiment with which soil type
1H-perfluoroheptane[a]	1	C7 H F15	0.14	4.736	368.9766	368.9764	Loring[b] and Robins
3-OH-7:3 acid	2	C10 H5 F15 O3	0.36	4.919	456.9926	456.9930	Loring[c]
1H-perfluorohexane	3	C6 H F13	-0.33	4.439	318.9798	318.9795	Loring[b]
Perfluoroheptanal	3	C7 H F13 O	-0.25	4.748	346.9747	346.9745	Loring[b] and Robins
7:3 u acid	3	C10 H3 F15 O2	0.24	4.937	438.9821	438.9822	Loring[c] and Robins
3-fluoro-7:3 acid	3	C10 H4 F16 O2	0.67	5.077	458.9883	458.9885	Loring[c]
6:2 FTCA	3	C8 H3 F13 O2	0.29	4.410	376.9853	376.9691	Loring[c]
7:3 u amide	4	C10 H4 F15 N O	-0.05	5.492	437.9981	437.9975	Loring[c] and Robins
6:2 FTUA	4	C8 H2 F12 O2	-0.09	4.522	356.9790	356.9785	Loring[c]
6:3 acid	4	C9 H5 F13 O2	1.25	4.877	391.0009	391.0009	Loring[c]

[a] Purchased from SynQuest Laboratories (Alachua, FL)

[b] Identified in both low-dosed and high-dosed treatment

[c] Identified in high-dosed treatment only

Table A.21 Microbial richness and diversity in Loring and Robins AFB soils.

Soil type	8:2 FTOH dose	Sampling time	Mapped reads	OTUs	Shannon	Chao1
Loring	N/A	Day 0	10882	742	5.32	755
Loring	N/A	Day 90	13790	483	4.19	583
Loring	Low	Day 90	17032	537	4.30	672
Loring	High	Day 90	13621	488	3.90	628
Robins	N/A	Day 7	15017	87	1.82	94
Robins	N/A	Day 90	12027	104	2.38	111
Robins	Low	Day 90	16960	122	2.69	133

Table A.22 Concentrations (nanomole per gram soil/dry weight) of individual PFAS in Loring AFB soil.

Category	PFAS	Loring AFB soil
Polyfluorinated compounds	8:2 FTOH	N.D.
	8:2 FTCA	N.D.
	8:2 FTUA	N.D.
	7:2 sFTOH	N.D.
	7:3 acid	0.034 ± 0.011
PFCAs	PFBA	0.031 ± 0.005
	PFPeA	0.048 ± 0.009
	PFHxA	0.032 ± 0.005
	PFHpA	0.011 ± 0.003
	PFOA	0.026 ± 0.005
	PFNA	0.012 ± 0.003
	PFDA	0.007 ± 0.002
	PFUnA	0.012 ± 0.004
	PFDoA	N.D.
PFSAs	PFBS	N.D.
	PFPeS	N.D.
	PFHxS	0.018 ± 0.002
	PFHpS	N.D.
	PFOS	3.412 ± 0.348

N.D.: analyte not detected in the sample.

Table A.23 Potential biotransformation products of 8:2 FTOH identified by LC-HRMS analysis

Abbreviated name	Formula	Mass (*m/z*)	Mass error [ppm]	Level of confidence[a]	Identified in microcosms
1H-perfluoroheptane	C_7HF_{15}	368.9764	0.14	1	Nitrate-reducing (ED & NA)
3-OH-7:3 acid	$C_{10}H_5F_{15}O_3$	456.9930	0.36	2	
7:3 U acid	$C_{10}H_3F_{15}O_2$	438.9822	0.24	3	
7:3 U amide	$C_{10}H_4F_{15}NO$	437.9975	-0.05	4	
3-F-7:3 acid	$C_{10}H_4F_{16}O_2$	458.9885	0.67	3	Sulfate-reducing (ED & NA), iron-reducing (ED)

[a]The level of confidence of each identified biotransformation product was assigned using a scheme reported by Schymanski et al.[201]

Table A.24 Background levels (nmole/g dw) of 6:2 FTS and its potential per- and polyfluorinated transformation products in Loring and Robins soils.

Category	PFAS	Loring AFB soil	Robins AFB soil
Polyfluorinated compounds	6:2 FTS	0.278 ± 0.067	2.821 ± 0.150
	6:2 FTOH	N.D.	N.D.
	6:2 FTCA	N.D.	N.D.
	6:2 FTUA	N.D.	N.D.
	5:2 sFTOH	N.D.	N.D.
	5:3 acid	0.071 ± 0.010	0.026 ± 0.006
	3:3 acid	0.036 ± 0.009	0.027 ± 0.007
Perfluorinated compounds	PFBA	0.033 ± 0.004	0.072 ± 0.013
	PFPeA	0.052 ± 0.010	0.073 ± 0.011
	PFHxA	0.036 ± 0.005	0.291 ± 0.039
	PFHpA	0.016 ± 0.004	0.035 ± 0.008

N.D.: not detected in the sample.

Table A.25 Changes in the mass (nmole) of 6:2 FTS and its potential transformation products in Loring soil microcosms.

Time (day)	6:2 FTS	6:2 FTOH	6:2 FTUA	6:2 FTCA	5:2 sFTOH	5:3 acid	3:3 acid	PFBA	PFPeA	PFHxA	PFHpA
Live treatment											
0	154.7 ± 15.8	N.D.	N.D.	N.D.	N.D.	0.203 ± 0.004	0.136 ± 0.005	0.093 ± 0.009	0.146 ± 0.038	0.097 ± 0.024	0.047 ± 0.011
7	143.0 ± 8.3	N.D.	N.D.	N.D.	N.D.	0.226 ± 0.026	0.116 ± 0.016	0.120 ± 0.031	0.179 ± 0.020	0.106 ± 0.005	0.061 ± 0.023
28	99.6 ± 13.7	N.D.	5.729 ± 0.834	N.D.	8.237 ± 0.660	1.632 ± 0.337	0.105 ± 0.026	0.120 ± 0.019	0.186 ± 0.008	1.221 ± 0.242	0.079 ± 0.009
56	60.7 ± 3.2	N.D.	3.752 ± 1.470	0.309 ± 0.001	15.746 ± 1.777	2.306 ± 0.917	0.137 ± 0.011	0.109 ± 0.011	0.578 ± 0.077	2.722 ± 0.006	0.095 ± 0.019
98	46.3 ± 11.7	N.D.	1.205 ± 0.762	0.048 ± 0.019	15.148 ± 1.947	7.083 ± 0.924	0.107 ± 0.025	0.136 ± 0.007	0.720 ± 0.126	2.423 ± 0.390	0.321 ± 0.034
154	0.3 ± 0.1	N.D.	3.217 ± 0.109	N.D.	17.840 ± 1.887	13.698 ± 1.925	0.098 ± 0.025	0.615 ± 0.078	1.988 ± 0.464	2.454 ± 0.402	0.138 ± 0.010
224	0.5 ± 0.1	N.D.	0.469 ± 0.205	N.D.	19.832 ± 9.649	0.261 ± 0.118	0.124 ± 0.018	2.300 ± 0.780	10.964 ± 4.215	8.196 ± 1.067	0.508 ± 0.165
Positive control											
0	0.835 ± 0.200	N.D.	N.D.	N.D.	N.D.	0.172 ± 0.014	0.094 ± 0.004	0.093 ± 0.013	0.141 ± 0.036	0.117 ± 0.004	0.034 ± 0.001
7	0.632 ± 0.446	N.D.	N.D.	N.D.	N.D.	0.219 ± 0.028	0.100 ± 0.031	0.103 ± 0.008	0.176 ± 0.011	0.096 ± 0.008	0.054 ± 0.000
28	0.002 ± 0.000	N.D.	N.D.	N.D.	0.161 ± 0.013	0.195 ± 0.040	0.112 ± 0.021	0.122 ± 0.003	0.150 ± 0.048	0.130 ± 0.022	0.070 ± 0.018
56	0.002 ± 0.002	N.D.	N.D.	N.D.	0.453 ± 0.045	0.493 ± 0.085	0.099 ± 0.027	0.113 ± 0.003	0.127 ± 0.020	0.141 ± 0.010	0.100 ± 0.020
98	0.028 ± 0.004	N.D.	0.005 ± 0.002	N.D.	0.410 ± 0.120	0.623 ± 0.050	0.090 ± 0.012	0.149 ± 0.010	0.154 ± 0.027	0.149 ± 0.016	0.255 ± 0.015
154	0.038 ± 0.018	N.D.	0.002 ± 0.001	N.D.	0.340 ± 0.060	0.534 ± 0.008	0.087 ± 0.003	0.174 ± 0.053	0.111 ± 0.006	0.239 ± 0.085	0.104 ± 0.009
224	0.029 ± 0.001	N.D.	N.D.	N.D.	0.303 ± 0.219	0.282 ± 0.061	0.087 ± 0.045	0.235 ± 0.010	0.464 ± 0.012	0.355 ± 0.045	0.309 ± 0.052
Abiotic control											
0	145.7 ± 3.6	N.D.	N.D.	N.D.	N.D.	0.183 ± 0.018	0.096 ± 0.013	0.101 ± 0.012	0.137 ± 0.024	0.105 ± 0.021	0.054 ± 0.012
7	145.4 ± 1.4	N.D.	N.D.	N.D.	N.D.	0.221 ± 0.001	0.142 ± 0.004	0.098 ± 0.008	0.175 ± 0.007	0.120 ± 0.006	0.053 ± 0.008
28	156.2 ± 3.3	N.D.	N.D.	N.D.	N.D.	0.226 ± 0.014	0.136 ± 0.001	0.124 ± 0.003	0.150 ± 0.022	0.132 ± 0.020	0.065 ± 0.003
56	159.1 ± 1.8	N.D.	N.D.	N.D.	N.D.	0.218 ± 0.025	0.107 ± 0.039	0.158 ± 0.014	0.121 ± 0.018	0.131 ± 0.003	0.084 ± 0.010
98	137.0 ± 5.5	N.D.	N.D.	N.D.	N.D.	0.286 ± 0.006	0.125 ± 0.009	0.118 ± 0.010	0.140 ± 0.014	0.158 ± 0.006	0.266 ± 0.019
154	153.8 ± 0.2	N.D.	N.D.	N.D.	N.D.	0.455 ± 0.025	0.091 ± 0.006	0.154 ± 0.040	0.178 ± 0.059	0.121 ± 0.020	0.117 ± 0.001
224	152.3 ± 7.8	N.D.	N.D.	N.D.	N.D.	0.214 ± 0.092	0.150 ± 0.112	0.245 ± 0.039	0.373 ± 0.050	0.267 ± 0.115	0.200 ± 0.010

Table A.26 Changes in the mass (nmole) of 6:2 FTS and its potential transformation products in Robins soil microcosms.

Time (day)	6:2 FTS	6:2 FTOH	6:2 FTUA	6:2 FTCA	5:2 sFTOH	5:3 acid	3:3 acid	PFBA	PFPeA	PFHxA	PFHpA
Live treatment											
0	186.1 ± 15.3	N.D.	N.D.	N.D.	N.D.	0.082 ± 0.006	0.091 ± 0.013	0.240 ± 0.054	0.212 ± 0.015	0.984 ± 0.139	0.108 ± 0.017
7	182.8 ± 2.1	N.D.	N.D.	N.D.	N.D.	0.098 ± 0.008	0.082 ± 0.014	0.249 ± 0.032	0.176 ± 0.014	1.126 ± 0.091	0.126 ± 0.022
28	182.5 ± 3.7	N.D.	N.D.	N.D.	N.D.	0.076 ± 0.017	0.081 ± 0.023	0.200 ± 0.015	0.219 ± 0.026	1.008 ± 0.217	0.100 ± 0.009
56	208.6 ± 19.8	N.D.	N.D.	N.D.	N.D.	0.081 ± 0.007	0.071 ± 0.011	0.188 ± 0.027	0.227 ± 0.015	0.833 ± 0.090	0.112 ± 0.026
98	149.8 ± 7.7	0.006 ± 0.000	N.D.	N.D.	N.D.	0.077 ± 0.025	0.082 ± 0.029	0.232 ± 0.025	0.233 ± 0.011	0.868 ± 0.146	0.135 ± 0.018
154	121.3 ± 12.2	0.188 ± 0.000	0.857 ± 0.685	0.064 ± 0.000	6.804 ± 1.387	0.929 ± 0.428	0.099 ± 0.002	0.555 ± 0.114	0.768 ± 0.000	4.709 ± 0.323	0.325 ± 0.105
224	118.5 ± 11.2	N.D.	3.872 ± 1.907	0.522 ± 0.378	3.743 ± 0.095	4.365 ± 3.474	0.228 ± 0.015	0.605 ± 0.194	0.821 ± 0.016	3.891 ± 0.467	0.651 ± 0.304
Positive control											
0	8.252 ± 0.347	N.D.	N.D.	N.D.	N.D.	0.089 ± 0.014	0.094 ± 0.003	0.174 ± 0.018	0.220 ± 0.037	0.798 ± 0.024	0.087 ± 0.005
7	8.871 ± 0.274	N.D.	N.D.	N.D.	N.D.	0.090 ± 0.004	0.093 ± 0.010	0.217 ± 0.048	0.216 ± 0.004	1.032 ± 0.032	0.107 ± 0.004
28	8.058 ± 0.020	N.D.	N.D.	N.D.	N.D.	0.058 ± 0.006	0.067 ± 0.012	0.232 ± 0.008	0.211 ± 0.044	0.935 ± 0.041	0.138 ± 0.018
56	9.920 ± 1.111	N.D.	N.D.	N.D.	N.D.	0.074 ± 0.001	0.065 ± 0.012	0.194 ± 0.025	0.270 ± 0.001	0.776 ± 0.208	0.092 ± 0.029
98	7.026 ± 2.009	N.D.	N.D.	N.D.	N.D.	0.057 ± 0.009	0.062 ± 0.013	0.207 ± 0.039	0.244 ± 0.048	0.898 ± 0.015	0.167 ± 0.018
154	3.637 ± 3.581	N.D.	0.625 ± 0.574	N.D.	1.079 ± 0.504	0.081 ± 0.017	0.111 ± 0.089	0.437 ± 0.211	0.664 ± 0.000	3.338 ± 1.084	0.536 ± 0.070
224	1.815 ± 0.914	N.D.	0.331 ± 0.130	0.053 ± 0.006	2.225 ± 1.085	0.480 ± 0.131	0.261 ± 0.188	0.350 ± 0.004	0.797 ± 0.005	2.436 ± 0.227	0.578 ± 0.108
Abiotic control											
0	189.2 ± 8.3	N.D.	N.D.	N.D.	N.D.	0.056 ± 0.001	0.066 ± 0.023	0.243 ± 0.033	0.211 ± 0.033	0.805 ± 0.058	0.109 ± 0.023
7	156.5 ± 2.0	N.D.	N.D.	N.D.	N.D.	0.080 ± 0.024	0.073 ± 0.017	0.228 ± 0.003	0.235 ± 0.038	0.860 ± 0.117	0.121 ± 0.037
28	188.6 ± 2.3	N.D.	N.D.	N.D.	N.D.	0.081 ± 0.016	0.044 ± 0.001	0.199 ± 0.033	0.202 ± 0.007	0.731 ± 0.086	0.142 ± 0.025
56	173.3 ± 4.5	N.D.	N.D.	N.D.	N.D.	0.058 ± 0.015	0.091 ± 0.002	0.236 ± 0.028	0.213 ± 0.045	0.780 ± 0.025	0.127 ± 0.025
98	186.5 ± 13.6	N.D.	N.D.	N.D.	N.D.	0.077 ± 0.019	0.074 ± 0.010	0.224 ± 0.072	0.208 ± 0.029	0.570 ± 0.035	0.160 ± 0.001
154	183.5 ± 7.3	N.D.	N.D.	N.D.	N.D.	0.101 ± 0.072	0.059 ± 0.046	0.240 ± 0.013	0.653 ± 0.139	1.574 ± 0.686	0.392 ± 0.020
224	174.7 ± 3.6	N.D.	N.D.	N.D.	N.D.	0.063 ± 0.000	0.050 ± 0.020	0.277 ± 0.053	0.512 ± 0.058	1.609 ± 0.005	0.307 ± 0.031

Table A.27 Comparison of 6:2 FTS biotransformation in environmental matrices and pure cultures under aerobic conditions.

Environmental matrix/pure culture	Duration (days)	Biotransformation rate (half-life, if applicable)	Biotransformation products at the end of experiment (yield in mol%, if determined)	Reference
Activated sludge	90	63.7 mol% remaining at day 90	5:2 ketone & 5:2 sFTOH (3.4), 5:3 acid (0.1), PFBA (0.1), PFPeA (1.5), PFHxA (1.1)	[45]
River sediment	90	1.9 mol% remaining at day 90 (<5 days)	6:2 FTOH (<2.5), 6:2 FTCA (12), 5:2 sFTOH (<8), 5:2 ketone (<8), 5:3 acid (16), PFPeA(21), PFHxA(20), PFHpA (0.6)	[54]
Wetland slurry	142	91.1 mol% remaining at day 142	5:3 acid (2.7), PFPeA (6.1), PFHxA (2.1)	[222]
Landfill leachate and sediment	90	~50 mol% remaining at day 90 (86 days)	5:2 sFTOH (0.6), 5:3 acid (0.2), PFBA (0.6), PFPeA (5.6), PFHxA (3.1)	[186]
Landfill leachate and sediment	10	80-93 mol% remaining at day 10	Sum of PFBA, PFPeA and PFHxA (2)	[224]
Pseudomonas sp. strain D2	1	Not available	Not available	[175]
Gordonia sp. strain NB4-1Y	5	56 mol% remaining at day 5	6:2 FTCA, 6:2 FTUA, 5:3 acid, and 5:3 U acid	[180]
Gordonia sp. strain NB4-1Y	7	0.1 mol% remaining at day 7	6:2 FTOH (4.1), 6:2 FTCA (4.3), 6:2 FTUA (13.7), 5:2 sFTOH (9.0), 5:2 ketone (43.9), 5:3 acid (0.4), PFBA (<0.1), PFPeA(<0.1), PFHxA(0.6)	[179]
Rhodococcus jostii RHA1	6	<1 mol% remaining at day 6	6:2 FTCA, 6:2 FTUA, α-OH-5:3 acid, and PFHpA	[106]
Dietzia aurantiaca J3	7	0 mol% remaining at day 6	6:2 FTCA, 6:2 FTUA, 5:3 acid, PFPeA, PFHxA	[105]
Loring AFB soil	224	0.2 mol% remaining at day 224 (43.3 days)	6:2 FTUA (0.3), 5:2 sFTOH (12.8), 5:3 acid (0.2), PFBA (1.3), PFPeA (7.0), PFHxA (5.3), and PFHpA (0.2)	This study
Robins AFB soil	224	63.7 mol% remaining at day 224	6:2 FTUA (2.1), 6:2 FTCA (0.3), 5:2 sFTOH (2.0), 5:3 acid (2.3), PFBA (0.3), PFPeA (0.1), and PFHxA (0.8)	This study

Table A.28 Microbial richness and diversity in Loring and Robins soils.

Soil type	6:2 FTS (μg/L)	Sampling time	Mapped reads	OTUs	Chao1	Shannon	Simpson
Loring AFB soil	0	Day 0	10428	554	726.6 ± 80.2	5.64 ± 0.12	0.99 ± 0.00
	0	Day 0	6148	483			
	0	Day 224	14522	285	460.5 ± 44.6	4.38 ± 0.09	0.96 ± 0.00
	0	Day 224	16627	326			
	~1700	Day 224	18059	322	502.8 ± 36.8	4.58 ± 0.07	0.97 ± 0.00
	~1700	Day 224	14988	326			
Robins AFB soil	0	Day 7	3609	30	27.6 ± 2.5	2.00 ± 0.06	0.81 ± 0.01
	0	Day 7	1878	25			
	0	Day 224	3034	86	123.9 ± 12.1	3.64 ± 0.37	0.95 ± 0.02
	0	Day 224	6343	120			
	~1700	Day 224	15083	109	149.9 ± 17.2	3.61 ± 0.08	0.95 ± 0.00
	~1700	Day 224	14554	131			

Table A.29 Potential biotransformation products of 6:2 FTS identified by HRMS analysis

Chemical name	Formula	Mass (*m/z*)	Mass error [ppm]	Level of confidence[a]
1H-perfluoropentane	C_5HF_{11}	268.98271	-1.00	1
1H-perfluorobutane	C_4HF_9	218.98587	-1.39	1
1,2,2,3,3,4,4,4-octafluorobutan-1-ol	$C_4H_2F_8O$	216.98912	-6.39	2
Perfluoropentanal	C_5HF_9O	246.98080	-1.16	4
N/A[b]	$C_7H_2F_8$	236.99543	-0.71	3
N/A	$C_7H_3F_9$	257.00159	-0.93	4
N/A	N/A	292.98316	0.6	5

[a] The level of confidence of each identified biotransformation product was assigned using a scheme reported by Schymanski et al [89].

[b] Not applicable.

Table A.30 The full names and corresponding acronyms of classified PFAS identified in non-targeted LC-HRMS analysis.

	Class name	Class acronym	Per-F chain length	Compound acronym
AFFF components	N-trimethyl ammonio propyl perfluoroalkane sulfonamide	**TAmPr-FASA**	**n = 4**	TAmPr-FBSA
			n = 5	TAmPr-FPeSA
			n = 6	TAmPr-FHxSA
	N-dimethyl ammonio propyl perfluoroalkane sulfonamide	**AmPr-FASA**	**n = 4**	AmPr-FBSA
			n = 5	AmPr-FPeSA
			n = 6	AmPr-FHxSA
			n = 7	AmPr-FHpSA
			n = 8	AmPr-FOSA
	N-carboxy ethyl dimethyl ammonio propyl perfluoroalkane sulfonamido propanoic acid	**CEt-AmPr-FASA-PrA**	**n = 4**	CEt-AmPr-FBSA-PrA
	N-dimethyl ammonio propyl perfluoralkane sulfonamido propanoic acid or N-trimethyl ammonio propyl perfluoroalkane sulfonamide acetic acid	**AmPr-FASA-PrA** or **TAmPr-FASA-AA**	**n = 4**	AmPr-FBSA-PrA/ TAmPr-FBSA-AA
			n = 5	AmPr-FPeSA-PrA/ TAmPr-FPeSA-AA
			n = 6	AmPr-FHxSA-PrA/ TAmPr-FHxSA-AA
			n = 7	AmPr-FHpSA-PrA/ TAmPr-FHpSA-AA
			n = 8	AmPr-FOSA-PrA/ TAmPr-FOSA-AA
	n:2 fluorotelomer sulfonamido betaine/fluorotelomer sulfonamido propyl betaine	**n:2 FTAB/FTSA-PrB**	**n = 6**	6:2 FTAB/FTSA-PrB
	N-carboxy ethyl dimethyl ammonio propyl perfluoroalkane amide	**CEt-AmPr-FAAd**	**n = 7**	CEt-AmPr-FOAd
	N-dimethylammonio propyl perfluoroalkane amide	**AmPr-FAAd**	**n = 6**	AmPr-FHpAd
			n = 7	AmPr-FOAd
	Perfluoroalkane sulfonic acids	**PFSA**	**n = 2**	PFEtS
			n = 3	PFPrS
			n = 4	PFBS
			n = 5	PFPeS
			n = 6	PFHxS
			n = 7	PFHpS
			n = 8	PFOS
			n = 9	PFNS

			n = 10	PFDS
	Perfluoroalkyl carboxylic acid	**PFCA**	**n = 4**	PFPeA
			n = 5	PFHxA
			n = 6	PFHpA
			n = 7	PFOA
			n = 9	PFDA
Transformation products	Perfluoroalkane sulfonamide	**FASA**	**n = 3**	FPrSA
			n = 4	FBSA
			n = 5	FPeSA
			n = 6	FHxSA
			n = 8	FOSA
	N-methyl ammonio propyl perfluoroalkane sulfonamide	**M-AmPr-FASA**	**n = 6**	M-AmPr-FHxSA
	N-oxide dimethyl ammonio propyl perfluoroalkane sulfonamide	**OAmPr-FASA**	**n = 4**	OAmPr-FBSA
			n = 6	OAmPr-FHxSA
			n = 7	OAmPr-FHpSA
			n = 8	OAmPr-FOSA
	N-methyl perfluoroalkane sulfonamido acetic acid	**N-MeFASAA**	**n = 6**	N-MeFHxSAA
	N-ethyl perfluoroalkane sulfonamido acetic acid	**N-EtFASAA**	**n = 6**	N-EtFHxSAA
	N-oxide dimethyl ammonio propyl perfluoroalkane amide	**OAmPr-FAAd**	**n = 5**	OAmPr-FHxAd
			n = 6	OAmPr-FHpAd
			n = 7	OAmPr-FOAd

Table A.31 Identification of 16 classes of PFAS in non-targeted LC-HRMS analysis.

	Acronym	Per-F chain length	Positive mode				Negative mode			
			confidence level	deltamass (ppm)	m/z	RT (min)	confidence level	deltamass (ppm)	m/z	RT (min)
AFFF components	**TAmPr-FASA**	**n = 4**	2a	1.31	399.07885	5.316				
		n = 5	2a	1.56	449.07583	6.304				
		n = 6	3d	1.84	499.07286	7.244				
	AmPr-FASA	**n = 4**	2a	0.55	385.06289	5.302	5a	0.61	383.04836	5.755
		n = 5	2a	0.78	435.05982	6.264	3c	0.34	433.04508	6.777
		n = 6	1a	0.23	485.05640	7.208	3c	0.78	483.04211	7.394
		n = 7	3d	2.29	535.05432	7.613				
		n = 8	1a	2.36	585.05129	7.786				
	CEt-AmPr-FASA-PrA	**n = 4**	5a	2.23	529.10611	5.567				
	AmPr-FASA-PrA or **TAmPr-FASA-AA**	**n = 4**	3a	0.55	457.08406	5.517	5a	0.95	455.06969	5.755
		n = 5	3a	1.66	507.08145	6.475	3d	0.94	505.06654	6.776
		n = 6	4	0.23	557.07755	7.298	3c	0.47	555.06312	7.447
		n = 7	5a	1.99	607.07543	7.629				
		n = 8	2a	2.27	657.07252	7.809				
	n:2 FTAB	**n = 6**	5a	1.59	571.09398	7.335				
	CEt-AmPr-FAAd	**n = 7**	5a	1.42	571.10805	7.036				
	AmPr-FAAd	**n = 6**	3d	1.65	449.09004	6.130				
		n = 7	3d	1.63	499.08692	6.964				
	PFSA	**n = 2**					2c	0.08	198.94939	2.871
		n = 3					3a	-0.24	248.94613	4.632
		n = 4					1a	0.47	298.94313	6.230
		n = 5					1a	0.90	348.94011	7.549
		n = 6					1a	0.38	398.93676	8.182

		n = 7					1a	0.76	448.93375	8.866
		n = 8					1a	0.27	498.93035	9.531
		n = 9					1a	0.63	548.92737	9.796
		n = 10					1a	0.53	598.92415	10.126
	PFCA	**n = 4**					1a	0.17	262.97605	4.983
		n = 5					1a	0.95	312.97311	6.210
		n = 6					1a	0.75	362.96989	7.438
		n = 7					1a	0.80	412.96680	7.957
		n = 9					1a	0.03	512.96006	9.322
Transformation products	**FASA**	**n = 3**					3d	0.23	247.96223	5.854
		n = 4					2b	0.50	297.95913	7.371
		n = 5					2b	1.01	347.95613	7.950
		n = 6					1a	0.38	397.95274	8.418
		n = 8					1a	0.63	497.94652	9.517
	M-AmPr-FASA	**n = 6**	4	1.61	471.04140	7.118	4	0.65	469.02639	7.305
	OAmPr-FASA	**n = 4**	5a	1.31	401.05812	5.453				
		n = 6	3d	1.40	501.05191	7.321	3c	1.33	499.03732	7.469
		n = 7	3d	1.62	551.04890	7.631				
		n = 8	3d	2.39	601.04625	7.780				
	N-MeFASAA	**n = 6**					5b	0.70	469.97405	8.477
	N-EtFASAA	**n = 6**					3c	0.93	483.98982	9.278
	OAmPr-FAAd	**n = 5**	3d	1.76	415.08814	5.350				
		n = 6	3d	1.08	465.08472	6.372				
		n = 7	2a	1.58	515.08184	7.136				

Table A.32 The average log2-fold changes (LFCs) of classified PFAS in the associated peak areas between certain sampling points and the initial sampling point (day 0).

	Acronym	Per-F chain length	Live treatment				Abiotic control			
			ESI+		ESI-		ESI+		ESI-	
			LFC (day 308/day 0)	LFC (max/day0)	LFC (day 308/day 0)	LFC (max/day0)	LFC (day 308/day 0)	LFC (max/day0)	LFC (day 308/day 0)	LFC (max/day0)
AFFF components	TAmPr-FASA	n = 4	-7.78				0.07			
		n = 5	-1.33				0.07			
		n = 6	-0.54				-0.23			
	AmPr-FASA	n = 4	-2.97		-0.93		0.49		0.16	
		n = 5	-3.98		-2.05		-0.03		0.04	
		n = 6	-3.52		-1.95		-0.52		-0.17	
		n = 7	-3.58				-0.64			
		n = 8	-2.58				-1.17			
	CEt-AmPr-FASA-PrA	n = 4	-0.47				-0.48			
	AmPr-FASA-PrA or TAmPr-FASA-AA	n = 4	-0.93		-0.94		0.16		0.18	
		n = 5	-2.53		-1.11		-0.59		0.03	
		n = 6	-2.31		-1.93		-0.18		-0.19	
		n = 7	-1.93				-0.85			
		n = 8	-2.74				0.31			
	n:2 FTAB	n = 6	-0.35				0.27			
	CEt-AmPr-FAAd	n = 7	-0.69				-1.08			
	AmPr-FAAd	n = 6	-3.54				-2.51			
		n = 7	-3.36				-2.47			
	PFSA	n = 2			0.02				0.96	
		n = 3			1.15				-2.77	
		n = 4			0.63				0.56	

		n = 5			1.00				0.13	
		n = 6			0.77				0.22	
		n = 7			0.09				0.37	
		n = 8			-0.04				-0.07	
		n = 9			0.29				-1.25	
		n = 10			-0.48				-1.11	
	PFCA	n = 4			0.62				-0.06	
		n = 5			0.69				-0.08	
		n = 6			0.57				-0.43	
		n = 7			-0.17				-0.21	
		n = 9			-0.19				-0.52	
Transformation products	FASA	n = 3			8.28				0.03	
		n = 4			8.74				1.76	
		n = 5			8.51				2.29	
		n = 6			7.32				2.06	
		n = 8			2.56				0.49	
	M-AmPr-FASA	n = 6	5.31	6.24	3.84	4.86	3.35		3.85	
	OAmPr-FASA	n = 4	3.33	5.07			2.39			
		n = 6	1.01	4.30	-0.55	2.80	4.87		4.41	
		n = 7	-0.70	1.35			5.47			
		n = 8	0.15	2.39			4.73	5.66		
	N-MeFASAA	n = 6			2.74	3.90			1.29	
	N-EtFASAA	n = 6			7.42				-0.30	
	OAmPr-FAAd	n = 5	2.65	4.88			4.85			
		n = 6	1.79	4.77			5.17			
		n = 7	0.46	3.66			5.59			

Color scale	-8.00	-4.50	-1.00	-0.50	0.00	0.50	1.00	5.00	9.00
Fold change	0.004X	0.044X	0.500X	0.707X	No change	1.414X	2X	32X	512X

Table A.33 Topological properties of the microbial co-occurrence networks in soils under different redox conditions (the control and constructed networks) and random networks with the same size as the constructed network.

	The control network	The constructed network	Randam network[a]
No. of nodes	262	269	269
No. of edges	1,638	1,627	1,627
Average degree	12.504	12.097	12.097
Network diameter	11	10	4.015
Average path length	4.007	3.474	2.517
Graph density	0.048	0.045	0.045
Modularity	0.807	0.766	0.238
Average clustering coefficient	0.792	0.826	0.045

[a] Topological properties of random network are calculated as the average value from 10,000 random networks, whose size is identical to the constructed network (same number of nodes and edges) based on Erdős-Rényi model.

Table A.34 Correlation coefficients (Cramer's *V* value) and significances (Chi-square *P*-value) between module and environmental factors.

	Cramer's *V*	Chi-square *P*
Module-Contaminant	0.8382	< 0.001
Module-Soil	0.8272	< 0.001
Module-Redox condition	0.6000	< 0.001

Table A.35 Count of genes with significant changes in abundance between treatment (microcosms exposed to fluorotelomer) and control (microcosms without fluorotelomer addition) in each set of microcosm experiment according to PICRUSt2 results.

Contaminant	FTOH					FTS	
Soil	Loring				Robins	Loring	Robins
Redox condition	Aerobic	Nitrate-reducing	Sulfate-reducing	Iron-reducing	Aerobic	Aerobic	Aerobic
Up[a]	55	1266	265	70	300	36	0
Down[b]	190	973	115	64	234	4	1

[a] genes with significantly higher abundance (log2-fold change > 2 and FDR-adjusted *P*-value 0.05).
[b] genes with significantly lower abundance (log2-fold change < -2 and FDR-adjusted *P*-value 0.05).

Table A.36 Potential functional genes encoding dehydrogenases and reductases identified in this study.

KO#	KO Description	Function	Reference
K07538	had; [EC:1.1.1.368] 6-hydroxycyclohex-1-ene-1-carbonyl-CoA dehydrogenase	Oxidizes the secondary alcohol to ketone in pathways of anaerobic degradation of benzoate and its derivatives	[298, 299]
K07535	badH; [EC:1.1.1.-] 2-hydroxycyclohexanecarboxyl-CoA dehydrogenase	Involved in benzoate degradation	[373]
K15514	boxD; [EC:1.2.1.77] 3,4-dehydroadipyl-CoA semialdehyde dehydrogenase	Involved in aerobic benzoyl-CoA catabolic pathway	[374]
K04109	hcrB, hbaD; [EC:1.1.7.1] 4-hydroxybenzoyl-CoA reductase subunit beta	Acts as phenolic ring dehydroxylating enzyme; plays a role in anaerobic degradation of aromatic compounds	[375, 376]
K16173	acd; [EC:1.3.99.32] glutaryl-CoA dehydrogenase (non-decarboxylating)	Acts as a key enzyme during catabolism of 3,3′-dithiodipropionic acid; involved in aerobic and anaerobic benzene degradation pathways	[377, 378]
K04117	aliB; [EC:1.3.99.-] cyclohexanecarboxyl-CoA dehydrogenase	Conversed cyclohexanecarboxyl-CoA to cyclohexenecarbonyl-CoA	[379]
K00217	[EC:1.3.1.32] maleylacetate reductase	Involved in dechlorination of chloroaromatics	[260, 300, 301]
K05797	pchF; [EC:1.17.9.1] 4-cresol dehydrogenase (hydroxylating) flavoprotein subunit	Involved in the catabolism of 2,4-xylenol and p-cresol	[380]

Table A.37 Potential functional genes encoding oxygenases identified in this study.

KO#	KO Description	Function	Reference
K04099	desB, galA; gallate dioxygenase [EC:1.13.11.57]	Involved gallate degradation	[381]
K04100	ligA; protocatechuate 4,5-dioxygenase, alpha chain [EC:1.13.11.8]	Involved gallate degradation and breaks aromatic rings	[381, 382]
K04101	ligB; protocatechuate 4,5-dioxygenase, beta chain [EC:1.13.11.8]	Involved gallate degradation and breaks aromatic rings	[381, 382]
K04098	chqB; hydroxyquinol 1,2-dioxygenase [EC:1.13.11.37]	Removes chlorines from chloroaromatics and cleavage of chlorinated rings	[305, 306]
K18243	nagH; salicylate 5-hydroxylase small subunit [EC:1.14.13.172]	Involved in degradation of PAHs	[383, 384]
K18242	nagG; salicylate 5-hydroxylase large subunit [EC:1.14.13.172]	Involved in degradation of PAHs	[383, 384]

Table A.38 Potential functional genes encoding other enzymes except oxidoreductases identified in this study.

KO#	KO Description	Function	Reference
K07544	bbsF; benzylsuccinate CoA-transferase BbsF subunit [EC:2.8.3.15]	Involved in toluene catabolic pathway	[385]
K10221	ligI; 2-pyrone-4,6-dicarboxylate lactonase [EC:3.1.1.57]	catalyzes the hydrolysis of lignin and lignin-derived aromatic compounds	[386, 387]
K07536	badI; 2-ketocyclohexanecarboxyl-CoA hydrolase [EC:3.1.2.-]	Involved in ring cleavage for anaerobic degradation of benzoate	[373, 388, 389]
K03382	atzB; hydroxydechloroatrazine ethylaminohydrolase [EC:3.5.4.43]	Acts on carbon-nitrogen bonds in a chlorinated triazine systemic herbicide	[308]
K07539	oah; 6-oxocyclohex-1-ene-carbonyl-CoA hydrolase [EC:3.7.1.21]	Responsible for anaerobically degrading benzoate and other monocyclic aromatic compounds, and defluorinating fluorinated aromatics	[307, 390]
K01617	dmpH, xylI, nahK; 2-oxo-3-hexenedioate decarboxylase [EC:4.1.1.77]	Involved in phenol degradation	[391]
K10220	ligJ; 4-oxalmesaconate hydratase [EC:4.2.1.83]	Involved in protocatechuate 4,5-cleavage pathway as well as vanillate and syringate degradation	[392]
K07537	dch; cyclohexa-1,5-dienecarbonyl-CoA hydratase [EC:4.2.1.100]	Involved in aromatics degradation	[393]
K16515	galB; 4-oxalomesaconate hydratase [EC:4.2.1.83]	Involved gallate degradation	[394]
K01865	hab; (hydroxyamino)benzene mutase [EC:5.4.4.1]	Involved in aromatic ring fission	[395]
K04116	aliA; cyclohexanecarboxylate-CoA ligase [EC:6.2.1.-]	Involved in degradation of benzoate and derivatives of alicyclic acid	[373, 389, 396]
K04105	hbaA; 4-hydroxybenzoate-CoA ligase [EC:6.2.1.27 6.2.1.25]	Involved in aromatics degradation	[397, 398]

Table A.39 Functional genes encoding enzymes involved in microbial defluorination and fluorotelomer transformation in prior studies.

KO#	KO Description	Reference
K01561	dehH; haloacetate dehalogenase [EC:3.8.1.3]	[309]
K01563	dhaA; haloalkane dehalogenase [EC:3.8.1.5]	[310-312]
K06199	crcB, FEX; fluoride exporter	[107, 399]
K00299	ssuE; FMN reductase [EC:1.5.1.38]	[105]
K04091	ssuD; alkanesulfonate monooxygenase [EC:1.14.14.5]	
K15553	ssuA; sulfonate transport system substrate-binding protein	
K15554	ssuC; sulfonate transport system permease protein	
K15555	ssuB; sulfonate transport system ATP-binding protein [EC:7.6.2.14]	
K01560	haloacid dehalogenase [EC:3.8.1.2]	[106]
K00496	alkB1_2, alkM; alkane 1-monooxygenase [EC:1.14.15.3]	
K16389	amphN, nysN, fscP, pimG; cytochrome P450 monooxygenase	

Table A.40 Packed dry porous media mass, total porosity, and pore volume (PV) for experimental columns.

Column	Porous media	Mass of packed porous media (dry weight, gram)	Total porosity (n)	PV (mL)
Abiotic 1	Loring soil and Federal Fine sand (1:1 w/w)	140.6	0.35	28.8
Abiotic 2		139.6	0.35	28.7
Biotic 1		138.7	0.35	28.6
Biotic 2		139.5	0.36	29.3

Table A.41 Oxidation-reduction potential (ORP) of biotic column samples collected at different time points.

Column samples	ORP (mV)*
Collected during Phase I (25.5-27.5 PVs)	
Influent	476.7 ± 3.7
Port 1	450.6 ± 53.4
Port 2	562.1 ± 39.7
Port 3	469.9 ± 7.5
Effluent	498.6 ± 9.0
Collected during Phase II (40.6-42.0 PVs)	
Influent	539.5 ± 0.6
Port 1	586.8 ± 21.3
Port 2	532.8 ± 14.2
Port 3	542.2 ± 19.8
Collected after Phase II-B (47.4-48.4 PVs)	
Port 3	569.5 ± 22.7

*Values are reported as E_h (mV), relative to standard hydrogen electrode (SHE).

Table A.42 The average molar yields of 6:2 FTS and its biotransformation products (unit: mol%) in different phases.

Phases	I-B (11.5-17.5 PVs)	I-C (17.5-33.1 PVs)	II-A (33.1-47.4 PVs)	II-B (47.4-54.1 PVs)	II-C (54.1-58.8 PVs)
6:2 FTS	41.5 ± 12.6*	70.8 ± 11.9	55.4 ± 15.0	45.1 ± 17.3	52.3 ± 5.8
6:2 FTCA	5.4 ± 3.4	5.2 ± 3.8	3.7 ± 2.6	6.6 ± 4.0	4.7 ± 3.4
6:2 FTUA	3.4 ± 1.9	5.1 ± 2.5	4.2 ± 2.6	6.0 ± 4.1	2.9 ± 2.6
5:2 sFTOH	2.4 ± 2.1	3.8 ± 3.2	1.4 ± 1.4	1.7 ± 1.6	2.9 ± 2.2
5:3 acid	1.8 ± 1.4	2.0 ± 1.9	4.7 ± 2.7	10.4 ± 3.4	7.3 ± 2.4
PFBA	0.1 ± 0.1	0.0 ± 0.1	0.1 ± 0.2	0.7 ± 0.3	0.7 ± 0.2
PFPeA	0.0 ± 0.0	0.1 ± 0.1	0.1 ± 0.1	0.3 ± 0.1	0.1 ± 0.0
PFHxA	0.3 ± 0.2	0.2 ± 0.2	0.7 ± 0.4	1.4 ± 0.4	0.6 ± 0.1
PFHpA	0.1 ± 0.1	0.0 ± 0.1	0.1 ± 0.1	0.1 ± 0.0	0.0 ± 0.0
Transformation products	13.5 ± 9.3	16.4 ± 11.7	15.1 ± 10.0	27.2 ± 13.8	19.1 ± 10.9
Total mass recovery	55.0 ± 21.9	87.1 ± 23.7	70.6 ± 24.9	72.3 ± 31.1	71.4 ± 16.7

* The average molar percent of one compound represents the average value of its molar yields measured in all sampling points during the corresponding phase.

Table A.43 Potential biotransformation products of 6:2 FTS identified by LC-HRMS analysis in the present column experiments and prior microcosms (Yan et al., 2022).

Chemical name	Formula	Mass (*m/z*)	Mass error [ppm]	Level of confidence[a]
N/A[b]	C_7HF_{11}[c]	292.98325[e]	0.89	3
1H-perfluoropentane	C_5HF_{11}[d]	268.98271	-1.00	1
1H-perfluorobutane	C_4HF_9[d]	218.98587	-1.39	1
1,2,2,3,3,4,4,4-octafluorobutan-1-ol	$C_4H_2F_8O$[d]	216.98912	-6.39	2
Perfluoropentanal	C_5HF_9O[d]	246.98080	-1.16	4
N/A	$C_7H_2F_8$[d]	236.99543	-0.71	3
N/A	$C_7H_3F_9$[d]	257.00159	-0.93	4
N/A	C_7HF_{11}[d]	292.98316[e]	0.6	5

[a] The level of confidence of each identified biotransformation product was assigned using a scheme reported by Schymanski et al.[7]

[b] Not applicable.

[c] Potential biotransformation product of 6:2 FTS identified in the present column experiments.

[d] Potential biotransformation products of 6:2 FTS identified in prior microcosms (Yan et al., 2022).

[e] The *m/z* are likely same, and the slight difference was because the LC-HRMS analysis on microcosm and column samples were conducted separately.

Table A.44 The average molar yields of 6:2 FTS and its biotransformation products (unit: mol%) at different time points in prior microcosm study (Yan et al., 2022).

	Day 7	Day 28	Day 56	Day 98	Day 154	Day 224
6:2 FTS	92.4 ± 5.2	64.4 ± 8.9	39.2 ± 2.1	29.9 ± 7.6	0.2 ± 0.0	0.3 ± 0.0
6:2 FTCA	N.D.	N.D.	0.4 ± 0.0	0.0 ± 0.0	N.D.	N.D.
6:2 FTUA	N.D.	3.7 ± 0.5	2.4 ± 0.9	0.8 ± 0.5	2.1 ± 0.1	0.3 ± 0.1
5:2 sFTOH	0.0 ± 0.0	5.3 ± 0.4	10.2 ± 1.1	9.8 ± 1.3	11.5 ± 1.2	13.3 ± 5.1
5:3 acid	0.0 ± 0.0	1.1 ± 0.2	1.5 ± 0.6	4.6 ± 0.6	8.9 ± 1.2	0.2 ± 0.1
PFBA	N.D.	N.D.	N.D.	N.D.	0.2 ± 0.0	1.3 ± 0.5
PFPeA	0.0 ± 0.0	0.0 ± 0.0	0.3 ± 0.0	0.4 ± 0.1	1.2 ± 0.3	7.0 ± 2.7
PFHxA	N.D.	0.8 ± 0.2	1.8 ± 0.0	1.6 ± 0.3	1.6 ± 0.3	5.3 ± 0.7
PFHpA	N.D.	N.D.	N.D.	0.0 ± 0.0	0.0 ± 0.0	0.2 ± 0.1
Transformation products	0.1 ± 0.0	10.9 ± 1.3	16.5 ± 2.7	17.2 ± 2.7	25.5 ± 3.1	27.6 ± 9.3
Total mass recovery	92.5 ± 5.4	75.3 ± 10.2	55.8 ± 4.8	47.1 ± 10.3	25.7 ± 3.2	27.9 ± 9.4

Table A.45 Richness and diversity of the free-living (FL) and porous media-attached (PMA) microbial communities in the biotic columns.

Microbial communities	Experimental stage	Sampling location	OTUs	Shannon	Chao1
Free-living (FL)	Phase I	Port 1	66 ± 4	2.331 ± 0.341	76.13 ± 5.13
		Port 2	63 ± 9	2.127 ± 0.601	75.97 ± 11.08
		Port 3	77 ± 2	2.340 ± 0.157	159.38 ± 6.38
	Phase II	Port 1	66 ± 3	2.595 ± 0.141	90.16 ± 4.02
		Port 2	67 ± 4	2.573 ± 0.076	75.54 ± 3.17
		Port 3	81 ± 1	2.544 ± 0.042	107.36 ± 2.68
Porous-media attached (PMA)	Termination	S1	275 ± 14	4.543 ± 0.356	355.84 ± 22.52
		S2	254 ± 11	4.932 ± 0.062	263.31 ± 19.8
		S3	263 ± 12	4.674 ± 0.092	296.6 ± 26.37
		S4	287 ± 1	4.335 ± 0.044	384.19 ± 35.22
		S5	279 ± 5	4.691 ± 0.002	319.94 ± 3.82

Table A.46 Regression parameters to obtain Freundlich coefficients (K_f and n) from soil properties according to equations (A-6) and (A-7).

	PFOA	PFOS		SDS	
i	b_i	a_i	b_i	a_i	b_i
0	1.7335	0.0807	0.0730	2.1725	0.2416
1	-0.4344	0.0315	0.3702	-0.6440	-0.3767
2	-0.0183	-0.0022	-0.0021	-0.0712	0.0135
3	-0.1175	-0.0088	0.0866	-0.2857	0.0704
4	0.0108	0.0006	-0.0140	0.0379	0.0046
5	0.0775	-0.0038	-0.0518	0.0920	0.0835
6	0.0026	0.0003	0.0005	0.0097	-0.0026
7	-0.0019	-0.0001	0.0020	-0.0052	-0.0011
8	1.7335	0.0807	0.0730	2.1725	0.2416

Table A.47 Description of spills for field-scale simulations.

Types of Spills	Site	Description
Fire training sessions	Wright-Patterson (Area 21)	FTA 5 was put in service in 1981. The current FTA was constructed adjacent to FTA 5 in 1996. Fire training activities are conducted at the current FTA (and previously FTA 5) from two to four times per year, using approximately 100 gallons of AFFF concentrate during each training event.
	Wright-Patterson (Area 22)	Fire fighter training was conducted at the two FTAs between 1960 and 1980. The estimated volume of AFFF used at former FTA 3 and FTA 4 sites would have been approximately 100 gallons of concentrate during two to four exercises per year. Given this assumption (200 to 400 gallons of AFFF released per year), it is possible that from 2,000 to 4,000 gallons of AFFF concentrate may have been released in this area over the 10- year period from 1970 to 1980.
	Wright-Patterson (Area 24)	The building was used for several years in the late 1980s to conduct training 2 to 3 times per year. An estimated 25 gallons of AFFF concentrate was used during each training event, for an estimated 50 to 75 gallons released per year.
	Altus (Area 1)	From 1960 to 1976, fire training sessions at FT3 were performed on a weekly basis with each training session including two to five fires. After 1976, training sessions were conducted with a typical frequency of eight fires per calendar quarter. Extinguishing agents included water, protein foam, chlorobromomethane, 1 AFFF, and possibly carbon tetrachloride in the early years of operation. The total amount of AFFF released at this location is unknown. However, based on the use of AFFF by the Air Force beginning in 1970, the potential exists for AFFF having been used to extinguish fires at Former FT3 during the operational period from 1970 through 1982.
Fire station	Wright-Patterson (Area 8)	There was one documented discharge of AFFF at this location. On January 24, 1997, a problem with an overfill vent pipe caused an over pressurization of the AFFF concentrate storage tank, resulting in the release of approximately 120 gallons of AFFF concentrate to the nearby pavement, parking area, and storm drains.
	Edwards (Fire station 3)	After nozzle spray tests, training exercises, and responses, the fire engines are washed outside east of the building. AFFF residue on the trucks is washed off and runs into the nearby dirt areas. Additionally, on January 30, 2010, an approximately 500-gallon release of AFFF occurred when a pipe burst inside a P-23 crash truck parked outside the building, and the contents spilled onto the unpaved ground adjacent to Building 250.
	Ellsworth (Area 4)	The Ellsworth spills database documented a 5-gallon spill (contained on concrete) when a line broke in November 1994.

Continuation of **Table A.47** Description of spills for field-scale simulations.

Types of Spill	Site	Description
Vehicle crash	Ellsworth (Area 7)	A vehicle crash in 2000 involving a fire truck and an AFFF trailer occurred on Taxiway West. The crash resulted in the release of 1000 gallons of AFFF. According to South Dakota Department of Environment and Natural Resources (SD DENR) spill records, approximately 900 gallons were recovered and 100 gallons infiltrated soil in adjacent grassed areas.
	Ellsworth (Area 9)	In 2001, 10 gallons of AFFF were spilled from a Base fire department crash truck designated as "Crash 4." The spill occurred near former Building 7140.
	Tyndall (Area 3)	The Tyndall AFB Fire Department responded to a 2001 QF-4 drone aircraft. Approximately 50 gallons of AFFF concentrate were reportedly used to extinguish the aircraft fire and the site of the crash is littered with aircraft debris fragments.
	Tyndall (Area 7)	On September 20, 2006, an unmanned BQM-167A drone aircraft crashed in the subscale drone launch buffer zone. The Tyndall AFB Fire Department extinguished the fuselage of the drone and several spot fires, then maintained a foam blanket until all components of the crashed drone were within acceptable temperature limits using approximately 50 gallons of AFFF concentrate.
	Tyndall (Area 8)	On November 15, 2012, a manned F-22 Raptor aircraft was on approach to Runway 32 and crashed at the end of the drone runway, initiating an emergency fire response. The Tyndall AFB Fire Department responded to the crash site and extinguished the fire on the fuselage of the F-22 and several spot fires in the area. A foam blanket was maintained in the area with repeated applications of AFFF and a total of approximately 700 gallons of AFFF were used during the emergency response and cool-down of aircraft components.
	Lackland (Area 10)	The plane crashed around 1981 and dispatch sent out a fire truck containing 2,000 gallons of AFFF/water mix (of which 25 gallons was AFFF concentrate). The entire quantity was used to extinguish the fire at the crash area.
	Lackland (Area 11)	The plane caught fire in 2012 and dispatch sent out a P23 fire truck containing 1,500 gallons of AFFF/water mix. Approximately 50 gallons of the AFFF/water mixture was used to extinguish the fire.

Continuation of **Table A.47** Description of spills for field-scale simulations.

Types of Spill	Site	Description
Vehicle crash	Lackland (Area 12)	A tar truck caught fire during runway repair activities. The tar truck attempted to drive to FS2 and was able to make it 100 yards east of the station. According to the Deputy Fire Chief, the tar truck fire occurred in the 1980s. FS2 dispatched a P23 fire truck to the area and extinguished the fire using approximately 50 gallons of AFFF in a 1,500 gallon foam/water mixture.
	Travis (Area 7)	The aircraft caught fire upon landing, igniting a small grass fire on the side of the runway. Less than 100 gallons of AFFF were reportedly used to extinguish the aircraft fire.
	Travis (Area 8)	On 15 October 1986, a C-141B aircraft made an emergency night landing. While the plane was being marshalled into a parking area, the aircraft made a hard right turn and the left wing struck a light pole, rupturing the aircraft's main fuel tank. Fuel ran down the light pole and into a high-voltage junction box at the base of the pole, igniting a fire that spread back up the pole and onto the aircraft's wing. Approximately 500 to 1,000 gallons of AFFF were used to extinguish the fire.
	Travis (Area 10)	In the late 1980s, a C-141B aircraft crash-landed due to a problem with the nose gear. Approximately 60 gallons of AFFF may have been used to extinguish the small fire that reportedly developed under the nose of the aircraft.
	Travis (Area 11)	In 2001, a small aircraft crashed southwest of the intersection of the connector from Perimeter Road/Collins Drive and Runway 03R-21L. The aircraft caught fire when it landed. Approximately 5 gallons of AFFF were used to extinguish the fire.
	Travis (Area 12)	On 4 May 2014, a Boeing E75 Stearman biplane was performing an aerial demonstration at the Travis Air Show. The aircraft was inverted when it contacted the runway, slid, and came to a stop near the northeastern terminus of Runway 03L-21R and Taxiway H. The aircraft caught fire shortly after the crash; however, fewer than 5 gallons of AFFF were needed to extinguish the fire.

Source: [362, 363, 365, 400-403].

Table A.48 Soil properties for Wright-Patterson Scenario 1 (AFFF Area 8).

					Soil Parameters					Particle Size Distribution		
Horizon	**Depth (cm)**	**USDA texture**	**Classification**	**Ksat (cm/d)**	**Bulk density (g/cm3)**	**Porosity (%)**	**Organic matter (%)**	**TOC (%)**	**pH**	**Sand (%)**	**Silt (%)**	**Clay (%)**
H1	0-28	Loam	CL, ML	14	1.4	47	3.5	2.03	6	42	38	20
H2	28-84	Clay loam, clay, gravelly	CL	8	1.48	44	1.25	0.73	6.2	40	30	30
H3	84-152	Very gravelly loamy sand	GP, SP, GM, SM	112	1.53	42	0.5	0.29	7.5	80	15	5
H4	152-400	Gravelly silty sand	SM	114	1.53	42	3.5	0.29	7.5	80	15	5

Note:
Sand: 0.05 to 2 mm
Silt: 0.002 to 0.05 mm
Clay: less than 0.002 mm

Table A.49 Soil properties for Wright-Patterson Scenario 2 (AFFF Area 22).

				Soil Parameters						Particle Distribution		
Horizon	**Depth (cm)**	**USDA texture**	**Classification**	**K_{sat} (cm/d)**	**Bulk density (g/cm^3)**	**Porosity (%)**	**Organic matter (%)**	**TOC (%)**	**pH**	**Sand (%)**	**Silt (%)**	**Clay (%)**
H1	0-60	Silty clay loam	CL	11	1.38	48	4.5	2.61	7	18	52	30
H2	60-114	Silty clay loam, clay loam, loam, silt loam	CL	10	1.4	47	0.8	0.46	7	19	52	29
H3	114-152	Stratified loam to silt loam to sandy loam to clay loam	CL, ML, SM	18	1.35	49	0.3	0.17	7	35	45	20
H4	152-274	Silty Clay	CL	23	1.35	49		0.5	7	22.1	59.8	18.1
H5	274-400		GP	1261	1.53			0.3	7.6	98.6	0.9	0.5

Note:
Sand: 0.05 to 2 mm
Silt: 0.002 to 0.05 mm
Clay: less than 0.002 mm

Table A.50 Soil properties for Tyndall Scenario (Map Unit 13)

				Soil Parameters						Particle Distribution		
Horizon	**Depth (cm)**	**USDA texture**	**Classification**	**Ksat (cm/d)**	**Bulk density (g/cm3)**	**Porosity (%)**	**Organic matter (%)**	**TOC (%)**	**pH**	**Sand (%)**	**Silt (%)**	**Clay (%)**
A	0-14	Sand	SP, SP-SM	768	1.38	48	2.3	1.33	5	94	3	3
E	14-47	Sand	SP, SP-SM	1064	1.50	43	0.3	0.17	5	98	2	1
Bh	47-66	Sand	SP, SP-SM	563	1.45	45	3	1.74	5	92	5	3
E’	66-150	Sand	SP, SP-SM	815	1.58	40	0.3	0.17	5	96	3	1

Note:
Sand: 0.05 to 2 mm
Silt: 0.002 to 0.05 mm
Clay: less than 0.002 mm
Total fragments: fragments of rock and other materials larger than 2

Table A.51 Soil properties for Ellsworth Scenario (Nunn clay loam, NcA).

				Soil Parameters						Particle Distribution		
Horizon	**Depth (cm)**	**USDA texture**	**Classification**	**K_{sat} (cm/d)**	**Bulk density (g/cm^3)**	**Porosity (%)**	**Organic matter (%)**	**TOC (%)**	**pH**	**Sand (%)**	**Silt (%)**	**Clay (%)**
A	0-18	Loam	CL, OH	11	1.4	42	3.0	1.74	8.1	35	40	25
Bt	18-58	Clay loam	CL	20	1.30	49	1.0	0.58	8.1	26	31	43
Ck	58-214	Clay loam	CL	14	1.33	46	0.5	0.29	8.2	30	37	33
	214-500	Gravelly sand	GW	53	1.5	38			8.3	69.4	21.6	9

Note:
Sand: 0.05 to 2 mm
Silt: 0.002 to 0.05 mm
Clay: less than 0.002 mm
Total fragments: fragments of rock and other materials larger than 2 mm

Table A.52 Soil properties for Ellsworth Scenario (LY210109 within area OU1).

				Soil Parameters						Particle Distribution		
Horizon	**Depth (cm)**	**USDA texture**	**Classification**	**K_{sat} (cm/d)**	**Bulk density (g/cm^3)**	**Porosity (%)**	**Organic matter (%)**	**TOC (%)**	**pH**	**Sand (%)**	**Silt (%)**	**Clay (%)**
A	0-213	Clay Loam	CL	8.54	1.5	43.4	-	1.35	8.1	78.9	13.9	7
Bt	213-500	Gravelly Sand	GW	1208	1.5	43.4	-	0.88	8.0	69.4	21.6	9

Table A.53 Estimated sorption parameters for Wright-Patterson Scenario 1.

Soil Horizon		$K_f \left[\frac{mg}{mg_{soil}}\left(\frac{cm^3}{mg}\right)^n\right]$			n		
Start (cm)	End (cm)	PFOA	PFOS	MASS	PFOA	PFOS	MASS
0	28	2.80E-04	1.10E-04	3.65E-03	0.94	0.59	0.68
28	84	3.49E-04	1.49E-04	1.17E-03	0.95	0.64	0.65
84	152	3.57E-04	4.71E-04	1.61E-03	0.9	0.75	0.74
152	400	3.60E-04	4.79E-04	1.53E-03	0.9	0.75	0.73

Table A.54 Estimated sorption parameters for Wright-Patterson Scenario 2.

Soil Horizon		$K_f \left[\frac{mg}{mg_{soil}}\left(\frac{cm^3}{mg}\right)^n\right]$			n		
Start (cm)	End (cm)	PFOA	PFOS	MASS	PFOA	PFOS	MASS
0	60	2.22E-04	5.61E-04	9.56E-04	0.85	0.77	0.61
60	114	3.76E-04	4.70E-04	4.32E-05	0.9	0.76	0.51
114	152	4.24E-04	4.24E-04	5.73E-05	0.91	0.74	0.53
152	274	3.38E-04	5.01E-04	1.23E-05	0.88	0.77	0.46
274	400	1.90E-04	3.32E-04	2.38E-03	0.89	0.73	0.85

Table A.55 Estimated sorption parameters for Tyndall.

Soil Horizon		$K_f \left[\frac{mg}{mg_{soil}}\left(\frac{cm^3}{mg}\right)^n\right]$			n		
Start (cm)	End (cm)	PFOA	PFOS	MASS	PFOA	PFOS	MASS
0	14	7.99E-04	3.53E-04	3.59E-03	1	0.64	0.65
14	47	2.99E-04	5.24E-05	2.72E-03	1	0.52	0.6
47	66	1.05E-03	5.58E-04	3.74E-03	1	0.67	0.66
66	150	3.05E-04	5.13E-05	2.65E-03	1	0.52	0.6

Table A.56 Estimated sorption parameters for Ellsworth (Nunn clay loam, NcA).

Soil Horizon		$K_f \left[\frac{mg}{mg_{soil}}\left(\frac{cm^3}{mg}\right)^n\right]$			n		
Start (cm)	End (cm)	PFOA	PFOS	MASS	PFOA	PFOS	MASS
0	18	3.86E-04	1.73E-03	8.62E-04	0.91	0.92	0.73
18	58	6.52E-04	1.57E-03	7.68E-04	0.9	0.85	0.67
58	214	9.24E-04	2.53E-03	3.21E-04	0.89	0.87	0.57
214	500	4.05E-04	9.46E-04	8.71E-04	0.92	0.83	0.84

Table A.57 Estimated sorption parameters for Ellsworth (LY210109 within area OU1).

Soil Horizon		$K_f \left[\frac{mg}{mg_{soil}}\left(\frac{cm^3}{mg}\right)^n\right]$			n		
Start (cm)	End (cm)	PFOA	PFOS	MASS	PFOA	PFOS	MASS
0	213	4.16E-04	4.38E-04	2.77E-02	1.00	0.78	1.00
213	500	4.42E-04	8.07E-04	3.13E-03	0.93	0.81	0.82

A.20 Supplementary figures

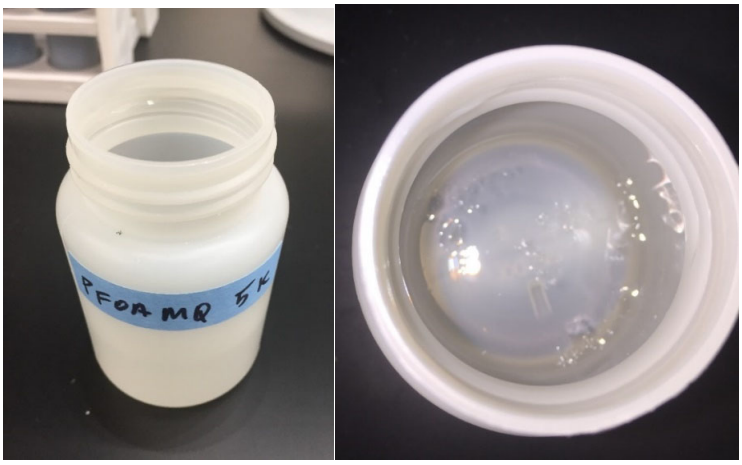


Figure A.1 Separate phase formation in a solution of 5,000 mg/L PFOA in ultrapure water.

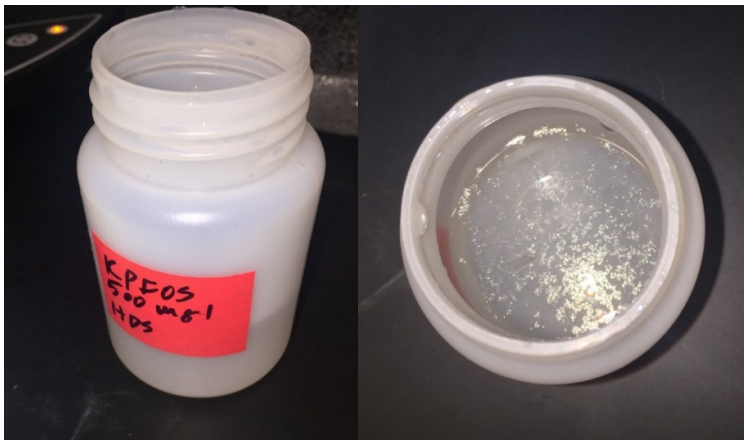


Figure A.2 Separate phase formation in a solution of 500 mg/L KPFOS in 1,741 mg/L Total Dissolved Solids.

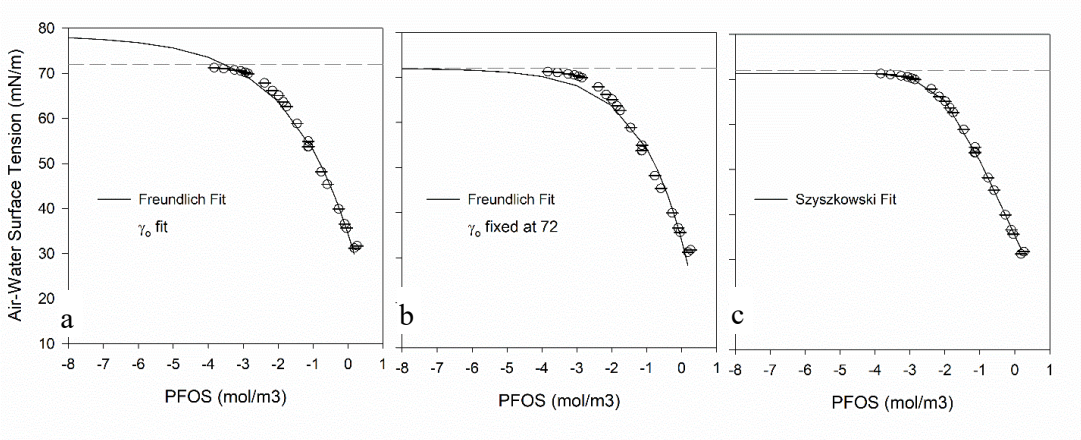


Figure A.3 Comparison between Freundlich and Szyszkowski fits of air-water surface tension curves for PFOS in 42 mM TDS solution.

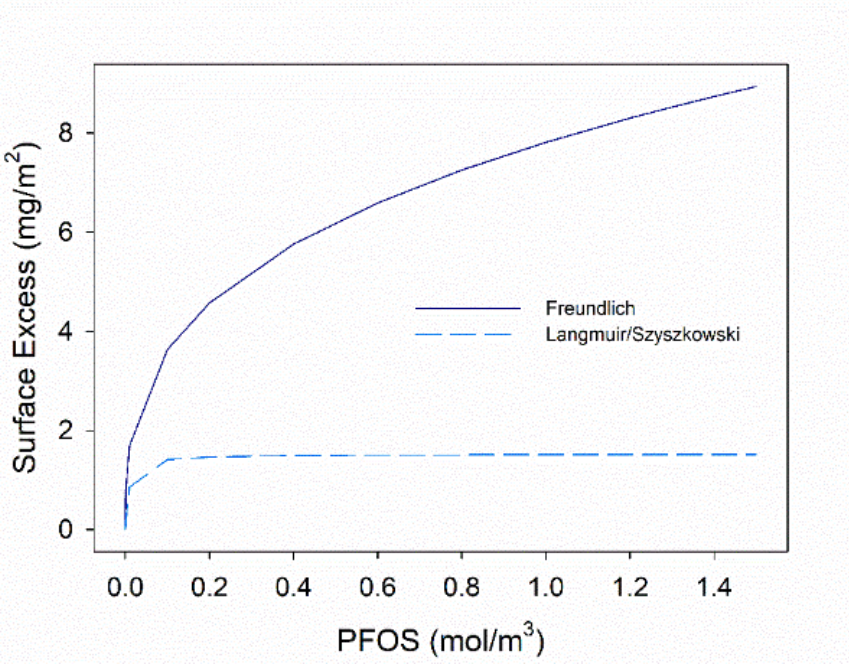


Figure A.4 Surface excess for PFOS in 42 mM solution determined from the Freundlich and Langmuir-Szyszkowski equations.

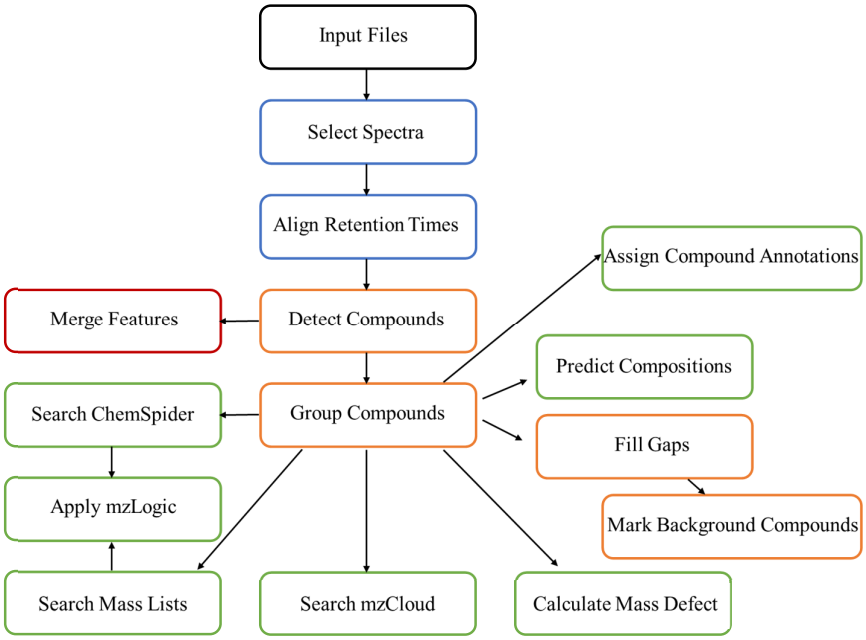


Figure A.5 Compound Discoverer Workflow.

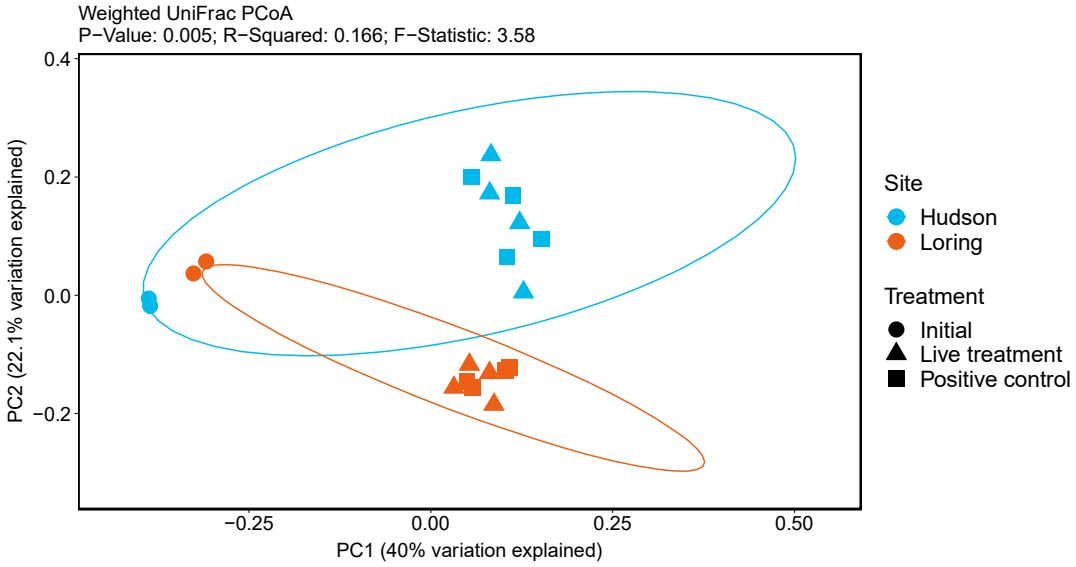


Figure A.6 Principal coordinate analysis (PCoA) plot of phylogenetic microbial community changes among the treatments from Loring and Hudson soil microcosms, as described by weighted UniFrac distance matrices. The PC1 and PC2 axes explain 40% and 22.1% of the variation, respectively.

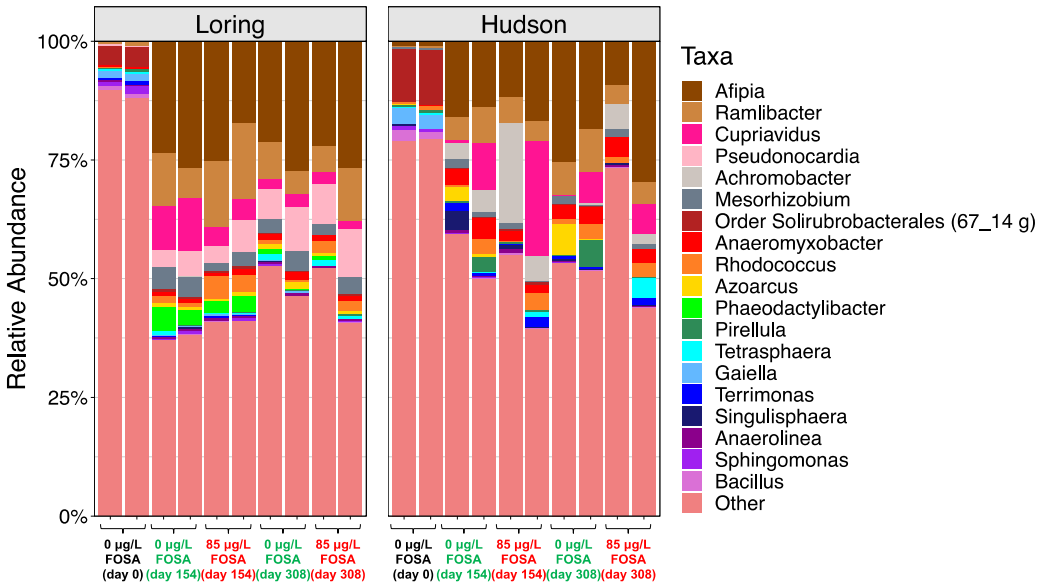


Figure A.7 The relative abundance of microbial community composition at the genus level in Loring (left) and Hudson (right) soil microcosms.

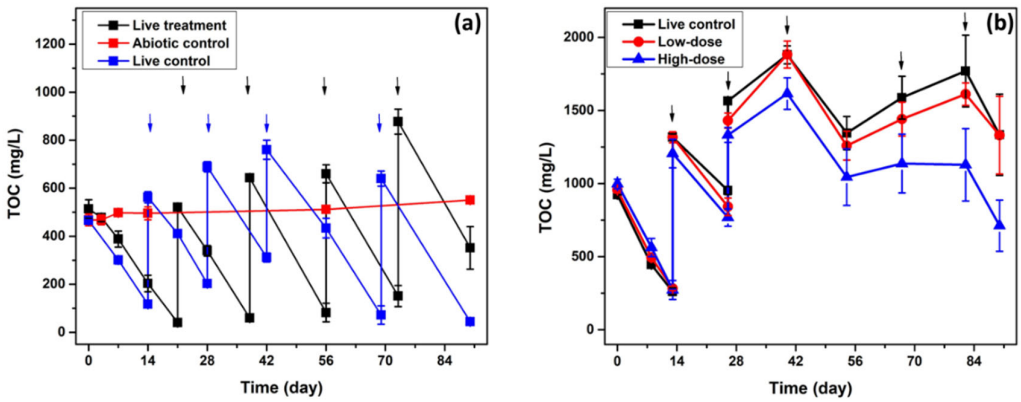


Figure A.8 Total organic carbon (TOC) in (a) Robins biotransformation experiment during 90-day incubation. DGBE amendment were made to live treatment (black arrow) and live control (blue arrow) and (b) Loring biotransformation experiment during 90-day incubation. Identical amount of DGBE was amended into all three groups at the same time points (black arrow). Error bars represent one standard deviation of triplicate live treatments and duplicate abiotic/live controls.

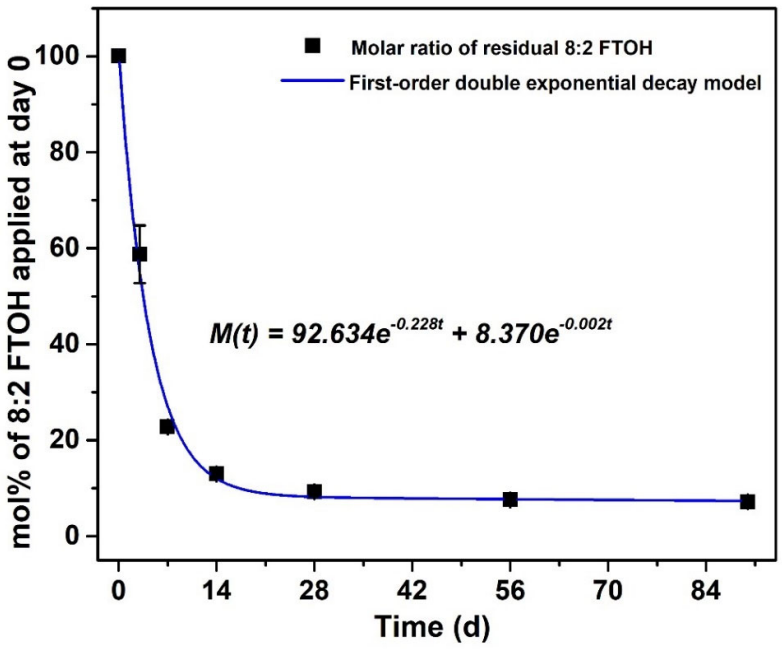


Figure A.9 Molar percentage of residual 8:2 FTOH in live treatment in Robins biotransformation experiment during 90-day incubation along with fitting curve of first-order double exponential decay model.

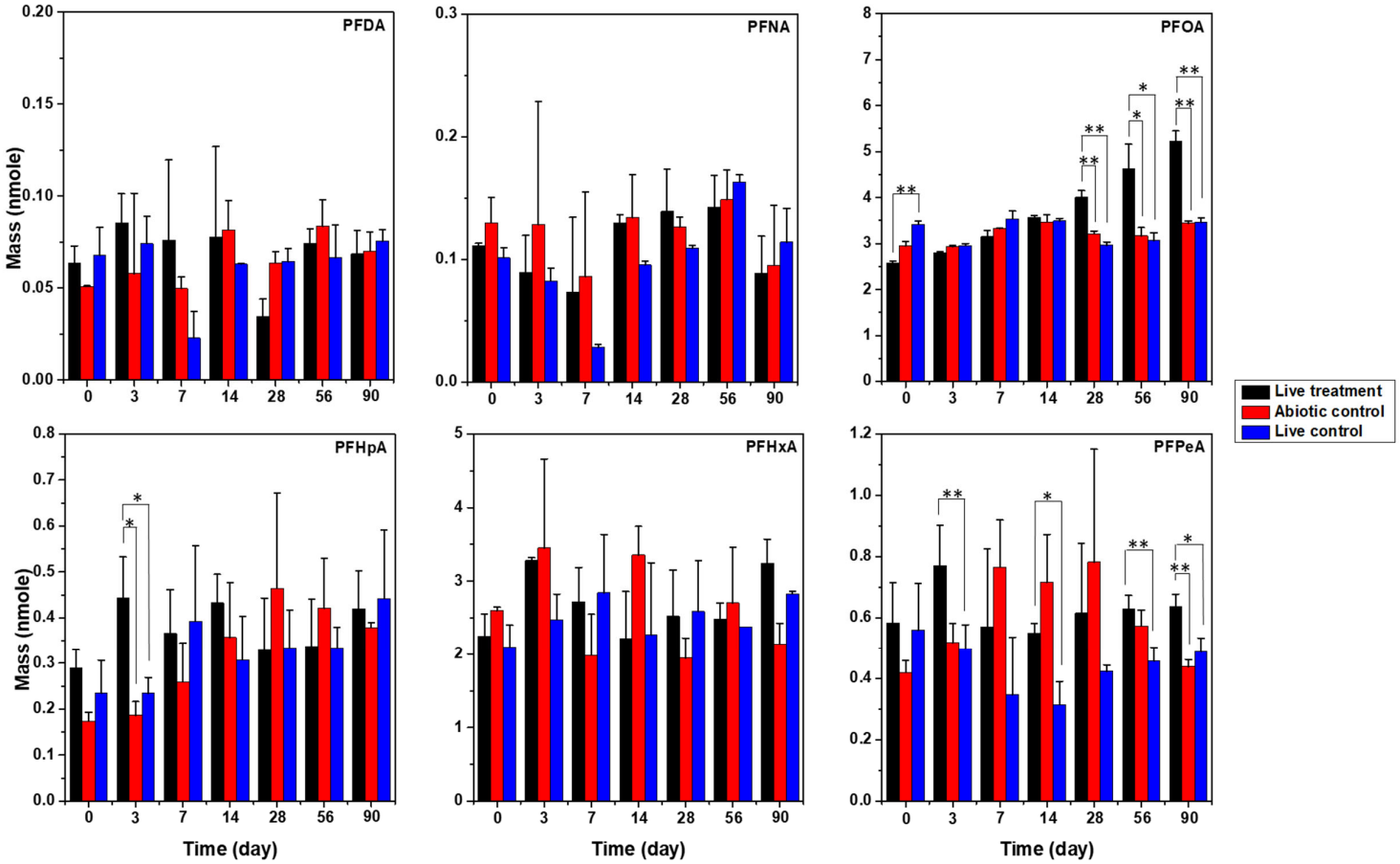


Figure A.10 Mass of PFCAs (C5-C10) in Robins biotransformation experiment during 90-day incubation. Error bars represent one standard deviation of triplicate of live treatments and duplicate abiotic and live controls. Asterisks indicate statistically significant differences between the live treatment and abiotic/live control (two sample *t*-test). The single asterisk indicates $p < 0.05$ and double asterisks indicate $p < 0.01$. Note that the y-axis scales for each PFCA are different.

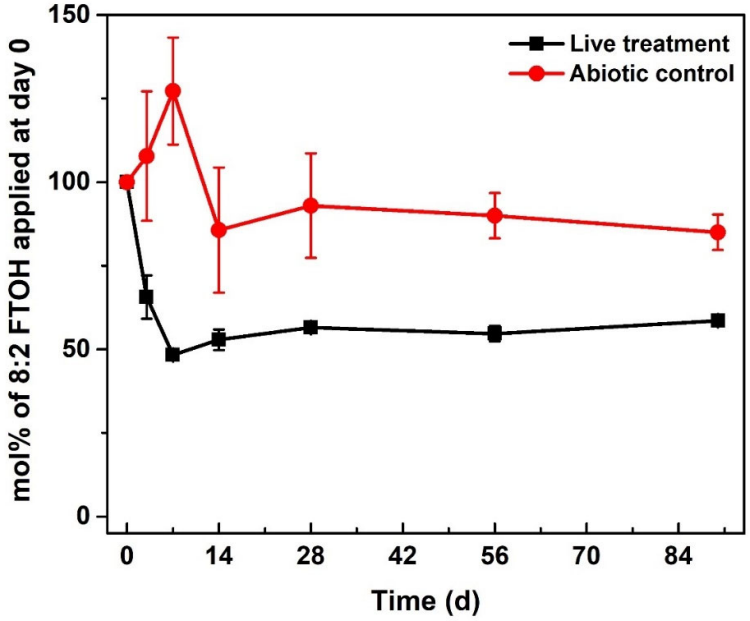


Figure A.11 The total molar recovery in Robins biotransformation experiment during 90-day incubation. Error bars represent one standard deviation of triplicate live treatments and duplicate abiotic controls.

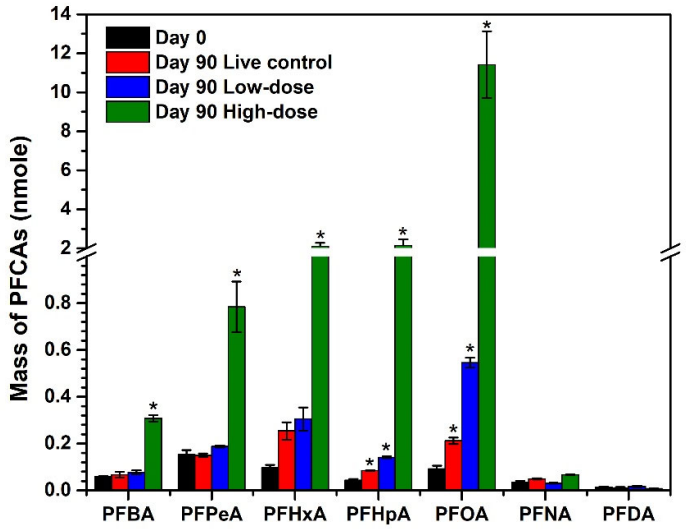


Figure A.12 Mass of PFCAs (C4-C10) in Loring biotransformation experiment. Asterisk indicates $p < 0.05$ compared with live control at day 90. Error bars represent one standard deviation of triplicate high-dose and low-dose treatments and duplicate live controls.

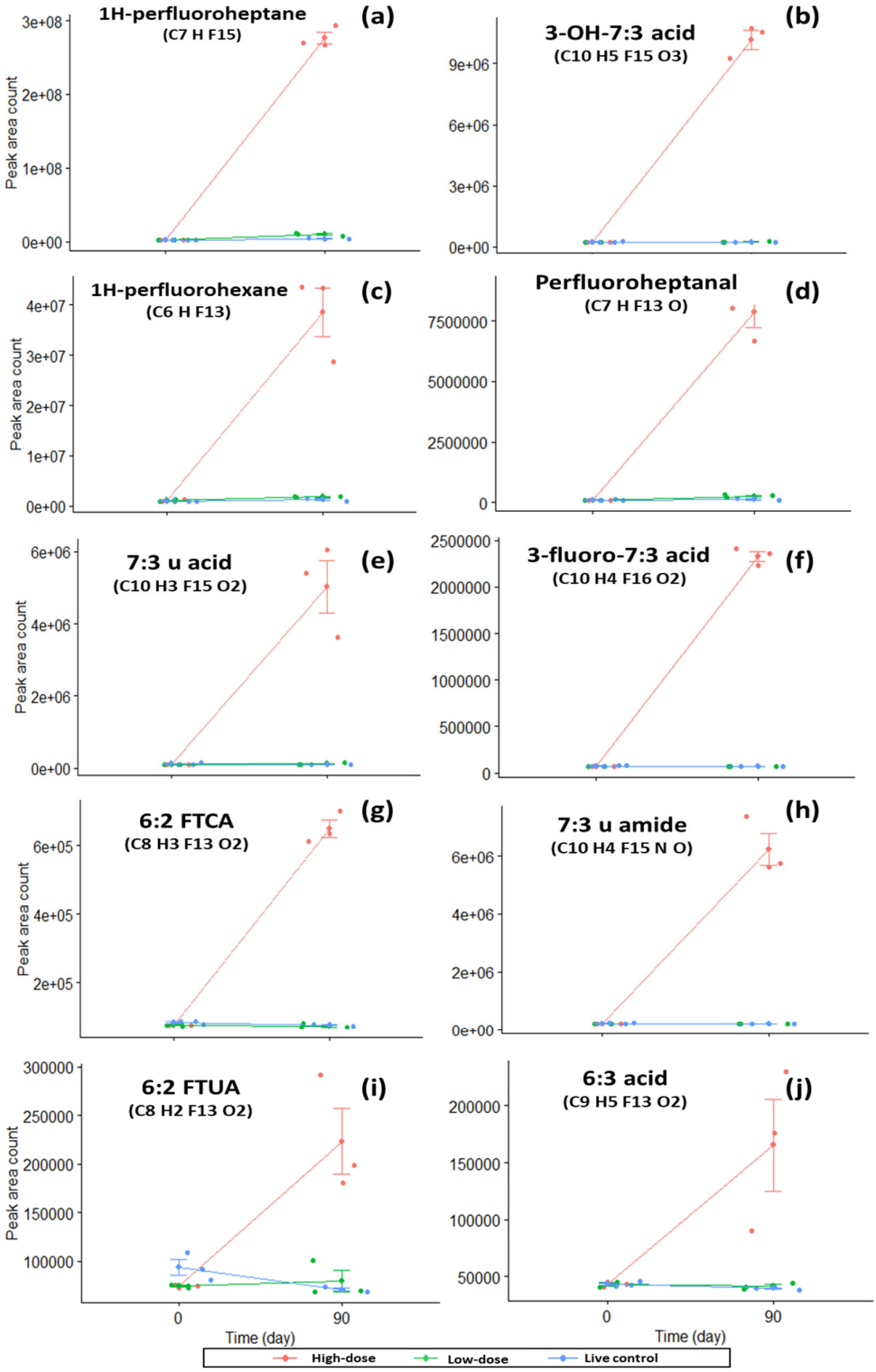


Figure A.13 Change of peak area count (mean value and standard error of three technical replicate) along with time at day 0 and day 90 for compounds selected by non-targeted analysis in Loring biotransformation experiment.

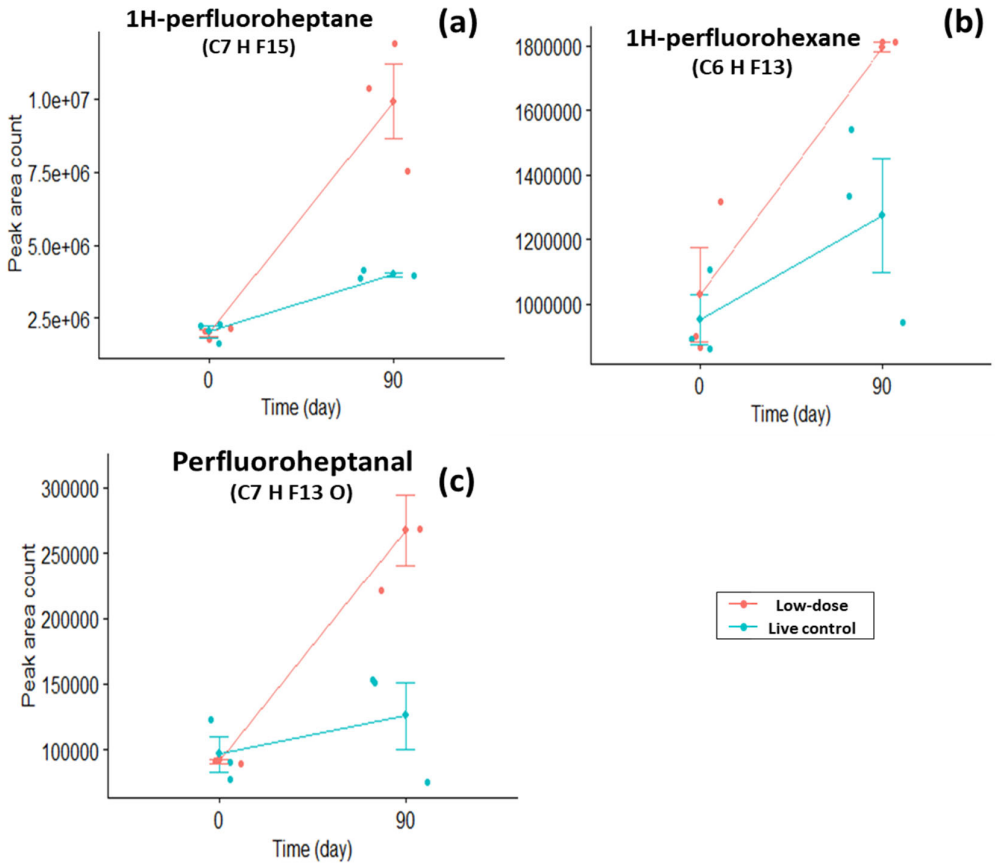


Figure A.14 Change of peak area count (mean value and standard error of three technical replicate) along with time at day 0 and day 90 for compounds selected by non-targeted analysis in Loring biotransformation experiment (Low-dose treatment only).

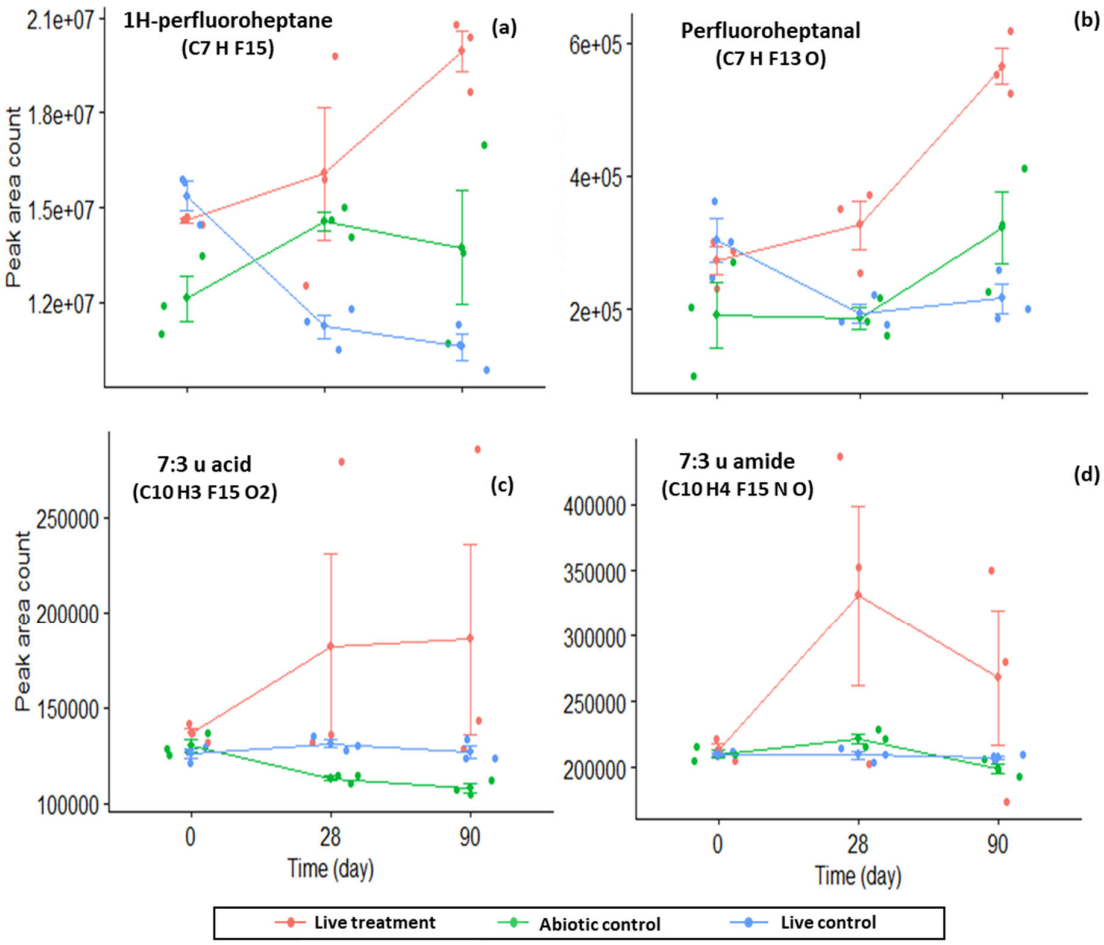


Figure A.15 Change of peak aera count (mean value and standard error of three technical replicate) along with time at day 0, day 28 and day 90 for compounds selected by non-targeted analysis in Robins biotransformation experiment.

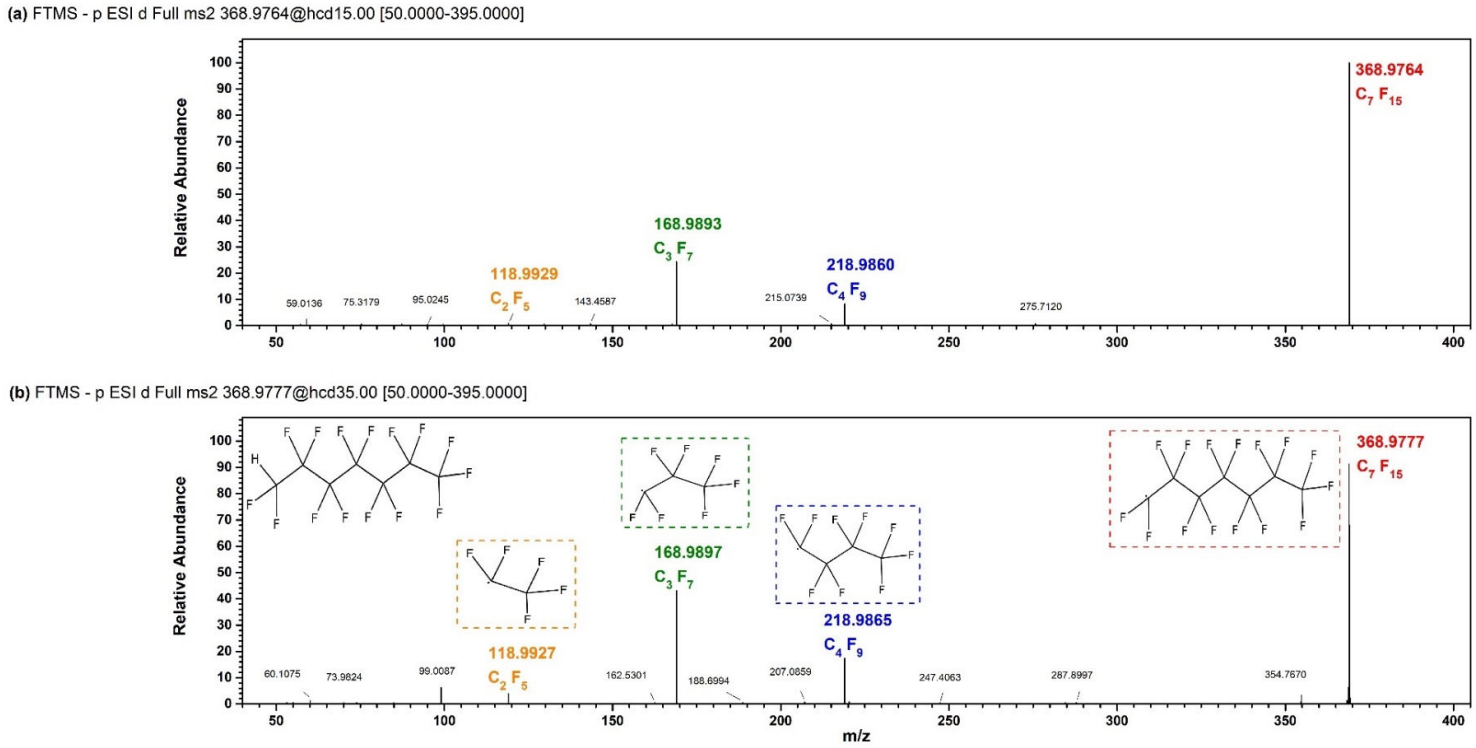


Figure A.16 Illustration of the elucidated high-resolution MS2 spectrum obtained for 1H-perfluoroheptane, identified at the confirmed structure confidence level (level 1): (a) microcosm sample; (b) 1H-perfluoroheptane reference standard (1 µg/L).

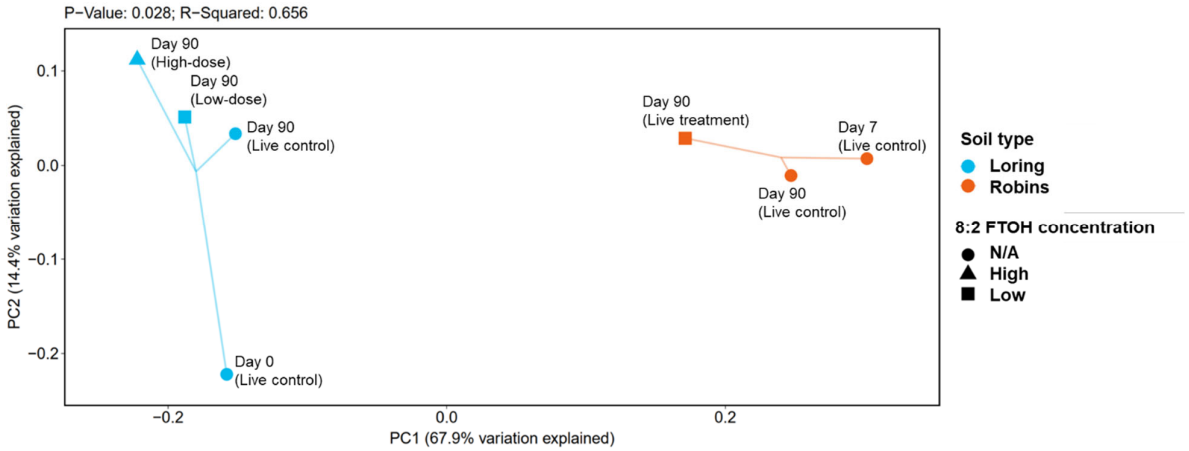


Figure A.17 Principal coordinate analysis (PCoA) plot of phylogenetic microbial community changes across different 8:2 FTOH dose treatments with Loring AFB soil or Robins AFB soil as described by weighted UniFrac distance matrices. PC1 explains 67.9% of the variation while PC2 explains 14.4%.

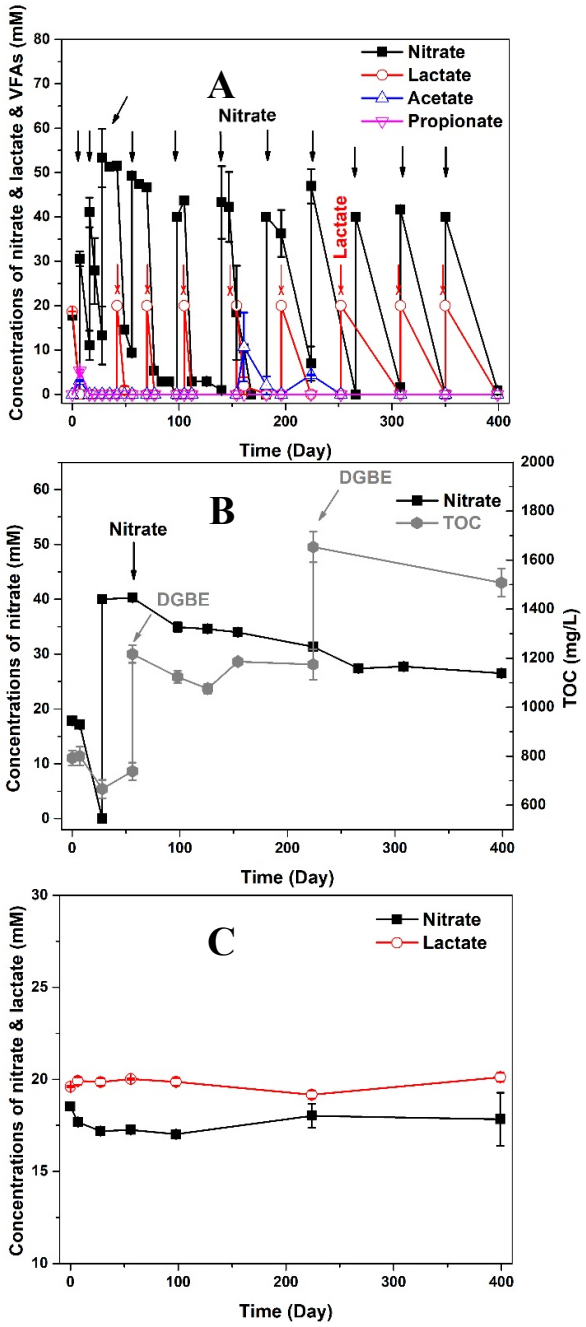


Figure A.18 Concentrations of nitrate and organic acids in ED treatment/positive control (Panel A); concentrations of nitrate and total organic carbon (TOC) in NA treatment (Panel B); concentrations of nitrate and lactate in abiotic control (Panel C). The black, red, and gray arrows represent the individual amendments of 40 mM nitrate, 20 mM lactate, and 5 mM DGBE to the microcosms, respectively. Note that a total of 11 nitrate and 8 lactate amendments were made to ED treatment/positive control due to the rapid depletion of both electron donor and acceptor. Error bars represent the standard deviation of triplicate ED/NA microcosms, and of duplicate control microcosms.

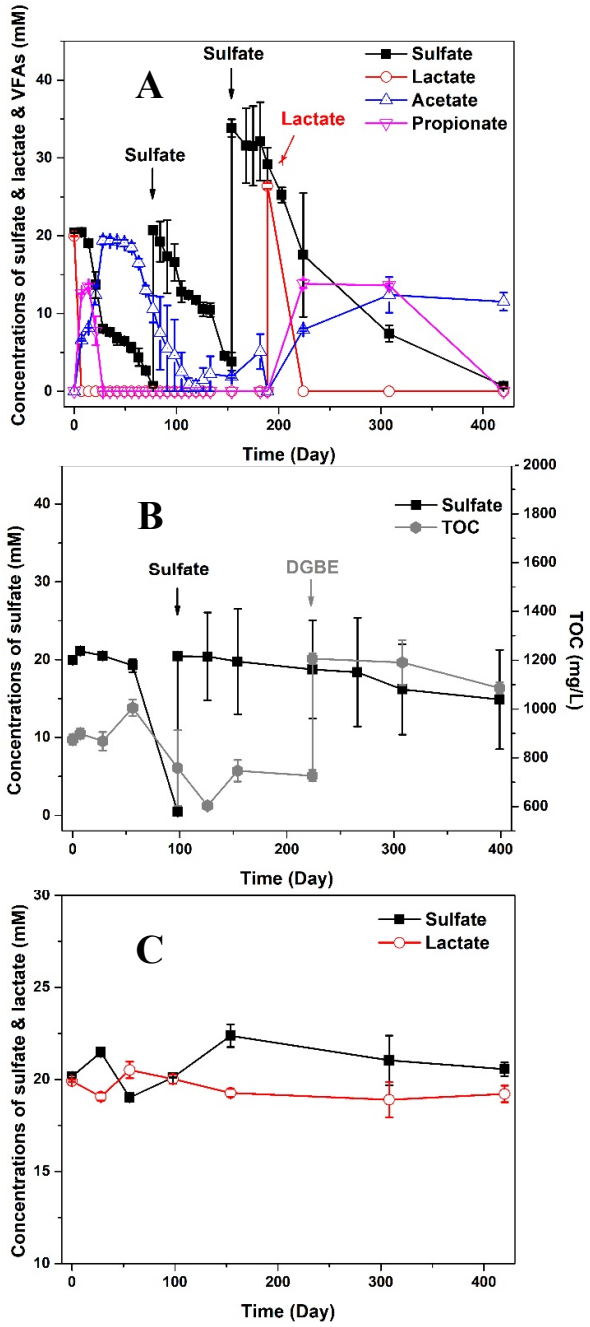


Figure A.19 Concentrations of sulfate and organic acids in ED treatment/positive control (Panel A); concentrations of sulfate and total organic carbon (TOC) in NA treatment (Panel B); concentrations of sulfate and lactate in abiotic control (Panel C). The black, red, and gray arrows represent the individual amendments of 20 mM sulfate, 20 mM lactate, and 5 mM DGBE to the microcosms, respectively. Error bars represent the standard deviation of triplicate ED/NA microcosms, and of duplicate control microcosms.

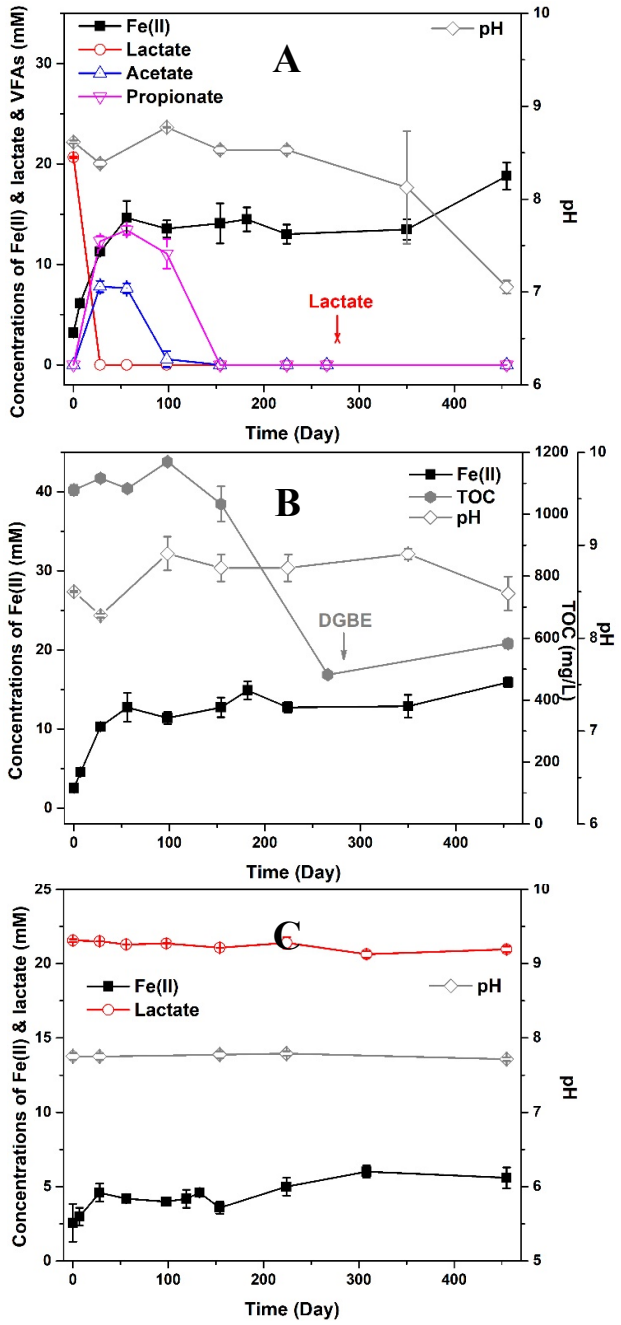


Figure A.20 Concentrations of Fe(II) and organic acids in ED treatment/positive control (Panel A); concentrations of Fe(II) and total organic carbon (TOC) in NA treatment (Panel B); concentrations of Fe(II) and lactate in abiotic control (Panel C). The red, and gray arrows represent the individual amendments of 20 mM lactate, and 5 mM DGBE to the microcosms, respectively. Note that the time variation of pH in each treatment was also plotted in respective Panel. Error bars represent the standard deviation of triplicate ED/NA microcosms, and of duplicate control microcosms.

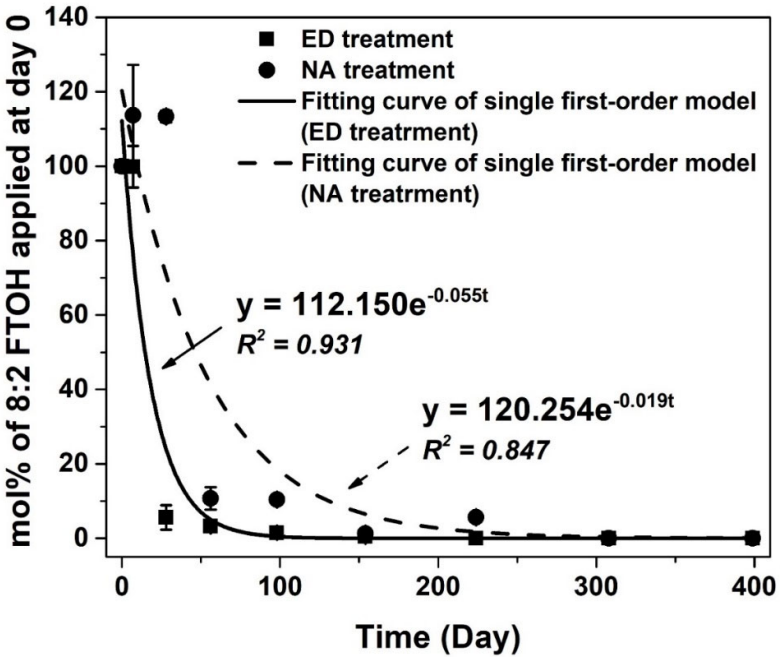


Figure A.21 Changes in molar ratio of residual 8:2 FTOH, and the fitting curves of single first-order kinetic models in ED and NA treatment under nitrate-reducing condition.

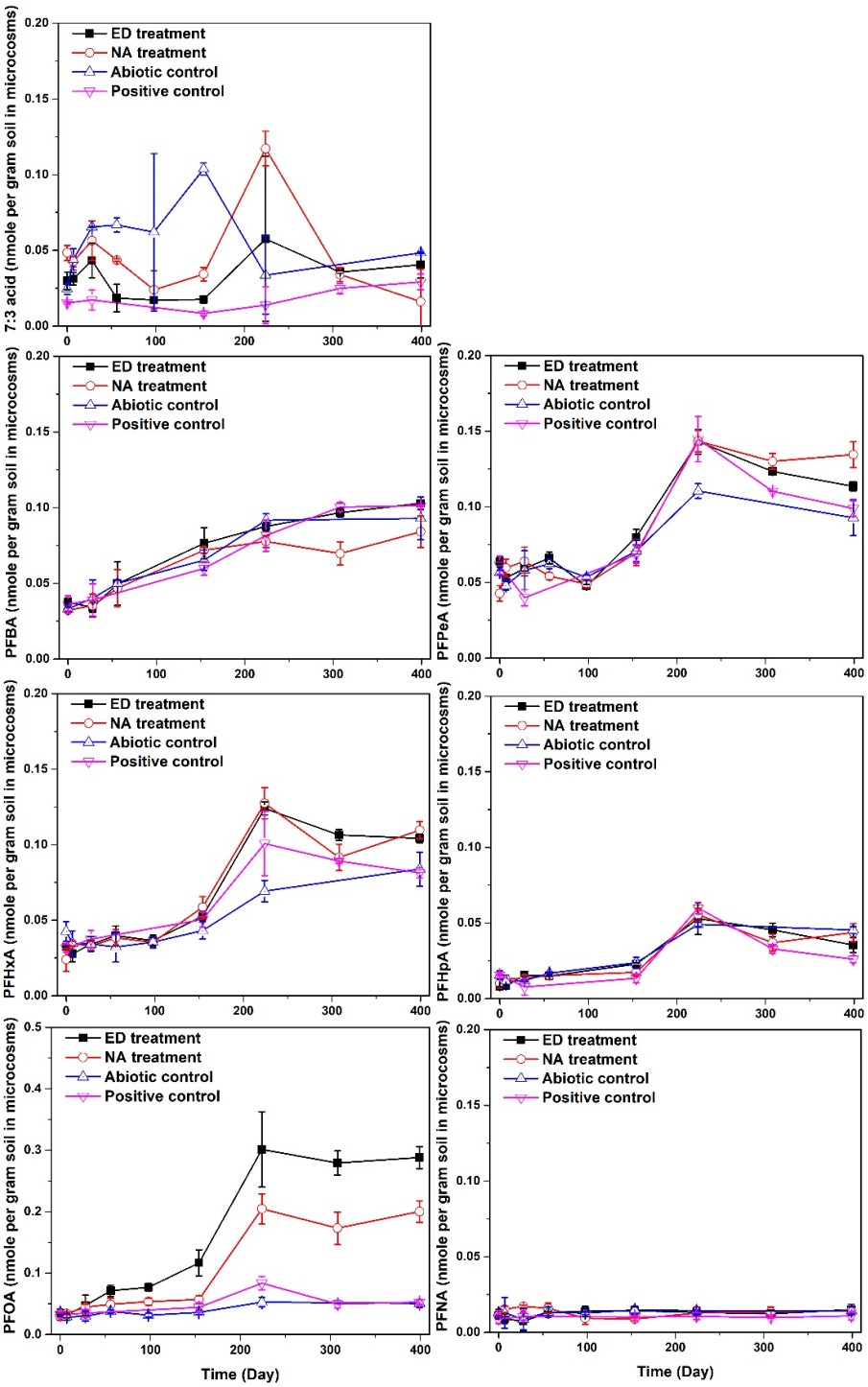


Figure A.22 Changes in the concentrations (nanomole per gram soil/dry weight) of 7:3 acid, and C4-C9 PFCAs in ED, NA treatment, abiotic controls, and positive controls under nitrate-reducing condition throughout the experiments. Note that the y-axis scales in PFOA plot is larger than the scales in other plots.

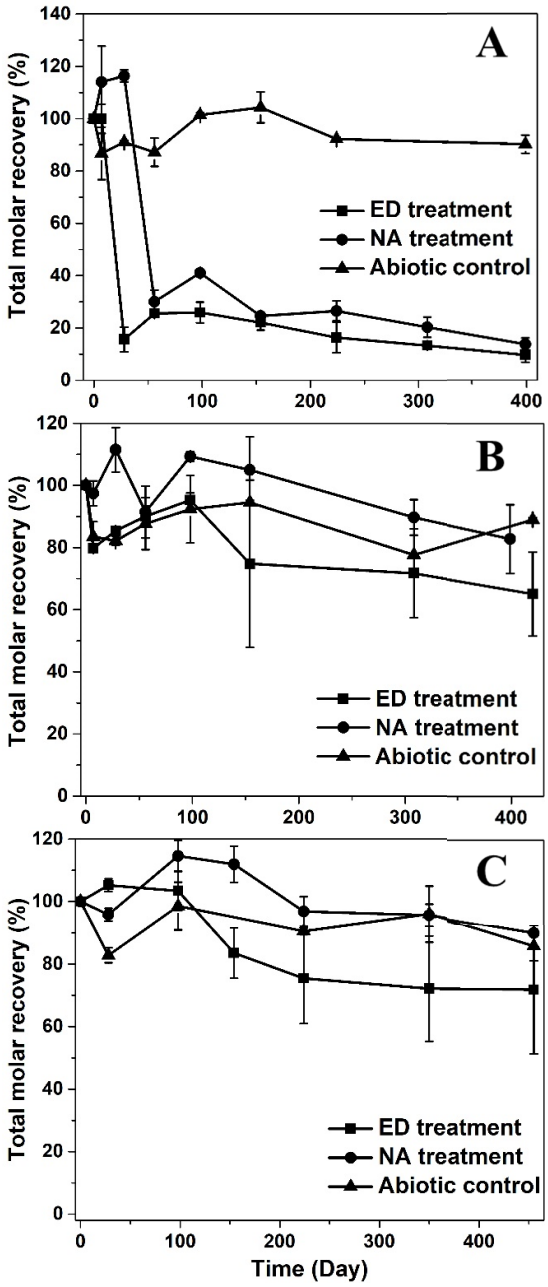


Figure A.23 The total molar recoveries (8:2 FTOH and quantifiable biotransformation products) during 8:2 FTOH biotransformation in ED, NA treatment, and abiotic controls under nitrate-reducing conditions (Panel A), sulfate-reducing conditions (Panel B), iron-reducing conditions (Panel C).

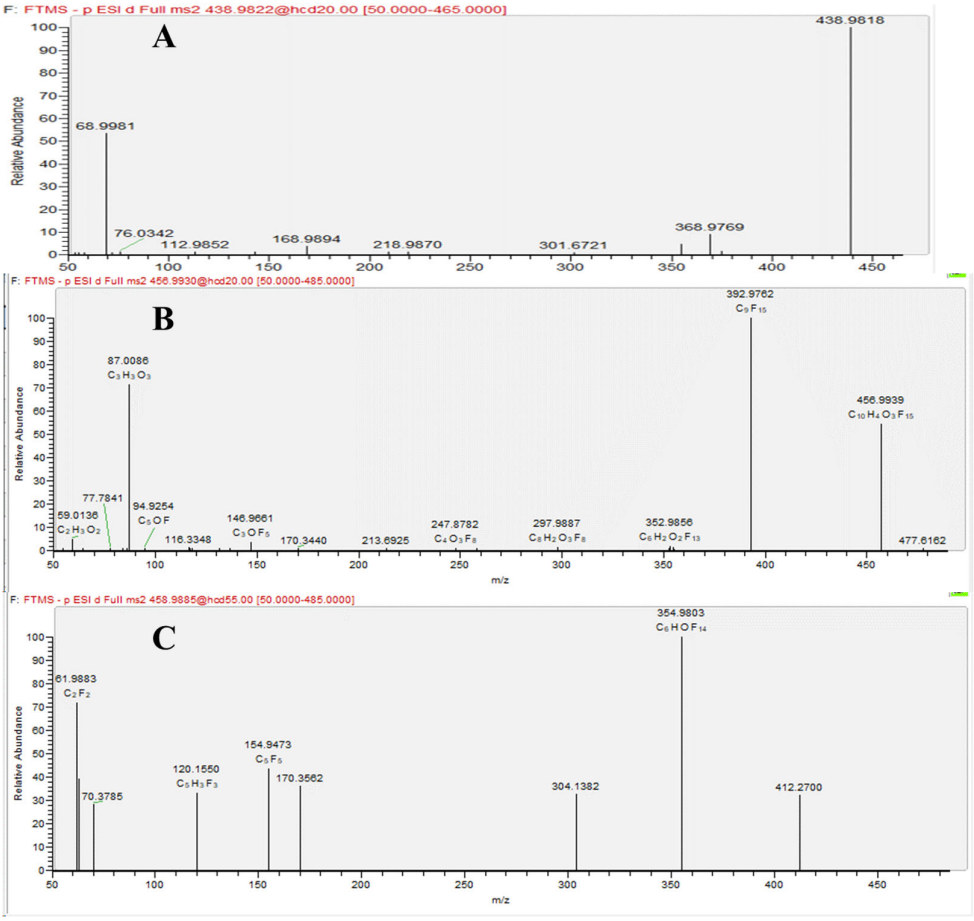


Figure A.24 The MS2 spectra of potential biotransformation products identified in the ED and/or NA treatments under nitrate, sulfate-, or iron-reducing conditions**.** Panel A, 7:3 U acid ($F(CF_2)_7CH{=}CHCOOH$, *m/z* 438.9822); Panel B, 3-OH-7:3 acid ($F(CF_2)_7CHOHCH_2COOH$, *m/z* 456.9930); Panel C, 3-F-7:3 acid ($F(CF_2)_7CFHCH_2COOH$, *m/z* 458.9885).

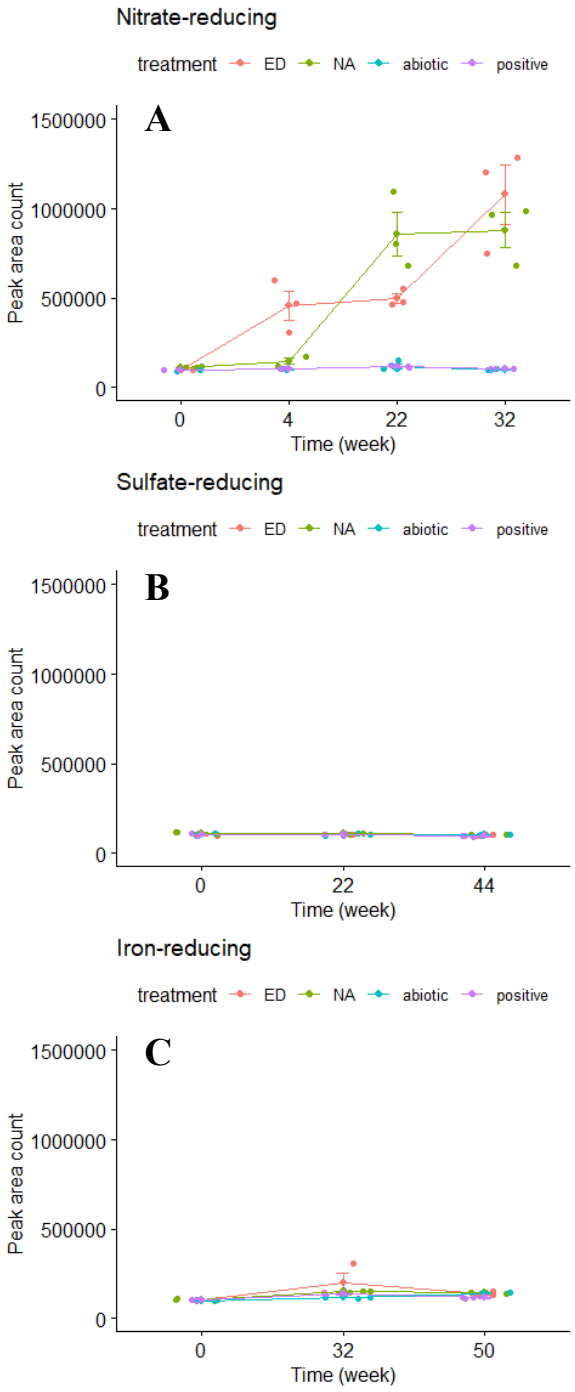


Figure A.25 The time trend of 7:3 U acid during 8:2 FTOH biotransformation in each treatment under (A) nitrate-reducing; (B) sulfate-reducing; and (C) iron-reducing conditions based on peak areas of extracted ion chromatograms.

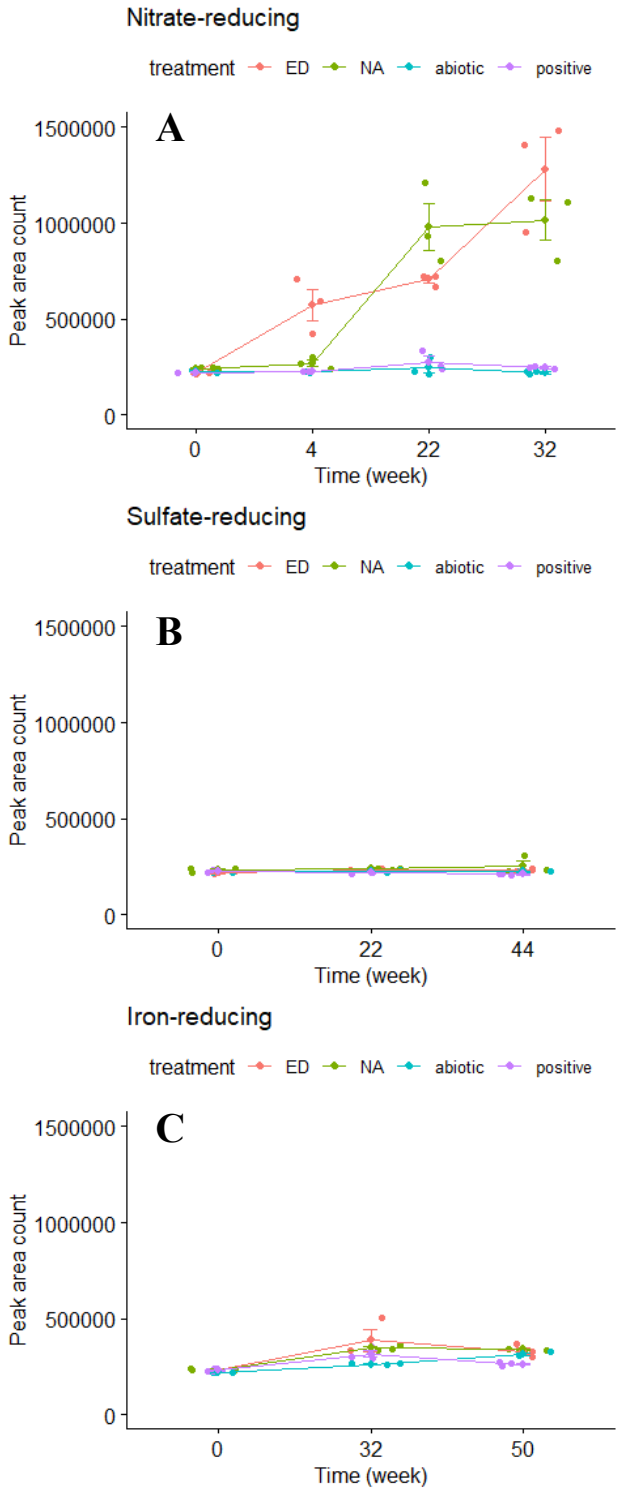


Figure A.26 The time trend of 3-OH-7:3 acid during 8:2 FTOH biotransformation in each treatment under (A) nitrate-reducing; (B) sulfate-reducing; and (C) iron-reducing conditions based on peak areas of extracted ion chromatograms.

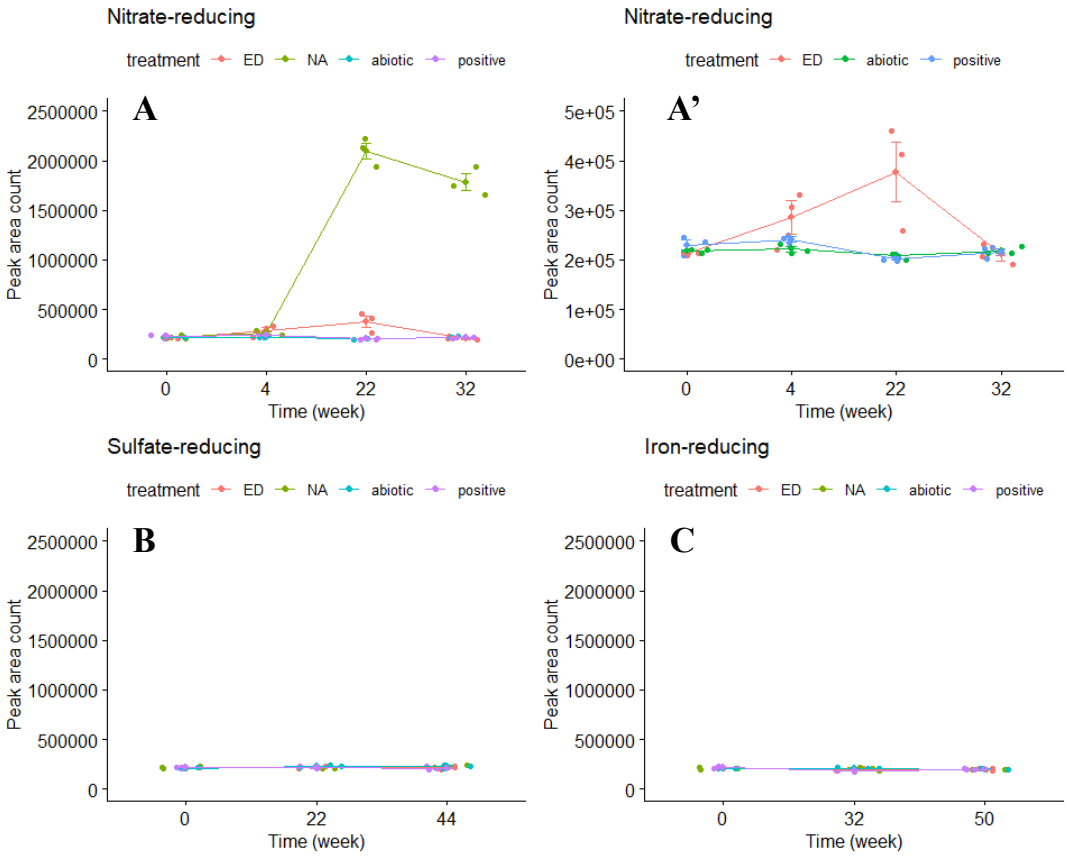


Figure A.27 The time trend of 7:3 U amide during 8:2 FTOH biotransformation in each treatment under (A) nitrate-reducing; (B) sulfate-reducing; and (C) iron-reducing conditions based on peak areas of extracted ion chromatograms. Note Panel A' is the zoom view of Panel A, excluding the NA treatment with a smaller y-axis scale, to illustrate the different time trends between the ED treatment and two controls.

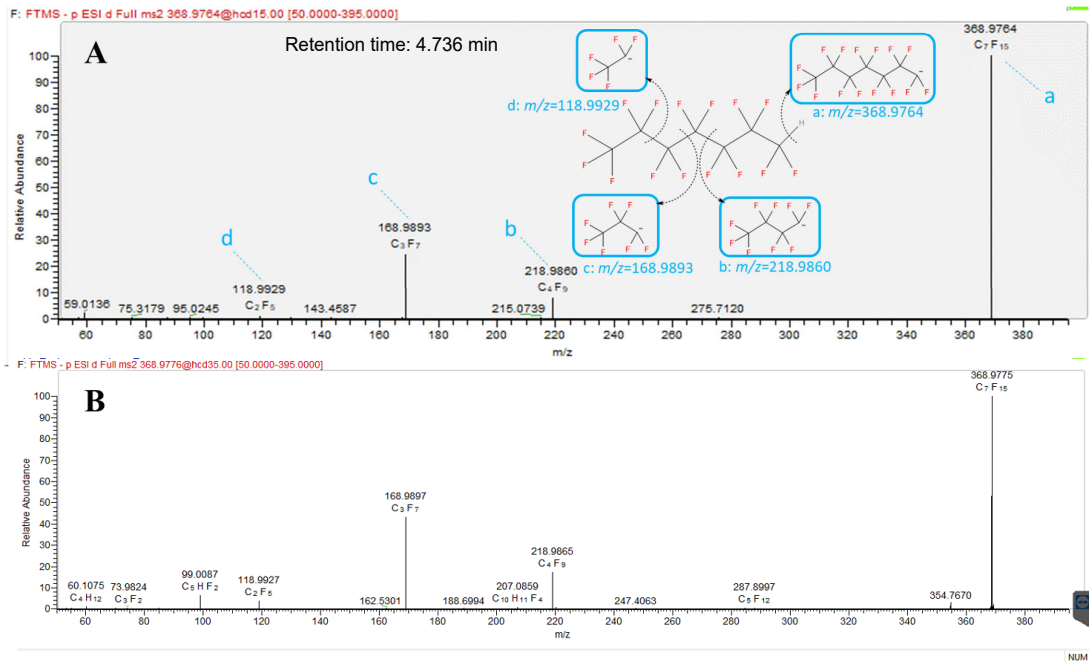


Figure A.28 The MS2 spectra of a novel biotransformation product identified as 1H-perfluoroheptane (m/z 368.9764). Panel A is the spectrum of samples collected from 8:2 FTOH nitrate-reducing microcosms. Panel B is the spectrum of 1 ppb 1H-perfluoroheptane standard.

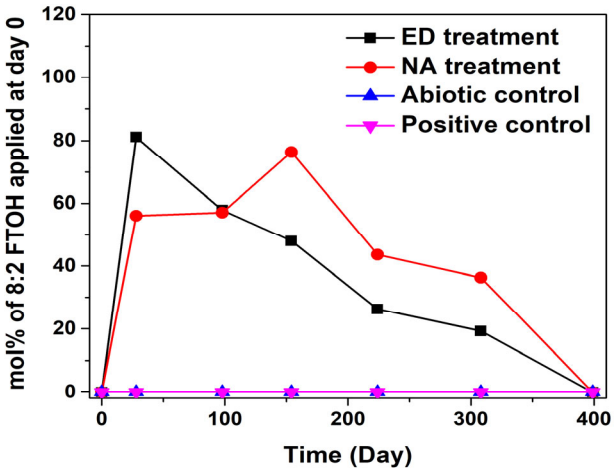


Figure A.29 The molar yields of 1H-perfluoroheptane during 8:2 FTOH biotransformation in each treatment under nitrate-reducing conditions, based on the GC-HRMS quantification results.

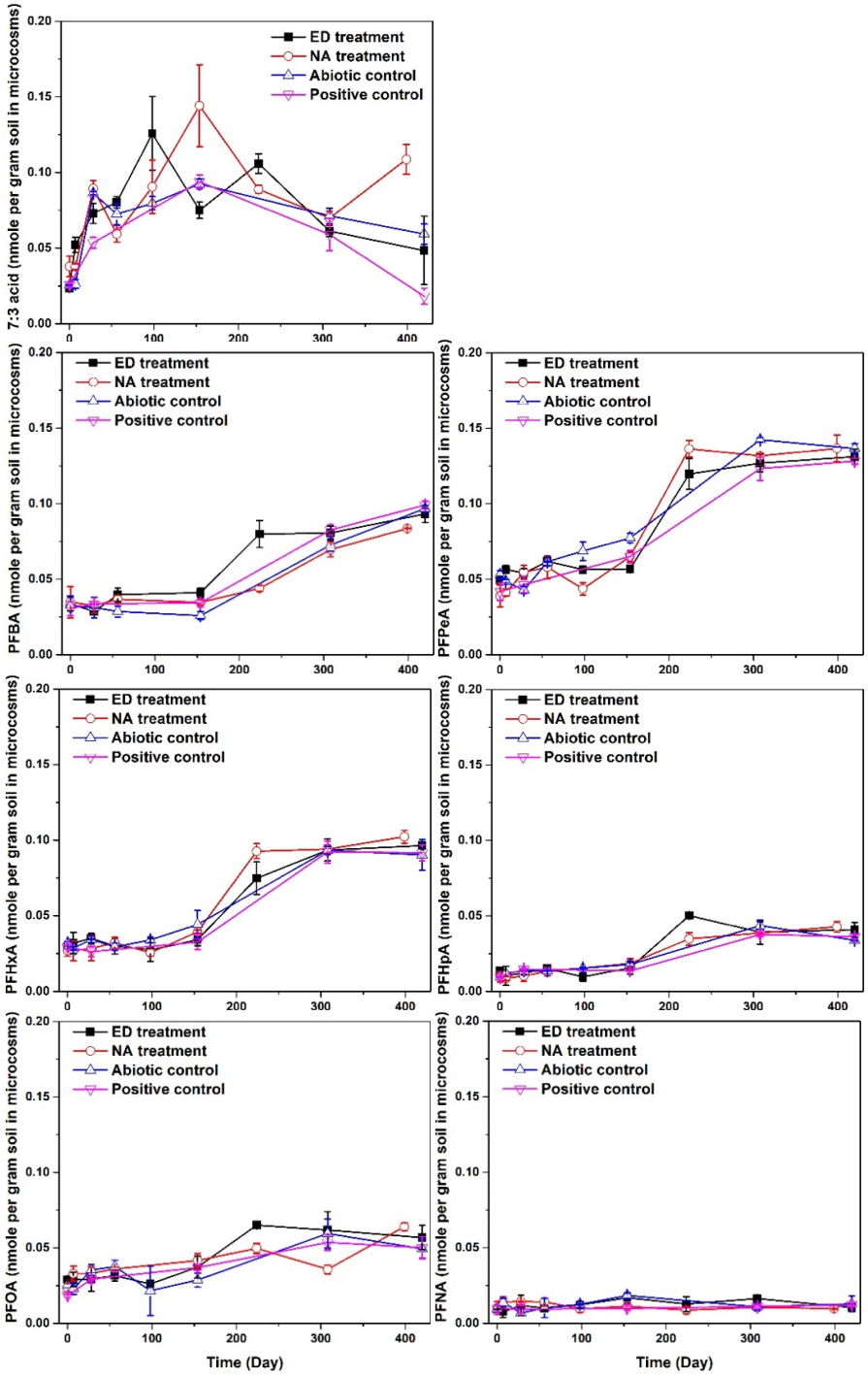


Figure A.30 Changes in the concentrations (nanomole per gram soil/dry weight) of 7:3 acid, and C4-C9 PFCAs in ED, NA treatment, abiotic controls, and positive controls under sulfate-reducing condition throughout the experiments.

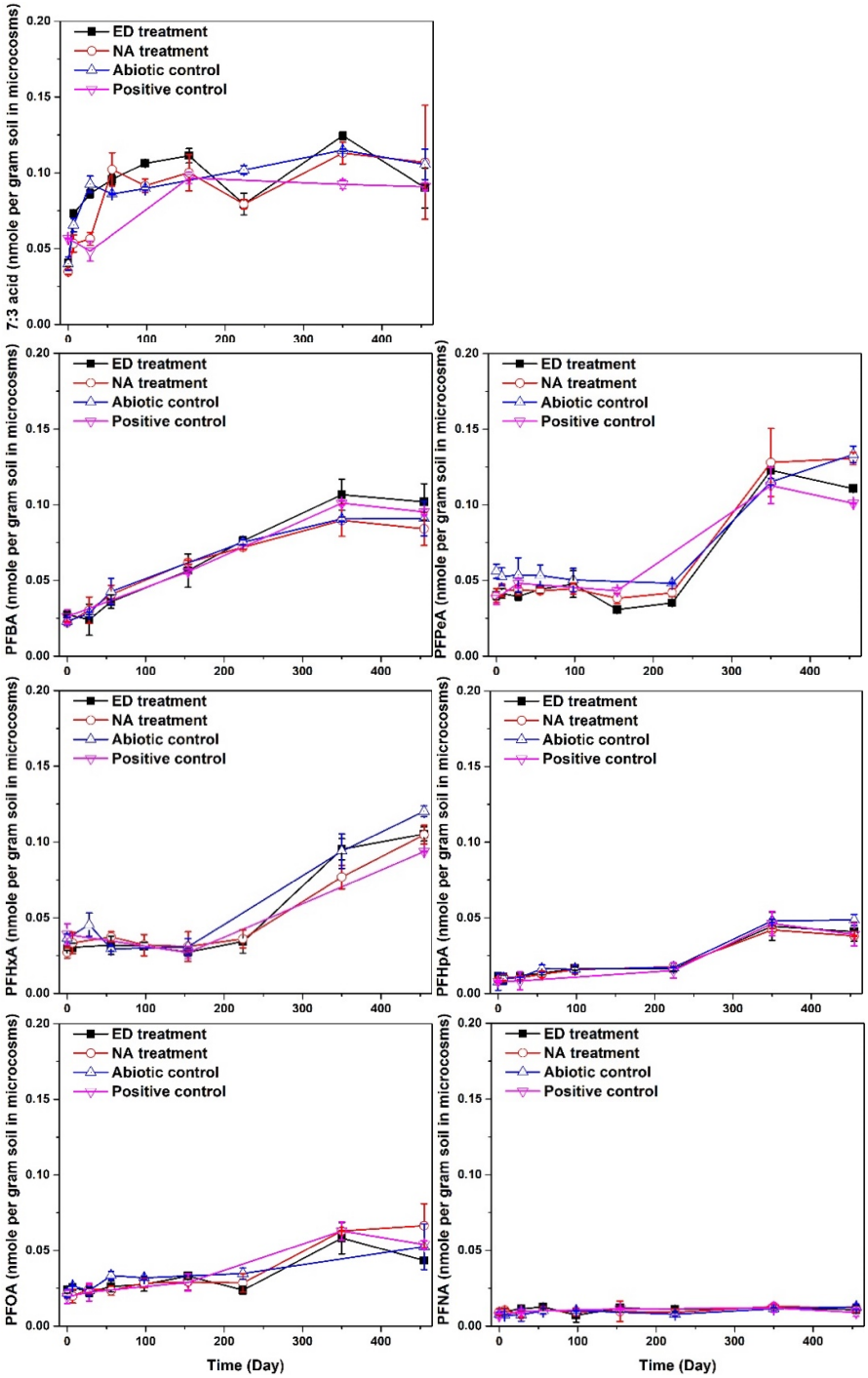


Figure A.31 Changes in the concentrations (nanomole per gram soil/dry weight) of 7:3 acid, and C4-C9 PFCAs in ED, NA treatment, abiotic controls, and positive controls under iron-reducing condition throughout the experiments.

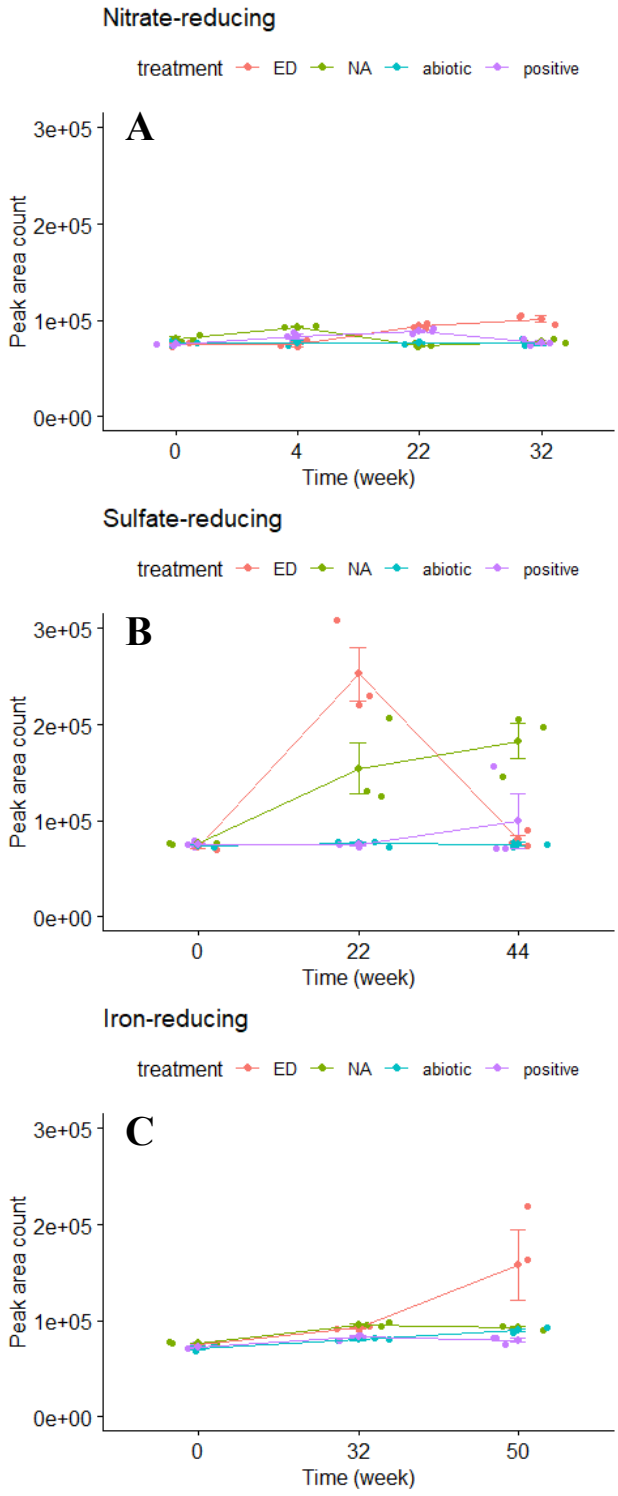


Figure A.32 The time trend of 3-F-7:3 acid during 8:2 FTOH biotransformation in each treatment under (A) nitrate-reducing; (B) sulfate-reducing; and (C) iron-reducing conditions based on peak areas of extracted ion chromatograms.

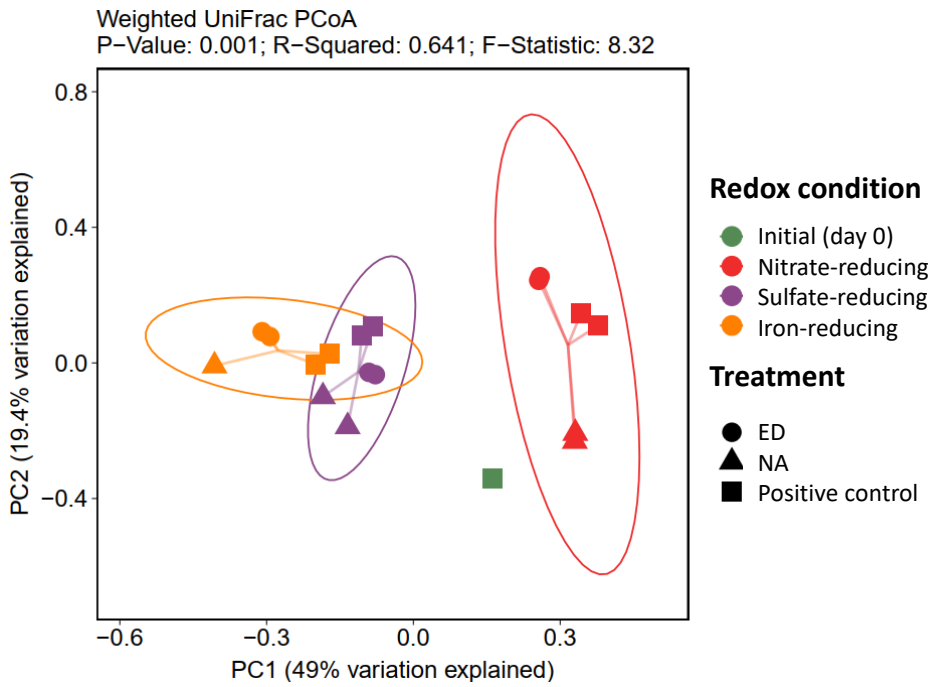


Figure A.33 Principal coordinate analysis (PCoA) plot of phylogenetic microbial community changes among the microcosms under different redox conditions, as described by weighted UniFrac distance matrices.

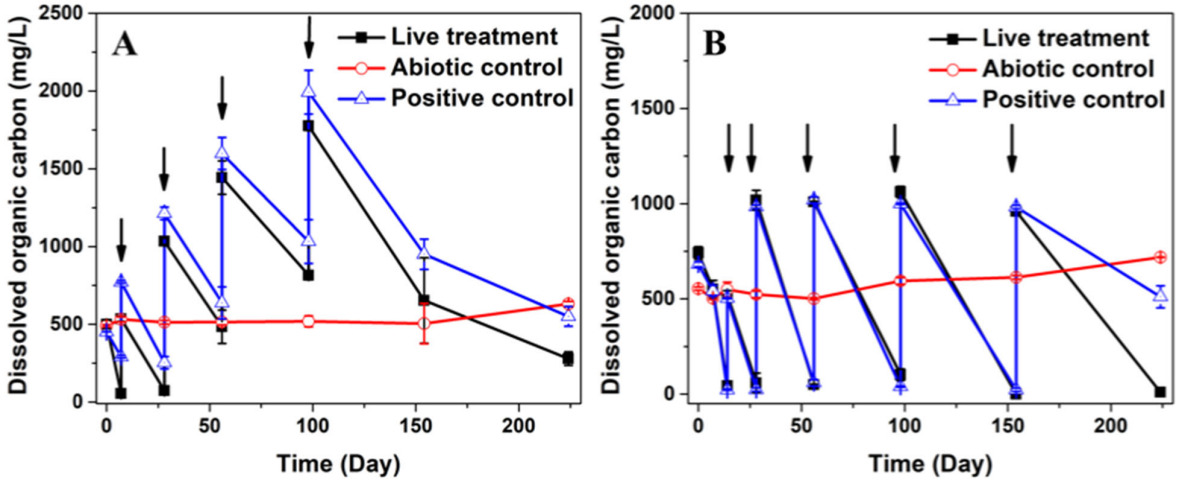


Figure A.34 Concentrations of dissolved organic carbon (DOC) in Loring (Panel A) and Robins (Panel B) soil microcosms. Solid arrows represent the amendment of 10 mM DGBE to live treatments and positive controls. Error bars represent the standard deviation of triplicate live treatment microcosms, and of duplicate control microcosms.

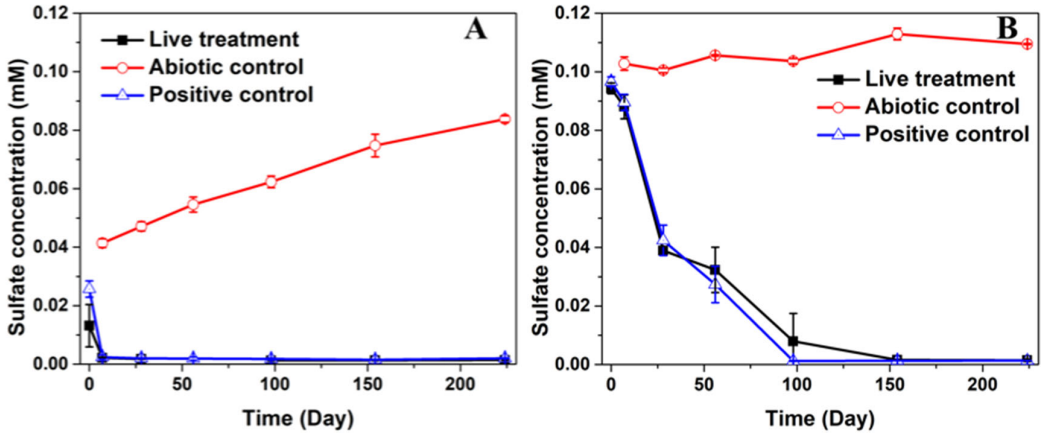


Figure A.35 Changes in sulfate concentrations during 6:2 FTS aerobic biotransformation in Loring (Panel A) and Robins (Panel B) soil microcosms. Error bars represent the standard deviation of triplicate live treatment microcosms, and of duplicate control microcosms.

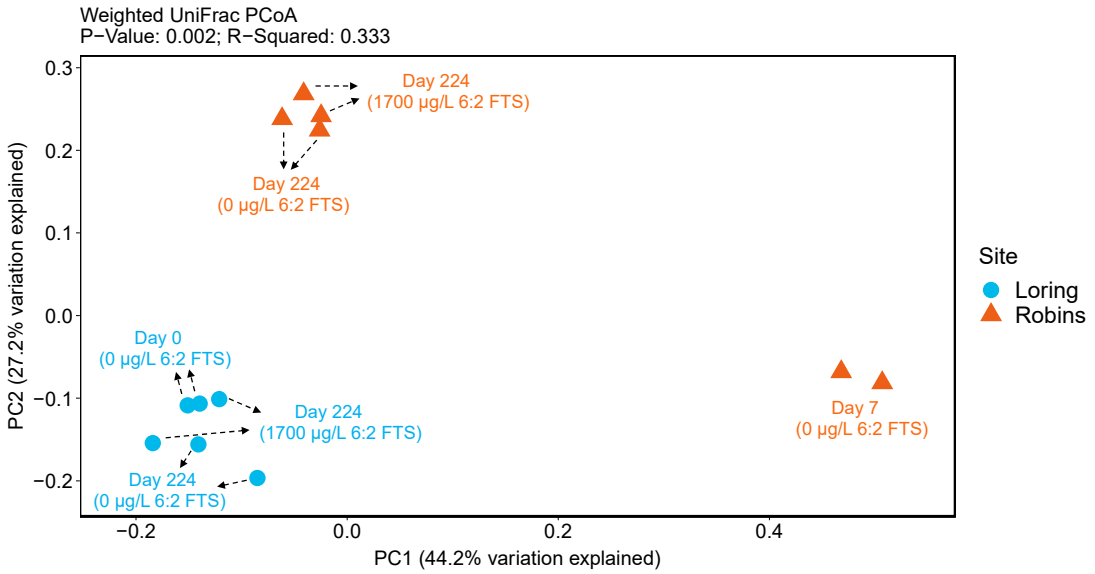


Figure A.36 Principal coordinate analysis (PCoA) plot of phylogenetic microbial community changes among the treatments from Loring or Robins soil microcosms, as described by weighted UniFrac distance matrices. The PC1 and PC2 axes explain 44.2% and 27.2% of the variation, respectively.

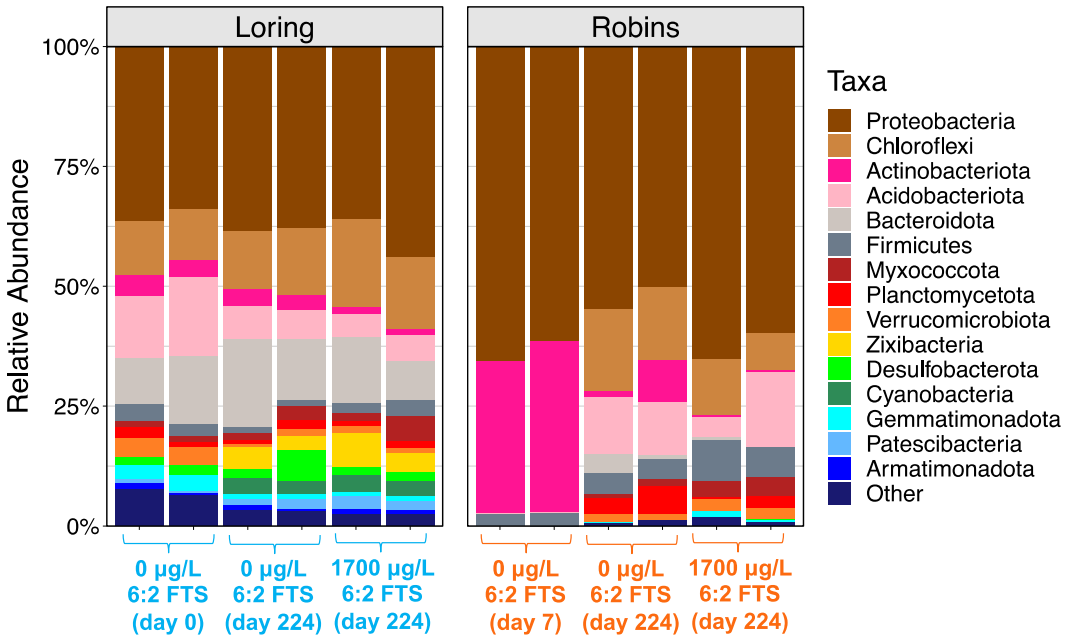


Figure A.37 The relative abundance of microbial community composition at the phylum level in Loring (left) and Robins (right) soil microcosms.

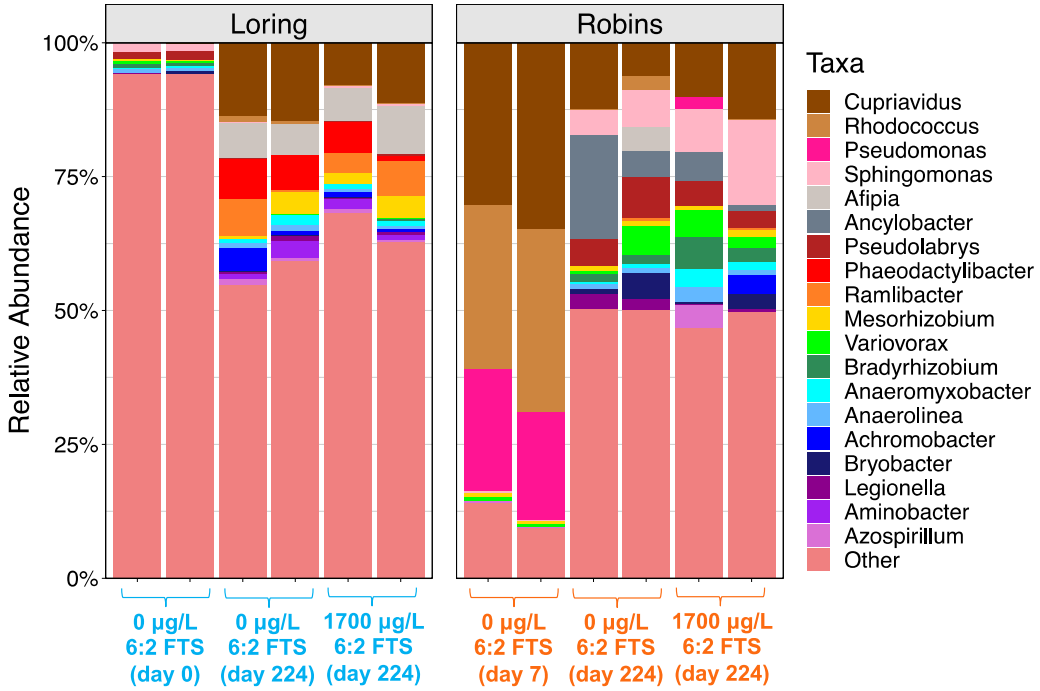


Figure A.38 The relative abundance of microbial community composition at the genus level in Loring (left) and Robins (right) soil microcosms.

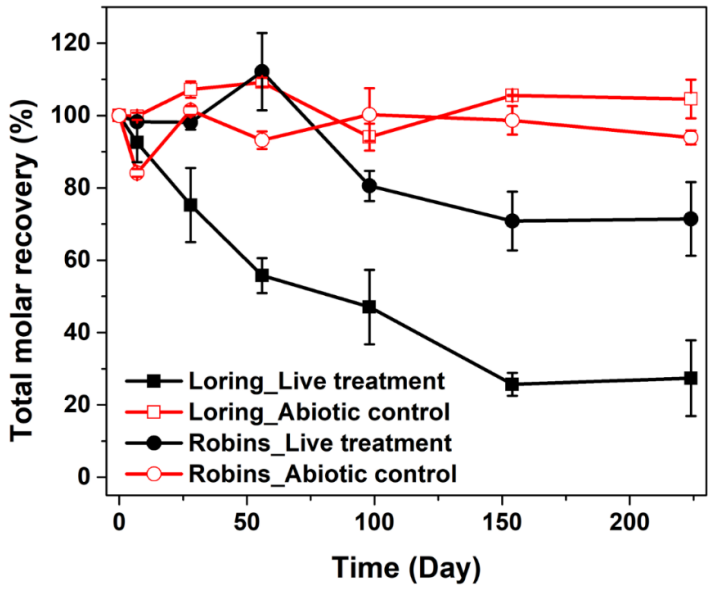


Figure A.39 The total molar recoveries (6:2 FTS and quantifiable biotransformation products) in live treatments and abiotic controls from Loring and Robins soil microcosms.

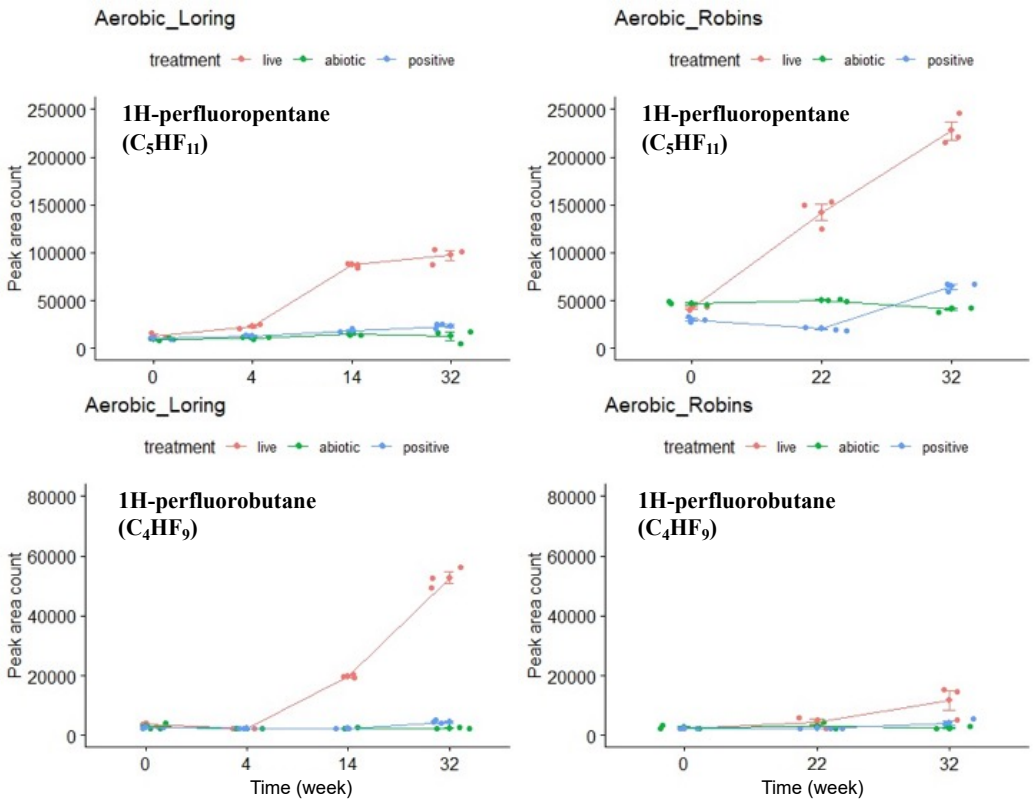


Figure A.40 The time trends of 1H-perfluoropentane (C_5HF_{11}, *m/z* 268.98271) and 1H-perfluorobutane (C_4HF_9, *m/z* 218.98587) during 6:2 FTS biotransformation in each treatment of Loring and Robins soil microcosms based on peak areas of extracted ion chromatograms.

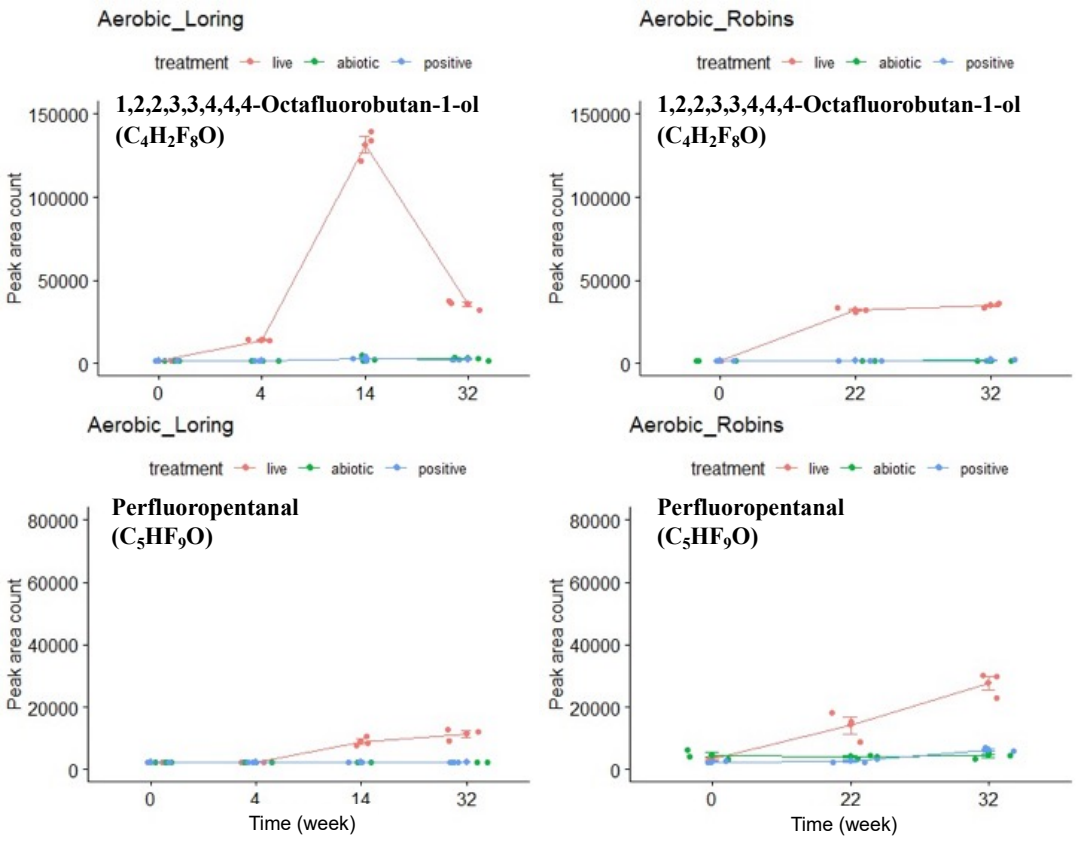


Figure A.41 The time trends of 1,2,2,3,3,4,4,4-Octafluorobutan-1-ol ($C_4H_2F_8O$, *m/z* 216.98912) and Perfluoropentanal (C_5HF_9O, *m/z* 246.9808) during 6:2 FTS biotransformation in each treatment of Loring and Robins soil microcosms based on peak areas of extracted ion chromatograms.

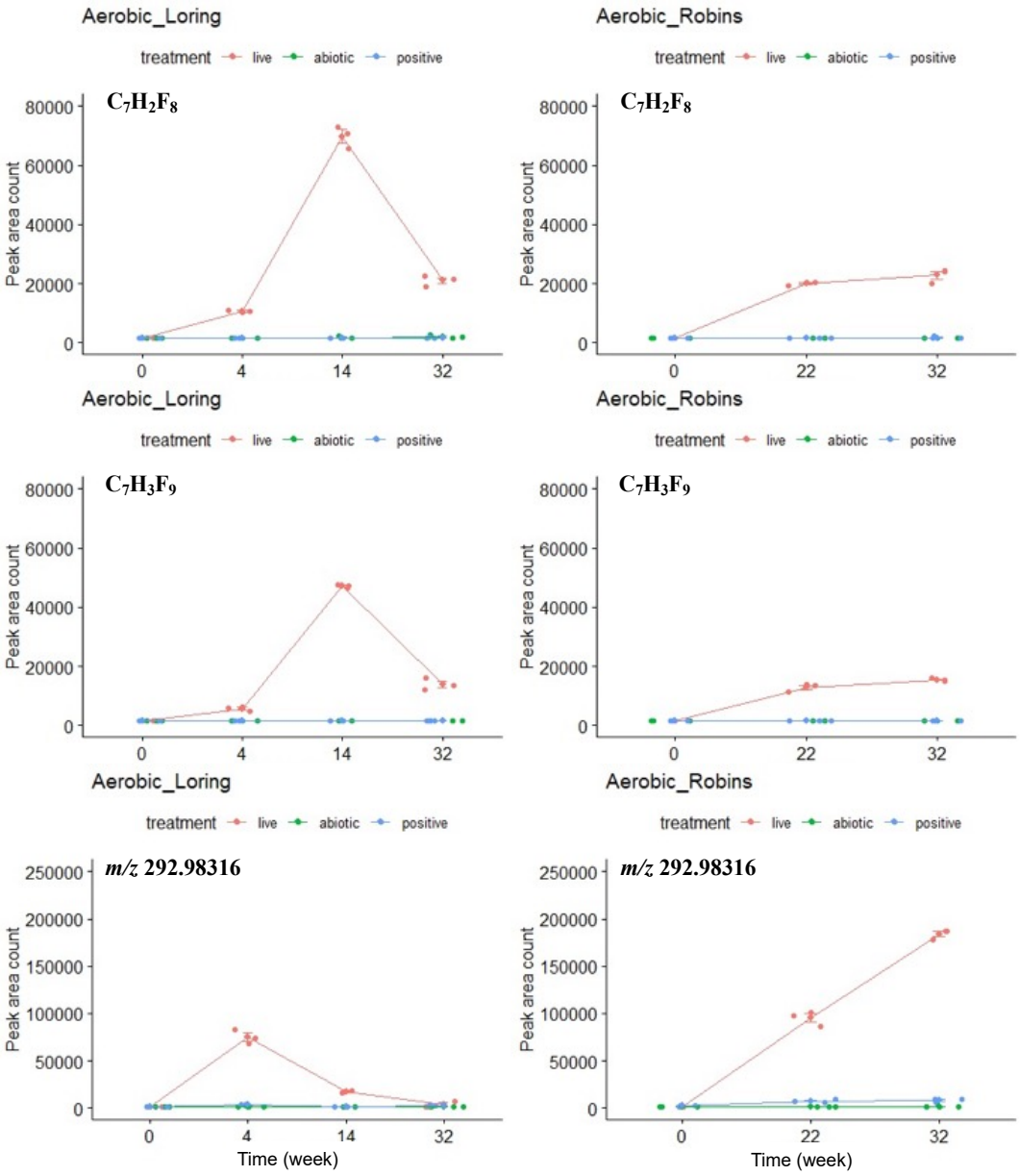


Figure A.42 The time trends of $C_7H_2F_8$ (m/z 236.99543), $C_7H_3F_9$ (m/z 257.00159), and m/z 292.98316 during 6:2 FTS biotransformation in each treatment of Loring and Robins soil microcosms based on peak areas of extracted ion chromatograms.

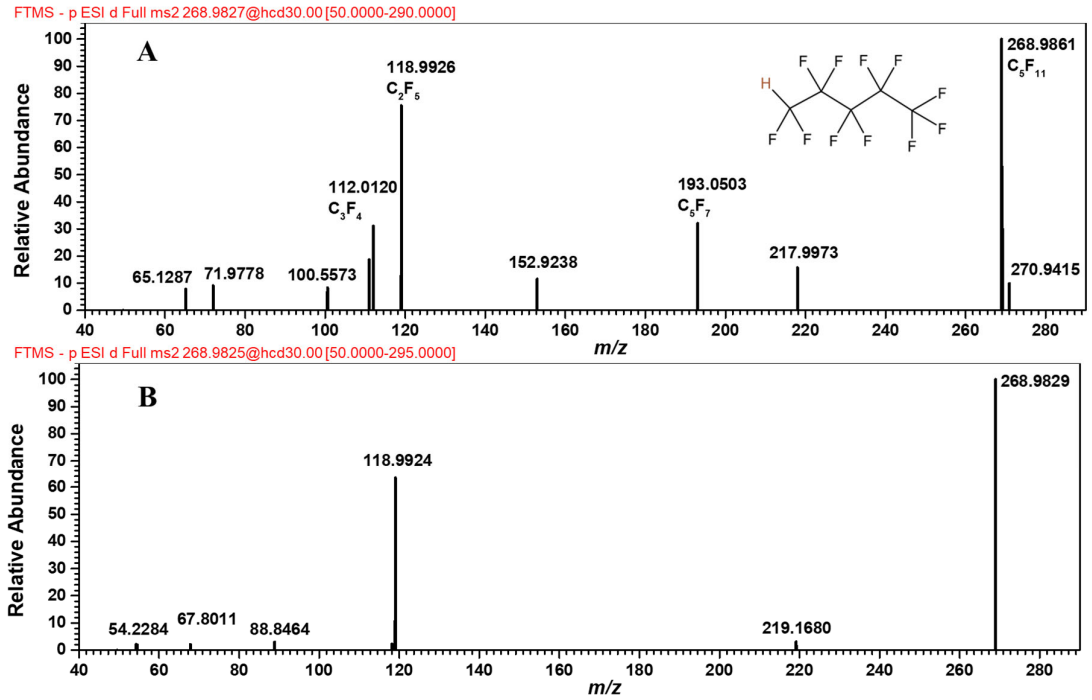


Figure A.43 MS^2 spectra of 1H-perfluoropentane (C_5HF_{11}, *m/z* 268.98271) obtained from the analysis of microcosm sample (Panel A), and the analysis of 1 ppb reference standard (Panel B).

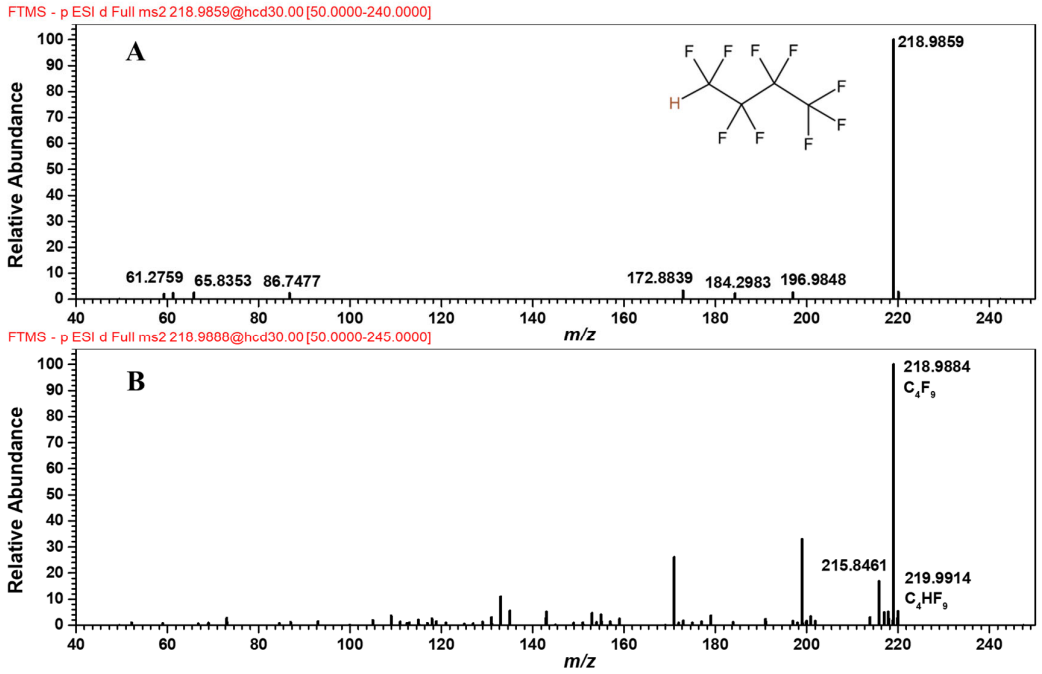


Figure A.44 MS^2 spectra of 1H-perfluorobutane (C_4HF_9, *m/z* 218.98587) obtained from the analysis of microcosm sample (Panel A), and the analysis of 1 ppb reference standard (Panel B).

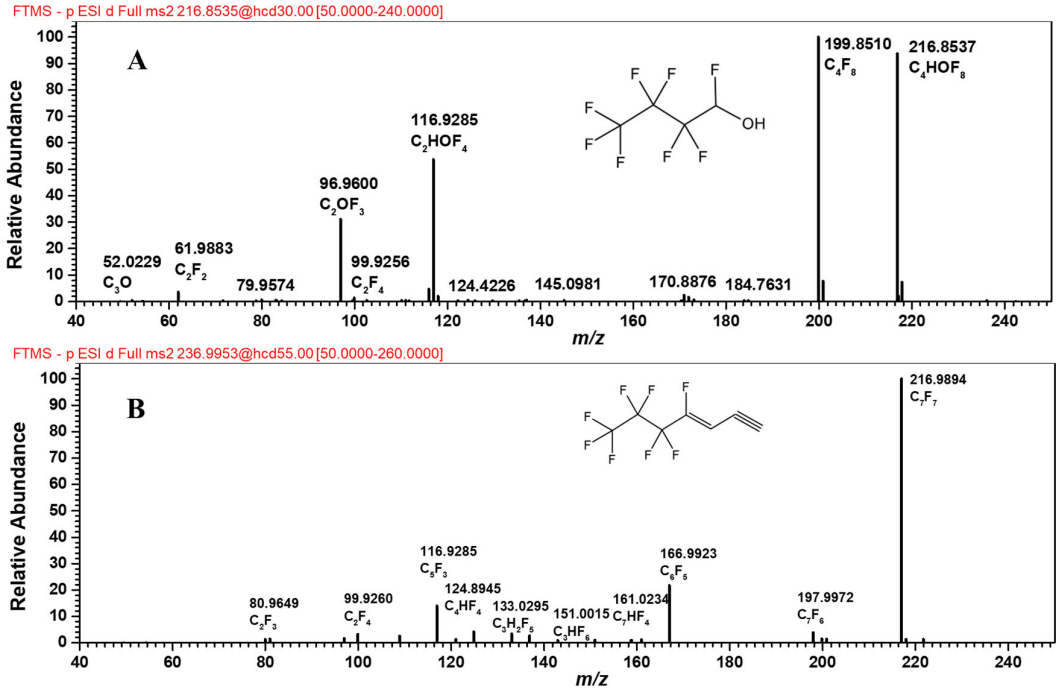


Figure A.45 MS^2 spectra of potential 6:2 FTS biotransformation products. Panel A, 1,2,2,3,3,4,4,4-octafluorobutan-1-ol ($C_4H_2F_8O$, m/z 216.98912); Panel B, $C_7H_2F_8$ (m/z 236.99543).

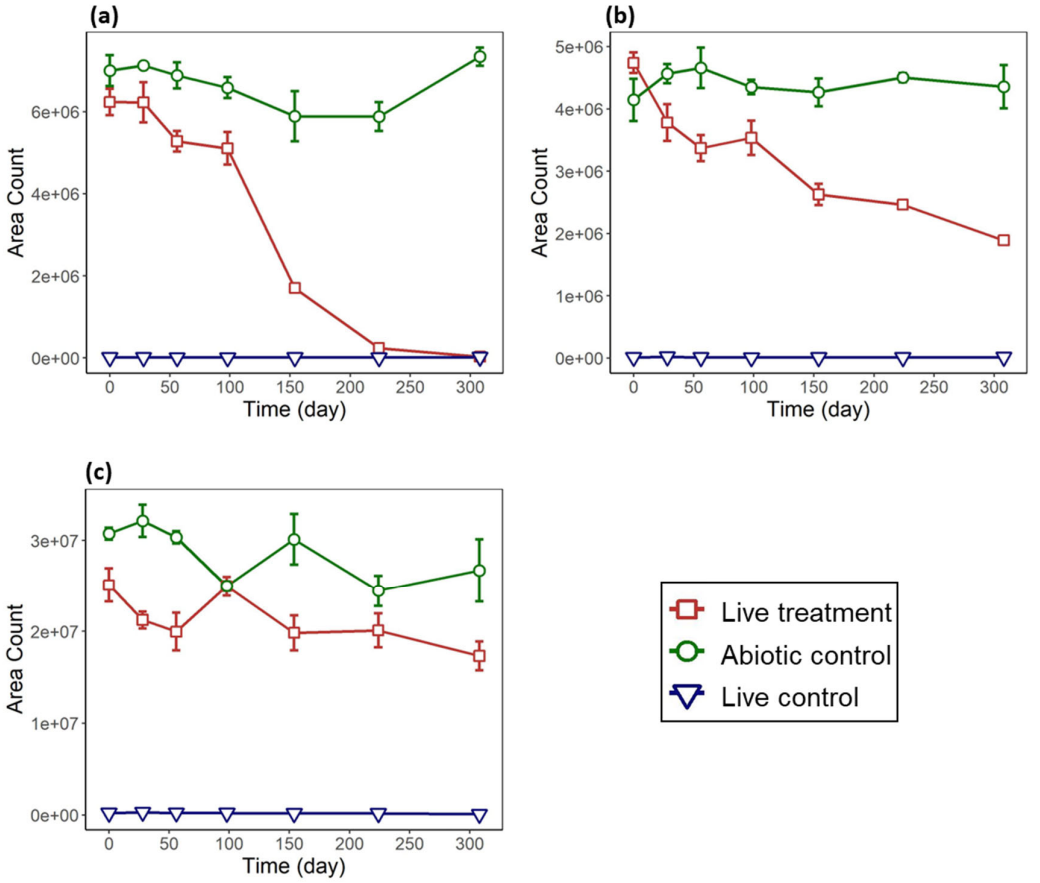


Figure A.46 Change of peak areas (mean value and standard error of three technical replicate) along with time (308 days) for **TAmPr-FASA** homologues with different perfluoroalkyl chain length (a) n = 4, (b) n = 5, (c) n =6. All these compounds were identified only in ESI+ mode.

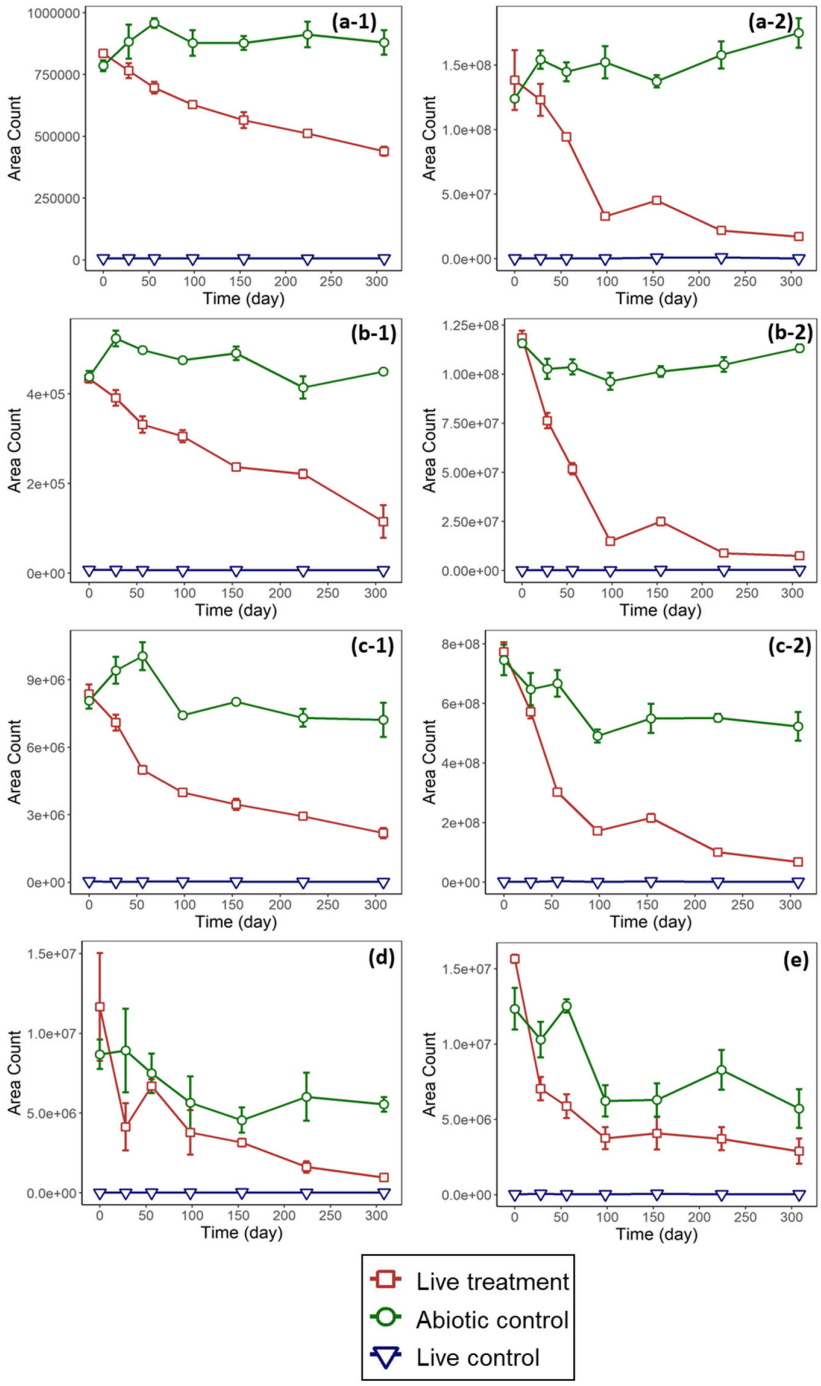


Figure A.47 Change of peak areas (mean value and standard error of three technical replicate) along with time (308 days) for **AmPr-FASA** homologues with different perfluoroalkyl chain length (a-1) n = 4, ESI-, (a-2) n = 4, ESI+; (b-1) n = 5, ESI-, (b-2) n = 5, ESI+; (c-1) n =6, ESI-, (c-2) n = 6, ESI+; (d) n = 7, ESI+; (e) n = 8, ESI+.

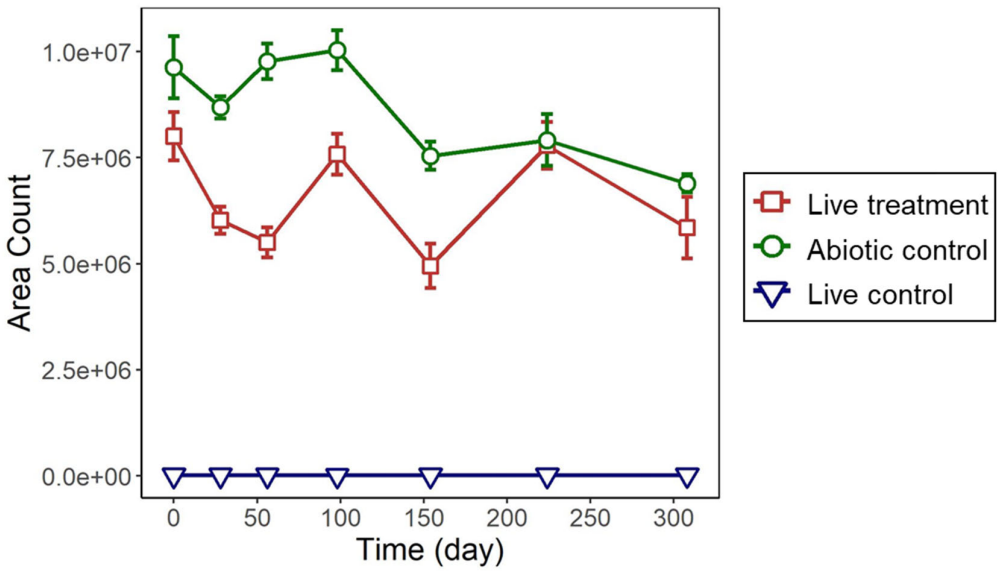


Figure A.48 Change of peak areas (mean value and standard error of three technical replicate) along with time (308 days) for **CEt-AmPr-FASA-PrA** homologue with perfluoroalkyl chain length n = 4, identified in ESI+ mode.

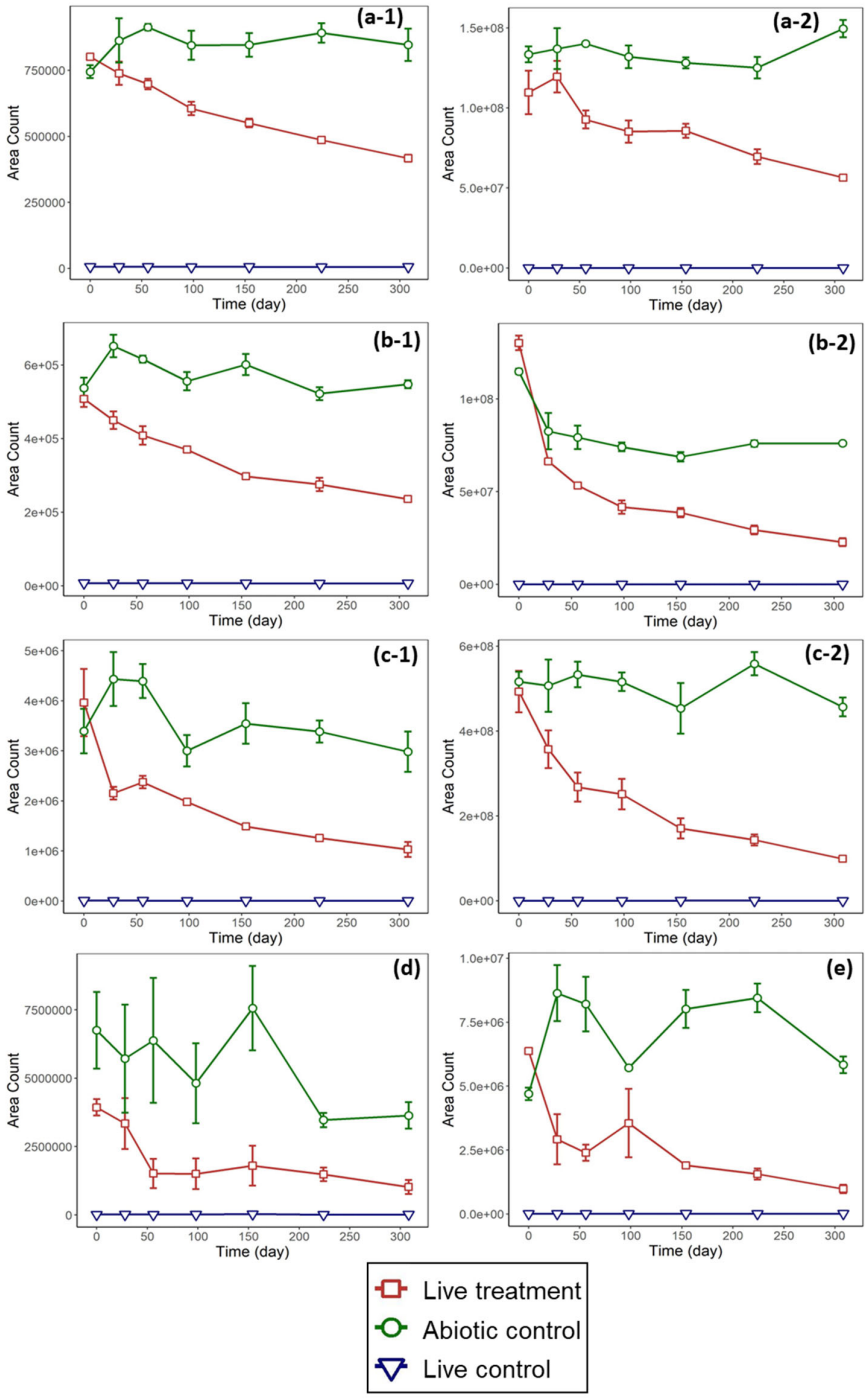


Figure A.49 Change of peak areas (mean value and standard error of three technical replicate) along with time (308 days) for **AmPr-FASA-PrA/TAmPr-FASA-AA** homologues with different perfluoroalkyl chain length (a-1) n = 4, ESI-, (a-2) n = 4, ESI+; (b-1) n = 5, ESI-, (b-2) n = 5, ESI+; (c-1) n = 6, ESI-, (c-2) n = 6, ESI+; (d) n = 7, ESI+; (e) n = 8, ESI+.

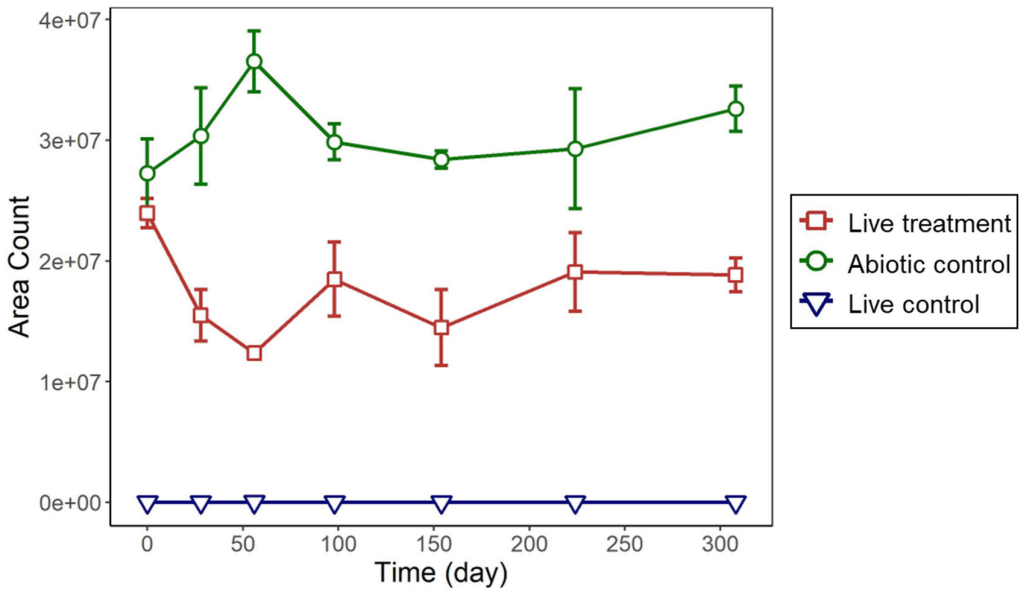


Figure A.50 Change of peak areas (mean value and standard error of three technical replicate) along with time (308 days) for **6:2 FTAB** identified in ESI+ mode.

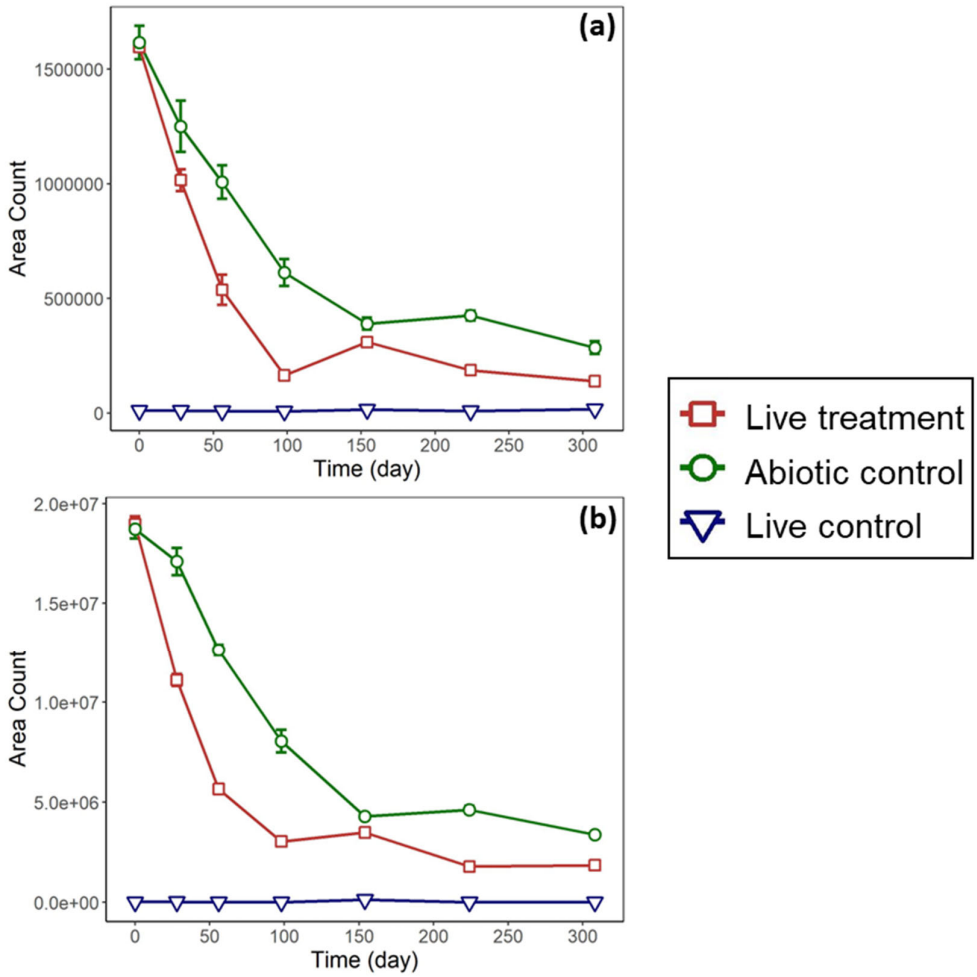


Figure A.51 Change of peak areas (mean value and standard error of three technical replicate) along with time (308 days) for **AmPr-FAAd** different with perfluoroalkyl chain length (a) n = 6 and (b) n = 7.

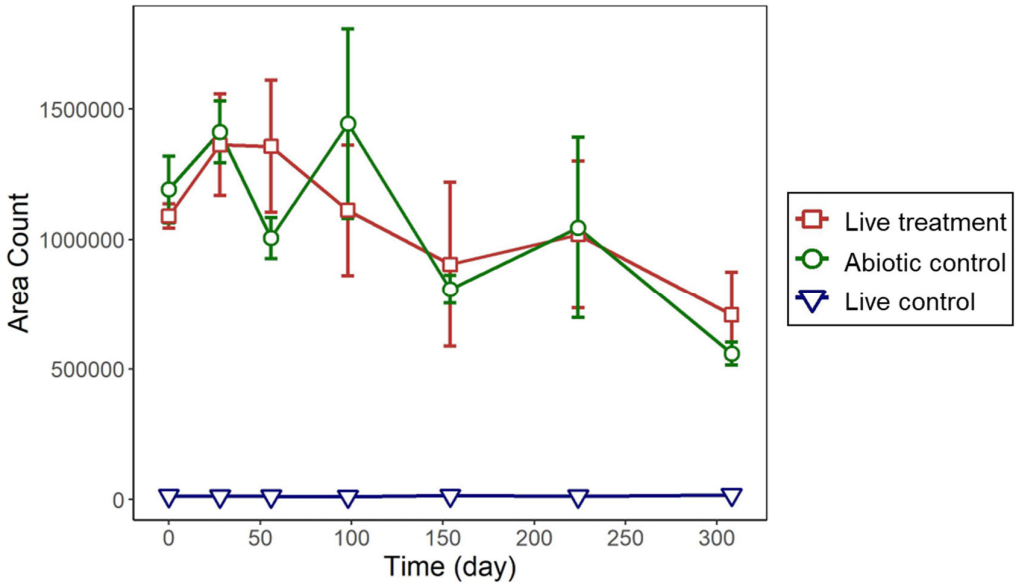


Figure A.52 Change of peak areas (mean value and standard error of three technical replicate) along with time (308 days) for **CEt-AmPr-FAAd** with perfluoroalkyl chain length n = 7 identified in ESI+ mode.

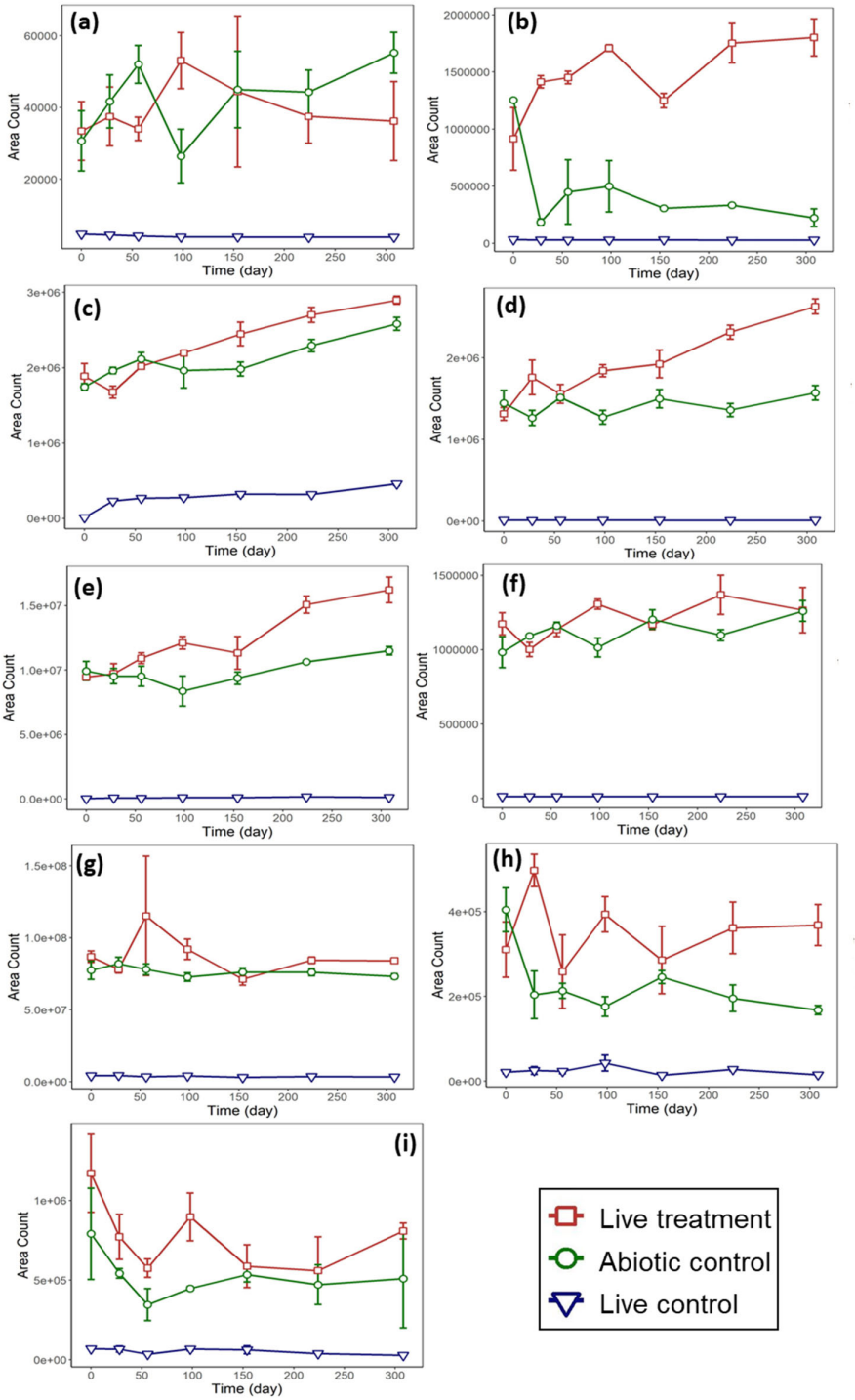


Figure A.53 Change of peak areas (mean value and standard error of three technical replicate) along with time (308 days) for **PFSA** homologues with different perfluoroalkyl chain length (a) n = 2, (b) n = 3, (c) n = 4, (d) n = 5, (e) n = 6, (f) n = 7, (g) n = 8, (h) n = 9, and (i) n = 10. All the homologues were identified in ESI- mode.

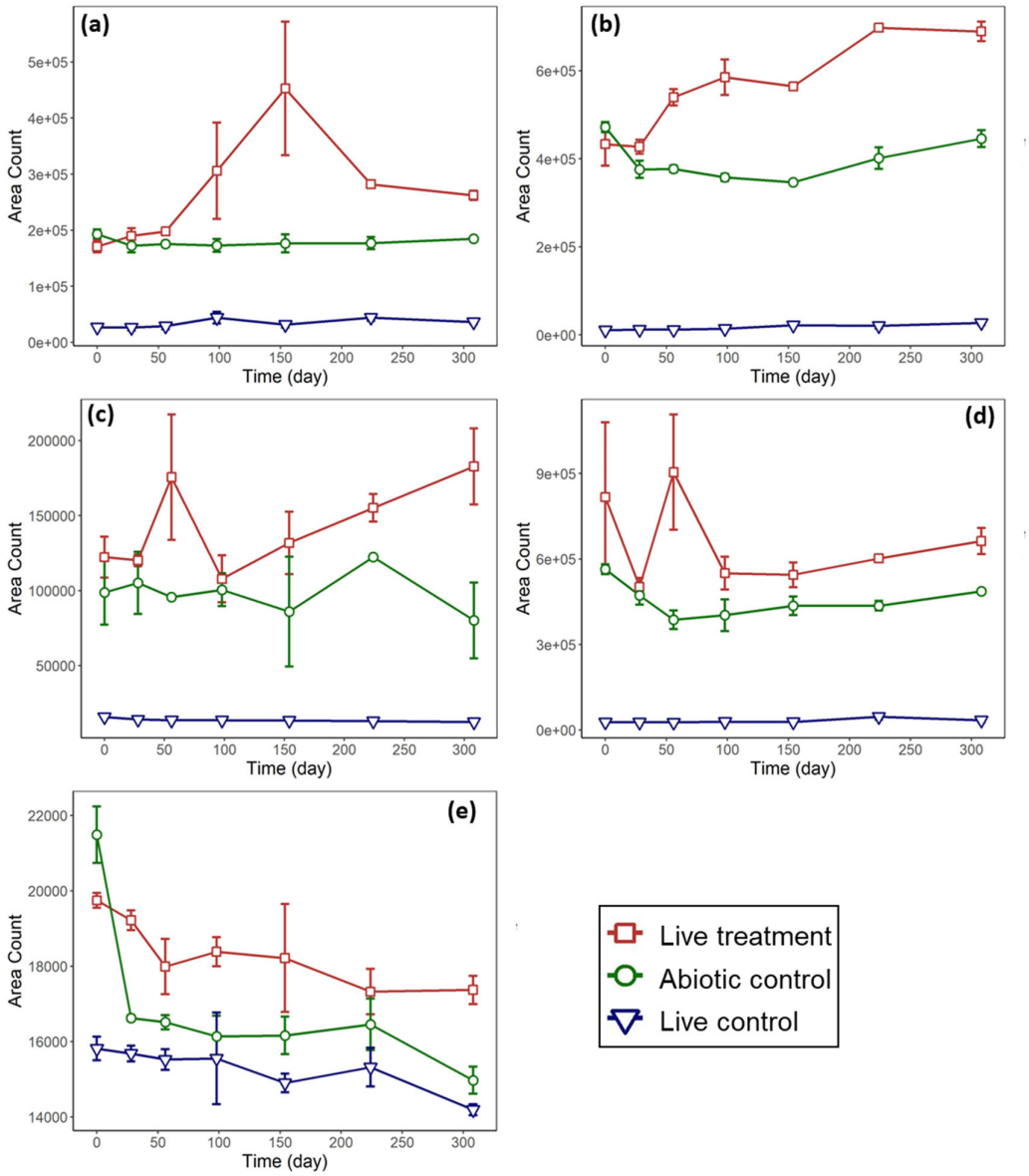


Figure A.54 Change of peak areas (mean value and standard error of three technical replicate) along with time (308 days) for **PFCA** homologues with different perfluoroalkyl chain length (a) n = 4, (b) n = 5, (c) n = 6, (d) n = 7, and (e) n = 9. All the homologues were identified in ESI- mode.

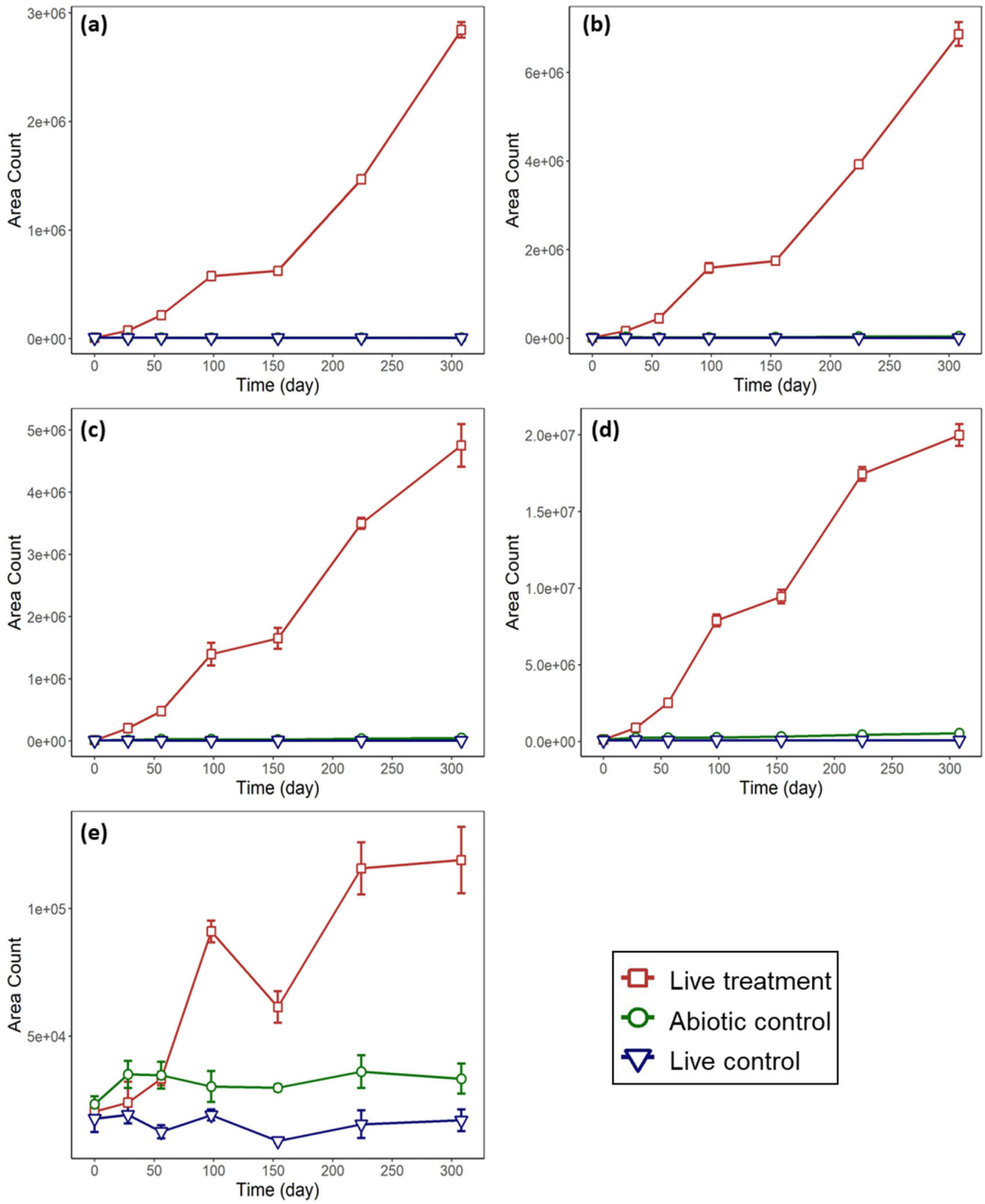


Figure A.55 Change of peak areas (mean value and standard error of three technical replicate) along with time (308 days) for **FASA** homologues with different perfluoroalkyl chain length (a) n = 3, (b-1) n = 4, (c) n = 5, (d) n = 6, and (e) n = 8. All the homologues were identified in ESI- mode.

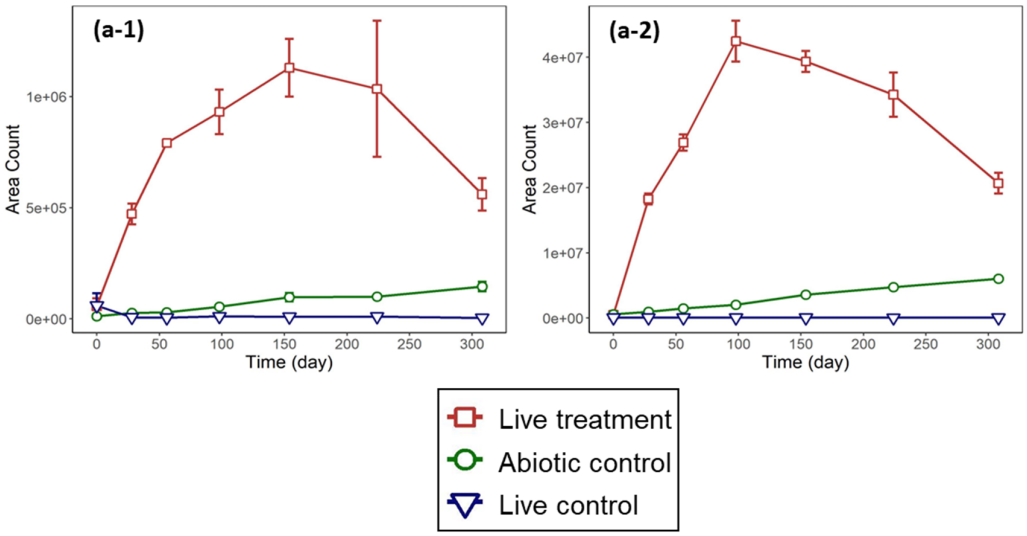


Figure A.56 Change of peak areas (mean value and standard error of three technical replicate) along with time (308 days) for **M-AmPr-FASA** with perfluoroalkyl chain length n = 6 identified in (a-1) ESI- mode and (a-2) ESI+ mode.

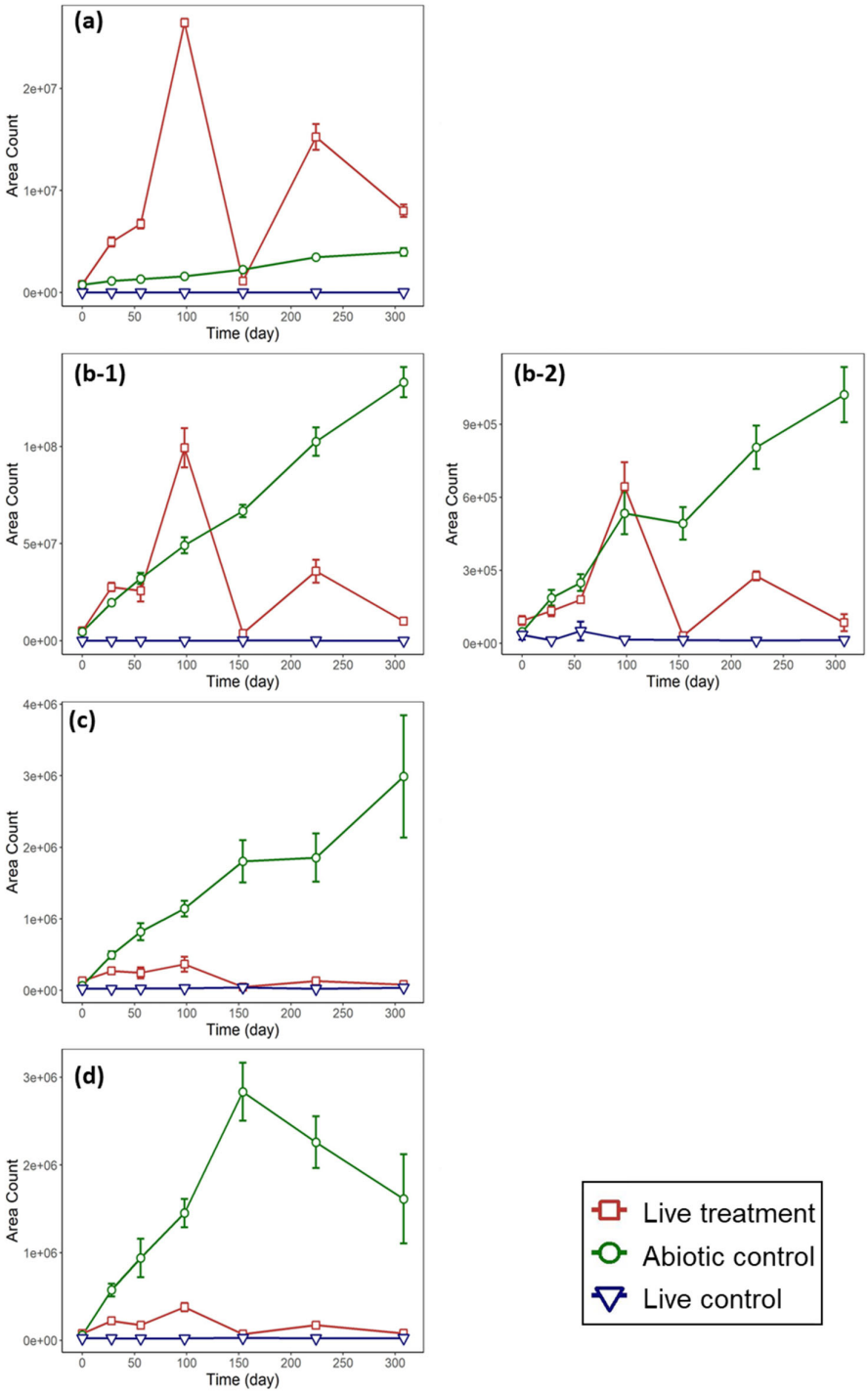


Figure A.57 Change of peak areas (mean value and standard error of three technical replicate) along with time (308 days) for **OAmPr-FASA** homologues with different perfluoroalkyl chain length (a) n = 4, (b-1) and (b-2) n = 6, (c) n = 7, and (d) n = 8. Except for (b-1) identified in ESI- mode, others were all identified in ESI+ mode.

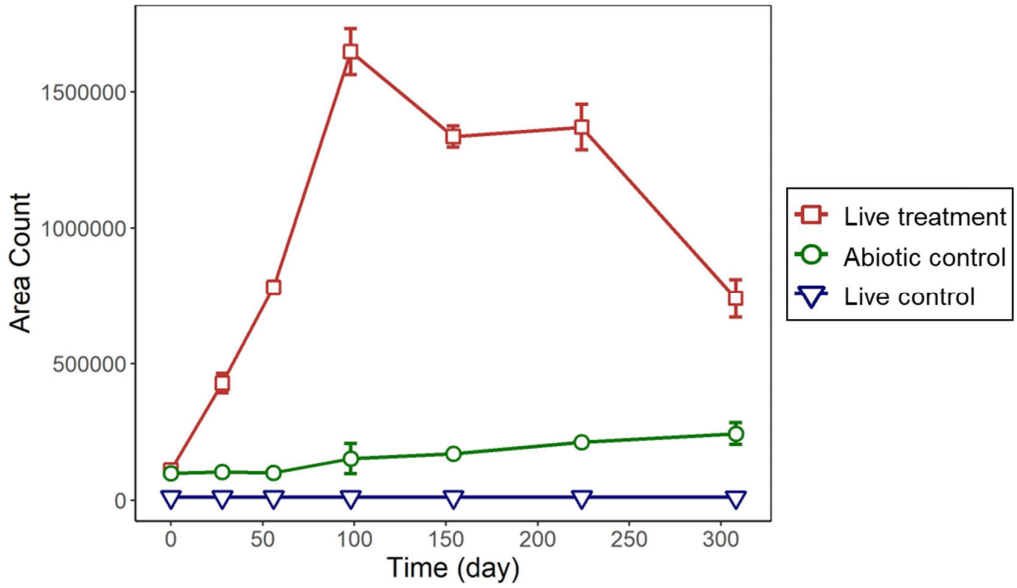


Figure A.58 Change of peak areas (mean value and standard error of three technical replicate) along with time (308 days) for **N-MeFASAA** with perfluoroalkyl chain length n = 6 identified in ESI- mode.

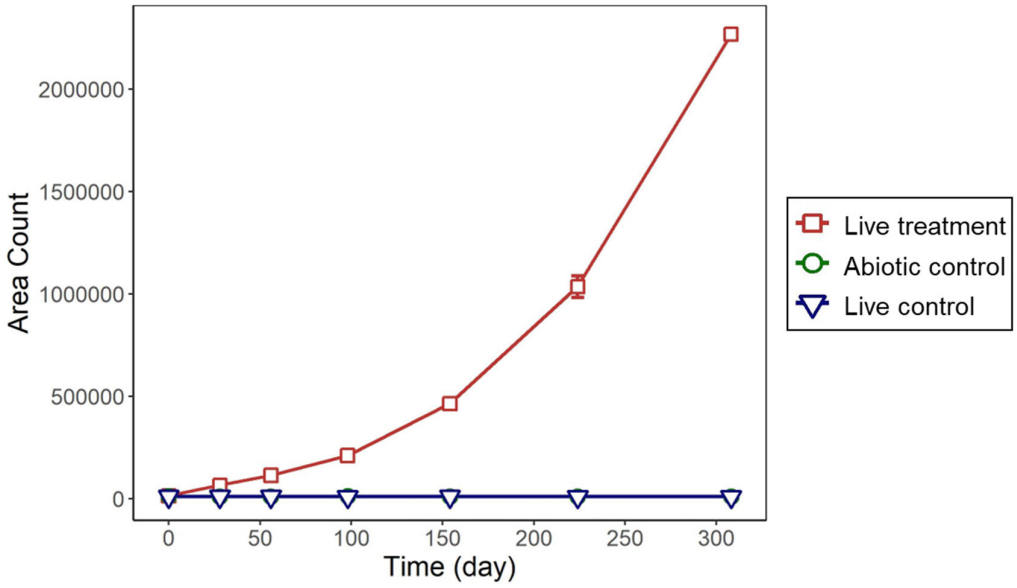


Figure A.59 Change of peak areas (mean value and standard error of three technical replicate) along with time (308 days) for **N-EtFASAA** with perfluoroalkyl chain length n = 6 identified in ESI- mode.

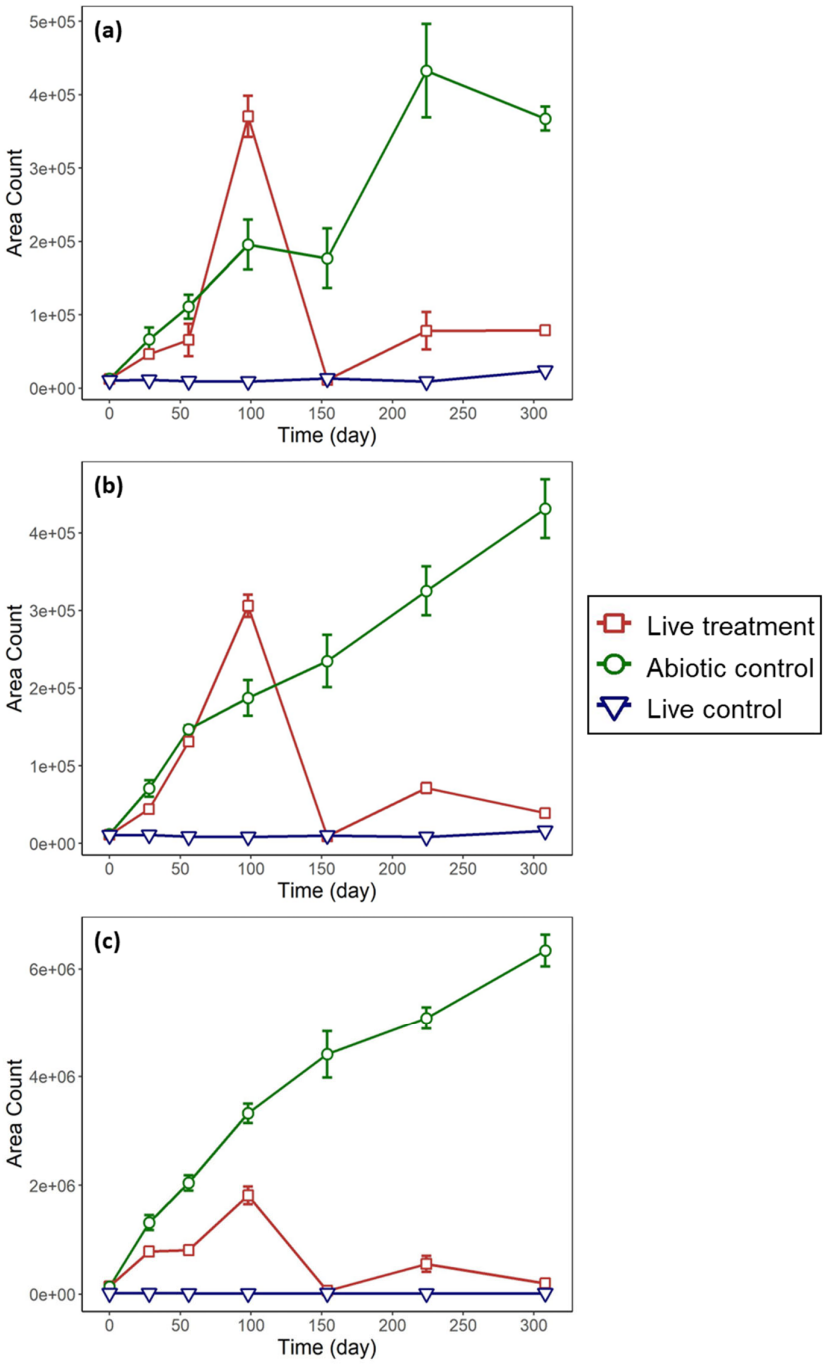


Figure A.60 Change of peak areas (mean value and standard error of three technical replicate) along with time (308 days) for **OAmPr-FAAd** homologues with different perfluoroalkyl chain length (a) n = 5, (b) n = 6, and (c) n = 7. All the homologues were identified in ESI+ mode.

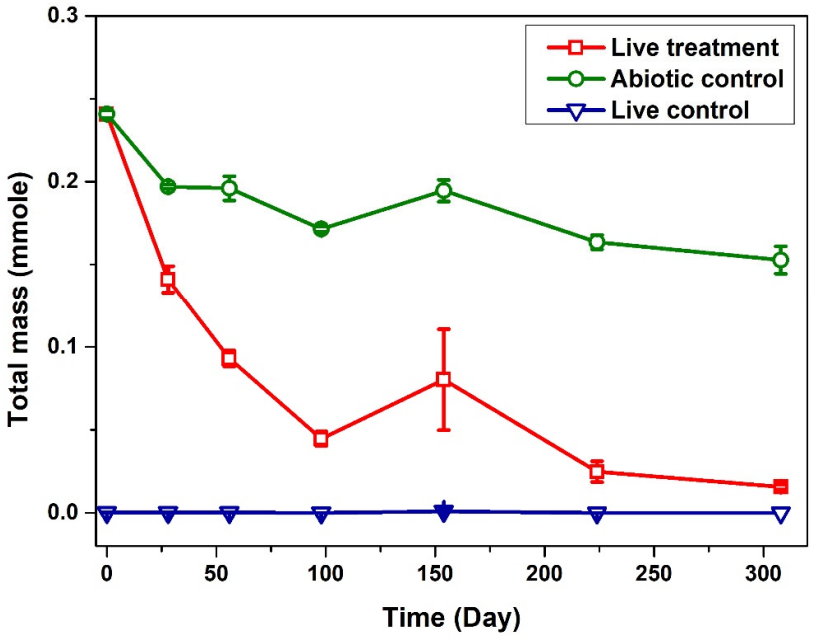


Figure A.61 Change of total mass (nanomole) over time (308 days) for C_6 homologue of AmPr-FASA based on LC-MS analysis. The red, green, and blue symbols/lines represent the live treatment, abiotic control, and live control, respectively. Error bar represents one standard deviation of replicates.

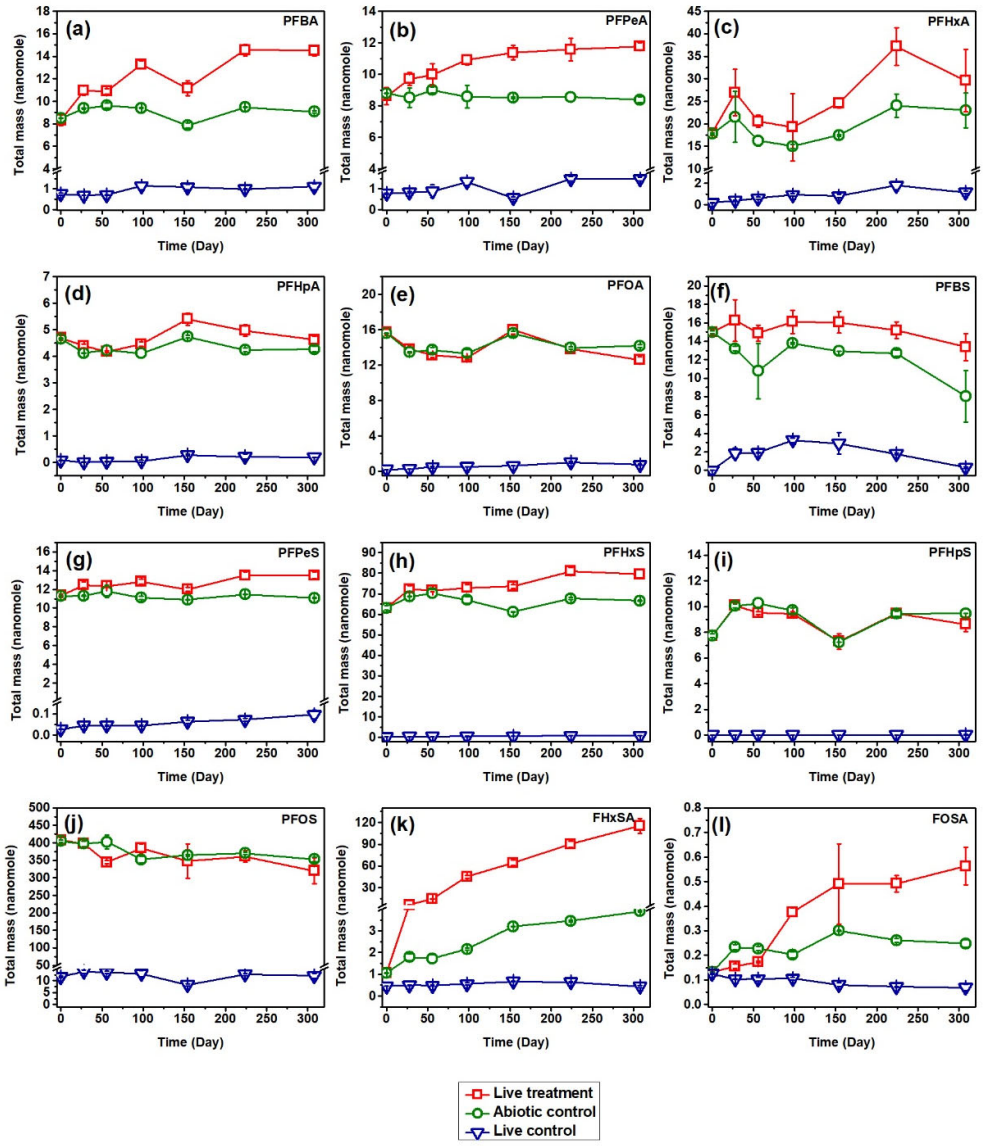


Figure A.62 Change of total mass (nanomole) over time (308 days) for homologues in PFCAs, PFSAs, and FASAs with available analytical standards based on LC-MS analysis: (a) PFBA, (b) PFPeA, (c) PFHxA, (d) PFHpA, (e) PFOA, (f) PFBS, (g) PFPeS, (h) PFHxS, (i) PFHpS, (j) PFOS, (k) FHxSA, and (l) FOSA. Error bar represents one standard deviation of replicates.

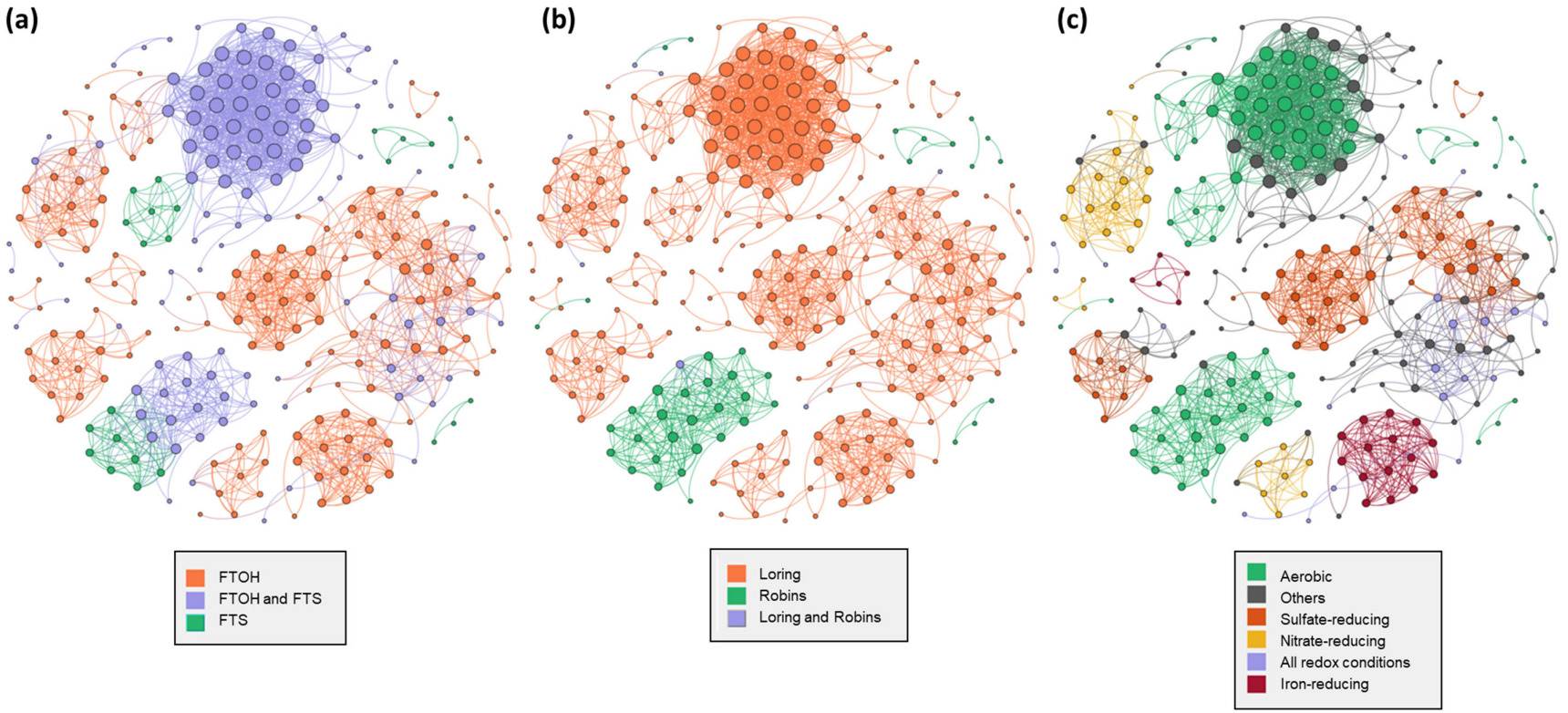


Figure A.63 Microbial co-occurrence networks in fluorotelomer contaminated soils under different redox conditions (constructed networks). An edge (connection) between nodes (ASVs) indicates a strong and significant correlation between two nodes. The size of each node is proportional to the number of connections (degree). The nodes are colored according to (a) contaminant added externally, (b) soil, and (c) redox condition maintained during the experiments.

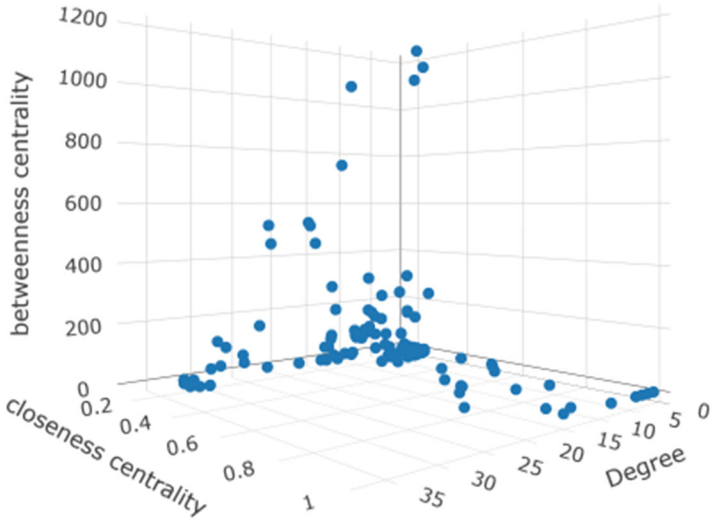


Figure A.64 The node distribution in the Degree-Closeness centrality-Betweenness centrality space.

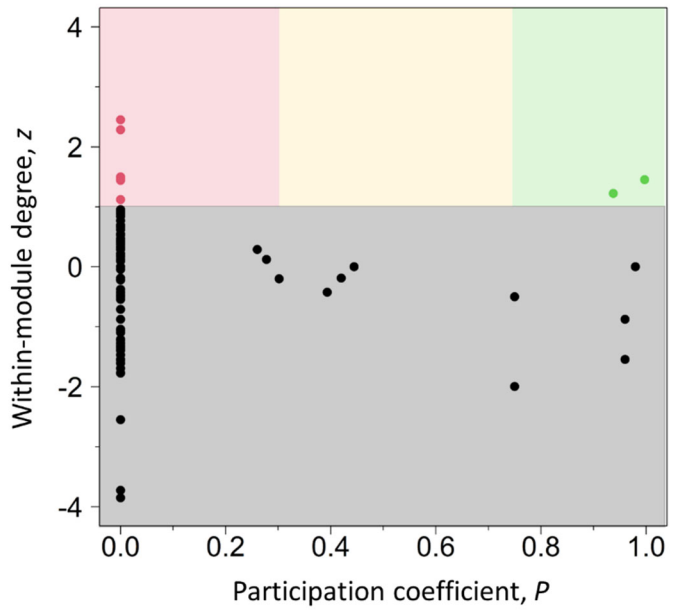


Figure A.65 The node positions and regions of roles in the z–P parameter space. The nodes in the bottom region are peripheral nodes, or non-hubs, ($z < 0.9$); the nodes in the top left region are modular hubs ($z \geq 0.9$, $P \leq 0.30$); the nodes in the top middle region are connector hubs ($z \geq 0.9$, $0.30 < P \leq 0.75$); and the nodes in the top right region are network hubs ($z \geq 0.9$, $P > 0.75$).

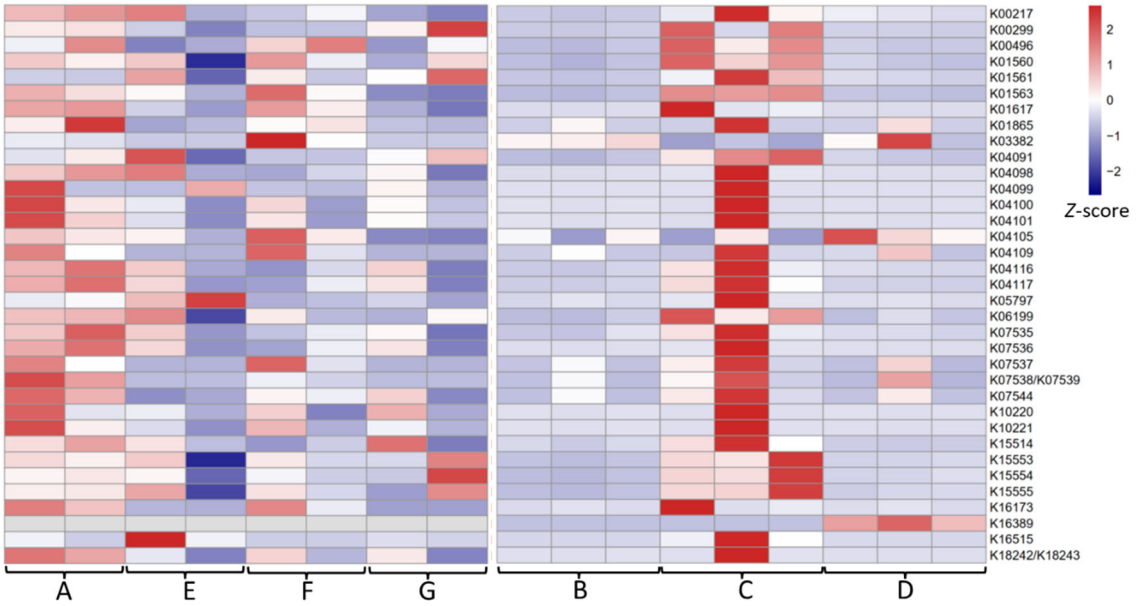


Figure A.66 Heatmap of selected functional gene abundances predicted by PICRUSt2 in different treatments of microcosm experiments. The left panel are from 4 sets of aerobic microcosms and there are 2 columns for each set (left column: live treatment with fluorotelomer added; right column: control without fluorotelomer). A and E, 8:2 FTOH, Loring soil and Robins soil, respectively; F and G, 6:2 FTS, Loring soil and Robins soil, respectively. The right panel are from 3 sets of anerobic microcosms with 3 columns for each set (left: live treatment with fluorotelomer and lactate added as extra electron donor and carbon source to mimic biostimulation; middle column: live treatment with fluorotelomer and only diethylene glycol monobutyl ether as external electron donor and caron source to mimic natural attenuation; right column: control without fluorotelomer). B, C, and D, 8:2 FTOH, Loring soil, under nitrate-, sulfate-, and iron-reducing conditions, respectively. The values of gene abundance were normalized (Z-score) and colored from red to blue to indicate high-to-low relative abundances.

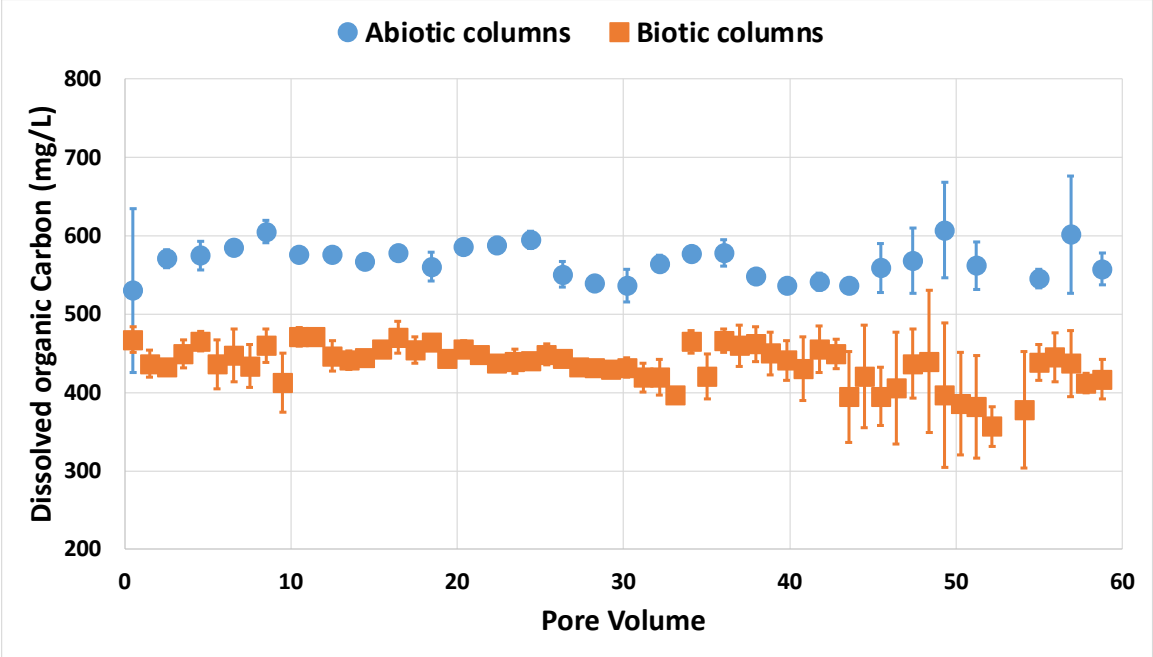


Figure A.67 Concentrations of dissolved organic carbon (DOC) in the effluent samples collected from abiotic and biotic columns.

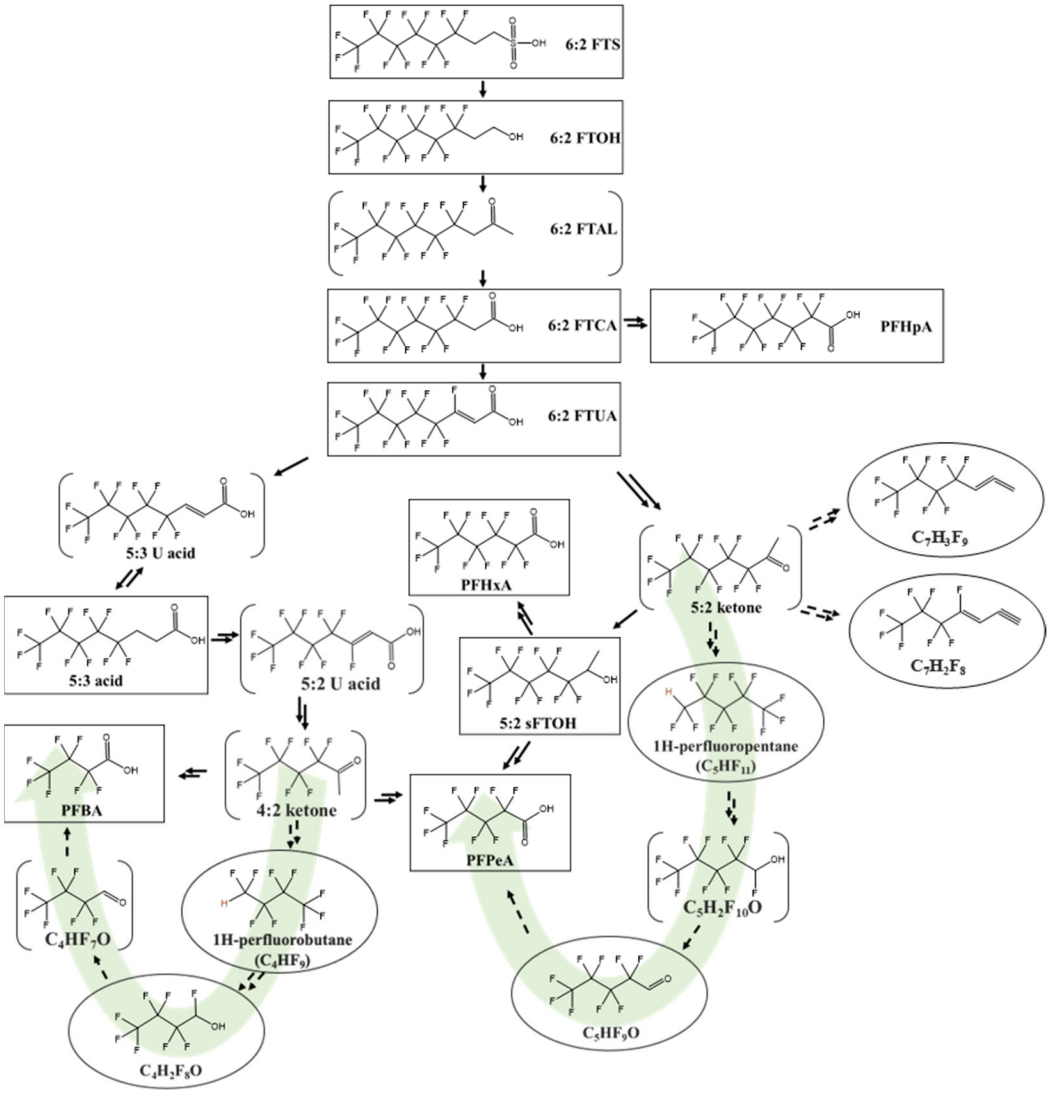


Figure A.68 Aerobic biotransformation pathways of 6:2 FTS in AFFF-impacted soils proposed in the previous study [332]. The compounds in the rectangular boxes were detected by LC-MS/MS analysis, and the compounds in the oval boxes were identified using non-targeted LC-HRMS analysis. The compounds in the brackets are proposed transformation products. The solid arrows represent the biotransformation steps expected to occur based on the present and previous studies. The dashed arrows represent the proposed reactions that may occur. The double arrows represent multiple enzymatic steps involved. The two large, curved arrows in green illustrate the proposed "fluorotelomer ketone to PFCA" pathway which elucidate the formation process of PFCAs.

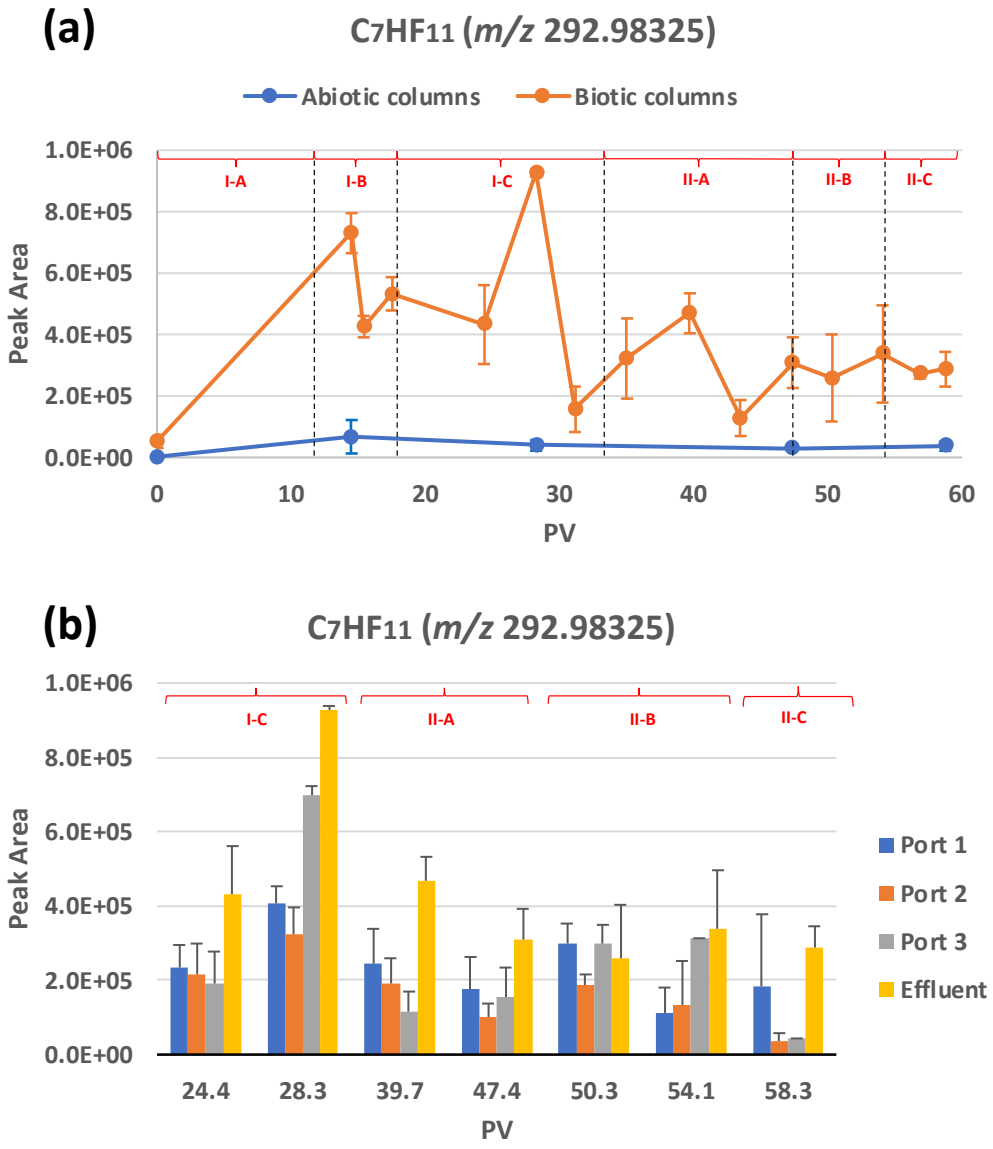


Figure A.69 The peak areas of extracted ion chromatograms of C_7HF_{11} (*m/z* 292.98325) in (a) abiotic and biotic column effluent, and (b) side-port and effluent samples from biotic columns during the column experiments.

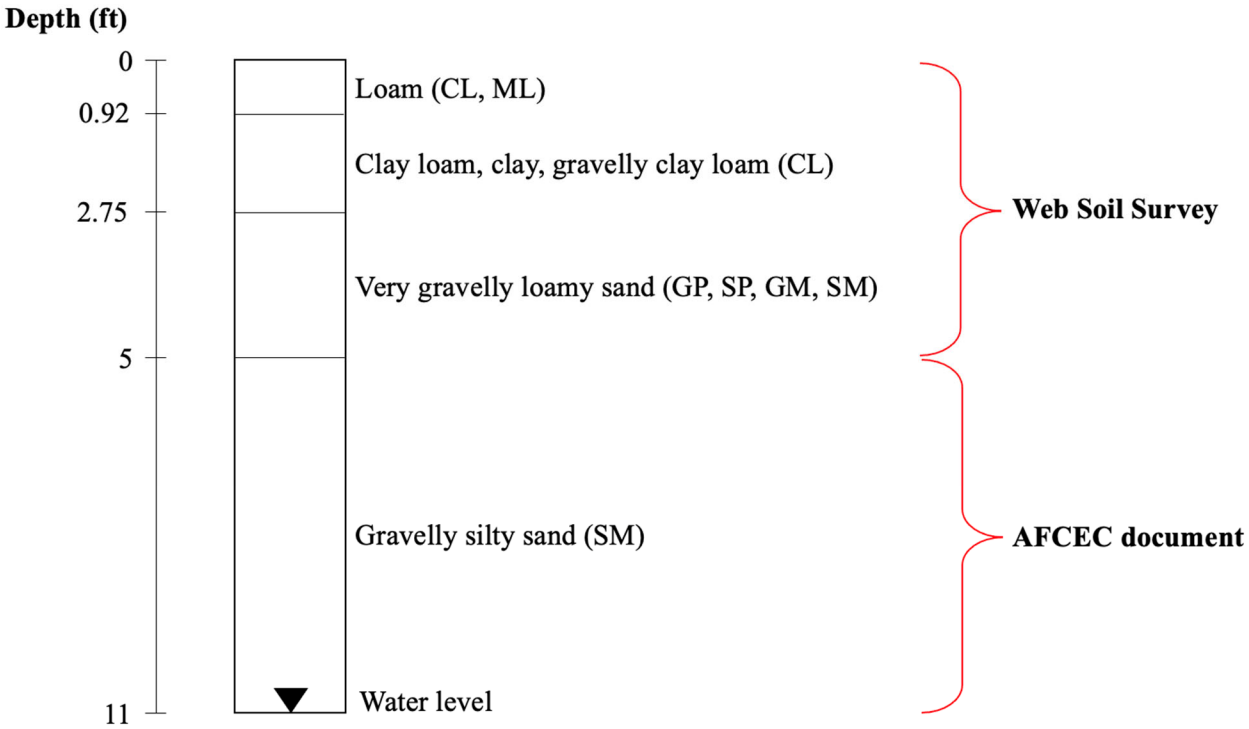


Figure A.70 Wright-Patterson Scenario 1.

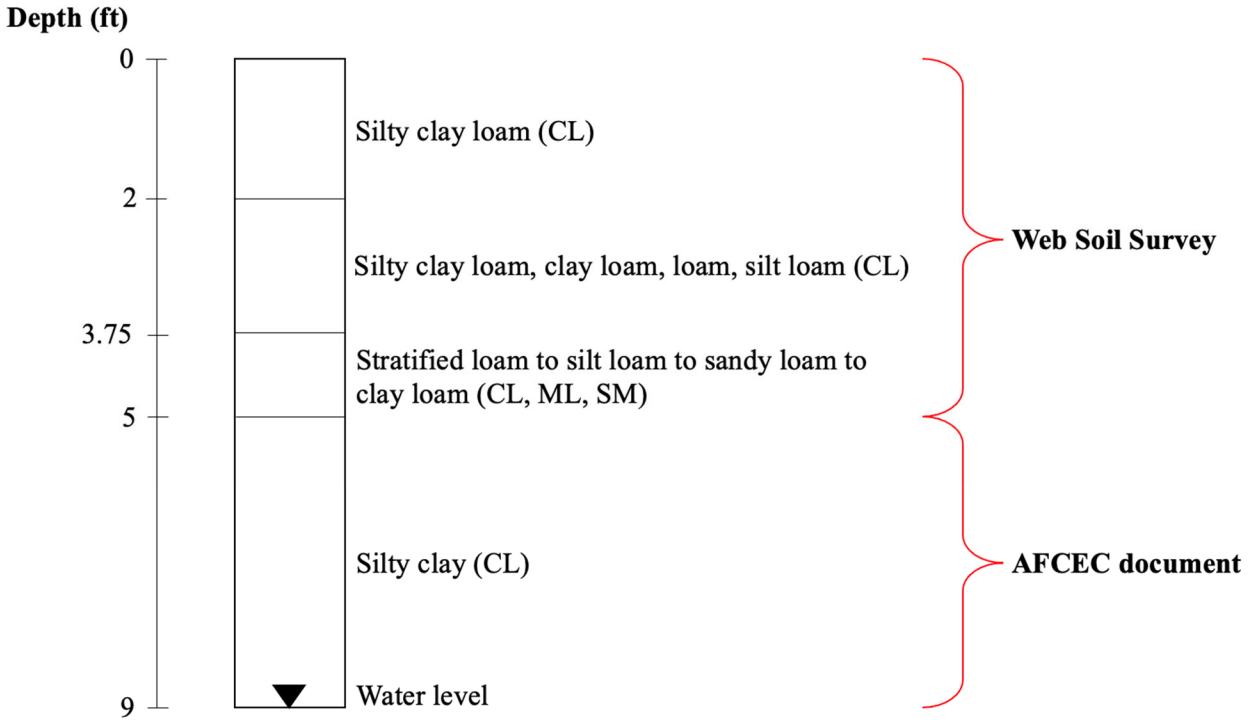


Figure A.71 Wright-Patterson Scenario 2.

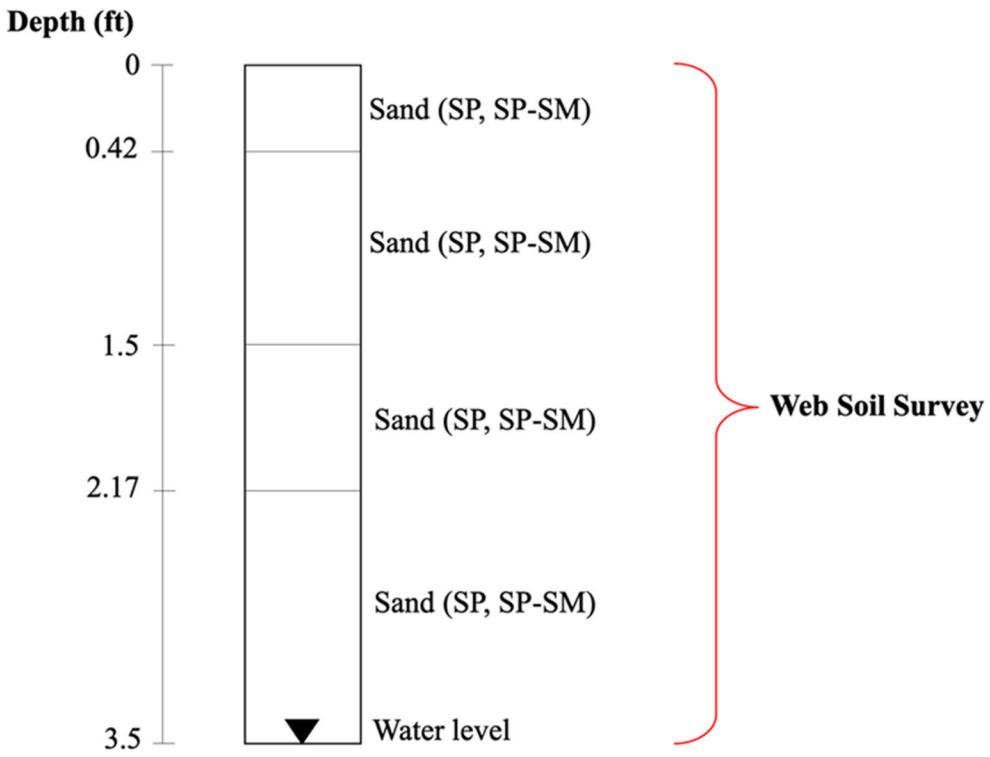


Figure A.72 Tyndall Scenario.

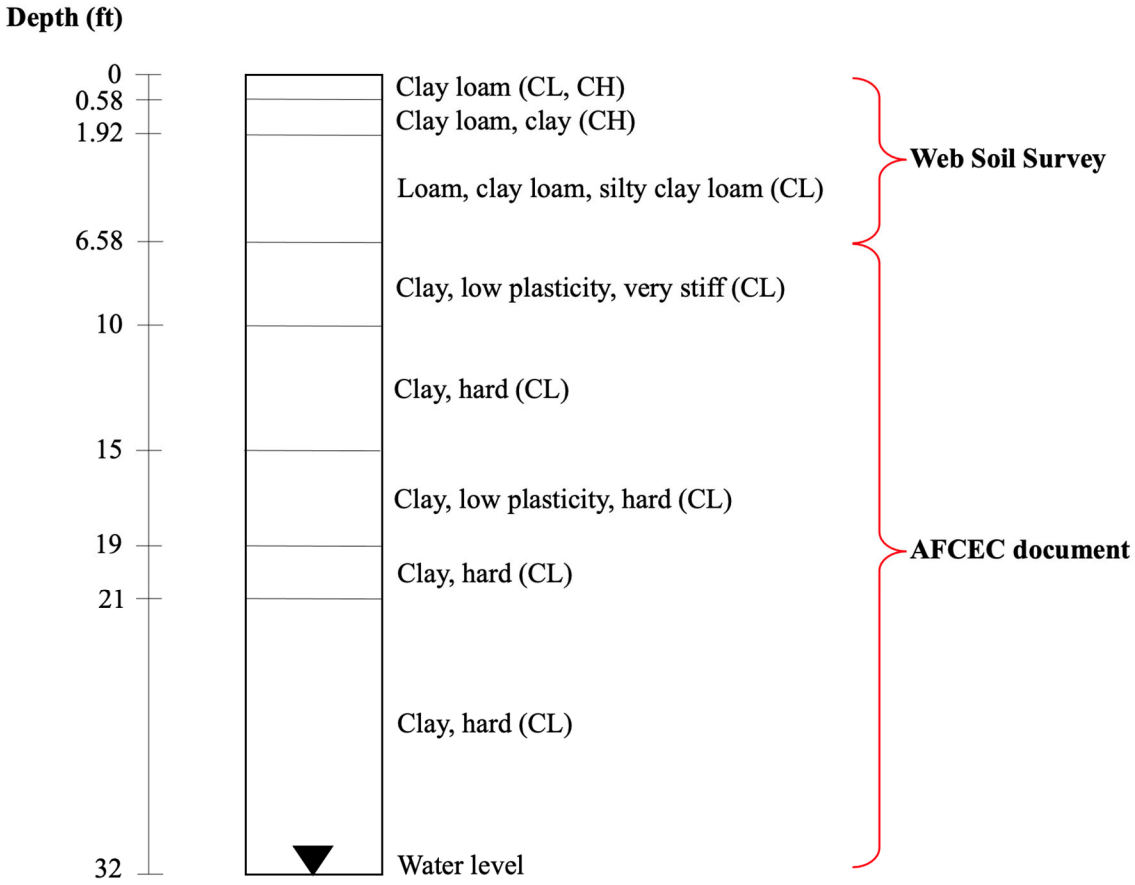


Figure A.73 Ellsworth Scenario.

Appendix B: List of Scientific/Technical Publications

B.1 Peer-Reviewed Papers

Yan, P., S. Dong, K. Manz, M. Woodcock, C. Liu, M. Mezzari, L. Abriola, K. Pennell and N. Capiro. 2022. Aerobic Biotransformation of 6:2 Fluorotelomer Sulfonate in Soils from Two Aqueous Film-Forming Foam (AFFF)-Impacted Sites, submitted to *Environ Sci & Technol*.

Dong, S., Yan, P.F., Liu, C., Manz, K.E., Mezzari, M.P., Abriola, L.M., Pennell, K.D. and Cápiro, N.L., 2023. Assessing aerobic biotransformation of 8: 2 fluorotelomer alcohol in aqueous film-forming foam (AFFF)-impacted soils: Pathways and microbial community dynamics. *Journal of Hazardous Materials*, 446, p.130629.; https://doi.org/10.1016/j.jhazmat.2022.130629

Yan, P.F., Dong, S., Manz, K.E., Liu, C., Woodcock, M.J., Mezzari, M.P., Abriola, L.M., Pennell, K.D. and Cápiro, N.L., 2022. Biotransformation of 8: 2 fluorotelomer alcohol in soil from aqueous film-forming foams (AFFFs)-impacted sites under nitrate-, sulfate-, and iron-reducing conditions. *Environmental Science & Technology*, 56(19), pp.13728-13739.; https://pubs.acs.org/doi/abs/10.1021/acs.est.2c03669

Liao, S., Arshadi, M., Woodcock, M.J., Saleeba, Z.S., Pinchbeck, D., Liu, C., Cápiro, N.L., Abriola, L.M. and Pennell, K.D., 2022. Influence of residual nonaqueous-phase liquids (NAPLs) on the transport and retention of perfluoroalkyl substances. *Environmental Science & Technology*, 56(12), pp.7976-7985.; https://doi.org/10.1021/acs.est.2c00858

Liao, S., Saleeba, Z., Bryant, J.D., Abriola, L.M. and Pennell, K.D., 2021. Influence of aqueous film forming foams on the solubility and mobilization of non-aqueous phase liquid contaminants in quartz sands. *Water Research*, 195, p.116975.; https://doi.org/10.1016/j.watres.2021.116975

Costanza, J., Abriola, L.M. and Pennell, K.D., 2020. Aqueous film-forming foams exhibit greater interfacial activity than PFOA, PFOS, or FOSA. *Environmental Science & Technology*, 54(21), pp.13590-13597; https://doi.org/10.1021/acs.est.0c03117

Arshadi, M., Costanza, J., Abriola, L.M. and Pennell, K.D., 2020. Comment on "uptake of poly- and perfluoroalkyl substances at the air–water interface". *Environmental Science & Technology*, 54(11), pp.7019-7020.; https://dx.doi.org/10.1021/acs.est.0c01838

Costanza, J., Arshadi, M., Abriola, L.M. and Pennell, K.D., 2019. Accumulation of PFOA and PFOS at the Air–Water Interface. *Environmental Science & Technology Letters*, 6(8), pp.487-491; https://pubs.acs.org/doi/full/10.1021/acs.estlett.9b00355.

B.2 Presentations/Posters:

Abriola, L.M., Cápiro N.L., Pennell, K.D., Phelan, T.J., Christ, J.A., Costanza, J., Dong, S., Yan, P., Liu, C., and Arshadi, M. Development and Laboratory Validation of Mathematical Modeling Tools for Prediction of PFAS Transformation, Transport, and Retention in AFFF Source Areas, *2019 SERDP and ESTCP Symposium*, Washington, DC, December 2019.

Abriola, L.M., Laboratory and Modeling Investigation of PFAS Transformation, Transport, and Retention in AFFF Source Areas, *SERDP and ESTCP Webinar* Series #116, July 23, 2020.

Abriola, L.M., Investigations of Per- and Polyfluoroalkyl Substance (PFAS) Transport and Retention in Soils, Invited Seminar, *MIT Parson's Laboratory*, October 2, 2020.

Abriola, L.M., Cápiro N.L., Pennell, K.D., Phelan, T.J., Christ, J.A., Costanza, J., Dong, S., Yan, P., Liu, C., and Arshadi, M., Development and Laboratory Validation of Mathematical Modeling Tools for Prediction of PFAS Transformation, Transport, and Retention in AFFF Source Areas, *2020 SERDP and ESTCP Symposium*, November 2020.

Christ, J.A., PFAS Concerns: An Introduction and Look at Ongoing and Future DoD Sponsored Research. *Society of American Military Engineers (SAME)*. Mobile Post Monthly Meeting, 2021.

Dong, S. Aerobic biotransformation of 8:2 fluorotelomer alcohol in AFFF-impacted soil, *Remediation Technology Summit*, 2021.

Yan, P. Anaerobic biotransformation of 8:2 FTOH in soil from AFFF-impacted sites under nitrate-, sulfate-, and iron-reducing conditions, *Remediation Technology Summit*, 2021.

Liao, S., Interactions of Aqueous Film Forming Foams with Non-aqueous Phase Liquids, *Remediation Technology Summit*, 2021.

Arshadi, M., S. Liao, C. Liu, K.D. Pennell, L.M. Abriola, Investigating the Influence of Non-Linear Interfacial Partitioning on Aqueous Film Forming Foam (AFFF) Transport and Retention in the Unsaturated Zone, Interpore 13th Annual Meeting, online, 2021.

Yan, P. Biotransformation of 6:2 fluorotelomer sulfonate in AFFF-impacted soil under oxic and anoxic conditions. *ACS Fall 2021*. Atlanta, GA, August 22-26, 2021.

Dong, S. Biotransformation of 8:2 FTOH in AFFF-impacted soils under different redox conditions. *ACS Fall 2021*. Atlanta, GA, August 22-26, 2021.

Abriola, L.M., Cápiro N.L., Pennell, K.D., Phelan, T.J., Christ, J.A., Costanza, J., Dong, S., Yan, P., Liu, C., and Arshadi, M., Development and Laboratory Validation of Mathematical Modeling Tools for Prediction of PFAS Transformation, Transport, and Retention in AFFF Source Areas, *2021 SERDP and ESTCP Symposium*, November 2021.

Abriola, L.M. and M. Arshadi. 2022. Recent Advances in Modeling PFAS Transport and Retention in AFFF Source Areas, *PFAS-∑-IT International PFAS Summit*, April 4-5, 2022, Tuebingen, Germany (virtual invited platform presentation).

Arshadi, M. S. Liao, C. Liu, K.D. Pennell, and L.M. Abriola. 2022. Experimental and Modeling Investigations on Accumulation of PFAS at the Air and NAPL-Water Interface. 12th International Conference on the Remediation of Chlorinated and Recalcitrant Compounds, Palm Springs, CA.

Yan, P.F., Dong, S., Manz, K.E., Woodcock M., Liu C., Pennell, K.D., Cápiro, N.L. Biotransformation of 6:2 fluorotelomer sulfonate in AFFF-impacted soil: microcosm and column experiments. *AEESP 2022 Environmental Engineering at the Confluence*. June 28-30 St. Louis, MO.

Cápiro, N.L., S. Dong, PF. Yan, C. Liu, K. E. Manz, M. J. Woodcock, and K. D. Pennell. Biotransformation of 8:2 Fluorotelomer Alcohol and 6:2 Fluorotelomer Sulfonate Using Microbial Communities from AFFF-Impacted Soils. American Chemical Society. Chicago, IL, August 21-25, 2022.

Cápiro, N.L. S. Dong, P. Yan, C. Liu, K. E. Manz, M. J. Woodcock, and K. D. Pennell. Biotransformation of 8:2 fluorotelomer alcohol using microbial communities from AFFF-impacted soils. (Invited). International CleanUp Conference. Adelaide, SA. September 11-14, 2022.

Dong, S., PF. Yan, M.P. Mezzari, L.M. Abriola, K.D. Pennell, and N.L. Cápiro. Microcosm Sample Sequencing Data for Fluorotelomer Biotransformation by Soil Microorganisms. RemTEC & Emerging Contaminants Summit. Westminster, CO, October 4-6, 2022

Christ, J.A. PFAS Contamination – Translating Research to Practice. ASCE Knowledge and Learning Webinar. Presented on 13 Dec 2022.

Abriola, L.M., Modeling the Transport and Retention of 'Emerging' Surface-Active Contaminants In the Vadose Zone, Keynote Address, Presented at the 10th International Conference on Water Resources and Arid Environments, Riyadh, Saudi Arabia, December 26-27, 2022 (virtual presentation).

Yan, P.F., Dong, S., Woodcock M., Manz, K.E., Abriola, L.M., Pennell, K.D., Cápiro, N.L. Biotransformation and microbial community dynamics of 6:2 fluorotelomer sulfonate in water-saturated one-dimensional flow-through columns. Presented at AEESP 2023, Boston, MA, June 20-23, 2023.

Garza-Rubalcava, U.J., Klevan C., Xia S., Greenley C., Pennell K., Abriola L. Competitive Adsorption at the Air-Water Interface Influences PFAS Transport in Unsaturated Porous Media. Presented at AEESP 2023, Boston, MA, June 20-23, 2023.

Appendix C: Other Supporting Materials

C.1 Per- and Polyfluoroalkyl Substances (PFAS) Analyte List

Project: ER18-1149

PI: Linda Abriola

Date: January 7, 2019

The following list of PFAS compounds are being quantitated using a Waters Ultra Performance Liquid Chromatograph (UPLC) connected to a Waters Xevo TQ-S tandem quadrupole mass spectrometer (MS/MS) located in the School of Engineering at Brown University.

Compound Name	Abbreviation	CAS	Labelled Surrogate
Perfluorobutanoic acid	PFBA	375-22-4	MPFBA
Perfluoropentanoic acid	PFPeA	2706-90-3	M5PFPeA
Perfluorohexanoic acid	PFHxA	307-24-4	M5PFHxA
Perfluoroheptanoic acid	PFHpA	375-85-9	M4PFHpA
Perfluorooctanoic acid	PFOA	335-67-1	M8PFOA
Perfluorononanoic acid	PFNA	375-95-1	M9PFNA
Perfluorodecanoic acid	PFDA	335-76-2	M6PFDA
Perfluoroundecanoic acid	PFUnA	2058-94-8	M7PFUnDA
Perfluorododecanoic acid	PFDoA	307-55-1	MPFDoA
Perfluorotridecanoic acid	PFTriA	72629-94-8	
Perfluorotetradecanoic acid	PFTreA	376-06-7	M2PFTeDA
Perfluorobutanesulfonic acid	PFBS	375-73-5	M3PFBS
Perfluoropentanesulfonic acid	PFPeS	2706-91-4	
Perfluorohexanesulfonic acid	PFHxS	355-46-4	M3PFHxS
Perfluoroheptanesulfonic acid	PFHpS	375-92-8	
Perfluorooctanesulfonic acid	PFOS	1763-23-1	M8PFOS
Perfluorononanesulfonic acid	PFNS	68259-12-1	
Perfluorodecanesulfonic acid	PFDS	335-77-3	
Perfluorooctanesulfonamide	PFOSA	754-91-6	M8PFOSA
Fluorotelomer sulfonic acid 4:2	FtS 4:2	757124-72-4	M24:2FTS
Fluorotelomer sulfonic acid 6:2	FtS 6:2	27619-97-2	M26:2FTS
Fluorotelomer sulfonic acid 8:2	FtS 8:2	39108-34-4	M88:2 FTS

2-(N-Ethylperfluorooctanesulfonamido) acetic acid	NEtFOSAA	2991-50-6	D3-N-EtFOSAA
2-(N-Methylperfluorooctanesulfonamido) acetic acid	NMeFOSAA	2355-31-9	D3-N-MeFOSSA

C.2 Standard Operating Procedures for PFAS Sample Collection Preparation, and Analysis

1. Sample Collection

Samples will be collected from laboratory-scale batch, column, and aquifer cell systems where technical grade PFAS precursors and transformation products have been introduced. The samples will be analyzed to determine concentrations of PFAS in aqueous and solid phases.

a. Equipment/Supplies

2 mL polypropylene (PP) centrifuge tubes

15 mL PP centrifuge tubes

3 mL PP syringe with rubber plunger and stainless-steel needle

50 mL and 100 mL high-density polyethylene (HDPE) bottles

Optima grade methanol (Fisher Scientific)

Isotopically labelled PFAS from Wellington Laboratories Inc. (Ontario, Canada)

b. Collection Process

Aqueous effluent samples will be collected with a fraction collector during column experiments in 15 mL PP centrifuge tubes. Additional aqueous samples will be collected from batch and aquifer cell systems using a 3 mL PP syringe with stainless steel needle and placed into 2 mL PP centrifuge tubes. Solid (soil) samples will be collected from batch, column, and aquifer cell systems and transferred into HDPE bottles.

c. Decontamination Procedures

Syringes will be used once and discarded, or they will be rinsed with Optima grade methanol followed by ultrapure water before collecting each sample. The PP centrifuge tubes and HDPE bottles will be used once and discarded.

d. QC Samples

The isotopically-labelled PFAS extraction standards paired with each PFAS introduced into each experiment (e.g., M8-PFOA when PFOA is present) will be added to each sample at the time of collection and prior to extraction and will serve as an internal standard to track the extraction process (i.e., extracted internal standard). The instrument response to the labelled PFAS will be used show recoveries are between 50% and 150% of added amounts (Table B-15, DOD/DOE QSM 5.1.1). If recoveries are outside these limits, the sample result will be discarded.

A method blank (MB) will be collected using the procedures described in section 1.b. during each sampling event from either the uncontaminated background solution or solids being utilized in the experiment. A matrix spike (MS) and a matrix spike duplicate (MSD) will be prepared with each batch of samples by adding a

low-level PFAS standard to the background solution or solids being used in each experiment. The MS and MSD will be used to show that the % recovery is within 70% to 130%, and the relative percent difference (RPD) is less than 30% (Table B-15, DOD/DOE QSM 5.1.1).

e. Sample Preservation, Shipping, and Hold Times

The PP centrifuge tubes and HDPE bottles will be placed in a 4 °C refrigerator immediately after sample collection. Aqueous samples will be analyzed within 28 days of collection. Solid samples will be extracted within 14 days of collection and extracts will be analyzed within 28 days of extraction.

2. Sample Preparation

Aqueous samples used for PFAS analysis will be prepared by collecting a small volume from each PP centrifuge tube and diluting this in a 2 mL autosampler vial to a final 80:20 water to methanol mix. Solid phase extraction (SPE) of the aqueous sample will not be employed as there will be insufficient volume of aqueous sample available (e.g., 250 mL). Solids samples for PFAS analysis will be extracted using methanol.

a. Equipment/Supplies

Optima grade methanol (Fisher Scientific)

HPLC grade water (Honeywell Burdick & Jackson)

2 mL glass autosampler vials

Pipette with PP tips

Centrifuge

b. Preparation Technique

For aqueous samples, each PP centrifuge tube containing an aqueous sample will be centrifuged at 4,000 rpm for 5 min to remove suspended solids. Thereafter, a 100 µL aliquot will be transferred from each PP centrifuge tube by pipette with PP tip and placed into a 2 mL glass autosampler vial. The 100 µL aliquot will be diluted by adding 700 µL of HPLC grade water and 200 µL of Optima grade methanol. Each sample will be vortexed for 15 seconds to ensure mixing.

For solid samples, a 5 to 10 mL volume of methanol will be added to each HDPE bottle containing a solid sample and then sonicated in a water bath for 20 minutes. Following sonication, a 100 µL sample of the supernatant will be collected from each bottle by pipette with PP tip and transferred to a 2 mL glass autosampler vial. The 100 µL sample will be diluted by adding 800 µL of HPLC grade water and 100 µL of Optima grade methanol. Each sample will be vortexed for 15 seconds.

c. Sample QC

Laboratory control spike (LCS) consisting of low-level PFAS added to an uncontaminated 80:20 water to methanol mix will be prepared with each batch of samples.

3. Sample Analysis

Samples consisting of 80:20 water to methanol will be analyzed for PFAS concentration by UPLC connected to a triple-quad MS. Aqueous samples will be analyzed by Ion Chromatography for fluoride.

a. Equipment/Supplies

Waters Acquity ultra performance liquid chromatograph (UPLC) connected to a Waters Xevo tandem quadrupole (TQ)-S micro mass spectrometer (MS).

Dionex DX500 modular ion chromatography system

Isotopically labelled PFAS from Wellington Laboratories, Inc

PFAS analytical standards from Sigma-Aldrich

SPEX CertiPrep standards for fluoride

b. Instrument Conditions

Analyte separation will be achieved with a Waters BEH C-18 column (1.7 µm dia., 2.1 × 50 mm) operated at a flow rate of 0.4 mL/min with an eluent gradient consisting of 10 mM ammonium acetate in water. Large volume injection (250 µL) will be employed to improve sensitivity. The Waters TQ-S micro will be operated in the negative ion electrospray mode with desolvation gas (nitrogen) flow at 450 L/hr and temperature of 55°C. Cone gas flow of 30 mL/min and collision gas (argon) flow at 0.2 mL/min. The source temperature will be maintained at 150°C and the electrospray capillary voltage at 0.6 kV. The multiple reaction monitoring (MRM) conditions for select PFAS are given in Table 1. These conditions will be optimized during the mass spectrometer tuning.

c. Analytical Standards and Calibration Procedure

The LC-MS/MS system will be mass calibrated and tuned using internal standards and the calibration and tune will be checked prior to each use. The mass spectra will be acquired at greater than 10 scans across each chromatographic peak.

The initial calibration (ICAL) will be performed using at least 5 concentrations of isotopically labeled PFOA and PFOS from Wellington Laboratories. These concentrations will cover the range of expected concentrations. No unknown samples will be analyzed until the initial calibration has achieved the following criteria:

- Signal to noise ratio of 10:1 for all quantification ions
- The %RSD of the response factors for all analytes is less than 20%
- The calibration curve is linear with an $r^2 = 0.99$

The initial calibration will be verified (ICV) using unlabeled PFAS analytical standards obtained from Sigma-Aldrich. After the initial calibration, the calibration samples will be analyzed prior to and after analyzing unknown samples to serve as a continuing calibration verification (CCV) where concentrations must be within 30% of the calibration standards.

d. Instrument Cleanliness

Two checks will be used to verify instrument cleanliness as well as to flush out the system after analyzing samples with high PFAS concentrations. One check is a zero-volume injection (i.e., instrument blank) to determine if there is carry-over on the UPLC column and the other check is the analysis of a PFAS-free 80:20 water to methanol to evaluate carry-over on the LC injection needle. These two checks will be performed after every 10 to 12 sample are analyzed to determine cleanliness of the instrument.

If the check results after a batch of 10 to 12 samples have significantly elevated PFAS concentrations compared to the other check results ($P > 0.05$) then the batch of samples will be analyzed again with additional blank checks included to determine which sample is causing carry-over.

e. Level of Quantitation (LOQ)

The LOQ is the smallest concentration that produces a quantitative result and will be set at or above the lowest ICAL concentration standard. The precision and bias of the LOQ will be established and verified quarterly by analyzing seven replicate standards prepared at the proposed LOQ and confirming the analysis results are within 50% of the lower and upper recovery limits.

Table 1 – Waters TQ-S Multiple Reaction Monitoring Conditions for Carboxylates								
Compound	Internal Standard	Molecular Ion	Cone Voltage (V)	Collision Energy (V)	Quant. Ion (m/z)	Cone Voltage (V)	Collision Energy (V)	Confirmation Ion (m/z)
PFBA	[$^{13}C_4$] PFBA	213	30	5	169	--	--	--
PFPeA	[$^{13}C_5$] PFPeA	263	35	5	219	--	--	--
PFHxA	[$^{13}C_5$] PFHxA	313	40	5	269	40	20	119
PFHpA	[$^{13}C_4$] PFHpA	363	20	7	319	20	16	169
PFOA	[$^{13}C_8$] PFOA	413	15	8	369	15	8	169
PFNA	[$^{13}C_9$] PFNA	463	8	10	419	8	14	219
PFDA	[$^{13}C_6$] PFDA	513	11	10	469	6	18	219
PFUnA	[$^{13}C_7$] PFUnA	563	13	12	519	20	18	269
PFDoA	[$^{13}C_2$] PFDoA	613	15	12	569	4	26	169
PFTriA	--	663	15	13	619	--	--	--
PFTreA	[$^{13}C_2$] PFTreA	713	14	13	669	--	--	--
Internal Standards								
[$^{13}C_4$] PFBA		217	10	8	172	--	--	--
[$^{13}C_5$] PFPeA		268	35	5	223	--	--	--
[$^{13}C_5$] PFHxA		318	19	7	273	--	--	--
[$^{13}C_4$] PFHpA		367	20	8	322	--	--	--
[$^{13}C_8$] PFOA		421	15	8	376	--	--	--
[$^{13}C_9$] PFNA		472	10	11	427	--	--	--
[$^{13}C_6$] PFDA		519	11	11	474	--	--	--
[$^{13}C_7$] PFUnA		570	13	12	525	--	--	--
[$^{13}C_2$] PFDoA		615	4	11	570	--	--	--
[$^{13}C_2$] PFTreA		715	20	14	670	--	--	--

Table 2 – Waters TQ-S Multiple Reaction Monitoring Conditions for Sulfonates								
Compound	Internal Standard	Molecular Ion	Cone Voltage (V)	Collision Energy (V)	Quant. Ion (m/z)	Cone Voltage (V)	Collision Energy (V)	Confirmation Ion (m/z)
PFBS	[$^{13}C_3$] PFBS	299	2	30	80	2	30	99
PFPeS	--	349	15	32	80	15	32	99
PFHxS	[$^{13}C_3$] PFHxS	399	10	34	80	10	32	99
PFHpS	--	449	14	38	80	14	38	99
PFOS	[$^{13}C_8$] PFOS	499	4	50	80	4	40	99
PFNS	--	549	10	43	80	10	43	99
PFDS	--	599	2	55	80	2	48	99
Internal Standards								
[$^{13}C_3$] PFBS		302	15	25	99	--	--	--
[$^{13}C_3$] PFHxS		402	25	25	99	--	--	--
[$^{13}C_8$] PFOS		507	15	32	99	--	--	--

Table 3 – Waters TQ-S Multiple Reaction Monitoring Conditions for Sulfonamide, Telomer Sulfonates, and Sulfonamidoacetatic Acids								
Compound	Internal Standard	Molecular Ion	Cone Voltage (V)	Collision Energy (V)	Quant. Ion (m/z)	Cone Voltage (V)	Collision Energy (V)	Confirmation Ion (m/z)
PFOSA	[$^{13}C_8$] FOSA	498	16	32	78	--	--	--
FtS 4:2	[$^{13}C_2$] FtS 4:2	327	5	17	307	5	25	81
FtS 6:2	[$^{13}C_2$] FtS 6:2	427	5	21	407	5	19	81
FtS 8:2	[$^{13}C_2$] FtS 8:2	527	10	26	507	10	35	81
NMeFOSAA	D3MeFOSA	570	5	18	419	5	20	512
NEtFOSAA	D5EtFOSAA	584	5	18	419	5	17	526
Internal Standards								
[$^{13}C_8$] FOSA		506	15	32	78	--	--	--
[$^{13}C_2$] FtS 4:2		329	5	18	309	5	20	81
[$^{13}C_2$] FtS 6:2		429	5	22	409	5	25	81
[$^{13}C_2$] FtS 8:2		529	10	27	509	10	35	81
D3MeFOSAA		573	10	19	419	5	20	515
D5EtFOSAA		589	10	19	419	10	18	531

C.3 Analytical Confirmation Whitepaper

Brown University. November 8, 2022.

C.3.1 Analytical Methodology Overview

PFAS sample analysis is performed in the Pennell laboratory at Brown University using a modified EPA Method 537.1 procedure involving liquid chromatography and mass spectrometry. Samples were split with Battelle Memorial Laboratory (BML) in Norwood, MA to verify the concentrations reported from the targeted analysis performed at Brown. BML is accredited by the National Environmental Laboratory Accreditation Program (NELAP). For this analysis EPA Method 537.1 was used because EPA Draft Method 1633 is not currently run in most commercial laboratories. However, we have implemented EPA draft Method 1633 in our laboratory as described in the SOP document.

In the Pennell laboratory at Brown University, samples are analyzed using a targeted LC-MS/MS method to quantify PFAS compounds. Solid samples undergo extraction using a 50% methanol solution. All samples undergo solid-phase extraction (SPE) with extracts analyzed by a modified EPA Method 537 procedure using liquid chromatography-mass spectrometry. Analyte separation is achieved using a Waters Acquity H-Class ultra-performance liquid chromatograph (UPLC) equipped with a Waters BEH C-18 column with an eluent gradient of ammonium acetate in water and methanol, the same as described in EPA Method 537.1. Quantification of PFAS is achieved using a Waters Xevo tandem quadrupole mass spectrometer (TQ-S Micro) fitted with a Unispray ionization source. The Waters Xevo TQ-S Micro is operated in negative ionization mode using multiple reaction monitoring with unit mass resolution to isolate precursor and product ions, specific to each substance, for quantitation. Mobile phases are prepared from liquid chromatography-mass spectrometry (LC-MS) grade water, methanol, and ammonium acetate. The initial instrument calibration is performed using at least five concentrations of PFAS obtained from Wellington Laboratories, covering the range of expected concentrations. Prior to sample analysis, the initial calibration utilized for targeted analysis must achieve the following criteria:

i. Signal to noise ratio of 10:1 for all quantification ions
ii. Concentration of each analyte calibrator calculated as an unknown, with concentration ≥MRL, and compared against its regression equation, is within ±30% of its true value. For calibrators with concentrations <MRL, ±50% is acceptable
iii. peak asymmetry factors at the mid-level CAL standard between 0.8 and 1.5 at 10% peak height for the first two eluting analytes

A method blank (MB) is included with each analytical batch to demonstrate the experimental systems are free of background PFAS contamination. A matrix spike (MS) and a matrix spike duplicate (MSD) are prepared with each batch of extracts by adding a trace-level PFAS standard to the background solvents or solids used in each experiment. The MS and MSD are used to demonstrate that the percent recovery is within 70 to 130 %, and the relative percent difference (RPD) is less than 30%. When available, isotopically-labelled PFAS extraction standards paired with each PFAS (e.g., M8-PFOA when PFOA is present) analyte are added to sample as an internal standard to monitor the extraction process. Instrument response to the labelled PFAS are used to show recoveries are between 50 and 150 % of the added amounts. If recoveries are outside these limits, the sample result is discarded. The analytical system is currently able to detect over 40 PFAS, precursors, and C-13 labeled standards within a total run time of approximately 20 min.

LC-MRL is verified at least bi-annually for all analytes, and in all matrices, for which data are reported.

Table C.1 Target PFAS Analyte List

Compound Name	Abbreviation	CAS	Labelled Surrogate
Perfluorobutanoic acid	PFBA	375-22-4	MPFBA
Perfluoropentanoic acid	PFPeA	2706-90-3	M5PFPeA
Perfluorohexanoic acid	PFHxA	307-24-4	M5PFHxA
Perfluoroheptanoic acid	PFHpA	375-85-9	M4PFHpA
Perfluorooctanoic acid	PFOA	335-67-1	M8PFOA
Perfluorononanoic acid	PFNA	375-95-1	M9PFNA
Perfluorodecanoic acid	PFDA	335-76-2	M6PFDA
Perfluoroundecanoic acid	PFUnA	2058-94-8	M7PFUnDA
Perfluorododecanoic acid	PFDoA	307-55-1	MPFDoA
Perfluorotridecanoic acid	PFTrDA	72629-94-8	MPFTeDA + MPFDoA
Perfluorotetradecanoic acid	PFTeDA	376-06-7	M2PFTeDA
Perfluorobutanesulfonic acid	PFBS	375-73-5	M3PFBS
Perfluoropentanesulfonic acid	PFPeS	2706-91-4	MPFHxS
Perfluorohexanesulfonic acid	PFHxS	355-46-4	M3PFHxS
Perfluoroheptanesulfonic acid	PFHpS	375-92-8	M8PFOS
Perfluorooctanesulfonic acid	PFOS	1763-23-1	M8PFOS
Perfluorononanesulfonic acid	PFNS	68259-12-1	M8PFOS
Perfluorodecanesulfonic acid	PFDS	335-77-3	M8PFOS
Perfluorododecanesulfonic acid	PFDoS	79780-39-5	M8PFOS
Fluorotelomer sulfonic acid 4:2	FtS 4:2	757124-72-4	M24:2FTS
Fluorotelomer sulfonic acid 6:2	FtS 6:2	27619-97-2	M26:2FTS
Fluorotelomer sulfonic acid 8:2	FtS 8:2	39108-34-4	M28:2 FTS
Perfluorooctanesulfonamide	PFOSA	754-91-6	M8PFOSA
N-methyl perfluorooctanesulfonamide	NMeFOSA	31506-32-8	D3-N-MeFOSA
N-ethyl perfluorooctanesulfonamide	NEtFOSA	4151-50-2	
2-(N-Methylperfluorooctanesulfonamido) acetic acid	NMeFOSAA	2355-31-9	D3-N-MeFOSSA
2-(N-Ethylperfluorooctanesulfonamido) acetic acid	NEtFOSAA	2991-50-6	D3-N-EtFOSAA
N-methyl perfluorooctanesulfonamidoethanol	NMeFOSE	24448-09-7	D7-NMeFOSE
N-ethyl perfluorooctanesulfonamidoethanol	NEtFOSE	1691-99-2	D9-NEtFOSE
Hexafluoropropylene oxide dimer acid	HFPO-DA	13252-13-6	13C3-HFPO-DA
4,8-Dioxa-3H-perfluorononanoic acid	ADONA	919005-14-4	13C3-HFPO-DA
Perfluoro-3-methoxypropanoic acid	PFMPA	377-73-1	13C5-PFPeA
Perfluoro-4-methoxybutanoic acid	PFMBA	863090-98-5	13C5-PFPeA
Nonafluoro-3,6-dioxaheptanoic acid	NFDHA	151772-58-6	13C5-PFHxA
9-Chlorohexadecafluoro-3-oxanonane-1-sulfonic acid	9Cl-PF3ONS	756426-58-1	13C3-HFPO-DA
11-Chloroeicosafluoro-3-oxaundecane-1-sulfonic acid	11Cl-PF3OUdS	763051-92-9	13C3-HFPO-DA
Perfluoro(2-ethoxyethane)sulfonic acid			

3-Perfluoropropyl propanoic acid	PFEESA	113507-82-7	13C5-PFHxA
2H,2H,3H,3H-Perfluorooctanoic acid	3:3FTCA	356-02-5	13C5-PFPeA
3-Perfluoroheptyl propanoic acid	5:3FTCA	914637-49-3	13C5-PFHxA
	7:3FTCA	812-70-4	13C5-PFHxA

C.3.2 Analytical Confirmatory Analysis of Soil Samples

Analytical confirmation with a NELAP-accredited laboratory was conducted for five soil samples collected from Eielson Air Base as part of an ESTCP-funded field project (ER20-5198). The samples were run in the Brown lab on 10/7/2022. Mean concentration values should be within ±30% of confirmatory laboratory values when reported concentrations of analyte are greater than or equal to the limit of quantitation (LOQ) for both laboratories. Comparison of data for 15 PFAS are shown in the Tables 2 through 6 below indicate that concentrations reported by the Brown lab were all within ±20% of confirmatory laboratory (BML) values.

Table C.2 Confirmatory Analysis of Soil Samples (Borehole 2, 0-6" depth)

	BH2-0/6-SO-02		
	BROWN	BML	Difference*
PFBA	<0.462	<2.02	0%
PFPeA	<0.462	<1.01	0%
PFHxA	<0.462	<1.01	0%
PFHpA	<0.462	<1.01	0%
PFOA	<0.462	<1.01	0%
PFNA	<0.462	<1.01	0%
PFDA	<0.462	<1.01	0%
PFUnA	<4.62	<1.01	0%
PFDoA	<4.62	<1.01	0%
PFTrDA	<4.62	<1.01	0%
PFTeDA	<4.62	<2.02	0%
PFBS	<0.462	<1.01	0%
PFPeS	<0.462	<2.02	0%
PFHxS	6.08	7.55	-19.5%
PFOS	18.8	23.1	-18.8%

*If both labs reported below their LOQs, or one lab reported below LOQ while the other reported a value below that LOQ, then 0% difference was recorded.

Table C.3 Confirmatory Analysis of Soil Samples (Borehole 2, 12-18” depth)

	BH2-12/18-SO-02		
	BROWN	BML	Difference*
PFBA	<0.481	<2.31	0%
PFPeA	<0.481	<1.15	0%
PFHxA	<0.481	<1.15	0%
PFHpA	<0.481	<1.15	0%
PFOA	<0.481	<1.15	0%
PFNA	<0.481	<1.15	0%
PFDA	<0.481	<1.15	0%
PFUnA	<4.81	<1.15	0%
PFDoA	<4.81	<1.15	0%
PFTrDA	<4.81	<1.15	0%
PFTeDA	<4.81	<2.31	0%
PFBS	<0.481	<1.15	0%
PFPeS	<0.481	<2.31	0%
PFHxS	1.36	1.30	4.4%
PFOS	4.16	4.49	-7.4%

*If both labs reported below their LOQs, or one lab reported below LOQ while the other reported a value below that LOQ, then 0% difference was recorded.

Table C.4 Confirmatory Analysis of Soil Samples (Borehole 3, 0-6” depth)

	BH3-0/6-SO-02		
	BROWN	BML	Difference*
PFBA	<0.458	<1.97	0%
PFPeA	<0.458	<0.984	0%
PFHxA	<0.458	<0. 984	0%
PFHpA	<0.458	<0. 984	0%
PFOA	<0.458	<0. 984	0%
PFNA	<0.458	<0. 984	0%
PFDA	<0.458	<0. 984	0%
PFUnA	<4.58	<0. 984	0%
PFDoA	<4.58	<0. 984	0%
PFTrDA	<4.58	<0. 984	0%
PFTeDA	<4.58	<1.97	0%
PFBS	<0.458	<0. 984	0%
PFPeS	<0.458	<1.97	0%
PFHxS	3.75	3.13	19.7%
PFOS	11.6	10.7	8.7%

*If both labs reported below their LOQs, or one lab reported below LOQ and the other reported a value below that LOQ, then 0% difference was recorded

Table C.5 Confirmatory Analysis of Soil Samples (Borehole 3, 12-18” depth)

	BH3-12/18-SO-02		
	BROWN	BML	Difference*
PFBA	<0.434	<1.97	0%
PFPeA	<0.434	<0.984	0%
PFHxA	<0.434	<0. 984	0%
PFHpA	<0.434	<0. 984	0%
PFOA	<0.434	<0. 984	0%
PFNA	<0.434	<0. 984	0%
PFDA	<0.434	<0. 984	0%
PFUnA	<4.34	<0. 984	0%
PFDoA	<4.34	<0. 984	0%
PFTrDA	<4.34	<0. 984	0%
PFTeDA	<4.34	<1.97	0%
PFBS	<0.434	<0. 984	0%
PFPeS	<0.434	<1.97	0%
PFHxS	3.28	3.14	4.5%
PFOS	11.2	10.3	8.7%

*If both labs reported below their LOQs, or one lab reported below LOQ and the other reported a value below that LOQ, then 0% difference was recorded.

Table C.6 Confirmatory Analysis of Soil Samples (Borehole 4, 0-6” depth)

	BH4-0/6-SO-02		
	BROWN	BML	Difference*
PFBA	<0.437	<2.20	0%
PFPeA	<0.437	<1.10	0%
PFHxA	<0.437	<1.10	0%
PFHpA	<0.437	<1.10	0%
PFOA	<0.437	<1.10	0%
PFNA	0.498	<1.10	0%
PFDA	<0.437	<1.10	0%
PFUnA	<4.37	<1.10	0%
PFDoA	<4.37	<1.10	0%
PFTrDA	<4.37	<1.10	0%
PFTeDA	<4.37	<2.20	0%
PFBS	<0.437	<1.10	0%
PFPeS	<0.437	<2.20	0%
PFHxS	0.498	0.494 J	0.8%
PFOS	3.04	3.45	-11.9%

*If both labs reported below their LOQs, or one lab reported below LOQ and the other reported a value below that LOQ, then 0% difference was recorded.

J- Analyte detected below limit of quantitation

C.3.3 Analytical Confirmatory Analysis of Water Samples

Analytical confirmation with a NELAP-accredited laboratory was conducted on four water samples collected from effluent scrubber system and co-collected field blank at Eielson Air Base as part of an ESTCP-funded field project (ER20-5198). These samples were run in the Brown Lab on 10/11/2022. Mean concentration values should be within ±30% of confirmatory laboratory values when reported concentrations of analyte are greater than or equal to the limit of quantitation (LOQ) for both laboratories. Comparison of data for 26 PFAS are shown in the Tables 7 through 10 below indicate that the concentrations of 95% (95 out 100 PFAS in four samples) reported by the Brown lab were all within ±30% of confirmatory laboratory (BML) values. The five outliers are highlighted in yellow below, and include PFPeA, PFOSA, PFHxS and 8:2 FTS in sample LP1 and PFPeA in sample LP1-2. Four out of 5 of these samples were at relatively low concentrations. For example, PFHpS in sample LP-1 was reported by BML as 9.38 ng/L, while Brown reported a concentration of 13.0 ng/L.

Table C.7 Confirmatory Analysis of Water Scrubber Samples (LP1)

Analyte	BML LP1 1020 2021	BROWN LP1 1020 2021	Difference*
LOQ	4.96	2.00	
PFBA	<4.96	<2.00	0.0%
PFPeA	13.1	7.05	46.2%
PFHxA	42.1	33.4	20.7%
PFHpA	6.32	5.51	12.8%
PFOA	22.2	20.6	-7.2%
PFNA	<4.96	<2.00	0.0%
PFDA	<4.96	<2.00	0.0%
PFUnA	<4.96	<2.00	0.0%
PFDoA	<4.96	<2.00	0.0%
PFTrDA	<4.96	<2.00	0.0%
PFTeDA	<4.96	<2.00	0.0%
NMeFOSAA	<4.96	<2.00	0.0%
NEtFOSAA	<4.96	<2.00	0.0%
PFOSA	117	28.5	75.6%
PFBS	<4.96	<2.00	0.0%
PFPeS	<4.96	<2.00	0.0%
PFHxS	9.38	13.0	38.6%
PFHpS	<4.96	<2.00	0.0%
PFOS	<4.96	<2.00	0.0%
PFNS	<4.96	<2.00	0.0%
PFDS	<4.96	<2.00	0.0%
4:2FTS	<4.96	<2.00	0.0%
6:2FTS	45.2	54.7	21.0%
8:2FTS	13.6	6.21	54.3%
HFPO-DA	<4.96	<2.00	0.0%
Adona	<4.96	<2.00	0.0%

*If both labs reported below their LOQs, or one lab reported below LOQ and the other reported a value below that LOQ, then 0% difference was recorded.

Table C.8 Confirmatory Analysis of Water Scrubber Samples (Field Blank)

Analyte	BML Field Blank 1026 2021	BROWN Field Blank 1026 2021	Difference*
LOQ	3.98	2.00	
PFBA	<3.98	<2.00	0.0%
PFPeA	<3.98	<2.00	0.0%
PFHxA	<3.98	<2.00	0.0%
PFHpA	<3.98	< 2.00	0.0%
PFOA	<3.98	<2.00	0.0%
PFNA	<3.98	<2.00	0.0%
PFDA	<3.98	<2.00	0.0%
PFUnA	<3.98	<2.00	0.0%
PFDoA	<3.98	<2.00	0.0%
PFTrDA	<3.98	< 2.00	0.0%
PFTeDA	<3.98	<2.00	0.0%
NMeFOSAA	<3.98	<2.00	0.0%
NEtFOSAA	<3.98	2.11	0.0%
PFOSA	<3.98	<2.00	0.0%
PFBS	<3.98	<2.00	0.0%
PFPeS	<3.98	< 2.00	0.0%
PFHxS	<3.98	<2.00	0.0%
PFHpS	<3.98	<2.00	0.0%
PFOS	<3.98	<2.00	0.0%
PFNS	<3.98	<2.00	0.0%
PFDS	<3.98	< 2.00	0.0%
4:2FTS	<3.98	< 2.00	0.0%
6:2FTS	<3.98	<2.00	0.0%
8:2FTS	<3.98	<2.00	0.0%
HFPO-DA	<3.98	<2.00	0.0%
Adona	<3.98	<2.00	0.0%

*If both labs reported below their LOQs, or one lab reported below LOQ and the other reported a value below that LOQ, then 0% difference was recorded.

Table C.9 Confirmatory Analysis of Water Scrubber Samples (LP2)

Analyte	BML LP2 1026 2021	BROWN LP2 1026 2021	Difference*
LOQ	4.36	2.00	
PFBA	<4.36	<2.00	0.0%
PFPeA	<4.36	2.43	0.0%
PFHxA	<4.36	8.24	NC
PFHpA	<4.36	<2.00	0.0%
PFOA	<4.36	6.47	NC
PFNA	<4.36	<2.00	0.0%
PFDA	<4.36	<2.00	0.0%
PFUnA	<4.36	<2.00	0.0%
PFDoA	<4.36	<2.00	0.0%
PFTrDA	<4.36	<2.00	0.0%
PFTeDA	<4.36	<2.00	0.0%
NMeFOSAA	<4.36	<2.00	0.0%
NEtFOSAA	<4.36	<2.00	0.0%
PFOSA	<4.36	9.82	NC
PFBS	<4.36	<2.00	0.0%
PFPeS	<4.36	<2.00	0.0%
PFHxS	<4.36	<2.00	0.0%
PFHpS	<4.36	<2.00	0.0%
PFOS	<4.36	<2.00	0.0%
PFNS	<4.36	<2.00	0.0%
PFDS	<4.36	<2.00	0.0%
4:2FTS	<4.36	<2.00	0.0%
6:2FTS	<4.36	9.41	NC
8:2FTS	<4.36	2.51	0.0%
HFPO-DA	<4.36	<2.00	0.0%
Adona	<4.36	<2.00	0.0%

*If both labs reported below their LOQs, or one lab reported below LOQ and the other reported a value below that LOQ, then 0% difference is reported. When one lab was below LOQ and other lab reported a value, then no calculation "NC" is reported.

Table C.10 Confirmatory Analysis of Water Scrubber Samples (LP1)

Analyte	BML LP1 1101 2021	BROWN LP1 1101 2021	Difference*
LOQ	4.81	2.00	
PFBA	<4.81	3.19	0.0%
PFPeA	30.6	13.1	-57.2%
PFHxA	35.8	31.2	-12.8%
PFHpA	8.31	7.01	-15.6%
PFOA	18.4	20.0	8.7%
PFNA	<4.81	<2.00	0.0%
PFDA	<4.81	<2.00	0.0%
PFUnA	<4.81	<2.00	0.0%
PFDoA	<4.81	<2.00	0.0%
PFTrDA	<4.81	<2.00	0.0%
PFTeDA	<4.81	<2.00	0.0%
NMeFOSAA	<4.81	<2.00	0.0%
NEtFOSAA	<4.81	<2.00	0.0%
PFOSA	409	395	-3.4%
PFBS	<4.81	<2.00	0.0%
PFPeS	<4.81	<2.00	0.0%
PFHxS	<4.81	3.71	0.0%
PFHpS	<4.81	<2.00	0.0%
PFOS	<4.81	2.42	0.0%
PFNS	<4.81	<2.00	0.0%
PFDS	<4.81	<2.00	0.0%
4:2FTS	<4.81	<2.00	0.0%
6:2FTS	14.7	19.0	29.3%
8:2FTS	9.53	11.0	15.4%
HFPO-DA	<4.81	<2.00	0.0%
Adona	<4.81	<2.00	0.0%

*If both labs reported below their LOQs, or one lab reported below LOQ and the other reported a value below that LOQ, then 0% difference is reported.